Durham E-Theses

Influence of fluid pressure on the diagenesis of clastic sediments

STRICKER, STEPHAN

How to cite:

STRICKER, STEPHAN (2016) *Influence of fluid pressure on the diagenesis of clastic sediments* , Durham theses, Durham University. Available at Durham E-Theses Online: http://etheses.dur.ac.uk/11713/

Use policy

The full-text may be used and/or reproduced, and given to third parties in any format or medium, without prior permission or charge, for personal research or study, educational, or not-for-profit purposes provided that:

- a full bibliographic reference is made to the original source
- a link is made to the metadata record in Durham E-Theses
- the full-text is not changed in any way

The full-text must not be sold in any format or medium without the formal permission of the copyright holders.

Please consult the full Durham E-Theses policy for further details.

Academic Support Office, Durham University, University Office, Old Elvet, Durham DH1 3HP
e-mail: e-theses.admin@dur.ac.uk Tel: +44 0191 334 6107
http://etheses.dur.ac.uk

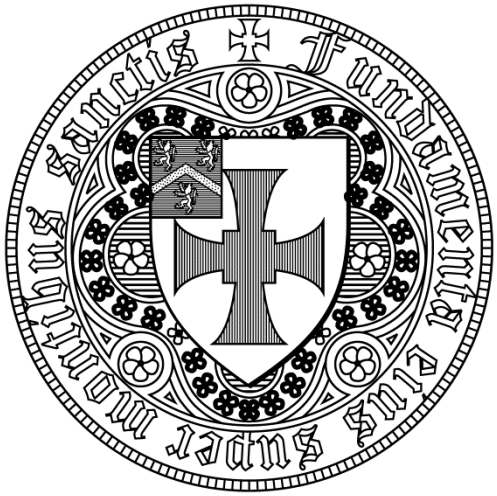

Influence of fluid pressure on the diagenesis of clastic sediments

Stephan Stricker

This thesis is submitted in partial fulfilment of the requirements for the degree of Doctor of Philosophy at Durham University

Department of Earth Sciences

University of Durham

2016

Abstract

As the exploration of hydrocarbon moves into more complex and deeper basinal settings the need to understand the effect of high pressures and high temperatures (HPHT) on reservoir quality and rock properties becomes more important. The complex fluvial sandstones of the Skagerrak Formation are the host for a number of HPHT reservoirs in the Central North Sea and exhibit anomalously high porosities and permeabilities considering their present-day depth of burial (>4500 m). The Skagerrak Formation reservoirs used in this study have encountered overpressures of >40 MPa and temperatures up to ~185°C at present-day maximum burial. This study has combined detailed petrographic analyses, core analysis and pressure history modelling to assess the impact of high pore fluid pressures (up to 80 MPa), differing vertical effective stress (VES) and authigenic clay mineral grain coatings on reservoir quality. It has been recognized that fluvial channel sandstones of the Skagerrak Formation in the UK sector have experienced, due to shallow onset and continuous maintenance of overpressure, significantly less mechanical compaction than their equivalents in the Norwegian sector. This difference in mechanical compaction has had a significant impact upon reservoir quality, even though the presence of chlorite grain coatings and the reduced VES inhibited extensive macroquartz cement overgrowths across all Skagerrak Formation reservoir sandstones. It is the combined effect of shallow overpressure onset, continuous overpressure maintenance and well-developed authigenic chlorite grain coatings which maintained anomalously high reservoir quality in the deeply buried HPHT reservoir sandstones of the Skagerrak Formation in the Central Graben, North Sea.

Contents

Declaration

I declare that this thesis, which I submit for the degree of Doctor of Philosophy at Durham University, is my own work, except where acknowledgement is made in the text, and not substantially the same as any work which has previously been submitted at this or any other university for any degree, diploma or other qualification.

June 2016

© Copyright, Stephan Stricker, 2016

The copyright of this thesis rests with the author. No quotation from it should be published in any form without the author's prior written consent. All information derived from this thesis must be acknowledged appropriately.

Acknowledgements

Many thanks to all the people who have supported me throughout my PhD and especially to my amazing supervisory team Stuart Jones, Neil Goulty and Andrew Aplin who have set up the GeoPOP3 project and helped me through this time. Firstly, I like to thank Stuart for being such a kind and helpful person. His door was always open and his support helped me not just to improve me as a researcher and scientist, it helped me growing as a person. His support is highly appreciated and became invaluable in my final year at Durham. Secondly, I like to thank Neil for being such a calm, knowledgeable and helpful person who got always great advice at hand. And last but not least, Andy for helpful scientific discussions and advice when needed. I also like to thank Neil Grant for his time and the great support during this project.

I also like to thank everyone from the Department of Earth Sciences for being great and making this a very enjoyable time. Special thanks to Shanvas Sathar, Jon Gluyas, Chris Saville, Sean O'Neil, Mark Brodie, and Peter Andras for providing great discussions and being very helpful. Furthermore, I like to thank Ian Chaplin for the preparation of hundreds of thin sections, Leon Bowen for his support and time at the scanning electron microscope, and Norman Oxtoby for the analysis of the fluid inclusions.

Finally, I would like to thank my wonderful wife, my family and all my friends for all the love and support they have given me throughout this time – I couldn't have done it without you.

So thank you all.

Chapter I

Introduction

1.1 Introduction

The inclusion of reservoir quality in pre-drill assessments is of paramount importance as hydrocarbon companies explore deeper targets. Exploration in deeply buried, high-pressure-high-temperature (HPHT; >69 MPa and >150 °C; Shadravan and Amani (2012)) reservoirs depends on identifying reservoir sandstones with sufficient porosity and permeability, especially where the reservoir has been exposed to elevated temperatures (>100 °C) by prolonged burial.

The reservoir quality of deeply buried sandstones is the combined product of depositional processes and subsequent diagenesis during progressive burial. Deposition controls the composition of the sand, including its grain size distribution which has an over-arching influence in determining siliciclastic reservoir properties. Relative porosity and permeability differences between sandstone facies are preserved during burial, so facies is a key factor in controlling reservoir performance (Chapter 6). Burial-related diagenesis also has an important role to play as it can destroy, preserve, or enhance the reservoir quality, whatever the facies (Chapter 4, 5 & 6).

In normally pressured reservoirs, sediments compact mechanically during burial as the vertical effective stress increases, so that the porosity is reduced. Mechanical compaction in sandstones has been reported to be dominant to burial depths of ~2000 m (>70-80°C) (Bjørlykke, 1999, 2014). The porosity loss in sandstones can generally be predicted to some degree of accuracy, giving rise to regional porosity-depth or porosity-temperature curves for many hydrocarbon basins (e.g., Ehrenberg et al., 2008). However, siliciclastic reservoirs with higher than expected porosity (i.e., regional porosity-depth or porosity-temperature curves) are common in several hydrocarbon basins, e.g., the Central Graben, North Sea, UK (Osborne and Swarbrick, 1999; Nguyen et al., 2013; Grant et al., 2014); the Gulf of Mexico, USA (Taylor et al., 2004;

Ehrenberg et al., 2008; Ajdukiewicz et al., 2010); the Santos Basin, Brazil (Anjos et al., 2003); and the Indus Basin, Pakistan (Berger et al., 2009). Their occurrence is commonly attributed to conditions that limit the degree of burial compaction and/or cementation, or to pre-existing cements and grain coatings (e.g., Bloch et al., 2002; Taylor et al., 2010, 2015; Nguyen et al., 2013).

Models for porosity preservation in deeply buried HPHT sandstone reservoirs tend to be focused on how clay (commonly chlorite) and microquartz detrital grain coatings can inhibit macroquartz cementation. There are many studies where deep reservoir porosity is linked to early diagenetic clay or microquartz grain coats (e.g., Pittman et al., 1992; Ehrenberg, 1993; Aase et al., 1996; Bloch et al., 2002; Ajdukiewicz and Lander, 2010; Ajdukiewicz and Larese, 2012; French et al., 2012; Worden et al., 2012; French and Worden, 2013). These studies have shown that quartz-rich sandstones with well-developed and continuous diagenetic clay or microquartz grain coats contain a much lower volume of quartz cementation than without such coatings (e.g., Berger et al., 2009; Ajdukiewicz and Lander, 2010) (Chapter 5).

Albeit controversial, early hydrocarbon emplacement in siliciclastic reservoirs may also play a crucial role in porosity preservation (Worden et al., 1998; Worden and Morad, 2000). Field-based (Marchand et al., 2002) and experimental (Sathar et al., 2012) studies have shown that quartz cementation is inhibited at high oil saturations. However, other studies (e.g., Saigal et al., 1992; Aase and Walderhaug, 2005; Molenaar et al., 2008) have suggested that there is no correlation between hydrocarbon emplacement and porosity preservation.

The role played by fluid overpressure in porosity preservation during the burial of sandstones has often been overlooked or considered less significant (e.g., Audet and McConnell, 1992; Gaarenstroom et al., 1993; Giles, 1997; Bloch et al., 2002; Taylor et

al., 2015). Increasing vertical effective stress (VES) caused by sediment loading is the major driver of mechanical compaction and porosity reduction during shallow burial. Pore fluid overpressure, defined as the excess pore pressure above the hydrostatic pressure for a given depth, reduces the effective stress acting on intergranular contacts and inhibits mechanical and chemical compaction (Osborne and Swarbrick, 1999) (Chapter 7). The shallow onset of pore fluid overpressure enhances porosity preservation, as noted for the Central North Sea (Nguyen et al., 2013; Grant et al., 2014) and the Gulf of Mexico (Sathar and Jones, 2016).

The primary focus of this thesis is the effect of HPHT reservoir conditions on porosity evolution in the deeply buried, siliciclastic reservoirs from the Skagerrak Formation in the Central Graben, North Sea. A multidisciplinary approach comprising petrographic, SEM, XRD, fluid inclusion, and burial history modelling studies has been adopted to investigate

- The inter-relationship between diagenesis and overpressure in siliciclastic reservoirs under HPHT conditions.
- The extent to which fluid pressure controls chemical compaction processes associated with other factors such as temperature and fluid composition.
- The effect of chlorite coatings on quartz cementation under HPHT conditions.

1.2 Methodology

A range of methods has been undertaken during the course of this research. The key methods used in this thesis are explained below.

1.2.1 Sampling

Core samples and thin sections examined in this study are from the Joanne and Judy Sandstone members of the Skagerrak Formation in the wider Central Graben area (see Chapter 3). The depth intervals have been chosen to cover the main reservoir unit and the core samples have been selected from the available core material as those expected to have the best reservoir quality (Appendix I). The focus on best reservoir quality has restricted the facies used in this study to ribbon sands, amalgamated ribbon sands, sheet sands and amalgamated sheet sands (Hirst, 1992; Gibling, 2006). The floodplain, playa and lacustrine facies, although part of the Skagerrak Formation, have not been the focus of this research.

1.2.2 Petrography

Core sample thin sections were used to measure optical porosity, grain size and fraction of clay-coated grains (Appendix I). Optical porosity was measured by using the digital image analysis technique, jPOR (Grove and Jerram, 2011), on blue epoxy-impregnated thin sections. Grain size distribution was analysed by using the Leica QWin (V. 3.5.0) software on thin section micrographs and the fraction of chlorite-coated grains were measured by point counting with 300 counts per thin section using a standard petrographic microscope (Leica DM2500P and DM750P) and point counting stage (PETROG – Conwy Valley Systems Limited). The resulting data (i.e., grain size and fraction of coated grains) were used to select samples for additional petrographic analysis, including intergranular volume (*IGV*) (Paxton et al., 2002), total cement

volume (*C*), porosity-loss by mechanical compaction (*COPL*) and porosity-loss by cementation (*CEPL*) (Lundegard, 1992) (Appendix I), conducted by point counting with 300 counts per thin section using a standard petrographic microscope (Leica DM2500P and DM750P) and point counting stage (PETROG - Conwy Valley Systems Limited).

1.2.3 Scanning electron microscope (SEM) and Energy-dispersive X-ray spectroscopy (SEM-EDS)

Selected thin sections were highly polished to 30μm and coated with carbon prior to analysis by a Hitachi SU-70 field emission gun scanning electron microscope (SEM) and equipped with an energy-dispersive detector (EDS). Scanning electron microscope analyses of thin section and bulk rock samples were conducted at 5 to 20kV acceleration voltage with beam currents of 1.0 and 0.6 nA, respectively. Point analyses had an average duration of 2 minutes, whereas line analyses were dependent on length. SEM-EDS was used for rapid identification of chemical species (i.e., chlorite Fe/Mg-ratio) and orientation on the sample. Cathodoluminescence analysis has been undertaken on selected thin sections with visible macroquartz overgrowths using a Gata MonoCL system with a panchromatic imaging mode operated at 8 kV.

1.2.4 Fluid inclusion analysis

Fluid inclusion analysis as part of the research was undertaken by Norman Oxtoby (Appendix III).

Microthermometry was conducted on double-polished detached wafers to determine the conditions of cementation and evidence for formation water salinity. Fragments were cut from double-polished rock wafers. The wafers were firstly checked under incident UV on a petrographic microscope to determine which contain petroleum inclusions and under transmitted light to determine the distribution of both aqueous and non-aqueous

fluid inclusions for subsequent analyses. A Linkam THM600/TS90 heating – cooling stage connected to a Nikon petrographic microscope was used to obtain temperature data. Instrumental precision is ± 0.1°C, while accuracy, dependent on the manufacturer's stated accuracy for the calibration standards used (synthetic inclusions and pure organic compounds), is better than ± 0.1°C, over the range of temperatures reported here. Routinely available measurements are homogenization temperatures (T_h) and final melting temperatures (T_m). Homogenization is the conversion of multiphase inclusion contents to a single phase, usually at temperatures above room temperature. Interpreting homogenization temperatures in carbonates, sulphates and halides can be complicated because aqueous inclusions can, though not necessarily do, reset to higher temperature if they are a) overheated beyond a threshold which is dependent on the mineral strength and inclusion geometry (Goldstein and Reynolds, 1994), or b) frozen. This can occur in the laboratory as well as through geological processes, so care is taken over the order in which analyses are made for each rock chip. If resetting has occurred, larger inclusions may give higher temperatures, homogenization temperature distributions may show a high temperature tail, and data from paragenetically distinct settings may overlap. Final melting occurs at the disappearance of the last trace of solid in the inclusion on heating, usually after cooling an inclusion to well below room temperature. If ice is the final phase to melt, as in the present study, salinities are calculated using the equation given by (Oakes et al., 1990).

1.2.5 XRD analysis

X-ray diffraction (XRD) analysis (bulk rock and clay fraction) was conducted by X-Ray Mineral Services Ltd (Appendix IV).

Selected bulk rock samples were de-oiled, disaggregated and powdered to a mean particle size between 5 and 10 μm for the XRD analysis. Samples were analysed by

using a Philips PW1730 Generator at 2Θ (theta) angles between 4.5˚ and 75˚, with a step size of 0.06˚ per second using X-ray radiation from a copper anode at 40 kV, 40 mA, equipped with a Philips PW1050 Goniometer with graphite monochromator and a PW1170 automatic sample changer. Identification of the minerals was achieved by using the X-ray Mineral Services Ltd in-house 'Traces' and 'Search-Match' software to compare the X-ray diffraction pattern with the International Centre for Diffraction Data PDF-4 Minerals database. The measured maximum intensity of each mineral was compared to the standard intensity of the pure mineral. The method does not take any amorphous content into account and the results were normalised to 100% based on the assumption that the whole mineral content accounted for the diffractogram.

Separation of the clay fraction (<2 μm fraction) samples was achieved by ultrasound and centrifugation of the suspension, with additional evaporation of the fluid content at 80˚C. The samples were analysed as untreated clay, after saturation with ethylene glycol vapour overnight and following heating at 380˚C for 2 hours, with further heating to 550˚C for one hour if required. The initial scan for these four treatments was performed with the same machine and at 2Θ angles between 3˚ and 35˚ with a step size of 0.05˚ per second using X-ray radiation from a copper anode at 40 kV, 40 mA. The untreated samples were also analysed between 24˚ and 27˚ 2Θ at a step size of 0.2˚ per 2 seconds to further define kaolinite/chlorite peaks. Interpretation was done by overlaying the four diffractograms to identify the clay mineral assemblages and to assess the effect of the treatment on the clay minerals. Peak intensities were measured and analysed to indicate the relative amounts of clay minerals present and have been referenced to the total amount of clay minerals present in the bulk rock analysis.

1.2.6 One-dimensional basin modelling

Pore pressure in the Skagerrak Formation sandstones was modelled in one dimension using Schlumberger's PetroMod (V. 2012.2) software. One-dimensional modelling provides a good insight into overpressure build-up by disequilibrium compaction and pore fluid expansion due to increasing temperature. However, the models do not include other mechanisms for generating excess pore pressure, such as fluid flow or hydrocarbon cracking, and are only able to take vertical stress into account. Any influence of clay mineral diagenesis on fluid pressure development is ignored. PetroMod is based on a forward modelling approach to calculate the geological evolution of a basin from the burial history. The burial history and lithology are inferred from the present-day well stratigraphy (Figure 3.2; Figure 3.3 & Figure 3.4), well log lithology and lithological description of the modelled units. We used the thermal upwelling basement palaeo-heat flow model of Allen and Allen (2005) with 63–110 mW/m^2 (average of 80 mW/m^2) during syn-rift phases and 37–66 mW/m^2 (average 50 mW/m^2) during post-rift phases combined with the palaeo-surface temperature history published by Swarbrick et al. (2000). The burial history models are calibrated against present-day RFT temperature measurements, corrected after Andrews-Speed et al. (1984), and measured Triassic sandstone porosities (Boyle's law), and carefully adjusted towards present-day RFT formation pressure measurements by considering late stage, high temperature overpressure mechanisms (Osborne and Swarbrick, 1997; Isaksen, 2004). The lithological unit types used in these models are mainly PetroMod (V. 2012.2) default lithology types, chosen on the basis of well log descriptions and core analysis reports for the investigated wells. Exceptions are the Hod lithology type present in the UK models and the lithology type of the Skagerrak sandstone members. The Hod chalk unit is modified to represent the North Sea non-reservoir chalk and

match the compaction trend and permeability trend (Table 5.3, Table 6.3 & Table 7.4) given by (Mallon and Swarbrick, 2002, 2008). The North Sea non-reservoir chalk is a laterally extensive low-permeability rock unit that represents the major vertical fluid flow barrier in the Central North Sea (Mallon and Swarbrick, 2008). The Triassic Skagerrak sandstone of the Joanne and Judy Sandstone members is simulated by a mixture of PetroMod (V. 2012.2) default lithologies (80% sand, 10% silt, 10% shale) combined with a regional compaction trend for shaly sandstone given by Sclater and Christie (1980). Assumptions used by Sclater and Christie (1980) are :

- All sedimentary sequences such as chalk, sandstone, clay and marl compact and dewater with burial, the only exception being salt.
- Porosity decays exponentially with depth in chalks, sandstones and clays, although the constants in the relationship differ because of the physical and chemical differences of the sediment matrix.
- Differences in compaction have been taken into account (corrected) when the sediments are ‘backstripped’.
- Only porosity data from normal/hydrostatic pressured sediments are taken into account for the porosity-depth relationship.

The porosity-depth trends for the Central North Sea by Sclater and Christie (1980) are widely used in industry.

1.3 Thesis outline

Chapters 2-8 are described individually below. The main data sections, chapters 4-7, have been written as standalone manuscripts and have all been submitted for publication in peer-reviewed international journals; these are recast and updated for the thesis where appropriate. As such, each chapter contains a specific introduction, background, discussion and conclusions. The background sections for each chapter represent a content-specific synopsis of the material in chapters 2 and 3, and may, therefore, be skipped at the reader's discretion. Co-authors for each manuscript provide scientific advice and discussion, appropriate editorial guidance, and content-specific data (i.e., fluid inclusion analysis conducted by Norman Oxtoby and X-ray diffraction analysis conducted by X-Ray Mineral Services Ltd). The thesis only contains manuscripts for which I am the first author, and I have been responsible for more than 90% of the primary data collection, interpretation and research manuscript writing.

1.3.1 Chapter II – Literature review

This chapter represents a summary of the present state of the literature regarding reservoir quality of siliciclastic reservoirs and discusses factors that control reservoir quality, such as clay mineral and microquartz coatings, the effect of oil emplacement, vertical effective stress, and the effect of pore fluid overpressure on the reservoir quality.

1.3.2 Chapter III - The geological context of the study area

This chapter presents a summary of the geology of the Central North Sea and Central Graben, with particular reference and focus on the Triassic succession, based on published references.

1.3.3 Chapter IV - Enhanced porosity preservation by pore fluid overpressure and chlorite coatings in the Triassic Skagerrak, Central Graben, North Sea, UK

This chapter is a comparison of the effects of pore fluid overpressure and chlorite grain coatings on reservoir quality in the Heron field (UK Quadrant 22) and the Judy field (UK Quadrant 30).

1.3.4 Chapter V - Exceptional reservoir quality in HPHT reservoir settings: Examples from the Skagerrak Formation of the Heron Cluster, North Sea, UK

This chapter focuses on the structural development of clay mineral coatings, the impact of clay mineral coatings on the reservoir quality, and the interrelationship of clay mineral coatings and quartz cementation in the HPHT reservoirs of the Heron Cluster, i.e., Egret, Heron and Skua (UK Quadrant 22).

1.3.5 Chapter VI - Reservoir quality of HPHT fluvial sandstone reservoirs in a salt-walled mini-basin, Seagull field, Central Graben, North Sea, UK

This chapter investigates the internal reservoir quality variations in minibasins by comparing two sample sets of the Seagull field. The focus is on the effect of contemporaneous salt movement on diagenesis and intra-basinal reservoir quality differences.

1.3.6 Chapter VII - Importance of vertical effective stress for reservoir quality in the Skagerrak Formation, Central Graben, North Sea

This chapter is a regional comparison of Skagerrak Formation sandstones from the wider Central Graben area, including the UK quadrants 22 and 30, and the Norwegian quadrants 6 and 7. The main focus is on the impact of shallow pore fluid overpressure development on maintaining porosity in the Skagerrak sandstones and the consequent enhancement of reservoir quality within them under their present-day HPHT conditions.

1.3.7 Chapter VIII - Discussion, conclusion, and future work

This chapter elaborates on the discussion sections from the preceding chapters with a more global perspective (e.g., HPHT basins: Gulf of Mexico, Malay Basin, and Taranaki Basin). Conclusions drawn throughout the body of the thesis are summarised. This chapter also reveals areas of future research that might develop the themes covered in this thesis.

Chapter II

Reservoir quality of sandstones: a review

2.1 Introduction

The reservoir quality of deeply buried sandstones is a cumulative product of depositional processes and subsequent diagenesis during shallow and deep burial. Deposition controls the composition of sands which has an over-arching influence on the development of the rock properties and the reservoir quality. Reservoir quality of sandstones is generally defined by the hydrocarbon storage capacity and the hydrocarbon deliverability. The hydrocarbon storage capacity of a reservoir depends on the effective porosity and the reservoir size, whereas the hydrocarbon deliverability is permeability-dependent. The development of porosity and permeability throughout time is strongly dependent on the burial-related diagenesis. Burial-related diagenesis can destroy, preserve, or enhance reservoir quality, whatever the depositional characteristics have been. Mechanical compaction at shallower depth (less than 2500 m) is known to decrease porosity (e.g., Bloch et al., 2002; Houseknecht, 1987; Paxton et al., 2002; Taylor et al., 2010) before chemical compaction, with pressure dissolution and mineral growth, takes over (e.g., Bjørlykke, 2014; Worden and Morad, 2003, 2000).

Pore fluid overpressure and low vertical effective stress are reported to decrease mechanical and chemical compaction throughout burial (e.g., Nguyen et al., 2013; Osborne and Swarbrick, 1999; Sathar and Jones, 2016; Sheldon et al., 2003), whereas clay mineral and microquartz coatings are known to reduce and inhibit quartz cementation (e.g., Pittman et al., 1992; Bloch et al., 2002; Ajdukiewicz and Lander, 2010; French et al., 2012). These processes have maintained anomalously high porosities and excellent reservoir quality in a number of hydrocarbon basins, e.g., the Central Graben, North Sea (Osborne and Swarbrick, 1999; Swarbrick et al., 2000; Nguyen et al., 2013; Grant et al., 2014); the Gulf of Mexico, USA (Taylor et al., 2004; Ehrenberg et al., 2008; Ajdukiewicz et al., 2010; Sathar and Jones, 2016); the Santos

Basin, Brazil (Anjos et al., 2003; Bahlis and De Ros, 2013); the Indus Basin, Pakistan (Berger et al., 2009).

This review chapter focusses on reservoir quality and the key factors that maintain high porosities in sandstones throughout burial, namely clay mineral coatings, microquartz coatings, the effect of oil emplacement, vertical effective stress, and the effect of pore fluid overpressure on reservoir diagenesis.

2.2 Reservoir quality controlling factors in siliciclastic rocks

Rock properties and reservoir quality are defined by depositional and diagenetic processes. The source area, the depositional environment and associated processes define through grain size, composition, sorting, sphericity, angularity, packing, and the abundance of matrix the initial rock properties, e.g., grain size and composition, initial porosity, and initial permeability. The rock properties develop by diagenetic processes involving mechanical compaction, cementation, dissolution, and recrystallization throughout the burial history. Diagenetic processes are widely controlled by the temperature, pore fluid chemistry, detrital grain composition, pore fluid pressure, and effective stress.

The main diagenetic processes that control reservoir quality are:

1. Near-surface diagenesis which includes chemical reactions with fresh groundwater or highly saline waters (evaporates) and may lead to early cementation or dissolution of cements, e.g., carbonates or halite, or the alteration of minerals, e.g., mica or feldspar.
2. Mechanical compaction, reducing the porosity by grain rotation and rearrangement into a tighter packing configuration, plastic deformation of ductile grains, and fracturing and crushing of brittle grains (e.g., Chuhan et al., 2002; Houseknecht,

1987; Paxton et al., 2002). Mechanical compaction is responsive to effective stress and increases with ongoing burial to a physical lower limit of compaction at around 2 km to 3 km burial depth (~25% intergranular volume; (Paxton et al., 2002)). Rocks containing mechanical labile grains such as clay clasts, altered rock fragments, or delicate fossils are more likely to experience significant porosity reductions through mechanical compaction compared to rocks made of ridged grains (i.e., quartz).

3. Chemical induced compaction including dissolution of minerals or amorphous material and precipitation of mineral cement. Through chemical diagenesis, the reservoir rock transforms towards a more stable thermodynamic equilibrium mineral assemblage with increasing temperatures. Chemical diagenesis is mainly driven by temperature, vertical effective stress and the pore fluid and mineral composition (Sheldon et al., 2003). Pressure dissolution (chemical compaction) is common at grain contacts in rocks made of rigid grains and generates tighter grain frameworks by moving the grain centres close together (Paxton et al. 2002). The rate of pressure dissolution is generally temperature-depended and increases with increasing temperature (Walderhaug, 1994a; Worden and Morad, 2000). The occurrence of clay minerals at grain contacts is also thought to be important: dissolution is enhanced or catalysed by mica and clay minerals at quartz grain contacts (Bjørkum, 1996).
4. The precipitation of authigenic cement (e.g., calcite or quartz cement) will strengthen the grain framework and infill the primary pore space (Paxton et al. 2002). Precipitation of quartz, calcite, dolomite, anhydrite, feldspar, kaolinite, smectite, illite and chlorite as authigenic cements is mainly controlled by fluid flow, pore fluid chemistry and the temperature, and usually reduces the reservoir quality

(e.g., Bloch et al., 2002). However, early precipitation of small amounts of mineral cements, e.g., quartz, calcite, dolomite, anhydrite, can also preserve porosity by strengthening the grain framework and preventing late stage compaction. Early precipitation of grain coatings, e.g., smectite, illite, chlorite, microquartz, can also preserve porosity by inhibit extensive quartz cementation (e.g., Jahren and Ramm, 2000; Worden and Morad, 2000; Bloch et al., 2002; Ajdukiewicz and Lander, 2010).

5. Dissolution of thermodynamically unstable minerals or cements driven by pore fluid chemistry, fluid flow and reservoir temperature may contribute significantly towards reservoir quality, but may also destabilise the grain framework.

2.3 Oil emplacement

2.3.1 Oil emplacement and control on diagenesis

Reservoir quality is modified during burial by various physical and chemical processes as a result of diagenesis. To evaluate the effect of oil emplacement on reservoir quality, the relationship between oil emplacement and diagenesis needs to be understood.

Early oil emplacement has been widely assumed to preserve reservoir quality in hydrocarbon reservoirs (e.g., Wilkinson and Haszeldine, 2011; Worden et al., 1998). However, other studies have provided evidence for cementation during and after oil emplacement in hydrocarbon reservoirs (e.g., Aase and Walderhaug, 2005; Molenaar et al., 2008; Saigal et al., 1992). The effect of oil emplacement on diagenesis has been investigated with various approaches and different datasets, such as cement volume trends in oil and water legs, oil inclusions in quartz cements, wettability and oil-water saturation, the effect on the supply and precipitation of solutes, and the effect on the transport of solutes in solution to understand the effect of oil emplacement on

diagenesis. Based on the observations of this datasets and approaches, two schools of thought have evolved regarding the effect of oil emplacement on diagenesis. These schools of thought can be broadly referred to as “oil-inhibits diagenesis” and “oil-does-not-inhibit-diagenesis”.

2.3.2 Cement volume trends in oil and water legs

Systematic studies on the relative distributions of diagenetic cements in the oil and water legs within an oil reservoir led to contrasting conclusions. Marchand et al. (2002) observed significant variations in the distributions of diagenetic quartz cement between the oil and water legs in a study of 103 samples from the deep water sandstone reservoirs of the Brae Formation, Miller field and Kingfisher field, North Sea, UK (Figure 2.1). They concluded that progressive oil filling inhibits diagenesis in oil reservoirs. Conversely, similar studies on the Cambrian reservoir sandstones from the Palaeozoic Baltic basin by Molenaar et al. (2008) found no significant variation in the distribution of porosity between the oil and water legs of the reservoir sandstones and concluded that oil emplacement does not necessarily result in preservation of primary porosity (Figure 2.2). Barclay et al. (2000) observed that the quartz cement volumes did not change significantly across the oil-water contact in the Magnus reservoir, North Sea, UK. Based on fluid inclusion, petrography and burial history modelling, Emery et al. (2016) ascribed the uniform distribution of quartz cement in oil and water legs in Magnus reservoir to synchronous oil emplacement and quartz cementation. Furthermore, these studies are inconclusive because the differences in quartz cement volumes were observed in different lithotypes within the same formation with different potential sources of cement and sites of precipitation (Worden and Morad, 2000). The timing of oil emplacement, the source of the cements and the duration of quartz cementation also play a major role in the distribution of quartz cements in oil reservoirs.

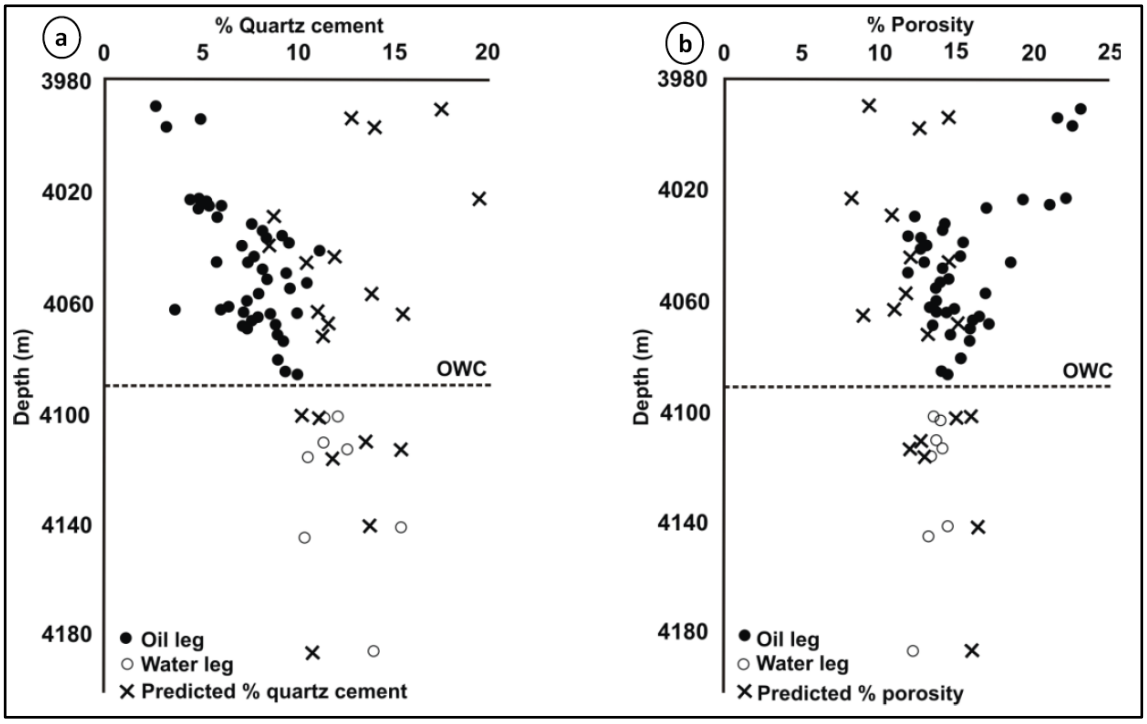

Figure 2.1 Variation of quartz cement and porosity distribution between the oil and water leg in the Miller field, UK sector, North Sea, from Marchand et al. (2002). Oil leg of the reservoir is marked with low quartz cement and high porosities thus supporting the view that oil emplacement inhibits diagenesis and preserves reservoir quality.

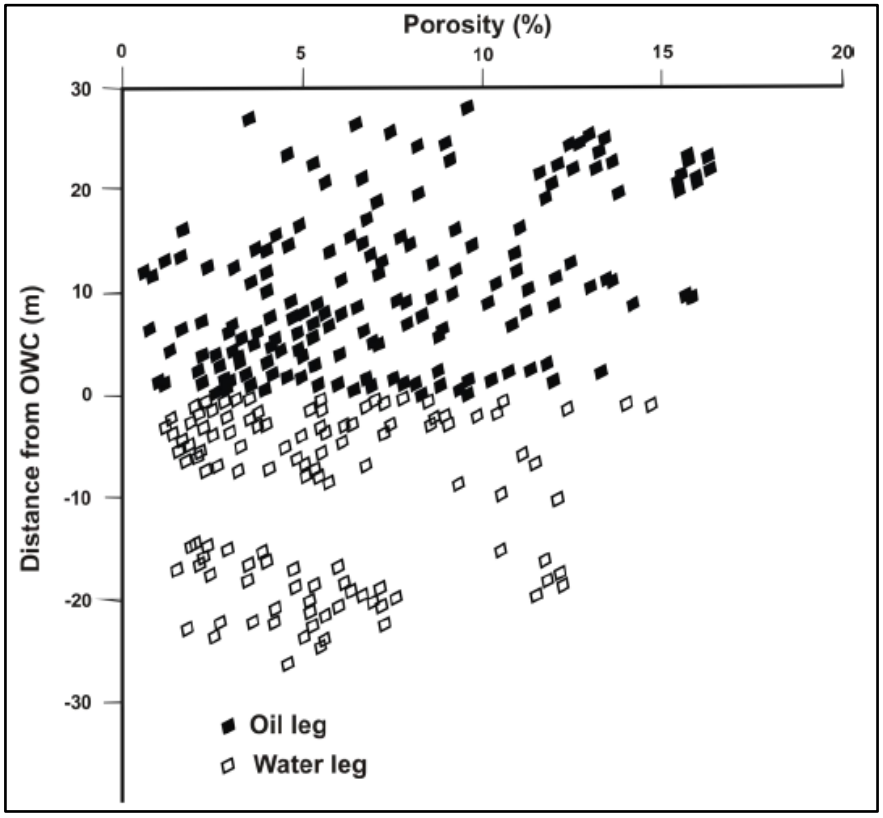

Figure 2.2 Porosity distribution in the Cambrian reservoir sandstones of the Kretinga oil field, Baltic basin, from Molenaar et al. (2008). No significant variation in porosity was observed between the oil leg and the water leg.

2.3.3 Oil inclusions in quartz cements

Oil inclusions within quartz cement have been used in numerous studies to understand the effect of oil emplacement on diagenesis (Walderhaug, 1990; Saigal et al., 1992; Gluyas et al., 1993; Oxtoby et al., 1995; Gluyas, 1997). Oil and aqueous fluid inclusions trapped between detrital quartz and euhedral quartz overgrowths have been studied to determine the homogenisation temperature of the different phases and components within the inclusions and the results have been correlated with the burial history of the rocks to estimate the reservoir-filling history. Walderhaug (1990) studied fluid inclusions from the oil leg of the Jurassic sandstones from the Haltenbanken area, offshore Norway, and observed that the homogenisation temperatures from fluid inclusions were similar to the present-day reservoir temperatures. From this similarity in temperature, it was concluded that quartz cement is ongoing in these reservoir rocks and oil emplacement did not inhibit diagenesis in the Haltenbanken area (Walderhaug, 1990). Moreover, Saigal et al. (1992) studied the Upper Jurassic sandstones from the Fulmar Formation, Central North Sea and observed lower volumes of quartz overgrowth and albitisation of K-feldspars in the oil leg compared to water leg of the same reservoir. The homogenisation temperatures of the fluid inclusions in both the oil leg and the water legs were estimated to be similar, in the range of 85°C to 125°C, and these observations led to the conclusion that quartz overgrowths can develop under high oil saturations and during oil emplacement (Saigal et al., 1992).

Worden and Morad (2000) have shown that the presence of primary oil inclusions in quartz cements cannot be unequivocally used to understand the cementation of sandstones at high oil saturation or during oil emplacement as the mechanism of formation of fluid inclusions in sandstones remains poorly understood. Aqueous films are generally absent in the oil inclusions present within quartz cements and thus the

mechanism of formation of oil inclusion in precipitated quartz cements remains controversial (Kvenvolden and Roedder, 1971). Moreover, the oil trapped inside the fluid inclusions is commonly of different composition and maturity (less mature) compared to the oil in the reservoir (Nedkvitne et al., 1993). Based on the above observations, it has been concluded that the majority of oil inclusions are formed during the initial stages of oil charging of the reservoir and sealed well before oil emplacement is complete (Larter and Aplin, 1995; Worden et al., 1998). It has been hypothesised that the irreducible water present within the pore spaces and grain contacts facilitated the cementation of the quartz cement which trapped the oil inclusions (Walderhaug, 1990).

2.3.4 Wettability and oil-saturation

Wettability refers to the degree of wetting of the system and is defined as the relative magnitude of the forces or affinities between the various liquid phases and the rock surfaces. It determines the tendency of a fluid to spread along the rock surface in the presence of another (immiscible) fluid (Crocker and Marchin, 1988; Drummond and Israelachvili, 2002). Different rocks exhibit different wettabilities as a function of rock and fluid type. Most reservoir rocks exhibit mixed wettabilities due to their mixture of minerals. In general, pure sandstones show water-wet to mixed-wet behaviour whereas carbonates tend to be oil-wet.

Studies on the effects of reservoir wettability by Barclay and Worden (2000) on quartz cementation in oil fields indicated that the wettability of the system has an enormous effect on the extent of the reduction of quartz cementation. In order for migrating oil to inhibit diagenesis, the grain surfaces are required to be entirely coated by oil to isolate the grains from aqueous fluids. This is easily achieved in oil-wet reservoirs, whereas in water-wet reservoirs diagenesis may resume unhindered during oil-filling (Figure 2.3).

Hence quartz cementation is likely to be inhibited sooner after oil-emplacement in an oil-wet reservoir compared to a water-wet reservoir.

With oil-filling, the formation water will be gradually expelled from the pore spaces. As a result of gradual oil filling, a gradational boundary commonly referred to as the oil-water contact (OWC) is formed between the oil-saturated interval and the water-saturated interval. A complete expulsion of water from a reservoir by oil filling never occurs. Thus, even under conditions of high oil saturation, a small amount of water referred to as the irreducible water (S_{wi}) is present adhering to the grain surface. The wettability of the reservoir rocks is strongly influenced by the S_{wi} values. The S_{wi} values in oil-wet reservoirs (0.1 to 0.15) tend to be lower than those in the water-wet reservoirs (0.2 to 0.25). Thus the effect of oil emplacement on diagenesis depends on the wettability state of the rocks and the nature of the reservoir fluids.

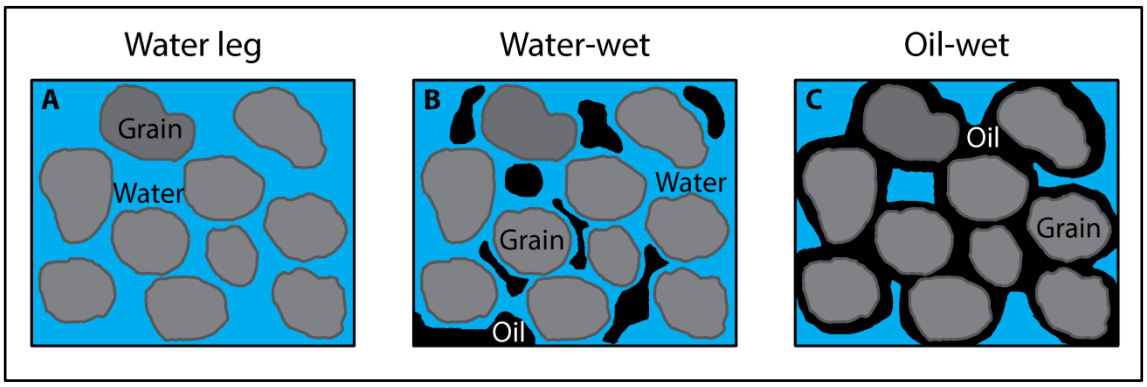

Figure 2.3 Cartoon showing the state of wettability in A) water leg of the reservoir, B) water-wet reservoir, and C) oil-wet reservoir. In the case of oil-wet reservoir, the aqueous fluids are isolated from being in contact with the mineral grains by a coat of oil and this prevents dissolution and precipitation of diagenetic cements.

2.3.5 Effect on the supply and precipitation of solutes

The presence of oil in the pore spaces can potentially influence the dissolution, diffusion/advection and precipitation of dissolved materials. The internal supply of silica for quartz cementation is likely to be severely affected as dissolution along grain

contacts will be severely affected due to oil emplacement. The degree to which dissolution is slowed down by oil emplacement is controlled by the wettability of the rocks (Barclay and Worden, 2000). In water-wet systems water is the medium of dissolution, i.e., water is in close proximity to the grain surface and dissolution is likely to proceed unhindered. However, in oil-wet systems the presence of oil around the grain surface impedes contact between the aqueous medium and the grain surface, which is expected to inhibit dissolution (Figure 2.3). In the case of a mixed-wettability system, overall dissolution is likely to be slowed down during oil emplacement (Worden and Morad, 2000).

Murphy et al. (1989) and Worden et al. (1998) studied the dependence of surface reaction rates (dissolution and precipitation) and diffusion on temperature and wettability states in the oil legs of sandstone reservoirs. Since quartz is generally water-wet in nature, the rates of dissolution and precipitation are unaffected. The diffusion rate is severely affected by the wettability of the reservoir. However, if the quartz grains are oil wet, then the rate of surface reactions are likely to be drastically reduced during oil emplacement.

The effect of oil emplacement on the rate of precipitation is governed by temperature, concentration of solute, and wettability of the rocks. If adequate temperature and concentration are achieved, the wettability of the system can play a major role in controlling the rate of precipitation. In the case of an oil-wet reservoir, oil coating the grain surfaces will block the access of dissolved solutes to the detrital grain surface. The reduced access for dissolved solutes to potential nucleation or precipitation sites is likely to result in reduced amounts of authigenic cements in the pores and thus will have a positive effect on reservoir quality preservation (Bloch et al., 2002). In the case of a

water-wet reservoir, precipitation is likely to proceed unhindered and the resulting effect on reservoir quality will be profound.

2.3.6 Effect on the transport of solutes in solution

The main process by which the dissolved solutes (silica and carbonates) are transported in reservoir rocks remains controversial (Worden et al., 1998). The dominant process of solute transport could be either advection involving large-scale fluid flow through rocks or diffusion involving small-scale fluid flow at pore scales. The rates of advection and diffusion of solutes is likely to be severely affected during oil emplacement as the pathways for advection and diffusion will become tortuous. Worden and Morad (2000) have shown the effect of evolving oil-water ratios and different wettability states on diffusion of silica in sandstone reservoirs (Figure 2.4). The silica diffusion is at least two orders of magnitude lower in the oil leg than in the water leg. Moreover, the magnitude of retardation in diffusion rate is amplified with increase in oil-wet behaviour.

2.3.7 Summary

The effect of oil emplacement on diagenesis remains a controversial topic amongst geoscientists. Observations and results both in favour of "oil inhibits diagenesis" and "oil does not inhibit diagenesis" have been reported from field based studies in various oil reservoirs and were therefore inconclusive. Theoretical and modelling studies have shown that the wettability of the system along with the degree of oil saturation can play a crucial role in slowing down the dissolution, diffusion and precipitation of solutes, thus inhibiting diagenesis.

However, hydrocarbon generation in the Central Graben area started at the end of the Cretaceous in the Upper Jurassic source rocks (Isaksen, 2004; Lines and Auld, 2004)

with hydrocarbon emplacement towards the mid-Miocene in the Skagerrak Formation reservoirs (Lines and Auld, 2004). Therefore, the hydrocarbon emplacement in the Skagerrak Formation occurred relatively late and hydrocarbon has played a less important role in porosity preservation and reservoir quality maintenance in the Skagerrak Formation than elsewhere.

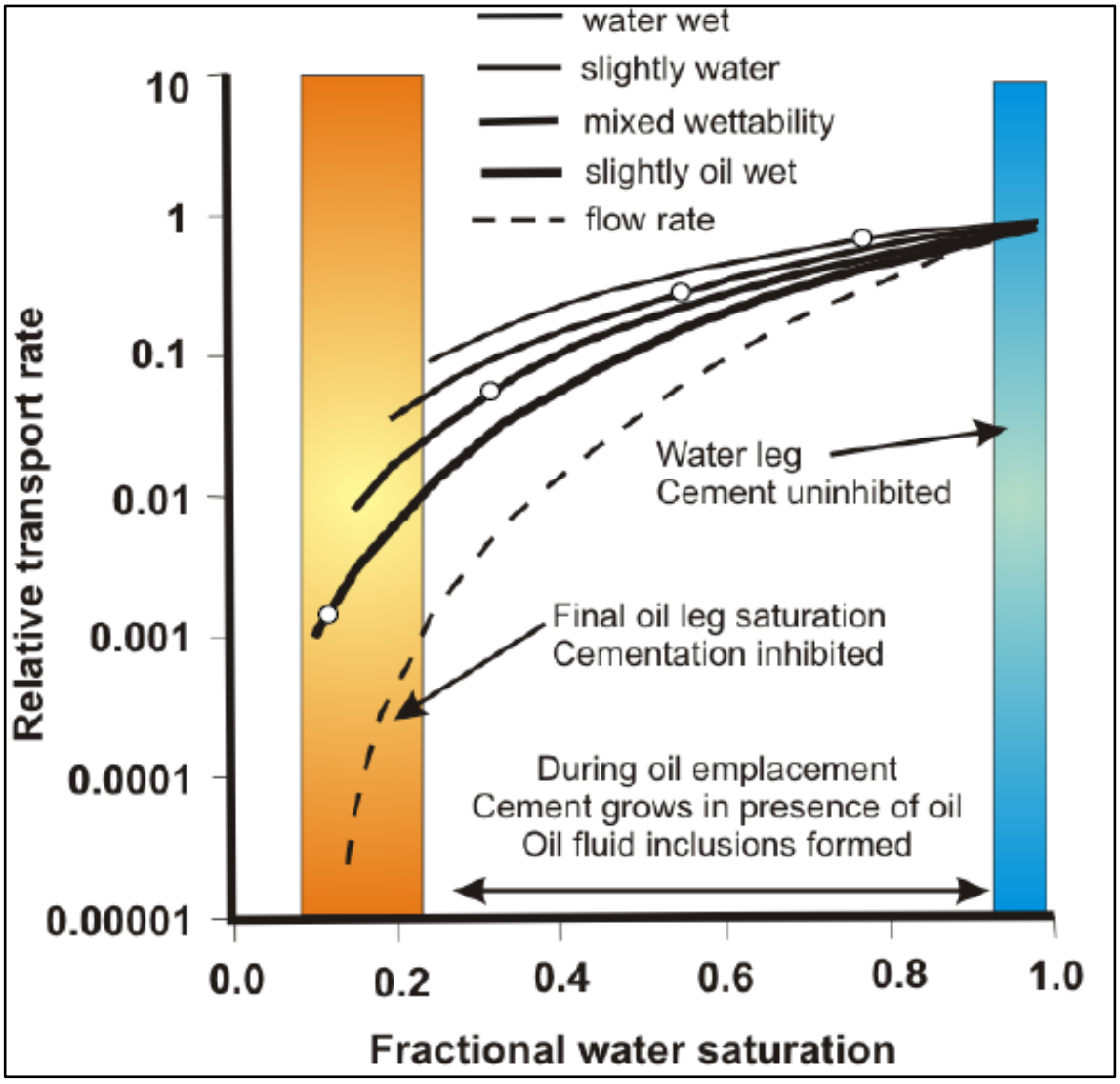

Figure 2.4 Effects of evolving oil-water ratios and different oil-water wettability states on diffusion of silica in sandstone reservoirs, from Worden and Morad (2000).

2.4 Clay mineral grain coatings and pore linings

2.4.1 Clay mineral coatings and control on reservoir quality

The presence of clay minerals can affect reservoir quality in siliciclastic reservoirs significantly. Clay mineral grain coatings are well known for their beneficial effect in inhibiting macroquartz cementation (e.g., Heald and Larese, 1974; Thomson, 1979; Pittman et al., 1992; Ehrenberg, 1993; Bloch et al., 2002; Anjos et al., 2003; Berger et al., 2009; Taylor et al., 2010, 2015; Ajdukiewicz and Larese, 2012; Bahlis and De Ros, 2013; Nguyen et al., 2013; Haile et al., 2015), but can also decrease reservoir quality by their pore filling nature (e.g., Dewers and Ortoleva, 1991; Worden and Morad, 2003; Morad et al., 2010; Taylor et al., 2010; Wilson et al., 2014). Absence of quartz cement is not exclusively related to clay mineral coatings (Heald and Larese 1974), but highest porosities are often documented where continuous and thick developed authigenic clay mineral coatings are present, regardless of coating mineralogy, origin and morphology (Pittman et al. 1992). Studies have shown that the completeness and thickness of clay coatings are the key for porosity maintenance in deeply buried sandstones (Bloch et al., 2002; Lander et al., 2008; Ajdukiewicz and Lander, 2010). However, clay mineral coatings associated with anomalous high porosity are mainly authigenic coatings of chlorite, illite, smectite-illite, smectite-chlorite or illite-chlorite in high temperature settings (Ajdukiewicz and Larese 2012).

The growth of authigenic clay mineral coatings has been subject of numerous laboratory experiments (e.g., Pittman et al., 1992; Aagaard et al., 2000; Ajdukiewicz and Larese, 2012; Haile et al., 2015). Growth experiments by Pittman et al. (1992) showed the importance of the coating root zones for the coating growth. The root zone represents the link between the authigenic coating and the detrital grain and is therefore important for the coating growth and the quartz inhabitation. The root zone is first to form and is

built by clay platelets oriented tangentially to the detrital grain surface. The root zone is generally hidden by superseding crystal structures (e.g., honeycomb), normally associated with authigenic clay coatings. Pittman et al. (1992) compared the growth of authigenic smectite coatings in hydrothermal reactor experiments to naturally grown coatings and observed a complete cover of the detrital grain by the root zones which provide an effective barrier against the nucleation of quartz overgrowth. Ajdukiewicz and Larese (2012) conducted similar hydrothermal reactor experiments at high temperatures (>120˚C) and observed abundant quartz overgrowth (i.e., microquartz) on detrital grain surfaces beneath the clay coatings. Ajdukiewicz and Larese (2012) interpreted this as evidence for a temperature dependence of the effectiveness of clay coatings. They proposed that clay coatings permit quartz nucleation of quartz at temperatures above 115˚C, but preserve porosity by limiting the quartz cement growth by their interconnected structure.

Detrital clay coatings on the other hand are commonly built from mechanically infiltrated clay (Matlack et al., 1989) and compared to authigenic coatings are less continuous and poorly developed, but commonly provide important precursors for authigenic clay mineral coatings (Matlack et al., 1989; Pittman et al., 1992; Bloch et al., 2002; Worden and Morad, 2003) (Figure 2.5). Infiltrated allogenic clay minerals are generally stable or metastable at surface conditions, but highly reactive in response to increasing temperature and pore fluid chemistry changes. Major changes in the clay mineral assemblage and the pore fluid chemistry occur during burial (Worden and Morad, 2003). Temperature is the main controlling factor for clay mineral transformation. Detrital clay minerals such as kaolinite, berthierine and smectite are replaced by authigenic high-temperature clay minerals such as dickite, illite and chlorite with increasing temperature (Figure 2.5) (Worden and Morad, 2003). Clay mineral

transformation is controlled by the temperature increase, the presence of reactants (e.g., K-feldspar) and the pore fluid chemistry.

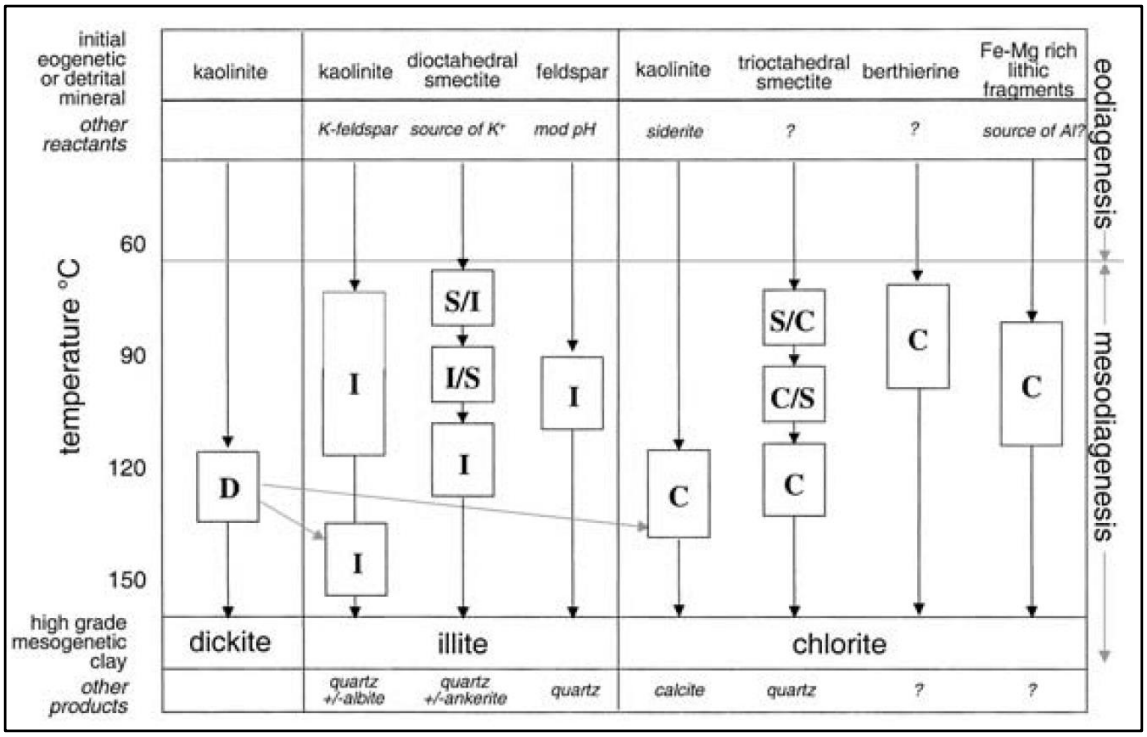

Figure 2.5 Common mesogenetic pathways for clay minerals in sandstones, where D is dickite, S is smectite, I is illite and C is chlorite, from Worden and Morad (2003). Randomly interstratified mixed-layer clay minerals are named according to the types of layers involved, with the most abundant layer type listed first: S/I is mixed-layer smectite–illite dominated by smectite; I/S is the same mineral mixture dominated by illite. The same naming rules apply for interlayered smectite–chlorite. High-grade diagenesis leads to dickite, illite and chlorite clay minerals in sandstones. Kaolinite forms predominantly during eodiagenesis and can be cannibalized to form dickite, illite or even chlorite during mesodiagenesis. Illite forms by at least three main routes during mesodiagenesis. Although it can be a detrital clay (following incomplete weathering) it does not form during eodiagenesis. Chlorite also seems to be unlikely to form during eodiagenesis and forms by at least four main pathways.

2.4.2 Smectite

Smectites are chemically complex clay minerals which have a poorly documented reservoir quality record. The occurrence of smectites in siliciclastic reservoirs is generally linked to shallow burial and low temperatures, due to their detrital or eogenetic nature. Nevertheless, smectite minerals play an important role as detrital grain coatings (Pittman et al., 1992) and represent a common precursor for authigenic, high-temperature clay minerals such as illite or chlorite.

Smectites are 2:1 (tetrahedral-octahedral-tetrahedral) layered silicates with $(0.5Ca,Na)_{0.7}(Al,Mg,Fe)_4(Si,Al)_8O_{20}(OH)_4 \times nH_2O$ as a general formula. Smectite minerals can expand structurally by binding water or organic molecules between their layers due to their cation exchange ability (Deer et al., 1992; McKinley et al., 2003; Worden and Morad, 2003). The smectite group is divided in two subgroups, the dioctahedral smectites and the trioctahedral smectites, of which the most common ones are montmorillonite and saponite, respectively (Deer et al., 1992). Dioctahedral smectites have two of the three sites in the three octahedral units occupied, due to the occupation of one octahedral site by cations such as Al^{3+} or Fe^{3+}. Trioctahedral smectites tend to have their octahedral units occupied by divalent cations such as Fe^{2+} or Mg^{2+} (Guven et al., 1980; Worden and Morad, 2003). Dioctahedral smectites tend to be Al-rich and trioctahedral smectites Mg-rich (McKinley et al., 2003).

Smectite minerals form mainly from weathered igneous material with dioctahedral smectites predominantly produced by weathering of acid and intermediate igneous material and silicic metamorphic rocks and trioctahedral smectites by weathering of more mafic and basaltic volcanics, volcaniclastics and metabasites (McKinley et al., 2003). Smectites can be emplaced in sandstones by mechanical infiltration or diagenetically by weathering and alteration of lithic fragments (e.g., volcanic fragments) during eodiagenesis. Smectite grain coatings are generally formed as clay particles oriented parallel to the grain surfaces, with curled edges (Matlack et al., 1989; Pittman et al., 1992; McKinley et al., 2003; Worden and Morad, 2003). Pittman et al. (1992) identified four growth or development stages for diagenetic smectite coatings in hydrothermal reactor experiments, similar to natural samples of authigenic smectite grain coatings (Figure 2.6 & Figure 2.7):

1. smectite wisps on the grain surface

2. smectite platelets, which form a root zone
3. an open polygonal boxwork
4. denser polygonal boxwork

The authigenic smectite coatings develop a flatly attached root zone on the detrital surface, covered by a less dense outer zone of well-developed smectite crystals leading to a dense and effective coating structure (Pittman et al., 1992; Worden and Morad, 2003). Low-temperature smectite coatings have commonly acted as precursor and nucleation grounds for authigenic high-temperature clay coatings (i.e., illite and chlorite).

The transformation of smectite to illite and/or chloritie is mainly controlled by temperature and the geochemical environment (i.e., pore fluid chemistry and reservoir mineralogy) (Figure 2.5) (McKinley et al., 2003; Worden and Morad, 2003). Smectites transform through mixed-layer stages of smectite/illite (S/I) and illite/smectite (I/S) or smectite/chlorite (S/C) and chlorite/smectite (C/S) to illite and/or chlorite (Figure 2.5) (McKinley et al., 2003; Worden and Morad, 2003; Morad et al., 2010). Dioctahedral smectites, richer in potassium, calcium or sodium, tend to transform into illite, whereas trioctahedral smectites, richer in magnesium and iron, tend to transform into chlorite (Figure 2.5) (Aagaard et al., 2000; Worden and Morad, 2000).

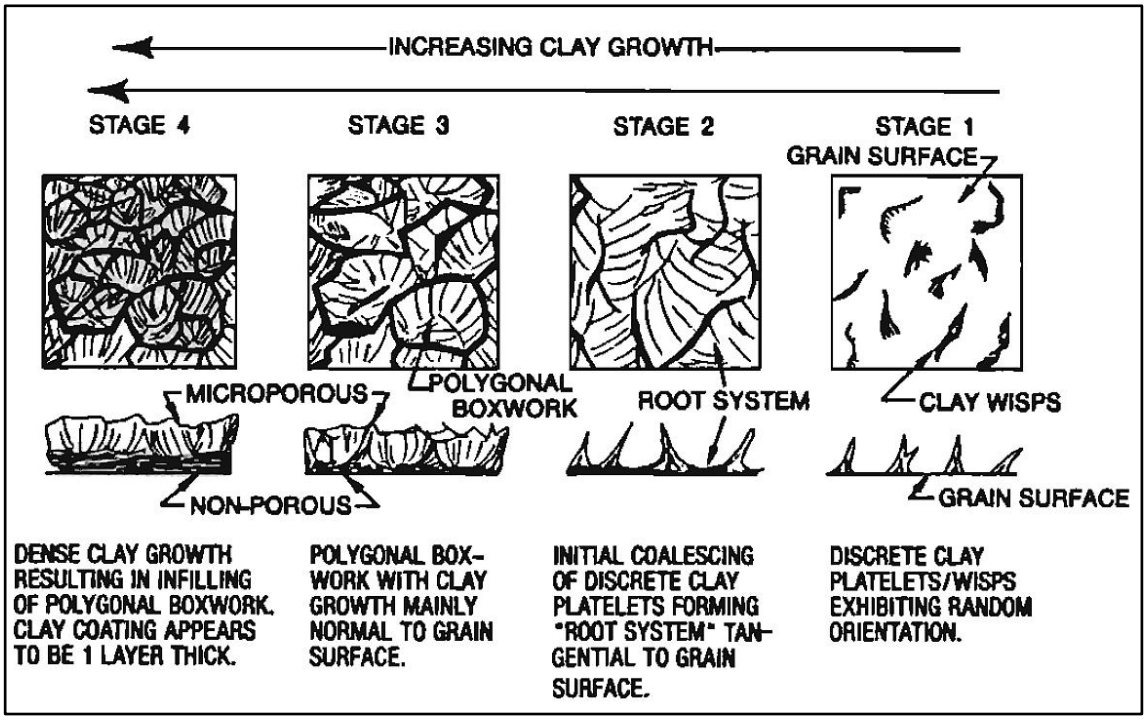

Figure 2.6 Schematic sketch of the four smectite growth stages from the hydrothermal reactor experiments, from Pittman et al. (1992)

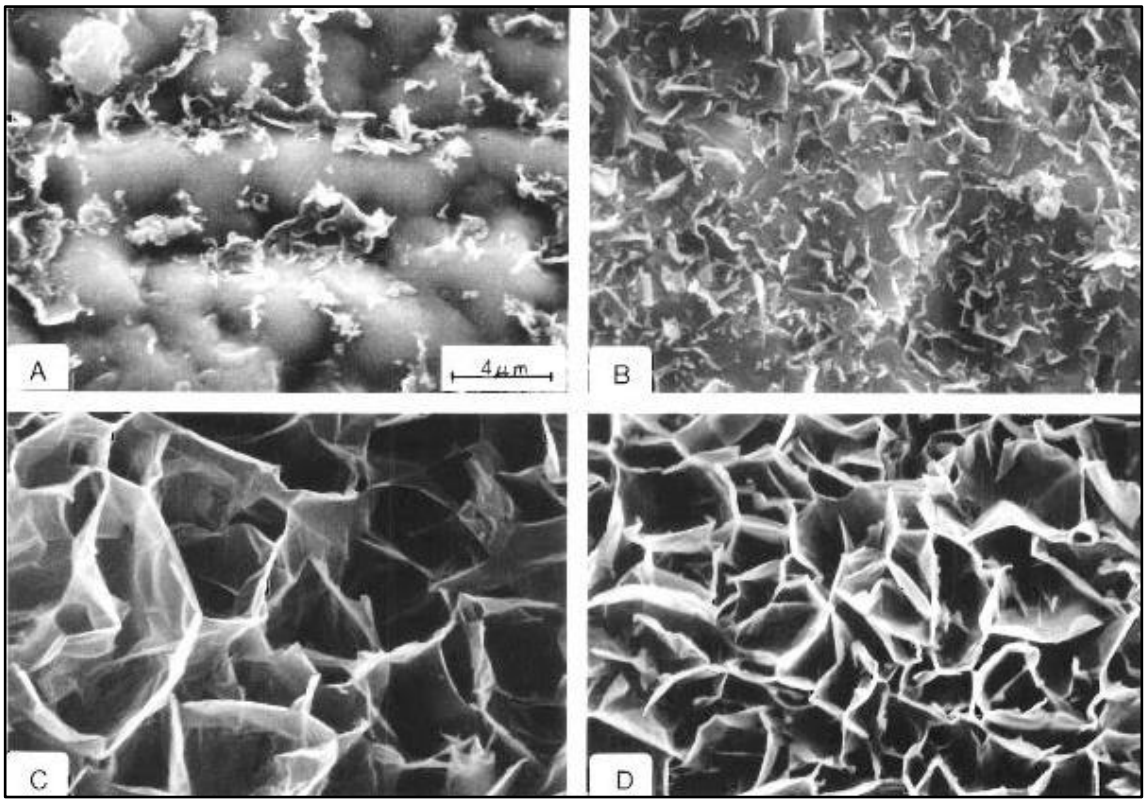

Figure 2.7 SEM images of the four growth stages of smectite coating development in reactor experiments, from Pittman et al. (1992).

2.4.3 Mixed-layer clay minerals

Mixed-layer clay minerals consist of interstratified layers of different clay mineral types in a single structure, commonly low- and high-temperature equivalents (Środoń, 1999). Mixed-layer clay minerals (i.e., smectite/illite, illite/smectite (allevardite), smectite/chlorite, chlorite/smectite (corrensite), illite/kaolinite, chlorite/kaolinite and dickite/kaolinite) represent intermediate stages of ongoing transformations between the low- and the high-temperature minerals (Worden and Morad, 2003). Mixed-layer clay mineral coatings can be present in siliciclastic reservoirs at high temperatures due to incomplete and ongoing transformation of the low-temperature clay mineral.

Mixed-layer high-temperature chlorite/illite is widely reported (e.g., Ajdukiewicz et al., 2010; Chen et al., 2011; Dixon et al., 1989; Humphreys et al., 1994; Storvoll et al., 2002) as the result of the interstratification of different mineral layers in a single structure. Chlorite/illite is commonly mainly chlorite interlayering with single illite crystals and rather less common as illite interlayering with single chlorite crystals (Ahn et al., 1988). Chlorite/illite has been interpreted as a result of the transformation of mixed dioctahedral-trioctahedral smectites, where illite replaces dioctahedral and chlorite trioctahedral smectites. Mixed high-temperature clay coatings are commonly reported, but usually represent minor amounts of the coating clay and are rather an intermediate product of the clay transformation process.

2.4.4 Chlorite

Chlorite is the most common and widely reported clay minerals regarding the issue of porosity preservation in reservoirs (e.g., Thomson, 1979; Ehrenberg, 1990, 1993; Billault et al., 2003; Berger et al., 2009; Ajdukiewicz et al., 2010; Bahlis and De Ros, 2013) (Table 2.1 & Figure 2.8). Authigenic chlorite is reported to form thick and continuous coatings on detrital grain surfaces (Figure 2.9B, C & E) and to inhibit nucleation and growth of quartz cement (e.g., Ajdukiewicz and Larese, 2012; Stricker et al., 2016b; Taylor et al., 2010).

Chlorite is a layered hydrous aluminosilicate with a three layer (tetrahedral-octahedral-tetrahedral) 2:1 type structure and is stable at high temperatures due to the interlayer filling of the positively charged octahedral sheet. The general formula is $(Mg,Fe^{2+},Fe^{3+},Mn,Al)_{12}[(Si,Al)_8O_{20}](OH)_{16}$ (Deer et al., 1992), but chlorite can be chemically very complex due to isomorphous substitution (Peng et al., 2009). The chlorite group can be subdivided into three major groups (Bayliss, 1975; Deer et al., 1992).

1. Fe-rich chlorites, e.g. chamosite
2. Mg-rich chlorites, e.g. clinochlore
3. Mn- rich chlorites, e.g. pennantite

with the Fe-rich and Mg-rich types as the most common ones.

Grain coating chlorite, mainly Fe-rich and Mg-rich chlorite, exists in two different mineralogical polytypes, the 1b polytype and the 2b polytype. Diagenetic Fe-rich chlorites (e.g. chamosite) are typically 1b polytypes and common as a lower temperature crystallization product. Mg-rich chlorites (e.g. clinochlore) are typically 2b polytypes mainly formed at higher temperatures (150°C - 200°C) (Hillier, 1994;

Worden and Morad, 2003; Peng et al., 2009). Chlorite coatings are reported to develop first as diagenetic 1b chlorites, which transform to a 2b polytype with increasing temperatures. The 1b to 2b transformation is reported to occur via recrystallization and replacement through polytype-mixtures (Hillier, 1994; Peng et al., 2009).

The origin of authigenic chlorite coatings in siliciclastic reservoirs is generally diagenetic and controlled by the clay mineral precursors, the mineralogical composition of the reservoir, the pore fluid chemistry and the temperature (Chen et al., 2011). Chlorite and chlorite coatings can develop by different transformation processes (chloritization), such as berthierine to chlorite, kaolinite to chlorite, odinite to chlorite and trioctahedral smectite to chlorite (Ehrenberg, 1993; Hillier, 1994; Aagaard et al., 2000; Worden and Morad, 2003; Morad et al., 2010; Taylor et al., 2010; Chen et al., 2011; Haile et al., 2015; Sathar 2015, *pers. com.*). Transformation of precursor Fe-rich clay minerals to chlorite commonly occurs at depths of 2-3 km and temperatures between 60-100°C (Ehrenberg, 1993; Aagaard et al., 2000; Worden and Morad, 2003). Berthierine and odinite are Fe-rich clay minerals, commonly occurring as early grain coatings, and evolve to Fe-rich chlorite (chamosite) upon burial (Hillier, 1994; Morad et al., 2010). Chlorite can also develop by solution and replacement from Fe-rich and Mg-rich lithic fragments, such as garnet, biotite, amphibole or volcanic rock fragments and glasses (Worden and Morad, 2003; Taylor et al., 2010).

Commonly reported chlorite precursors are detrital or eogenetic trioctahedral smectites (e.g., saponite) (Deer et al., 1992; Hillier, 1994; Humphreys et al., 1994; McKinley et al., 2003). Based on the Al/Si ratio of trioctahedral smectites, two transformation pathways are possible, with one requiring a source of aluminium and conservation of silica in the structure and the other requiring conservation of aluminium and release of silica from the structure (Worden and Morad, 2003). The transformation occurs

progressively through mixed-layer stages, starting with randomly distributed phases via more regular distributed phases to a 1:1 structure (corrensite) with increasing temperature (Worden and Morad, 2003; Chen et al., 2011). Chloritization is reported to be accompanied by a decrease of magnesium and increase of iron and aluminium, commonly resulting in iron-rich chlorite. However, Mg-rich chlorite is also common and is proposed to form in association with Mg-rich brines or from Mg-rich smectite precursors (Gaupp et al., 1993; Hillier, 1994). The chloritization of smectite may lead to quartz and carbonate precipitation by the release of silica, calcium, sodium and magnesium (McKinley et al., 2003; Worden and Morad, 2003).

Chlorite coatings tend to line or coat the interface between detrital quartz grains and the pore space, and thereby minimize the accessible detrital quartz surfaces for quartz cement nucleation. The effectivity of chlorite coatings usually increases with increasing surface coverage and thickness (Ajdukiewicz and Lander, 2010). Well-developed chlorite coatings show generally a two layered structure (Billault et al., 2003), with an inner layer or root zone (sensus Pittman et al., 1992) and an outer layer. The root zone is in direct contact with the detrital grain and consists of amorphous to poorly-developed chlorite crystals. The outer layer usually consists of well-developed crystals, covering the root zone. The outer layer of Fe-rich chlorite coatings consists commonly of euhedral, randomly interconnected crystals oriented perpendicular or sub-perpendicular to the grain surface. Crystals in the outer layer of Mg-rich coatings are typically more anhedral and characterized by a honeycomb or boxwork crystal orientation (Hillier, 1994; Haile et al., 2015). The crystal arrangement creates significant microporosity in the chlorite coating structure between the single chlorite crystals (Figure 2.9A, D & F). This microporosity is negligible in terms of the effective reservoir porosity, but

represents an excellent pathway for chemical reactants alongside the detrital grains (Ajdukiewicz and Larese, 2012; Friis et al., 2014).

Ajdukiewicz and Larese (2012) conducted high-temperature reactor experiments with chlorite-coated quartz sands and observed significant amounts of microquartz below the chlorite grain coatings. They also observed similar microquartz cement in deeply buried natural samples and concluded that chlorite coatings inhibit the nucleation of quartz cementation at temperatures up to 115°C, but allow nucleation between chlorite crystals above 115°C. The observations of Ajdukiewicz and Larese (2012) are supported by studies of the Panyu low-uplift sandstones from the Pearl River Mouth Basin (Chen et al., 2011), the Tuscaloosa Sandstone (Pittman et al., 1992), and by nanopetrographic investigations of chlorite coatings (Billault et al., 2003). Ajdukiewicz and Larese (2012) also observed that nucleated quartz crystals or microquartz have been blocked by the interconnected crystal structure of the outer chlorite coating layer. Therefore, pore-filling quartz has been only observed at breaks or gaps in the coating (Figure 2.9B).

The microporosity is also important for the development of chlorite coatings and the coating growth after oil emplacement (Friis et al., 2014). Friis et al. (2014) observed growth of chlorite coatings after oil emplacement in Paleocene sandstones in the Faroe-Shetland Basin, and related the growth to diffusion though the water-wet microporosity. The ongoing development of chlorite crystals has also been observed by Hillier (1994), who found that individual chlorite crystals grow with increasing temperature. He observed an increase in crystal thickness (c-axis) with temperature, after subjecting chlorite samples to temperatures between 90°C and 220°C. The increase in thickness of chlorite crystals closes and tightens the coating structure (Figure 2.9F), providing a better blocking mechanisms for quartz crystal growth at temperatures above 115°C (Ajdukiewicz and Larese, 2012).

Country	Location	Formation	Formation Age	Publication	Coating Clay	Burial Depth	Porosity		Temperature
							Average	Maximum	
[-]	[-]	[-]	[-]	[-]	[-]	[m]	[%]	[%]	[°C]
Brazil	Santos Basin	Itajaí-Açu Formation	Upper Cretaceous	(Anjos et al., 2003)	Fe-Chlorite	4000 - 5000	20	-	-
				(Bahlis and De Ros, 2013)	Fe-Chlorite	4030 - 5123	22	29	-
China	Pearl River Mouth Basin	Panyu low-uplift		(Chen et al., 2011)	Fe-Chlorite	3224 - 3242	19	21	130
	Sichuan Basin, Western China	Xujiahe Formation	Upper Triassic	(Sun et al., 2014)	Chlorite	4500 - 5000	8	12	-
Indonesia	North Sumatra Back-Arc Basin	Keutapang Formation	Miocene	(Humphreys et al., 1994)	Fe-Chlorite	950 - 1850	-	-	-
Pakistan	Middle Indus Basin	Goru Formation	Cretaceaous	(Berger et al., 2009)	Fe-Chlorite	3000 - 3500	16	25	175
Norway	Norwegian Continental Shelf, North Sea	Garn Formation	Middle Jurassic	(Ehrenberg, 1993)	Fe-Chlorite	~3500	20	25	-
		Tilje Formation	Lower Jurassic			3400 - 4300	17	32	-
		Tofte Formation				3800 - 4200	17	25	-
		Statfjord Formation	Upper Jurassic			~3000	20	30	-
UK	Central Graben, North Sea	Skagerrak Formation	Middle to Late Triassic	(Nguyen et al., 2013)	Mg-Chlorite	3400 - 5000	-	33.9	-
				(Taylor et al., 2015)	Chlorite	3400 - 4800	22	26.7	130 - 165
	Judd Subbasin, Faroe-Shetland Basin	Sullom Formation and Vaila Formation	Early to Middle Paleocene	(Friis et al., 2014)	Chlorite	3500 - 3600	-	-	-
USA	South Texas	Vicksburg Formation	Early Oligocene	(Grigsby, 2001)	Fe-Chlorite	3568 - 4099	30	-	-
	Louisiana	Woodbine/Tuscaloosa Formation	-	(Thomson, 1979)	Chlorite	6050 -6460	16	29	-
	Lower Mobile Bay, Alabama	Norphlet Formation	Upper Jurassic	(Dixon et al., 1989)	Chlorite/Illite	4500 - 7000	9 – 14.2	21 – 26.4	>180
				(Ajdukiewicz et al., 2010)	Chlorite/Illite	6126 - 6645	-	20	215

Table 2.1 Selection of siliciclastic reservoirs reported in the literature with chlorite coatings and anomalous high porosities, including country, location, formation, formation age, author, type of coating, burial depth, average porosity, maximum porosity, and temperature.

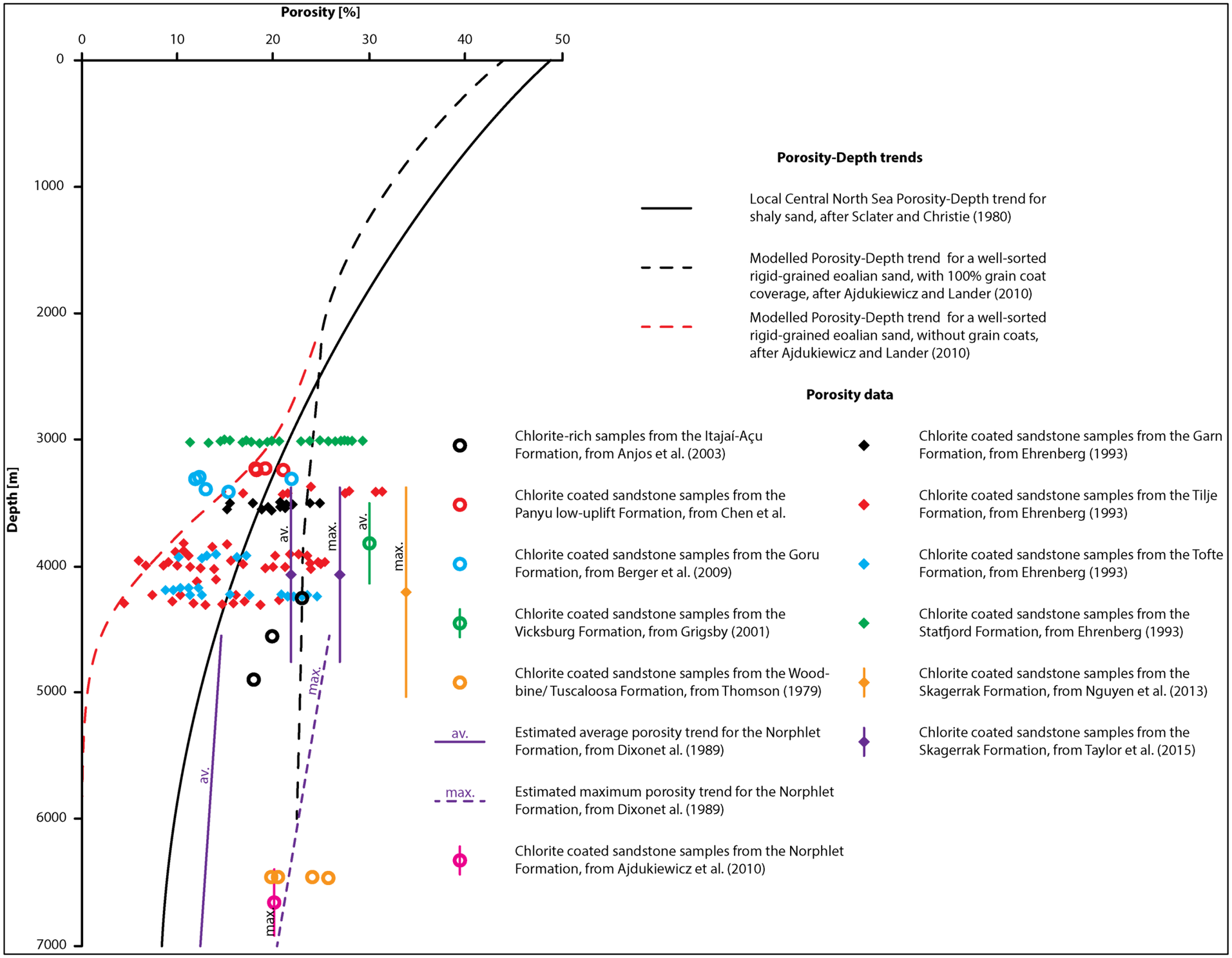

Figure 2.8 Porosity data or porosity trends reported in the literature with chlorite coatings and anomalous high porosities, with a local porosity-depth trend for shaly-sand after Sclater and Christie (1980), and two modelled porosity-depth trends (0% and 100% clay coating coverage) for well-sorted rigid-grain eolian sands, after Ajdukiewicz and Lander (2010).

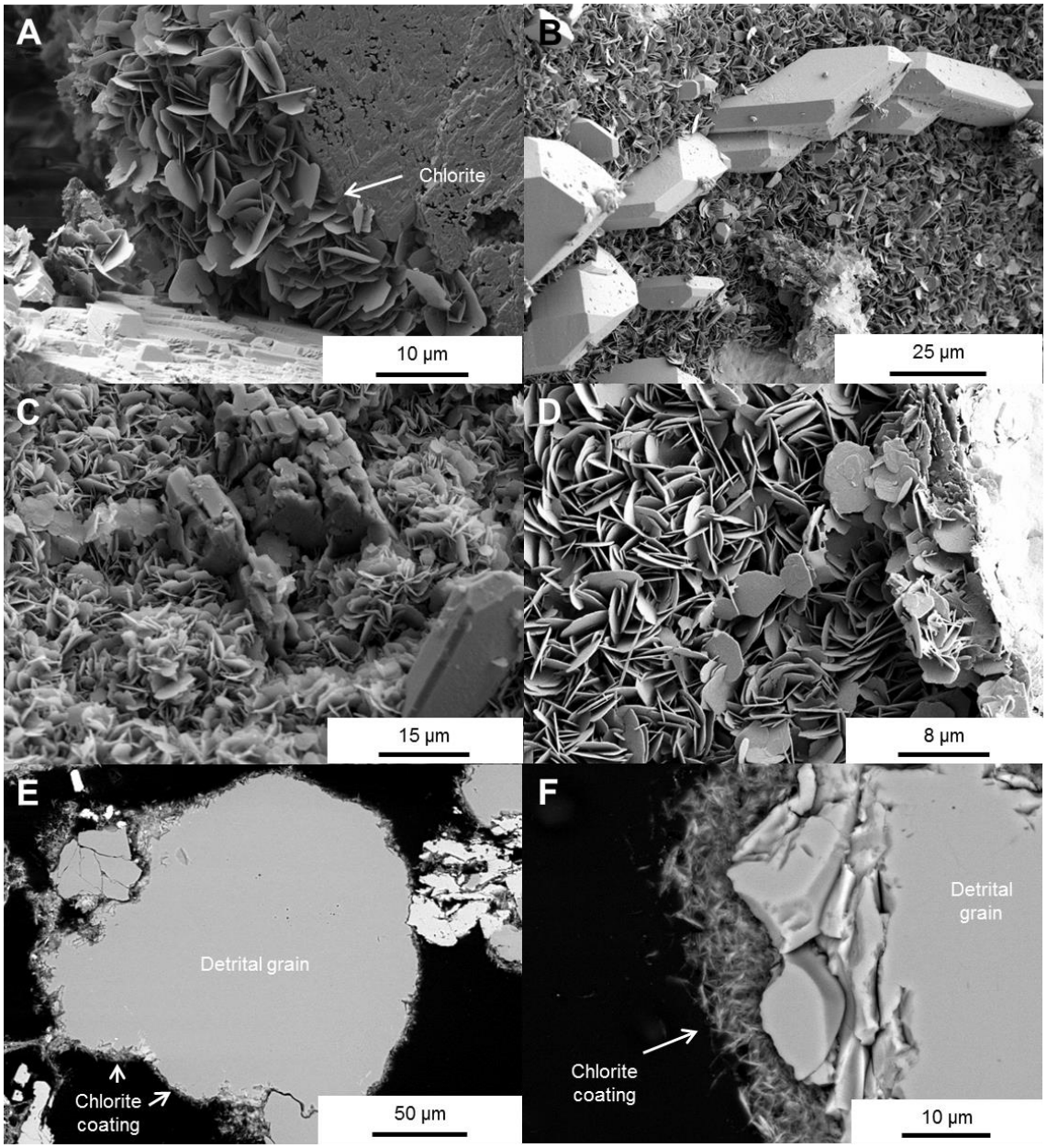

Figure 2.9 SEM images of A) well-developed chlorite platelets on a feldspar grain (Egret; 14997'2"); B) a grain coating chlorite with single quartz crystals growing at a coating break (Seagull 22/29-2; 13627'11"); C) a dense and well-developed chlorite grain coating with edge-to-face dominated pattern (Haile et al., 2015) (Heron; 15715'10"); D) rosette-like clusters in a chlorite grain coating (Seagull 22/29-2; 13627'11"); E) a detrital quartz grain with a well-developed and complete chlorite coating (Heron; 15714'7"); F) a cross section of a well-developed chlorite coating with crystals oriented randomly (Skua; 11939'3").

2.4.5 Illite

Illite is one of the most common diagenetic clay minerals in sandstone reservoirs (Heald and Larese, 1974; Guven et al., 1980; Kantorowicz, 1990; Pittman et al., 1992; Gaupp et al., 1993; Lanson et al., 1996; Storvoll et al., 2002) where it tends to coat detrital grains. Grain coating illite is known to be double-edged for reservoir quality. Illite can inhibit extensive quartz cementation, but its fibrous structure also decreases permeability significantly (Figure 2.10A, B, C & E) (Kantorowicz, 1990).

Illite is a mainly dioctahedral, rarely trioctahedral layered sheet silicate. The general formula is $K_{1.5\text{-}1.0}Al_4[Si_{6.5\text{-}7.0}Al_{1.5\text{-}1.0}O_{20}](OH)_4$ (Deer et al., 1992) with an octahedral layer sandwiched by two inward-pointing tetrahedral layers (2:1 layer structure). The origin of diagenetic illite and illite coatings is controlled by many factors, such as general rock material, pore fluid chemistry, precursor clays or coatings and the temperature. Several precursors and pathways are known for the development of illite, e.g. kaolinite to illite, dickite to illite, muscovite to illite, k-feldspar to illite and dioctahedral smectite to illite (Storvoll et al., 2002; Worden and Morad, 2003). The transformation processes or illitization of lower temperature clay minerals, e.g., smectite or kaolinite has been the subject of various studies (e.g., Abercrombie et al., 1994; Altaner and Ylagan, 1997; Charpentier et al., 2003; McKinley et al., 2003; Worden and Morad, 2003).

The illitization of detrital or early diagenetic smectite coatings is a common process in siliciclastic reservoirs. The illitization of smectite normally starts at temperatures around 70°C with the gradual replacement of dioctahedral smectite layers (Abercrombie et al., 1994; Storvoll et al., 2002), but was also observed at very low temperatures of 50°C and high temperatures around 120°C for very slow or rapid burial conditions, respectively (Abercrombie et al., 1994). The illitization process occurs through

disordered layer pattern (low illite content) via regular 1:1 layered illite/smectite (allevardite) to illite with low or no smectite content (McKinley et al., 2003; Worden and Morad, 2003; Morad et al., 2010). Dioctahedral smectites have typically a low Al/Si ratio and contain calcium, iron and magnesium which provide two major transformation pathways. One conserves silica and requires a source of aluminium, while the other conserves aluminium and releases silica (Worden and Morad, 2000, 2003; McKinley et al., 2003). The illitization of dioctahedral smectite also requires a source of potassium and the release of calcium, magnesium and iron, which can lead to carbonate cementation in combination with bicarbonate (McKinley et al., 2003).

Kaolinite is a thin layered, eogenetic or detrital precursor clay mineral with a booklet-like, pseudohexagonal structure. Kaolinite is common in sandstones and transforms with increasing temperatures (70°C to 130°C) into its high-temperature equivalent, dickite with blocky pseudohexagonal crystals (Figure 2.5) (Worden and Morad, 2003). Illitization of kaolinite can start around 70°C (Worden and Morad, 2003), but has mostly been reported at higher temperatures of 120°C to 140°C (Lanson et al., 2002; Storvoll et al., 2002). The transformation of kaolinite to illite or dickite is mainly controlled by the geochemical environment, and dickite is less susceptible to illitization due to the better ordered structure (Figure 2.5) (Morad et al., 1994; Worden and Morad, 2000). The illitization of kaolinite and/or dickite is not beneficial in terms of reservoir quality due to the tendency of the illite to retain the pseudohexagonal form and the pore-filling character of kaolinite (Deer et al. 1992; Lanson et al. 2002; Storvoll et al. 2002). Furthermore, the illitization of kaolinite releases silica, and the transformation temperature is beyond the quartz precipitation temperature (Worden and Morad, 2003).

Illite grain coatings are generally thickly developed (Figure 2.10E): 6 to 8 µm (Storvoll et al., 2002); 5 to 20 µm (Gaupp et al., 1993); 20 to 50 µm with microcrystalline quartz

intergrowth (Ajdukiewicz and Larese, 2012), and show a fibrous (Figure 2.10A, B & D) or flaky structure (Figure 2.10C). Illite grain coatings are commonly associated with the absence of quartz cement and are reported to inhibit extensive quartz cementation due to their grain coating nature. The illite coatings commonly grow from a root zone of flatly attached crystals, which is in direct contact with the detrital grain surface (Figure 2.10D). This root zone is essential for the inhibition of quartz cement overgrowth because it stops the nucleation of quartz cement on the detrital quartz surface. Without the root zone, quartz crystals can nucleate between the fibres of the grain coating at the detrital quartz surface and will outgrow and grow over the coating. The intergrowth of illite and quartz cement is possible due to the open, fibrous or flaky structure of the illite coating, which does not entirely seal the detrital surface. Quartz intergrowth at illite grain coatings has been observed by Kantorowicz (1990) in the Cormorant fields, North Sea, by Heald and Larese (1974) in the Tuscarora Sandstone, USA, and by Ajdukiewicz and Larese (2012) in reactor experiments. Grain coating illite is often described as flower-like (Figure 2.10C) and shows a tendency to bridge between grain surfaces, grow into the pore space, and block pore throats (Figure 2.10E), all of which significantly decrease the reservoir quality (Kantorowicz, 1990; Gaupp et al., 1993).

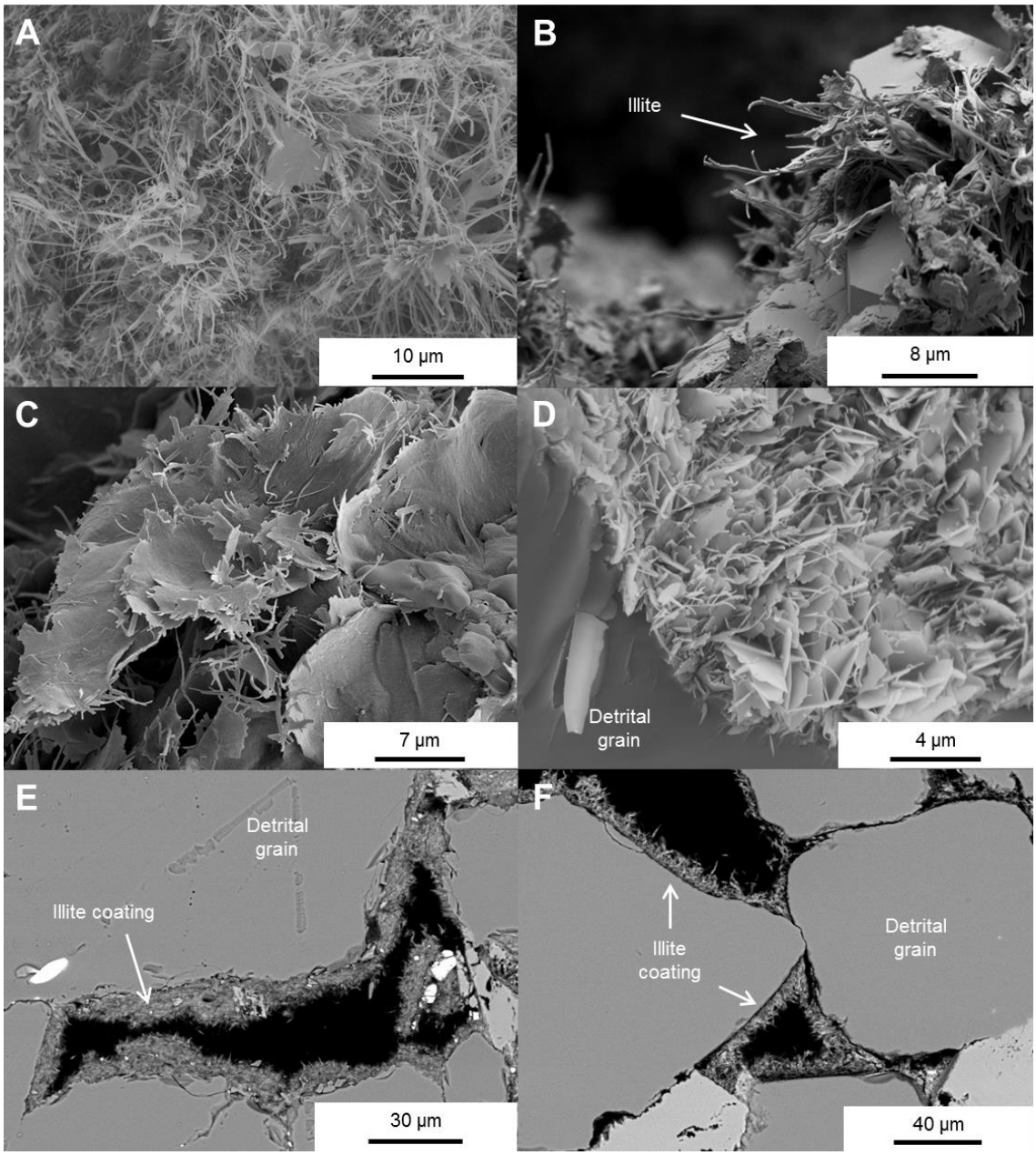

Figure 2.10 SEM images of A) fibrous and grain coating illite (Seagull 22/29-3; 13799'6"); B) long illite fibres filling pore space (Skua; 11971'1"); C) flaky illite in a flower-like or rosette-like structure (Seagull 22/29-2; 13880'3"); D) a cross section through fibrous illite coating a quartz grain (Seagull 22/29-3; 13799'6"); E) an illite-lined and infilled pore space (Seagull 22/29-3; 13910'0"); F) a cross section of illite-coated quartz grains (Egret; 14500').

2.5 Microquartz grain coatings

The occurrence of microcrystalline quartz coatings on detrital quartz grains has been identified as an effective mechanism for inhibiting the formation of pore-filling quartz overgrowths (e.g., Aase et al., 1996; French and Worden, 2013; French et al., 2012; Jahren and Ramm, 2000; Weibel et al., 2010). Microcrystalline quartz is difficult to detect in thin section using standard light microscopy due to the crystal size, but easily identified using standard scanning electron microscopy (SEM) (Figure 2.11). The term microquartz is here used for micro-sized quartz crystals, ranging from 1 to 10 μm in length, that are in optical continuity or discontinuity with detrital quartz grain (Aase et al., 1996; French and Worden, 2013).

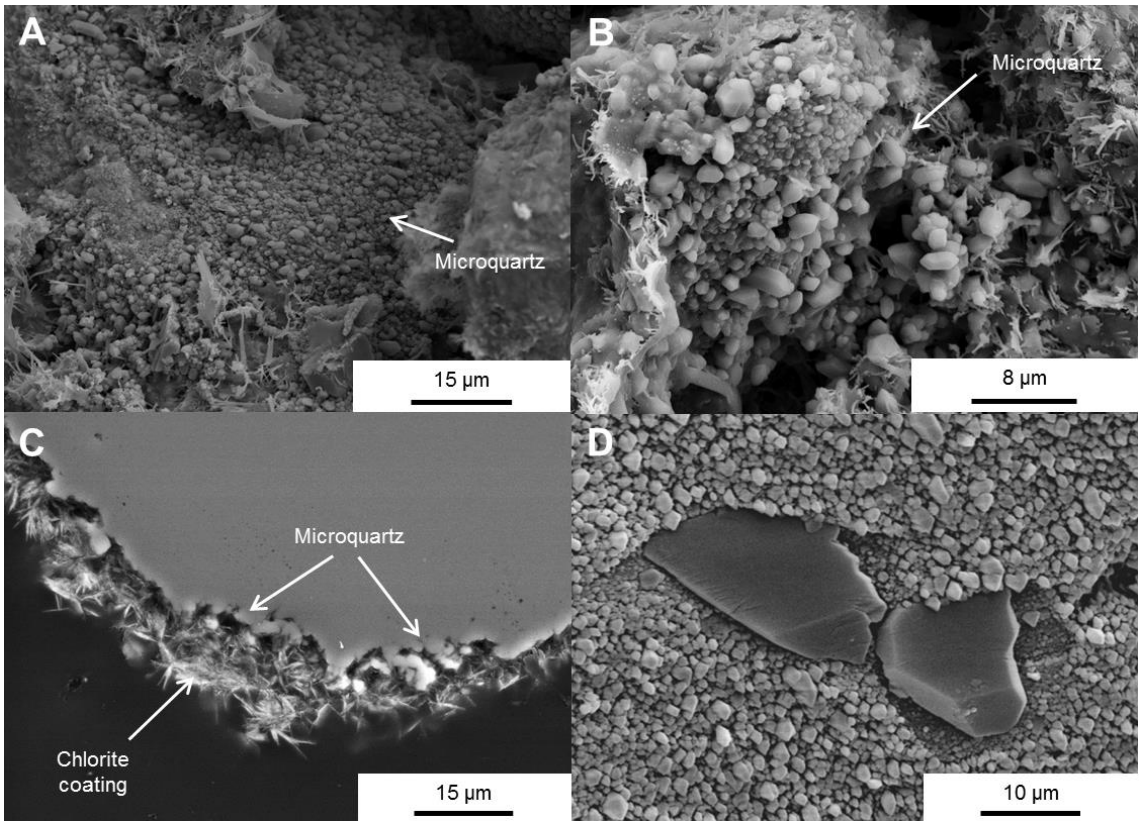

Figure 2.11 SEM images of A) microquartz coating from the Fulmar Formation (Elgin 22/30c-13; 6384.28); B) micro-sized quartz crystals on a detrital quartz grain (Elgin 22/30c-10; 5688.00); C) microquartz overgrowth below a chlorite grain coating (Heron; 15714'7"); D) microquartz coating from the Tyr Member

Microquartz in sandstones is typically derived from biologically derived silica (Vagle et al., 1994; Hendry and Trewin, 1995; Lima and De Ros, 2002) and occurs as fine coatings of crystallites on quartz grains. These fine and randomly oriented crystallites prevent the growth of ordinary macroquartz cement, which is optically continuous to the host grain (McBride, 1989; Vagle et al., 1994; Aase et al., 1996; Bloch et al., 2002; Lima and De Ros, 2002). Microquartz coats consist of a single layer or multiple layers of prismatic quartz crystals. Microquartz has been found in sandstones from regions as diverse as Brazil (Lima and De Ros, 2002), Colombia (Warren and Pulham, 2001), the United States (Haimson and Lee, 2004), the North Sea basins (Vagle et al., 1994; Hendry and Trewin, 1995; Aase et al., 1996; Ramm et al., 1997; Weibel et al., 2010) and North Africa (Goldstein and Rossi, 2002). Quartz cement grows generally in optical and crystallographic continuity with the host detrital quartz grain (McBride, 1989). In contrast, microquartz does not grow in optical continuity with the host quartz grain (e.g., French and Worden, 2013; Haddad et al., 2006; Hendry and Trewin, 1995; Worden et al., 2012), but rather grows as randomly oriented crystals <10 μm in length. Microquartz is commonly associated with sandstone beds rich in biogenic silica, such as sponge spicules (Hendry and Trewin, 1995; Aase et al., 1996), and seems to develop at the expense of bioclasts at temperatures of ~50°C (Vagle et al., 1994). Once detrital grains have a full coating of optically and crystallographically random oriented microquartz crystals, the overgrowth of optically and crystallographically continuous quartz cement is prevented as the random oriented microquartz crystals block each other in further growth. Therefore, early microquartz inhibits ordinary quartz cement growth, preserves porosity, and leads to anomalously high porosity in deeply buried petroleum sandstone reservoirs. It has been suggested that elevated silica saturation, resulting from the presence of microquartz, inhibits quartz dissolution during burial and prevents

quartz cementation (Hendry and Trewin, 1995), but until recently we have had no mechanistic data that explained why or how microquartz grows. Worden et al. (2012) provided the first mechanistic explanation on how microquartz grows and potentially maintains reservoir quality (Figure 2.12). The quality of the microquartz coatings seems to be a driver for determining porosity preservation, as with chlorite coatings of detrital quartz grains. If any breaks in the coating occur, the performance of the coating is compromised. However, as microquartz tends to precipitate rapidly from silica supersaturated solutions and often at lower temperatures than macroquartz cements, it provides an early method of porosity preservation during burial.

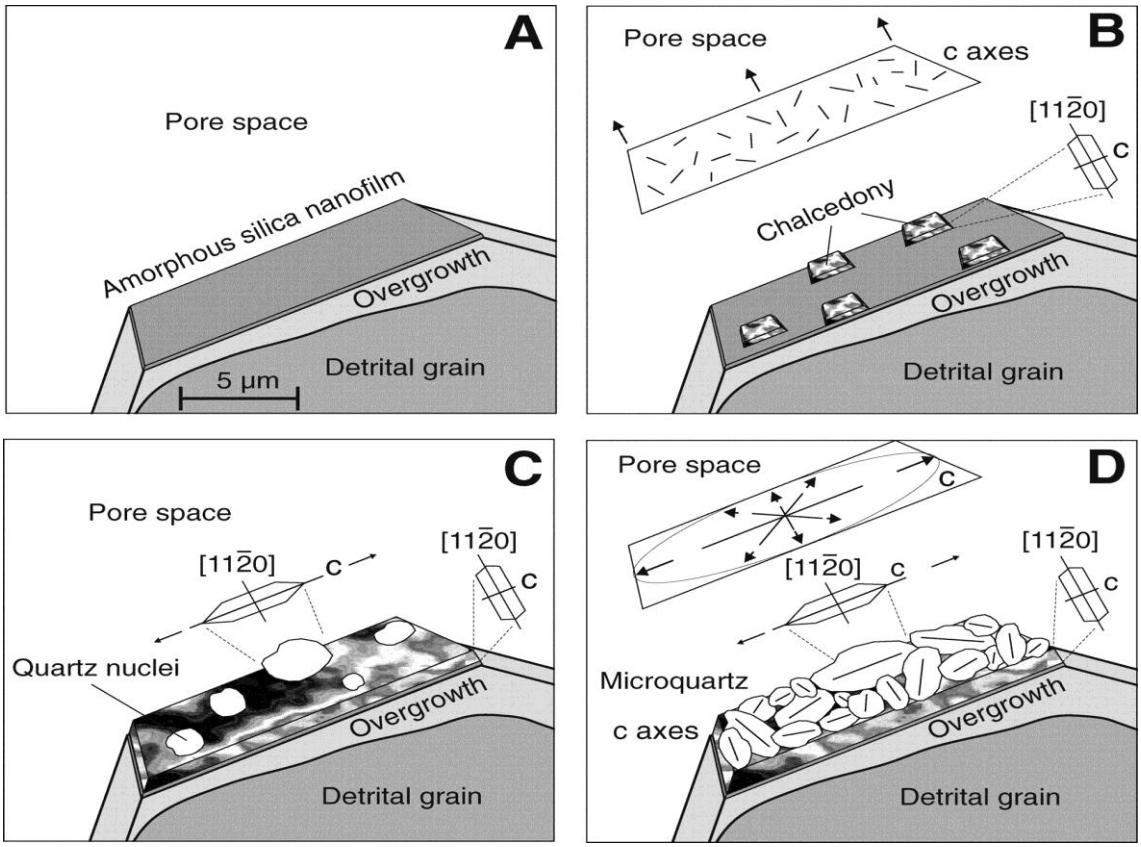

Figure 2.12 : Model showing microcrystalline quartz growing on amorphous silica nanofilms. A) During early diagenesis, pore-filling quartz overgrowths with the same crystallographic orientation as detrital grain form around detrital quartz sand grains. An amorphous silica nanofilm is deposited on overgrowth. B) Fibrous chalcedony crystals crystallize in the amorphous silica and grow into the pore space with their [1120] directions perpendicular to the local surface. The c-axes of the chalcedony crystals are always perpendicular to [1120] and are thus parallel to the detrital grain surface and randomly oriented within the nanofilm plane. C) Microcrystalline quartz nucleates on chalcedony-coated substrate and uses chalcedony crystal structure and orientation (c axis parallel to grain surface) as template. D) Microcrystalline quartz grows along the chalcedony crystal c-axis and parallel to the detrital grain surface (French et al., 2012; Worden et al., 2012)

2.6 Overpressure and vertical effective stress

2.6.1 Overpressure and its generation mechanisms

Pore fluid overpressure, sometimes termed geopressure, is common in subsurface rocks. Pore fluid overpressure is defined as the amount of pressure that exceeds the hydrostatic pressure at a specific depth (Figure 2.13). The hydrostatic pressure is the pressure that is exerted by a continuous column of static fluid, e.g. water or formation brine (Figure 2.13) (Osborne and Swarbrick, 1997). Overpressured pore fluids are generally common in closed or semi-closed geological systems where pore fluids are trapped and unable to drain (Jeans, 1994; Osborne and Swarbrick, 1997; Swarbrick and Osborne, 1998).

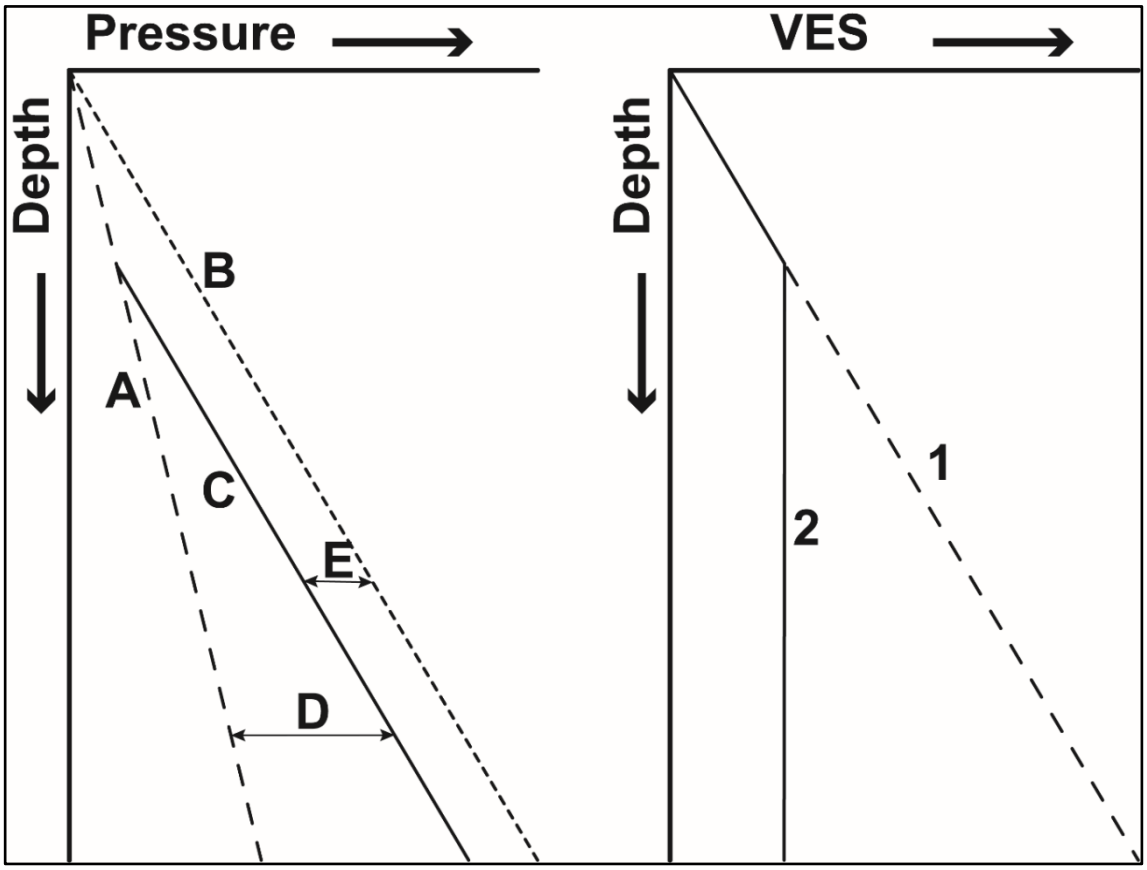

Figure 2.13 Fluid pressure scenarios shown as a function of depth, with the hydrostatic pressure (A), lithostatic stress (B), the pore pressure (C), the pore fluid pressure at a specific depth (D), the vertical effective stress (VES) at a specific depth (E), and equivalent vertical effective stress, with the hydrostatically pressured scenario (1) and the overpressured scenario (2).

Osborne and Swarbrick (1997) and Swarbrick and Osborne (1998) propose a wide variation of mechanims for the generation of pore fluid overpressure in sedimentary basins. The mechanisms are generally divided into three main categories:

1. Stress-related, (i.e., compression leading to pore volume reduction)

   Mechanisms:

   Disequilibrium compaction (vertical loading stress)

   Tectonic compression (lateral compressive stress)

2. Fluid volume increase

   Mechanisms:

   Temperature increase (aquathermal pressuring)

   Water release due to mineral diagenesis (e.g., smectite dehydration)

   Hydrocarbon generation

   Cracking of oil to gas

3. Fluid movement and buoyancy

   Mechanisms:

   Osmosis

   Hydraulic (potentiometric) head

   Buoyancy due to density contrasts

However, the contribution of some of the mechanisms towards overpressure is still poorly understood. Mineral transformation (e.g., smectite illitization or smectite dehydration) is generally assumed to have a minor impact on overpressure generation in sandstones due to small clay fractions and low volumes of water released, but may be of

significance in mudrocks. Aquathermal expansion is also considered to be less important (Figure 2.14). The volumetric expansion due to temperature rise is so small that highly impermeable seals would be required throughout geological timescales (Swarbrick et al., 2002). Disequilibrium compaction, however, is considered to be the most important overpressure generating mechanism in sedimentary basins at shallow depth, with gas generation, hydrocarbon buoyancy and pressure transfer at greater depths (Osborne and Swarbrick, 1997; Swarbrick et al., 2002).

The following paragraphs focus in detail on the key mechanisms thought to be important for the generation of pore fluid overpressure in the Triassic reservoirs of the Central North Sea (Swarbrick et al., 2000; Isaksen, 2004; Nguyen et al., 2013; Grant et al., 2014).

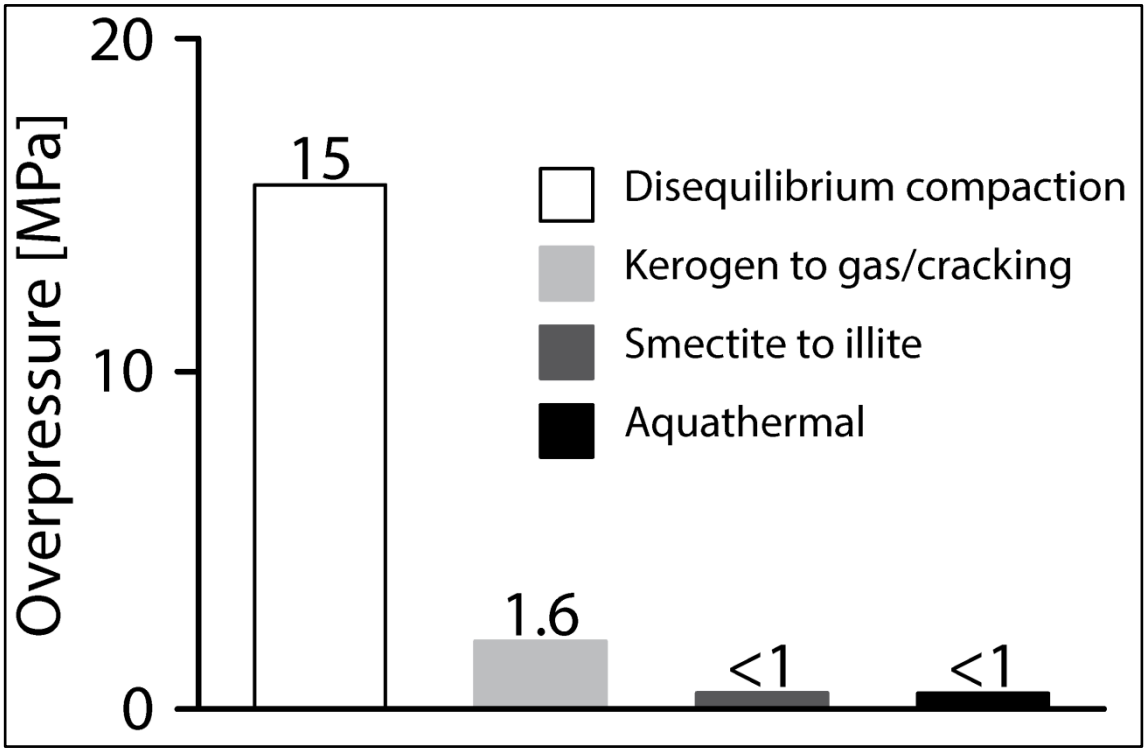

Figure 2.14 Comparison of overpressure magnitude for stress and volume expansion mechanisms of the north Carnarvon Basin, northwest Australia, showing the importance of disequilibrium compaction in relation to other overpressure generating mechanisms, after Swarbrick et al. (2002).

2.6.1.1 Disequilibrium compaction

Disequilibrium compaction in sediments is driven by overburden stress σ which is induced by vertical load due to the overlying sediments and can be described as:

$$\sigma = Z \times \rho_b \times g \qquad (2.1)$$

where Z is the thickness of the overburden, ρ_b is the average bulk density of the overburden and g is gravity. Some of the overburden stress, is borne by the fluid, with the pore pressure u and the remaining stress (vertical effective stress, σ') is born by the grain framework (grain-to-grain contacts) of the rock. The relationship between VES and overburden stress is given by Karl von Terzaghi's equation:

$$\sigma' = \sigma - u \qquad (2.2)$$

If the VES is small (high pore pressure), porosity values will also remain high, whereas if the VES increases porosity will decrease, the rock will compact and formation fluids will be forced out (William J. Plumley, 1980; Swarbrick and Osborne, 1998). Where the fluids cannot be expelled fast enough, the pore pressure rises above hydrostatic, i.e., overpressure is generated (Figure 2.13). This process is known as disequilibrium compaction.

Overpressure development by disequilibrium compaction is generated by insufficient drainage of the rock, which is common in fine-grained sediments (e.g., shales) or can be induced by stratigraphic isolation of permeable sediment packages due to surrounding sediments of low permeability or sealing faults. The initiation point of overpressure is known as the fluid isolation depth (intersection of hydrostatic gradient (A) and the formation pressure gradient (C) in Figure 2.13). If no fluid escapes the pore pressure would rise along a pressure-depth path parallel to the lithostatic gradient. However,

rocks are not entirely impermeable in reality, so some fluid will continue to be expelled, and the profile will be subparallel to the lithostatic gradient.

Disequilibrium compaction is the favoured mechanism to explain pore fluid overpressure at shallow depths (<2 – 3 km) in a number of basins, including the Gulf of Mexico (Hart et al., 1995; Audet, 1996; Burrus, 1998; Sathar and Jones, 2016), the Caspian Sea (Bredehoeft et al., 1988), the Nile Delta (Mann and Mackenzie, 1990), the Mahakam Delta (Burrus, 1998), and the North Sea (Audet and McConnell, 1992; Aplin et al., 2000; Swarbrick et al., 2000; Isaksen, 2004; Neumann, 2006; Nguyen et al., 2013). Disequilibrium compaction favours generally conditions of rapid burial and low permeability, and is therefore likely to be found in thick clay, mud, marl, and shale successions during continuous rapid burial (Osborne and Swarbrick, 1997; Burrus, 1998; Swarbrick et al., 2002).

2.6.1.2 Hydrocarbon generation and cracking to gas

The transformation of kerogen (solid) to liquid or gaseous hydrocarbon is kinetically controlled and dependent on a combination of time and temperature, and generally accompanied by volume increase (Meissner, 1978; Ungerer et al., 1981; Osborne and Swarbrick, 1997; Swarbrick et al., 2002). Maturation of kerogen occurs typically at depths of around 2000 m to 4000 m, and at temperatures in the range of 70°C to 120°C. Meissner (1978) studied the Bakken shale type II source rock in the Williston Basin, Montana and North Dakota, USA and observed a volume increase of 25% due to oil generation from kerogen, with a further increase when maturation proceeded to wet and later to dry gas. Swarbrick et al. (2002) analysed observations of Ungerer et al. (1981) on kerogen maturation, vitrinite reflectance, and volume changes, and concluded that gas generation rather than oil generation is responsible for significant volume increases.

This observation show that temperature/maturity of kerogen is the controlling factor on overpressure generation by hydrocarbon generation.

2.6.2 Vertical effective stress and reservoir quality

Reservoir quality of siliciclastic reservoirs is highly dependent on the vertical effective stress history undergone during burial. Primary or depositional porosity is first reduced by irreversible mechanical compaction processes, such as grain rotation, rearrangement, plastic deformation of ductile grains, fracturing and crushing of brittle grains (Houseknecht, 1987; Chuhan et al., 2002; Paxton et al., 2002). Vertical effective stress caused by sediment loading during burial is the major physical force driving mechanical compaction and the reduction of reservoir quality in siliciclastic reservoirs. Mechanical compaction is the dominant process during shallow burial and is responsible for porosity reduction from depositional values of around 45% (e.g., Beard and Weyl, 1973) to typical values between 25% and 32% prior to lithification (Houseknecht, 1987; Paxton et al., 2002; Taylor et al., 2010).

Only a small number of studies have tried to appraise the role of low vertical effective stress and pore fluid overpressure on reservoir quality and especially porosity maintenance (e.g., Ramm and Bjørlykke, 1994; Gluyas and Cade, 1997; Bloch et al., 2002; Taylor et al., 2010). Studies by Gluyas and Cade (1997) and Ramm and Bjørlykke (1994) developed algorithms based on empirical relationships between present-day porosity and present-day pore fluid overpressures. Gluyas and Cade (1997) derived an empirical relationship for overpressure and equivalent depth of poorly lithified to unlithified sandstones by using laboratory compaction experiments and field data. They developed an equation for the porosity loss as a function of effective stress and proposed that 1 MPa of overpressure offsets the increase in VES due to 80 m of

burial with hydrostatic pore pressure, so overpressure leads to less mechanical compaction and higher porosity in unlithified sands.

Overpressure initiation depth and evolution during burial are both critical to quantify and predict the effect of overpressure on reservoir quality (Bloch et al., 2002; Taylor et al., 2010; Nguyen et al., 2013). Bloch et al. (2002) showed in numerical models, using the Lander and Walderhaug (1999) model, that early overpressure onset provides a potential porosity preservation window until temperatures reach the point where significant quartz cementation can occur (>90°C). Bloch et al. (2002) conclude from the modelling that deeply developed overpressure has a much smaller effect on reservoir quality in siliciclastic reservoirs than shallow developed overpressure, due to its minor effect on mechanical compaction. Research by Osborne and Swarbrick (1999) has shown that the early overpressure build-up certainly created a low VES setting and reduced the amount of quartz cementation in the Fulmar Formation.

Two mechanisms for maintaining enhanced reservoir quality by overpressure or low vertical effective stress have been proposed:

1. Overpressure reduces the effective stress acting on the grain framework and porosity that would be lost to mechanical compaction is held open (e.g., Gluyas and Cade, 1997; Grant et al., 2014; Nguyen et al., 2013).
2. Overpressure reduces quartz cementation by forestalling and eliminating intergranular pressure dissolution at grain contacts, a presumed primary source of silica for quartz cementation (Osborne and Swarbrick, 1999; Sheldon et al., 2003).

Both experimental and empirical evidence indicates that compaction of sand is an irreversible process (Houseknecht, 1987; Giles, 1997; Paxton et al., 2002). The development of pore fluid overpressure always lessens the vertical effective stress and

reduces the load borne by intergranular contacts within buried sand (Gluyas and Cade, 1997). Therefore, overpressures can slow the rate of compaction (mechanical and chemical) due to the reduction in vertical effective stress but does not result in a volume or porosity increase, apart from a minor poroelastic effect that is negligibly small when considering reservoir quality.

The occurrence of sheet silicates at grain contacts is also thought to play a significant role in chemical compaction. Silica dissolution is thought to be promoted by mica or clay minerals at quartz grain contacts. It has been proposed that this process is independent of the application of stress (Bjørkum, 1996; Oelkers et al., 1996). However, it might be the case that sheet silicates enhance dissolution at grain contacts, but it is unlikely that significant dissolution occurs without the application of stress at the grain contacts (Sheldon et al., 2003).

2.6.3 Overpressure and reservoir quality – a more global view

Pore fluid overpressure in the northern Gulf of Mexico deep-water region can be used as a proxy for the compaction state and the reservoir quality of the turbiditic sands. Overpressures are established in the northern Gulf of Mexico at relatively shallow depths by disequilibrium compaction and tend to increase and tend to increase with depth (Ostermeier, 1995). The reservoir sandstones in deep-water Gulf of Mexico region are mainly affected by mechanical compaction due to the low thermal gradient and the lack of quartz or other volumetrically significant cements. The low vertical effective stress maintains porosities of up to 35% in many of the isolated sands in the deep-water Gulf of Mexico region and vertical effective stress can be used as a proxy for reservoir quality (Sathar and Jones, 2016).

Interestingly, Miocene to Pleistocene sediments on the New Jersey continental slope (Ocean Drilling Program Site 1073) are undercompacted, with porosities between 40% and 65%, and are interpreted to record fluid pressures that reach 95% of the lithostatic stress (Dugan and Flemings, 2000). Dungan and Flemings (2000) used a two-dimensional model with rapid Pleistocene sedimentation of permeable sandy silt of Miocene age to predict observed overpressures. The model describes how lateral pressure equilibration in permeable beds produces fluid pressures that approach the lithostatic stress where overburden is thin. This may not be widely applicable, but does demonstrate the importance of early overpressure generation and how overpressure can be responsible for abnormally high porosities in sediments at shallow depths.

Recent research has also demonstrated that even deeper and older reservoirs can retain anomalous porosities due to early onset of overpressure (Osborne and Swarbrick, 1999; Swarbrick et al., 2000; Nguyen et al., 2013; Grant et al., 2014). The HPHT Elgin and Franklin fields (>5km, 200°C, ~110MPa) retain good reservoir quality in the Fulmar Formation sandstones, with average porosities of 17% (up to 32%) and average permeability of 100 mD (up to 2800 mD). Osborne and Swarbrick (1999) clearly showed that the early overpressure build-up certainly created a low VES setting and reduced the amount of quartz cementation in the Fulmar Formation. Moreover Grant et al. (2014) and Nguyen et al. (2013) have demonstrated that even diagenetically and structurally complex sandstone reservoirs can retain anomalous porosities due to the early onset of overpressure. Sandstones of the Triassic fluvial Skagerrak Formation of the Central Graben, North Sea hold remarkably good porosity, as much as 35%, with respect to their present-day depths of burial (3.5-5 km).

2.6.4 Summary

The best-case scenario for significant porosity preservation by fluid overpressure development is in rapidly deposited sandstones that are encased in low-permeability lithologies such as shales, e.g., Miocene and Pliocene, Gulf of Mexico (Sathar and Jones, 2016). In such cases, the extent of porosity preservation due to reduced compaction is maximized because fluid overpressures develop at shallow depths in response to disequilibrium compaction.

Porosity preservation by overpressure in older and deeper reservoirs (e.g., the Skagerrak Formation) is more complex and requires a more holistic and integrated approach to understanding the pore-system evolution during burial. It is more difficult to maintain high fluid overpressures to the present-day using reasonable shale permeabilities (Harrison and Summa, 1991; Swarbrick et al., 2002). However, a number of mechanisms could be responsible for maintaining some overpressure through geological time, such as:

- Tight carbonate, salt or mudstone baffles/barriers with picodarcy permeability
- Isolated sand bodies in low permeability mudstones, associated with complex diagenesis may maintain porosity and overpressure
- Compartmentalised reservoir sandstones
- Deep overpressure generating mechanisms associated with hydrocarbon reactions or quartz cementation
- Transformation of clay cements which usually occur at temperatures above 100°C

Chapter III

The geological context of the study area

3.1 The Central North Sea and the Central Graben

The Central Graben of the North Sea is part of the NW-SE trending southern extension of a trilete rift system (i.e., an incipient ridge-ridge triple junction), with the S-SW trending Viking Graben as the northern arm and the NW-SE trending Inner and Outer Moray Firth as the western arm. The North Sea Central Graben is 70-130 km wide with an approximate length of 550 km. The rift system separates the Norwegian basement in the east from the UK continental shelf in the west. The North Sea Central Graben consists of the West and the East Central Graben, divided by the Forties-Montrose High and Josephine Ridge horst blocks and flanked by marginal platform areas (Figure 3.1). The geological history and sediments that infill the Central Graben have commonly been divided into pre-rift, syn-rift and postrift by using a tectonostratigraphic approach, based on the major rifting periods during basin evolution (Clark et al., 1999). The rift system developed in at least two major rifting phases, one during the Permian-Triassic (280-210 Ma) and the second during the Late Jurassic (155-140 Ma) (Gowers and Saeboe, 1985; Hodgson et al., 1992; Glennie, 1998). Furthermore, Hodgson et al. (1992) suggested an earlier Permian rift phase, prior to the deposition of the Zechstein evaporites, but basement extension during this rifting event is difficult to track in the geological record due to the overprint of subsequent rifting and salt tectonics (Erratt et al., 1999). The Triassic to Middle Jurassic rift event, with Early Triassic basement extension, is related to syn-rift salt ridge generation located over Permian fault systems, early salt movement and post-rift sediment deposition in the subsiding basin, with subsequent volcanism related to regional thermal uplift. The Late Jurassic to Tertiary rift event is related to Mid Jurassic doming and volcanism in the Forties region, prior to the rifting during the Late Jurassic (159-144 Ma). The main rifting event was accompanied by fault movement, commonly by reactivation of Permian faults, and

followed by post-rift thermal subsidence and passive halokinesis, forming early large peripheral sinks around isolated diapiric structures (Hodgson et al., 1992). Rift-related doming, centred at the triple junction of the trilete system, and extensive related inversion during the Mid Jurassic resulted in widespread erosion of previously deposited strata in the northern Central Graben area (Clark et al., 1999). This was followed by a sag phase starting in the Late Cretaceous linked with the majority of the present-day basin infill. Further details of the structural evolution of the Central Graben area can be found in Erratt et al. (1999), Evans et al. (2003), Gibbs (1984) and Roberts et al. (1990).

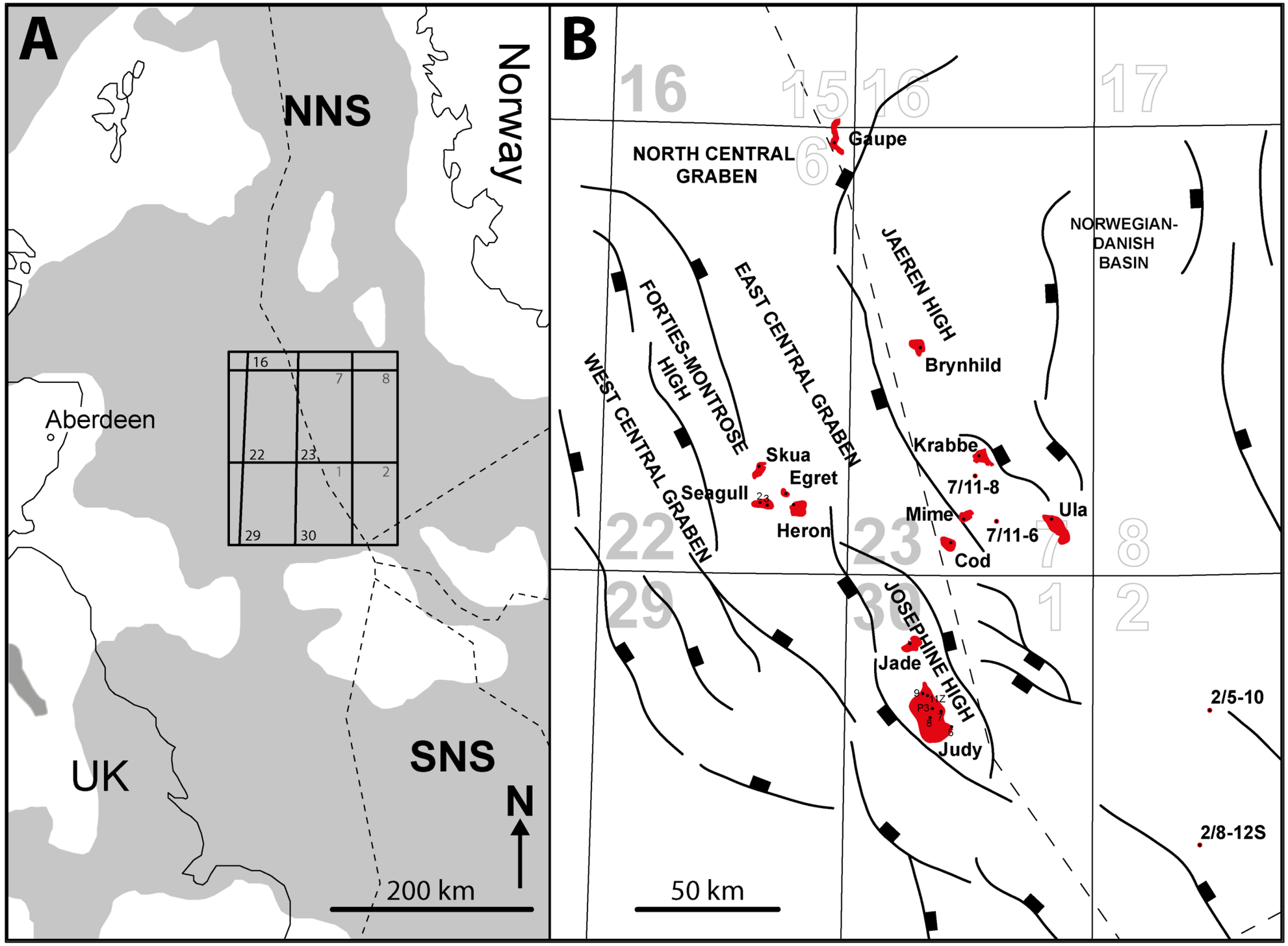

Figure 3.1 A) Regional map of the Central North Sea, with the outline of Triassic sediments (grey). B) Central Graben map showing Triassic fields (red) and wells (black) of the UK quadrants 22 and 30, the Norwegian quadrants 2, 6 and 7, with major structures of the Central Graben.

3.2 Central North Sea stratigraphy

The following text identifies the stratigraphy as used in this research. It is compiled from several sources, as outlined below, but builds primarily upon the seminal work of Goldsmith et al. (2003). It provides an important reference stratigraphy used for the 1D PetroMod modelling as part of this research. The Central Graben Stratigraphy is shown in a schematic stratigraphic column for the wider Central Graben area in Figure 7.2 and divided into pre-rift, syn-rift and post-rift deposits by using a tectonostratigraphic approach, based on the major rifting periods during basin evolution (Clark et al., 1999). Pre-rift sediments in the Central Graben area are the Devonian Buchan Group sands which are overlain by the Permian continental sediments of the Rotliegend Group and the Late Permian Zechstein evaporites. The syn-rift sediments are mainly siliciclastic Triassic and Jurassic sediments of as much as 2000 m in thickness and commonly represent the main reservoir rocks of the Central Graben area, including fluvial sandstones of the Triassic Skagerrak Formation and shoreface and mass-flow sandstones of the Upper Jurassic Fulmar and Ula Formations. The Upper Jurassic oil-prone, marine shales and the Middle to Upper Jurassic gas-prone, coaly shales and coals of the top of the syn-rift sequence represent the main hydrocarbon source rocks of the Central Graben area. The post-rift sediments from the Cretaceous to Holocene are up to 4500m in thickness and are mainly siliciclastic rocks dominated by shale, sandstone and silty sandstone with a thick Upper Cretaceous Chalk section (Glennie, 1998; Goldsmith et al., 2003). The Upper Cretaceous Chalk units, including the Ekofisk, Tor and Hod formations, form the main seal for the highly overpressured Mesozoic reservoirs in the Central Graben, North Sea (Mallon and Swarbrick, 2002, 2008; Mallon et al., 2005; Swarbrick et al., 2010). After the North Atlantic Ocean opened, the Eocene and younger Stronsay, Westray and Nordland Groups comprising up to 2500 m of predominantly

siltstone and shale were deposited (Figure 3.2; Figure 3.3 & Figure 3.4). The Eocene and younger sediments are important for the overpressure development by disequilibrium compaction, due to their rapid deposition.

3.3 The study area

This study focuses on the wider Central Graben area including various Triassic reservoir sandstones in UK quadrants 22 and 30 and Norwegian quadrants 2, 6 and 7 in the North Sea (Figure 3.1).

The investigated Triassic reservoirs of UK Quadrant 22 are the Egret field (well 22/24d-10), the Heron field (wells 22/29-5; 5RE & 5RES1), the Seagull field (wells 22/29-2; 2S1 & 3), and the Skua field (well 22/24b-7) (Figure 3.2; Appendix I). The fields are all located at the southern end of the Forties-Montrose High, and are commonly referred to as the ETAP or Eastern Trough Area Project (Pooler and Amory, 1999; McKie and Audretsch, 2005).

The investigated Triassic fields in UK Quadrant 30 are the Jade field (well 30/2c-4) and the Judy field (wells 30/7a-7; 8; 8; 11Z; P3 & 30/13-5) (Figure 3.3; Appendix I). The Jade and Judy fields are both located on the Josephine Ridge in Quadrant 30 commonly referred to as the J-Block.

The investigated Norwegian Triassic reservoirs or sandstones are in Quadrant 2 from the well 2/5-10 and 2/8-12S, in Quadrant 6 from the Gaupe field (well 6/3-1), and in Quadrant 7 from the Brynhild field (well 7/7-2), the Krabbe field (well 7/8-3), the Cod field (wells 7/11-7 & 7R), the Mime field (well 7/11-10S), the Ula field (well 7/12-6), and wells 7/11-6 and 7/11-8 (Figure 3.4; Appendix I).

The areas are part of a larger HPHT province that includes the Triassic strata of the Central Graben and the southern part of the Viking Graben (Goldsmith et al., 2003).

The regional water depth is generally 70 m to 90m. This broad areal coverage allows a regional perspective on the post-depositional processes that have influenced porosity preservation in the Skagerrak Formation.

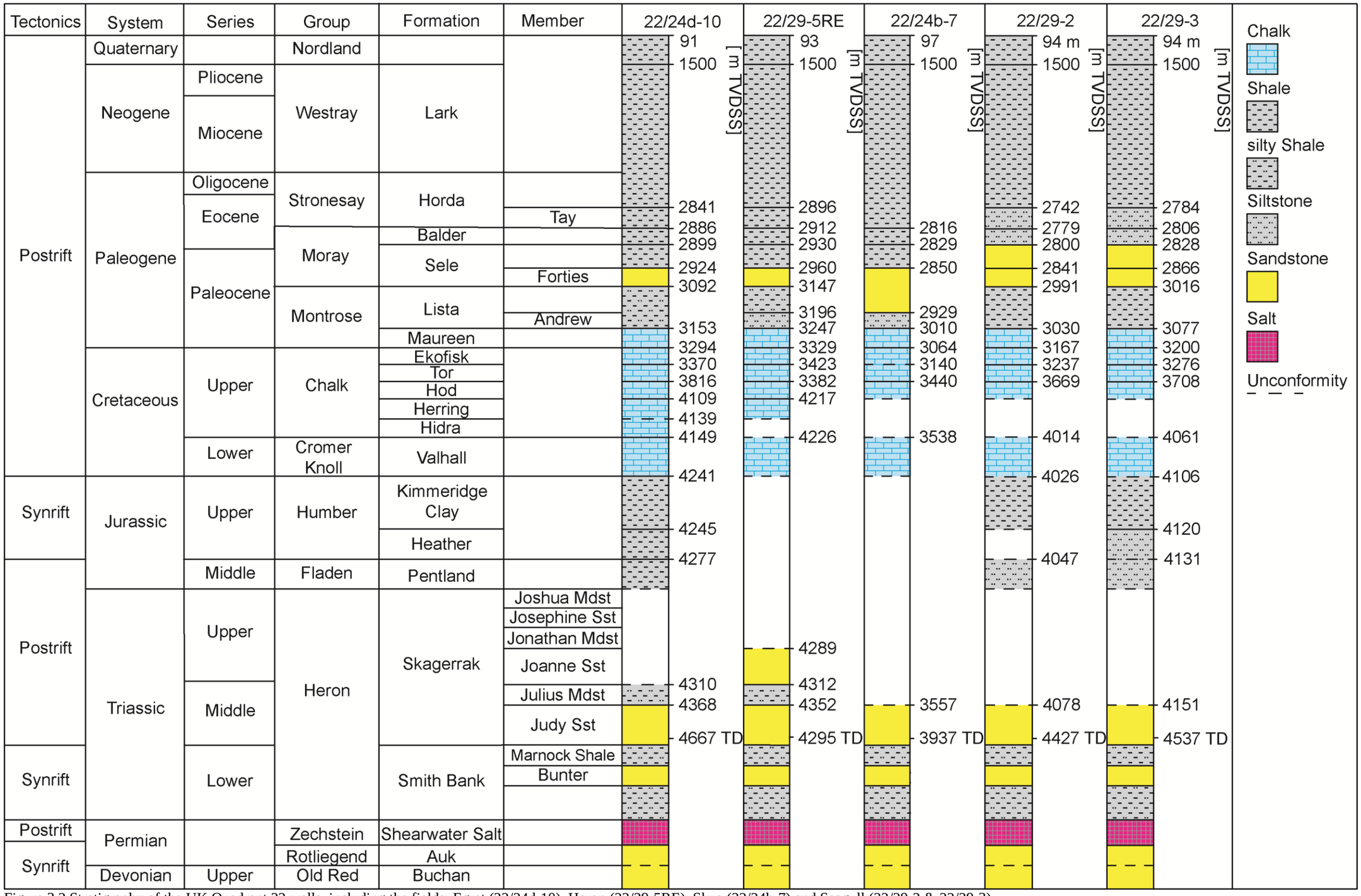

Figure 3.2 Stratigraphy of the UK Quadrant 22 wells, including the fields: Egret (22/24d-10), Heron (22/29-5RE), Skua (22/24b-7) and Seagull (22/29-2 & 22/29-3).

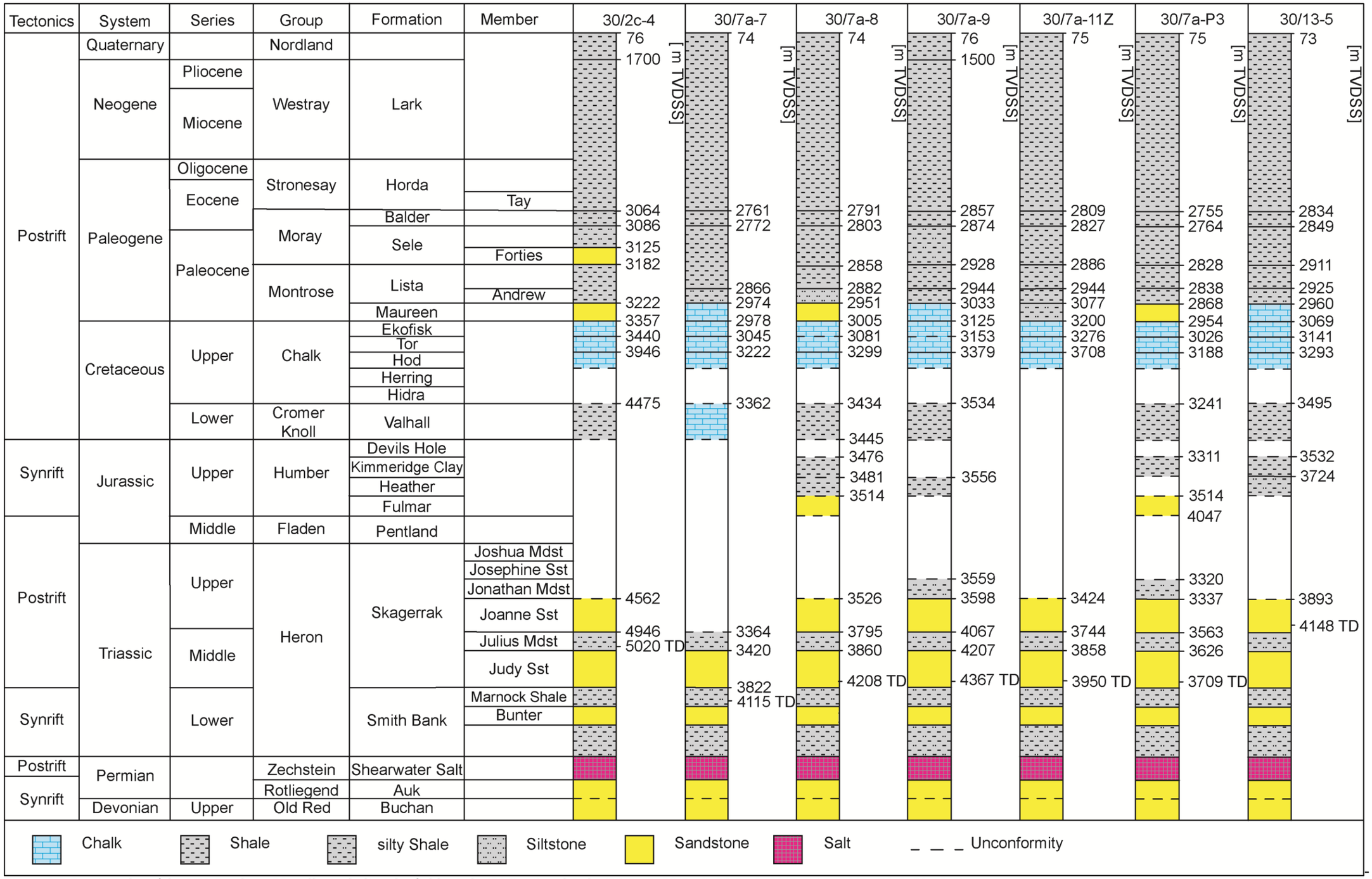

Figure 3.3 Stratigraphy of the UK Quadrant 30 wells, including the fields: Jade (30/2c-4) and Judy (30/7a-7, 30/7a-8, 30/7a-9, 30/7a-11Z, 30/7a-P3 & 30/13-5).

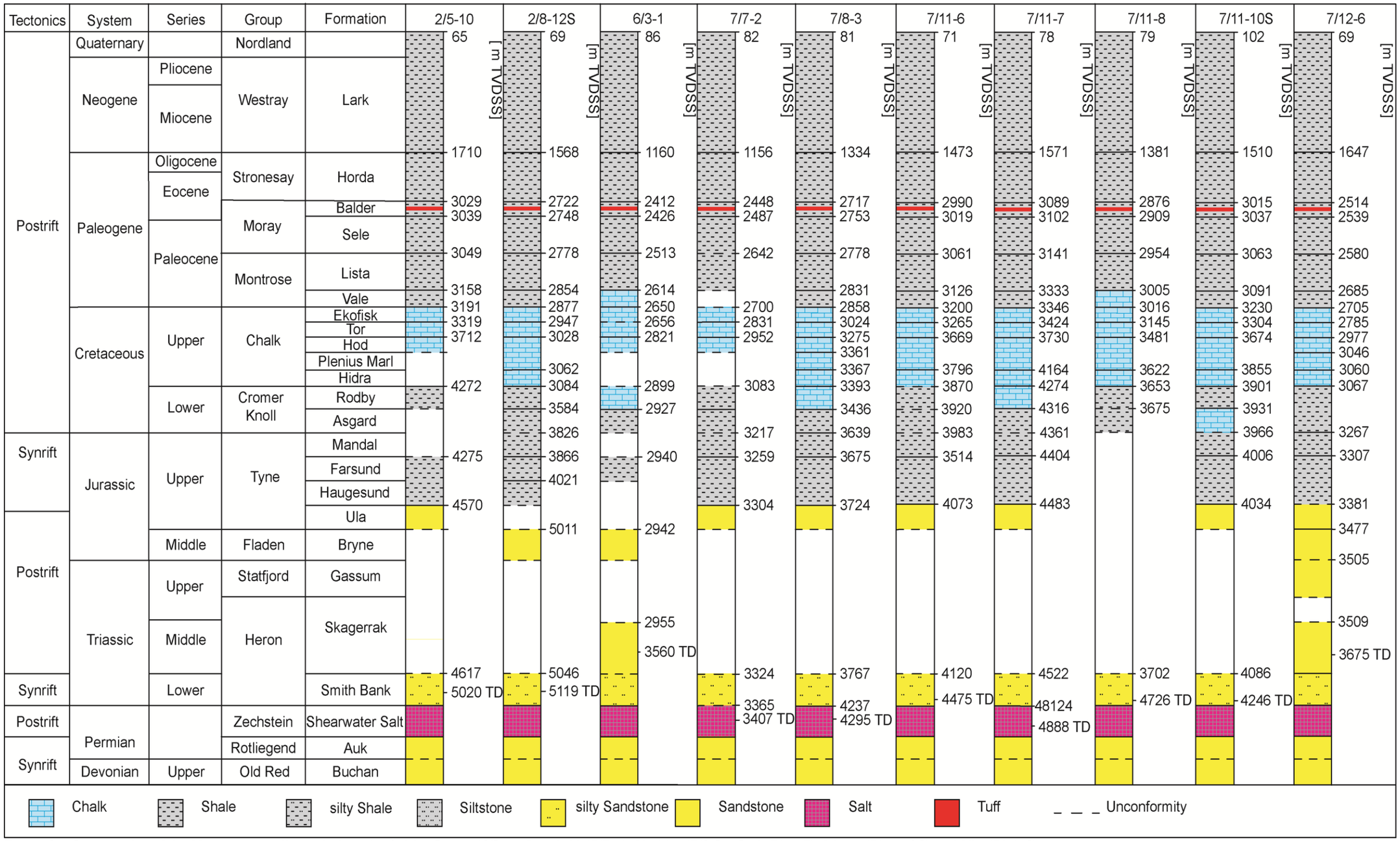

Figure 3.4 Stratigraphy of the Norwegian wells, including the fields: Gaupe (6/3-1), Brynhild (7/7-2), Krabbe (7/8-3), Cod (7/11-7), Mime (7/11-10S) and Ula (7/12-6).

3.4 Triassic stratigraphy of the Central North Sea

The stratigraphic nomenclature of the Triassic for the Central Graben for the UK sector was defined by Goldsmith et al. (1995), based on detailed biostratigraphic and lithostratigraphic correlation of wells from the Josephine Ridge and was extended and correlated towards the ETAP (Eastern Trough Area Project) area by McKie and Audretsch (2005). The stratigraphic nomenclature of the Norwegian sector is based on the 2014 Norwegian Petroleum Directorate (NPD) lithostratigraphic chart for the Central North Sea (e.g., Lervik, 2006; Vollset and Dore, 1984). The Central Graben Triassic succession consists of sediments belonging to the Early Triassic Smith Bank Formation (shales, evaporites and thin sands) and the Middle to Late Triassic Skagerrak Formation (thickly interbedded sands and shales). The Triassic Smith Bank and Skagerrak sediments accumulated directly on top of the Late Permian Zechstein salt in a series of salt and fault controlled mini-basins or pods. The Smith Bank sediments represent the bulk and basal part of the mini-basin infill, whereas the overlying Skagerrak is found as intra-basin sediments in the upper parts of the mini-basins and as inter-basin sediments between the mini-basins.

The Skagerrak Formation of the Central Graben (UK sector) is further subdivided into three sand-dominated units (Judy, Joanne and Josephine) and three mud-dominated units (Julius, Jonathan and Joshua), but not for the Norwegian sector (Goldsmith et al., 2003). The sand-dominated units include ribbon sands, amalgamated ribbon sands, sheet sands and crevasse splay sands (Goldsmith et al., 1995; McKie and Audretsch, 2005), whereas the mud-dominated units include a variation of basinwide floodplain, lacustrine shale, loess and playa deposits. The thick and laterally extensive mud-dominated units provide the main correlative units for the Triassic Skagerrak in the

Central Graben (McKie and Audretsch, 2005). The Judy Sandstone Member (UK Quadrant 22) is also further subdivided by McKie & Audretsch (2005) into a lower terminal splay dominated interval and an upper channelised interval, separated by a shale-prone section. The lower terminal splay facies is characterized by fine-grained, planar cross-bedded and ripple-laminated sandstones. In comparison, the upper interval is dominated by channel-fill deposits, which are organized into fining upward packages with coarse lag deposits (usually with ripped-up calcrete nodules) commonly occurring at the base. Channel-fill deposits are characterized by well sorted cross-bedded sandstones and can be separated into channel and sheet-dominated sandstones (McKie and Audretsch, 2005; McKie and Williams, 2009; McKie, 2011).

The resultant Triassic stratigraphy in the wider Central Graben area is generally incompletely preserved due to deep erosion during the Middle and Late Jurassic (Erratt et al., 1999).

3.5 Fluvial facies

The Triassic strata of the Central North Sea area are dominated by thick alluvial successions deposited in a closed or internally draining basin with no apparent connection to a marine realm (Goldsmith et al., 1995). The Middle to Late Triassic Skagerrak Formation comprises deposits of 500-1000 m of predominantly continental braided and meandering fluvial systems and terminal fluvial fans with lacustrine facies in the Central Graben, North Sea (McKie and Audretsch, 2005; de Jong et al., 2006; McKie and Williams, 2009; Kape et al., 2010). The sand-dominated units (Judy, Joanne and Josephine) include ribbon sands, amalgamated ribbon sands, sheet sands, amalgamated sheet sands and crevasse splay sands (e.g., Goldsmith et al., 1995; McKie and Audretsch, 2005). Ribbon sands are classified by their width to thickness ratio of

<15 and show characteristic wings attached to the central bodies of coarse-grained overbank deposits (levees) (Hirst, 1992; Gibling, 2006). Ribbon sands form in fluvial systems, when palaeochannels become plugged with sediments prior to any significant lateral migration of the original scour (Figure 3.5). Sheet sands, on the other hand, are characterised by a width to thickness ratio of >15 and commonly >100. They can be subdivided into three main groups, of 1) channelised/confined flow sheet sands, 2) poorly channelised flow sheet sands and 3) unconfined flow sheet sands, depending on the form of basal erosion surface and the development of cutbanks (Figure 3.5) (Hirst, 1992). Channelized flow sheet sands are characterised by well-developed cutbanks, which indicates channelized flow, but the channels were laterally unstable and therefore deposited broader units. Poorly channelized sheet sand bodies are defined by their distinctive form with laterally wedged out bodies and poorly defined banks and cutbanks (Hirst, 1992). Sheet sands from unconfined flow show generally a large width relative to their thickness (typically <1.5 m and often <0.5 m) and are defined by a general absence of cutbanks (Hirst, 1992; Gibling, 2006).

However, the ribbon sands and the channelized/confined sheet sands, especially in amalgamated complexes, are assumed to provide best reservoir sands with the best reservoir quality in the Skagerrak Formation. Unconfined sheet sands and crevasse splay sands on the other hand are expected to have low reservoir quality. Samples for this research are chosen on the basis of expected best reservoir quality in ribbon sands and channelized/confined sheet sands. Furthermore, the assumption has been made that ‘like’ facies represent the best reservoir quality in all the areas and wells.

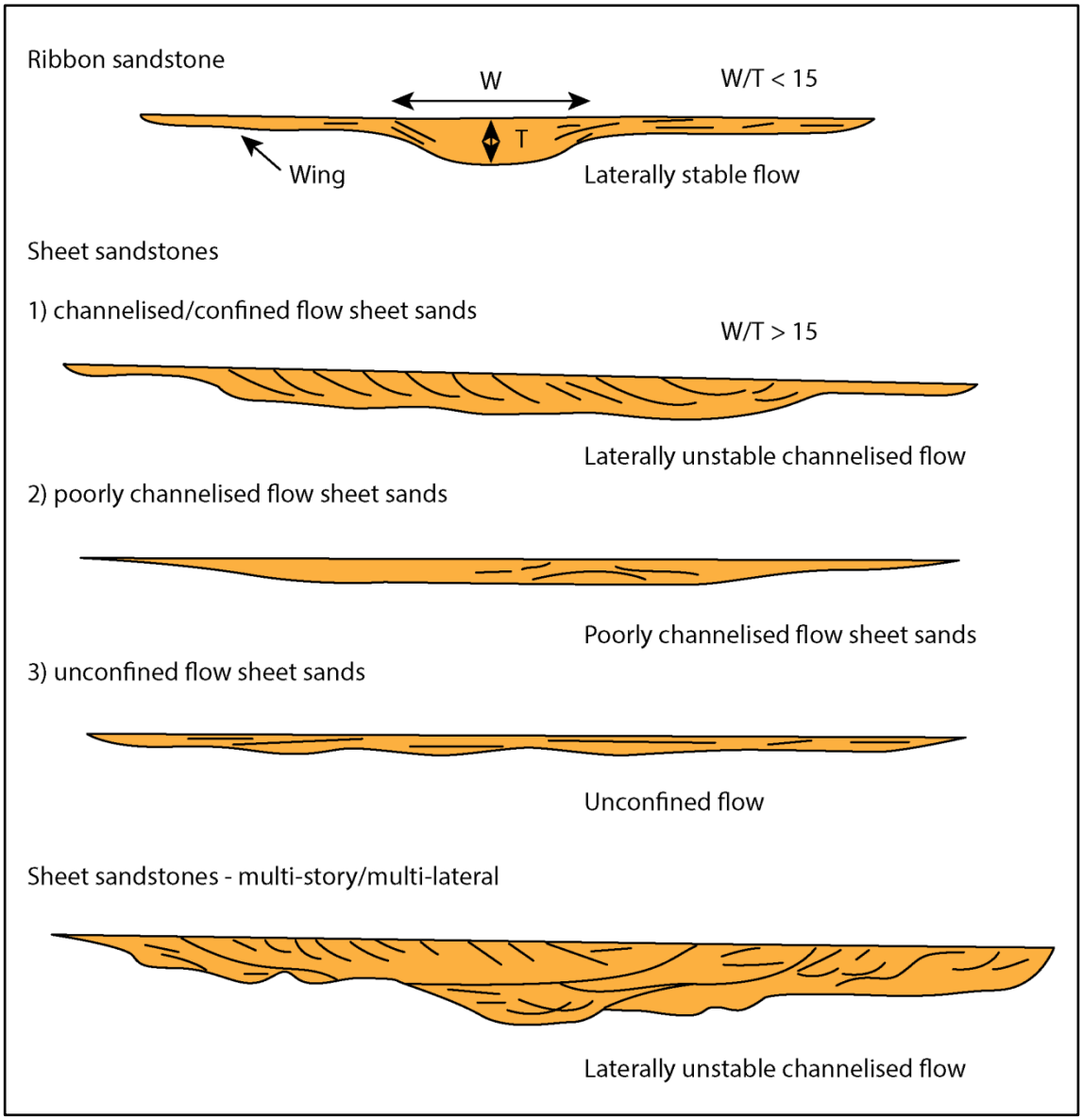

Figure 3.5 Illustration of ribbon sands and sheet sands, with 1) channelised/confined flow sheet sands, 2) poorly channelised flow sheet sands, and 3) unconfined flow sheet sands. After Hirst (1992).

3.6 Triassic palaeoenvironment

The Triassic Period is generally considered as a relatively stable 'hot-house' world, with ice-free poles and an arid to semi-arid climate. However, the overall arid to semi-arid Triassic climate was also variable from arid and to humid conditions, with the strongest climate changes in the early Triassic and the Carnian, especially in the Tethys realm (McKie and Williams, 2009; Preto et al., 2010). The Central Graben area during

Triassic times was an internally drained basin with no connection to the marine realm. Due to the general absence of eustatic control, sedimentation was controlled by tectonics and the climate. Long-term fluctuations in the hinterland climate are generally thought to control the generation of the alternating sandstone and mudstone members within the Skagerrak Formation (Goldsmith et al., 1995, 2003).

Goldsmith et al. (2003) suggested that the thick and laterally extensive mudstone members of the Skagerrak Formation represent more humid climate periods with lacustrine or swamp environments, and that the sandstone members represent a fluvial system that prograded and extended basinward during more arid to semi-arid climate periods (Figure 3.6).

However, Archer et al. (2010) suggested, based on observations from core, cuttings and wireline log data, a reversed climate curve with the more humid periods during the deposition of the sandstone members and the arid periods during the deposition of the mudstone members (Figure 3.6). The more recent climate curve by Archer et al. (2010) is based on observed evaporates (anhydrite) interbedded in the Julius, Jonathan and Joshua Mudstone members and the general absence of lacustrine laminites in the core record.

The Early Triassic Smith Bank Formation with its entirely reddened silty mudstones and absence of palynomorphs is generally interpreted as representative of a continuation of the generally harsh conditions and intense hot-house climate of the Permian/Triassic boundary into the Early Triassic. The Smith Bank Formation reflects a widespread, Early Triassic terminal splay/playa environment deposited in an arid to semi-arid climate with rare palaeosols and biogenic traces (Goldsmith et al., 2003; Péron et al., 2005; McKie and Williams, 2009; Preto et al., 2010) (Figure 3.6).

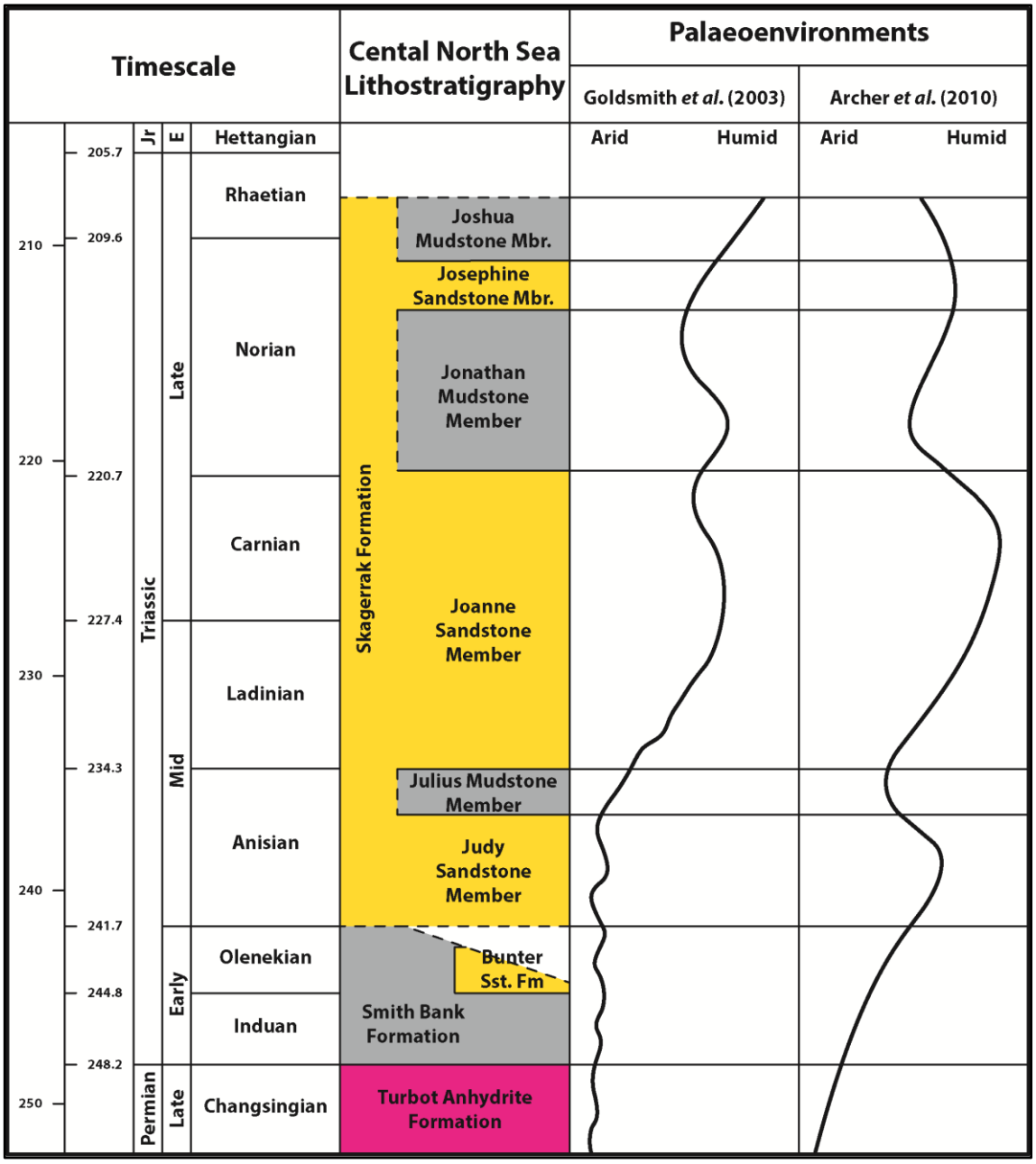

Figure 3.6 Palaeoenvironmental interpretations by Goldsmith et al. (2003) and Archer et al. (2010) for the Central Graben area.

The Judy Sandstone Member represents a more humid hinterland climate with major sand transport into the basin by the fluvial system according to Archer et al. (2010) and McKie (2014), in agreement with more general observations about Triassic climate changes made by Preto et al. (2010). The subsequent deposition of the Julius Mudstone Member reflects a more arid to semi-arid hinterland climate with a retrograde fluvial

system, a general lack of sand transport into the basin, and the presence of evaporites (anhydrite) in the shaly rock record. Archer et al. (2010) referred to the commonly observed symmetrical nature of the Julius Mudstone wireline log character, with a more resistive, denser and sonically faster centre portion, which indicates a more-evaporite rich and drier phase during the middle Julius times than the transitional periods towards the Judy and Joanne Sandstone times. The overlying Joanne Sandstone Member shows a progressive increase in hinterland affinities with a wetter sub-humid climate, where higher discharges activated and sustained a competent fluvial system. The Jonathan Mudstone Member shows increased reddening and interbedding with evaporites in the core material, which indicates a tendency to more aridity during the deposition of the mudstone member. This climatic cyclicity was repeated during the depositional times of the Josephine Sandstone Member, with a relatively wet period, and the Joshua Mudstone Member, with a relatively arid period (Archer et al., 2010) (Figure 3.6).

3.7 Mini-basin development in the Central North Sea

The Triassic sediments of the Central North Sea area accumulated directly on top of the Late Permian Zechstein salt within a series of salt and fault controlled mini-basins or pods. The initiation of mini-basin subsidence or creation of salt-walled mini-basins requires the presence of salt with a sufficient thickness to allow halokinesis (Hudec et al., 2009), and a mechanisms to initiate halokinesis, i.e., extension, compression, differential loading, or buoyancy (Banham and Mountney, 2013b). The salt structures in the Central North Sea, i.e., mini-basins and salt walls, are generally in alignment with the overall rift-controlled basement structure, i.e., the Permian fault system. The halokinesis of the Late Permian Zechstein evaporites and the development of mini-basins started during the Triassic rifting due to reactivation of the Permian fault system

and localised loading by Triassic sediments in the Central Graben (Hodgson et al., 1992; Smith et al., 1993; Bishop, 1996; Matthews et al., 2007). The salt was unevenly distributed across Central Graben area (Glennie et al., 2003), which led to an uneven distribution and variable development of mini-basins and accommodation space in the Central Graben throughout the Triassic period. The coeval halokinesis of the thickly developed Zechstein salt significantly influenced the depositional environment of the Triassic deposits in the Central Graben. This probably controlled the overall subsidence of the mini-basins, sediment transport pathways, and the reworking of previously deposited sediments (Banham and Mountney, 2013b).

The syn-rift and halokinesis controlled Smith Bank sediments generally represent the bulk and basal part of the mini-basin infill, whereas the overlying post-rift and halokinesis controlled Skagerrak Formation sediments are mainly found as intra-basin sediments in the upper parts of the mini-basins and as inter-basin sediments between the mini-basins. The overall mini-basin development was mainly responsible for the preservation of the Middle to Late Triassic Skagerrak Formation in the study area. The thick Late Permian evaporite sediments often prevented grounding of mini-basins on the underlying Rotliegend basement in the Central Graben. Salt withdrawal has allowed considerable thicknesses of Skagerrak Formation sediments to accumulate within mini-basins as well as being responsible for facies variability between intra-basin and inter-basin areas that influenced reservoir thickness and diagenetic cementation (e.g., Nguyen et al., 2013).

Chapter IV

Enhanced porosity preservation by pore fluid overpressure and chlorite coatings in the Triassic Skagerrak, Central Graben, North Sea, UK

This chapter has been published in the Special Publication 435 - Reservoir Quality of Clastic and Carbonate Rocks: Analysis, Modelling and Prediction by the Geological Society of London (05/02/2016).

Stricker, S., & Jones, S. J., (2016). Enhanced porosity preservation by pore fluid overpressure and chlorite grain coatings in the Triassic Skagerrak, Central Graben, North Sea, UK. *In:* Armitage, P. J., Butcher, A. R., Churchill, J. M., Csoma, A. E., Hollis, C., Lander, R. H., Omma, J. E. & Worden, R. H. (eds.) Reservoir Quality of Clastic and Carbonate Rocks: Analysis, Modelling and Prediction. *Geological Society, London, Special Publications*, 435, http://doi.org/10.1144/SP435.4

4.1 Summary

Current understanding of porosity preservation in deeply buried sandstone reservoirs tends to be focused on how diagenetic grain coats of clay minerals and microquartz can inhibit macroquartz cementation. However, the importance of overpressure developed during initial (shallow) burial in maintaining high primary porosity during subsequent burial has generally not been appreciated. Where pore fluid pressures are high, and the vertical effective stress is low, the shallow arrest of compaction can allow preservation of high porosity and permeability at depths normally considered uneconomic. The deeply buried fluvial sandstone reservoirs of the Triassic Skagerrak Formation in the Central Graben, North Sea, show anomalously high porosities at depths greater than 3500 m. Pore pressures can exceed 80 MPa in the upper part of the Skagerrak Formation at depths of 4000 to 5000 m, where temperatures are above 140°C. The Skagerrak reservoirs commonly have high primary porosities of up to 35%, little macroquartz cement and variable amounts of diagenetic chlorite grain coats. This research sheds light on the complex controls on reservoir quality in the fluvial sandstones of the Skagerrak Formation by identifying the role of shallow overpressure in arresting mechanical compaction and the importance of chlorite detrital grain coatings in inhibiting macroquartz cement overgrowth as temperature increases during progressive burial.

4.2 Introduction

Deeply buried sandstone reservoirs are the cumulative product of depositional processes and diagenesis during burial at both shallow and greater depths. Simple porosity-depth trends can offer some useful guidance but are not always successful in predicting reservoir porosity. Reservoirs with anomalously high porosities are common in several hydrocarbon basins, e.g., Central Graben, North Sea, UK (Osborne and Swarbrick, 1999; Nguyen et al., 2013; Grant et al., 2014); the Gulf of Mexico, USA (Taylor et al., 2004; Ehrenberg et al., 2008; Ajdukiewicz et al., 2010); the Santos Basin, Brazil (Anjos et al., 2003) and the Indus Basin, Pakistan (Berger et al., 2009). Current understanding of porosity preservation in deeply buried sandstone reservoirs (>4000 m) tends to be focused on how coatings of clay and microquartz on detrital grains can inhibit macroquartz cementation. There are many studies where deep reservoir porosity is linked to early diagenetic clay or microquartz grain coats (Pittman et al., 1992; Ehrenberg, 1993; Aase et al., 1996; Bloch et al., 2002; Berger et al., 2009; Ajdukiewicz and Lander, 2010; Ajdukiewicz and Larese, 2012; French et al., 2012; Worden et al., 2012; Bahlis and De Ros, 2013). These studies have proven that quartz-rich sandstones with robust and continuous diagenetic clay or microquartz grain coats contain a much lower volume of macroquartz cement than expected (Berger et al., 2009; Ajdukiewicz and Lander, 2010).

The role played by fluid overpressure in porosity preservation during the burial of sandstones has often been overlooked or considered less significant (e.g., Audet and McConnell, 1992; Gaarenstroom et al., 1993; Giles, 1997; Bloch et al., 2002; Taylor et al., 2010). The preservation of enhanced secondary porosity has also been attributed to high overpressures and increased porosity at depth (e.g., Wilkinson et al., 1997; Haszeldine et al., 1999). Increasing vertical effective stress (VES) caused by sediment

loading is the major driver of mechanical compaction and porosity reduction during shallow burial. Pore fluid overpressure reduces the stress on intergranular and cement-grain contacts and inhibits both mechanical compaction and pressure dissolution (Swarbrick and Osborne, 1998). The shallow onset of pore fluid overpressure enhances porosity preservation, as noted for the Triassic Skagerrak Formation of the Central North Sea (Nguyen et al., 2013; Grant et al., 2014).

The Triassic Skagerrak Formation is one of the main reservoirs in the high pressure high temperature (HPHT) province in the Central Graben, North Sea. Pore pressures can exceed 80 MPa in the upper part of the Skagerrak Formation at depths of 4000-5000 m where temperatures are in the range 166-200°C (Swarbrick et al., 2000; di Primio and Neumann, 2008; Nguyen et al., 2013). Overpressures are widespread in the Mesozoic reservoirs in the Central North Sea, a region which since the early Cretaceous has experienced almost continuous sedimentation of dominantly fine-grained lithologies (Osborne and Swarbrick, 1999; Swarbrick et al., 2000; Yardley and Swarbrick, 2000).

Typical porosity-depth trends for siliciclastic reservoirs, show porosities of 10-15% at depths of 4000-5000 m (Ehrenberg et al., 2009). However, the Skagerrak reservoir sandstones retain remarkably good porosity, up to 35%, and a low degree of compaction with respect to their present-day depths of burial. It is these higher than expected porosities that form the focus of this study. Here we present new results for the diagenesis and pore pressure evolution of the Triassic Skagerrak Formation in the Josephine High (J-Block), located within the Central Graben in UK Quadrant 30, and in the Heron field located further north in UK Quadrant 22.

Basin analysis and burial history modelling have been undertaken to investigate the role of pore fluid overpressure evolution in the maintenance of high primary porosity during shallow burial (<2500 m burial), where mechanical compaction dominates. The basin

model was then compared to petrographic data to investigate the role of palaeo-pressures on maintenance of high primary porosity at depth. Furthermore, detailed SEM and petrographic analysis was applied to investigate the role of clay mineral grain coatings in maintaining high primary porosity in the high-temperature deep burial phase (>2500 m burial). This simple approach yields results that allow important inferences to be made about the controls on porosity preservation in HPHT reservoirs. These results complement previous studies in the Central Graben, North Sea (e.g., Nguyen et al., 2013; Grant et al., 2014).

4.3 Geological setting

The Central Graben of the North Sea is part of the NW-SE trending southern extension of a trilete rift system (i.e., an incipient ridge-ridge triple junction), with the Viking Graben as the northern arm and the Inner and Outer Moray Firth as the western arm. The North Sea Central Graben is 70-130 km wide with an approximate length of 550 km. The rift system separates the Norwegian basement in the east from the UK continental shelf in the west. The North Sea Central Graben consists of the West Central Graben and the East Central Graben, divided by the Forties-Montrose High and Josephine Ridge horst blocks and flanked by marginal platform areas (Figure 4.1). The rift system developed in at least two major rifting phases, one during the Permian-Triassic (290-210 Ma) and the second during the Late Jurassic (155-140 Ma) (Gowers and Saeboe, 1985; Glennie, 1998). The geological history has commonly been divided into pre-rift, syn-rift and post-rift phases (Clark et al., 1999). Syn-rift sediments are mainly siliciclastic Triassic and Jurassic sediments of as much as 2000 m in thickness. The post-rift sediments from the Cretaceous to Holocene are up to 4500m in thickness (Figure 4.2). Post-rift sediments are mainly siliciclastic rocks dominated by shale,

sandstone, silty-sandstone and a thick Upper Cretaceous Chalk section (Goldsmith et al., 2003). Importantly, Upper Cretaceous Chalk units including the Ekofisk, Tor and Hod formations (Figure 4.2), are the main reservoir seals for the sub-Chalk reservoirs in the Central Graben, North Sea (Mallon and Swarbrick, 2002, 2008; Swarbrick et al., 2010). These highly cemented and mechanically compacted chalk units have got the potential to seal high overpressure in the underlying highly pressured reservoirs (Mallon et al., 2005; Mallon and Swarbrick, 2008; Swarbrick et al., 2010). After the North Atlantic Ocean opened, the Eocene and younger Hordaland and Nordland groups were deposited, comprising up to 2500 m of predominantly siltstone and shale.

This study focuses on two HPHT key areas in the Central Graben, North Sea: the Heron Cluster in UK Quadrant 22, part of the ETAP area at the southern end of the Forties-Montrose High; and the J-Block area in UK Quadrant 30, located on the Josephine Ridge (Figure 4.1). Both areas are part of a wider HPHT province that includes the Triassic strata of the Central Graben and the southern part of the Viking Graben (Goldsmith et al., 2003).

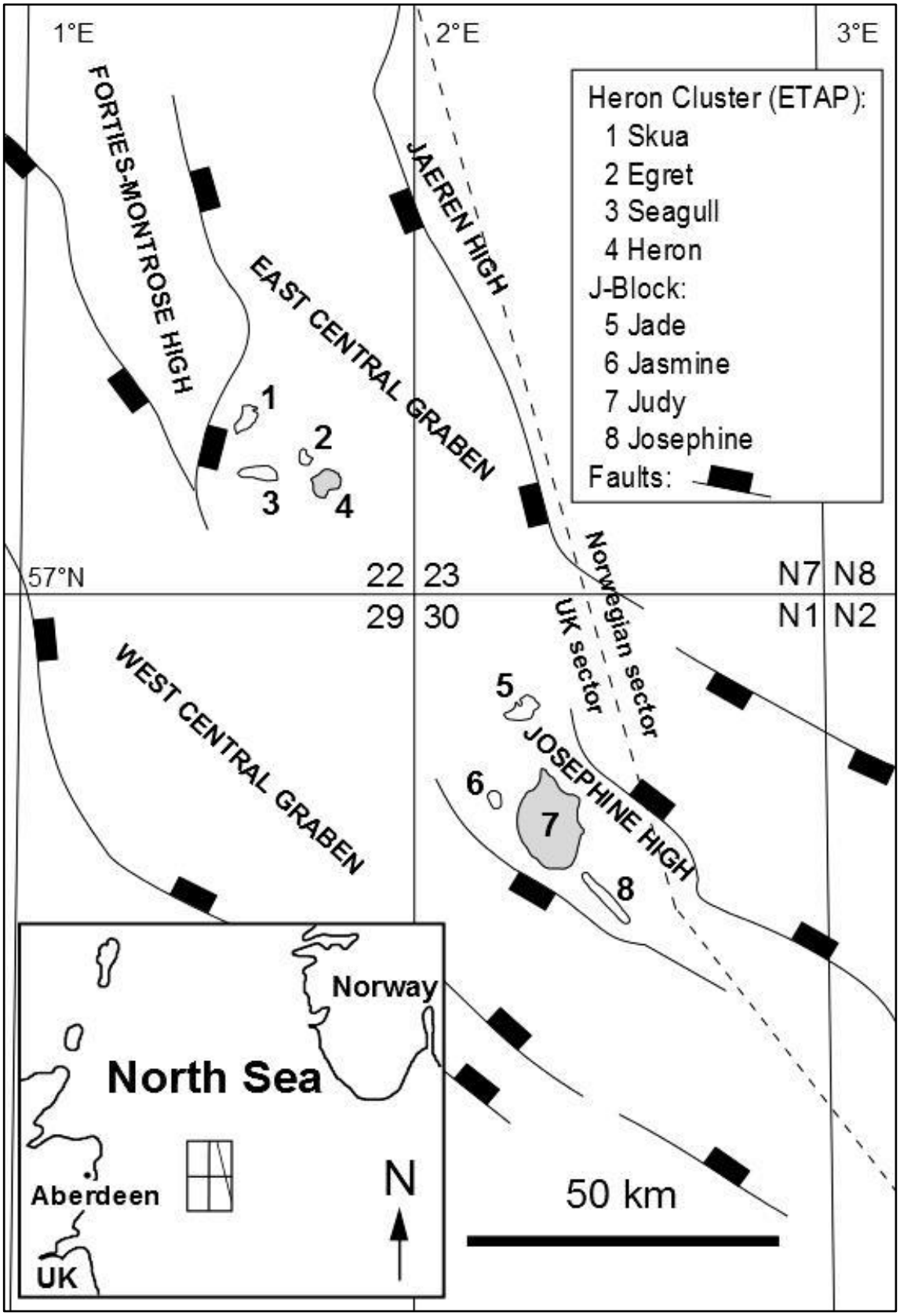

Figure 4.1 Location map showing the Central Graben, North Sea, major structural elements (East Central Graben, Forties-Montrose High, Josephine High and West Central Graben) and some Triassic targets within the UK Quadrant 22 (Heron Cluster) and UK Quadrant 30 (J-Block).

4.3.1 Triassic Skagerrak stratigraphy

The Triassic Skagerrak Formation in the Central Graben, North Sea comprises 500-1000 m of predominantly continental braided and meandering fluvial systems and terminal fluvial fans with lacustrine facies (McKie and Audretsch, 2005; de Jong et al., 2006). The Skagerrak sediments accumulated in a series of fault- and salt-controlled mini-basins, or pods, within the overall rift basin (Smith et al., 1993; Matthews et al., 2007). The thick Zechstein salt, of late Permian age, strongly influenced sedimentation by forming withdrawal basins due to a combination of localised loading and structural extension (Smith et al., 1993; Bishop, 1996; Matthews et al., 2007). Mini-basin development was active in the study area throughout the Triassic and provided localised depocentres for the south-easterly flowing Skagerrak fluvial system. The mini-basins were largely responsible for the preservation of the Skagerrak Formation in the study area. However, the salt mini-basins do create facies variability between intra-basin and inter-basin that has influenced reservoir thickness and diagenetic cementation (Nguyen et al., 2013).

The stratigraphic nomenclature of the Triassic for the Central Graben was defined by Goldsmith et al. (1995), based on detailed biostratigraphic and lithostratigraphic correlation. The Central Graben Triassic succession consists of sediments belonging to the Early Triassic Smith Bank Formation and the Middle to Late Triassic Skagerrak Formation (Figure 4.2). The Triassic Skagerrak Formation is subdivided into three sand-dominated units (Judy, Joanne and Josephine) and three mud-dominated units (Julius, Jonathan and Joshua). The sand-dominated units comprise sheetflood deposits and multi-storey stacked channel sandbodies (Goldsmith et al., 1995; McKie and Audretsch, 2005), whereas the mud-dominated units comprise non-marine, basinwide floodplain and playa deposits. The thick and laterally extensive mud-dominated units provide the

main correlative units for the Triassic Skagerrak in the Central Graben (McKie and Audretsch, 2005).

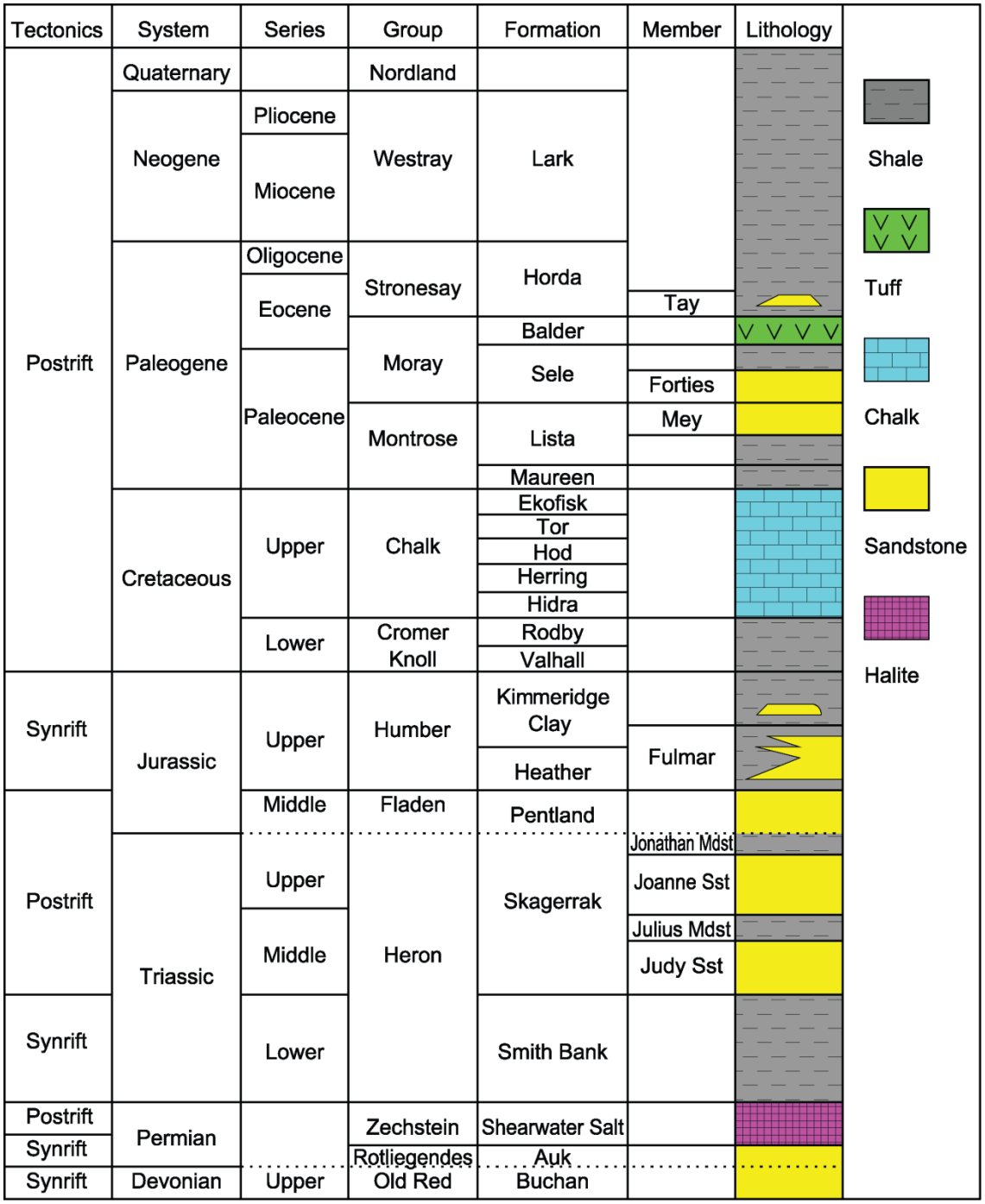

Figure 4.2 Regional stratigraphy of the Central Graben, North Sea. North Sea stratigraphic nomenclature based on Knox and Cordey (1992). Also see Figure 3.2 and Figure 3.3.

The resultant Triassic stratigraphy is incompletely preserved due to deep erosion during the Middle and Late Jurassic (Erratt et al., 1999). The resultant Triassic Skagerrak Formation in the UK Quadrant 22 (i.e., the Heron field; well 22/29-5RE) consists of the Julius Mudstone Member and the Judy Sandstone Member (Figure 3.2), whereas the UK Quadrant 30 stratigraphy (i.e., the Judy field; wells 30/7a-7; 8; 8; 11Z; P3 & 30/13-5) consists of the Joanne and Judy sandstone members and the Jonathan and Julius mudstone members (Figure 3.3). The thick and laterally extensive mud-dominated units (e.g., Julius Mudstone Member) provide the main correlative units for the Triassic Skagerrak in the Central Graben (McKie and Audretsch, 2005).

4.4 Methodology

4.4.1 Sampling

Core samples and thin sections from one well in the Heron field (well 22/29-5RE) and six wells in the Judy field (wells 30/7a-7; 30/7a-8; 30/7a-9; 30/7a-11Z; 30/7a-P3; 30/13-5) have been examined in this study/chapter (Figure 3.2 & Figure 3.3).The 136 Heron core samples were chosen from 4300 to 4500 m below seafloor to cover the main reservoir facies of the Judy Sandstone Member (Figure 4.2). The 74 Judy core samples were chosen from 3400 to 4000 m below seafloor to cover the main reservoir fluvial facies for the Joanne and Judy Sandstone members (Figure 4.2).

4.4.2 Petrography

Optical porosity, grain size and the fraction of chlorite-coated grains were measured for this study. Optical porosity was measured by using the digital image analysis technique, jPOR (Grove and Jerram, 2011), on blue epoxy-impregnated thin sections. Grain size distribution was analysed by using the Leica QWin (V. 3.5.0) software on thin section micrographs and the fraction of chlorite-coated grains were measured by point counting

with 300 counts per thin section. The resulting data were used to select samples for additional petrographic analysis (i.e., intergranular volume (IGV) (Paxton et al., 2002), total cement volume, porosity-loss by mechanical compaction (COPL) and porosity-loss by cementation (CEPL) (Lundegard, 1992). The samples for further petrographic analysis were also selected by grain size (0.1 mm to 0.15 mm) to exclude grain size effects on the porosity and intergranular volumes. The intergranular volume and the total cement volume were measured by point counting with 300 counts per thin section.

All thin sections were highly polished to 30 µm and coated with carbon prior to analysis by a Hitachi SU-70 field emission gun scanning electron microscope (SEM) and equipped with an energy-dispersive detector (EDS). Scanning electron microscope analyses of thin section and bulk rock samples were conducted at 5 to 20 kV acceleration voltage with beam currents of 1.0 and 0.6 nA, respectively. Point analyses had an average duration of 2 min, whereas line analyses were dependent on length. SEM–EDS was used for rapid identification of chemical species and orientation on the sample.

4.4.3 One-dimensional basin modelling

The pore pressure modelling was achieved by one-dimensional burial modelling, which provides a good insight into the development of overpressure caused by disequilibrium compaction and pore fluid expansion due to increasing temperatures. Nevertheless one-dimensional models are limited in terms of integrating pore pressure mechanisms such as fluid transfer or hydrocarbon generation. The burial history simulations were undertaken using Schlumberger's PetroMod (V. 2012.2) software. The software is based on a forward modelling approach to calculate the geological evolution of a basin and burial history. The one-dimensional burial models are set up from the present-day well stratigraphy, well log lithology and lithological description of the modelled units (Table 4.1).

To create optimum one-dimensional models, it is essential have accurate palaeo-heat flow models. Several heat flow models have been published for the North Sea and especially for the Central Graben. The published models can be subdivided into two main types, the constant heat flow models (e.g., Schneider and Wolf, 2000) and the thermal upwelling models (e.g., Swarbrick et al., 2000; Carr, 2003; di Primio and Neumann, 2008). In this study we used the palaeo-basement heat flow and palaeo-surface temperature history published by Swarbrick et al. (2000). These data provide the best fit to the rifting events of the Central Graben, North Sea. The lithological unit types used in this model are mainly PetroMod default lithology types or mixed default lithology types based on well log descriptions and core analysis reports for the Central Graben lithologies. The only exceptions are the modelled chalk units, which were modified to match the specific characteristics of the North Sea non-reservoir chalk (Mallon and Swarbrick, 2002; Mallon et al., 2005; Swarbrick et al., 2010).

Time				Heron			Judy		
Start	**End**	**Formation**	**Subformation**	**T.**	**E.**	**Lithology**	**T.**	**E.**	**Lithology**
[Ma]	**[Ma]**			**[m]**	**[m]**		**[m]**	**[m]**	
53	0	Hordaland							
10	0		Hordaland 2	1407		shale	1424		shale
53	10		Hordaland 1	1396		shale	1357		shale
54.1	53	Tay Sand		15		silty sh			
54.3	54.1	Balder		18		shale	17		silty sh
54.8	54.3	Sele				shale	54		silty sh
54.45	54.3		upper Sele	7					
54.65	54.45		Rogerland	16					
54.8	54.65		lower Sele	8					
56.1	54.8	Forties		187		sst			
58.5	56.1	Lista		49		silty sh	16		shale
60	58.5	Andrew		51		silt			
59	58.5		Andrew Clay				18		shale
59.1	59		Andrew Sand				8		sst
59.7	59.1		Andrew Silt				50		silty sh
60	59.7		Andrew Clay				13		shale
61	60	Maureen		82		marl			
60.5	60		M.- Melange				37		sst
61	60.5		M.- Marl				55		marl
65	61	Ekofisk		94		chalk	28		chalk
74	65	Tor		459		chalk	226	0	chalk
93.5	74	Hod		335		chalk	154		chalk
98.9	93.5	Herring		9		chalk			
136.5	127	Valhall					22	0	sandy sh
129.5	127		upper Valhall	43	15	marl			
136.5	129.5		lower Valhall	20		marl			
160	144	upper Jurassic		0	50	sandy sh	0	50	sandy sh
180	160	mid Jurassic		0	20	shale	0	20	shale
188	184	Lias					3		shale
205.7	195	lower Jurassic		0	150	sst	0	150	sst
241.7	205.7	Skagerrak							
211	205.7		Joshua	0	50	silty sh	0	50	silty sh
214	211		Josephine	0	100	70%sst30%sh	0	100	70%sst30%sh
220.7	214		Jonathan	0	40	silty sh	38		silty sh
234.3	220.7		Joanne	23	375	70%sst30%sh	469		70%sst30%sh
237	234.3		Julius	41		silty sh	140		silty sh
241.7	237		Judy	339		70%sst30%sh	385		70%sst30%sh
251.2	241.7	Smith Bank		200		silty sh	200		silty sh
259	251.2	Zechstein		208		salt	208		salt

Table 4.1 Basic model parameters, with estimated depositional periods in millions of years, layer thicknesses (T.), modelled erosion (E.) and lithology for the Heron and Judy 1D burial history models.

4.5 Petrography and diagenesis of the Skagerrak Formation

The present-day reservoir quality of the Triassic Skagerrak samples is a cumulative product of depositional attributes, mechanical compaction and diagenesis during early and later stages of burial.

4.5.1 Grain size and porosity distribution

The 136 investigated samples from the Heron field show a wide range of porosity from below 1% up to a maximum of 31% (Figure 4.3). The porosity distribution shows a very high fraction (>90% of the samples) at porosities below 15% which leads to an average porosity of 3.9% for the Heron field samples. The grain sizes vary from coarse silt to medium-grained sand, with the majority of samples being very fine-grained and fine-grained (Figure 4.4). The average grain size is 0.147 mm. The Heron field samples have a narrow range of compositions with most in the range of arkosic to lithic-arkosic arenites (McKie and Audretsch, 2005; Nguyen et al., 2013).

The 74 samples from the six Judy field wells show porosities ranging from below 1% up to a maximum of 28% (Figure 4.3). The porosity distribution of the Judy field samples shows two-thirds of the porosities below 15% porosity which leads to an average porosity of 9.4% for the Judy field samples. The grain size distribution of the Judy field samples range from coarse silt to medium-grained sand, with the majority of samples being very fine-grained and fine-grained (Figure 4.4). The average grain size is 0.131 mm. The Judy field samples show a similar narrow range of compositions from arkosic to lithic-arkosic arenites (McKie et al., 2010; Nguyen et al., 2013).

4.5.2 Mechanical compaction

Mechanical compaction in sandstones can be identified by bending of weak grains (mica), deformed soft lithic grains, local fracturing and dissolution at grain contacts which produces concavo-convex or sutured/stylolitic grain contacts. The Heron field samples show features of low degrees of mechanical compaction such as deformation of soft lithic grains, slight bending of micas and concavo-convex grain contacts of some detrital quartz (4391 m; Figure 4.5A). In comparison, the Judy field samples show no mechanical compaction features and have being recognised to have a low compaction state at their current depth of burial (3558 m; Figure 4.5B).

4.5.3 Diagenetic cements and grain coatings

The diagenesis of the Skagerrak Formation has been the subject of a number of research papers (e.g., Smith et al., 1993; Weibel, 1998; Kape et al., 2010; Nguyen et al., 2013). These have highlighted the complex diagenetic history of the sandstone reservoirs and how grain size and facies play an important role. The main diagenetic cements recognised include quartz, localised carbonate (ferroan dolomite) and feldspar, and early precipitates of halite cement as identified by Nguyen et al. (2013). Detrital grain coatings such as chlorite are common and their presence has been correlated to low quartz cement volumes. The major cement types and detrital grain clay coatings important for reservoir quality in this study are discussed in more detail below.

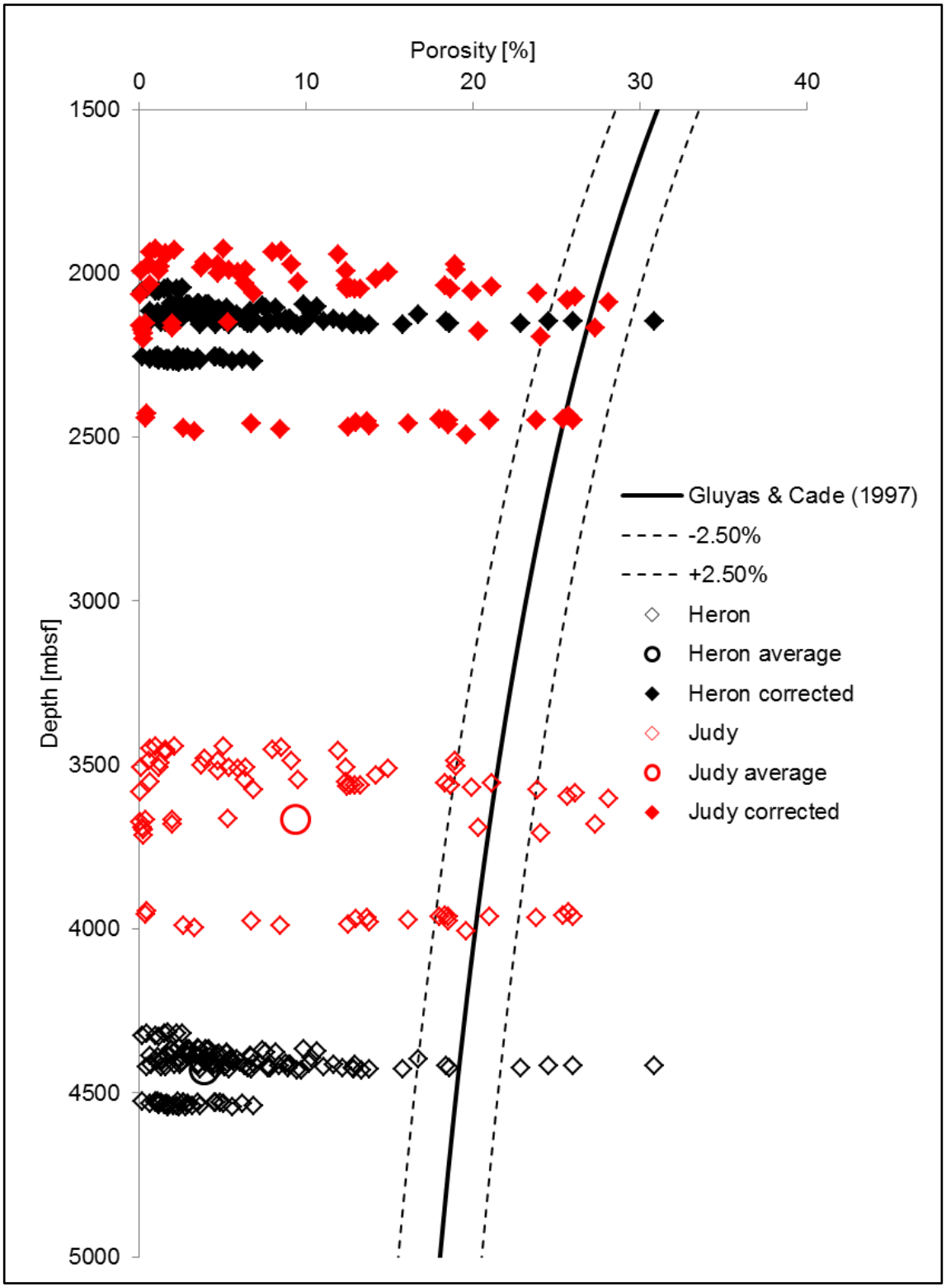

Figure 4.3 Optical porosity distribution with original sample depth and the corrected sample depth (calculated after Gluyas and Cade (1997)) and the porosity-depth relationship after Gluyas and Cade (1997).

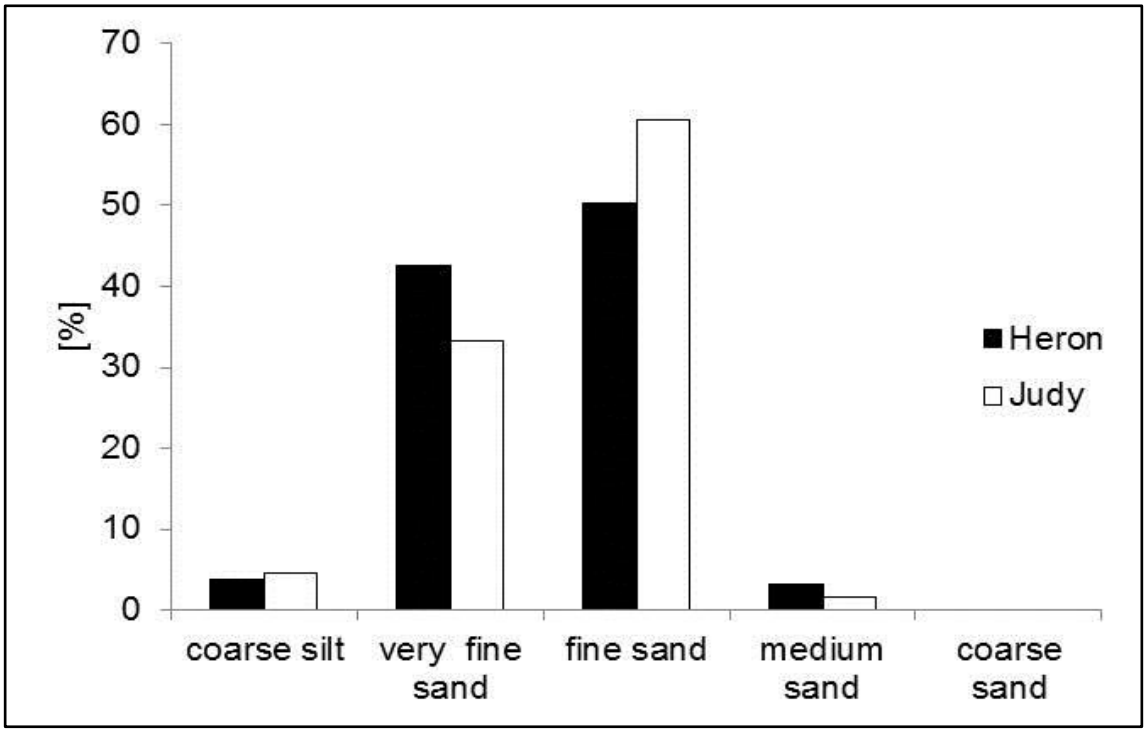

Figure 4.4 Grain size distribution for samples from the Heron (136) and the Judy (74) fields.

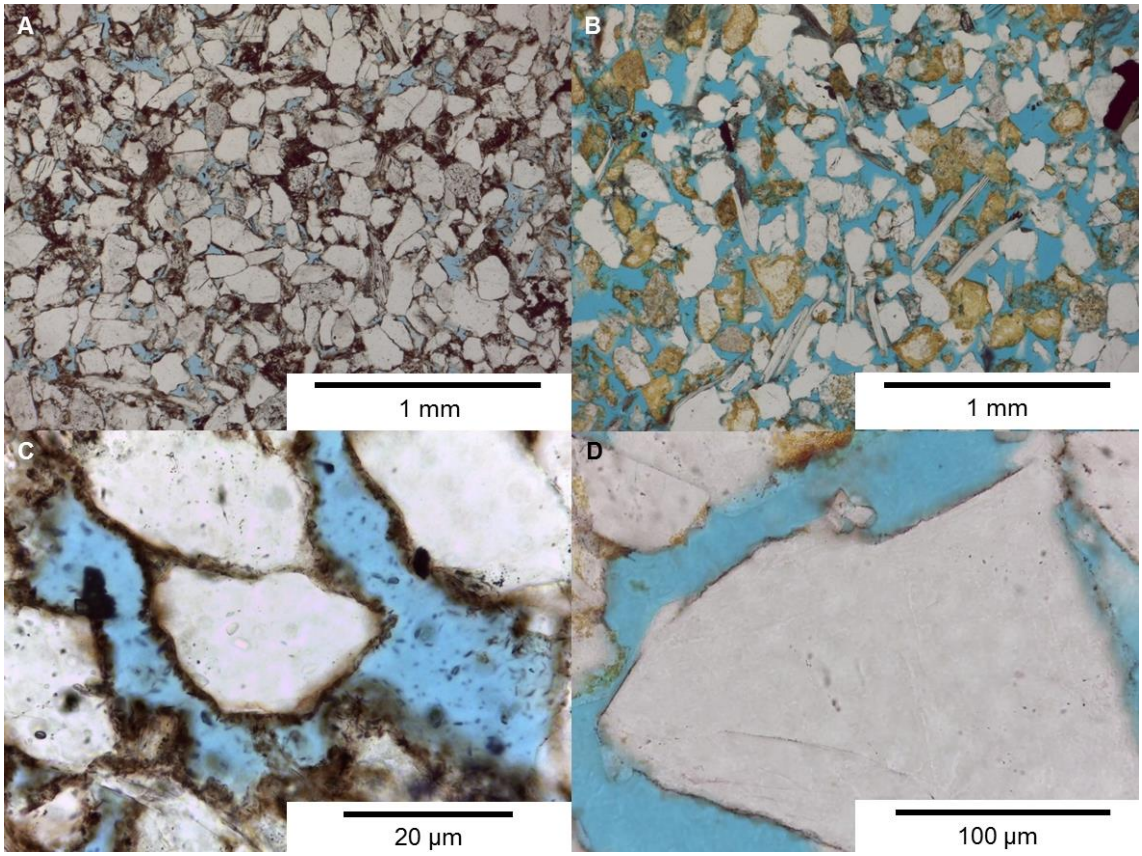

Figure 4.5 Micrographs from (A) the Heron field sample 15591'10"with mechanical compaction features (e.g., bended mica grain, concavo-convex grain); (B) the Judy field, with no mechanical compaction features and high porosity (30/7a-8, 11763.00); (C) the Heron field sample 15599'10" with thick and complete covering chlorite coating; (D) the Judy field with thin, partly covering chlorite coating (30/7a-8; 11731.00).

4.5.4 Quartz cements

The quartz cements recognised in this study were precipitated at two diagenetic stages. An earlier microquartz overgrowth is present below and in between the chlorite grain coatings, and a later macroquartz overgrowth is present on quartz grain surfaces without chlorite coatings or at breaks in the chlorite grain coatings. The term microquartz overgrowth is used here for polycrystalline growth patterns of individual micro-sized (1 μm to 5 μm in length) quartz crystals, which are in optical continuity or discontinuity with the detrital quartz grain. In comparison, the macroquartz overgrowth is defined as syntaxial quartz overgrowth larger than 20 μm in optical continuity with the detrital quartz grain.

Minor amounts of macroquartz (<<1% bulk volume) are recognised in the Heron Cluster dataset and typically are only present at rare gaps or breaks in the chlorite grain coatings. Microquartz is more common and can be observed between the detrital quartz grain and the well-developed chlorite grain coatings. The microquartz overgrowths tend to fill small cavities in the detrital quartz grain surface and infill the void space between the detrital surface and the chlorite crystals. Hydrothermal experiments of fluvial-deltaic sediments at similar temperatures as encountered in the Skagerrak Formation (~160°C) have identified that quartz cement can fill significant microporosity within diagenetic chlorite coats, potentially affecting mechanical and petrophysical rock properties (Ajdukiewicz and Larese, 2012).

Quartz cements play a more significant role in the Judy field data sets, where macroquartz overgrowths commonly occur in all wells but are particularly common in the deepest wells (Figure 4.5B). In the deeper buried sandstones, macroquartz overgrowths commonly occur where there are breaks in the thinner, less well developed

chlorite coatings. Furthermore, small syntaxial quartz overgrowths were also observed on grain surfaces beneath chlorite grain coatings.

4.5.5 Chlorite grain coatings and cement

Detailed SEM analysis identified that chlorite is the most common clay grain coating for all data sets in this study. Chlorite coatings represent over 95% of the clay mineral coatings recognised but commonly occur in close association with illite and mixed-layer chlorite-smectite or illite-smectite. A complex structural pattern for the chlorite grain coatings is observed in all cases, regardless of coating thickness. A root zone (*sensus* Ehrenberg, 1993; Pittman et al., 1992) with platey crystals parallel to the surface of the detrital grain is superseded by well-defined platey to curly crystals that grew perpendicular to the detrital surface (Figure 4.6A).

The Heron field samples show in general a high fraction (80% to 100%) of chlorite-coated grains (Figure 4.7). Grain coatings are very well developed and range from 1 μm to >20 μm thick, with an average thickness of 11 μm. The coatings are generally absent at grain-grain contacts, but show a very high detrital grain surface coverage of around 95% (Figure 4.5C).

The fraction of the chlorite-coated grains in the Judy field samples is more variable, ranging between 10% and 70% (Figure 4.7). Chlorite grain coatings vary in thickness from 1 μm to 15 μm, with average thicknesses of ~7 μm. The coatings are absent at grain-grain contacts and commonly incomplete in their surface coverage of detrital quartz grains (Figure 4.5D). Furthermore, there appears to be a direct relationship between the measured porosity of the sandstone data sets and the fractions of chlorite-coated grains (Figure 4.8). The Heron data set demonstrates a constant lower porosity (<15%) for lower fractions of coated grains (<15%), whereas high porosity of up to

30% for higher fractions (>50%) of chlorite-coated grains are common. The Judy data set, in contrast, does not illustrate such a close relationship between porosity and percentage of coated grains (Figure 4.8).

Authigenic chlorite cements are the most important and effective grain coating in the Skagerrak sandstones in terms of limiting early extensive quartz cementation. However, pore-filling chlorite, illite and chlorite-illite mixtures commonly occur in the sandstones from the Heron samples. The pore-filling cements comprise small chlorite plates that are orientated parallel to each other and arranged with a denser packing than seen for grain coatings (Figure 4.6B). Chlorite-coated grains are locally covered by pore-filling chlorite cements. They represent between 10% and 15% of the bulk rock sample and can fill up to 50% of the remaining intergranular volume (Figure 4.5A). In the Skagerrak sandstones from the Judy field authigenic pore-filling chlorite is rarely identified (<5%), (Figure 4.5B). This may in part reflect the less well developed chlorite grain coatings and occurrence in the Judy field compared to the Heron field (McKie et al., 2010; Nguyen et al., 2013).

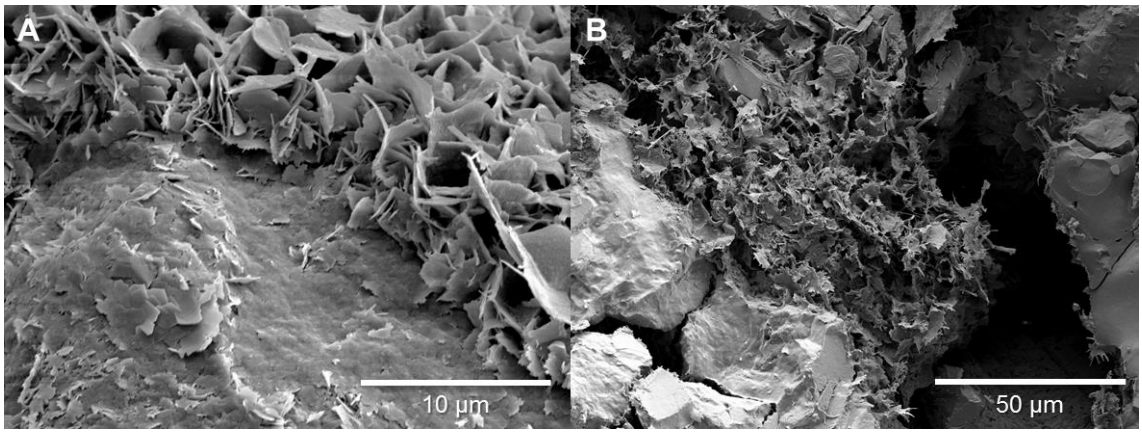

Figure 4.6 SEM images from (A) the Heron field sample 15599'10" with a clay coating root zone of crystals attached parallel to the detrital grain surface and a second layer of well-defined chlorite crystals oriented perpendicular to the detrital surface; and (B) the Heron field sample 15714'7" with a pore filling clay mixture of chlorite and illite.

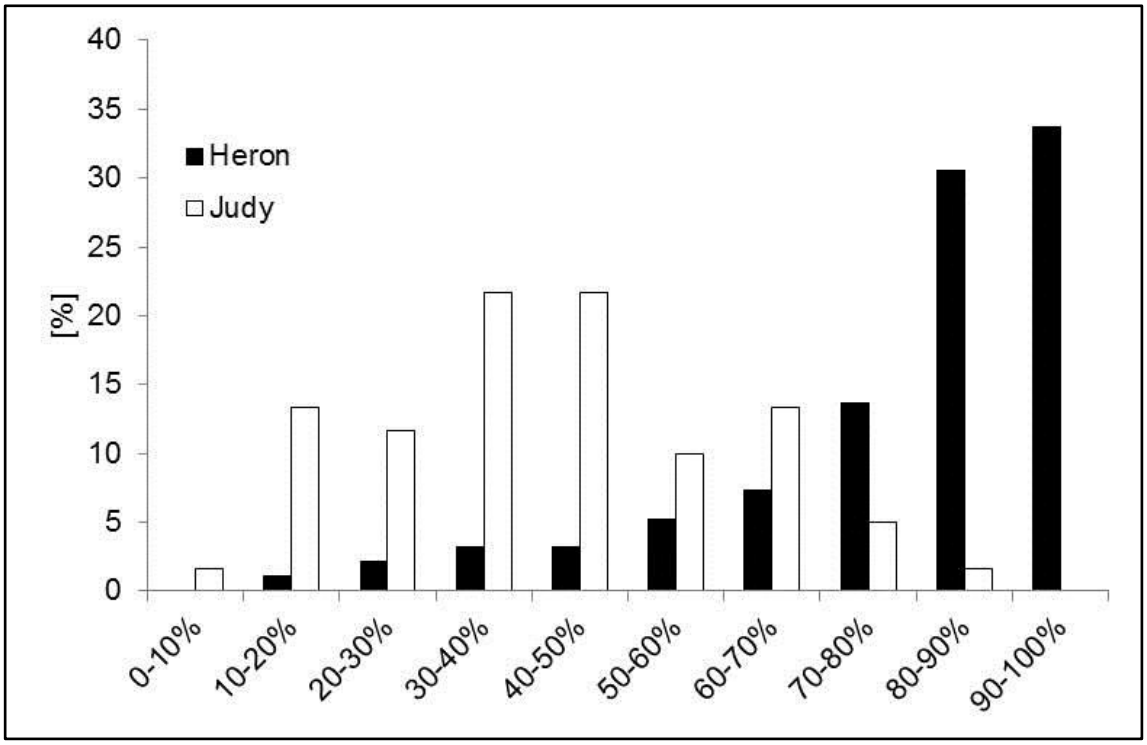

Figure 4.7 Fraction of chlorite-coated detrital grains per 300 counts for the 136 Heron samples and the 74 Judy samples.

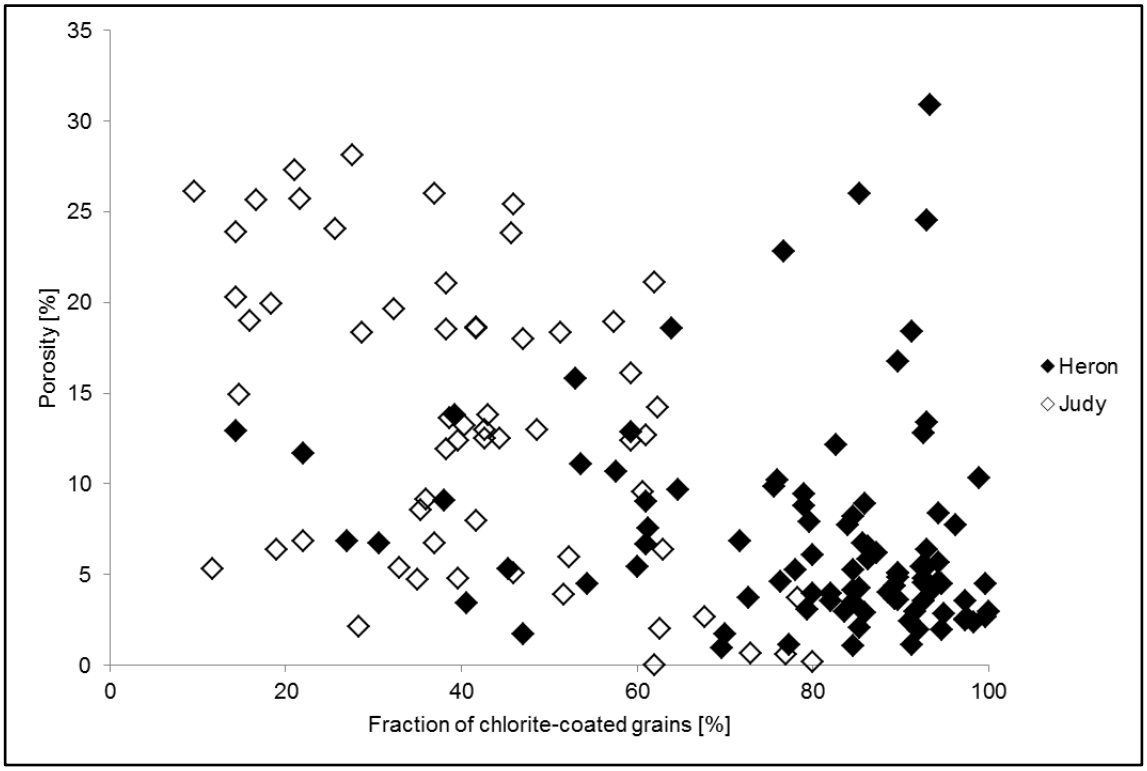

Figure 4.8 Measured porosity versus fraction of chlorite-coated detrital grains for the Heron and Judy samples.

4.5.6 K-feldspar dissolution

K-feldspar dissolution and alteration can be observed in both sample sets but is less common in the Heron field samples (Figure 4.5). K-feldspar dissolution occurs generally at a late burial stage, after the precipitation of the chlorite grain coating. This is indicated by chlorite grain coatings which preserve the original K-feldspar grain shape of the partly or fully dissolved grain.

4.5.7 Intergranular volume and total cement volume

Intergranular volume and total cement volume measurements were undertaken on samples with grain sizes between 0.1 mm and 0.15 mm to reduce the effect of grain-size variations on the measurements. The intergranular volume, or minus-cement porosity, is the sum of intergranular pore space, intergranular cement and depositional matrix (Paxton et al., 2002). The results of the IGV measurements show wide variations for both sample sets. The Heron field intergranular volumes vary from 13% to 44%, with the majority between 20% and 30% and a mean of 22.8%. The Judy field intergranular volumes range between 20% and 42%. The Judy field IGV plots in two clusters, between 20% to 25% and 31% to 42%, with an overall mean of 24.6% (Figure 4.9). The total cement volume represents the volume of all pore-filling diagenetic cements, including quartz, chlorite, illite and other clay mineral cements. The total cement volume is used to calculate the porosity loss by mechanical compaction and the porosity loss by cementation (Lundegard, 1992). The total cement volume varies for the Heron samples from 8% up to 37%, with an average of 19%. The Judy field samples show total cement volumes from 4% to 35%, with a lower average of 12% (Table 4.2). The measured total cement volume (C) can be used to calculate the porosity losses caused by compaction ($COPL$) and cementation ($CEPL$) using the following equations after Lundegard (1992):

$$COPL = P_i - \left(\frac{(100 - P_i) P_{mc}}{100 - P_{mc}} \right) \quad (4.1)$$

$$CEPL = (P_i - COPL) \left(\frac{C}{P_{mc}} \right) \quad (4.2)$$

where P_i is the initial or depositional porosity and P_{mc} is the intergranular volume or minus-cement porosity calculated from by subtracting the total cement volume, *C*, from the total optical porosity, P_o (Table 4.2). The calculated porosity losses *COPL* and *CEPL* are only accurate if three conditions are met. First, the assumed initial porosity P_i must be correct. Second, the amount of cement derived by local grain dissolution must be negligible or known. And third, the amount of framework mass exported by grain dissolution must be negligible or known (Lundegard, 1992). The initial or depositional porosity assumed for the Skagerrak sandstones samples is 45% (Beard and Weyl, 1973; Lundegard, 1992). The COPL-CEPL results show porosity loss for both sample sets was predominantly by mechanical compaction (Figure 4.10), with averages of 26% and 24% for the Heron and the Judy sample sets, respectively. Furthermore, the results show porosity loss by cementation of 15% for the Heron sample set, 5% higher than the porosity loss by cementation of 8% for the Judy sample set (Table 4.2).

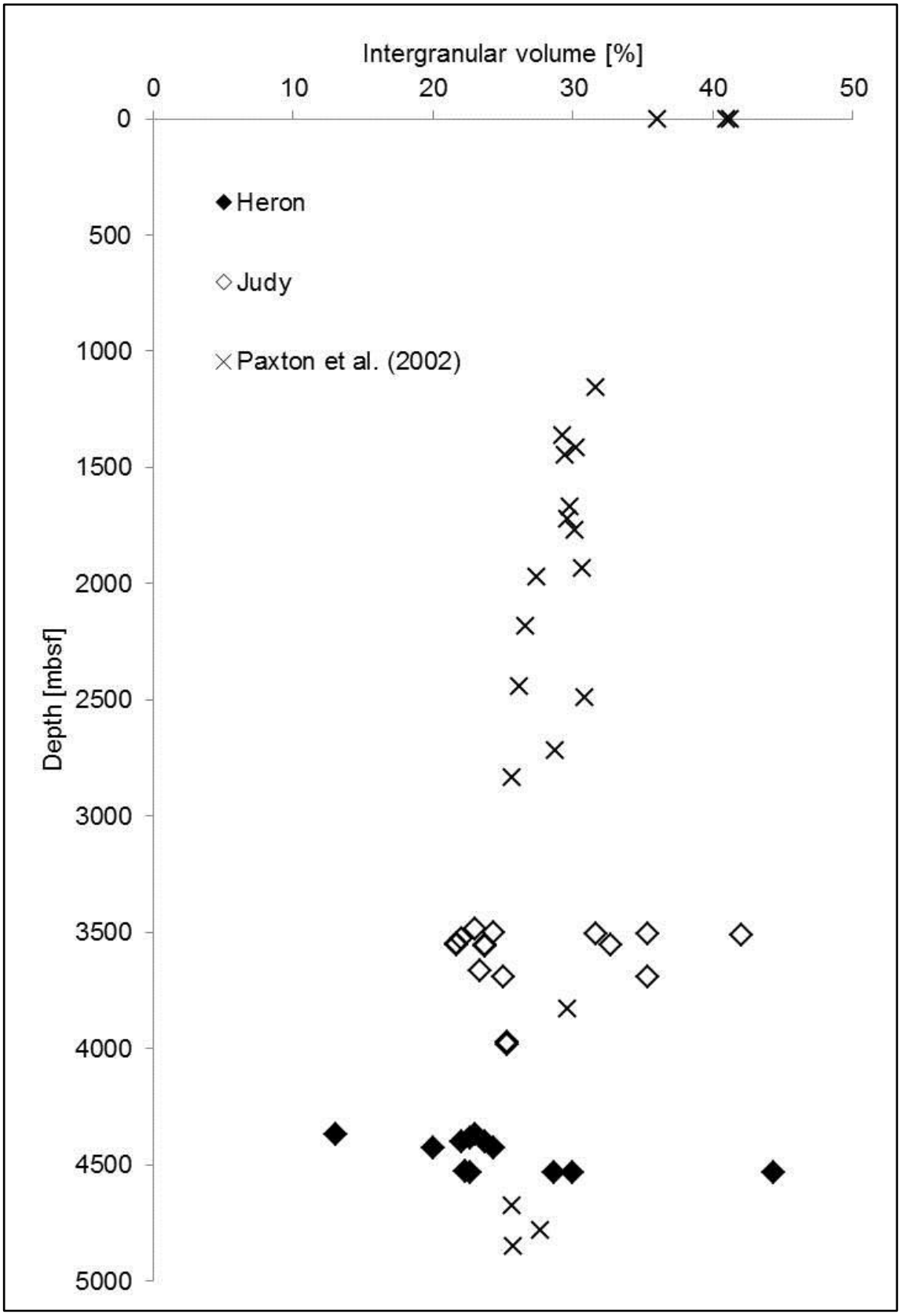

Figure 4.9 Intergranular volume (IGV) versus depth for the Heron samples and the Judy samples, with observed reference IGV from Paxton et al. (2002).

Field	*C*	P_o	P_{mc}/*IGV*	*COPL*	*CEPL*
	[%]	[%]	[%]	[%]	[%]
Heron	17.00	6.00	23.00	28.57	12.14
	11.00	2.00	13.00	36.78	6.95
	15.00	7.67	22.67	28.88	10.67
	11.67	10.33	22.00	29.49	8.23
	18.00	5.67	23.67	27.95	12.97
	8.33	11.67	20.00	31.25	5.73
	14.33	10.00	24.33	27.31	10.42
	21.00	1.33	22.33	29.18	14.87
	19.67	3.00	22.67	28.88	13.99
	28.67	1.33	30.00	21.43	22.52
	37.00	7.33	44.33	1.20	36.56
	28.67	0	28.67	22.90	22.10
Average	19.19	5.53	24.72	26.15	14.76
Judy	11.00	12.00	23.00	28.57	7.86
	5.00	19.33	24.33	27.31	3.63
	20.33	11.33	31.67	19.51	16.37
	35.67	6.33	42.00	5.17	33.82
	5.67	16.00	21.67	29.79	3.98
	15.67	17.00	32.67	18.32	12.80
	13.00	10.33	23.33	28.26	9.33
	7.33	17.67	25.00	26.67	5.38
	13.00	22.33	35.33	14.95	11.06
	20.00	15.33	35.33	14.95	17.01
	8.67	13.33	22.00	29.49	6.11
	15.67	6.00	21.67	29.79	11.00
	4.33	19.33	23.67	27.95	3.12
	5.67	18.00	23.67	27.95	4.08
	10.00	18.67	28.67	22.90	7.71
	4.00	15.67	19.67	31.54	2.74
	10.00	15.33	25.33	26.34	7.37
	14.00	11.33	25.33	26.34	10.31
Average	12.17	14.74	26.91	24.21	9.65

Table 4.2 Total cement volume (*C*), measured porosity (P_o), minus-cement porosity (P_{mc}) or inter-granular volume (*IGV*), porosity-loss by mechanical compaction (*COPL*) and porosity-loss by cementation (*CEPL*) for the Heron and Judy sample sets.

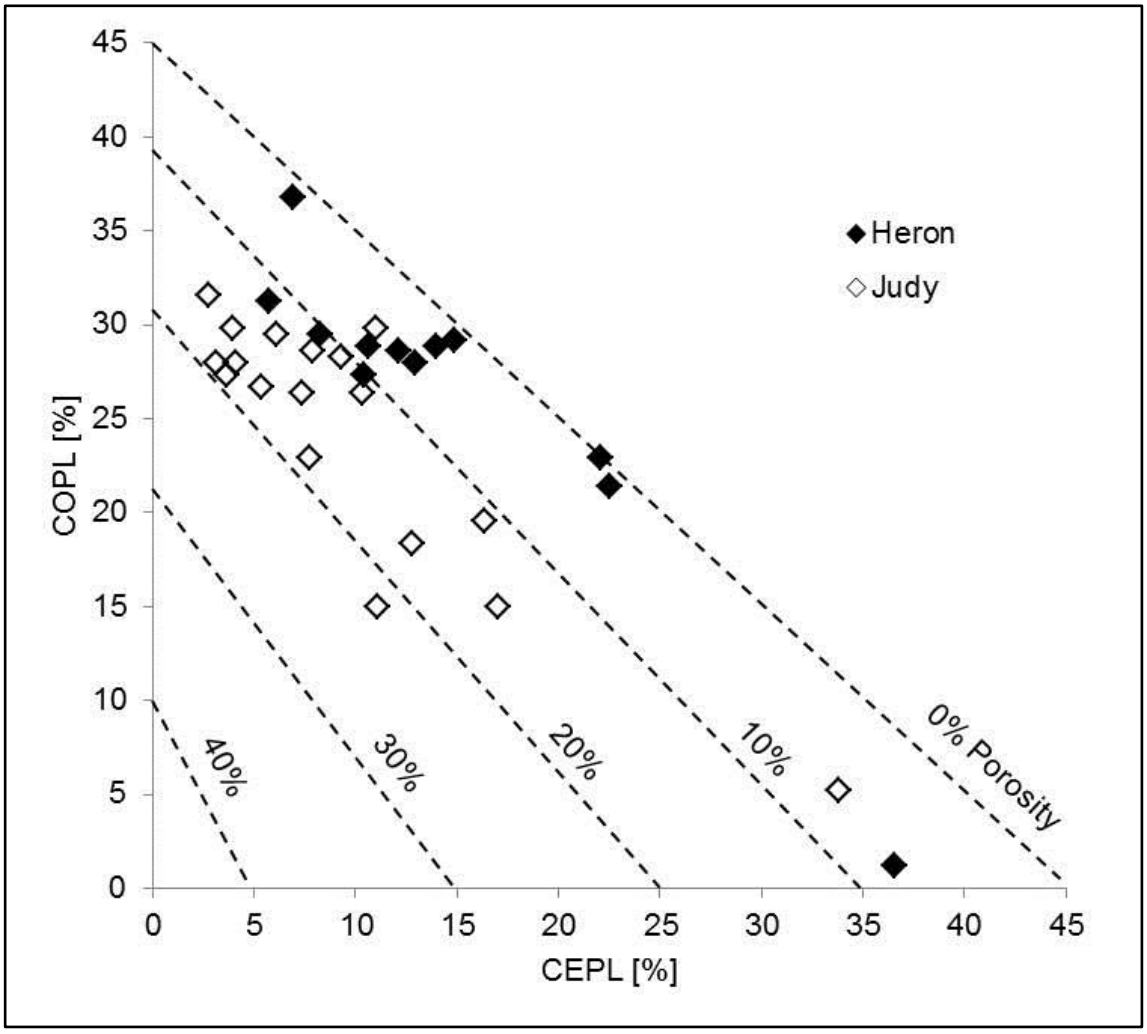

Figure 4.10 Mechanical compaction (COPL) and cementational (CEPL) porosity-loss for the Heron and the Judy sample sets. Calculated after Lundegard (1992).

4.5.8 Burial history modelling

The one-dimensional burial history models show the Triassic Skagerrak units at maximum burial depth and maximum temperature at present day (Figure 4.11). The Skagerrak Formation experienced a long shallow burial phase (<1800 m below seafloor) between deposition and 80 Ma, followed by a phase of rapid burial to its present burial depths. During this rapid burial phase, overpressure started to build up at around 80 Ma in the Heron field (Figure 4.12A) and at around 70 Ma in the Judy field (Figure 4.12B). The onset of the overpressure in both fields occurred during shallow burial at around 650 m burial depth for the Heron field (Figure 4.12A) and around 500 m burial depth for the Judy field (Figure 4.12B). The pore fluid pressure increased during ongoing burial to a present-day maximum for the whole study area. The increase in pore fluid pressure causes a reduction in vertical effective stress with ongoing burial (Figure 4.12). The present-day pore fluid pressures for both wells increase downwards through the chalk units (Ekofisk, Tor and Hod formations) to the Triassic Skagerrak units (Figure 4.13). In this burial model only disequilibrium compaction and fluid expansion have been taken into account as overpressure generating mechanisms. Nevertheless, the models for the Judy field, based on the well 30/7a-9 (Figure 4.13A), and the Heron field, based on the well 22/29-5 (Figure 4.13B), show pore fluid pressure trends in agreement with measured RFT pressure data trends.

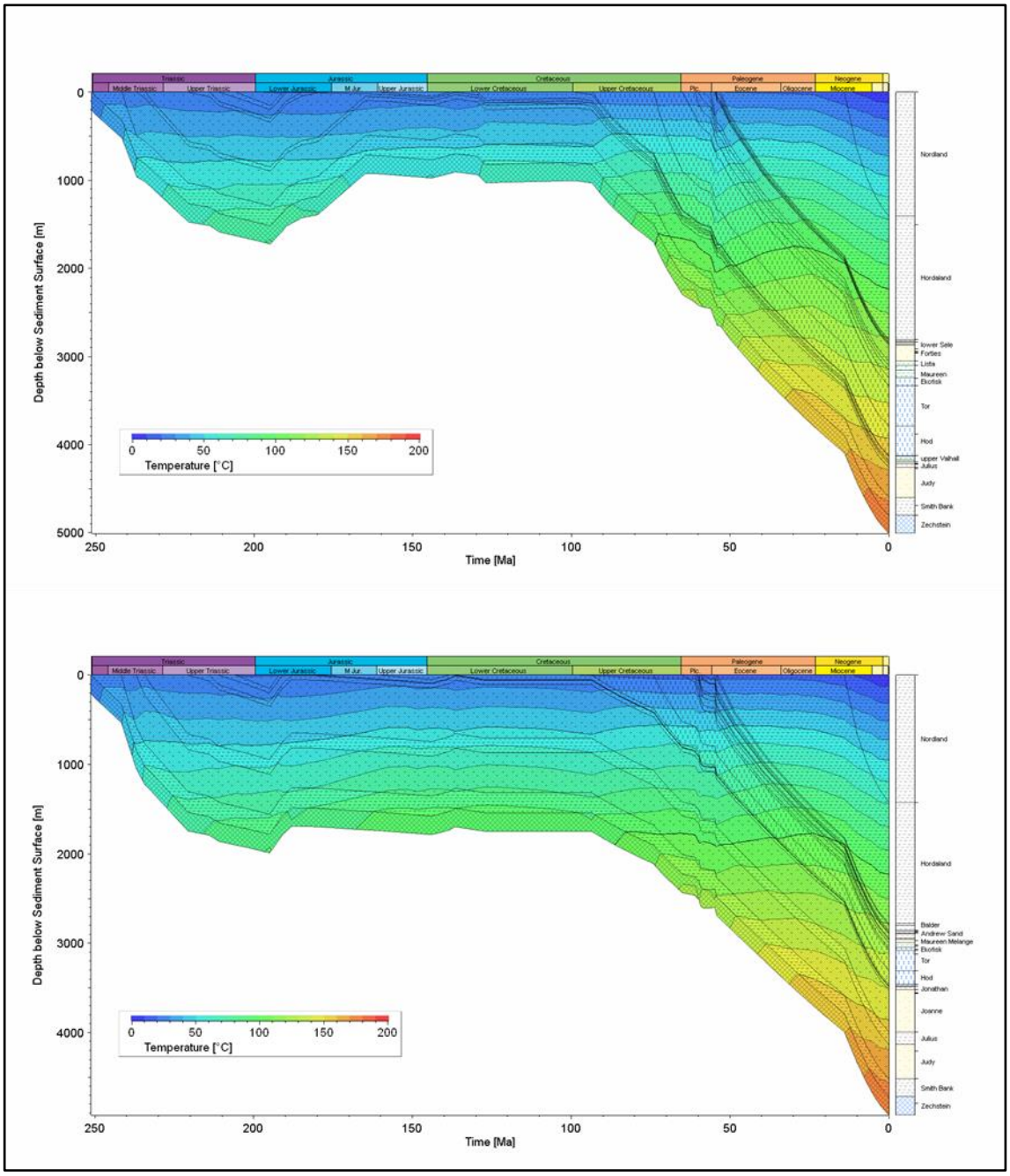

Figure 4.11 1D burial-temperature history plot for Heron well (22/29-5) (top) and Judy well (30/7a-9) (bottom).

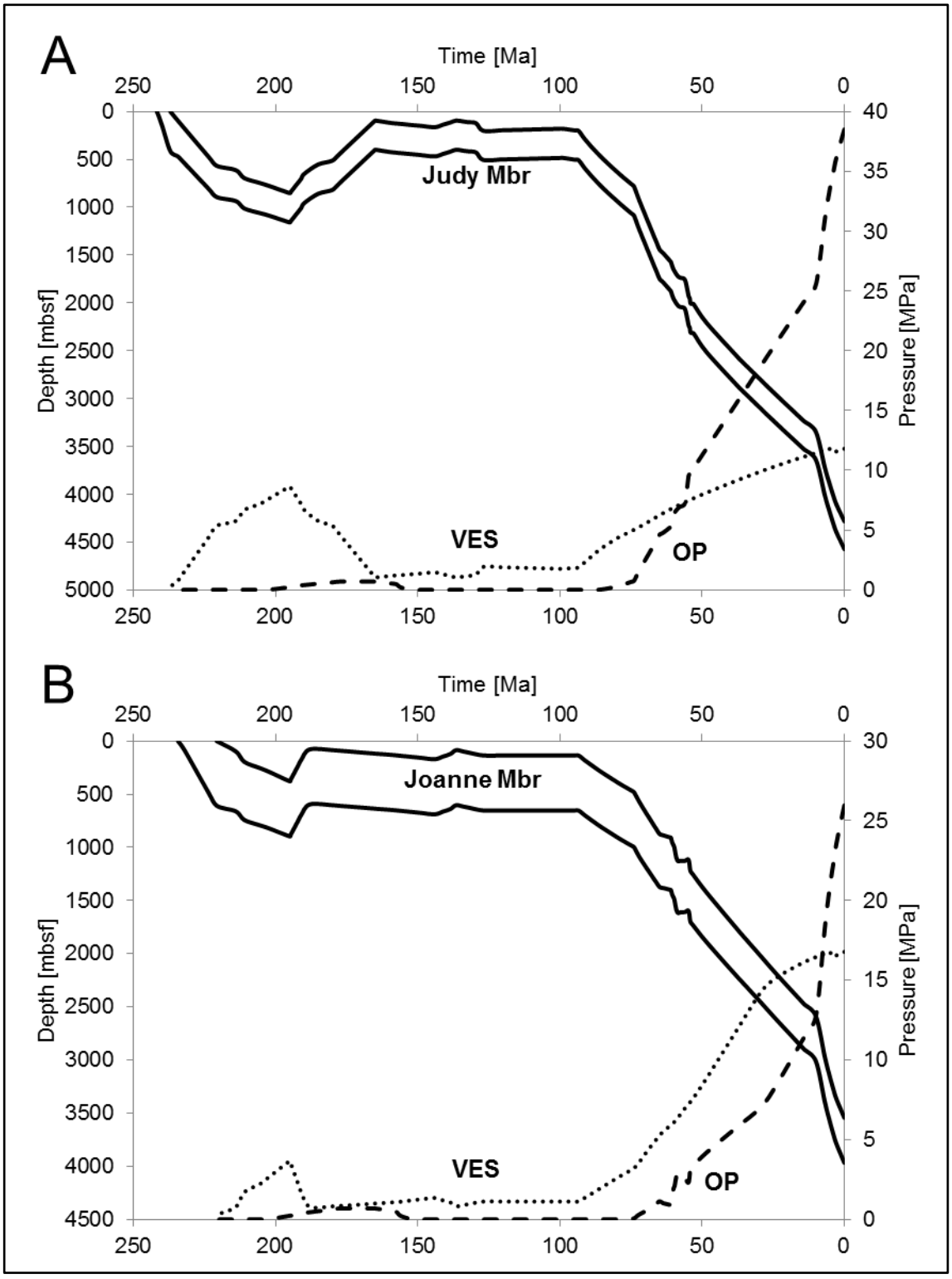

Figure 4.12 Burial history, pore fluid overpressure (OP) and vertical effective stress (VES) development for the Judy Sandstone Member, the uppermost succession within the Skagerrak Formation in the Heron well (22/29-5) (A), and the Joanne Sandstone Member, the uppermost succession within the Skagerrak Formation in the Judy well (30/7a-9) (B).

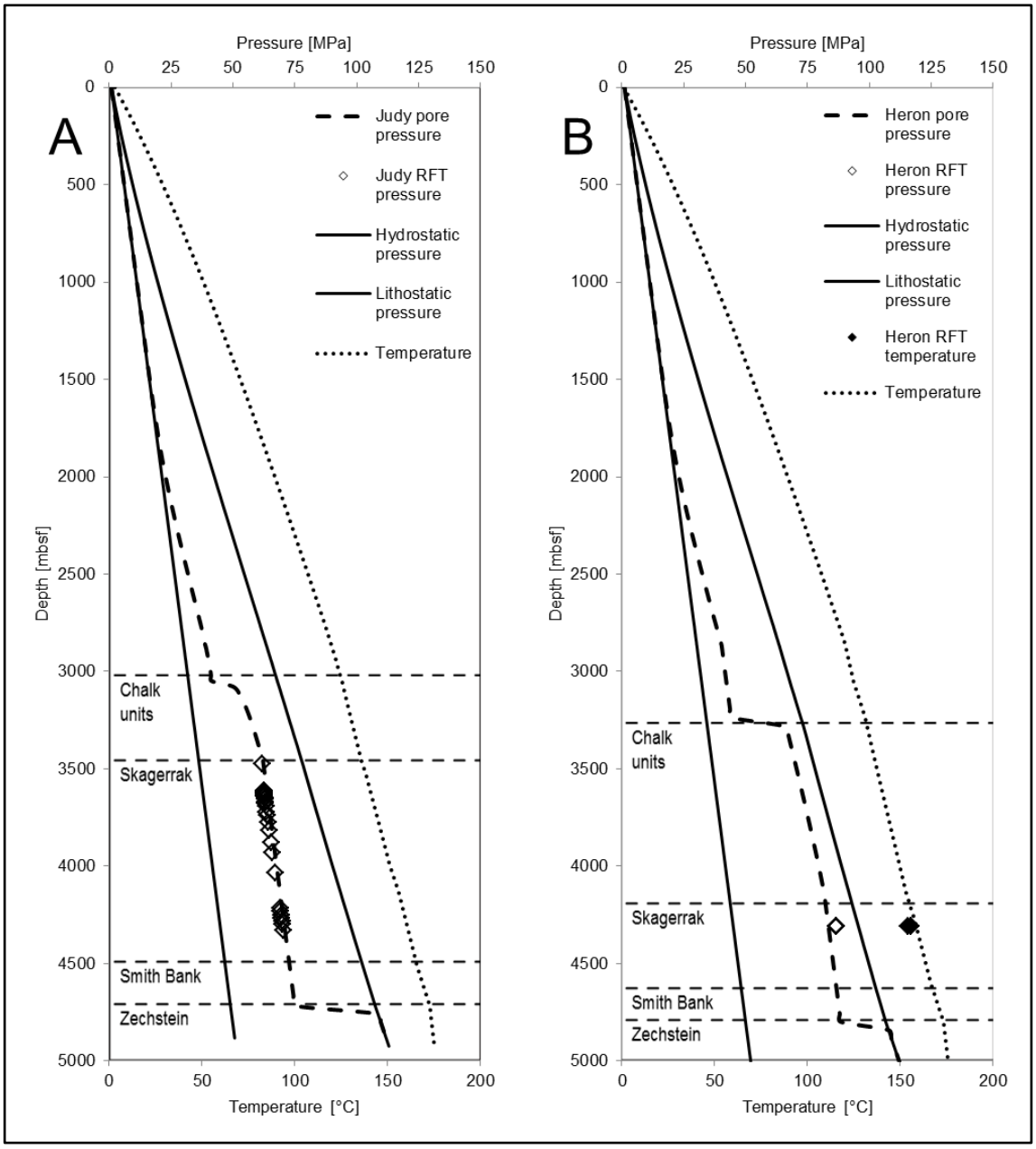

Figure 4.13 Modelled formation pressures caused by disequilibrium compaction with hydrostatic pressure, lithostatic pressure and formation temperature, measured RFT pressure and temperature data for the Judy field (30/7a-9) (A) and the Heron field (22/29-5) (B). Pore fluid pressure can exceed 80 MPa at depths between 4000 to 5000 m bsf (m below seafloor) in the Skagerrak Formation.

4.5.9 Overpressure-depth correction

The modelled pore fluid overpressure, generated by disequilibrium compaction, can be used to estimate the equivalent depth where the measured porosity would be found on the normal compaction curve, i.e., if the pore pressure were hydrostatic. As the normal

compaction curve, we used the porosity-depth relationship of Gluyas and Cade (1997), which is based on experimental data from laboratory compaction experiments for uncemented sandstones under hydrostatic burial:

$$\varphi = 50\exp\left(\frac{-10^{-3}z}{2.4+5\times10^{-4}z}\right) \tag{4.3}$$

where φ is porosity expressed as a percentage and z is depth in metres. The depth and the rate of mechanical compaction are corrected by scaling the porosity to vertical effective stress, rather than to depth (Gluyas and Cade, 1997). The compaction-only porosity-depth relationship is:

$$z' = z - \left(\frac{u}{(\rho_r - \rho_w)\times g\times(1-\varphi_\Sigma)}\right) \tag{4.4}$$

where *z'* is the equivalent depth in metres, *z* is the depth in metres, *u* the overpressure in pascals, ρ_r is the rock density in kilograms per cubic metre (typically 2650 kg/m^3), ρ_w is the water density in kilograms per cubic metre (typically 1050 kg/m^3), *g* is the gravity in metres per second squared (typically 9.8 m/s^2), and φ_Σ is the average porosity of the overburden expressed as a fraction (typically 0.2). The corrected depths for the Heron field samples are around 2200 m shallower, corrected from ~4400 m depth to ~2200 m depth (Figure 4.3). The corrected depths for the Judy field samples are around 1500 m shallower, corrected from ~3500 m to ~2000 m depth (Figure 4.3). The formerly anomalous high porosities of 25% to 30% in the Skagerrak sandstones are within the range of the porosity-depth relationship introduced by Gluyas and Cade (1997) at their corrected depths.

4.6 Discussion

4.6.1 Interpretation and diagenetic development

All the observed petrographic features can be linked into a relative timing sequence for both reservoirs. The eodiagenetic, dolomitic cements were precipitated early during the initial phase of mechanical compaction and decrease of IGV. This is indicated by high intergranular volumes (close to depositional IGV) in the dolomitic-cemented samples in both samples sets. The dolomite cement is likely to have been sourced by reworked calcrete or dolocrete fragments (McKie and Audretsch, 2005), as indicated by the association of the dolomitic cements with slightly deformed clay clasts. Mechanical compaction had the strongest impact during the shallow burial phase when mechanical compaction dominated (<2500 m), despite the shallow onset of the pore fluid overpressure which reduced the VES and probably reduced the amount of mechanical compaction. The dolomitic cements were followed by the early microquartz overgrowths, which are proven by the lack of microquartz on detrital grains surrounded by dolomitic cement. The following phase of authigenic grain-coating chlorite precipitation is probably the most important diagenetic phase for the Heron field and the Judy field. The authigenic chlorite covers the earlier microquartz on the detrital quartz grains. The authigenic chlorite coatings possibly developed during the early mesodiagenesis, at temperatures of 60°C to 100°C. Their origin was probably from precursor clay minerals such as smectite, berthierine and kaolinite (Grigsby, 2001; Worden and Morad, 2003; Berger et al., 2009) or the dissolution and reprecipitation of syndepositional chlorite (Anjos et al., 2003). These authigenic chlorite grain coatings inhibited a further stage of quartz cementation above temperatures of 70°C (Worden and Morad, 2000) in the Heron field and partly inhibited further quartz cementation in the Judy field. The later stage macroquartz cement is present at the non-covered detrital

quartz grain surfaces. Due to the incompleteness of the authigenic coatings, the amount of macroquartz cement is higher in the Judy field samples. The grain-coating chlorite was also followed by a stage of extensive feldspar dissolution in the Judy field and, less prominently, in the Heron field. The feldspar dissolution phase occurred with, or was closely followed by, a phase of secondary precipitation of pore-filling chlorite and illite which is likely to have been synchronous with the feldspar alteration and dissolution (Worden and Morad, 2003).

4.6.2 Role played by chlorite grain coatings

The occurrence of quartz overgrowths is closely related to chlorite grain coatings (Pittman and Lumsden, 1968; Dixon et al., 1989; Pittman et al., 1992; Ehrenberg, 1993; Anjos et al., 2003; Berger et al., 2009; Ajdukiewicz and Lander, 2010; Bahlis and De Ros, 2013). Therefore, the role played by the chlorite grain coatings is important for the maintenance of primary porosity. This role could not be more different in the two investigated reservoirs.

The Heron field chlorite coatings are thickly developed and, in the main, cover the detrital quartz grain surfaces completely (Figure 4.5A & Figure 4.5C). The general appearance of the fully covering, robust chlorite grain coatings with their well-developed root zone and their second layer of well-defined perpendicular-oriented crystals seem to have been key in inhibiting extensive macroquartz cement overgrowth at temperatures above 70°C (Worden and Morad, 2000). Similar effects on quartz overgrowth have been described by Dixon et al. (1989), Pittmann et al. (1992), Ehrenberg (1993), Anjos et al. (2003), Bahlis & De Ros (2013), Berger et al. (2009) and Ajdukiewicz & Lander (2010) for other formations with thick and fully covering chlorite grain coatings. The inhibition of quartz cement is potentially the cause of the

correlation between porosity and the fraction of coated grains in the Heron field samples (Figure 4.8).

The investigated Judy field samples show thin chlorite grain coatings with major gaps where macroquartz overgrowths are present (Figure 4.5D). The impact of grain coatings on the porosity maintenance is highly dependent on their completeness (Ajdukiewicz and Lander, 2010; Ajdukiewicz and Larese, 2012). Despite their incomplete coverage, the Judy field coatings are still inhibiting extensive quartz cement precipitation on around 80% of the detrital surfaces. The main nucleation points for the quartz overgrowth are the gaps in the chlorite coatings on the surface of the detrital quartz grains where macroquartz overgrowths can be observed (Figure 4.5D). Nevertheless, macroquartz overgrowth is less extensive than expected with the incomplete coating coverage in the Judy field samples. This could be due to a low concentration of dissolved silica in the pore fluid. The Judy reservoir experienced pore fluid overpressure at relatively shallow depths, which leads to a semi-closed system, low vertical effective stress, less mechanical compaction and less pressure dissolution at grain contacts. Therefore, less silica was dissolved in the reservoir and due to the pore fluid overpressure, lateral transfer of pore fluid is less likely to have occurred. This could be a possible explanation for a lower ratio of dissolved silica in the Judy field reservoir.

Nevertheless, it has been reported that thick and extensive chlorite coatings could reduce the reservoir quality by decreasing the porosity and, probably of greater significant, the permeability by bridging and closing of pore throat (Anjos et al., 2003; Bahlis and De Ros, 2013). Therefore, it seems that the thickly developed chlorite coatings in the Heron reservoir have also had contrary impacts on the porosity by bridging from one grain coating to another across open pore space and filling that pore space with chlorite cement. Some of the thick chlorite coatings actually have a net effect

of decreasing the overall porosity, and also reduce the permeability of the reservoir sandstones instead of increasing it. This observation is confirmed by the 5% higher cementational porosity loss in the Heron samples compared with the Judy samples (Figure 4.10). This porosity reduction is not caused by quartz cementation but by bridging and pore-filling chlorite.

4.6.3 Effect of pore fluid overpressure on porosity preservation

The positive effect of pore fluid pressure on the maintenance of primary porosity is well known, according to Terzaghi's concept of effective stress, and overpressured reservoirs are often associated with higher porosities. However, a combination of magnitude and timing of onset of overpressure needs to be considered in reservoirs with enhanced primary porosity preservation. Pore fluid overpressure can arrest and slow down mechanical compaction, but cannot increase porosity. Therefore the timing of the onset of overpressure is the crucial factor in maintaining primary porosity by overpressure to depth. Furthermore, overpressured reservoirs are often closed or at least semi-closed systems with minimal or no external fluid exchange, so they have evolved in their own fluids (Jeans, 1994). The exclusion of external sources reduces the number of possible cementation processes in the reservoir and allows better predictions of them.

The overpressure onset in the Heron field was around 80 Ma, which provides an onset burial depth of around 650 m for the investigated samples (Figure 4.12A). The pore fluid overpressure then started to ramp up significantly due to the rapid burial and the massive overlaying packages. The vertical effective stress on the Heron field grain framework further increased during the rapid burial of the Triassic Skagerrak units, but the rapidly increasing pore fluid overpressure reduced the rate of increase for the vertical effective stress dramatically (Figure 4.12). This slower than expected vertical effective stress increase from the shallow burial depth of 650 m reduced the effects of

mechanical compaction on the grain framework significantly. This reduced mechanical compaction can be seen in the investigated samples, where mechanical compaction characteristics of a medium compaction state are present (slight bending mica, grain contact dissolution with concavo-convex contacts), but no features of a high compaction state (sutured or stylolitic grain contacts and grain fracturing) (Figure 4.5A) as would be expected in this deep burial stage.

The overpressure onset in the Judy field was around 70 Ma, which provided an overpressure onset at around 500 m burial depth for the investigated samples (Figure 4.12B). The pore fluid pressure started to ramp up, which led to a reduced rate of increase for the vertical effective stress. The lower than expected vertical effective stress led to less mechanical compaction in the Judy field, as can be observed in the investigated samples. There are no common mechanical compaction features such as bent mica grains, fractured grains, pressure dissolution or concavo-convex or sutured grain contacts in the Judy field samples (Fig. 7B). Consequently, greater primary porosity was maintained in the Judy field.

Nevertheless, in both case studies the overpressure only had an impact on the porosity preservation because of its shallow onset. In the case of a deeper onset, most of the preserved primary porosity would have been lost due to ongoing mechanical compaction. There would have been almost no effect with a deeper (>2500 m below seafloor) onset, because sandstones at that depth are sufficiently lithified that mechanical compaction is reduced to a minimum (Gluyas and Cade, 1997; Paxton et al., 2002).

The porosity-preserving impact of the overpressure is shown by the overpressure-depth correction after Gluyas and Cade (1997). The anomalously high porosities for deeply buried sandstone reservoirs, above 20%, are well within the expected range of the

hydrostatic porosity-depth relationship after the overpressure-depth correction (Figure 4.3).

Furthermore, the IGV and the total cement measurements show that even if most of the porosity loss in both reservoir sandstones has been due to mechanical compaction (Figure 4.10), the impact of pore fluid overpressure on porosity maintenance seems to have been considerable. However, it is not just the overpressure or the magnitude of overpressure which is important. The depth of onset controls the vertical effective stress; the depth of onset is therefore crucial: the shallower the onset, the higher is the potential for preserving high primary porosity.

4.6.4 Implications for deeply buried sandstone reservoirs

Anomalously high porosities can be found in deeply buried sandstone reservoirs where a good combination of porosity-preserving mechanisms has been operating. The onset of shallow (<2000 m) pore fluid overpressure reduces the vertical effective stress on the grain framework and hence reduces the amount of mechanical compaction. Nevertheless, the impact of pore fluid overpressure on the precipitation of cements seems to be negligible, given that temperature and availability of dissolved material is the main driver of cementation (Walderhaug, 1994b; Oelkers et al., 1996; Osborne and Swarbrick, 1999). Therefore, clay mineral or microquartz coatings are important for inhibiting extensive quartz cementation at temperatures above 70°C (Worden and Morad, 2000), during deeper burial, where porosity loss is dominated by cementation processes. The effect of grain coatings on inhibiting quartz cement growth is highest in quartz-rich sandstones with silica-rich pore fluids.

It has clearly been shown by the two Triassic Skagerrak case studies that a shallow onset of pore fluid overpressure has a high potential for preserving primary porosities to

depth. However, mechanisms that inhibit extensive quartz cementation are also important for porosity preservation during deeper burial (Pittman et al., 1992; Jeans, 1994; Ajdukiewicz and Lander, 2010). Primary porosity maintained by overpressure during shallow burial can be reduced significantly by extensive quartz cementation during later burial. Therefore, a combination of shallow overpressure onset and high fraction of grains with chlorite coatings, without the development of pore-filling chlorite, is the best possible scenario for maintaining high primary porosities to depth.

4.7 Conclusions

1. High porosities (up to 35%) at depths of >3500 m and temperatures around 150°C are found in the Triassic Skagerrak fluvial sandstones of the J-Block and the Heron Cluster fields in the Central Graben, North Sea.
2. The rate of porosity decline with increasing burial depth has been significantly arrested by a combination of shallow overpressure development and chlorite coatings of detrital grains.
3. Timing of overpressure development was crucial. Later overpressure development would probably have resulted in poorer reservoir quality for the Skagerrak Formation sandstones. It seems the isolated nature of the intra-basin reservoir units in both areas contributed to the onset of overpressure at shallow burial depths.
4. Authigenic chlorite coatings maintain porosity by inhibiting quartz cement overgrowth at temperatures >70°C (Worden and Morad, 2000). However, the chlorite coatings also reduce porosity due to their very presence, especially when their growth bridges between detrital quartz grains and fills the intervening pore space.
5. This research has shed light on the controls on reservoir quality in the complex fluvial sandstones of the Skagerrak Formation. It clearly identifies the need to understand the timing of overpressure generation for arresting mechanical compaction, and the importance of chlorite detrital grain coatings in inhibiting quartz cement overgrowth as temperature increases during progressive burial.
6. Compaction is still active at the present day, and its deleterious effects are only too evident where chlorite grain coatings are absent, even where the VES is very low.

Chapter V

Exceptional reservoir quality in HPHT reservoir settings: Examples from the Skagerrak Formation of the Heron Cluster, North Sea, UK

This chapter has been accepted for publication in Marine and Petroleum Geology (02/02/2016).

Stricker, S., Jones, S. J., Sathar, S., Bowen, L., & Oxtoby, N., (2016). Exceptional reservoir quality in HPHT reservoir settings: examples from the Skagerrak Formation of the Heron Cluster, North Sea, UK. *Marine and Petroleum Geology*, http://doi.org/10.1016/j.marpetgeo.2016.02.003

5.1 Summary

As the exploration of hydrocarbons moves into more complex and deeper basinal settings, the need to understand the effect of high temperatures and high pressures on reservoir quality and rock properties becomes even more important. The fluvial channel sandstone reservoirs of the Skagerrak Formation in the Central North Sea exhibit anomalously high porosities and permeabilities considering their depth of burial (> 3500 m). Despite the complex depositional setting, diagenetic history, high overpressure and temperatures encountered in the Skagerrak Formation, hydrocarbons are currently being produced. The Skagerrak Formation reservoirs used in this study have encountered overpressures of >40 MPa and temperatures up to ~185°C at present-day maximum burial. To identify the role played by the high pressure and high temperature encountered in the reservoir sandstones, a multidisciplinary approach involving petrographic, fluid inclusion, microthermometry, and burial history modelling studies has been adopted.

Our interpretation of the results is that the generation of shallow overpressure in these fields limited mechanical compaction and also played an important role in minimizing pressure dissolution in the chemical compaction regime, as evidenced by reduced quartz cementation. Fluid inclusions found in the quartz overgrowths indicate late-stage development with temperatures of formation in the range 130 to 170°C, coincident with late-stage deeper burial. Hydrocarbon emplacement occurred after quartz cementation and has had little to no effect on porosity preservation. The formation of well-developed authigenic chlorite (>70% surface coating) and, to a lesser extent, illite clay coats with burial had a positive effect on porosity preservation even though permeability was marginally reduced in the illite-rich sandstones. A schematic porosity and quartz cement

evolution model has been developed which allows for pre-drill prediction of reservoir quality in the Heron Cluster and provide valuable insights for other complex high-pressure high-temperature reservoirs.

5.2 Introduction

The inclusion of reservoir quality in pre-drill assessments is of paramount importance as hydrocarbon companies explore deeper targets. Exploration in deeply buried, high-pressure-high-temperature (HPHT; >69 MPa and >150°C) reservoirs depends on identifying reservoir sandstones with sufficient porosity and permeability, especially where the reservoir has been exposed to elevated temperatures (>100°C) by prolonged burial.

In normally pressured reservoirs, sediments compact mechanically during burial as the vertical effective stress increases, so that the porosity is reduced. Mechanical compaction in sandstones has been reported to be dominant to burial depths of ~2000 m (>70 to 80°C) (Bjørlykke, 1999, 2014). Porosity loss in sandstones can be generally predicted to some degree of accuracy giving rise to regional porosity-depth or porosity-temperature curves for many hydrocarbon basins (e.g., Ehrenberg et al., 2008). However, occurrences of sandstone reservoirs with higher than expected porosity are commonly attributed to conditions that limit the degree of burial compaction and/or cementation, or to pre-existing cements and grain coatings (e.g., Bloch et al., 2002; Taylor et al., 2010, 2015; Nguyen et al., 2013).

Models for porosity preservation in deeply buried HPHT sandstone reservoirs (>4000 m) tend to be focused on how clay (commonly chlorite) and microquartz detrital grain coatings can inhibit macroquartz cementation. There are many studies where deep reservoir porosity is linked to early diagenetic clay or microquartz grain coats (e.g.,

Pittman et al., 1992; Ehrenberg, 1993; Aase et al., 1996; Bloch et al., 2002; Ajdukiewicz and Lander, 2010; Ajdukiewicz and Larese, 2012; French et al., 2012; Worden et al., 2012). These studies have shown that quartz-rich sandstones with well-developed and continuous diagenetic clay or microquartz grain coats contain a much lower volume of macroquartz cement than without such coatings (Ajdukiewicz and Lander, 2010).

Albeit controversial, early hydrocarbon emplacement into a reservoir may also play a crucial role in the preservation of porosity (Worden et al., 1998; Worden and Morad, 2000). Field-based (Marchand et al., 2002) and experimental (Sathar et al., 2012) studies have shown that quartz cementation is inhibited at high oil saturations. However, other studies (e.g., Saigal et al., 1992; Aase and Walderhaug, 2005; Molenaar et al., 2008) have suggested that there is no correlation between hydrocarbon emplacement and porosity preservation.

Fluid overpressure, defined as the excess pore pressure above the hydrostatic pressure for a given depth, reduces the effective stress acting on intergranular contacts and inhibits mechanical and chemical compaction (Osborne and Swarbrick, 1999; Sathar and Jones, 2016). The shallow onset of pore fluid overpressure has been noted to enhance porosity preservation in the Skagerrak Formation of the Central North Sea (Nguyen et al., 2013; Grant et al., 2014).

In this study we investigate the effect of HPHT reservoir conditions on sandstone porosity and permeability evolution in three deeply buried, siliciclastic reservoirs from the Skagerrak Formation in the Heron Cluster (Egret, Heron and Skua, UK Quadrant 22), Central Graben, North Sea. Pore pressures exceed 80 MPa in the reservoir sandstones at present-day depths of 4000 to 5000 m below sea floor where temperatures are around 170 to 180°C (Table 5.1). A multidisciplinary approach comprising

petrographic, SEM, fluid inclusion, and burial history modelling studies has been adopted in the present study to understand the evolution of reservoir quality in HPHT environments, with an explicit focus on:

- How does the vertical effective stress history influence the porosity evolution of reservoir sandstones?
- How do authigenic grain coatings control quartz cementation and reservoir quality in HPHT settings?

Field		**Egret**	**Heron**	**Skua**
Well		**22/24d-10**	**22/29-5RE**	**22/24b-7**
Top Skagerrak Formation	[m TVDSS]	4310	4289	3557
Top Judy Member	[m TVDSS]	4368	4312	3557
RFT Formation pressure (Judy Mbr)	[MPa]	85.6 - 86.8	86.8	63.7 - 66.8
RFT Temperature (Judy Mbr)	[°C]	175 - 183	176 - 178	160
Fluid inclusion sample 1	[m TVDSS]	4565	4412	3608
Fluid inclusion sample 2	[m TVDSS]		4419	3615

Table 5.1 Present-day formation tops (Skagerrak Formation and Judy Sandstone Member) and formation pressure and formation temperature of the Judy Sandstone Member in the Egret, Heron and Skua fields.

5.3 Geological setting

The Central Graben of the North Sea is a prolific hydrocarbon province containing more than 20 billion barrels of discovered hydrocarbons. The Central Graben is 70 to 130 km wide with an approximate length of 550 km. It is the southern arm of a trilete rift system (i.e., an incipient ridge-ridge triple junction) in the North Sea with the Viking Graben as the northern arm and the Moray Firth Basin as the western arm. The Central Graben is divided into the West and East sections by the Forties-Montrose and Josephine Ridge horst blocks (Figure 5.1) and is flanked by the Norwegian basement in the east and the UK continental shelf in the west. The rift system developed in at least two major extension phases, one Permian-Triassic (290-210 Ma) and a Late Jurassic one (155-140

Ma) (Gowers and Saeboe, 1985; Glennie, 1998). The geological history of the Central Graben is commonly divided into pre-rift, syn-rift and post-rift phases. The syn-rift sediments are the mainly siliciclastic Triassic and Jurassic sediments of approximately 2000 m thickness. The post-rift sediments from the Cretaceous to the Holocene are as much as 4500m thick and dominated by shale, sandstones, silty sandstones and a thick chalk section (Glennie, 1998).

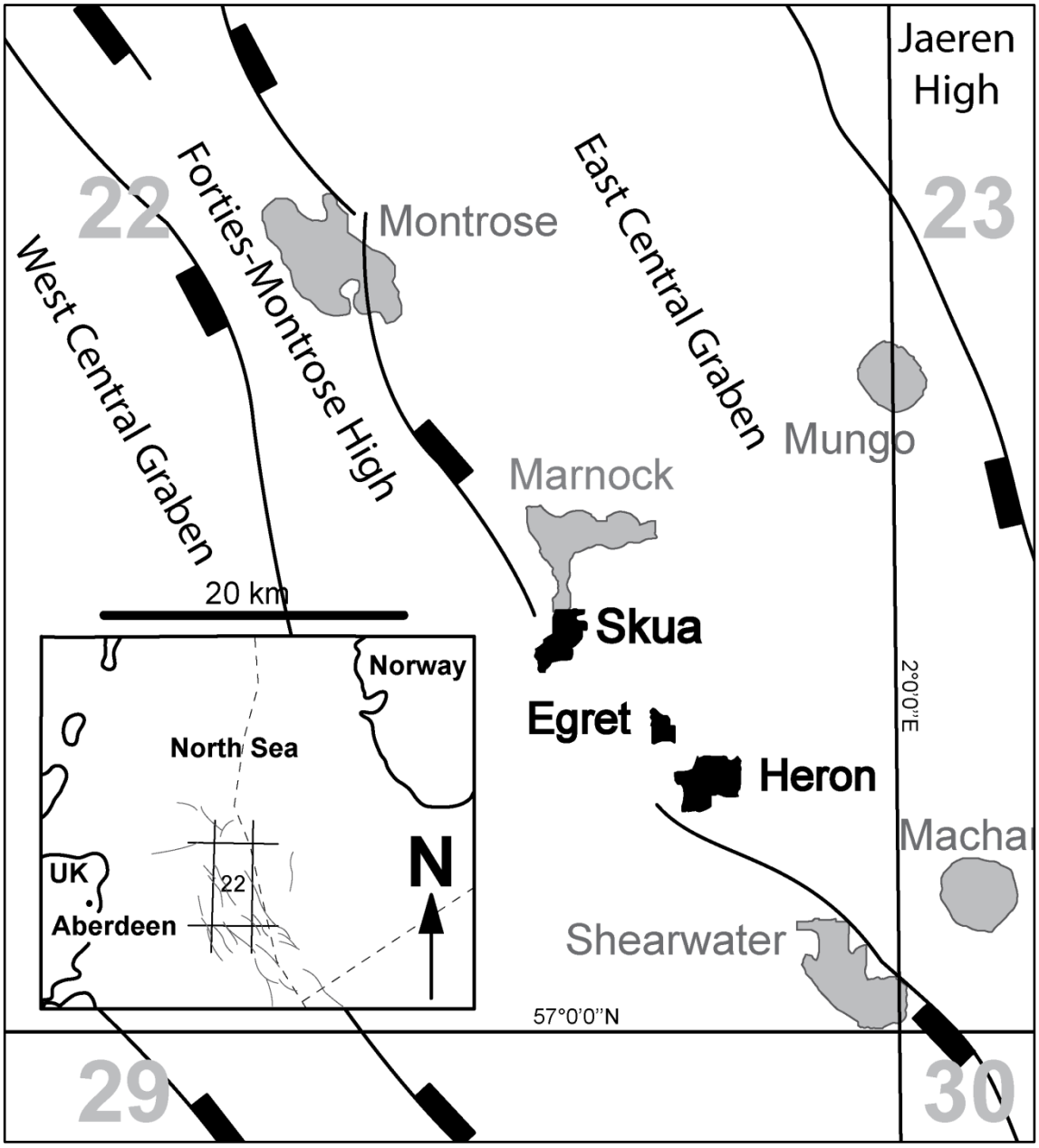

Figure 5.1 Map of the southern part of UK Quadrant 22 with important regional structural features indicated.

The focus of this study is on the HPHT sections at the southern end of the Forties-Montrose High in UK Quadrant 22 (Figure 5.1). Cores of Skagerrak Formation reservoirs from three fields, Egret, Heron and Skua, were utilized in this study (Figure 5.1) The area is a part of a wider HPHT province, including the Triassic strata of the Central Graben and the southern Viking Graben (Goldsmith et al., 2003).

5.3.1 Triassic Skagerrak Formation stratigraphy

The Triassic strata of the Central North Sea area are dominated by thick alluvial successions with no connection to a marine realm (Goldsmith et al., 2003). The Middle to Late Triassic Skagerrak Formation comprises deposits of 500 to 1000 m of predominantly continental braided and meandering fluvial systems and terminal fluvial fans with lacustrine facies in the Central Graben, North Sea (McKie and Audretsch, 2005; de Jong et al., 2006; Kape et al., 2010). The stratigraphic nomenclature of the Triassic for the Central Graben was defined by Goldsmith et al. (1995, 2003), based on detailed biostratigraphic and lithostratigraphic correlation of wells from the Josephine Ridge and was extended and correlated towards the ETAP (Eastern Trough Area Project) area by Mckie and Audretsch (2005). The Central Graben Triassic succession is subdivided into the Early Triassic Smith Bank Formation (shales, evaporites and thin sands) and the Middle to Late Skagerrak Formation (thickly interbedded sands and shales) (Figure 5.2). The Skagerrak Formation is subdivided into three sand-dominated successions (Judy, Joanne and Josephine) and three mud-dominated successions (Julius, Jonathan and Joshua) (Figure 5.2). The sand-dominated units include sheetflood deposits and multi-storey stacked channel sandbodies (Goldsmith et al., 1995; McKie and Audretsch, 2005), whereas the mud-dominated units include a variety of non-marine, basinwide floodplain, lacustrine shale, loess and playa lake deposits. The thick and laterally extensive mud-dominated units provide the main correlative units for the

Skagerrak in the Central Graben (McKie and Audretsch, 2005). The resultant Triassic stratigraphy in the Central Graben is incompletely preserved due to deep erosion during the Middle and Late Jurassic (Erratt et al., 1999).

The Triassic Smith Bank and Skagerrak sediments accumulated directly on top of the thickly developed Late Permian Zechstein salt in a series of salt- and fault-controlled mini-basins or pods. The Late Permian Zechstein salt strongly controlled the deposition by forming salt withdrawal mini-basins due to a combination of localised loading and structural extension within an overall rift controlled basin (Smith et al., 1993; Bishop, 1996; Matthews et al., 2007). The Smith Bank sediments represent the bulk and basal part of the mini-basin infill, whereas the overlying Skagerrak is found as intra-basin sediments in the upper parts of the mini-basins and as inter-basin sediments between the mini-basins. Mini-basin development was active throughout the Triassic and is mainly responsible for the preservation of Middle to Late Skagerrak Formation in the study area. The thick Late Permian evaporite sediments (>2 km) prevented grounding of mini-basins on the underlying Rotliegend basement in the Central Graben. The salt tectonics created variable thicknesses between intra-basin and inter-basin Skagerrak sediments and allowed thick accumulations within the mini-basins. Furthermore, the salt mini-basins created facies variability between intra-basin and inter-basin that influenced reservoir thickness and diagenetic cementation (e.g., Nguyen et al., 2013).

The Skagerrak stratigraphy in the study area consists of the Judy Sandstone Member, and is bounded by the Marnock and Heron shales, which are regional markers representing equivalents to the Julius Mudstone Member and the upper Smith Bank Formation (Figure 5.2) (McKie and Audretsch, 2005). The Judy Member is further subdivided in the ETAP area by McKie & Audretsch (2005) into a lower terminal splay-dominated interval and an upper channelised interval, separated by a shale-prone

section. The lower terminal splay facies is characterized by fine-grained, planar cross-bedded and ripple-laminated sandstones. In comparison, the upper interval is dominated by channel-fill deposits, which are organized into fining upward packages with coarse lag deposits (usually with ripped-up calcrete nodules) commonly occurring at the base. Channel-fill deposits are characterized by well sorted cross-bedded sandstones and can be separated into channel and sheet-dominated sandstones (McKie and Audretsch, 2005; McKie, 2011).

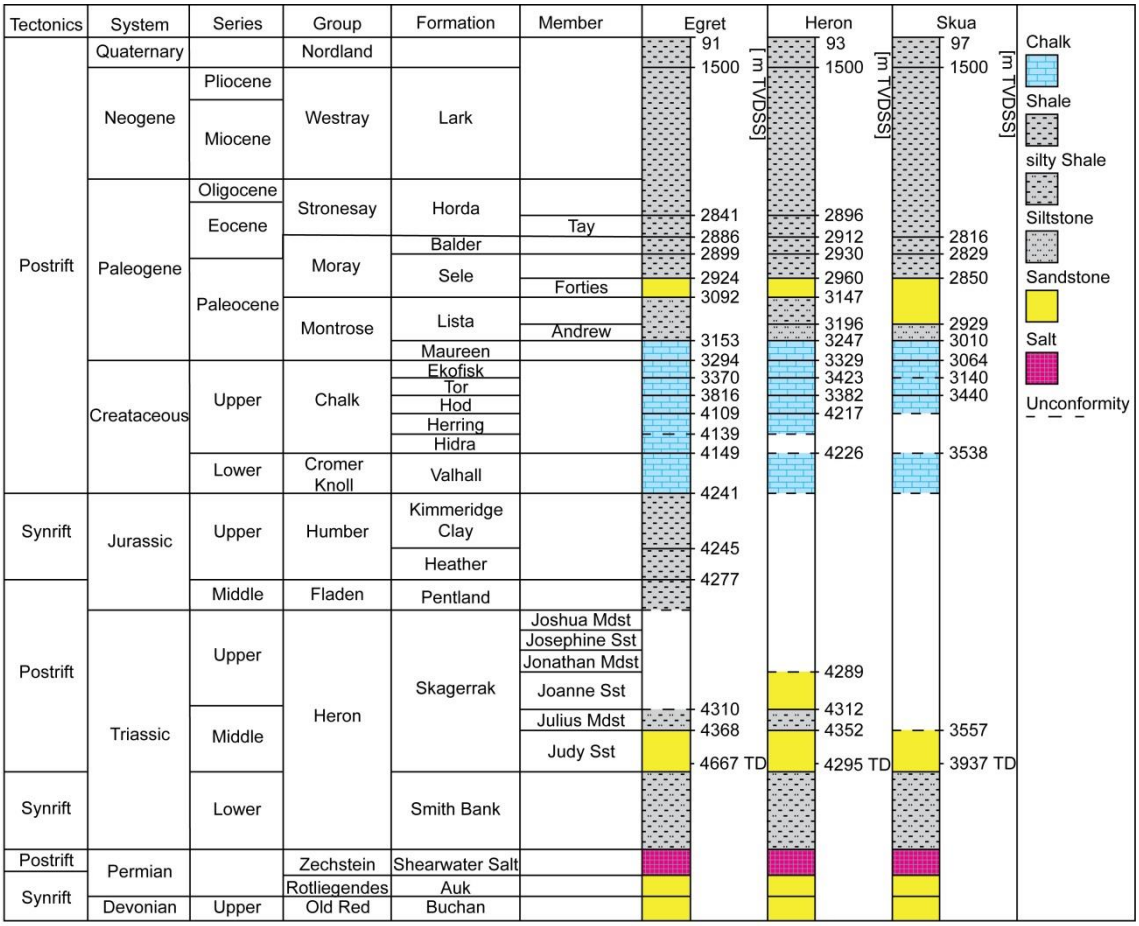

Figure 5.2 Stratigraphy of the Heron Cluster fields: Egret (well 22/24d-10), Heron (well 22/29-5) and Skua (well 22/24b-7). Also see Figure 3.2.

5.4 Methodology

5.4.1 Sampling

Core samples and thin sections examined in this study are from the Skagerrak Formation reservoirs from three fields, Egret (well 22/24d-10), Heron (well 22/29-5RE) and Skua (well 22/24b-7). A total of 274 core samples have been taken from the Egret field (106) (22/24d-10) at depths between 4350 to 4570 m TVDSS (true vertical depth minus elevation above mean sea level), from the Heron field (136) (22/29-5RE) at depths between 4300 to 4500 m TVDSS, and from the Skua field (32) (22/24b-7) from 3600 to 3660 m TVDSS. The depth intervals have been chosen to cover the main reservoir unit, the Judy Sandstone Member, and the samples have been selected on a best expected reservoir quality strategy from the available core material. The focus on best reservoir quality has restricted the facies used in this study to confined, channelised and unconfined, sheetflood and crevasse splay components of the Skagerrak fluvial system (N. Meadows 2015, *pers. comm.*). The Skagerrak sandstone reservoirs are currently at maximum burial depth and experiencing maximum temperatures and formation pressures (Table 5.1).

5.4.2 Petrography

Core sample thin sections were used to measure optical porosity, grain size and fraction of clay-coated grains for this study. Optical porosity was measured by using the digital image analysis technique, jPOR (Grove and Jerram, 2011), on blue epoxy-impregnated thin sections. Grain size distribution was analysed by using the Leica QWin (V. 3.5.0) software on thin section micrographs and the fractions of chlorite-coated grains were measured by point counting with 300 counts per thin section. Furthermore, additional petrographic analysis (i.e., intergranular volume (IGV) (Paxton et al., 2002) and total

cement volume (C)) were undertaken and measured by point counting with 300 counts per thin section using a standard petrographic microscope.

Thin sections from all three fields were highly polished to 30μm and coated with carbon prior to analysis by a Hitachi SU-70 field emission gun scanning electron microscope (SEM) and equipped with an energy-dispersive detector (EDS). Scanning electron microscope analyses of thin section and bulk rock samples were conducted at 5 to 20kV acceleration voltage with beam currents of 1.0 and 0.6nA, respectively. Point analyses had an average duration of 2 minutes, whereas line analyses were dependent on length. SEM-EDS was used for rapid identification of chemical species (i.e., chlorite Fe/Mg-ratio) and orientation on the sample. Scanning electron microscopy - cathodoluminescence (SEM-CL) analysis has been undertaken on selected thin sections with visible macroquartz overgrowths using a Gata MonoCL system with a panchromatic imaging mode operated at 8 kV.

5.4.3 Fluid inclusion analysis

Microthermometry was conducted on double-polished detached wafers to determine the conditions of cementation and evidence for formation water salinity. Fragments were cut from double-polished rock wafers. The wafers were firstly checked under incident UV on a petrographic microscope to determine which contain petroleum inclusions and under transmitted light to determine the distribution of both aqueous and non-aqueous fluid inclusions for subsequent analyses. A Linkam THM600/TS90 heating – cooling stage connected to a Nikon petrographic microscope was used to obtain temperature data. Instrumental precision is ± 0.1°C, while accuracy, dependent on the manufacturer's stated accuracy for the calibration standards used (synthetic inclusions and pure organic compounds) is better than ± 0.1°C over the range of temperatures reported here. Routinely available measurements are homogenization temperatures (T_h)

and final melting temperatures (T_m). Homogenization is the conversion of multiphase inclusion contents to a single phase, usually at temperatures above room temperature. Interpreting homogenization temperatures in carbonates, sulphates and halides can be complicated because aqueous inclusions can, though not necessarily do, reset to higher temperature if they are a) overheated beyond a threshold which is dependent on the mineral strength and inclusion geometry (Goldstein and Reynolds, 1994), or b) frozen. This can occur in the laboratory as well as through geological processes, so care is taken in the order in which analyses are made for each rock chip. If resetting has occurred, larger inclusions may give higher temperatures, homogenization temperature distributions may show a high temperature tail, and data from paragenetically distinct settings may overlap. Final melting occurs at the disappearance of the last trace of solid in the inclusion on heating, usually after cooling an inclusion to well below room temperature. If ice is the final phase to melt, as in the present study, salinities are calculated using the equation given by Oakes et al. (1990).

5.4.4 One-dimensional basin modelling

One-dimensional basin modelling provides an insight into the burial history of a reservoir and especially the temperature and pore fluid pressure evolution of the reservoir. Pore pressure built up by disequilibrium compaction and pore fluid volume expansion can be modelled with one-dimensional basin models such as the burial history simulation software PetroMod. Schlumberger's burial history simulation software PetroMod (V. 2012.2) was used in this study to model the temperature and pore pressure evolution of the Egret, Heron, and Skua fields. One-dimensional models are generally well suited to model pore pressure mechanisms such as disequilibrium compaction and pore fluid expansion but are limited in terms of integrating mechanisms such as lateral fluid transfer or hydrocarbon generation. PetroMod is based on a forward

modelling approach to calculate the geological evolution of a basin and burial history. Present-day well stratigraphy, well log lithology and lithological description were used to set the one-dimensional burial models (Figure 5.2 & Table 5.2). Palaeo-basement heat flow was assumed according to Allen and Allen (2005) with 63 to 110 mW/m^2 (average of 80 mW/m^2) during syn-rift phases and 37 to 66 mW/m^2 (average 50mW/m^2) during post-rift phases. The burial history models are calibrated against present-day RFT temperature measurements corrected after Andrews-Speed et al. (1984) and measured Skagerrak Formation porosities (Figure 5.3), and carefully adjusted towards present-day formation pressure measurments by considering late stage, high temperature overpressure mechanisms (Osborne and Swarbrick, 1997; Isaksen, 2004). Vitrinite reflectance data, maximum temperatures obtained from apatite fission-track analyses, palaeotemperatures and palaeopore pressures obtained from fluid inclusions in mineral cements were used to help calibrate the model (Swarbrick et al., 2000; di Primio and Neumann, 2008). We also conducted new fluid inclusion analysis in quartz cements to further constrain palaeotemperatures. The lithological unit types used in the models are PetroMod default lithology types or mixed default lithology types, chosen on the basis of well log descriptions and core analysis reports. Exceptions are the Hod lithology type and the lithology type of the Triassic Skagerrak sandstones. The Hod chalk unit is modified to represent the North Sea non-reservoir chalk and to match the compaction trend and permeability trend given by Mallon and Swarbrick (2002, 2008) (Table 5.3). The Triassic Skagerrak sandstone of the Judy Sandstone Member is simulated by a mix of PetroMod (V. 2012.2) default lithologies (80% sand, 10% silt, 10% shale) in combination with a regional compaction trend for shaly sandstone given by Sclater and Christie (1980).

Group/ Formation	Egret		Heron		Skua	
	Thick.	Lithology	Thick.	Lithology	Thick.	Lithology
	[m]	[-]	[m]	[-]	[m]	[-]
Water	91	Water	93	Water	97	Water
Nordland	1409	Shale	1407	Shale	1762	Shale
Lark/Horda	1341	Shale	1396	Shale	957	Shale
Tay	45	Shale	15	Sandy Sh.		
Balder	13	Shale	18	Shale	12	Shale
Sele	25	Sandy Sh.	31	Sandy Sh.	21	Shale
Forties	168	Sandstone	187	Sandstone	79	Sandstone
Lista	60	Silty Sh.	49	Silty Sh.		
Andrew			51	Siltstone	81	Siltstone
Maureen	142	Marl	82	Marl	54	Marl
Ekofisk	76	Chalk	94	Chalk	76	Marl
Tor	446	Chalk	459	Chalk	300	Chalk
Hod	293	Non-Res.	335	Non-Res.	98	Non-Res.
Herring	30	Chalk	9	Marl		
Hidra	10	Shale				
Valhall	92	Chalk	63	Marl	19	Marl
Kimmeridge Clay	4	Shale	0	Shale	0	Shale
Heather	33	Shale	0	Shale	0	Shale
Pentland	33	Shale				
Joshua	0	Silty Shale	0	Silty Shale	0	Silty Sh.
Josephine	0	Res. Sst	0	Res. Sst	0	Res. Sst
Jonathan	0	Silty Sh.	0	Silty Sh.	0	Silty Sh.
Joanne	0	Res. Sst	23	Res. Sst	0	Res. Sst
Julius	58	Silty Sh.	41	Silty Sh.	0	Silty Sh.
Judy	302	Res. Sst	339	Res. Sst	468	Res. Sst
Smith Bank	230	Silty Sh.	200	Silty Sh.	118	Silty Sh.
Zechstein	200	Salt	208	Salt	207	Salt

Table 5.2 Lithology thickness and type of the modelled layers for the Egret, Heron, Skua fields, with Sh: Shale, Sst: Sandstone, Non-Res.: Non-Reservoir Chalk and Res. Sst.: Reservoir Sandstone (80% Sand, 10% Silt and 10% Clay).

Model Parameter (Hod Formation)			
Mechanical compaction		**Permeability**	
Porosity	**Depth**	**Porosity**	**Permeability**
[%]	**[m]**	**[%]**	**[log(mD)]**
70.00	0	70.00	1.00
18.00	1300	30.00	-1.00
12.50	2100	25.00	-3.00
8.00	3100	20.00	-5.50
5.00	4500	12.50	-7.20
		9.00	-7.20
		5.00	-7.20

Table 5.3 Non-reservoir North Sea chalk model parameters after Mallon and Swarbrick (2002, 2008)

5.5 Petrography, burial modelling and diagenesis

The present-day reservoir quality of the deeply buried Skagerrak Formation in the Egret, Heron, and Skua fields is a cumulative product of depositional attributes (e.g., facies architecture, grain composition, sorting, and size), mechanical compaction and diagenesis during shallow and deep phases of burial.

5.5.1 Burial history modelling results

The one-dimensional burial history models are based on well data and are calibrated with measured RFT pore pressure data, measured and corrected RFT temperatures and aqueous fluid inclusion homogenization temperatures of the Judy Sandstone Member (Table 5.4). The burial history models show the Skagerrak Formation reservoir sandstones at maximum burial depth and temperatures at present day (Table 5.1). The Skagerrak Formation experienced in general a long shallow burial phase (~150 million years) followed by a phase of rapid burial starting between 90 and 70 Ma to their present maximum burial depth (Figure 5.4). The phase of rapid burial was accompanied by significant temperature and pore pressure increases to their present-day maxima. The present-day pore fluid pressure profiles of the three wells increase through the Chalk

units (Ekofisk, Tor and Hod Formations) from hydrostatic to highly overpressured in the Skagerrak Formation reservoir sandstones.

The Egret burial history model shows a burial rate increase from ~90 Ma onwards, leading to a present-day maximum burial depth of ~4300 m below seafloor (Formation top). Modelled reservoir temperature and pore fluid overpressure increase constantly during the rapid burial phase to present-day maxima of 180°C and 39 MPa, respectively (Figure 5.4 & Table 5.1). The rapid overpressure increase in the Skagerrak Formation induces a reduction of the vertical effective stress (VES) accrual, which led to a maximum VES of ~24 MPa at around ~10 Ma and a present-day VES of 10.4 MPa.

The Judy Sandstone Member of the Heron field underwent a shallow burial phase (<1150 m below seafloor) followed by rapid burial from 90 Ma onwards to its present-day maximum depth of around ~4300 m below seafloor (Formation top; Figure 5.4). The burial history model shows an increase of pore fluid overpressure from 60 million years ago towards a maximum present-day overpressure of 40 MPa which leads to a decrease of the VES in the Skagerrak Sandstone reservoirs to a maximum VES of 21.5 MPa at 10 Ma and a present-day VES of 6 MPa (Figure 5.4). The modelled temperature of the Judy Sandstone Member in the Heron field is below 50°C for the early shallow burial phase and starts to increase during the rapid burial phase to a present-day maximum of 178°C.

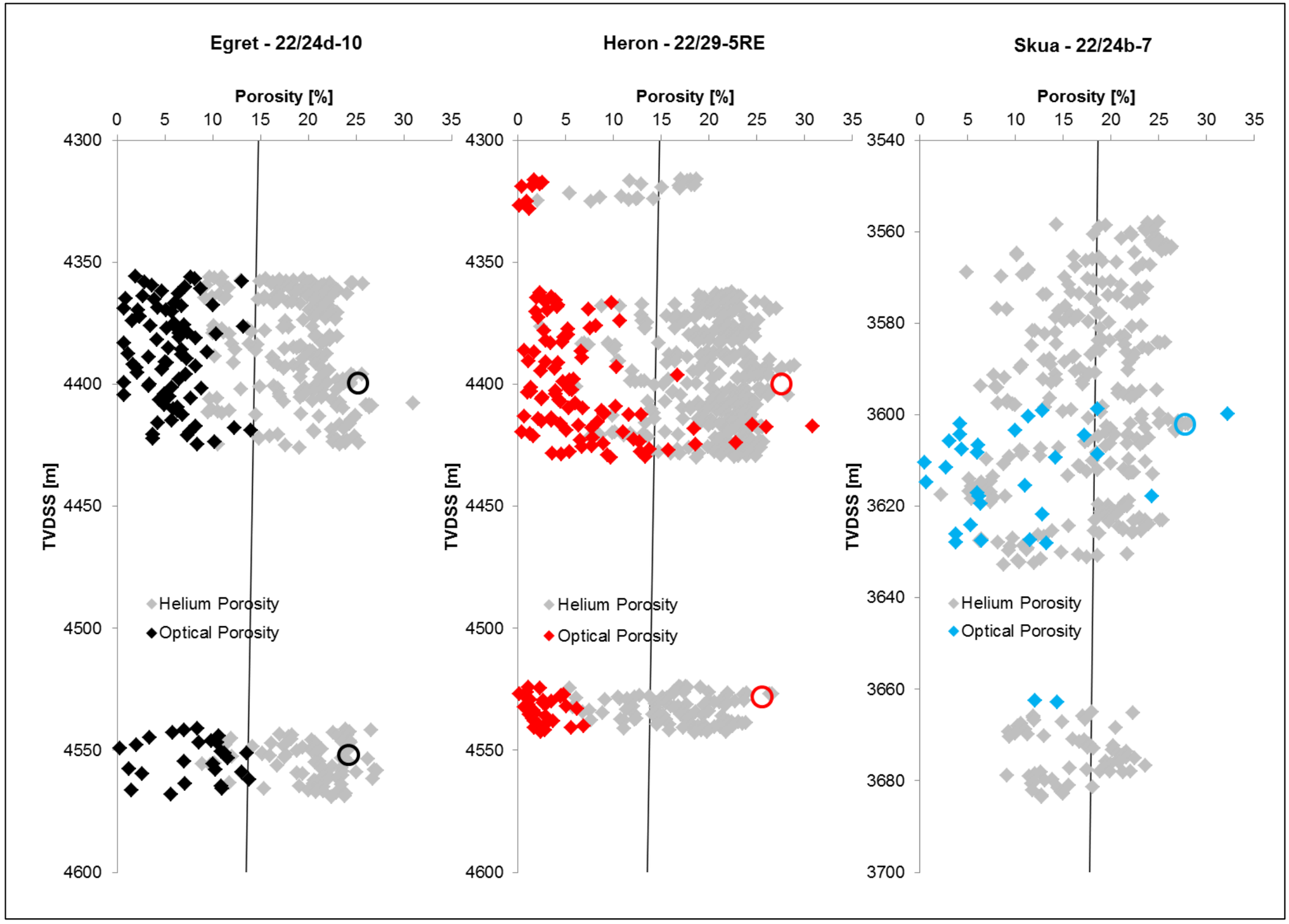

Figure 5.3 Optical and helium porosities of the Heron Cluster sample sets with a regional Central North Sea porosity–depth relationship for hydrostatically pressured shaly sandstone (Sclater and Christie, 1980) and the modelled sandstone porosities (circles).

FI Host	Egret		Heron				Skua			
	15068'11''		15691'6''		15721'11''		11909'4''		11931'0''	
	Aqu. [°C]	Non [°C]	Aqu. [°C]	Non [°C]	Aqu. [°C]	Non [°C]	Aqu. [°C]	Non [°C]	Aqu. [°C]	Non [°C]
Quartz OG	145.4		104.0	69.8	133.7		133.4		132.6	83.3
Quartz OG	146.0		106.0	72.1	141.5		135.8		133.1	
Quartz OG	147.9		111.0	75.3	143.1		135.9		133.3	
Quartz OG	149.0		116.0	76.1	143.6		137.1		133.5	
Quartz OG	149.4			76.3	144.4		137.3		136.1	
Quartz OG	150.2				145.4		137.3		137.3	
Quartz OG	150.2				162.2		139.3		138.6	
Quartz OG	150.7				163.3		139.9		139.9	
Quartz OG	151.6						140.4			
Quartz OG	152.2						140.8			
Quartz OG	152.3						140.8			
Quartz OG	153.4						141.5			
Quartz OG	154.4						142.3			
Quartz OG	155.0						143.0			
Quartz OG	155.8						144.0			
Quartz OG	160.1						144.2			
Quartz OG	166.5						144.6			
Quartz OG	166.6						145.7			
Quartz OG	171.0						146.8			
Quartz OG							154.5			
Quartz OG							156.2			
Feldspar	145.7			60.0		44.8		81.6		83.6
Feldspar	147.0			61.4		66.7		85.6		88.1
Feldspar	148.2			61.9		67.0		85.7		
Feldspar				62.3		70.8		87.9		
Feldspar				75.4		74.4		88.6		
Feldspar				75.5		75.4		88.7		
Feldspar				77.0		75.5		88.9		
Feldspar				77.3		75.8		91.0		
Feldspar				77.8		75.9		91.7		
Feldspar				78.9		76.4		100.1		
Feldspar				87.9		77.1		100.5		
Feldspar						81.4		118.2		
Carbonate									138.5	79.4
Carbonate									140.0	80.4
Carbonate									140.4	84.0
Carbonate									141.5	87.2
Carbonate									141.8	87.4
Carbonate									142.1	88.0
Carbonate									142.3	107.3
Carbonate									142.4	111.6
Carbonate									142.7	
Carbonate									143.4	
Carbonate									144.5	

Table 5.4 Homogenization temperatures of aqueous (Aqu.) and non-aqueous (Non) fluid inclusions in quartz overgrowth, feldspar and carbonate cements.

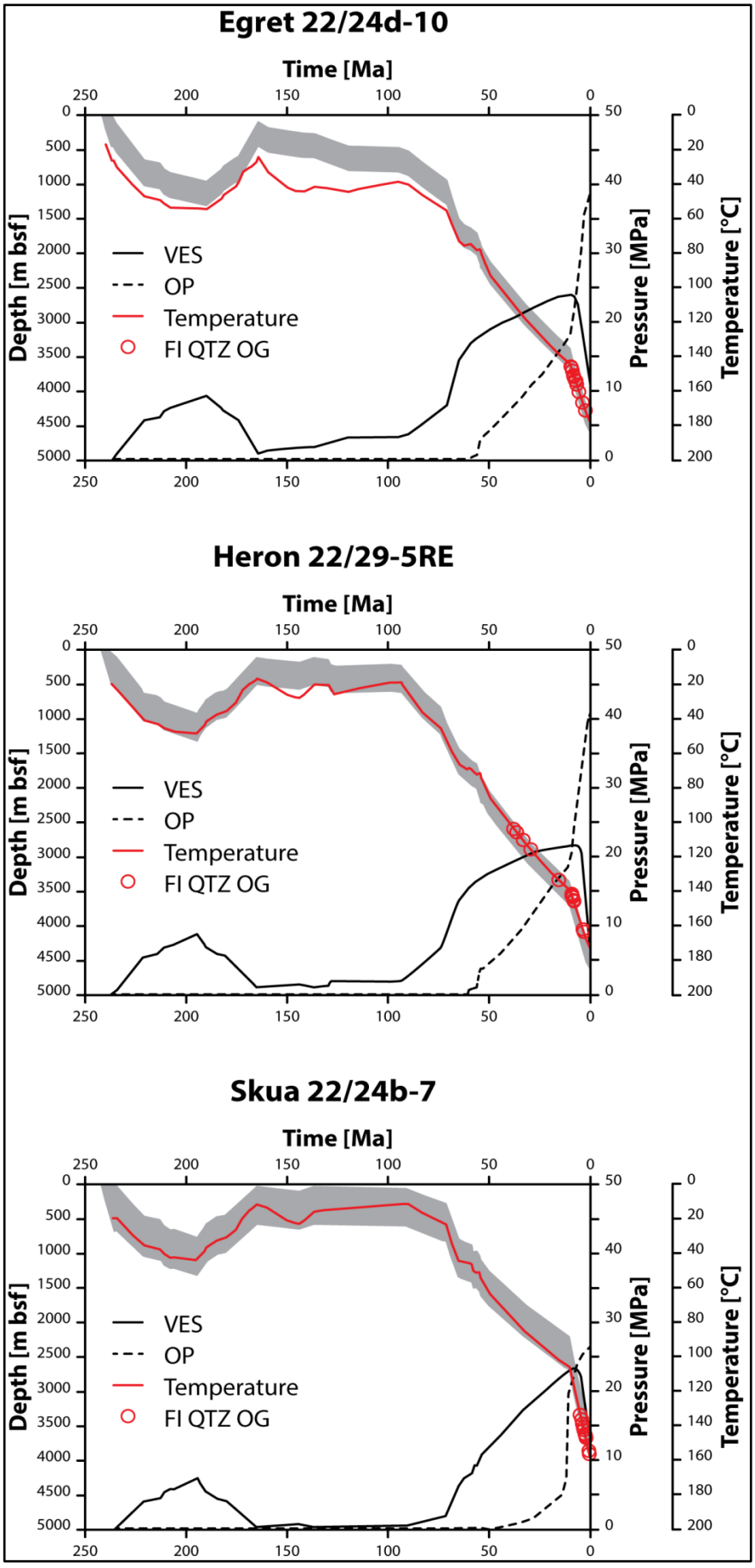

Figure 5.4 Modelled vertical effective stress (VES) evolution, overpressure (OP) evolution, temperature evolution with aqueous quartz overgrowths fluid inclusion homogenization temperatures and burial depth for the Triassic Judy Sandstone Member of the Egret, Heron and Skua fields.

The Judy Member of the Skua reservoir is subjected to a phase of a rapid burial from around 70 Ma with an even greater burial rate in the last 10 million years towards present-day maximum burial depth of 3500 m below seafloor (formation top; Figure 5.4). The phase of rapid burial is coupled with temperature and pore fluid overpressure increases, especially in the last 10 million years, towards 152°C and 26.6 MPa at present day (Figure 5.4). The overpressure increase with ongoing burial reduced the VES accrual significantly to a lower maximum VES of 21.5 MPa at ~10 Ma and a present-day VES of 12 MPa.

5.5.2 Grain size, porosity and degree of compaction

The 274 investigated samples from the Egret, Heron and Skua fields show a wide porosity range from <1% up to a maximum of 34% (Figure 5.3). The measured optical porosity data is complemented by helium core plug porosities (measured after Boyle's law, uncorrected for decompaction effects). The Skagerrak reservoir sandstones in this study cover a narrow range of compositions and are classified as arkosic to lithic-arkosic arenites.

The Egret field (well 22/24d-10) dataset shows optical porosities from <1% to up to 14% porosity, with an average of 7% and helium core plug porosities from 10% to 31%, with a mean around 20% (Figure 5.3). The grain sizes vary from coarse silt to medium-grained sand, with an average grain size of 0.136 mm and the majority of the samples between very fine and fine-grained sand (Figure 5.5).

The Heron field (well 22/29-5RE) dataset in comparison shows a wider optical porosity range from <1% to up to 31%, with the majority of the porosity values below 15% and a mean of 6%. The helium core plug porosities are in general higher with a maximum of 29% and a mean of 20% (Figure 5.3). The grain sizes vary from coarse silt to medium-

grained sand, with a mean grain size of 0.136 mm and the majority being very fine and fine-grained sand (Figure 5.5).

Porosity data from the Skua field samples (well 22/24b-7) show a wide range from <1% to 31% for the optical porosities and 3% to 27% for the helium porosities (Figure 5.3). The mean of optical and helium porosities is around 11% and 17%, respectively. The grain sizes correspond to very fine and fine-grained sand (Figure 5.5), with an average grain size of 0.169 mm.

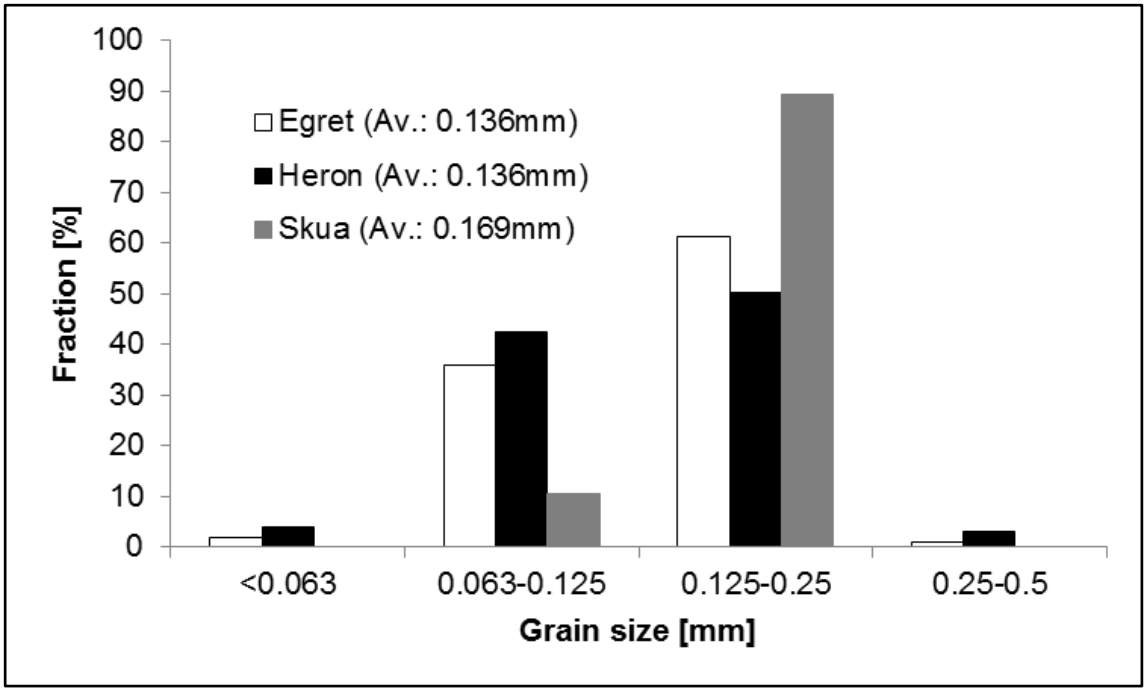

Figure 5.5 Grain size distribution of the Egret, Heron and Skua sample sets, with average grain size (Av.).

Interestingly, grain-size variability is limited across all facies, with most of the sandstones being fine and very fine-grained and grain sizes between 0.063 and 0.25 mm (Figure 5.5). Coarser grain sizes are encountered within the lower parts of the confined channelized sands, with a mean grain size of 0.35 mm (medium grain size).

The Egret, Heron, and Skua samples show features of mechanical compaction of soft grains, such as deformed lithic clay grains, kinked mica grains and minor chemical

compaction features such as concavo-convex grain contacts at detrital quartz grain boundaries. However, the sample sets indicate under-compaction in relation to hydrostatically pressured sandstones at equivalent burial depth (porosity-depth relationship for hydrostatically pressured shaly sandstone by Sclater and Christie (1980)) to the present-day burial depth of the Judy Sandstone Member. The under-compaction of the Skagerrak sandstones is further highlighted by the general absence of strong chemical compaction features, such as sutured or stylolitic grain contacts.

5.5.3 Diagenetic cements and grain coatings

The complex diagenetic history of the Skagerrak Formation sandstone reservoirs has been described by several authors (e.g., Smith et al., 1993; Weibel, 1999; Swarbrick et al., 2000; Kape et al., 2010; Nguyen et al., 2013). The main diagenetic cements recognised include quartz, localised carbonate (ferroan dolomite), feldspar, and early precipitates of halite cement as identified by Nguyen et al. (2013). Detrital quartz grains were reported to be coated by clay minerals such as chlorite and more rarely illite in the Skagerrak Formation, and the presence of clay mineral coatings has been correlated to low quartz cement volumes (Taylor et al., 2010, 2015; Nguyen et al., 2013). The major cement types and the clay mineral coatings, important for reservoir quality, are discussed in more detail below.

5.5.3.1 Carbonate cements

Carbonate cements are very localised throughout the Skagerrak Formation and sourced from syn-depositional calcitic palaeosols in very fine-grained floodplain deposits or by calcrete and dolocrete rip-up clasts at channel bases (McKie et al., 2010). The scarce carbonate cements in the three datasets are mainly present as deformed carbonate-clay rip-up clasts (Figure 5.6A) or as pore-filling cements often associated with “megapores”

in channel-base samples. The clay-free carbonate cements show a rhombic crystal structure with a prominent cleavage pattern and tend to infill the pore space completely where they are present (Figure 5.6B). Fluid inclusion analysis on carbonate cement in Skua sample 11931'0'' shows high aqueous and lower non-aqueous fluid inclusions homogenization temperatures of 138°C to 144.5°C and 79°C to 112°C, respectively (Table 5.4).

5.5.3.2 Grain coatings

Grain coatings and especially authigenic clay minerals are common in all of the Skagerrak sandstones (e.g., Nguyen et al., 2013; Taylor et al., 2015). Detailed petrography, SEM and SEM-EDS analysis presented in this study has identified authigenic clay mineral grain coatings on detrital quartz grains, consisting of mainly authigenic chlorite in the Heron and the Skua fields (Figure 5.7B & Figure 5.7C) and a mixture of authigenic chlorite and illite in the Egret field (Figure 5.7A). The authigenic clay coatings appear to be fully transformed at present day because no precursor clay minerals are detected. Grain-coating chlorite is analysed using SEM-EDS and classified according to the Fe/Mg-ratio (Hillier and Velde, 1992):

$$Fe/Mg = \frac{Fe}{(Fe + Mg)} \qquad (5.1)$$

Chlorite coats are classified as intermediate to Fe-rich (Grigsby, 2001) for the Egret and Heron samples, with Fe/Mg-ratio of 0.4-0.55 (Egret) and 0.45-0.6 (Heron) and as intermediate to Mg-rich for Skua (0.35-0.5) (Table 5.5).

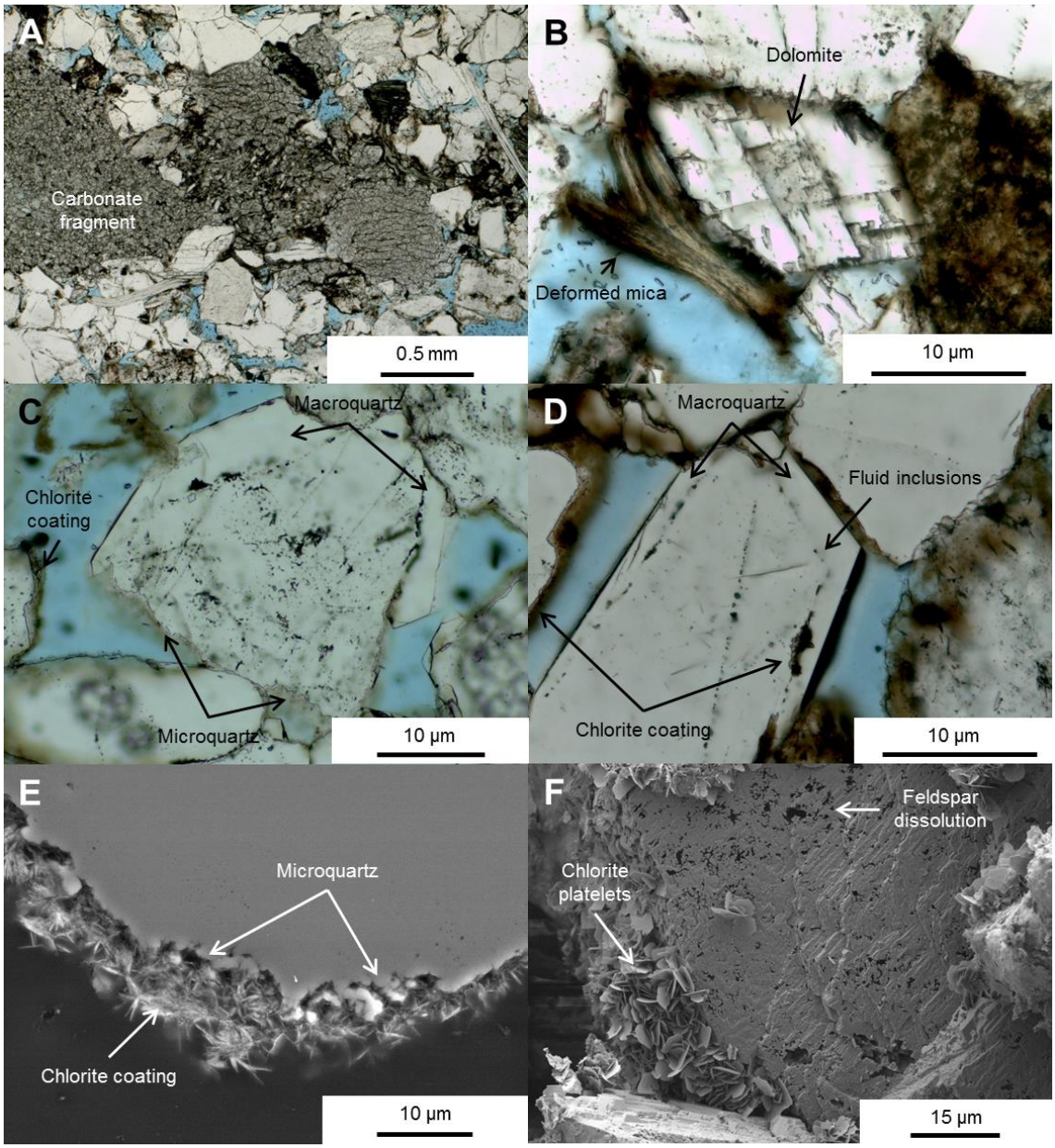

Figure 5.6 Micrographs of A) calcrete/dolocrete fragments (Heron; 15724'11"); B) a single dolomite crystal next to a deformed mica grain (Heron; 15724'11"); C) a detrital quartz grain with macroquartz (blocky) and microquartz overgrowth (Skua; 11882'2"); D) a detrital non-coated quartz grain with macroquartz overgrowth and fluid inclusions at the boundary between detrital grain and overgrowth (Heron; 15718'10"); and SEM images of E) a detrital grain with chlorite coating and microquartz between the coating and the detrital grain (Heron; 15714'7"); F) a partial dissolved feldspar with chlorite coating (Egret; 14997'2").

The majority of samples have measured grain-coating values of more than 70% and several are almost completely coated (Figure 5.8). The Heron and Skua datasets have high measured grain-coating coverage of 79.2% and 70.1%, respectively (Figure 5.8). The grain coatings are, in general, continuously developed and range from 1 μm to 20 μm thickness, with an average thickness of ~11 μm. The chlorite coatings show a complex structural pattern, regardless of their thickness, with a dense root zone (Pittman et al., 1992) of laminated crystals oriented parallel to the detrital quartz grain surface (Figure 5.7D). These are superseded by well-defined chlorite crystals growing normal to the root zone (Figure 5.7B, Figure 5.7C & Figure 5.7D). In comparison, the Egret dataset has a higher fraction of chlorite-coated detrital quartz grains of 86.1% (Figure 5.8). These chlorite coatings are better developed with an average thickness >15 μm, but commonly coexist with illite on detrital quartz surfaces (Figure 5.7A & Figure 5.7E). Furthermore, these coating root zones have a more dense structure of amorphous to poorly defined chlorite and illite crystals (Figure 5.7F) and are superseded by well-developed chlorite platelets and fibrous and flaky illite, which are randomly orientated to each other, but normally oriented to the detrital grain surface (Figure 5.7A, Figure 5.7E & Figure 5.7F). The observed coating structure, with a root zone and superseding crystals, has been described by several authors for authigenic clay mineral coatings (e.g. Pittman and Lumsden, 1968; Wilson and Pittman, 1977; Pittman et al., 1992; Ajdukiewicz and Larese, 2012; Haile et al., 2015).

The occurrence of grain-coating chlorite and its importance for reservoir quality in the Skagerrak sandstone reservoirs has been reported from the J-Ridge area (Nguyen et al., 2013; Grant et al., 2014) and the Heron Cluster (McKie et al., 2010; Taylor et al., 2015). However, the mixed chlorite/illite coatings of the Egret samples show a tendency to bridge between grain coatings and thereby fill the pore space and block pore throats.

This is less common in the Heron and Skua sample sets where the overall clay mixture consists predominantly of chlorite and <5% illite. In general, pore-filling cements comprise smaller and less well developed chlorite crystals within a denser packing arrangement than seen for the grain coatings. The optical porosity loss by pore-filling clay cements can be up to 15% in some samples.

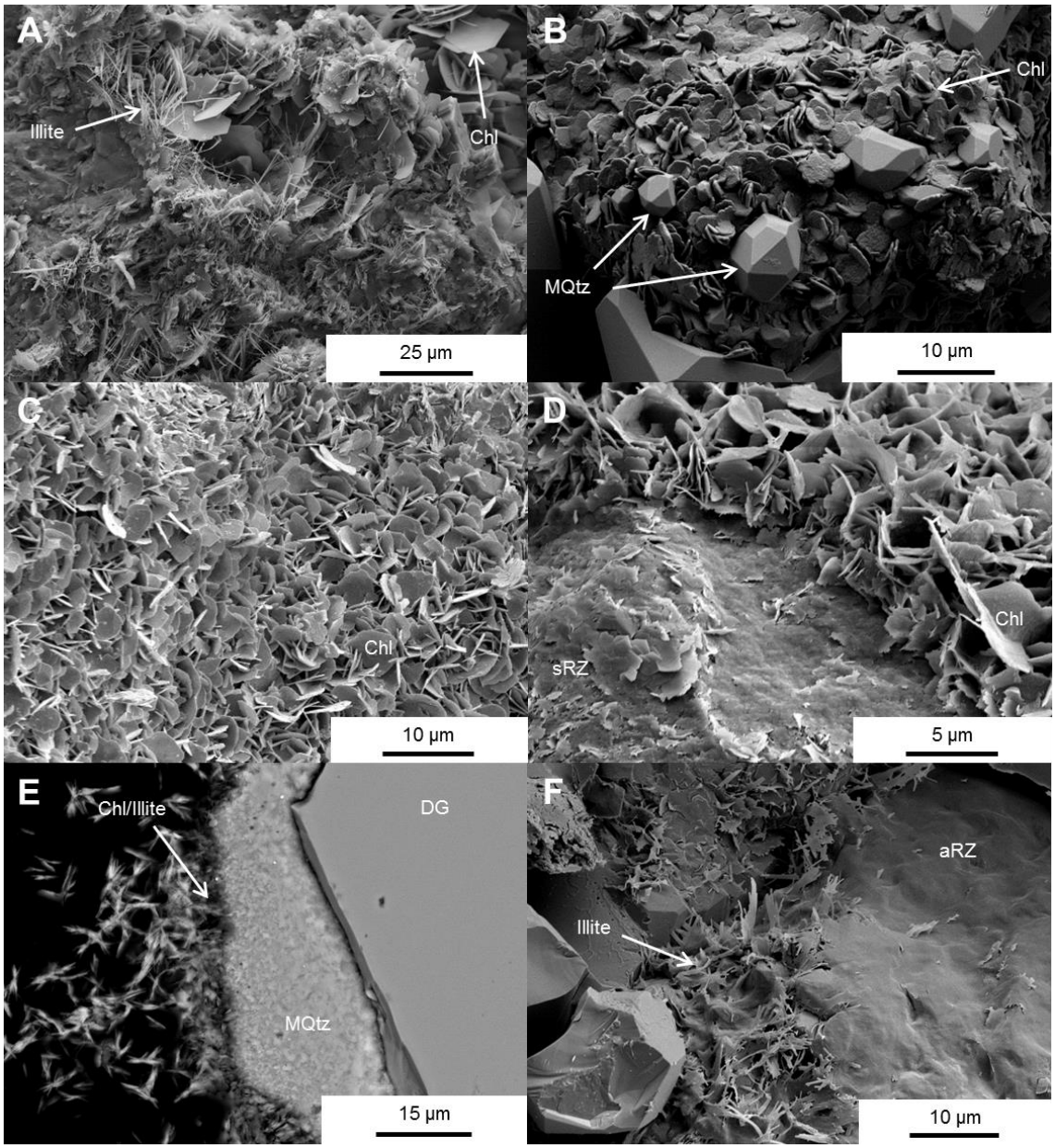

Figure 5.7 SEM images of A) chlorite (chl) and illite mixed clay mineral coats (Egret; 15042'10"); B) chlorite (chl) coatings with single outgrowing microquartz crystals (MQtz) (Heron; 15599'10"); C) well developed authigenic chlorite (chl) grain coating (Skua; 11887'); D) well developed authigenic chlorite (chl) coatings with a structured root zone (sRZ) (Skua; 11952'4"); E) a detrital grain with microquartz overgrowth (MQtz) underlying mixed clay mineral coating (chl/illite) (Egret; 14500'); F) amorphous root zone (aRZ) underlying illite grain coating (Egret; 14418'11").

Fe/Mg-ratio		
Egret	**Heron**	**Skua**
0.49	0.49	0.52
0.49	0.59	0.49
0.48	0.45	0.39
0.49	0.54	0.35
0.48	0.51	0.37
0.48	0.49	0.37
0.45	0.52	0.38
0.45	0.52	0.38
0.48	0.51	0.45
0.50	0.50	0.50
0.49	0.49	0.47
0.48	0.49	0.47
0.46	0.47	0.47
0.44	0.50	0.50
0.47	0.51	0.47
0.46	0.54	0.51
0.46	0.56	0.40
0.47	0.62	0.47
0.48	0.58	0.44
0.44	0.61	0.41
0.47	0.52	0.49
0.49	0.49	0.45
0.52	0.46	0.51
0.50	0.44	0.50
0.46	0.47	0.48
0.50	0.47	0.51
0.54	0.50	0.49
0.55	0.50	0.51
0.59	0.52	0.53
0.55	0.56	0.48
0.41	0.50	0.51
0.48	0.47	0.49
0.46		
0.47		
0.44		
0.46		
0.44		
0.42		
0.48	**0.51**	**0.46**

Table 5.5 Fe/Mg-ratio from SEM-EDS measurements of chlorite coats of the Egret, Heron and Skua samples, with the average values (grey fields).

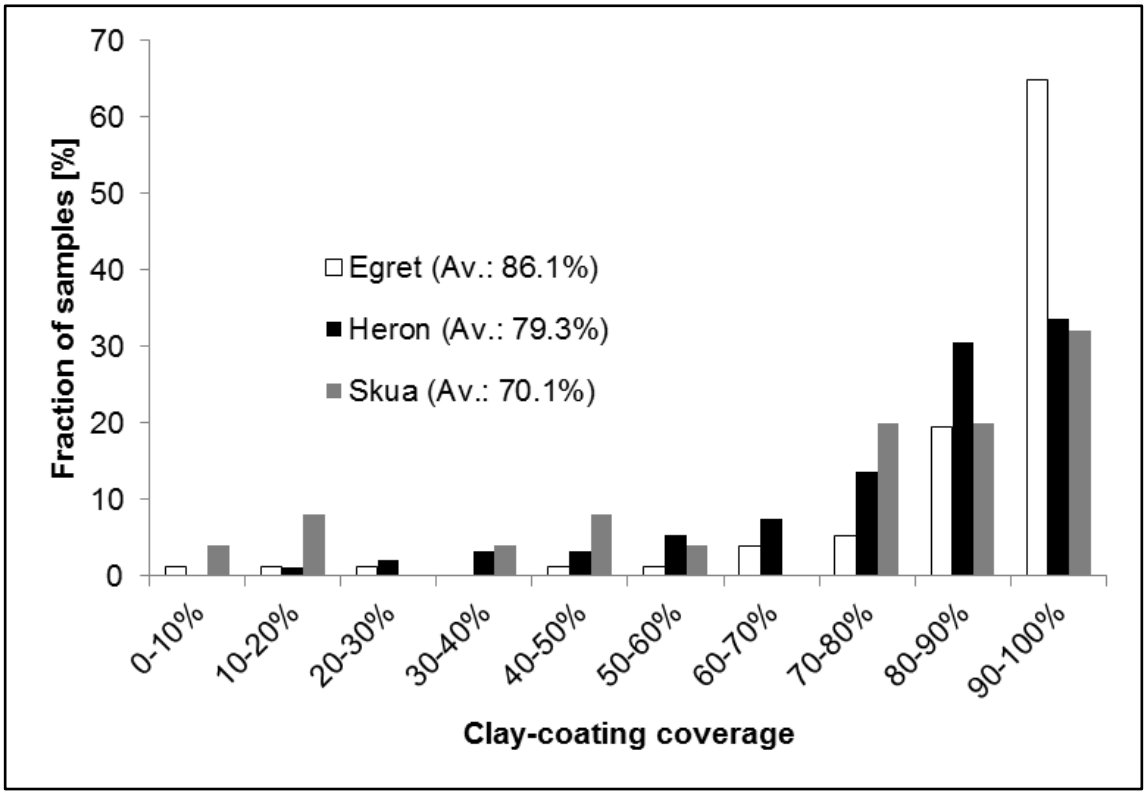

Figure 5.8 Clay-coating coverage of detrital grains in Egret, Heron, and Skua sample sets, with the average of coated grains (Av.).

5.5.3.3 Quartz cements

Quartz cements can be recognised in all three sample sets and is common in two types, either as very thin microquartz grain coatings (Figure 5.6C, Figure 5.7B & Figure 5.9A) or as more blocky and thick macroquartz overgrowths, present at non-coated grain surfaces or at breaks within the chlorite coatings (Figure 5.6C, Figure 5.6D & Figure 5.9B). The term microquartz overgrowth is here used for polycrystalline growth patterns of individual micro-sized quartz crystals ranging from 1 to 10 μm in length, which are in optical continuity or discontinuity with the detrital quartz grain (Aase et al., 1996; French and Worden, 2013). In comparison, macroquartz overgrowth is defined as syntaxial quartz overgrowth larger than 20 μm in optical continuity with the detrital quartz grain. The amount of quartz cement is generally very low in the three

investigated sample sets (<5% bulk volume), but can exceed 5% bulk volume in single samples.

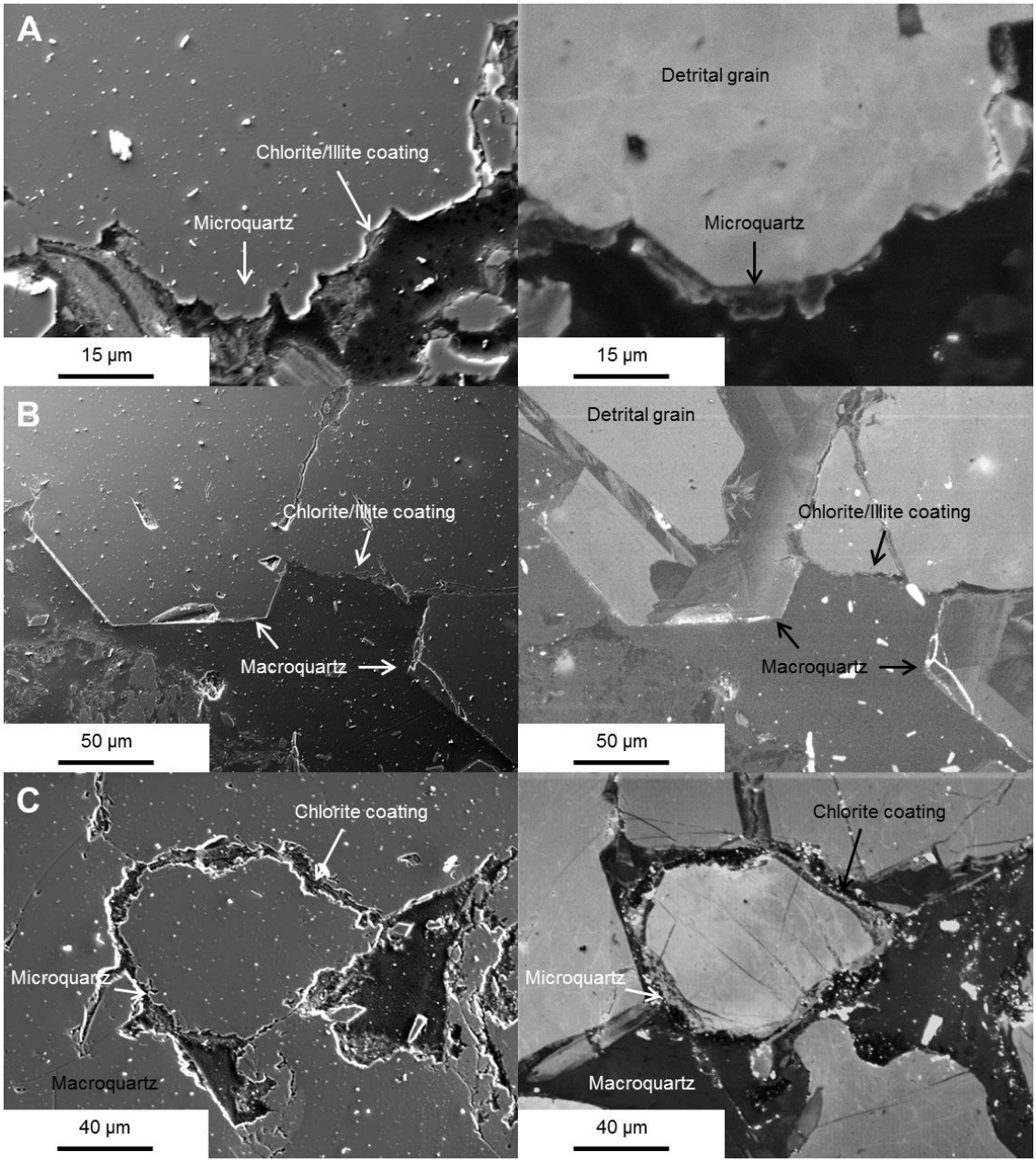

Figure 5.9 SEM and SEM-CL image pairs of A) microquartz growing on an detrital quartz grain (Egret; 15068'11"); B) macroquartz overgrowth on a detrital quartz grain next to an clay-coated grain without quartz overgrowth (Egret; 15068'11"); C) a fully chlorite-coated grain with minor microquartz between the detrital grain and the chlorite coating (Skua; 11895'7").

Fluid inclusion analyses have been undertaken on selected samples with higher quantities of quartz overgrowths and show high homogenization temperatures. The aqueous homogenization temperatures range from 145°C to 171°C for the Egret sample 15068’11’’, 104°C to 116°C and 133°C to 163°C for the Heron samples 15691’6’’ and 15721’11’’, and 133°C to 156°C for the Skua samples 11909’4’’ and 11931’0’’ (Table 5.4). The non-aqueous fluid inclusions are generally less common in the sample sets. Homogenization temperatures are between 70°C to 77°C for the Heron sample 15691’6’’ and are at 83°C for one inclusion in the Skua sample 11931’0’’ (Table 5.4).

The microquartz overgrowth tends to fill small cavities in the detrital quartz grain surface and to infill void spaces between the detrital quartz grain surface and the chlorite mineral coating (Figure 5.6C, Figure 5.6E & Figure 5.9C). Single microquartz crystals (<5 μm) can be found in between the chlorite platelets and the illite fibres (for Egret samples) and tend to outgrow the clay mineral coatings (Figure 5.7B & Figure 5.9C). This sublayer of microquartz precipitation beneath and between chlorite grain coatings has previously been recognized in high-temperature experimental studies by Ajdukiewicz and Larese (2012).

5.5.3.4 K-feldspar dissolution and cementation

K-feldspar dissolution and alteration can be observed in each of the sample sets. K-feldspar dissolution occurs generally during late burial, as indicated by clay mineral coatings, which preserve the original K-feldspar grain shape of partly or fully dissolved grains. The volume of K-feldspar cement ranges from approximately 1% to a maximum of 5%. Minor amounts of late-stage blocky authigenic K-feldspar overgrowth can be observed on uncoated and partly dissolved K-feldspar grains. Aqueous fluid inclusions in feldspar overgrowths in the Egret sample 15068’11’’ indicate cementation at high temperatures above 140°C. Non-aqueous fluid inclusions encountered in feldspars show

significantly lower temperatures between 45°C and 118°C across the three sample sets (Table 5.4). Highly altered and dissolved K-feldspar grains can coexist in close proximity to unaltered grains. Variations in feldspar microtextures exert control on reactivity, as demonstrated by Parsons et al. (2005).

5.5.4 Paragenetic sequence

The diagenetic development of the Skagerrak Formation in the investigated reservoirs is similar and therefore can be linked into a general relative sequence by their observed petrographic features (Figure 5.10 & Figure 5.6).

Evidence of mechanical compaction is present in Egret, Heron and Skua sample sets and, despite the overall shallow overpressure initiation and associated VES reduction, mechanical compaction is still the main driver of porosity reduction during the first 2500 m of burial (Figure 5.4). Nevertheless, the reduced VES accrual limited the effect of mechanical compaction significantly in the Skagerrak sandstones. Therefore, mechanical compaction is lower than in equivalent hydrostatically pressured sandstones (represented by the porosity-depth relationship for hydrostatically pressured shaly sandstone by Sclater and Christie (1980)) at equivalent depth (Figure 5.3).

Diagenesis started at shallow burial with localised carbonate cementation (e.g., ferroan dolomite), mainly internally sourced by dissolution of reworked calcrete or dolocrete fragments (Fig. 7A; McKie and Audretsch, 2005). Shallow carbonate precipitation is indicated by high IGVs, close to the assumed initial sandstone porosity of 45% (Beard and Weyl, 1973), in the cemented channel-base samples. High fluid inclusion homogenization temperatures in the Skua sample set and large single crystals indicate further diagenetic changes at higher temperatures (Table 5.4 & Figure 5.6B).

Authigenic clay mineral coatings developed after shallow carbonate cementation and prior to major quartz cementation (Figure 5.6C & Figure 5.6D). SEM and SEM-EDS analysis identified chlorite as the main coating clay mineral, with a minor amount of illite.

Feldspar dissolution occurs after the start of, but generally alongside, the continuous precipitation of authigenic chlorite and illite, which is indicated by clay mineral-coated feldspar grains where chlorite and illite tend to infill and overgrow dissolution cavities of partly dissolved feldspars (Figure 5.6F)

Fluid inclusions from blocky quartz overgrowths indicated late occurrence of quartz cementation at high temperatures of around 130°C to 170°C in the Skagerrak Formation. Quartz cement can be recognised as either very thin microquartz grain coatings (e.g., Figure 5.6C, Figure 5.7B & Figure 5.9A) or blocky and thick macroquartz overgrowths, present at non-coated grain surfaces or at breaks within chlorite coatings (e.g., Figure 5.6C, Figure 5.6D & Figure 5.9B). Several precipitation events can be observed for microquartz, indicated by various growth stages in SEM-CL images (Figure 5.9A & Figure 5.9C). High homogenization temperatures of up to 170°C for aqueous fluid inclusions in blocky macroquartz overgrowths indicate very late quartz cementation in the Judy Sandstone Member (Figure 5.10).

The non-aqueous fluid inclusions suggest that hydrocarbon emplacement occurred late in the burial history of the Egret, Heron and Skua fields. The microthermometry results from the coexisting hydrocarbon and aqueous inclusions reveals a temperature of around 60°C to 120°C for hydrocarbon inclusions and around 130°C to 170°C for aqueous fluid inclusions (Table 5.4). However, the homogenization temperature for the aqueous inclusions (i.e., 130°C to 170°C) represents the trapping temperature for both fluids as the oil was undersaturated with gas for the trapping pressure and temperature

(Munz et al., 1999; Munz, 2001). The fluid inclusion results concur with the commencement of hydrocarbon generation from the end of the Cretaceous and is completed by mid-Miocene times (Lines and Auld, 2004). Furthermore, feldspathic cementation can be observed and is identified as late-stage cement by aqueous fluid inclusion homogenization temperatures (Table 5.4).

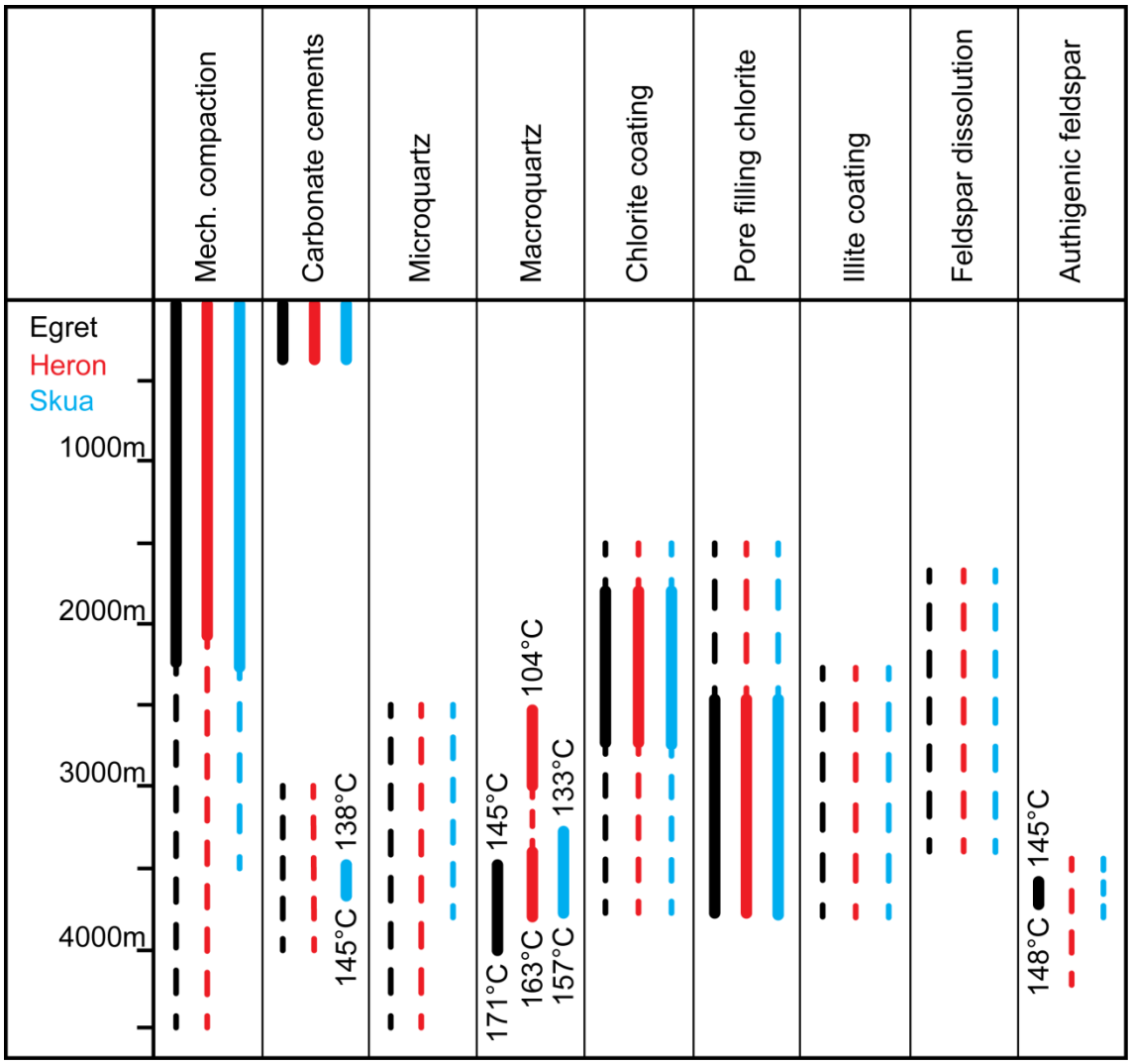

Figure 5.10 Paragenetic sequence of the main diagenetic processes for the Egret, Heron, and Skua fields, based on petrographic relationships and basin modelling, with fluid inclusion homogenization temperatures for aqueous carbonate, feldspar and quartz inclusions.

5.5.5 Porosity loss by mechanical compaction vs. cementation

Additional petrographic data such as intergranular volume (IGV) (Paxton et al., 2002) and total cement volume (C) can be used to calculate the porosity loss due to mechanical compaction (COPL) and cementation (CEPL) after Lundegard (1992):

$$COPL = P_i - \left(\frac{(100 - P_i) P_{mc}}{100 - P_{mc}} \right) \quad (5.2)$$

$$CEPL = (P_i - COPL) \left(\frac{C}{P_{mc}} \right) \quad (5.3)$$

where P_i is the initial or depositional porosity (here assumed to be 45%; Beard and Weyl, 1973) and P_{mc} is the intergranular volume or minus-cement porosity calculated by subtracting the total cement volume (C) from the optical primary porosity. The calculated COPL and CEPL are only accurate if three conditions are met. First, the assumed initial porosity P_i must be correct. Second, the amount of cement derived by local grain dissolution must be negligible or known. And third, the amount of framework mass exported by grain dissolution must be negligible or known (Lundegard, 1992). The calculated porosity losses by mechanical compaction (COPL) and by cementation (CEPL) show a similar pattern for the Egret, Heron and Skua fields (Figure 5.11). The average values of COPL and CEPL are 26.8% and 9.2%, with 29.1% and 8.8% for Egret, 24.8% and 9.6% for Heron and 26.4% and 9.1% for Skua sample sets. These values show that the main porosity loss in the Egret, Heron and Skua is due to mechanical compaction rather than cementation (Figure 5.11).

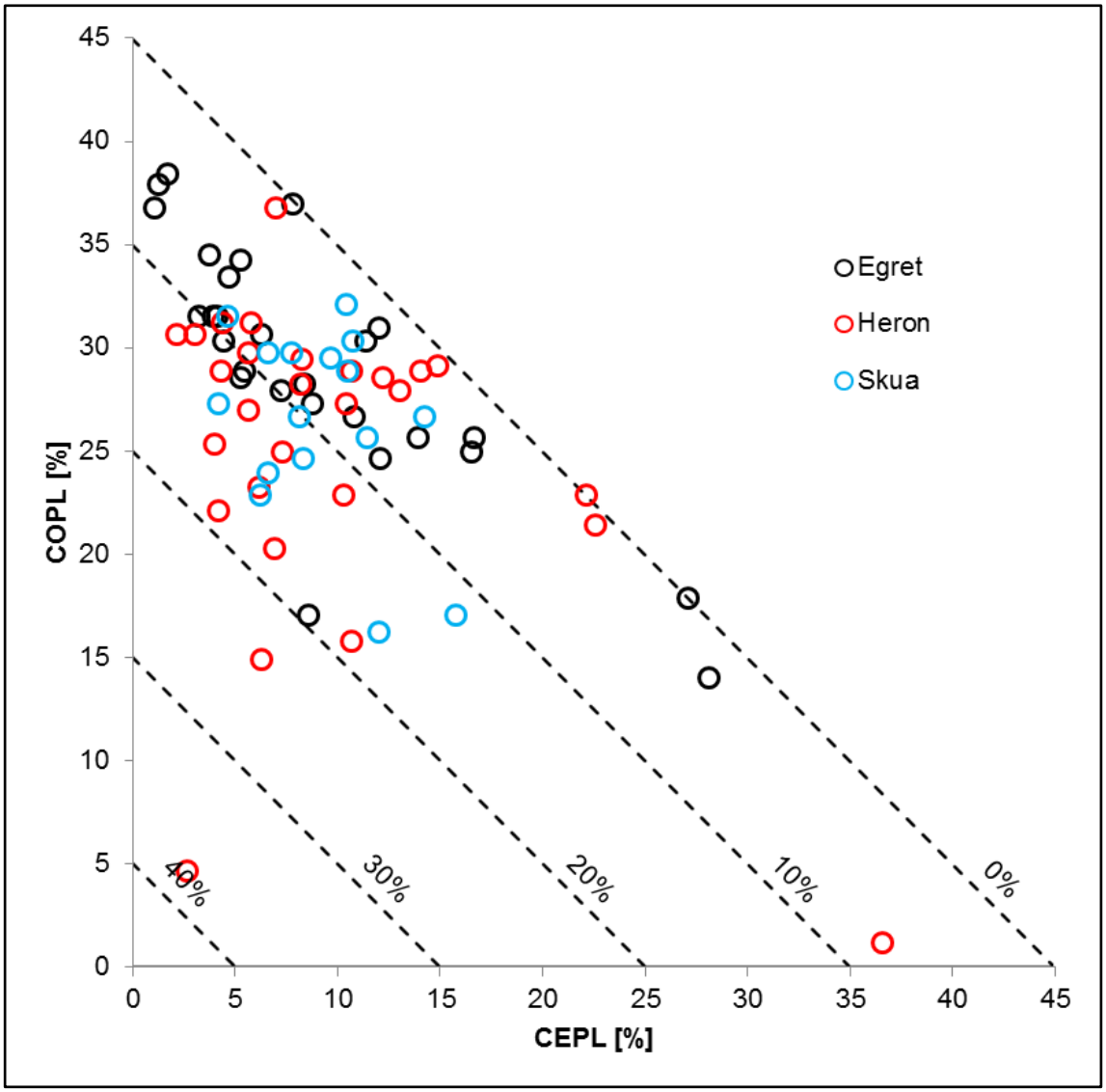

Figure 5.11 Compactional porosity loss (COPL) and cementational porosity loss (CEPL) for Egret, Skua, and Heron datasets, calculated according to Lundegard (1992).

5.6 Discussion

5.6.1 Vertical effective stress and porosity evolution

The positive effect of pore fluid pressure and low VES on porosity preservation has been well known since Terzaghi developed the concept of effective stress. However, a combination of magnitude and timing of onset of overpressure needs to be considered for enhanced porosity preservation in siliciclastic reservoirs. Pore fluid overpressure can slow down or arrest mechanical compaction by reducing the vertical effective stress during ongoing burial, but cannot increase porosity. Therefore, overpressure developed during (shallow) initial burial is crucial for maintaining primary porosity and good reservoir quality to depth (e.g., Ramm and Bjørlykke, 1994; Osborne and Swarbrick, 1999; Schneider and Hay, 2001; Sathar and Jones, 2016). Furthermore, overpressured reservoirs have no fluid influx from surroundings with lower overpressure, which allows them to evolve within their own fluids (Jeans, 1994). This reduces the overall number of diagenetic processes that may affect the overall reservoir quality.

The pore fluid overpressure in the Skagerrak sandstone reservoirs initiated (0.01 MPa) at around 60 Ma (Egret & Heron) and 50 Ma (Skua) at shallow burial and increased with ongoing burial to the present-day maximum. The very shallow onset and rapid increase of overpressure enabled the pore fluids to reduce the load borne by intergranular and cemented grain contacts within the sandstones (Figure 5.12). It is to be noted that late development and deeper onset of overpressure would have had a much smaller to negligible effect on porosity preservation in the reservoir sandstones. The reduced stress on the grain framework causes a reduction in mechanical compaction and chemical compaction (pressure dissolution) at grain contacts (Osborne and Swarbrick, 1999). The reduced mechanical compaction rate can be easily observed in the datasets, where a predominance of point, long or concavo-convex grain contacts occurs

compared with sutured or stylolitic quartz grain contacts which would be expected in deeply buried hydrostatic reservoirs. The effect of overpressure on reservoir quality is the highest with onset depths above 1500 m because the reduction of porosity and intergranular volume is particularly strong in hydrostatically pressured sandstones over this depth range (from 42% to 28% on average; Paxton et al., 2002). Nevertheless, low VES can still have an impact on compaction processes beyond 1500m burial depth due to the lower limit of physical grain compaction of approximately 26% porosity or IGV at 2500 m (Paxton et al., 2002), and late-stage chemical compaction.

Significant porosity preservation is commonly suggested to occur during late-stage chemical compaction due to the occurrence of authigenic chlorite grain coatings (e.g. Bloch et al., 2002; Ajdukiewicz and Larese, 2012). However, it has been recognized that the rate of quartz cementation increases as an exponential function of temperature during burial and estimated that the rate may increase by a factor of 1.7 for every 10°C temperature increase (Walderhaug, 1996). Temperature has been considered by far the most important control on the rate of quartz precipitation in deeply buried sandstones (Bjørkum, 1996; Walderhaug, 1996; Lander et al., 2008). The amount of quartz cementation and porosity can be modelled as an exponential function (Arrhenius equation) of the temperature integrated over time, and forms the basis of many commercially available programs for predicting reservoir quality. The occurrence of minerals at grain contacts are also thought to be important and dissolution is considered to be enhanced by mica or clay minerals at quartz grain contacts (Bjørkum, 1996).

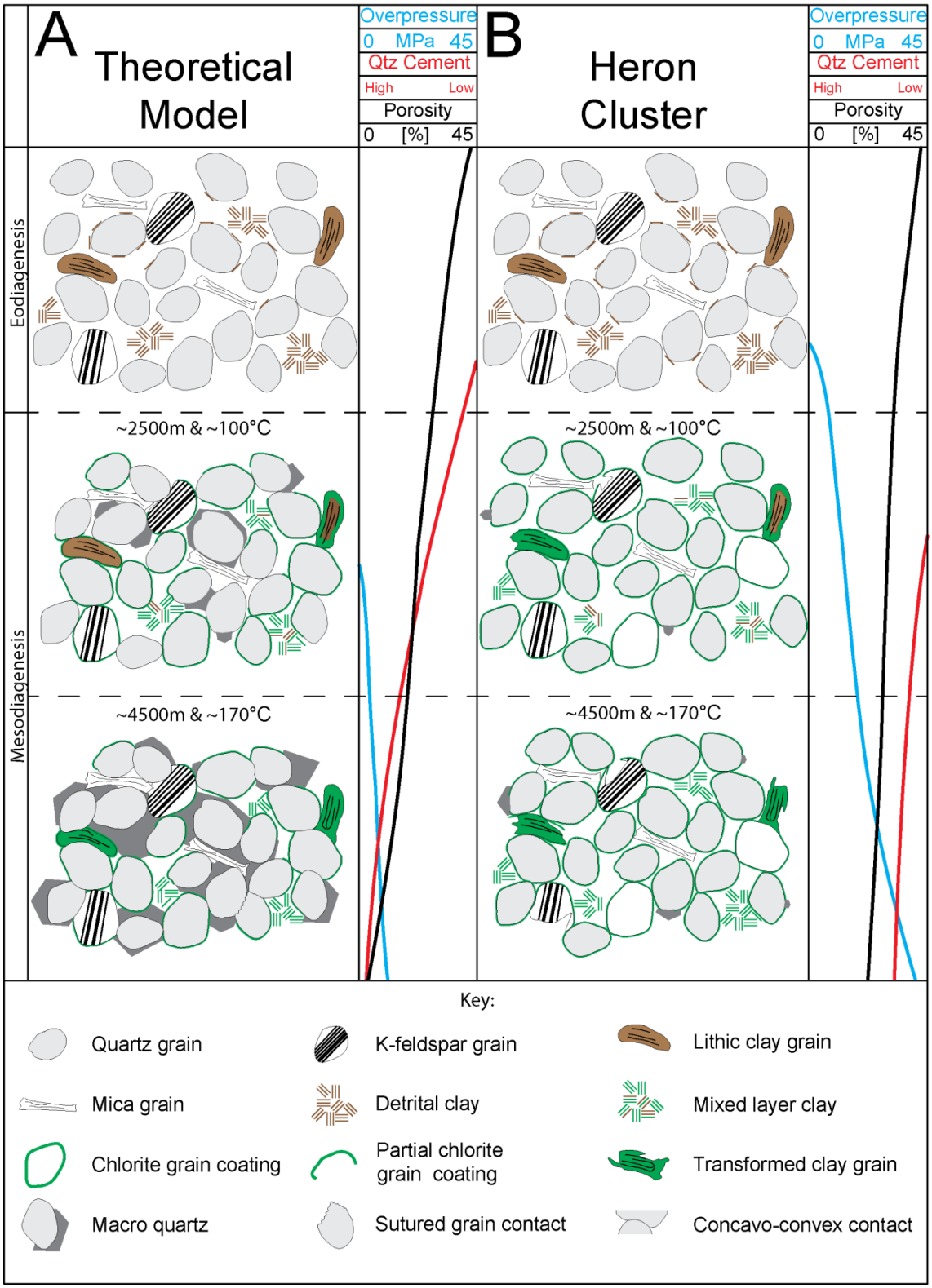

Figure 5.12 Schematic diagram for the comparison of A) a theoretical representation of a deeply buried siliciclastic reservoir with the same starting composition and grain size as the Skagerrak sandstone reservoirs and B) the HPHT Skagerrak sandstones from the Egret, Heron and Skua fields.

This study has provided evidence from the Skagerrak Formation sandstones that shallow onset of pore fluid pressure can arrest the rate of quartz cementation and maintain an enhanced porosity to greater burial depths than normally would be expected under hydrostatic conditions and as a function of temperature alone (Figure 5.12). Quartz cementation is far more sensitive to pore fluid overpressure than has previously been recognised. This is in part due to the significant role that the low VES plays in limiting and forestalling the onset of intergranular pressure dissolution at grain contacts (e.g., Osborne and Swarbrick, 1999; Swarbrick et al., 2000; Sheldon et al., 2003; Becker et al., 2010). Quartz cementation and especially quartz overgrowths on detrital quartz grains are widely reported as diagenetic and porosity reducing processes in deeply buried quartz-rich sandstones (e.g., McBride, 1989; Walderhaug, 1990, 1994a; Vagle et al., 1994; Worden and Morad, 2000). Stylolitisation and dissolution at intergranular grain contacts have often been reported as the main internal source of quartz cement in many siliciclastic reservoirs (e.g., Houseknecht, 1988; Bjørkum et al., 1993; Walderhaug, 1994a, 1994b). The low VES halted stylolitisation in the Skagerrak Formation sandstones and reduced stress on the grain framework and grain contacts (Figure 5.12). The supply of dissolved silica to the pore fluid was thereby reduced, which led to a lower silica saturation of the pore fluid and finally to lower and later quartz cement precipitation (Osborne and Swarbrick, 1999; Sathar and Jones, 2016).

5.6.2 Authigenic clay coatings and reservoir quality

The development of clay mineral coatings is often reported to be closely linked to the absence of extensive quartz cementation. The role played by clay mineral coatings in siliciclastic reservoirs is of significant interest for the maintenance of exceptional reservoir quality (e.g., Taylor et al., 2010; Ajdukiewicz and Larese, 2012).

Clay mineral coatings in the Skagerrak Formation are generally well developed and consist mainly of authigenic chlorite, with minor amounts of authigenic illite (especially in the Egret field). SEM-EDS analyses of the chlorite coatings classify them as intermediate to Fe-rich for the Egret and Heron samples, with Fe/Mg-ratio of 0.4-0.55 (Egret) and 0.45-0.6 (Heron) and as intermediate to Mg-rich for Skua (0.35-0.5) (Table 5.5) (Hillier and Velde, 1992; Grigsby, 2001). The observed Fe/Mg-ratios correlate well with reported ratios in the range 0.25–0.65 for terrestrial sediments (Dowey et al., 2012). The SEM-EDS analysis also showed that the authigenic chlorite and illite is fully transformed without any remnant precursor clay composition.

Dowey et al. (2012) reported three possible building mechanisms for chlorite grain coatings in fluvial environments; firstly grain coating Fe-rich clay minerals, secondly the mechanical infiltration of precursor clay minerals (e.g., smectite) and, thirdly the alteration of detrital grains. The chloritization and illitization of smectite is the most likely diagenetic pathway for authigenic chlorite and illite grain coatings in the Skagerrak Formation. Mechanically infiltrated smectite was probably attached flatly to the detrital grains during or shortly after deposition (Matlack et al., 1989) (Figure 5.12). The chloritization of smectite requires a source of aluminium (e.g., Hillier, 1994; Humphreys et al., 1994) and takes place at temperatures between 60°C and 100°C (e.g., Worden and Morad, 2003). Illitization of smectite also requires a source of aluminium and potassium and is reported to occur at temperatures above 90°C (e.g., Worden and Morad, 2003). Detrital smectite coatings have been continuously transformed into authigenic chlorite with increasing temperatures and dissolution of detrital K-feldspar (Figure 5.6F & Figure 5.12).

The authigenic chlorite grain coatings in the Heron Cluster fields are well developed and cover more than 70% of the detrital grain surfaces (Figure 5.8 & Figure 5.12).

Nevertheless, there are differences in composition and appearance. The coatings in the Heron and Skua sample sets are typical edge-to-edge chlorite coatings with a platy crystal structure similar to those observed by Pittman et al. (1992). The clay mineral coatings in the Egret field are generally thicker and contain a higher amount of fibrous illite (Figure 5.7A & Figure 5.7F). The Egret field coatings are structurally more variable in their morphology, compared with the Heron and Skua coatings. The general coating structure, described by Pittman et al. (1992), is consistent in all three sample sets, with a flatly attached root zone and superseding chlorite and/or illite crystals (Figure 5.7D). Where high amounts of fibrous illite occur, the root zone is structurally less well developed and amorphous in comparison to a pure chlorite grain coating (Figure 5.7F)

Ajdukiewicz and Larese (2012) observed quartz nucleation below the root zone and in between the crystals of the chlorite coatings at temperatures above 115°C, and concluded that chlorite coatings may retard quartz nucleation at moderate temperatures, but permit quartz nucleation at high temperatures similar to those encountered in the Skagerrak Formation. This quartz tends to infill the microporosity of the chlorite coatings and produces a sub-layer beneath them. Intact chlorite coatings provide an effective barrier for potential quartz crystal growth from the detrital surface into the pore space, due to the high crystal interconnection (Pittman et al., 1992; Ajdukiewicz and Larese, 2012; Haile et al., 2015). Illite coatings, on the other hand, are less able than chlorite coatings to prevent quartz outgrowths due to the normally oriented, fibrous crystals and the low degree of crystal interconnection (Guven et al., 1980; Storvoll et al., 2002; Wilson et al., 2014). The mixed clay coatings in the Egret field have a very high surface coverage (>85%; Figure 5.8).

High homogenization temperatures for the aqueous fluid inclusions in the quartz overgrowths (Table 5.4 ; 145°C to 171°C) indicate the importance of clay mineral coatings and vertical effective stress for retardation of quartz precipitation (Figure 5.12). Mixed chlorite/illite coatings (Figure 5.7F) show commonly a more amorphous root-zone, which lead to a better surface coverage and provide a more effective barrier to quartz nucleation than pure chlorite coatings alone.

5.6.3 Microquartz grain coatings

Microquartz grain coatings are polycrystalline growth patterns of individual micro-sized quartz crystals ranging from 1 to 10 μm in length, which are in optical continuity or discontinuity with the detrital quartz grain (Aase et al., 1996; French and Worden, 2013) and often reported to be closely linked to the absence of extensive macroquartz cementation.

Microquartz coatings have been described as layers of randomly oriented, micro-sized quartz crystals crystallographically misoriented with respect to the host grain (e.g., French et al., 2012; French and Worden, 2013). Microquartz can be observed in several forms in the Skagerrak sandstones, such as coating layers below clay coatings (Figure 5.6C & Figure 5.6E) or as single crystals, outgrowing clay mineral coatings (Figure 5.7B). Cathodoluminescence analysis of the microquartz in the three sample sets indicated multiple precipitation and growth events (Figure 5.9A & Figure 5.9C), mainly below the chlorite grain coatings and in between the chlorite crystals (Figure 5.6E, Figure 5.7E, Figure 5.7B & Figure 5.9C). The microquartz is likely to have been precipitated at higher temperatures (>115°C), as demonstrated by Ajdukiewicz and Larese (2012).

However, the contribution of the microquartz coatings towards the preservation of reservoir quality is minor to negligible in the Skagerrak Formation. The presence of well-developed chlorite grain coatings and high pore fluid pressures have played a more significant role to inhibit extensive macroquartz cementation.

5.6.4 Macroquartz cementation and reservoir quality

Quartz cementation is generally scarce in the Skagerrak Formation but can be observed as microquartz and macroquartz cement at non-coated detrital grain surfaces in all three sample sets. Quartz cementation starts generally at temperatures around 70°C to 80°C (e.g., McBride, 1989; Walderhaug, 1994a, 1994b; Worden and Morad, 2000) with very slow precipitation rates, which increase with increasing temperatures (Walderhaug, 1994a). Walderhaug (1994b) expressed the temperature dependence of macroquartz precipitation mathematically:

$$r = 1.98 \times 10^{-22} \times 10^{0.022 \times T} \qquad (5.4)$$

where r is the precipitation rate in moles per square centimetre and T is the temperature in degrees Celsius. The quartz precipitation rate can be converted into a linear outwards growth rate for quartz cement in cm/s by multiplying r by the molar mass of quartz (60.08 g/mol) and dividing by the density of quartz (2.65 g/cm^3). This leads to linear quartz cement outgrowth rates as a function of temperature, e.g., 0.04908 μm/Ma at 70°C or 1.70210 μm/Ma at 140°C (Table 5.6). The calculated linear quartz growth rates can be used to estimate the time necessary to enclose a small fluid inclusion (4 μm) at certain temperatures (Table 5.6).

The comparison of the quartz growth rates for overgrowth and the rapid burial rates for the Triassic Skagerrak show that fluid inclusions are unlikely to form at temperatures below 100°C to 110°C due to the slow quartz growth rates (Table 5.6) and the rapid

burial rates of the Skagerrak Formation (Figure 5.4). The lowest aqueous homogenization temperatures from quartz cements are consistent with this observation (Heron; Table 5.4), but the majority of the aqueous homogenization temperatures are above 130°C.

We have already argued for potential inhibition of quartz cementation by clay coatings, microquartz coatings and particularly overpressure, and suggest that the combined effect of all these processes produces predominantly high temperature quartz overgrowths.

Temperature	**Precipitation rate [r]**	**Linear outgrowth [g_l]**		**Critical time [t_c]**
[°C]	[mol/cm^2]	[cm/s]	[µm/Ma]	[Ma]
70	6.86539E-21	1.55661E-19	0.049089	81.48414
80	1.13937E-20	2.58333E-19	0.081468	49.09905
90	1.89089E-20	4.28726E-19	0.135203	29.5851
100	3.13809E-20	7.11509E-19	0.224381	17.82679
110	5.20793E-20	1.18081E-18	0.37238	10.7417
120	8.64301E-20	1.95966E-18	0.617998	6.472515
130	1.43438E-19	3.25222E-18	1.025621	3.900076
140	2.38048E-19	5.39735E-18	1.702107	2.350028
150	3.95062E-19	8.95737E-18	2.824795	1.416032
160	6.5564E-19	1.48655E-17	4.687993	0.853244
170	1.08809E-18	2.46706E-17	7.780131	0.51413

Table 5.6 Calculated, temperature-dependent quartz precipitation rates, with the temperature, the precipitation rate, the linear outgrowth rate and the critical time to enclose a fluid inclusion of 4 µm.

5.7 Conclusions

1. The HPHT Skagerrak Formation sandstone reservoirs of the Egret, Heron and Skua fields (UK Quadrant 22) have enhanced porosities in the range of 18 to 35%, despite their depths of burial and elevated temperatures.
2. Porosity in the Skagerrak Formation was preserved through a combination of shallow onset of pore fluid pressures, reducing mechanical compaction, and well developed chlorite and mixed chlorite/illite grain coatings, inhibiting quartz cementation.
3. The shallow onset of high pore fluid pressure (at end of Cretaceous) and its maintenance to the present day contributed to the inhibition of macroquartz overgrowths by reducing pressure dissolution at detrital quartz grain contacts.
4. Authigenic chlorite and mixed chlorite/illite coat most detrital quartz grain surfaces (>70% surface coating) and restricted the development of abundant pore-filling quartz cement despite elevated temperatures (up to ~180°C at the present day). The abundance of quartz cement correlates well with grain coat coverage and shows no relationship to the presence of hydrocarbon pore fluids.
5. Burial history modelling using detailed fluid inclusion analyses and quantitative petrography of the Skagerrak Formation reservoir sandstones has revealed that macroquartz overgrowths have been inhibited up to very high burial temperatures (~185°C) by low vertical effective stress and well developed clay mineral coatings. The results indicate that the range of porosities preserved provide potential for exploration in the deeper (>5500 m below seafloor) and HPHT portions of the Central Graben, North Sea.

Chapter VI

Reservoir quality of fluvial HPHT sandstone reservoirs in a salt-walled mini-basin, Seagull field, Central Graben, North Sea, UK

6.1 Introduction

Deposition controls clastic reservoir quality by determining the overarching starting rock characteristics such as composition and grain size which are primary controlling factors. The depositional setting and its effects on reservoir quality are of particular interest for clastic reservoirs in evaporitic basins, where contemporaneous salt movement influences sedimentation and resulting facies distribution (e.g., Fox, 1998; Banham and Mountney, 2013a, 2013b). Contemporaneous salt movement influences the rate of basin subsidence, sediment transport pathways and potential sediment reworking due to the partial uplift in evaporitic basins (Banham and Mountney, 2013b). Burial-related diagenesis also plays a significant role for governing reservoir quality, as it can destroy, preserve, or enhance porosity and permeability, whatever the grain size or starting composition.

Hydrocarbon reservoirs in evaporitic basins have always been of interest for the hydrocarbon industry. Recent research have contributed to a deeper understanding of salt tectonics and related processes in salt-walled mini-basins (e.g., Hudec and Jackson, 2007; Archer et al., 2012; Hudec et al., 2013). Such studies have increased our understanding of salt movement, the development of salt-walled mini-basins, and on the effects of coeval halokinesis on sedimentary processes and facies distribution (e.g., Fox, 1998; Hudec et al., 2009; Banham and Mountney, 2013a, 2013b). However, a detailed understanding of the complex effects of contemporaneous salt movement on diagenesis and reservoir quality is yet to be established.

The fluvial sediments of the Triassic Skagerrak Formation were deposited in an array of salt-walled mini-basins within the Central Graben, Central North Sea (see Chapter 3; e.g., Smith et al., 1993; Bishop, 1996; Helgeson, 1999; McKie, 2014). This study

investigates the effect of contemporaneous salt movement on diagenetic processes and reservoir quality of the high-pressure, high-temperature (HPHT; >65 MPa and >150°C) sandstone reservoirs in a salt-walled mini-basin setting. Fluvial channel sandstone samples of the Skagerrak Formation from two wells of the Seagull field (22/29-2 and 22/29-3) have been investigated to:

- Identify how the salt-walled mini-basin setting controls the reservoir quality in the fluvial sandstones of Triassic Skagerrak Formation within the Central North Sea
- Identify the influences of contemporaneous salt movement on fluvial sand deposition and early diagenesis
- Identify the influence of halokinesis on fracturing and clay infiltration to guide prediction of the best reservoir quality in salt-walled mini-basins

6.2 Geological setting

The Central Graben of the North Sea is a prolific hydrocarbon province containing more than 20 billion barrels of discovered hydrocarbons. The Central Graben is 70-130 km wide and 550 km long. It forms the southern arm of a trilete rift system (i.e., an incipient ridge-ridge triple junction) in the North Sea with the Viking Graben as the northern arm and the Moray Firth Basin as the western arm (Figure 6.1A). The Forties-Montrose High and Josephine Ridge horst blocks divide the Central Graben into the East Central Graben and the West Central Graben, flanked by the Norwegian basement in the east and the UK continental shelf in the west. The rift system developed in at least two major extension phases, one during the Permian-Triassic (290-210 Ma) and another in the Late Jurassic (155-140 Ma) (Gowers and Saeboe, 1985; Glennie, 1998).

This study focuses on the Seagull field (wells: 22/29-2 & 22/29-3) at the southern end of the Forties-Montrose High in UK Quadrant 22 (Figure 6.1B) which is a part of the ETAP (Eastern Trough Area Project) area and a wider HPHT province, including Triassic strata of the Central Graben and the southern Viking Graben (Goldsmith et al., 2003).

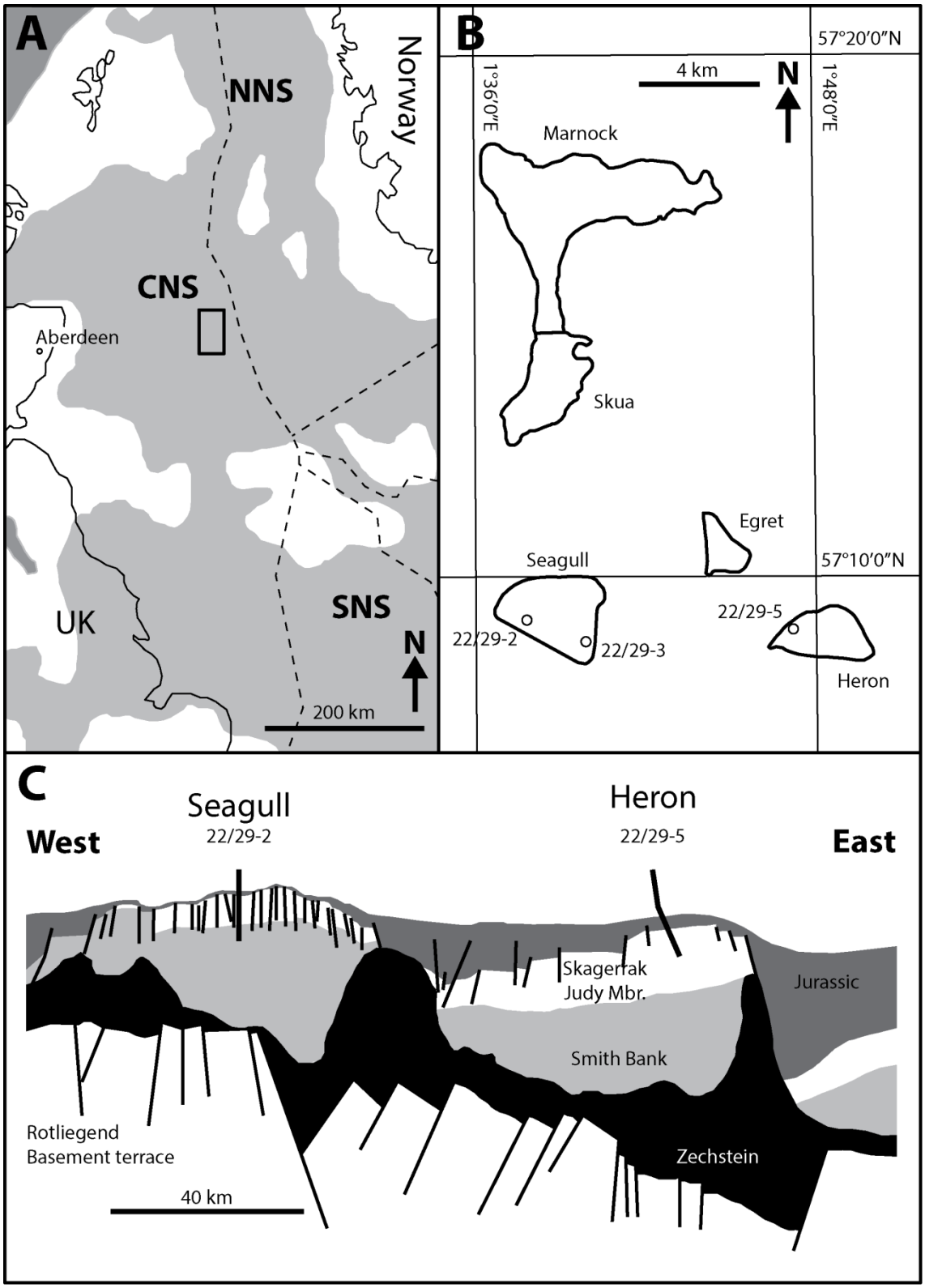

Figure 6.1 Central North Sea location with A) Regional distribution of the Triassic basin-fill in the North Sea region (grey) after McKie and Shannon (2011) and Mckie et al. (2010) with NNS: Northern North Sea, CNS: Central North Sea, SNS: Southern North Sea; B) Detailed outline of the study area with the Skagerrak Formation reservoirs of the area (outlined in black on the regional map A); C) Schematic cross section of the Seagull field and the Heron field after (McKie et al., 2010; McKie, 2011).

6.2.1 Skagerrak Formation stratigraphy

The Triassic strata of the Central North Sea area are dominated by thick alluvial successions which show no connection to a marine realm (Goldsmith et al., 2003). The Central Graben Triassic succession is subdivided into the Early Triassic Smith Bank and Bunter Formations (shales, evaporites and thin sands) and the Middle to Late Triassic Skagerrak Formation (thickly interbedded sands and shales). The Middle to Late Triassic Skagerrak Formation in the Central Graben, North Sea comprises 500-1000 m of predominantly continental braided and meandering fluvial systems and terminal fluvial fans with lacustrine facies (McKie and Audretsch, 2005; de Jong et al., 2006; Kape et al., 2010). The stratigraphic nomenclature of the Triassic for the Central Graben was defined by Goldsmith et al. (1995), based on detailed biostratigraphic and lithostratigraphic correlation of wells from the Josephine Ridge and was extended and correlated towards the ETAP area by McKie and Audretsch (2005).

The Skagerrak Formation in the Central Graben is subdivided into three sand-dominated successions (Judy, Joanne and Josephine) and three mud-dominated successions (Julius, Jonathan and Joshua). The sand-dominated units include sheetflood deposits and multi-storey stacked channel sandbodies (Goldsmith et al., 1995; McKie and Audretsch, 2005), whereas the mud-dominated units include a variation of non-marine, basin-wide floodplain, lacustrine shale, loess and playa lake deposits. The thick and laterally extensive mud-dominated units provide the main correlative units for the Triassic Skagerrak in the Central Graben (McKie and Audretsch, 2005). The present-day Triassic stratigraphy of the ETAP area is incomplete due to deep erosion during the Middle and Late Jurassic (Erratt et al., 1999; McKie et al., 2010). The stratigraphy comprises the Early Triassic Smith Bank and Bunter Formations and the lowermost

members of the Skagerrak Formation (Judy Member and Julius Member) (McKie and Audretsch, 2005; McKie et al., 2010).

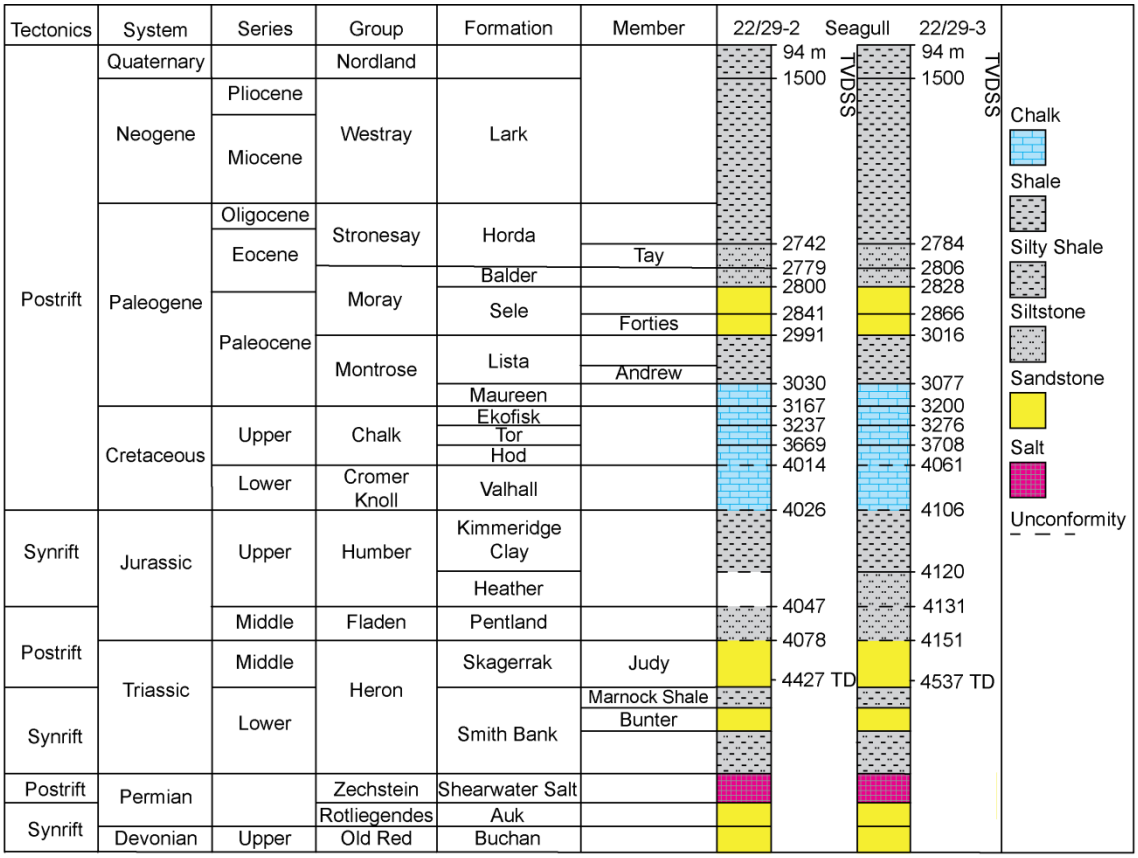

Figure 6.2 Stratigraphy of the Seagull field wells 22/29-2 and 22/29-3. Also see Figure 3.2.

The Skagerrak Formation of the Seagull field comprises a major sandstone reservoir, the Judy Sandstone Member, which is bound by regional shale markers of the Marnock and Heron Shales, equivalent to the Julius Mudstone Member and the upper Smith Bank (Figure 6.2; McKie and Audretsch, 2005). McKie and Audretsch (2005) subdivided the Judy Member into a lower terminal splay-dominated interval and an upper channelised interval, separated by a shale-prone section. The lower terminal splay facies is characterized by fine-grained, planar cross-bedded and ripple-laminated sandstones. In comparison, the upper interval is dominated by channel-fill deposits, which are organized into fining upward packages with coarse lag deposits (usually with ripped-up

calcrete nodules) commonly occurring at the base. Channel-fill deposits are characterized by well sorted cross-bedded sandstones and can be separated in channel and sheet-dominated sandstones (McKie and Audretsch, 2005; McKie, 2011).

6.2.2 Mini-basin development and halokinesis

Triassic sediments of the Central Graben, North Sea, accumulated directly on top of the Late Permian Zechstein salt within a series of salt-controlled and fault-controlled mini-basins or pods (Figure 6.1C). The Late Permian Zechstein salt strongly controlled the Triassic deposition by forming salt withdrawal mini basins within an overall rift-controlled basinal tectonic setting (Smith et al., 1993; Bishop, 1996; Matthews et al., 2007). The initiation of mini-basin subsidence or creation of salt-walled mini-basins requires the presence of salt with a sufficient thickness to allow halokinesis (Hudec et al., 2009), and a mechanism to initiate halokinesis, i.e., extension, compression, differential loading, or buoyancy (Banham and Mountney, 2013b). The mini-basins and salt walls in the Central Graben are generally in alignment with the overall rift-controlled basement structure, i.e., the Permian fault system. The halokinesis of the Zechstein evaporites started during the Triassic rifting due to reactivation of the Permian faults system and localised loading by Triassic sediments in the Central Graben (Hodgson et al., 1992; Smith et al., 1993; Bishop, 1996; Matthews et al., 2007). The salt had been unevenly distributed across Central Graben area (Glennie et al., 2003). This led to variations in the mini-basin development, the variable creation of accommodation space throughout the Triassic period, and the potential grounding of mini-basins on the basement (Figure 6.1C). The coeval halokinesis of the thickly developed Zechstein salt significantly influenced the depositional environment of the Triassic deposits in the Central Graben. It controlled the overall subsidence of the mini-basins, sediment transport pathways, and the reworking and uplifted sediments

(Banham and Mountney, 2013b). Salt withdrawal has allowed considerable thicknesses of Triassic sediment to accumulate within mini-basins in the Central Graben area. Reduced salt thickness allowed the grounding of the Seagull mini-basin in the Late Triassic on the underlying Rotliegend basement (Figure 6.1C) (McKie and Audretsch, 2005; McKie et al., 2010). The syn-rift and halokinesis controlled Smith Bank Formation sediments represent the bulk and basal part of the Seagull mini-basin infill, whereas the overlying post-rift and halokinesis controlled Skagerrak Formation sediments are the thinner upper part of the mini-basin infill. The coeval halokinesis has been responsible for depositional variations in the Judy Sandstone Member in the Seagull mini-basin and general facies variability between the centre and margins of all the mini-basins. The varying Zechstein salt thickness created variable Skagerrak sediment thicknesses within mini-basins and between different mini-basins. Furthermore, the salt mini-basins created facies variability within mini-basins and between mini-basins that has influenced reservoir thickness and diagenetic cementation including halite cements relating to the underlying Zechstein salt mobilisation (Nguyen et al., 2013).

6.3 Methodology

6.3.1 Sampling

Core samples and thin sections examined in this study have been from ribbon and channel sandstones selected as having the best reservoir quality. A total of 65 sandstone samples have been taken from the cored Skagerrak intervals of the 22/29-2 well (36) and the 22/29-3 well (29). The samples have been collected from depth intervals of 4090 to 4200 m TVDSS (22/29-2) and 4170 to 4235 m TVDSS (22/29-3). The 65 samples represent confined fluvial channel sands (48 in total: 26 in 22/29-2 and 21 in

22/29-3), unconfined fluvial sands (11 in total: 8 in 22/29-2 and 3 in 22/29-3) and lacustrine shore facies sediments (7 in total: 4 in 22/29-2 and 3 in 22/29-3). Solely channel sandstone samples have been used for the reservoir quality analysis throughout this study (Figure 6.3).

6.3.2 Petrography

Core sample thin sections were used to determine optical porosity, grain size distribution and the fraction of clay-coated grains. Optical porosity was measured by using the digital image analysis technique, jPOR (Grove and Jerram, 2011), on blue epoxy-impregnated thin sections. Grain size distribution was analysed by using the Leica QWin (V. 3.5.0) software on thin section micrographs and the fraction of clay-coated grains was measured by point counting with 300 counts per thin section. Additional petrographic analysis, i.e. intergranular volume (IGV) (Paxton et al., 2002) and total cement volume (C) (Lundegard, 1992) were performed exclusively on channel sandstones and measured by point counting, again with 300 counts per thin section using a standard petrographic microscope (Leica DM2500P and DM750P) and point counting stage (PETROG – Conwy Valley Systems Limited).

Thin sections were highly polished to 30 μm and coated with carbon prior to analysis by a Hitachi SU-70 field emission gun scanning electron microscope (SEM), equipped with an energy-dispersive detector (EDS). Scanning electron microscope analyses of thin section and bulk rock samples were conducted at 5 to 20 kV acceleration voltage with beam currents of 1.0 and 0.6 nA, respectively. Point analyses had an average duration of 2 minutes, whereas line analyses were dependent on length. SEM–EDS was used for rapid identification of chemical species and orientation on the sample. Cathodoluminescence analysis has been undertaken on selected thin sections with

visible macro-quartz overgrowths using a Gata MonoCL system with a panchromatic imaging mode operated at 8 kV.

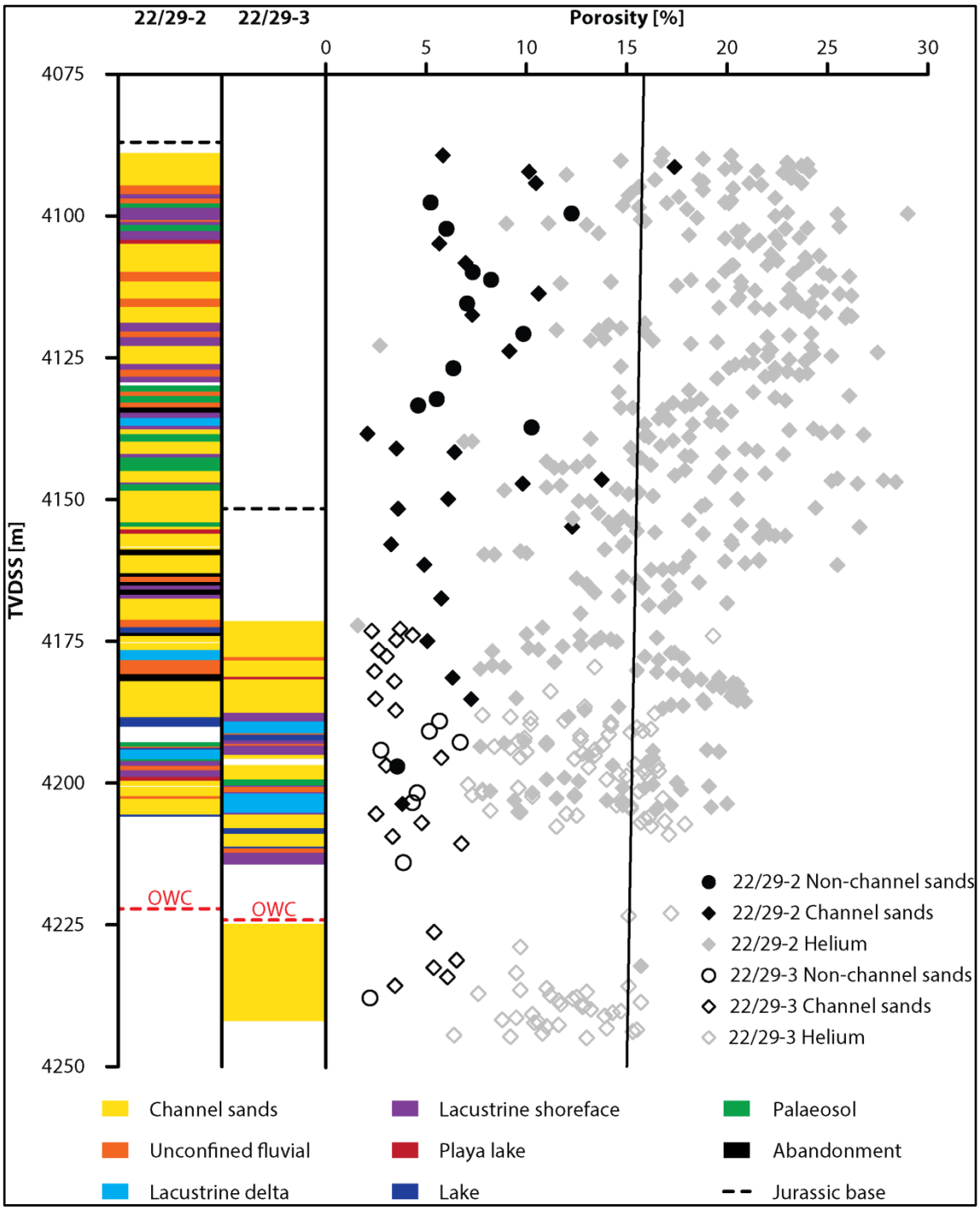

Figure 6.3 Facies interpretation of the cores of 22/29-2 and 22/29-3 (N. Meadows 2015, *pers. comm.*) and optical porosity distribution of the channel sand samples (diamonds) and non-channel sand samples (points/circles) of the 22/29-2 well (solid symbols) and the 22/29-3 well (open symbols) with helium porosity measurements (grey) and a regional Central North Sea porosity-depth relationship for shaly sandstone by Sclater and Christie (1980).

X-ray diffraction analysis

X-ray diffraction (XRD) analysis (bulk rock and clay fraction) was conducted by X-Ray Mineral Services Ltd. Selected bulk rock samples were de-oiled, disaggregated and powdered to a mean particle size between 5 and 10 µm for the XRD analysis. Samples were analysed by using a Philips PW1730 Generator at 2Θ (theta) angles between 4.5˚ and 75°, with a step size of 0.06° per second using x-ray radiation from a copper anode at 40 kV, 40 mA, equipped with a Philips PW1050 Goniometer with graphite monochromator and a PW1170 automatic sample changer. Identification of the minerals was achieved by using the X-ray Mineral Services Ltd in-house 'Traces' and 'Search-Match' software to compare the x-ray diffraction pattern with the International Centre for Diffraction Data PDF-4 Minerals database. The measured maximum intensity of each mineral was compared to the standard intensity of the pure mineral. The method does not take any amorphous content into account and the results were normalised to 100% based on the assumption that the whole mineral content accounted for the diffractogram.

Separation of the clay fraction (<2 µm fraction) samples was achieved by ultrasound and centrifugation of the suspension, with additional evaporation of the fluid content at 80°C. The samples were analysed as untreated clay, after saturation with ethylene glycol vapour overnight and following heating at 380°C for 2 hours, with further heating to 550°C for one hour if required. The initial scan for these four treatments was performed with the same machine and at 2Θ angles between 3° and 35° with a step size of 0.05° per second using x-ray radiation from a copper anode at 40 kV, 40 mA. The untreated samples were also analysed between 24° and 27° 2Θ at a step size of 0.2° per 2 seconds to further define kaolinite/chlorite peaks. Interpretation was done by overlaying the four diffractograms to identify the clay mineral assemblages and to

assess the effect of the treatment on the clay minerals. Peak intensities were measured and analysed to indicate the relative amounts of clay minerals present and have been referenced to the total amount of clay minerals present in the bulk rock analysis.

6.3.3 Fluid inclusion analysis

Microthermometry was conducted on double-polished detached wafers to determine the conditions of cementation and evidence for formation water salinity. Fragments were cut from double-polished rock wafers. The wafers were firstly checked under incident UV on a petrographic microscope to determine which contain petroleum inclusions and under transmitted light to determine the distribution of both aqueous and non-aqueous fluid inclusions for subsequent analyses. A Linkam THM600/TS90 heating-cooling stage connected to a Nikon petrographic microscope was used to obtain temperature data. Instrumental precision is ± 0.1°C, while accuracy, dependent on the manufacturer's stated accuracy for the calibration standards used (synthetic inclusions and pure organic compounds), is better than ± 0.1°C, over the range of temperatures reported here. Routinely available measurements are homogenization temperatures (T_h) and final melting temperatures (T_m). Homogenization is the conversion of multiphase inclusion contents to a single phase, usually at temperatures above room temperature. Interpreting homogenization temperatures in carbonates, sulphates and halides can be complicated because aqueous inclusions can, though not necessarily do, reset to higher temperature if they are a) overheated beyond a threshold which is dependent on the mineral strength and inclusion geometry (Goldstein and Reynolds, 1994), or b) frozen. This can occur in the laboratory as well as through geological processes, so care is taken over the order in which analyses are made for each rock chip. If resetting has occurred, larger inclusions may give higher temperatures, homogenization temperature distributions may show a high temperature tail, and data from paragenetically distinct

settings may overlap. Final melting occurs at the disappearance of the last trace of solid in the inclusion on heating, usually after cooling an inclusion to well below room temperature. If ice is the final phase to melt, as in the present study, salinities are calculated using the equation given by Oakes et al. (1990).

6.3.4 One-dimensional basin modelling

Pore pressure evolution in the Judy Sandstone Member of the Seagull field was modelled in one dimension using Schlumberger's PetroMod (V. 2012.2) software. This one-dimensional modelling provides a good insight into overpressure build-up by disequilibrium compaction and pore fluid expansion due to increasing temperature. However, the models do not include other mechanisms for generating excess pore pressure, such as fluid flow or hydrocarbon cracking, and are only able to take vertical stress into account. PetroMod is based on a forward modelling approach to calculate the geological evolution of a basin from the burial history. The burial history and lithology are inferred from the present-day well stratigraphy, well log lithology and lithological description of the modelled units (Figure 6.2 & Table 6.1). The thermal upwelling basement palaeo-heat flow model of Allen and Allen (2005) was used with 63–110 mW/m^2 (average of $80mW/m^2$) during syn-rift phases and 37–66 mW/m^2 (average 50 mW/m^2) during post-rift phases combined with the palaeo-surface temperature history published by Swarbrick et al. (2000) and di Primio and Neumann (2008). The burial history models are calibrated against present-day RFT temperature measurements corrected after Andrews-Speed et al. (1984), and measured Skagerrak Formation porosities (Figure 6.3) and carefully adjusted towards present-day formation pressure measurements by considering late stage, high temperature overpressure mechanisms (Osborne and Swarbrick, 1997; Isaksen, 2004). Vitrinite reflectance data, maximum temperatures obtained from apatite fission-track analyses, palaeotemperatures and

palaeopore pressures obtained from fluid inclusions in mineral cements were used to help calibrate the model (Swarbrick et al., 2000; di Primio and Neumann, 2008). We also conducted new fluid inclusion analysis in quartz cements to further constrain palaeotemperatures (Table 6.2). The lithological unit types used in these models are mainly PetroMod (V. 2012.2) default lithology types, based on well log descriptions and core analysis reports for the two wells, and generalised Central Graben lithology descriptions (Evans et al., 2003). The only exceptions are the Hod lithology type and the lithology type of the Triassic Skagerrak sandstone members. The Hod chalk unit is modified to represent the North Sea non-reservoir chalk (Table 6.3) and to match the compaction trend and permeability trend given by Mallon and Swarbrick (2008, 2002). The North Sea non-reservoir chalk is a laterally extensive low-permeability rock unit and represents the major vertical fluid flow barrier in the Central North Sea (Mallon and Swarbrick, 2008). The Triassic Skagerrak sandstone lithology is a mix of PetroMod (V. 2012.2) default lithologies (80% sand, 10% silt, 10% shale) in combination with the regional compaction trend for shaly sandstone given by Sclater and Christie (1980), to match the general Judy Sandstone Member characteristics.

Group/ Formation	Seagull (22/29-2)		Seagull (22/29/3)	
	Thickness	Lithology	Thickness	Lithology
	[m]	[-]	[m]	[-]
Water Depth	94	Water	94	Water
Nordland	1402	Shale	1406	Shale
Lark/Horda	1245	Shale	1284	Shale
Tay	37	Siltstone	22	Siltstone
Balder	21	Siltstone	22	Siltstone
Sele	41	Sandstone	38	Sandstone
Forties	150	Sandstone	149	Sandstone
Lista	39	Silty Shale	62	Shale
Maureen	137	Marl	123	Marl
Ekofisk	70	Chalk	76	Marl
Tor	432	Chalk	432	Chalk
Hod	345	Non-Reservoir Chalk	353	Non-Reservoir Chalk
Valhall	12	Marl	44	Marl
Kimmeridge Clay	21	Shale	14	Shale
Heather			12	Siltstone
Pentland	31	Siltstone	20	Siltstone
Fladen	0	Sandstone	0	Sandstone
Joshua	0	Silty Shale	0	Silty Shale
Josephine	0	Reservoir Sandstone	0	Reservoir Sandstone
Jonathan	0	Silty Shale	0	Silty Shale
Joanne	0	Reservoir Sandstone	0	Reservoir Sandstone
Julius	0	Silty Shale	0	Silty Shale
Judy	**378**	**Reservoir Sandstone**	**386**	**Reservoir Sandstone**
Smith Bank	244	Silty Shale	213	Silty Shale
Zechstein	200	Salt	200	Salt

Table 6.1 Lithology type and respective thickness of the modelled layers for the Seagull PetroMod models (the modelled key Skagerrak Formation reservoir unit in bold), with Non-Reservoir Chalk after (Mallon and Swarbrick, 2002, 2008) and Reservoir Sandstone comprising 80% Sand, 10% Silt and 10% Clay.

FI Host	Seagull							
	22/29-2				22/29-3			
	13786.00		13819.05		13834.01		13875.25	
	Aqu. [°C]	Non [°C]	Aqu. [°C]	Non [°C]	Aqu. [°C]	Non [°C]	Aqu. [°C]	Non [°C]
Quartz OG	137.9	75	134.7		132.9	65	132	
Quartz OG	143.4	72.3	142.3		138.1		128.5	
Quartz OG	136.2	82.1	144		141.1		134.3	
Quartz OG		108.6	136.1		135.7		136.6	
Quartz OG		72.7	130.9		139		131.3	
Quartz OG		72.9	143.4		145.4		144	
Quartz OG			139.3		141.3		142.6	
Quartz OG			129.5					
Quartz OG			134.1					
Feldspar			135.9	79.3				67
Feldspar			136.1	76.4				69.4
Feldspar			137	68.4				68.4
Feldspar			133.7	76.4				67.1
Feldspar			132.5	115.7				67.1
Feldspar				71.9				
Feldspar				74.4				
Feldspar				79.8				
Feldspar				84.9				
Feldspar				97.9				
Feldspar				138.5				
Feldspar				80				
Feldspar				78.6				
Feldspar				75.6				
Feldspar				74.3				
Carbonate	135.8							
Carbonate	134.5							
Carbonate	84.8							
Carbonate	125							
Carbonate	116.7							
Carbonate	85.9							

Table 6.2 Homogenization temperatures of aqueous (Aqu.) and non-aqueous (Non) fluid inclusions in quartz overgrowth, feldspar and carbonate cements.

Model Parameter (Hod Formation)			
Mechanical compaction		Permeability	
Porosity	Depth	Porosity	Permeability
[%]	[m]	[%]	[log(mD)]
70.00	0	70.00	1.00
18.00	1300	30.00	-1.00
12.50	2100	25.00	-3.00
8.00	3100	20.00	-5.50
5.00	4500	12.50	-7.20
		9.00	-7.20
		5.00	-7.20

Table 6.3 Non-reservoir North Sea chalk model parameters after Mallon and Swarbrick (2008, 2002).

6.4 Petrography, burial modelling and diagenesis

The present-day reservoir quality of the Triassic Skagerrak Formation in the Seagull field is a cumulative product of depositional attributes (e.g. facies architecture, grain composition, sorting, and size), mechanical compaction and diagenesis during shallow and deeper phases of burial.

6.4.1 Burial history modelling results

The one-dimensional burial history models of the Seagull wells 22/29-2 and 22/29-3 show the evolution of burial depth, pore fluid overpressure, VES and temperature for the top of the Judy Sandstone Member throughout the geological history (Figure 6.4). The models are based on present-day well stratigraphy, well log lithology and lithological description (Table 6.1) and are carefully calibrated against RFT temperatures corrected after Andrews-Speed et al. (1984), aqueous fluid inclusion homogenization temperatures of the Judy Sandstone Member (Table 6.2), measured porosities of the Judy Sandstone Member (Figure 6.3), and carefully adjusted towards measured present-day RFT formation pressures by considering late stage, high temperature overpressure mechanisms (Osborne and Swarbrick, 1997; Swarbrick and Osborne, 1998; Isaksen, 2004). The burial history models show the Judy Sandstone Member at maximum burial depth and temperatures (>160°C) at present day (Figure 6.4). The Judy Member experienced a long shallow burial phase (~150 million years) followed by a phase of rapid burial starting between 90 and 70 Ma to their present maximum burial depth. The phase of rapid burial was accompanied by significant temperature and pore pressure increases. The present-day pore fluid pressure profiles of the two wells increase through the Chalk units (Ekofisk, Tor and Hod Formations) from hydrostatic to highly overpressured in the Skagerrak Formation reservoir sandstones.

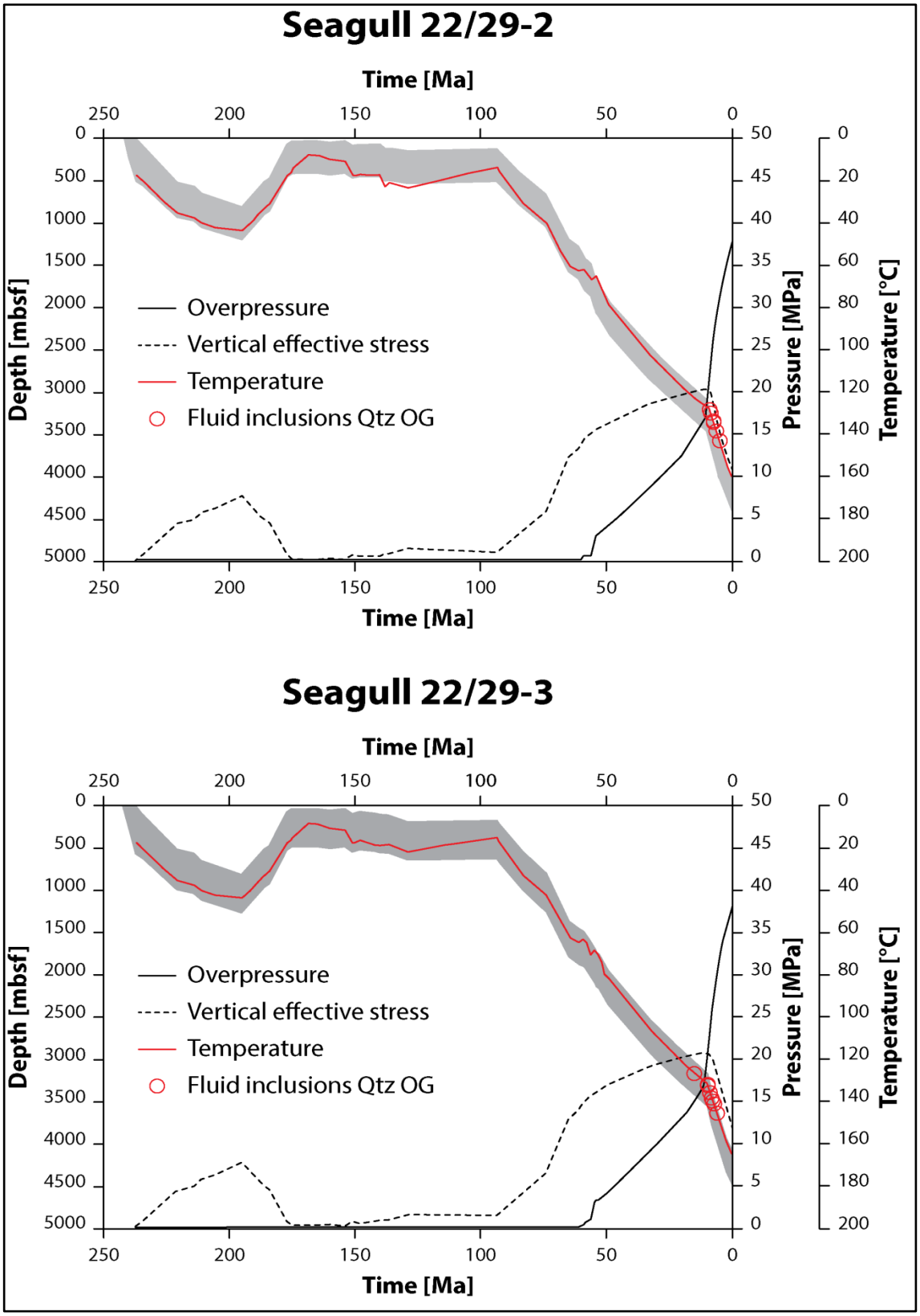

Figure 6.4 Burial history of the top of the Judy Sandstone Member Skagerrak of the Seagull field (well 22/29-2 & well 22/29-3), with temperature evolution, overpressure evolution and vertical effective stress evolution (VES), including aqueous fluid inclusion temperatures enclosed in quartz overgrowth (Qtz OG).

The burial history models shows a burial rate increase from ~90 Ma onwards, leading to a present-day maximum burial depth of ~4000 m below seafloor (Formation top). Modelled reservoir temperatures and pore fluid overpressures increase constantly during the rapid burial phase to present-day maxima of 160°C and ~38 MPa, respectively (Figure 6.4). The rapid overpressure increase in the Skagerrak Formation limited the increase in vertical effective stress (VES) during the rapid burial phase to a maximum VES of ~21 MPa at around ~10 Ma and present-day VES of 11.5 MPa (22/29-2) and 12.5 MPa (22/29-3) (Figure 6.4). The late rapid overpressure increase (from around 10 Ma) is caused by migration of overpressured fluids and hydrocarbon cracking (Isaksen, 2004; Lines and Auld, 2004; Winefield et al., 2005), which is indicated by the VES reduction (Swarbrick, 2012; Stricker et al., 2016a, 2016b).

6.4.2 Grain size and porosity

The 65 samples from the two samples sets (36 from 22/29-2 and 29 from 22/29-3) vary compositionally within a narrow range of arkosic arenites (Figure 6.5). The grain sizes vary from very fine-grained to medium-grained sand (Figure 6.6 & Table 6.4). The sample sets show a wide range of optical porosity from 2% up to 17%, with the higher porosities occurring in the 22/29-2 sample set (Figure 6.3). The measured optical porosity is complemented by helium core plug porosities (measured after Boyle's law, uncorrected for decompaction effects). The higher helium core plug porosities indicate the presence of microporosity (Figure 6.3 & Table 6.4).

Interestingly, grain-size variability is limited across all facies, with most of the sandstones being fine to very fine-grained sand (Figure 6.6 & Table 6.4). Lacustrine shoreface samples (LSF) show marginally finer grain sizes of very fine to fine-grained sand, whereas the channel sands (CS) and unconfined fluvial sands (UCF) range from very fine to medium-grained sand (Figure 6.6). The medium grain sized samples of the

22/29-2 sample set represent coarser grained basal parts of the channel and unconfined sheet sandbodies.

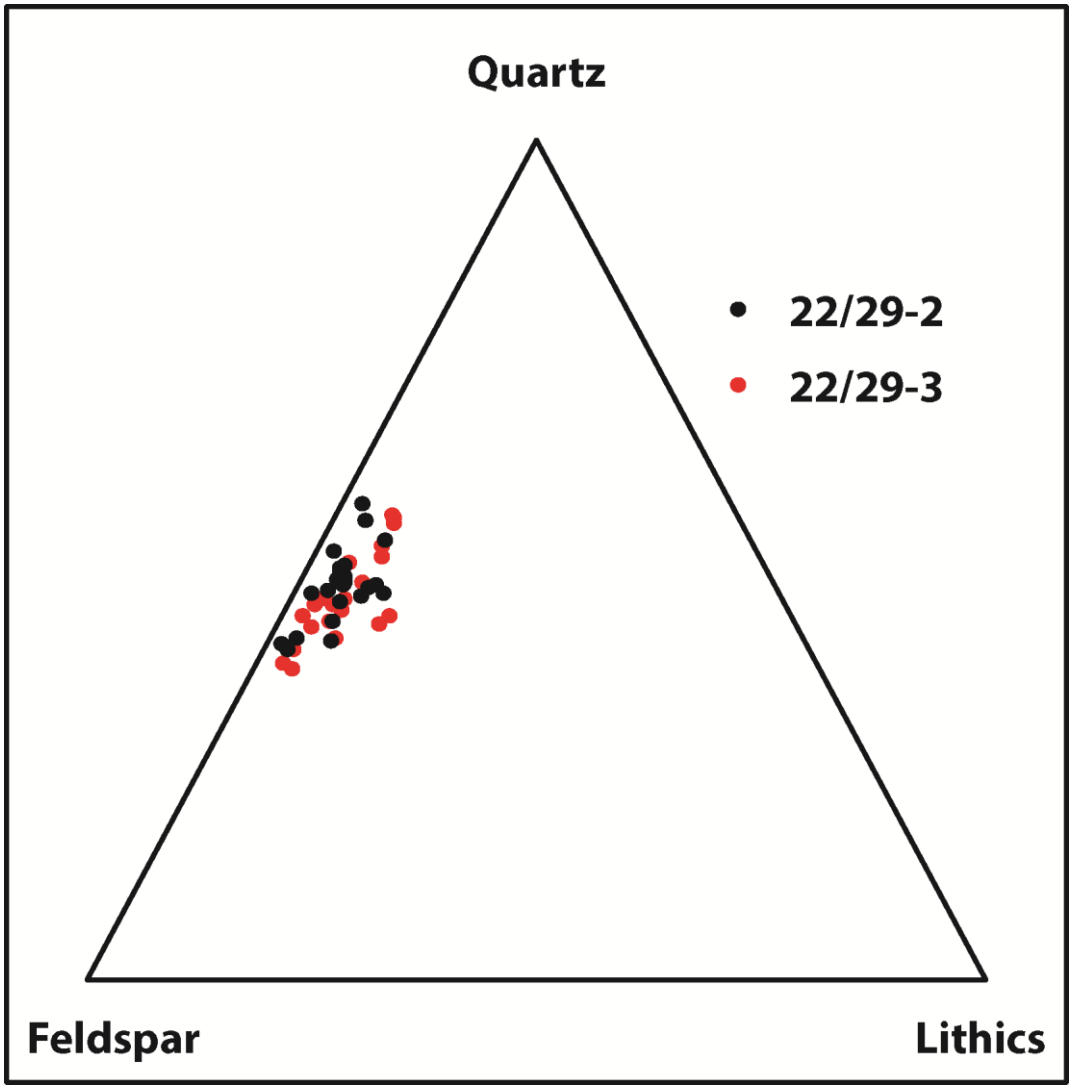

Figure 6.5 QFR diagram of the channel sandstones from the 22/29-3 and the 22/29-3 sample sets

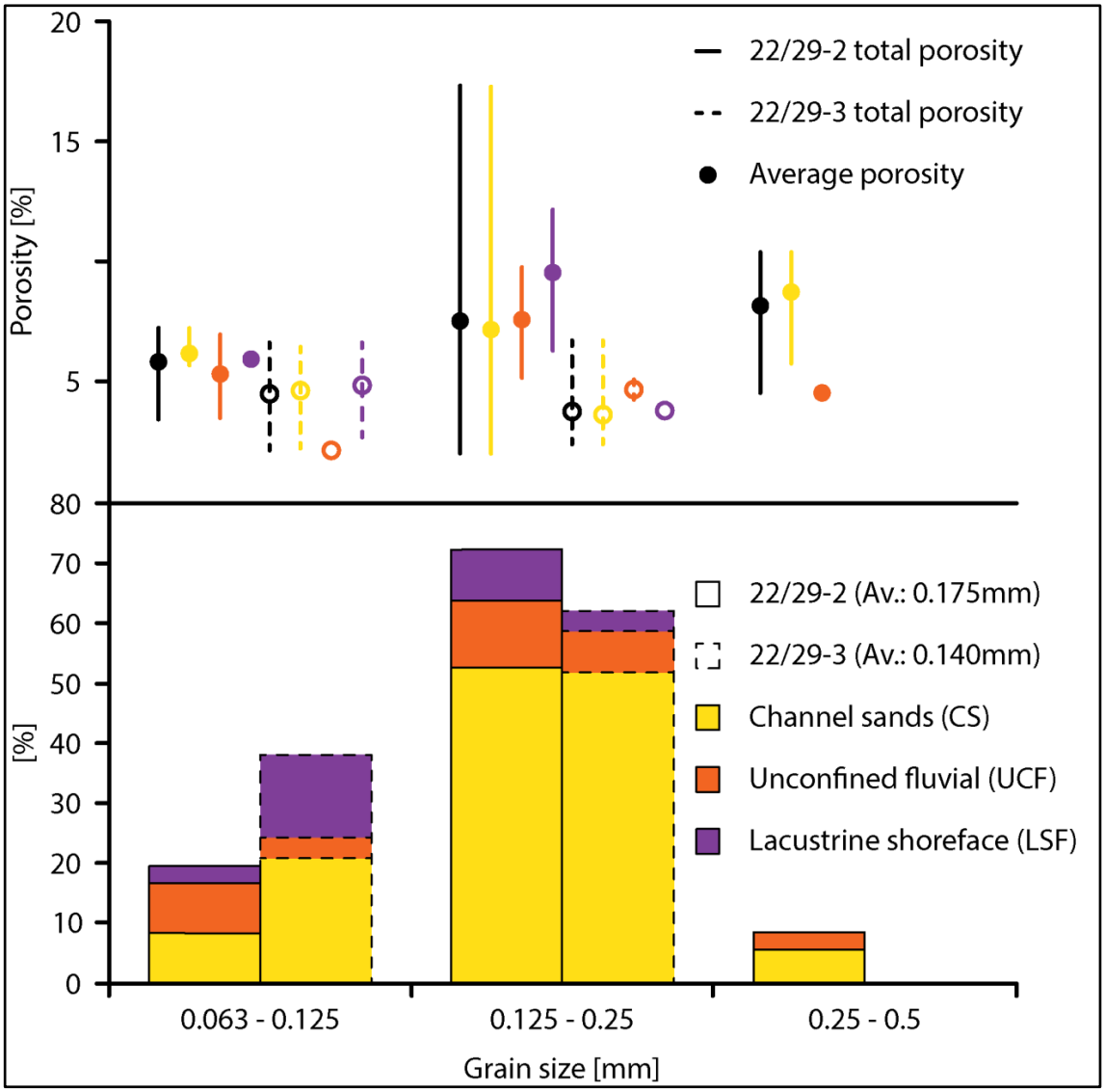

Figure 6.6 Grain size and porosity distribution of the sample sets 22/29-2 (36) and 22/29-3 (29), porosity arranged by grain size (black) and facies (channel sands (CS): yellow; unconfined fluvial (UCF): orange; lacustrine shoreface (LSF): purple) with minimum, average and maximum porosity.

Seagull well		Optical porosity				Helium Porosity	Grain size
		Total	By grain size				
			Sand				
			Very fine	Fine	Medium		
		[%]	[%]	[%]	[%]	[%]	[mm]
22 29-2	Minimum	2.1	6	2.1	4.6	1.6	0.096
	Average	7.3	5.9	7.6	8.4	17.9	0.175
	Maximum	17.4	7.3	17.4	10.5	29	0.298
22 29-3	Minimum	2.2	2.2	2.4		6.4	0.096
	Average	4.1	6.6	3.8		12.8	0.14
	Maximum	6.8	6	6.8		19.3	0.209

Table 6.4 Optical porosity, optical porosity distribution by grain size, helium porosity and grainsize for the 22/29-2 and 22/29-3 sample sets.

6.4.3 Diagenetic cements and grain coatings

The diagenetic history of Skagerrak Formation reservoirs has been described by several authors (e.g., Smith et al., 1993; Weibel, 1999; Kape et al., 2010; Nguyen et al., 2013; Stricker and Jones, 2016; Stricker et al., 2016b). The main diagenetic cements include quartz, localised carbonate, feldspar, and early precipitation of halite cement. Authigenic clay mineral coatings, i.e., chlorite or illite, are common throughout the Skagerrak Formation, and the presence of clay mineral coatings has been correlated to low quartz cement volumes (e.g., Taylor et al., 2015). The major cements types, important for the reservoir quality of the Seagull sample sets, are discussed in more detail below.

6.4.3.1 Carbonate cements

Carbonate cements are reported to be generally very localised throughout the Skagerrak Formation (McKie and Audretsch, 2005; McKie and Williams, 2009; Nguyen et al., 2013). Carbonate cement is scarce in the Seagull sample sets and either present as deformed carbonate rip-up clasts (Figure 6.7A) or as pore-filling cement associated with

"megapores" in channel base samples. McKie and Audretsch (2005) described calcrete and/or dolocrete rip-up clasts at the channel bases which seem to provide excellent nuclei for subsequent groundwater carbonate cementation shortly after deposition. The pore-filling carbonate cements show generally a rhombic crystal structure with a prominent cleavage pattern and tend to infill the pore space completely where present (Figure 6.7A). Fluid inclusion analysis on carbonate cement in the Seagull sample 22/29-2 – 13786.00 shows high aqueous fluid inclusions homogenization temperatures of 85°C to 135°C (Table 6.2).

6.4.3.2 Authigenic clay mineral cements

Authigenic clay minerals cements are widely reported for the sandstone members of the Skagerrak Formation in the Central Graben, North Sea (e.g., Humphreys et al., 1989; McKie and Audretsch, 2005; Nguyen et al., 2013; Grant et al., 2014; Stricker and Jones, 2016; Stricker et al., 2016b). Authigenic clay mineral cements in the Seagull sample sets are common as grain coatings (Figure 6.7B & C) or as pore-filling clay cements (Figure 6.7F). Detailed SEM, SEM-EDS and XRD analysis shows that clay mineral cements consists of chlorite and illite (Table 6.5 & Table 6.6). Authigenic clay mineral coatings consist of authigenic chlorite (Figure 6.7B) and authigenic illite (Figure 6.7C), and are common as mixtures of authigenic chlorite and illite (Figure 6.7D). SEM-EDS analysis show, that the authigenic clay coatings are fully transformed at the present day and no-precursor clay minerals are detected. Chlorite coatings were analysed and classified according to the Fe/Mg-ratio (Hillier and Velde, 1992) using SEM-EDS:

$$Fe/Mg = \frac{Fe}{(Fe + Mg)} \qquad (6.1)$$

Chlorite coatings are classified as intermediate to Fe-rich according to Grigsby (2001) with an Fe/Mg-ratio of 0.43-0.49.

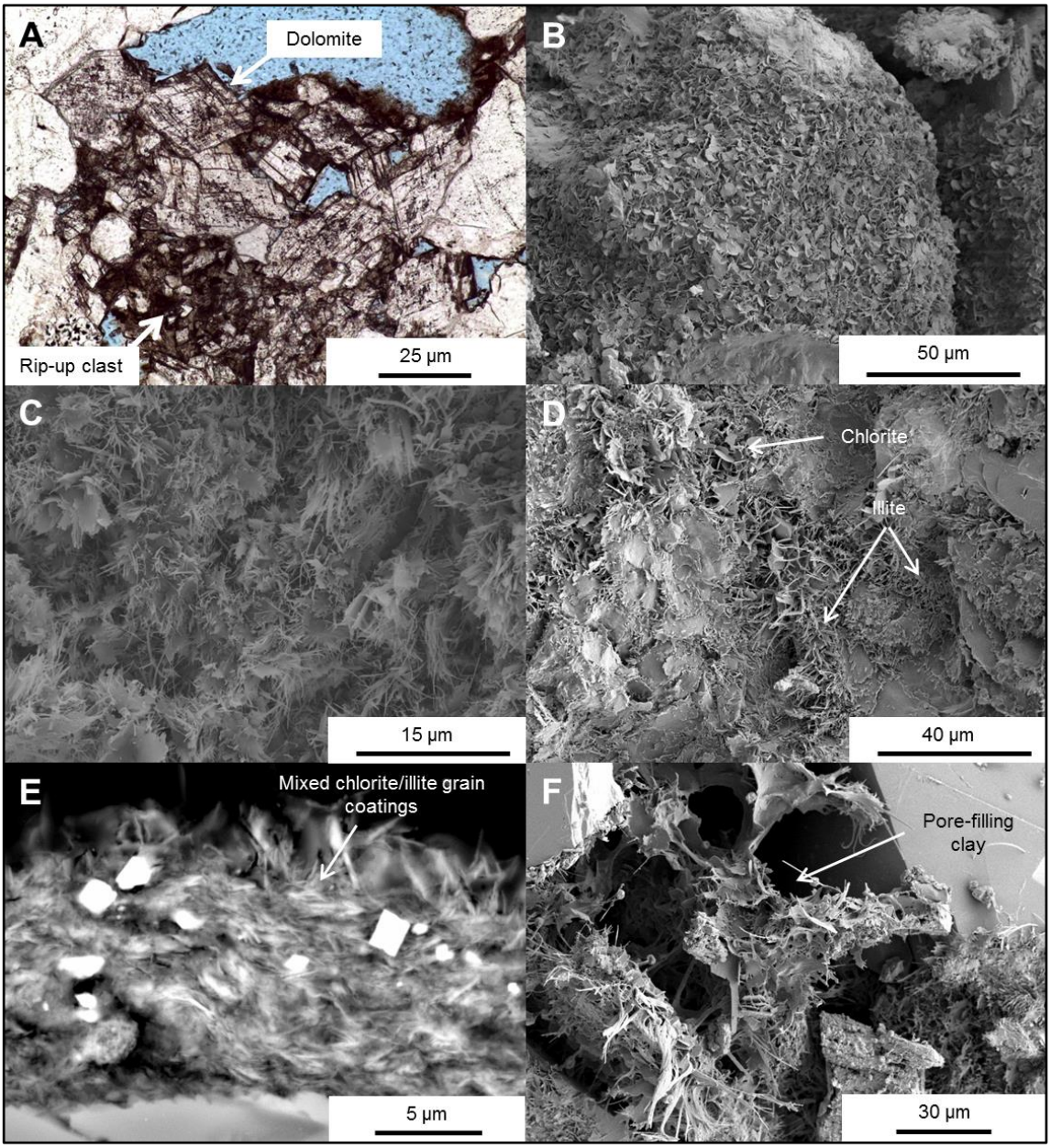

Figure 6.7 Micrographs and SEM images of A) calcrete/dolocrete rip-up clast with dolomite crystals (22/29-2; 13786'0"); B) well-developed authigenic chlorite coating (22/29-2; 13538'4"); C) well-developed authigenic illite coating (22/29-3; 13799'6"); (D) authigenic clay mineral coating, comprising chlorite and illite (22/29-3; 13910'0"); E) cross-section of a well-developed authigenic chlorite/illite coatings (22/29-3; 13775'0"); F) pore-filling illite/chlorite mix (22/29-3; 13775'0").

The authigenic clay coatings are generally widely spread in both Seagull sample sets and show average grain coating values of 72.1% (22/29-2) and 66.4% (22/29-3). The grain coatings are generally continuously developed and show variable thicknesses from 5μm to 20μm, with average thicknesses of around 10 μm (Figure 6.7E). The clay coating thickness is generally dependednt on the illite content and increases with increasing illite content. The clay coatings show a two-layered structure, with an inner layer or root zone (*sensus* Pittman et al., 1992) and an outer layer. The root zone is commonly densely packed and consists of laminated crystals, oriented parallel to the detrital quartz grain surface (Figure 6.7E). These crystals are overgrown by a layer of well-defined chlorite crystals or illite fibres, normally oriented to the root zone.

SEM and SEM-EDS identified the pore-filling clay cements in the Seagull sample sets as chlorite and illite. Detailed petrographic analysis indicates a wider occurrence of pore-filling clay cement within the channel sandstones of the 22/29-3 sample set, in comparison to the 22/29-2 channel sandstones (Figure 6.8). SEM analysis showed that pore-filling clay assemblages comprise mainly fibrous illite and small chlorite crystals in densely packed arrangements (Figure 6.7F). The pore-filling clay cements can represent up to 40% of the bulk rock and can infill up to 90% of the remaining intergranular volume (Figure 6.8; 22/29-3 – 13805.33ft).

Well	Sample	Quartz	K-feld.	Plagioclase	I/S	I+M	Chlorite	Kaolinite	Barite
		[wt%]	[wt%]	[wt%]	[wt%]	[wt%]	[wt%]	[wt%]	[wt%]
22/29-2	13692'6"	81.7	7.9	3.5	0.0	3.1	1.8	0.0	2.1
	13695'0"	71.5	9.6	5.1	TR	9.4	2.0	0.0	2.3
	13703'9"	58.2	9.5	6.8	0.0	17.4	7.6	0.0	0.6
	13709'4"	73.8	7.8	4.9	0.0	8.8	3.8	0.0	0.9
	13719'11"	74.4	7.1	4.0	0.0	8.0	6.0	0.0	0.5
	13730'0"	68.5	9.5	6.2	0.0	12.6	3.0	0.0	0.0
22/29-3	13781'4"	76.3	8.2	2.8	TR	9.3	3.3	0.0	0.0
	13787'3"	79.6	6.6	2.2	TR	8.2	3.4	0.0	0.0
	13790'10"	78.9	6.2	1.2	TR	10.8	2.8	0.0	0.0
	13799'6"	73.6	8.5	0.6	0.0	15.1	2.2	0.0	0.0
	13805'4"	74.6	7.8	0.0	TR	15.3	2.3	0.0	0.0
	13815'6"	86.7	5.2	0.4	0.0	6.2	1.5	0.0	0.0

Table 6.5 Bulk rock XRD results for the channel sandstone samples from the 22/29-2 and the 22/29-3 sample set, with quartz, K-feldspar (K-feld.), plagioclase, illite/smectite (I/S), illite and mica (I+M), chlorite, kaolinite and barite in weight%.

Well	Sample	<2µm	Illite/smectite			Illite		Chlorite		Quartz	Barite
		[wt%]	[wt%]	Order	% Illite	[wt%]	Crys	[wt%]	Crys	[wt%]	[wt%]
22/29-2	13692'6"	4.7	0.0			51.0	P	37.7	M	3.8	7.6
	13695'0"	4.1	TR	O	70-80	47.6	P	42.4	M	3.9	6.1
	13703'9"	4.6	0.0			42.7	M	48.5	M	6.3	2.5
	13709'4"	2.8	0.0			33.5	P	59.6	M	3.5	3.5
	13719'11"	3.0	0.0			15.5	P	77.9	M	3.9	2.7
	13730'0"	2.4	0.0			55.5	P	36.4	M	8.1	0.0
22/29-3	13781'4"	3.8	TR	O	70-80	40.1	M	54.8	M	5.1	0.0
	13787'3"	4.8	TR	O	70-80	33.2	M	62.9	M	3.9	0.0
	13790'10"	3.0	TR	O	70-80	32.4	M	63.4	M	4.2	0.0
	13799'6"	3.4	0.0			57.3	M	38.3	M	4.4	0.0
	13805'4"	3.7	TR	O	70-80	52.0	M	43.9	M	4.1	0.0
	13815'6"	3.2	0.0			51.6	M	41.0	M	7.5	0.0

Table 6.6 Clay fraction XRD results for the channel sandstone samples from the 22/29-2 and the 22/29-3 sample set, with the weight percentage of the clay fraction (<2µm), the weight percentage of the clay minerals relative to the size fraction for illite/smectite, illite, chlorite, quartz and barite, the mixed-layer ordering of illite/smectite (Order; RI: Random Interstratified (R0); O: Ordered Interstratification (R1); LR: Long-range Ordering (R3)) and the crystallinity of the clay minerals (Crys; VW: Very Well Crystallised; W: Well Crystallised; M: Moderately Crystallised; P: Poorly Crystallised)

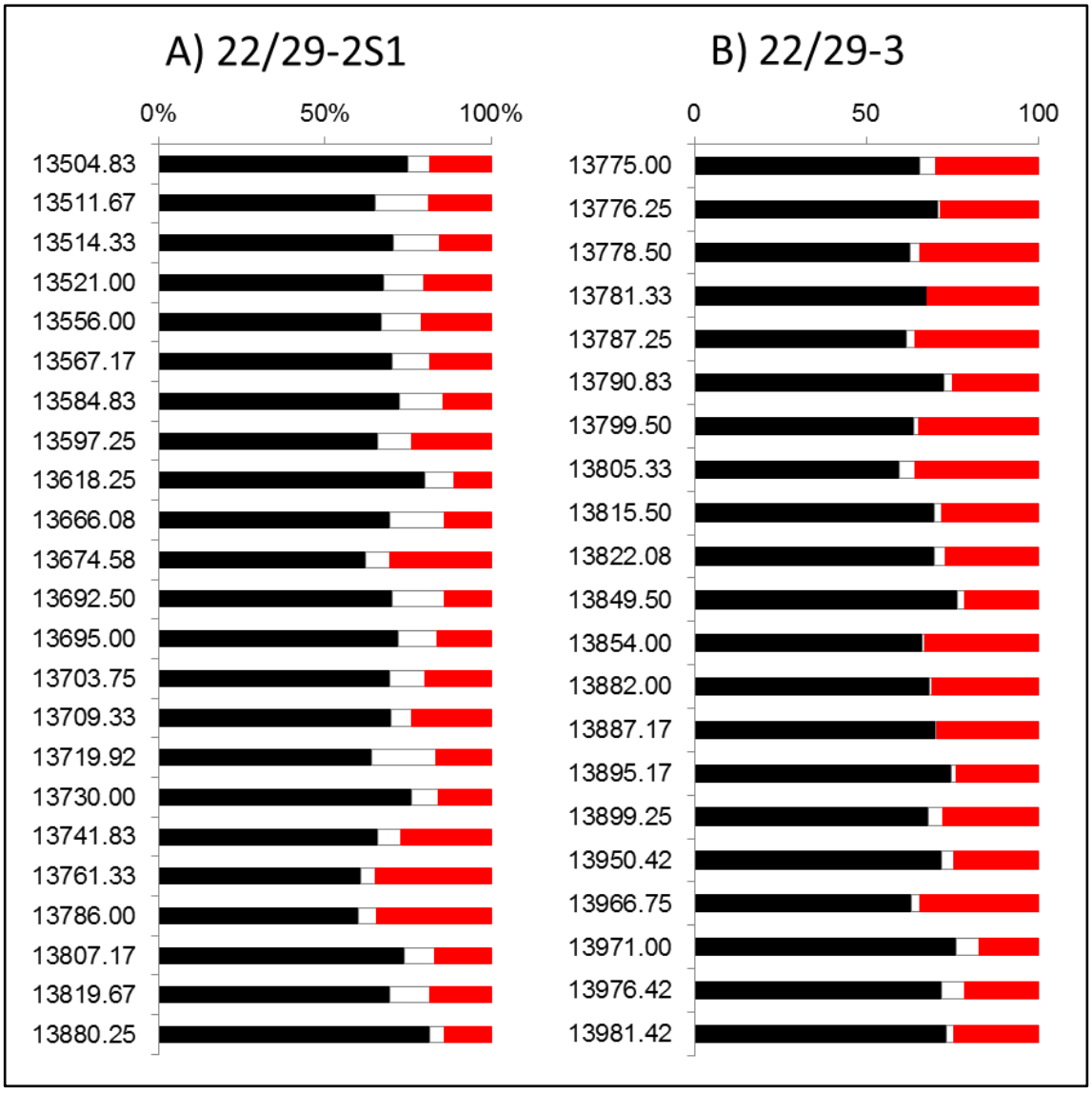

Figure 6.8 Fraction of detrital grains (black), cement (red) and porosity (white) of the channel sandstone samples of the 22/29-2 and the 22/29-3 sample sets, in percentage. Sample number is drillers depth given in feet.

6.4.3.3 Quartz cements

Quartz cement is common in two types, either as thick and blocky macroquartz overgrowths (Figure 6.9A & B), present at non-coated grain surfaces (Figure 6.9C) and breaks within the chlorite coatings, or as very thin microquartz grain coatings (Figure 6.9D). The term microquartz overgrowth is here used for polycrystalline growth patterns of individual micro-sized quartz crystals ranging from 1 to 10µm in length, which are in optical continuity or discontinuity with the detrital quartz grain (Aase et

al., 1996; French and Worden, 2013). In comparison, macroquartz overgrowth is defined as syntaxial quartz overgrowth larger than 20 μm in optical continuity with the detrital quartz grain. The amount of quartz cement is generally low to medium (<10% bulk volume) in the samples, but can exceed 10% bulk volume in single samples.

Fluid inclusion analyses have been undertaken on selected samples with higher quantities of quartz overgrowths and show high homogenization temperatures. The aqueous homogenization temperatures range from 129.5°C to 144°C for the 22/29-2 sample set, and from 128.5°C to 145.5°C for the 22/29-3 sample set (Table 6.2). The non-aqueous fluid inclusions are generally less common in both sample sets. Homogenization temperatures are between 72.3°C to 108.6°C for the 22/29-2 sample set and are at 65°C for one inclusion in the 22/29-3 sample set (Table 6.2).

6.4.3.4 K-feldspar dissolution & cements

K-feldspar dissolution and alteration is common in the Seagull sample sets (Taylor et al., 2015). K-feldspar dissolution occurs generally after the clay mineral transformation during late burial, indicated by clay mineral coatings (Figure 6.9E), which preserve the original grain shape of partly or fully dissolved grains. Late stage blocky authigenic K-feldspar overgrowth (<5% bulk rock) can be observed on uncoated and partly dissolved K-feldspar grains (Figure 6.9F). Aqueous fluid inclusions in feldspar overgrowths in the 22/29-2 sample set indicate cementation at high temperatures above 130°C (Table 6.2). Non-aqueous fluid inclusions encountered in feldspars show significantly lower temperatures between 67°C and 138.5°C across the two sample sets (Table 6.2). Highly altered and dissolved K-feldspar grains can coexist in close proximity to unaltered grains, consistent with the understanding that variations in feldspar microtextures exert control on reactivity as demonstrated by Parsons et al. (2005).

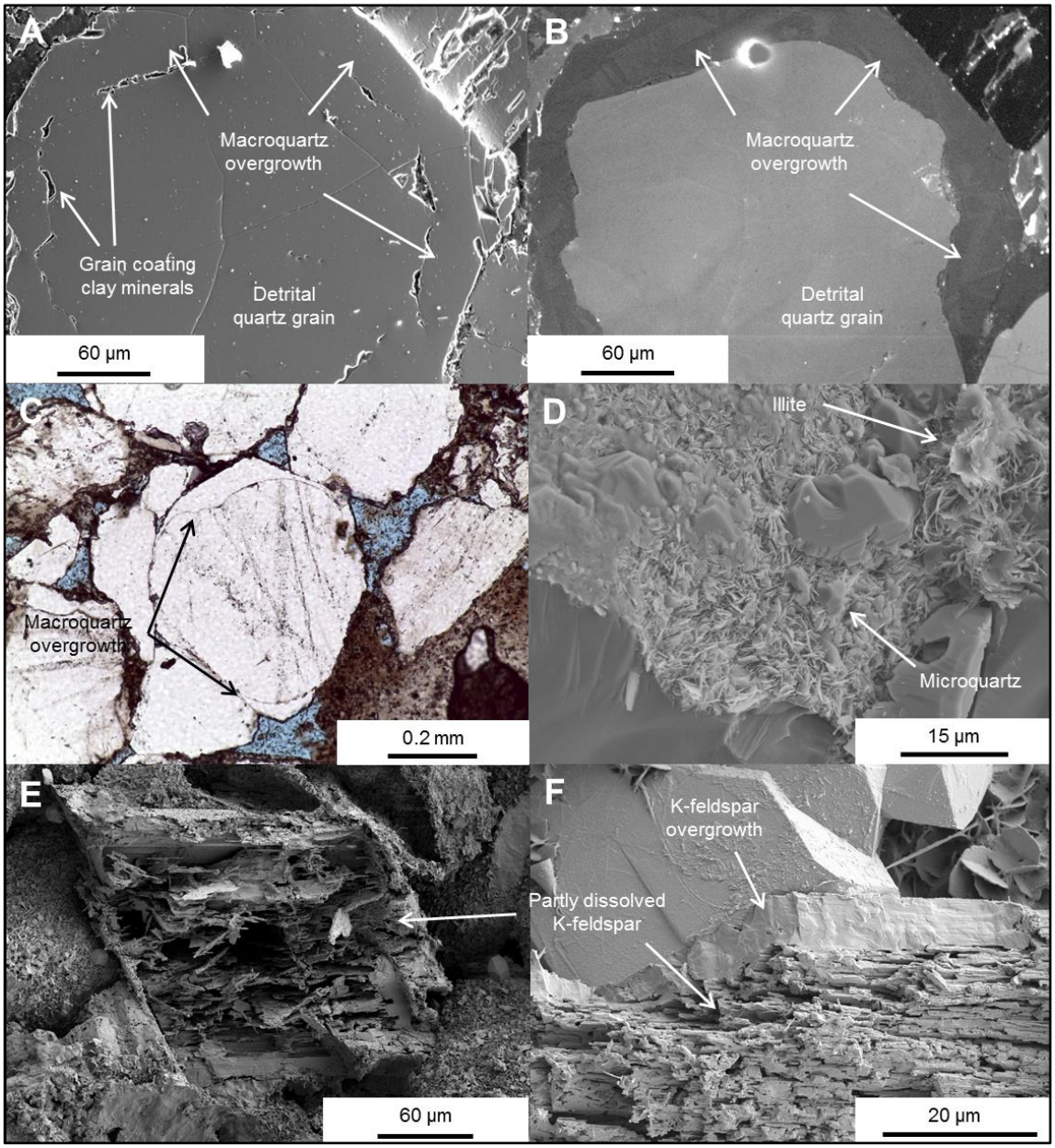

Figure 6.9 CL images, micrographs and SEM images of A & B) a detrital quartz grain with macroquartz overgrowth and grain-coating clay minerals (A: SEM & B: CL) (22/29-2; 13786'0"); C) macroquartz overgrowth on a detrital quartz grain (22/29-2; 13514'4"); D) illite grain coating with microquartz intergrowth (22/29-3; 13799'6"); E) partly dissolved K-feldspar (22/29-2; 13538'4"); F) partly dissolved K-feldspar with K-feldspar overgrowth (22/29-3; 13834'1").

6.4.4 Intergranular volume (IGV)

Intergranular volume (IGV), or minus-cement porosity, represents the sum of intergranular pore space, intergranular cement and depositional matrix (Houseknecht, 1987, 1988; Paxton et al., 2002). As discussed by Houseknecht (1987, 1988), Lundegard (1992), Ehrenberg (1995), and Paxton et al. (2002) IGV decreases with ongoing burial depth or increased VES, reflecting the degree of mechanical and chemical compaction. Nevertheless, IGV can also be influenced by early cementation (grain framework strengthening or locally pore-filling) or early pore fluid overpressure.

The IGV values of the two sample sets show similar values, but comprise wide internal variations from 18.3% to 40% (22/29-2) and from 23.6% to 42.3% (22/29-3) (Table 6.7). The IGV values are grain-size dependent, with the very fine-grained samples showing higher values than the fine or medium-grained samples. Facies, however, has no impact on the intergranular volume (Table 6.7). Total cement (C) values were determined, comprising clay mineral cement, carbonate cement and quartz cement. The comparison of the total cement values shows more cementation for the 22/29-3 (average 29.2%) than for the 22/29-2 sample set (average 19.9%). The increased cementation, mainly clay cements, led to significant lower porosities in the 22/29-3 sample set (Figure 6.8).

				Seagull well					
				22/29-2			22/29-3		
				Minimum	Average	Maximum	Minimum	Average	Maximum
Intergranular volume (IGV)	**Total**		[%]	18.3	30.3	40	23.6	32.5	42.3
	By grain size	Very fine	[%]	25	32.5	39.3	24	33.5	42.3
		Fine	[%]	18.3	29.8	40	23.6	31.9	40.3
		Medium	[%]	19.3	26.5	32.3			
	By facies	CS	[%]	18.3	30.4	40	23.6	31.3	40.3
		UCF	[%]	19.3	29.9	38.3	27.6	31.5	35.3
		LSF	[%]	29	30.3	36	33.6	37.9	42.3
Total cement (C)	**Total**		[%]	11.3	19.9	34.3	17.3	29.5	39
	By grain size	Very fine	[%]	18.3	24.8	35	17.3	30	39
		Fine	[%]	9.3	18.8	34.3	20	29.2	36
		Medium	[%]	12	15.6	20.3			
	By facies	CS	[%]	11.3	20	34.3	17.3	28.7	36
		UCF	[%]	9.3	20.3	30.3	20	28.7	34.6
		LSF	[%]	15	18.9	24.3	27	33.3	39

Table 6.7 Intergranular volume (IGV) and total cement (C) values for channel sands (CS), unconfined fluvial sands (UCF) and lacustrine shoreface sands (LSF).

6.4.5 Porosity loss by compaction vs. cementation

Total cement volume (C) and intergranular volume (IGV) can be used to calculate the porosity loss by compaction (*COPL*) and by cementation (*CEPL*) using the following equations by Lundegard (1992):

$$COPL = P_i - \left(\frac{(100 - P_i) P_{mc}}{100 - P_{mc}} \right) \tag{6.2}$$

$$CEPL = (P_i - COPL) \left(\frac{C}{P_{mc}} \right) \tag{6.3}$$

where P_i is the initial or depositional porosity and P_{mc} is the intergranular volume or minus-cement porosity calculated by subtracting the total cement volume, *C*, from the total optical porosity, P_o. The initial or depositional porosity for the Judy Member sandstone samples is assumed to be around 45% (Beard and Weyl, 1973; Chuhan et al.,

2002). The calculated COPL and CEPL are only accurate if three conditions are met. First, the assumed initial porosity P_i must be correct. Second, the amount of cement derived by local grain dissolution must be negligible or known. And third, the amount of framework mass exported by grain dissolution must be negligible or known (Lundegard, 1992).

The COPL-CEPL results indicate compaction as the main driver for porosity loss within the Seagull sample sets, especially in the 22/29-2 sample set, whereas the 22/29-3 sample set shows a strong addition of cementational porosity loss (Figure 6.10).

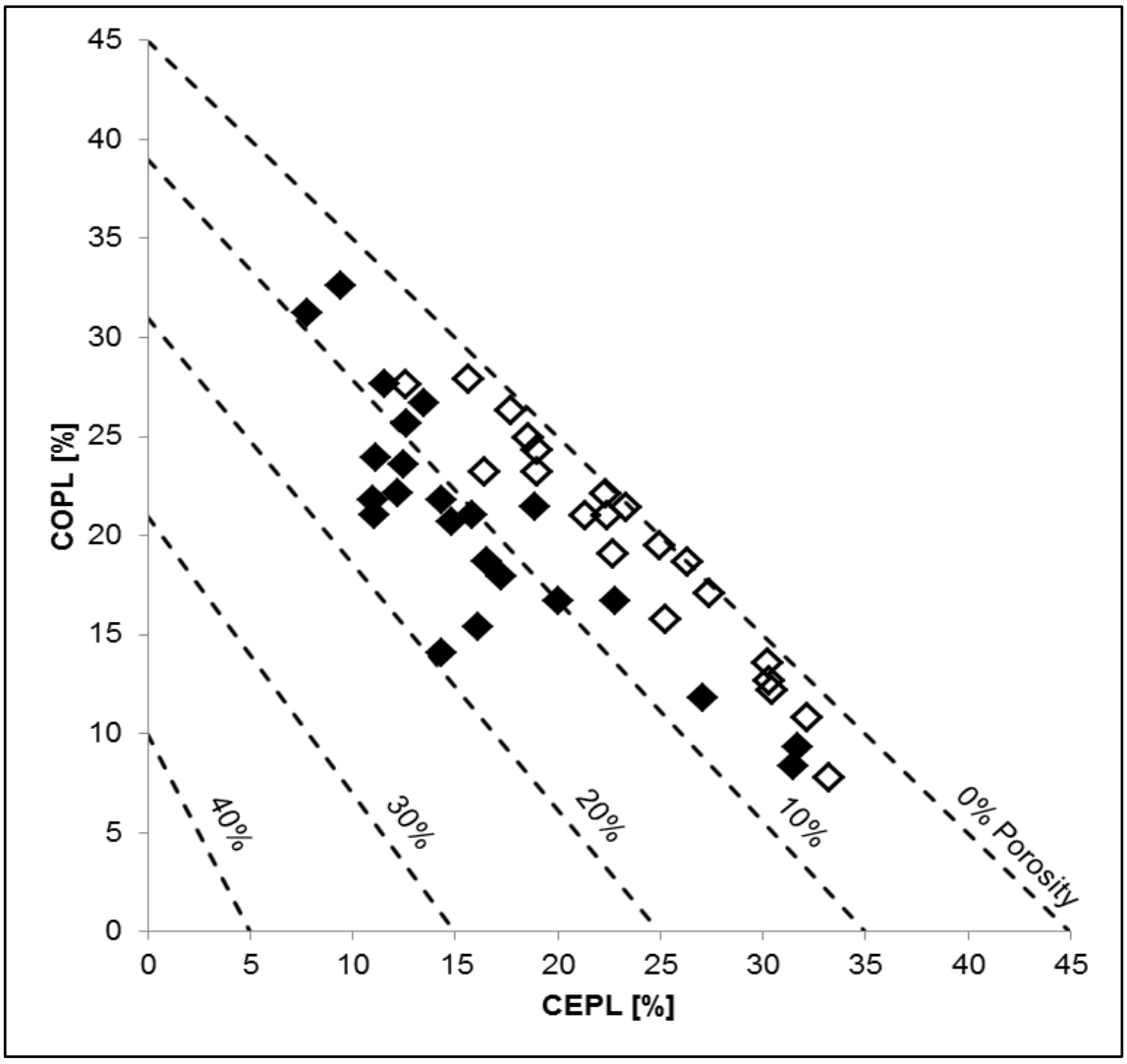

Figure 6.10 Compactional porosity loss (COPL) and cementational porosity loss (CEPL) for the Seagull data sets, 22/29-2 solid diamonds and 22/29-3 open diamonds, calculated according to Lundegard (1992).

6.4.6 Fractures and dilatant disaggregation bands

The diagenesis of the Skagerrak Formation in the Seagull field mini-basin is overall linked to the tectonic setting of the mini-basin. The structural evolution of the Skagerrak Formation is generally controlled by the overall extensional regime within the Central Graben and the underlying Zechstein salt, even though each reservoir has been affected differently due to the timing and magnitude of the salt movement (McKie and Audretsch, 2005; McKie et al., 2010). The Seagull mini-basin or pod is grounded on an edge of one of the underlying Rotliegend basement blocks and is tilted as a result of the ongoing evacuation of salt from under the subsiding mini-basin (Helgeson, 1999; McKie and Audretsch, 2005). The grounding of the mini-basin and ongoing evacuation of salt from below the mini-basin led to fracturing and faulting of the semi-consolidated sediments at flanks. The fracturing and faulting occurred as a result of the withdrawal from the margins after the initial grounding of the mini-basin centre. Fractures can be observed in both of the Seagull core sections (22/29-2 & 22/29-3) with a significantly higher density in the 22/29-3 core (e.g., Figure 6.11).

Six core samples that are highly fractured from the 22/29-3 core have been chosen and investigated (4177.44 m TVDSS; 4186.37 m TVDSS; 4191.18 m TVDSS; 4193.26 m TVDSS; 4202.43 m TVDSS; 4208.92 m TVDSS). The orientation and thickness of the fractures varies in the core samples (1 mm up to 50 mm thickness). The fractures are generally characterised by small shear offsets (Figure 6.11 & Figure 6.12A) and show no indicators of cataclastic deformation (fractured grains or reduced grain size), grain dissolution, or quartz/carbonate cementation (Figure 6.12D & E). Minor shear-related grain alignment can be observed within the fractures (Figure 6.12D & E). The fractures are classified as shear-related, often dilatant, disaggregation bands (Du Bernard et al., 2002; Fossen and Bale, 2007; Fossen et al., 2007). Dilatant disaggregation bands are

commonly reported for poorly consolidated sandstones at surface or near-surface conditions (<1000 m), with minor vertical effective stress applied to the grain framework (Mandl et al., 1977; Du Bernard et al., 2002; Fossen et al., 2007; McKie et al., 2010). Dilatant disaggregation bands are commonly charactierised by small shear displacement, larger pores, a reduced grain framework density, and a small porosity increase with respect to the host rock (up to 8%) (Antonellini et al., 1994; Du Bernard et al., 2002; Fossen and Bale, 2007). The small porosity increase and the larger pores of the dilatant disaggregation bands makes them a suitable pathway for meteoric water influx and associated clay infiltration. This is highlighted by intensive cementation of authigenic clay minerals in the investigated rock samples with disaggregation bands (Figure 6.12).

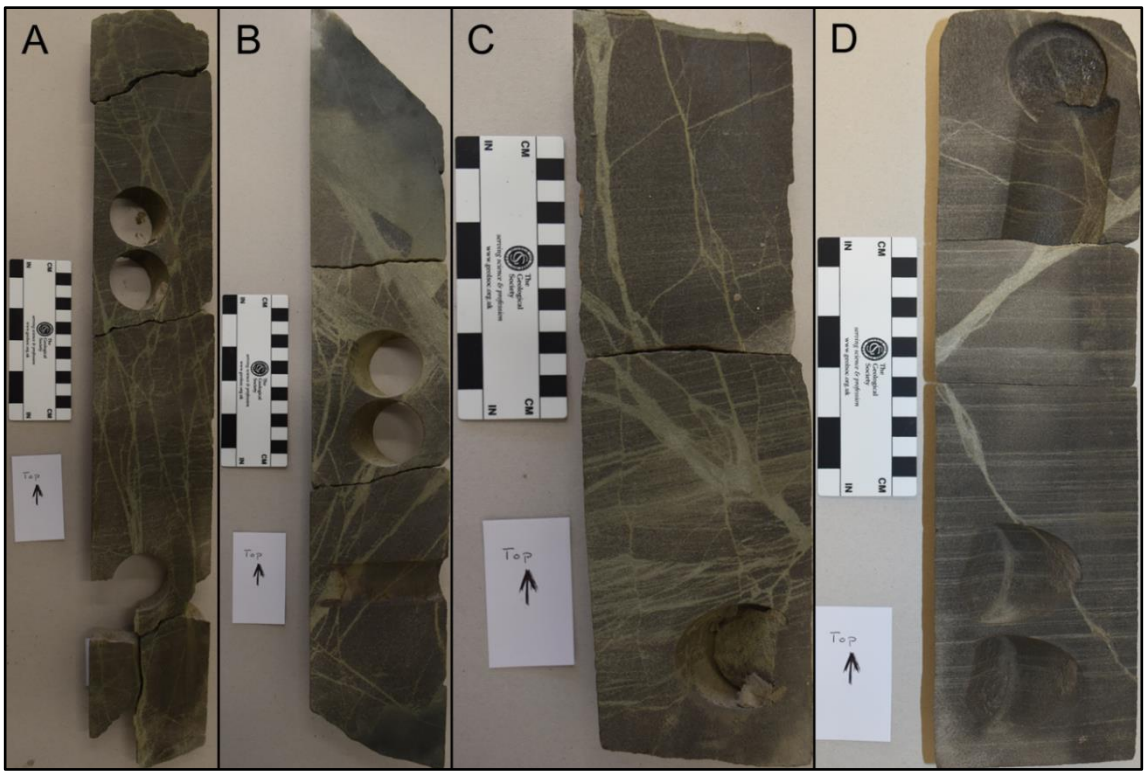

Figure 6.11 Fractures and disaggregation band distribution in core sections from A) 4177.09 m TVDSS to 4177.70 m TVDSS; B) 4192.90 m TVDSS to 4193.43 m TVDSS; C) 4208.72 m TVDSS to 4209.02 m TVDSS; D) 4209.36 m TVDSS to 4209.70 m TVDSS.

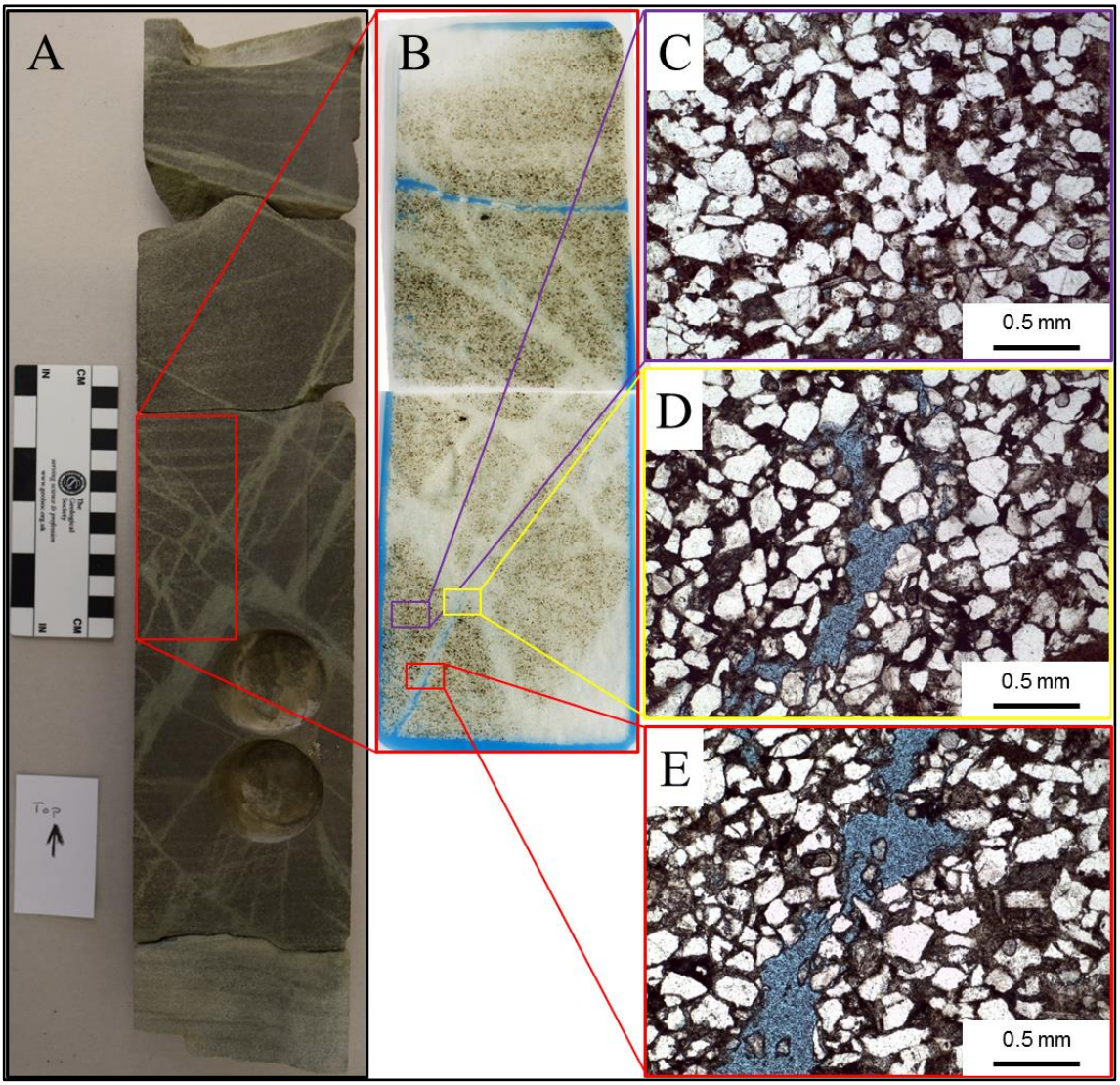

Figure 6.12 Images and micrographs of A) disaggregation bands in the core of 22/29-3 (4186.12 m TVDSS to 4187. 04 m TVDSS); B) disaggregation bands in thin section (4186.37 m TVDSS); C) the grain arrangement of the host rock; D & E) the grain arrangement of the disaggregation band with minor grain alignment and fracture porosity (blue).

6.5 Discussion

6.5.1 Reservoir quality and clay mineral cementation

Amount, distribution and morphology of clay minerals can have significant effects on the reservoir quality of sandstones. Infiltrated clay minerals and authigenic clay cements can enhance or reduce effective porosity and permeability (also shown in chapter 4 & 5). The development of clay mineral coatings in sandstones is, for example, often reported to be closely linked with the absence of extensive quartz cementation and porosity preservation (e.g., Billault et al., 2003; Ajdukiewicz and Larese, 2012; Taylor et al., 2015). Pore-filling clay cements, however, are known to affect effective porosity and to reduce the reservoir permeability significantly (e.g., Worden and Morad, 2003; Wilson et al., 2014). Authigenic clay minerals are widely reported for the Skagerrak Formation, especially grain-coating chlorite which has been linked to the absence of extensive quartz cementation in the Skagerrak Formation sandstones (e.g., Humphreys et al., 1989; Nguyen et al., 2013; Taylor et al., 2015; Stricker and Jones, 2016; Stricker et al., 2016b).

The clay assemblage of the Judy Sandstone Member in the Seagull field consists of authigenic chlorite and authigenic illite. The ratio between chlorite and illite varies from 83% chlorite and 17% illite to 40% chlorite and 60% illite with an average 54% to 46%, respectively. Kaolinite, as reported by Taylor et al. (2015), has not been observed in the sample sets (Table 6.5). The clay mineral cements in the Seagull field are common as authigenic clay coatings (Figure 6.7B & C) and authigenic pore-filling clay aggregates (Figure 6.7F). Clay mineral coatings are commonly well developed and tend to cover around 72.1% (22/29-2) and 66.4% (22/29-3) of the detrital grains (Figure 6.13). The authigenic clay mineral coatings tend to enhance the reservoir quality, where well developed and fully coating (Figure 6.7B, C & D), inhibition of quartz cement is noted.

However, where the authigenic coatings are poorly developed, quartz cement nucleated and the pore space has been commonly infilled by macroquartz cement (Figure 6.9A, B & C). A comparison of the ETAP area fields (Heron, Egret, Seagull and Skua) shows a lower fraction of chlorite-coated grains and lower surface coverage rates for the Seagull field (Figure 6.13). This is reflected by an increase of pore-filling and porosity reducing macroquartz cement (Figure 6.9A, B & C) in comparison to the Heron, Egret or Skua fields (Taylor et al., 2015).

Pore-filling clays within the reservoir sandstones of the Seagull field are a mixture of authigenic illite and chlorite (Figure 6.7F) and play an important role in controlling reservoir quality. The pore-filling clay mixture can fill up to 90% of the present-day intergranular volume (Figure 6.8; 22/29-3 - 13805.33) and decreases reservoir quality significantly. The authigenic pore-filling clay minerals are most likely to originate from post-depositional, mechanical infiltrated, allogenic clay minerals. Post-depositional clay infiltration by muddy water has been widely described as an effective mechanism to emplace allogenic clay mineral aggregates and allogenic clay mineral coats into sand in arid and semi-arid climates (Matlack et al., 1989; Moraes and de Ros, 1990; Worden and Morad, 2003; Ajdukiewicz et al., 2010). The clay minerals are infiltrated during rain or flood events through fractures and disaggregation bands into semi-consolidated sands (McKie et al., 2010). The high amounts of infiltrated allogenic clay minerals resulted in thick allogenic clay coatings, allogenic clay bridges between detrital grains, and pore-filling allogenic clay aggregates (Matlack et al., 1989; Moraes and de Ros, 1990). The allogenic clay minerals transformed with increasing temperatures along existing structures into authigenic chlorite and illite which led to present-day authigenic clay coatings (Figure 6.7B, C & D), pore-bridging clay structures, and pore-filling clay aggregates (Figure 6.7F).

Variations in the authigenic clay minerals assemblage between the 22/29-2 and 22/29-3 sample sets are proposed to relate to variations of meteoric water influx through fractures and disaggregation bands (Figure 6.14). Pore-filling clay mineral aggregates are common in each facies, but are particularly common in the 22/29-3 sample set (Table 6.7). Even though the pore-filling clay mineral aggregates comprise significant microporosity (Figure 6.3), they infill the open pore space, tend to block pore throats and significantly decrease fluid flow. McKie and Audretsch (2005) reported significant permeability reductions (hundreds of mD) in the channel sandstones of the Seagull field, in comparison to channel sandstone permeabilities of the Heron field (>10000 mD), where the clay minerals tend to line the pore space and pore-filling clay aggregates are less common (Stricker et al., 2016b).

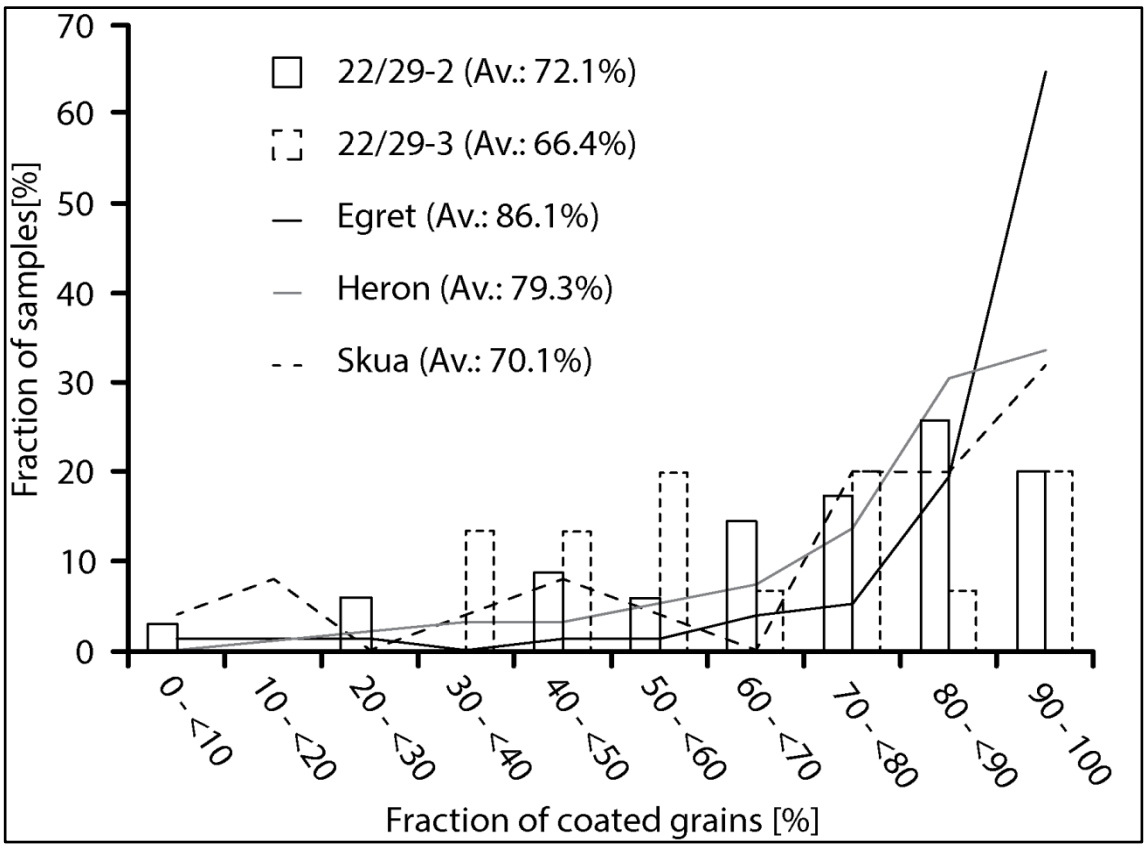

Figure 6.13 Fraction of clay mineral coated detrital grains per 300 counts for the two Seagull sample sets, in comparison to the ETAP fields Egret, Heron and Skua, from Stricker et al. (2016b).

6.5.2 Spatial variations of reservoir quality within salt-walled mini-basins

The Seagull mini-basin formed because differential loading induced withdrawal of Late Permian Zechstein salt. The Permian salt has negligible shear strength on long time scales and hence is easy to deform by differential sedimentary or tectonic loading. The coeval halokinesis had a strong influence on the deposition of the fluvial Triassic sediments and their present-day reservoir quality within the mini-basins. The coeval halokinesis dictated the distribution of fluvial channels and accommodation space which led to strong facies variations between the mini-basin centre and the mini-basin margins (e.g., Banham and Mountney, 2013a, 2013b). Furthermore, reservoir quality has been affected by post-depositional halokinesis due to diagenetic variations, induced by spatial variations in the pore fluid chemistry (meteoric to hypersaline pore fluids) (Figure 6.14) and halokinesis-induced faults and fractures (syn-depositional and/or post-depositional) (Figure 6.11) which enhance or reduce fluid flow and reservoir quality.

The Judy Sandstone Member within the Seagull mini-basin shows strong reservoir quality variations between the basin centre and the basin margin. The 22/29-3 sample set (located towards the margin) shows generally lower porosities and poorer reservoir quality than the 22/29-2 sample set (located towards the centre) (Figure 6.3). Both sample sets have undergone a similar burial history, with similar VES and temperature histories (Figure 6.4) and show comparable average IGV values (30.3% for 22/29-2 and 32.5% for 22/29-3), indicating a similar degree of compaction. The cement volumes, however, show significant variations (19.9% for 22/29-2 and 29.5% for 22/29-3; Figure 6.8, Figure 6.10 & Table 6.7), indicating a strong relationship between reservoir quality, diagenesis, and location within the mini-basin. Detailed petrographic analysis of the channel sandstone samples show up to 10% more authigenic clay mineral cements within the 22/29-3 samples (Figure 6.8). Clay mineral cements in both sample sets are

solely authigenic chlorite and illite cements (Table 6.5 & Table 6.6). The variations in clay cement correlate to the increased occurrence of fractures and disaggregation bands at the mini-basin margin (Figure 6.11 & Figure 6.12).

Disaggregation bands and fractures can be encountered in both cores, but are significantly more common in the 22/29-3 core. Faulting of mini-basin infill can commonly be encountered at the mini-basin margins, proximal to tectonically active salt-walls. The contemporaneous salt movement and post-depositional salt withdrawal at the mini-basin flanks lead to higher densities of fractures and disaggregation bands in the sedimentary sequence (Figure 6.14) (e.g., Fox, 1998; Rowan et al., 1999). The fractures and disaggregation bands represent ideal pathways for meteoric fluids and generate local fluid chemistry variations within mini-basin. The higher fracture densities at the marginal areas hold the potential for increased meteoric influx and localised pore fluid changes, leading to diagenetic variations of the clay assemblage within the reservoir sandstones. The occurrence of greater intensity of disaggregation bands at the mini-basin margins further complicate fluid flow prediction and reservoir compartmentalisation at different scales for the Skagerrak Formation. Fractures, faults and disaggregation bands create a complex system of permeable fluid pathways and cemented baffles at deeper burial (Fossen et al., 2007).

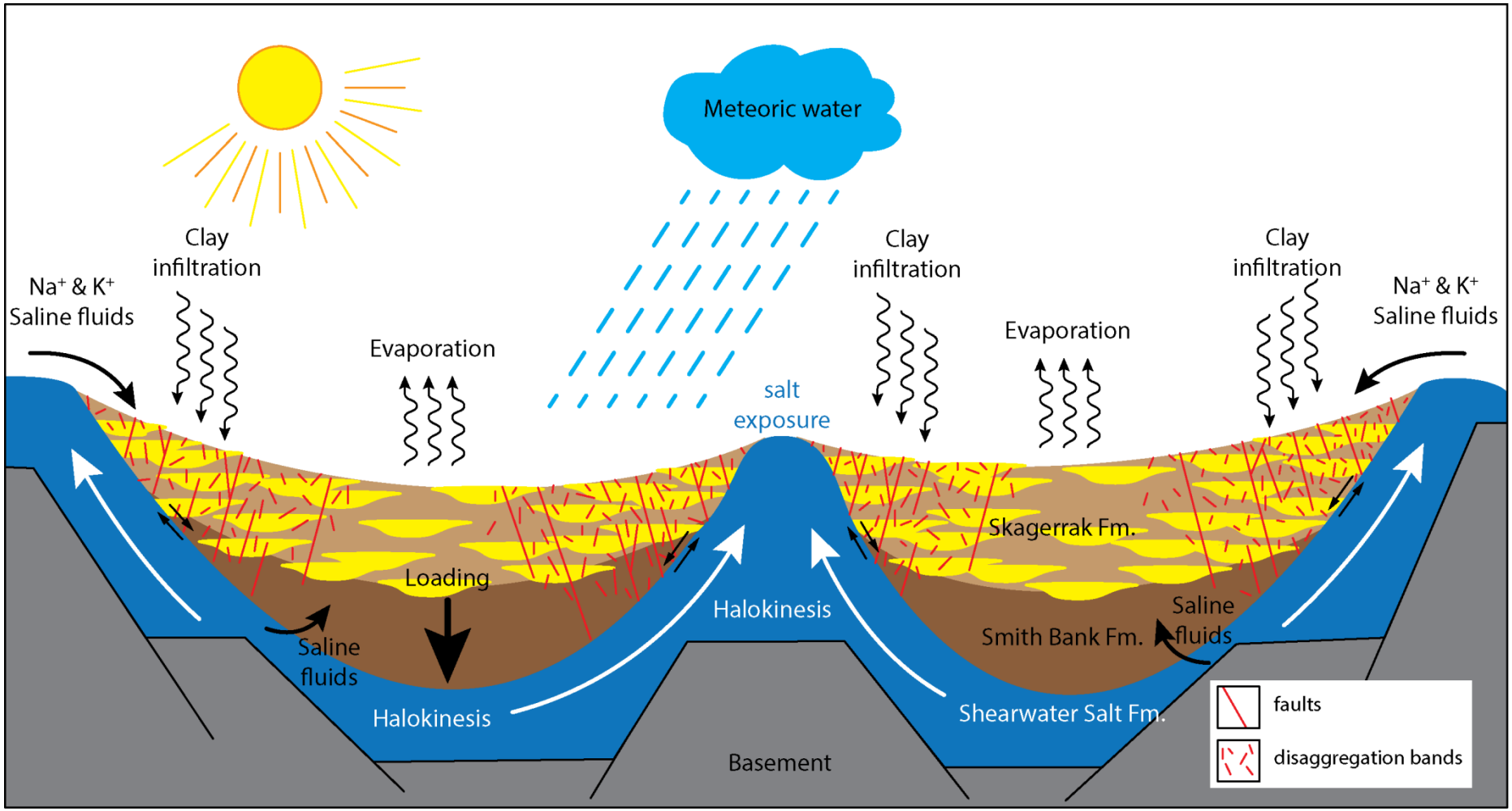

Figure 6.14 Schematic illustration of the mini-basin development and reservoir quality influencing processes. For stratigraphy see Figure 6.2.

6.5.3 Implications for exploration in salt-walled mini-basins in the North Sea

Hydrocarbon exploration in salt basins can be challenging due to the wide range of potential tectonostratigraphic controls on the temporal and spatial facies distribution and the diagenetic interplay between salt and sediments during burial (e.g., Smith et al., 1993; Barde et al., 2002; Matthews et al., 2007). The tectonic effects of halokinesis on salt-walled mini-basins are tremendous and can influence the shape and orientation of the mini-basin, as well as the depositional environment and diagenetic alteration within it. Salt-walled mini-basins are commonly faulted and tilted in the Central North Sea (McKie et al., 2010), which commonly creates structural highs at the marginal areas of the mini-basin. These structural highs commonly form structural traps with up-dip closure against impermeable salt and provide excellent hydrocarbon plays. However, this research has highlighted strong intra-basin reservoir quality variations between the margin and centre areas of the mini-basins. Banham and Mountney (2013b) have highlighted depositional variations within salt-walled mini-basins and have shown higher reservoir potential with more stacked channel sandstones for the mini-basin centres. This research has taken spatial reservoir quality analysis even further and provides valuable insights into the diagenesis of the channel sandstones. It has been shown that the centre of the mini-basin exhibits higher reservoir quality than the marginal areas due to less clay mineral cementation and a lower density of fracture and disaggregation bands compared to the marginal mini-basin areas.

Central areas of salt-walled mini-basins exhibit better reservoir quality due to higher ratios of stacked channel sandstones, less clay infiltration, and less diagenetic alteration, whereas marginal areas provide often excellent traps but poorer reservoir quality.

6.6 Conclusions

1) Excellent reservoir quality with anomalously high porosities of up to 29% at burial depths of >4000 m below sea floor is preserved in Skagerrak Formation sandstones of the Seagull field (UK Quadrant 22, 22/29-2 and 22/29-3).
2) Shallow overpressure and continuous increase of overpressure has maintained a low VES through time in the Seagull field and resulted in under-compaction of the fluvial channel reservoirs for their present-day depths of burial.
3) Despite similar burial and diagenetic histories, a marked spatial variation of reservoir quality occurs between the mini-basin centre and the mini-basin margin (29% and 17% porosity, respectively) within the Judy Sandstone Member in the Seagull field.
4) Higher fracture and disaggregation band density has led to high fractions of pore-filling authigenic chlorite and illite within channel sandstones towards the mini-basin margin.
5) Reservoir quality is clearly influenced by spatial positioning within salt-walled mini-basins. Moderate net to gross fluvial facies occurrences at mini-basin margins are likely to demonstrate poorer reservoir quality associated with disaggregation bands and localised faulting. These deformation bands provide localised pathways for infiltrated clays and porosity reduction.

Chapter VII

Importance of vertical effective stress for reservoir quality in the Skagerrak Formation, Central Graben, North Sea

This chapter has been accepted for publication in Marine and Petroleum Geology (01/03/2016).

Stricker, S., Jones, S. J., & Grant, N. T., (2016). Importance of vertical effective stress for reservoir quality in the Skagerrak Formation, Central Graben, North Sea. *Marine and Petroleum Geology*, http://doi.org/10.1016/j.marpetgeo.2016.03.001

7.1 Summary

The complex fluvial sandstones of the Triassic Skagerrak Formation are the host reservoir for a number of high-pressure, high-temperature (HPHT) fields in the Central Graben, North Sea. All the reservoir sandstones in this study compromise fine-grained to medium-grained sub-arkosic to arkosic sandstones that have experienced broadly similar burial and diagenetic histories to their present-day maximum burial depths. Despite similar diagenetic histories, the fluvial reservoirs show major variations in reservoir quality and preserved porosity. Reservoir quality varies from excellent with anomalously high porosities of up to 35% at burial depth of >3500 m to non-economic with porosities <10% at burial depths of 4300 m.

This study has combined detailed petrographic analyses, core analysis and pressure history modelling to assess the impact of differing vertical effective stresses (VES) and high pore fluid pressures (up to 80 MPa) on reservoir quality. It has been recognized that fluvial channel sandstones of the Skagerrak Formation in the UK sector have experienced significantly less mechanical compaction than their equivalents in the Norwegian sector. This difference in mechanical compaction has had a significant impact upon reservoir quality, even though the presence of chlorite grain coatings inhibited macroquartz cement overgrowths across all Skagerrak Formation reservoirs. The onset of overpressure started once the overlying Chalk seal was buried deeply enough to form a permeability barrier to fluid escape. It is the cumulative effect of varying amounts of overpressure and its effect on the VES history that is key to determining the reservoir quality of these channelised sandstone units. The results are consistent with a model where vertical effective stress affects both the compaction state and subsequent quartz cementation of the reservoirs.

7.2 Introduction

The reservoir quality of deeply buried sandstones is the combined product of depositional processes and subsequent diagenesis during progressive burial. Deposition controls the composition of the sand, including its grain size distribution which has an over-arching influence in determining reservoir properties. Relative differences between sandstone facies in terms of porosity and permeability are preserved during burial, so facies is a key factor in controlling reservoir performance. Burial-related diagenesis also has an important role to play as it can destroy, preserve, or enhance the reservoir quality, whatever the facies. High porosities in deeply buried siliciclastic reservoirs are exceptional and have commonly resulted from diagenetic cementation followed by dissolution (e.g., Bloch et al., 2002; Taylor et al., 2010). The role played by vertical effective stress (VES) during initial mechanical and chemical compaction processes is generally considered to be less significant. Primary porosity is reduced by mechanical compaction processes at shallow depths, where grain rearrangement (frictional slippage, rotation and sliding), deformation of soft grains (e.g., lithic fragments), and fracturing of ridged grains (e.g., quartz and feldspar), can occur. At the higher temperatures and pressures of deep burial, chemical compaction takes over and includes mineral growth and inter-granular pressure dissolution (e.g., Houseknecht, 1987; Chuhan et al., 2002; Paxton et al., 2002). Mechanical and chemical compaction processes are irreversible and eliminate inter-granular volume (IGV) that would otherwise remain fluid-filled or become occupied by cements that might dissolve during later diagenesis (Houseknecht, 1987). Thus inhibition of compaction is vital for porosity maintenance to depth.

Two processes are known to inhibit sediment compaction: (1) cement precipitation that strengthens the grain framework and (2) the development of pore fluid overpressure. Stabilization of the framework and enlargement of the grain contact areas can be

achieved by the precipitation of small quantities of cement such as carbonate, halite or quartz, and the porosity preservation is strongest if precipitation occurs at shallow depth. Fluid overpressure supports the grain framework and reduces the effective stress acting on the framework. Both processes can significantly reduce mechanical and chemical compaction. Pore fluid pressures in sedimentary basins remain hydrostatic during burial where the rocks can drain freely. Overpressure occurs where the fluid cannot drain rapidly enough for the pore pressure to remain hydrostatic as the bulk rock volume is reduced by compaction processes. Low permeability retards fluid flow and so overpressures develop preferentially where rocks are sealed by thick successions of fine-grained sediment. Fluid volume expansion due to cracking of oil to gas, transformation of smectite to illite, lateral transfer, and temperature increase can also lead to the development of excess pore pressure (e.g., Osborne and Swarbrick, 1997; Swarbrick and Osborne, 1998; Swarbrick et al., 2002). The overpressure supports the grain framework and decreases the stress acting on the grain contacts, which leads to lower normal effective stresses (Terzaghi's effective stress concept).

The aim of this paper is to investigate the reason for the porosity variations in the Skagerrak Formation in the Central North Sea and how anomalously high porosities have been preserved even though the reservoir is deeply buried and at high temperatures (Table 7.1). One-dimensional pore pressure and burial history models are combined with detailed petrography to assess the role played by overpressure on VES and reservoir quality. Analysis of the key processes responsible for this porosity preservation requires depositional effects to be taken into account. This has been done by careful focus on reservoir facies with similar grain size and sorting. The results can be used to help predict reservoir quality in undrilled structures.

Field		Heron	Skua	Jade	Judy	Cod	Gaupe
Well		22/29-5RE	22/24b-7	30/2c-4	30/7a/9	7/11-7	6/3-1
Water Depth	[m]	92	97	80	76	70	86
TRD	[m TVDSS]	4356	3556	4561	3639	4310	2955
TRPP	[MPa]	89.5	64.2	84.1	62.7	80.4	37.3
HWC	[m TVDSS]	4656	3680	5441	3581		3013
HC Gradient	[MPa/km]	4.750	5.429	3.845	5.429		3.167
Overpressure	[MPa]	39.3	24.1	27.2	22.4	32.6	4.1
BHT Measured	[°C]	155.5	160	175	161.6	167.7	147.7
BHT Corrected	[°C]	178	183.3	200.5	185	192.1	169.1
BHT Depth	[m TVDSS]	4298	4016	5020	4329	4618	3536

Table 7.1 Well data of the Heron, Skua, Jade, Judy, Cod and Gaupe fields used in this study, such as water depth, top reservoir depth (TRD) top reservoir pore pressure (TRPP), hydrocarbon-water-contact (HWC), hydrocarbon gradient (HC), overpressure, and measured as well as corrected (corrected after Andrews-Speed et al. (1984)) bottom hole temperature (BHT), including bottom hole depth, based on Grant et al. (2014).

7.3 Geological setting

The Central Graben of the North Sea is approximately 550 km long with a width of 70-130 km and is part of a NW-SE trending extension of a trilete rift system, with the Viking Graben as the northern arm and the Inner and Outer Moray Firth as the western arm. The North Sea Central Graben is divided into the East Central Graben and the West Central Graben by the Forties-Montrose High and the Josephine Ridge medial horst blocks, and separates the Norwegian platform in the east from the UK continental shelf in the west (Figure 7.1). The complex rift system developed in at least two major extensional phases, one in the Permian-Triassic (290-210 Ma) and another in the Late Jurassic (155-140 Ma) (Gowers and Saeboe, 1985; Glennie, 1998). The geological history has commonly been divided into pre-rift, syn-rift and post-rift phases. The syn-rift sediments are mainly siliciclastic Triassic and Jurassic sediments with a cumulative thickness of 1000-4000 m. The post-rift sediments comprise the Cretaceous to Holocene successions, of up to 4500 m in total thickness, which are dominated by shale, sandstone, silty sandstone and thick Upper Cretaceous chalk units including the

Ekofisk, Tor and Hod Formations (Figure 7.2) (Goldsmith et al., 2003). These highly cemented and compacted chalk units provide the main seal for the highly overpressured sub-Chalk reservoirs in the Central Graben, North Sea (Mallon and Swarbrick, 2002, 2008; Swarbrick et al., 2010).

The focus area for this chapter includes the Heron (well 22/29-5RE) and Skua (well 22/24b-7) fields from the Heron Cluster in UK Quadrant 22, the Jade (well 30/2c-4) and Judy (wells 30/7a-7, -8, -9, 11Z, -P3 & 30/13-5) fields from the Josephine Ridge in UK Quadrant 30, and the Cod (well 7/11-7) and Gaupe (well 6/3-1) fields in Norwegian quadrants 7 and 6, respectively (Figure 7.1). This broad areal coverage allows a regional perspective on the post-depositional processes that have influenced porosity preservation in the Skagerrak Formation.

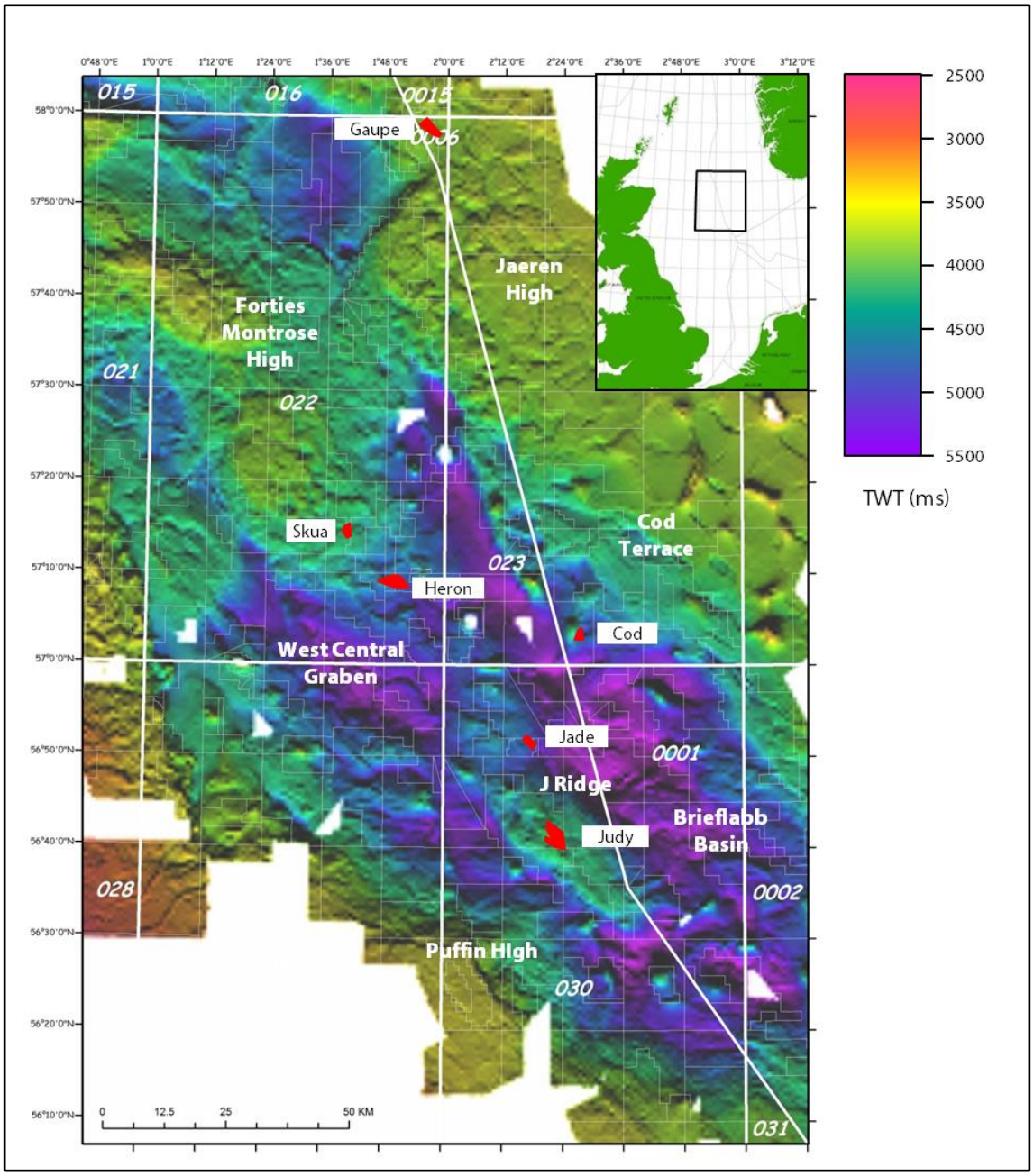

Figure 7.1 Regional base Cretaceous unconformity two-way time (TWT) map of the Central Graben, North Sea, highlighting the location of the six investigated Skagerrak Formation fields (N. Grant 2015, *pers. comm.*).

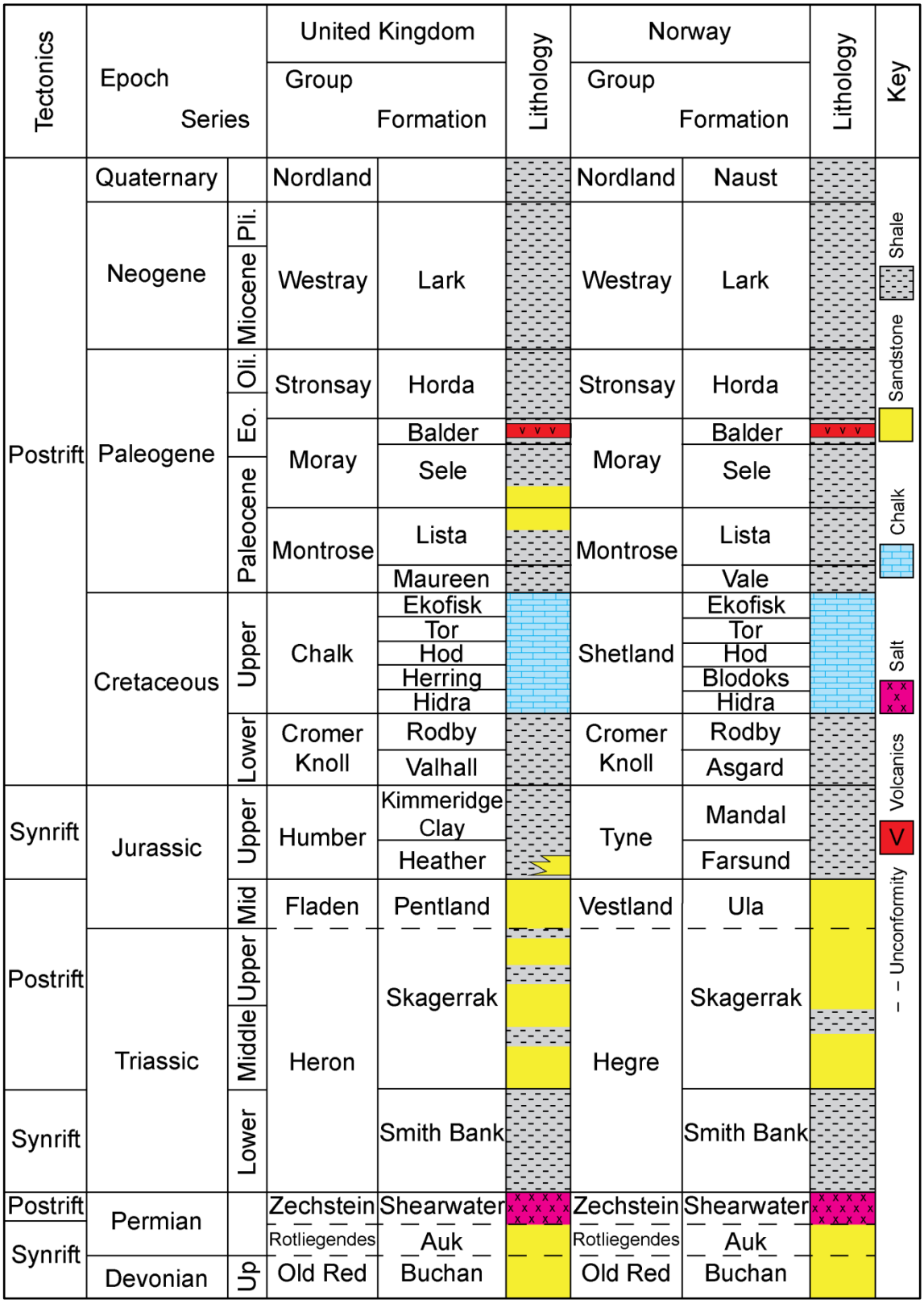

Figure 7.2 Regional stratigraphy of the Central Graben, North Sea. Also see Figure 3.2; Figure 3.3 and Figure 3.4.

7.3.1 Triassic Skagerrak stratigraphy

The Triassic strata of the Central North Sea area are dominated by thick alluvial successions deposited in a closed or internally draining basin with no apparent connection to a marine realm (Goldsmith et al., 2003). The general Triassic succession is subdivided into the Early Triassic Smith Bank Formation (shales, evaporites and thin sands) and the Middle to Late Triassic Skagerrak Formation (a thick sequence of interbedded sands and shales) (Figure 7.2). The Middle to Late Triassic Skagerrak Formation comprises 500-1000 m of predominantly continental braided and meandering fluvial deposits, terminal fluvial fans and lacustrine shale (McKie and Audretsch, 2005; de Jong et al., 2006; Kape et al., 2010).

The stratigraphic nomenclature of the Triassic for the Central Graben was defined by Goldsmith et al. (1995, 2003), based on detailed biostratigraphic and lithostratigraphic correlation of wells from the Josephine Ridge. This nomenclature has been extended and correlated towards the Forties-Montrose High area by Mckie and Audretsch (2005). The Skagerrak Formation can locally be subdivided into three sand-dominated members (Judy, Joanne and Josephine) and three mud-dominated members (Julius, Jonathan and Joshua) for UK quadrants 22 and 30, but is not subdivided in Norwegian quadrants 6 and 7 (Goldsmith et al., 2003). The sand-dominated units include sheetflood deposits and multi-storey stacked channel sandbodies (Goldsmith et al., 1995; McKie and Audretsch, 2005), whereas the mud-dominated units include basinwide floodplain, lacustrine shale, loess, and playa deposits. The thick and laterally extensive mud-dominated units provide the main correlative units for the Skagerrak Formation in the Central Graben (McKie and Audretsch, 2005). The Triassic stratigraphy is incompletely preserved due to deep erosion during the Middle and Late Jurassic (Figure 7.2) (Erratt et al., 1999).

The Triassic Smith Bank and Skagerrak sediments accumulated directly on top of the thick Late Permian Zechstein salt in a series of salt-controlled and fault-controlled mini-basins or pods. The Late Permian Zechstein salt strongly controlled the deposition by forming withdrawal basins due to a combination of localised loading and structural extension (Smith et al., 1993; Bishop, 1996; Matthews et al., 2007) within an overall rift setting. The predominantly fine-grained Smith Bank Formation represents the basal part of the mini-basin infill, and was deposited in lacustrine and playa settings within confined minibasins. The minibasins enlarged and amalgamated during deposition of the overlaying Skagerrak Formation as salt budgets waned and diapirism became localised rather than the salt continuing to form extensive salt walls. Mini-basin development was active throughout the Triassic and is mainly responsible for the preservation of Middle to Late Triassic Skagerrak Formation in the study area. Where the Late Permian salt was thickly developed, it prevented grounding of the mini-basins on the underlying Rotliegend basement. Salt withdrawal has allowed considerable thicknesses of Skagerrak sediment to accumulate within mini-basins as well as being responsible for great variation in thickness both within and between mini-basins. The consequent facies variability has influenced sandstone reservoir thickness and subsequent diagenetic cementation (Nguyen et al., 2013).

7.4 Methodology

7.4.1 Sampling

Core samples and the thin sections examined in this study are from Triassic Skagerrak Formation sandstones in the four fields in the UK sector: Heron (well 22/29-5RE; 136 samples), Skua (well 22/24b-7; 32 samples), Jade (well 30/2c-4; 20 samples), and Judy (wells 30/7a-7, -8, -9, -11Z, -P3 & 30/13-5; 85 samples in total) and from two fields in

the Norwegian sector: Cod (7/11-7; 39 samples) and Gaupe (6/3-1; 90 samples). The samples were selected from channel sands, the sedimentary facies in the available core material that is expected to have the best reservoir properties because of good sorting and an absence of matrix.

7.4.2 Petrography

Thin sections of core samples were used to measure optical porosity, grain size, composition and inter-granular volume. Optical porosity was measured by the digital image analysis technique jPOR (Grove and Jerram, 2011) on blue epoxy-impregnated thin sections. Uncorrected helium porosity measurements, making use of Boyle's law on core samples, were taken from core analysis reports. Grain size distribution was determined from analysis of thin section micrographs with the Leica QWin (V. 3.5.0) software. Sandstone composition was measured by point counting, with 300 counts per thin section using a standard petrographic microscope (Leica DM2500P and DM750P) and point counting stage (PETROG – Conwy Valley Systems Limited). Further petrographic analysis, such as intergranular-volume (IGV), total cement volume (C) and grain contact analysis, were exclusively performed on fine-grained samples with similar sorting. Inter-granular volume and total cement volume were measured by point counting with 300 counts per thin section. Grain-to-grain contacts were counted and classified by counting a line of 50 grain contacts per thin section.

7.4.3 One-dimensional basin modelling

Pore pressure in the Skagerrak sandstones for all six fields was modelled in one dimension using Schlumberger's PetroMod (V. 2012.2) software. This one-dimensional modelling provides a good insight into overpressure build-up by disequilibrium compaction and pore fluid expansion due to increasing temperature. However, the

models do not include other mechanisms for generating excess pore pressure such as fluid flow or hydrocarbon cracking, and are only able to take vertical stress into account. Any influence of clay mineral diagenesis on fluid pressure development is ignored. PetroMod is based on a forward modelling approach to calculate the geological evolution of a basin from the burial history. The burial history and lithology are inferred from the present-day well stratigraphy, well log lithology and lithological description of the modelled units (Table 7.2 & Table 7.3). We used the thermal upwelling basement palaeo-heat flow model of Allen and Allen (2005) with 63–110 mW/m^2 (average of 80 mW/m^2) during syn-rift phases and 37–66 mW/m^2 (average 50 mW/m^2) during post-rift phases combined with the palaeo-surface temperature history published by Swarbrick et al. (2000). The burial history models are calibrated against present-day RFT temperature measurements, corrected after Andrews-Speed et al. (1984), measured Triassic sandstone porosities (Boyle's law) and carefully adjusted towards present-day formation pressure measurements by considering late-stage, high-temperature overpressure mechanisms (Osborne and Swarbrick, 1997; Isaksen, 2004). The lithological unit types used in these models are mainly PetroMod (V. 2012.2) default lithology types, based on well log descriptions and core analysis reports for the investigated wells. Exceptions are the Hod lithology type present in the UK models and the lithology type of the Skagerrak sandstone members. The Hod chalk unit is modified to represent the North Sea non-reservoir chalk (Table 7.4) and match the compaction trend and permeability trend given by Mallon and Swarbrick (2002, 2008). The North Sea non-reservoir chalk is a laterally extensive low-permeability rock unit that represents the major vertical fluid flow barrier in the Central North Sea (Mallon and Swarbrick, 2008). The Triassic Skagerrak sandstone of the Joanne and Judy Sandstone Members is simulated by a mixture of PetroMod (V. 2012.2) default lithologies (80%

sand, 10% silt, 10% shale) combined with a regional compaction trend for shaly sandstone given by Sclater and Christie (1980).

Group/ Formation	Heron (22/29-5RE)		Skua (22/24b-7)		Jade (30/2c-4)		Judy (30/7a-9)	
	Thick	Lithology	Thick	Lithology	Thick	Lithology	Thick	Lithology
	[m]	[-]	[m]	[-]	[m]	[-]	[m]	[-]
Nordland	1407	Shale	1762	Shale	1624	Shale	1424	Shale
Lark/Hord	1396	Shale	957	Shale	1364	Shale	1357	Shale
Tay	15	Sandy Sh.						
Balder	18	Shale	12	Shale	22	Silty Sh.	17	Silty Sh.
Sele	31	Sandy Sh.	21	Shale	39	Silty Sh.	54	Silty Sh.
Forties	187	Sandstone	79	Sandstone	58	Sandstone		
Lista	49	Silty Sh.			16	Shale	16	Shale
Mey					24	Shale		
Andrew	51	Siltstone	81	Siltstone			89	Silty Sh.
Maureen	82	Marl	54	Marl	135	Sandstone	92	Sst/Marl
Ekofisk	94	Chalk	76	Marl	83	Marl	28	Chalk
Tor	459	Chalk	300	Chalk	506	Marl	226	Chalk
Hod	335	Non-Res.	98	Non-Res.	529	Non-Res.	154	Non-Res.
Herring	9	Marl						
Valhall	63	Marl	19	Marl	87	Shale	22	Sandy Sh.
Humber	0	Shale	0	Shale	0	Shale	0	Shale
Lias							3	Shale
Fladen	0	Sandstone	0	Sandstone	0	Sandstone	0	Sandstone
Joshua	0	Silty Shale	0	Silty Sh.	0	Silty Sh.	0	Silty Sh.
Josephine	0	Res. Sst	0	Res. Sst	0	Res. Sst	0	Res. Sst
Jonathan	0	Silty Sh.	0	Silty Sh.	0	Silty Sh.	38	Silty Sh.
Joanne	23	Res. Sst	0	Res. Sst	**384**	**Res. Sst**	**469**	**Res. Sst**
Julius	41	Silty Sh.	0	Silty Sh.	54	Silty Sh.	140	Silty Sh.
Judy	**339**	**Res. Sst**	**468**	**Res. Sst**	400	Res. Sst	385	Res. Sst
Smith Bank	200	Silty Sh.	118	Silty Sh.	600	Silty Sh.	200	Silty Sh.
Zechstein	208	Salt	207	Salt	500	Salt	208	Salt

Table 7.2 Lithology type and respective thickness of the modelled layers for the Heron, Skua, Jade and Judy PetroMod models (the modelled key Skagerrak Formation reservoir unit in bold), with Sh: Shale, Sst: Sandstone, Non-Res.: Non-Reservoir Chalk and Res. Sst.: Reservoir Sandstone (80% Sand, 10% Silt and 10% Clay)

Group/ Formation	Cod (7/11-7)		Gaupe (6/3-1)	
	Thick.	Lithology	Thick.	Lithology
	[m]	[-]	[m]	[-]
Nordland	1503	Shale	1211	Shale
Hordaland	1317	Shale	1115	Shale
Balder	13	Shale	14	Shale
Sele	39	Shale	87	Shale
Lista	190	Sandy Sh.	1	Shale
Maureen	13	Sandy Sh.	136	Chalk
Ekofisk	79	Chalk	6	Chalk
Tor	405	Chalk	165	Chalk
Hod	324	Chalk	78	Chalk
Blodoks	8	Shale		
Hidra	109	Chalk		
Rodby	41	Marl		
Asgard	42	Marl	41	Shale
Mandal	42	Shale		
Farsund	78	Shale	2	Shale
Ula	38	Sandstone		
Gassum			13	Sandstone
Skagerrak	**287**	**Res. Sst**	**545**	**Res. Sst**
Smith Bank	200	Silty Sh.	200	Silty Sh.
Zechstein	200	Salt	200	Salt

Table 7.3 Lithology type and respective thickness of the modelled layers for the Cod and Gaupe models (the modelled key Skagerrak Formation reservoir unit in bold), with Sh: Shale and Res. Sst.: Reservoir Sandstone (80% Sand, 10% Silt and 10% Clay)

Model Parameter (Hod Formation)			
Mechanical compaction		Permeability	
Porosity	Depth	Porosity	Permeability
[%]	[m]	[%]	[log(mD)]
70.00	0	70.00	1.00
18.00	1300	30.00	-1.00
12.50	2100	25.00	-3.00
8.00	3100	20.00	-5.50
5.00	4500	12.50	-7.20
		9.00	-7.20
		5.00	-7.20

Table 7.4 Non-reservoir North Sea Hod chalk model parameters, after Mallon and Swarbrick (2002, 2008)

7.5 Results

7.5.1 Grain size, composition and porosity distribution

The 347 investigated samples from the Heron Cluster fields (Heron – 136 and Skua – 32), the J-Ridge fields (Jade – 20 and Judy – 85), and the Norwegian fields (Cod – 30) and Gaupe – 90) vary compositionally within a narrow range of arkosic and lithic-arkosic sandstones. The grain size of the samples varies between silt and coarse-grained sand, with small regional differences (Figure 7.3). The sample sets show a wide range of optical porosities from below 1% up to 35% (Figure 7.3, Figure 7.4 & Figure 7.5) with higher maximum porosities occurring at coarser grain sizes (Figure 7.3 & Table 7.5). The optical porosity data sets have been complemented by additional helium core plug porosity data, measured using Boyle's law (uncorrected for possible decompaction effects). The helium core plug porosities measure the total porosity and are mostly greater than the optical measured porosity values (Figure 7.4, Figure 7.5 & Table 7.5), indicating the presence of significant microporosity within the sandstones. This is likely to reside within the clay cements and matrix, within partially dissolved grains and as small voids along grain boundaries.

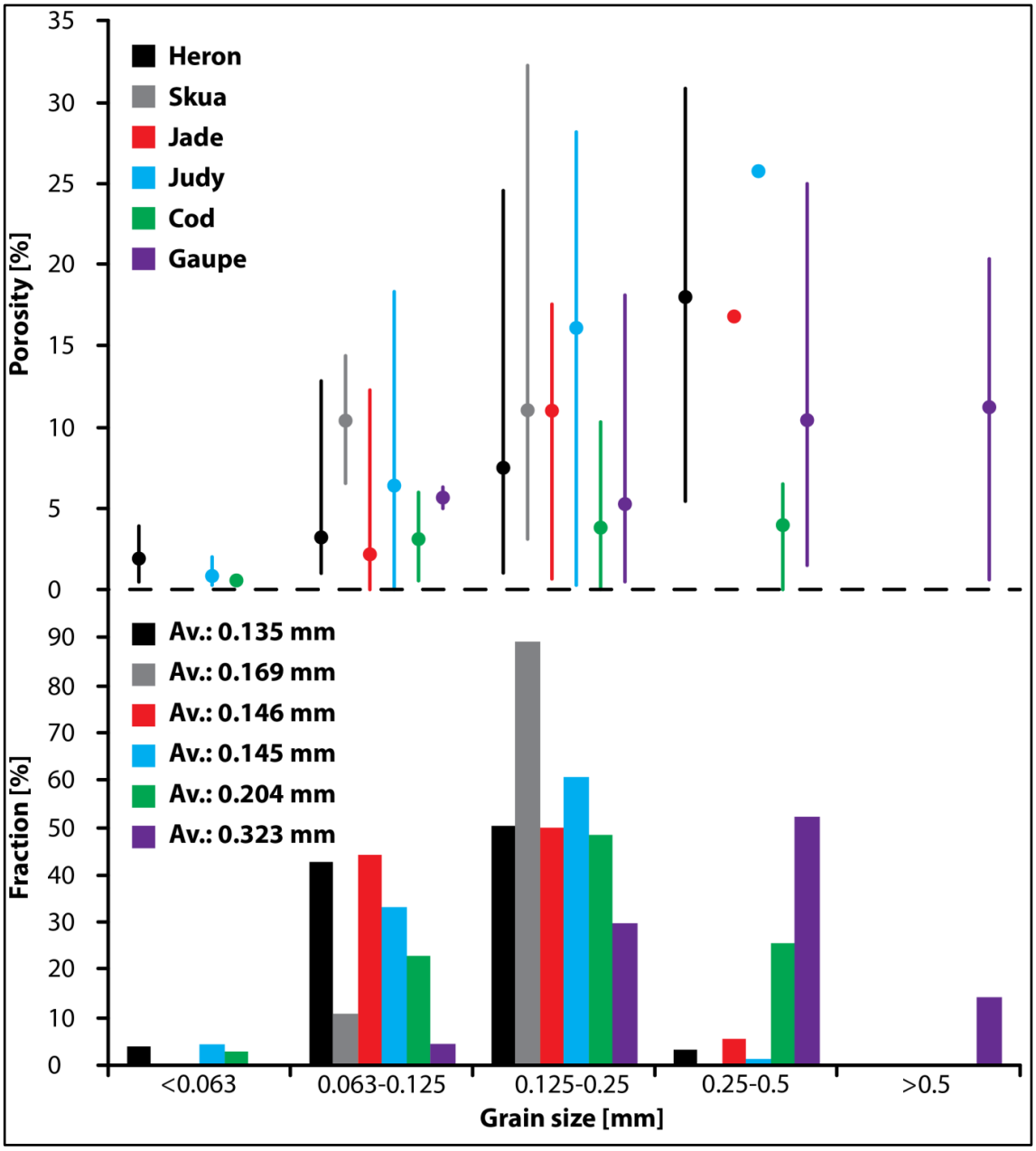

Figure 7.3 Grain size distribution and porosity for the Heron (136 samples), Skua (32), Jade (20), Judy (85), Cod (39) and Gaupe (90) sample sets, with the average (point), maximum and minimum porosity per grain size.

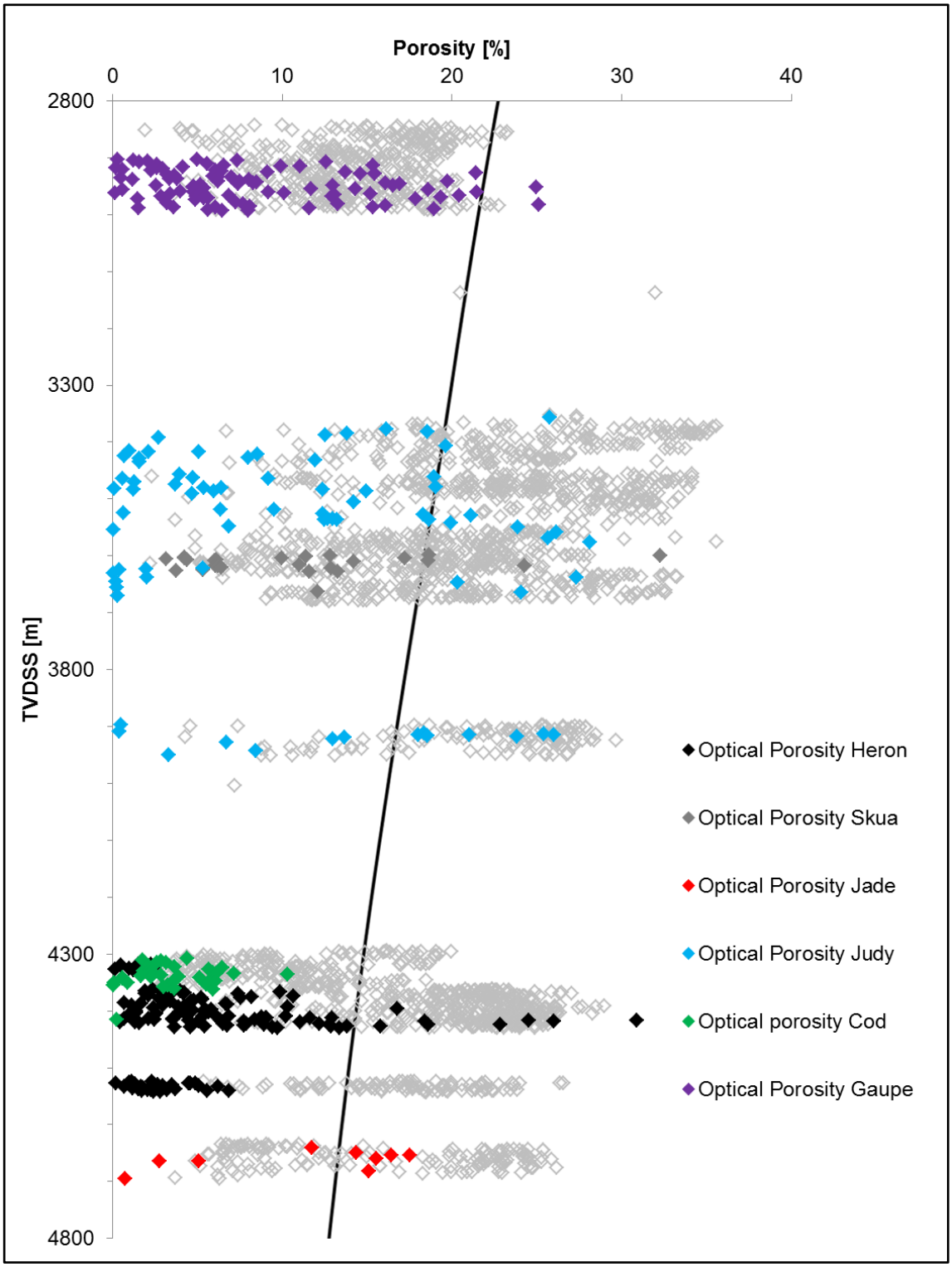

Figure 7.4 Helium (grey) and optical porosity (colour) distribution with depth (in true vertical depth below sea level) for the Heron, Skua, Jade, Judy, Cod and Gaupe sample sets, with a regional Central North Sea porosity-depth relationship for hydrostatically pressured shaly sandstone (Sclater and Christie, 1980).

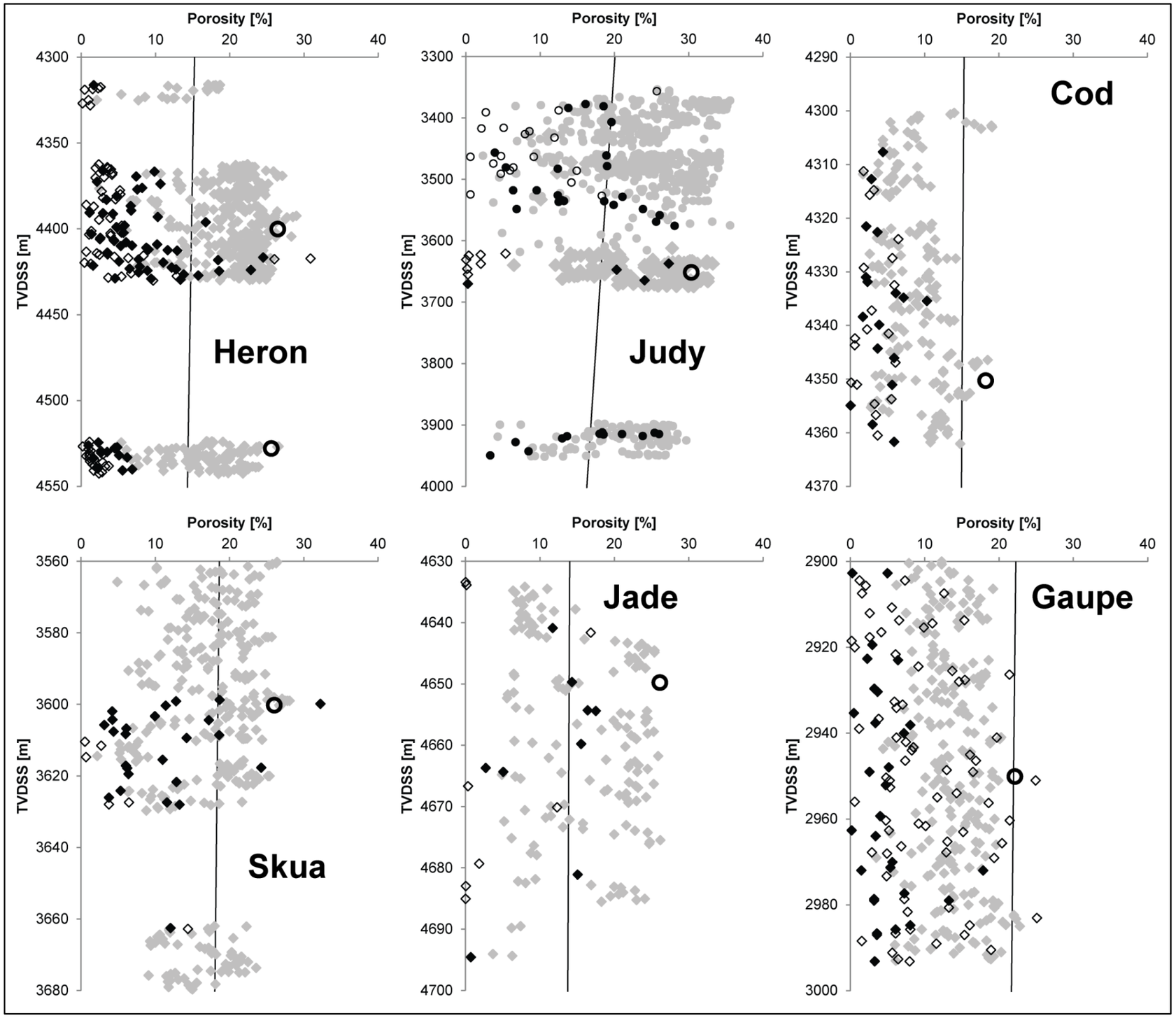

Figure 7.5 Helium (grey) and optical porosity (black) distribution with depth (in true vertical depth below sea level) for the Heron, Skua, Jade, Judy (diamonds: 30/7a-9; points: 30/7a-7, -8, -11Z, -P3 & 30/13-5), Cod and Gaupe sample sets, with optical porosity of fine-grained samples in solid black, a regional Central North Sea porosity-depth relationship for hydrostatically pressured shaly sandstone (Sclater and Christie, 1980). Large black circles represent PetroMod calibration porosity of the respective Skagerrak Formation sandstone.

Field	Porosity	Optical porosity by grain size					Helium porosity	Average grain size
		Silt	Sand					
		Silt	very fine	fine	medium	coarse		
		[mm]	[mm]	[mm]	[mm]	[mm]	[%]	[mm]
Heron	Maximum	3.9	12.9	24.5	30.9		29	0.136
	Average	1.8	3.2	7.6	18		19.5	
	Minimum	0.4	1	0.9	5.4		2.1	
Skua	Maximum		14.4	32.2			27.8	0.169
	Average		10.4	11			17.4	
	Minimum		6.5	3.1			2.2	
Jade	Maximum		12.3	17.5			26.2	0.146
	Average		2.2	11	16.8		15.8	
	Minimum		0.3	0.7			3.7	
Judy	Maximum	2	18.3	28.1			35.6	0.145
	Average	0.9	6.4	16.1	25.7		23.3	
	Minimum	0.3	0.2	0.3			2.3	
Cod	Maximum		5.9	10.3	6.5		20.4	0.204
	Average	0.6	3.1	3.9	3.9		9.8	
	Minimum		0.6	0.3	0.1		1.8	
Gaupe	Maximum		6.1	17.8	25.1	20.4	24.9	0.323
	Average		5.4	4.9	10.4	11.1	14.3	
	Minimum		4.9	0.2	1.5	0.6	1.9	

Table 7.5 Optical porosities categorised by grain size, helium porosities and average grain size per sample set.

7.5.2 Intergranular volume and porosity loss

Intergranular volume (IGV), or minus-cement porosity, is the sum of intergranular pore space, intergranular cement and depositional matrix (Houseknecht, 1987, 1988; Paxton et al., 2002). IGV is an excellent indicator for the degree of mechanical compaction of clastic sediments due to its dependence on vertical effective stress (VES) and its diminishing trend with ongoing compaction. Nevertheless, IGV can also be influenced by factors such as early cementation (grain framework strengthening or locally pore filling) or early pore fluid overpressure.

The IGV values of the six sample sets show both wide internal variations and variations between the different sample sets (Table 7.6). IGV averages of the shallower buried sample sets (e.g., from the Judy and Skua fields) are generally higher than those of the

deeper sample sets (e.g., Cod and Jade). This difference points to variations in compaction state between fields. Mechanical compaction of a fine-medium grained, well sorted sand, typical of the Skagerrak channel facies, should be able to reduce IGV from a starting point around 45% at deposition (e.g., Beard and Weyl, 1973) to around 26% when tightly packed grain framework has been established (e.g., Paxton et al., 2002). The grain composition will influence the amount of compaction with feldspars more likely to fracture and deform than quartz grains. Early framework stabilising cements or overpressure development help retard compaction during burial.

Field	IGV		
	Minimum	**Average**	**Maximum**
Heron	20	27.3	36
Skua	19	27.1	34.3
Jade	15	22.2	28
Judy	19.33	28.2	36.3
Cod	15	21.1	34
Gaupe	9.3	25.7	35

Table 7.6 Measured intergranular volume (IGV) of the Heron, Skua, Jade, Judy, Cod and Gaupe fine-grained samples.

The total cement volume has been measured and can be used in combination with the IGV to calculate the porosity loss by compaction (COPL) and by cementation (CEPL) using the following equations by (Lundegard, 1992):

$$COPL = P_i - \left(\frac{(100 - P_i) P_{mc}}{100 - P_{mc}} \right) \tag{7.1}$$

$$CEPL = (P_i - COPL) \left(\frac{C}{P_{mc}} \right) \tag{7.2}$$

where P_i is the initial or depositional porosity and P_{mc} is the intergranular volume or minus-cement porosity calculated from by subtracting the total cement volume, C, from the total optical primary porosity, P_o. The calculated COPL and CEPL are accurate if three conditions are met. First, the assumed initial porosity P_i must be correct. Second,

the amount of cement derived by local grain dissolution must be negligible or known. And third, the amount of framework mass exported by grain dissolution must be negligible or known (Lundegard, 1992). The initial or depositional porosity for the Triassic Skagerrak sandstones samples is assumed to be 45% (Beard and Weyl, 1973; Houseknecht, 1987; Lundegard, 1992; Chuhan et al., 2002; Paxton et al., 2002). The COPL-CEPL results (Figure 7.6) indicate mechanical and chemical compaction as the main drivers for porosity loss of the Heron, Skua, Jade, Judy and Cod sample sets, whereas the COPL-CEPL results of the Gaupe sample set indicate a higher porosity loss by cementation, albeit with stronger tendency towards compactional porosity loss.

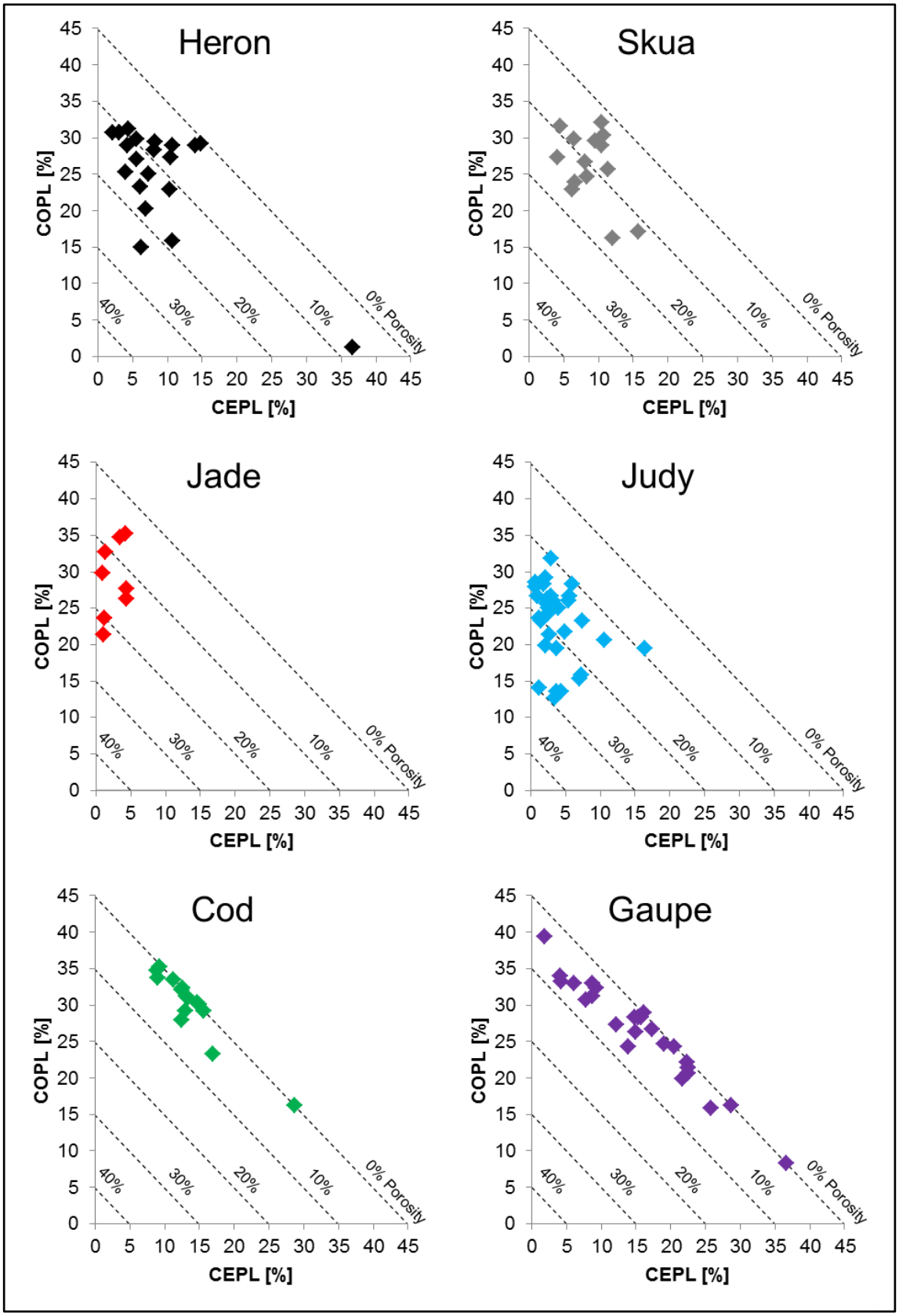

Figure 7.6 Compactional (COPL) and cementational (CEPL) porosity loss for the Heron, Skua, Jade, Judy, Cod and Gaupe fine-grained data sets with remaining sample porosity (dashed lines). COPL and CEPL calculated after Lundegard (1992).

7.5.3 Compaction indicators

Evidence for both mechanical and chemical compaction can be observed in the investigated fine-grained sandstone samples. Mechanical compaction is recorded by features such as grain rearrangement, grain deformation, denser grain packing, and the frequency of distinctive grain contacts, such as point and long/tangential grain contacts for low mechanical compaction (Table 7.7). Chemical compaction of quartz-rich sandstones occurs by pressure dissolution at grain contacts and is indicated by the presence of concavo-convex and/or sutured grain contacts.

The Judy sample set displays a low grain-packing density, often with apparently 'floating' grains, i.e., grains surrounded by pores in two-dimensional space (Figure 7.7A), and a high number of point contacts between the grains (Table 7.7). These features are characteristic of a relatively low compaction state or under-compaction in relation to similar hydrostatically pressured sandstones at equivalent burial depth (porosity-depth relationship for hydrostatically pressured shaly sandstone by Sclater and Christie (1980)). 'Floating' grains are not observed in the Heron Field sample set which has a slightly denser grain packing, a lower number of point contacts and slight bending of mica grains, but still has a low compaction state. The Jade and Skua sample sets generally show more mechanical compaction with denser grain arrangements and bent mica grains, and more features characteristic of chemical compaction, such as a higher frequency of concavo-convex contacts than the Heron and Judy field samples (Table 7.7 & Figure 7.7B). The Gaupe and Cod samples have a high grain-packing density and a high number of grain-to-grain contacts per grain (Figure 7.7C). These characteristics indicate a high degree of mechanical compaction, also recorded by the high frequency of soft grain deformation, such as bent micas (Figure 7.7D) and deformed lithic fragments. Chemical compaction is very common in the Norwegian data sets with

petrographic evidence such as concavo-convex and sutured grain contacts in both the Gaupe and, especially, the Cod samples (Figure 7.7E & Figure 7.7F). The grain framework of the Cod samples is dominated by concavo-convex grain contacts and shows the highest frequency of sutured grain contacts. Evidence of strong chemical compaction, i.e., sutured grain contacts, is rarely observed in the Jade and Skua samples, and is completely absent in the Judy and Heron field samples (Table 7.7).

Sample data			Grain contacts [%]			
Field	**Well**	**Sample**	**Point**	**Long**	**C&C**	**Sutured**
Heron	22 29-5RE	15614'9"	16.00	52.00	32.00	0.00
		15675'10"	12.00	48.00	40.00	0.00
		15691'6"	18.00	46.00	36.00	0.00
		15724'11"	16.00	46.00	38.00	0.00
		15749'1"	22.00	36.00	42.00	0.00
		15760'11"	14.00	46.00	40.00	0.00
		Average	**16.33**	**45.67**	**38.00**	**0.00**
Skua	22 24b-7	11909'4"	8.00	42.00	44.00	6.00
		11932'"	4.00	50.00	42.00	4.00
		11882'2"	12.00	42.00	46.00	0.00
		12086'3"	18.00	44.00	38.00	0.00
		11971'1"	16.00	40.00	42.00	2.00
		11908'3"	10.00	44.00	44.00	2.00
		Average	**11.33**	**43.67**	**42.67**	**2.33**
Jade	30 2c-4	s8 - 15615.94	10.00	52.00	34.00	4.00
		15645.00	22.00	46.00	32.00	0.00
		15660.00	14.00	44.00	36.00	6.00
		s11 - 15660.33	8.00	46.00	46.00	0.00
		15678.00	20.00	36.00	40.00	4.00
		15748.00	16.00	32.00	50.00	2.00
		Average	**15.00**	**42.67**	**39.67**	**2.67**
Judy	30 7a-7	11496.00	24.00	46.00	30.00	0.00
	30 7a-8	11688.00	32.00	46.00	22.00	0.00
		11731.00	32.00	46.00	22.00	0.00
		11820.00	44.00	34.00	22.00	0.00
	30 7a-9	12077.00	34.00	42.00	24.00	0.00
		12167.00	30.00	46.00	24.00	0.00
	30 7a-11Z	s12 - 11438.98	36.00	44.00	20.00	0.00
		s42 - 11660.53	32.00	42.00	26.00	0.00
		Average	**33.00**	**43.25**	**23.75**	**0.00**
Cod	7 11-7	4614.06	0.00	20.00	70.00	10.00
		4606.44	6.00	32.00	60.00	2.00
		4594.86	6.00	24.00	60.00	10.00
		4609.19	2.00	32.00	56.00	10.00
		4616.20	0.00	24.00	60.00	16.00
		Average	**2.80**	**26.40**	**61.20**	**9.60**
Gaupe	6 3-1	3063.00	8.00	48.00	42.00	2.00
		3102.03	10.00	34.00	52.00	4.00
		3107.77	12.00	42.00	44.00	2.00
		3108.75	4.00	42.00	46.00	8.00
		3061.10	6.00	48.00	44.00	2.00
		Average	**8.00**	**42.80**	**45.60**	**3.60**

Table 7.7 Distribution of distinctive grain contacts (point contact, long or tangential contact, concavo-convex (C&C) contact, sutured contact) for selected fine-grained samples of the Heron, Skua, Jade, Judy, Cod and Gaupe sample sets.

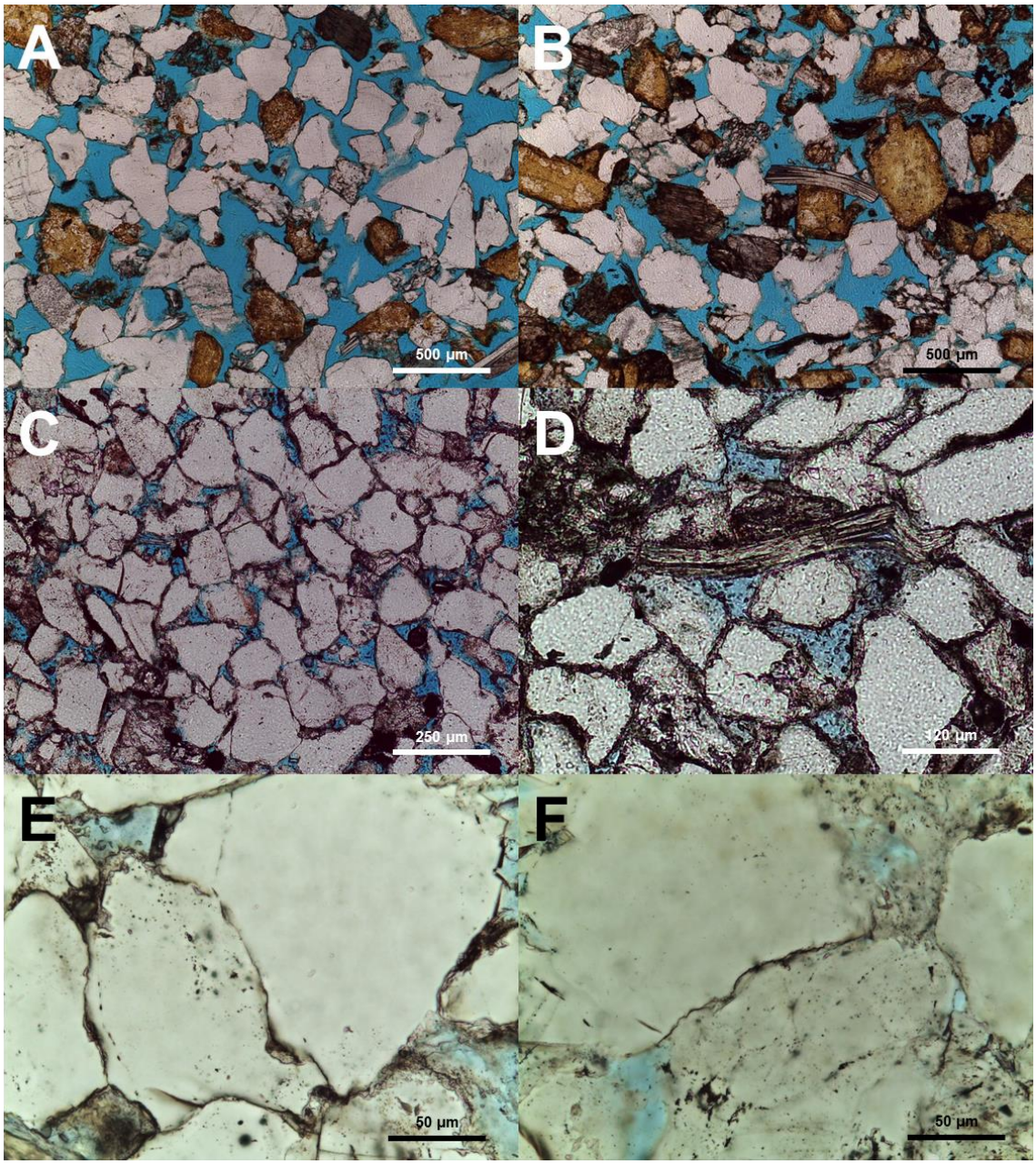

Figure 7.7 Micrographs of thin sections highlighting different compaction stages, A) Judy (30/7a-8; 11820.00): grain framework with ~28% optical porosity and 'floating' grains; B) Jade (30/2c-4; 15748.00): sample with 15.1% optical porosity; C) Gaupe (6/3-1; 3095.00): densely packed grain framework with 7.5% optical porosity; D) Gaupe (6/3-1; 3094.35): bended and compressed mica grain; E) Cod (7/11-7; 4610.10): concavo-convex grain contact; F) Cod (7/11-7; 4614.06): sutured grain contact.

7.5.4 One-dimensional basin modelling

The one-dimensional models show the evolution of burial depth, pore fluid overpressure and VES throughout the geological history for the top of the Triassic Skagerrak reservoir formation in the investigated fields/wells. Each model was set up from the present-day well stratigraphy, well log lithology and lithological description (Table 7.2 & Table 7.3) and carefully calibrated against measured Skagerrak sandstone porosities (Figure 7.5). Calibration was achieved by using observed and published rock properties for key horizons, as described above. Furthermore, each model was calibrated against corrected RFT temperatures and carefully adjusted towards measured present-day formation pressures by considering late-stage, high-temperature overpressure mechanisms (Osborne and Swarbrick, 1997; Swarbrick and Osborne, 1998; Isaksen, 2004). The burial history of the Skagerrak Formation can generally be subdivided into two main phases. The first episode of burial occurred at a relatively slow rate from the time of deposition (220 Ma) until 100-70 Ma. Because all the hydrocarbon fields studied are located on structural highs, the impact of Late Jurassic rift-related subsidence is largely absent from the burial history plots, or is obscured by erosion associated with the Base Cretaceous (end-rift) unconformity. The second phase of burial is related to post-rift subsidence and infilling of accommodation space within the Central Graben from around 90 Ma until the present-day. The fields now all reside at maximum burial depth. The burial histories of the Heron Cluster fields, the J-Ridge fields and the Norwegian fields show similar burial histories due to their proximity to each other (Figure 7.1).

The Judy Sandstone Member in the Heron and Skua fields experienced a phase of burial with maximum depths of around 1200 m (240 Ma to 200 Ma) followed by a phase of uplift (200 Ma to 165 Ma). Burial depth remained shallow, with maximum depths of

around 500 m from 165 Ma until 90 Ma. From 90 Ma onwards, burial was rapid and the Triassic sandstone members are at their maximum burial depths at the present day (Figure 7.8). The calculated overpressure started to build up in the Judy Sandstone Member at the Heron and Skua fields at around 60 Ma and 45 Ma, respectively, with onset burial depths of around 1550 m and 1250 m for the reservoir formation tops, respectively. The development of this overpressure reflects disequilibrium compaction beneath the overlying Chalk. Overpressure increased continuously with ongoing burial and reached 1 MPa at burial depths of 1650 m and 1750 m in the Heron and Skua fields. Overpressures are at their maxima at the present day, around 39 MPa for the Heron field and 24 MPa for the Skua field (Table 7.1). The continuous overpressure increase from its onset around 60 Ma has reduced the rate of VES accrual. The modelled maximum VES is reached around 10 Ma, with a value of approximately 21.5 MPa in the Heron Field and 23 MPa in the Skua Field. The modelled maximum VES was followed by a trend of decreasing VES until the present day due to significant overpressure build-up in the last 10 million years. The present-day VES values for the two fields are around 6 MPa for Heron and 15 MPa for Skua (Figure 7.8). The late rapid overpressure increase (from around 10 Ma) is caused by fluid expansion, migration of overpressured fluids, and hydrocarbon and gas charge (Isaksen, 2004; Lines and Auld, 2004; Winefield et al., 2005), which is indicated by the VES reduction (Swarbrick, 2012).

Present-day overpressure in Jade and Judy are 27 MPa and 22.5 MPa, with present-day VES of 17 MPa and 16.5 MPa, respectively (Table 7.1). Pore fluid pressure onset is at around 1250 m and 1350 m burial depth at 65 Ma and 50 Ma with maximum VES of 22 MPa and 19.5 MPa reached at approximately 10 Ma (Figure 7.8).

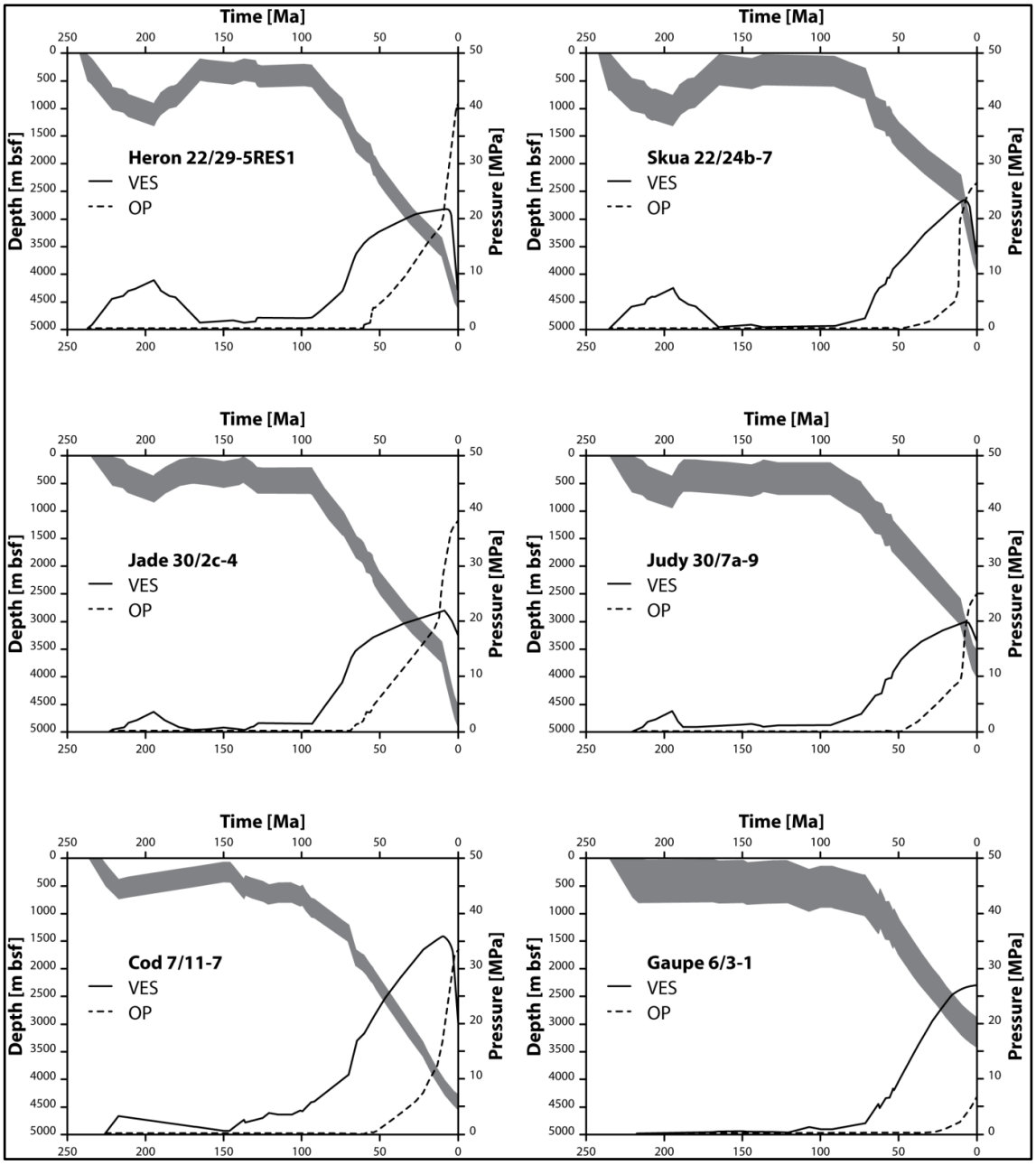

Figure 7.8 Evolution of burial depth (grey), pore fluid overpressure (OP) and vertical effective stress (VES) for the top of the Heron (22/29-5RE), Skua (22/24b-7), Jade (30/2c-4), Judy (30/7a-9), Cod (7/11-7) and Gaupe (6/3-1) Skagerrak sandstone reservoirs.

The Triassic sandstones of the Norwegian Cod and Gaupe fields also experienced a shallow burial phase from deposition to around 140 Ma and 60 Ma, followed by a phase of continuous burial towards present-day maximum depths (Figure 7.8). Modelled overpressure in the reservoir sandstones started to build up during the continuous burial at depths of around 1350 m and 1150 m, respectively. The overpressure increased

during ongoing burial and reached 1 MPa at 50 Ma and 20 Ma at burial depths of around 2200 m and 2300 m in the Cod and the Gaupe fields, respectively. Overpressure in the Cod field increased significantly from the Late Miocene to the present-day overpressure of 32.5 MPa (Table 7.1). Overpressuring of the Triassic reservoir sandstones led to a VES reduction from around a maximum modelled value of 36 MPa to 19 MPa at the present day (Figure 7.8). The VES history of the Gaupe field is less affected by overpressure due to its late onset and low magnitude. Present-day overpressure in the Gaupe Field is modelled as 6.5 MPa, with a VES of around 27 MPa for the Gaupe sandstones (Figure 7.8 & Table 7.1).

7.6 Discussion

7.6.1 Implications of overpressure on vertical effectives stress

Vertical effective stress (VES) has long been recognised as the main driver of early porosity loss by mechanical compaction processes during shallow burial (0–2500 m) (Houseknecht, 1987, 1988; Paxton et al., 2002). Limiting the rate of increasing VES during burial by pore fluid overpressure can slow down or arrest mechanical compaction and reduce its effect on porosity loss, leading to the maintenance of enhanced primary porosity to depth (Bloch et al., 2002; Nguyen et al., 2013; Stricker and Jones, 2016). Even though this effect has been well known since Terzaghi's introduction of the effective stress concept, the impact of low VES due to overpressure has often been overlooked or underestimated in reservoir quality studies (e.g., Taylor et al., 2015). However, to preserve enhanced reservoir quality by overpressure, the magnitude of overpressure, its continued maintenance during progressive burial, and the depth where the overpressures first started to develop must all be considered. Late development of overpressure at greater depth (for example by fluid transfer or expansion) will not be associated with a reduced compaction state and enhanced porosity.

7.6.2 IGV as a proxy for maximum VES and shallow overpressure development

As discussed by Houseknecht (1987, 1988), Lundegard (1992), Ehrenberg (1995), and Paxton et al. (2002), IGV decreases with ongoing burial depth or increased VES, reflecting the degree of mechanical and chemical compaction.

The quantification of the IGV development with depth has been the subject of various studies (e.g., Houseknecht, 1987, 1988; Paxton et al., 2002) which highlighted significant IGV loss by mechanical compaction during shallow burial, with a physical

lower limit of 26% to 30% established at burial depths of 2000 m to 2500 m, depending on the grain size, sorting and rock composition. A global study by Paxton et al. (2002) resulted in an intergranular volume compaction curve with depth, which identified major IGV loss (10% to 12%) during shallow burial (<1500 m) in uncemented, rigid-grained sandstones and established a physical lower limit of around 26% at 2500 m burial depth. Therefore IGV values of less than 26% reflect significant chemical compaction (e.g., pressure dissolution) within the rigid grain framework (Paxton et al., 2002).

Following Paxton et al. (2002), who proposed a lower limit of 26% for mechanical compaction, the six Triassic Skagerrak datasets indicate low compaction in three Central Graben samples sets (Judy, Heron and Skua) compared with significant chemical compaction in the Cod sample set (Table 7.6 & Figure 7.9). The low mechanical compaction state of the Judy, Heron and Skua fields is further supported by petrographic evidence, such as floating grains and the frequency of low mechanical compaction grain contacts. Low compaction in overpressured sandstones probably results from the retardation of early mechanical compaction by overpressure development during shallow burial (<2500 m) (Bloch et al., 2002; Paxton et al., 2002). Overpressure that has developed at shallow depth and continuously increased with ongoing burial has reduced the rate of VES built-up and typically leads to under-compaction, relative to hydrostatically pressured sandstones at equivalent burial depth (Sclater and Christie, 1980) because a lower maximum VES has acted on the grain framework. This can be observed in the Judy field, where IGV values are higher than expected (>26%, Table 7.6), due to shallow overpressure development and a constantly reduced VES accrual rate (Figure 7.8), resulting in the experience of lower maximum VES and a low mechanical compaction state for the present-day burial depth (e.g.,

Nguyen et al., 2013; Stricker and Jones, 2016). A similar correlation can be made for the present-day IGV values and the experienced maximum VES of the Heron and Skua fields, where IGV values are slightly higher than the expected 26% (Table 7.6 & Figure 7.9). The Cod sample set, demonstrated evidence for a high compaction state due to pressure dissolution at grain-to-grain contacts and a lower average IGV of around 21% (Table 7.7). This is most likely caused by the normal VES development prior to the deep overpressure onset (Figure 7.8), with a slow increase rate, which results in a higher VES accrual rate and higher experienced maximum VES (36 MPa) during the burial history. The relationship between IGV and maximum VES in the Skagerrak samples sets demonstrate mechanical compaction is the main reservoir quality controlling factor, where measured IGV represents a good proxy (Figure 7.9).

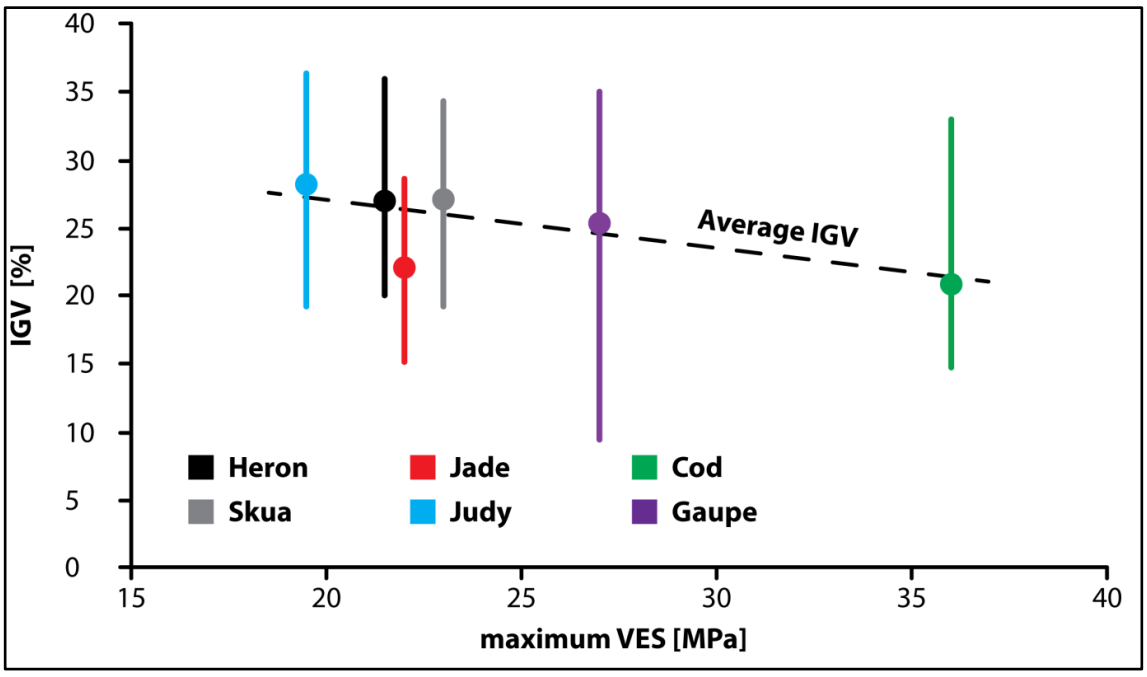

Figure 7.9 Average values of intergranular volumes, with maximum and minimum values, for Heron, Skua, Jade, Judy, Cod and Gaupe fine-grained samples plotted against maximum vertical effective stress (VES) with a best-fit trend line for average IGV.

7.6.3 VES development and influence on reservoir quality

Porosity maintenance by pore fluid overpressure/low VES has been the subject of several empirical studies (e.g., Ramm and Bjørlykke, 1994; Gluyas and Cade, 1997) where the present-day porosities have been related to present-day pore fluid overpressures. Hence the effect of overpressure development (i.e., timing, increase rate and maintenance) was not considered. However, the interaction of overpressure and the VES throughout the burial history must be considered to predict porosity preservation based on low mechanical compaction. Late development of overpressure at greater depth (for example by fluid transfer or expansion) will not be associated with a reduced compaction state. We infer that compaction has taken place by stress-sensitive porosity loss, both as mechanical compaction (i.e., grain rearrangement) and chemical compaction (i.e., pressure dissolution and cementation). The present-day compaction state of the sandstones has been determined by IGV measurements and the frequency measurements of distinctive petrographic features (i.e., grain contact types) in the fine-grained sandstones (Figure 7.10 & Table 7.7).

The importance of the VES development for the porosity preservation is highlighted by the comparison of two endmembers of this study; the Judy and Cod fields. Even though both selected sample sets show the same primary depositional attributes, they exhibit different present-day compaction states, reflecting different VES histories. The development of VES in the Joanne Sandstone Member of the Judy Field occurred from 90 Ma onwards. The rate of VES increase was arrested with early onset of overpressure at a depth of 1350 m (Figure 7.8). The shallow overpressure development in the Joanne Sandstone Member reduced the rate of VES increase, which led to a reduced VES acting on the grain framework. This VES evolution is reflected by anomalously high

present-day porosities (Figure 7.4 & Figure 7.5), high average IGV values (Figure 7.9) and a high frequency of point contacts (Table 7.7 & Figure 7.10) in the Judy sample set.

In comparison, the higher present-day compaction state of the Cod sandstone reflects a more normal VES development (Figure 7.8). VES in the sands started to increase slowly at around 150 Ma, with a significant increase of the VES accrual at 100 Ma (Figure 7.8). VES increased to around 20 MPa and led to the significant mechanical compaction and porosity loss prior to the main phase of overpressure development at a burial depth of around 2200 m (Figure 7.8). The Cod field sample data supports the burial and pressure modelling, where low porosities (Figure 7.4 & Figure 7.5), low average IGV (Table 7.6) and high frequencies of concavo-convex and sutured grain contact types indicate a higher degree of compaction and pressure dissolution (Figure 7.10).

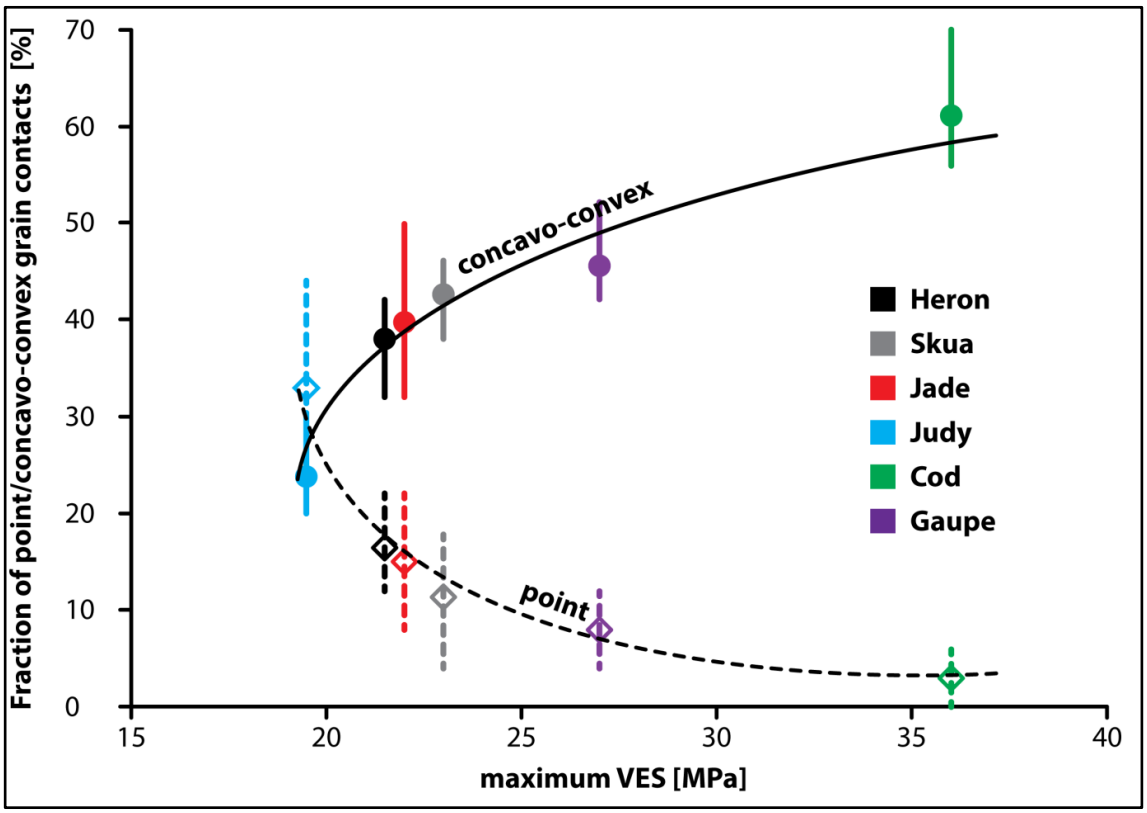

Figure 7.10 Fraction of point and concavo-convex grain contacts of Heron, Skua, Jade, Judy, Cod and Gaupe fine-grained samples plotted against maximum vertical effective stress (VES) with best-fit trend lines for average fraction point and concavo-convex contacts.

The comparison of the Judy and Cod sample sets shows that the compaction state and reservoir quality in the Skagerrak Formation sandstones in the North Sea are highly dependent on the experienced maximum VES, which has been controlled by the interplay of burial depth (i.e., stress induced by the overburden) and the pore fluid overpressure (Figure 7.10). The positive effect of overpressure or low VES towards retardation of mechanical compaction has been previously observed by modelling studies of Lander and Walderhaug (1999) and Paxton et al. (2002). Furthermore, high primary porosities, maintained by shallow overpressure have been documented for the Skagerrak Formation sands of the Judy Field (Nguyen et al., 2013; Stricker and Jones, 2016). The early work undertaken by Osborne and Swarbrick (1999) clearly recognised the importance of overpressure to arrest quartz cementation and preserve porosity in the Jurassic Fulmar Formation of the Central Graben, North Sea. The research in this study, has confirmed the observations made by Osborne and Swarbrick (1999) and, importantly, has identified the need to consider overpressure development for reservoir quality predictions and studies of deeper and hotter reservoirs, such as the Skagerrak Formation.

A recent study by Taylor et al. (2015), partly focusing on the Skagerrak Formation (Egret, Heron, Seagull & Skua), refutes the contribution of shallow overpressure development and reduced VES towards the excellent reservoir quality in UK Quadrant 22 and attributes the enhanced porosity solely to chlorite grain coatings. The role played by chlorite coatings in these reservoirs is significant in reducing quartz cementation and correlates with quantities of quartz cement, but does not reflect the present-day compaction state, the high IGV values, and low frequency of concavo-convex and sutured grain contacts in this region (Stricker et al., 2016b). We propose that a combination of low maximum VES and high fraction of chlorite-coated grains has been

responsible for the porosity preservation in the Heron and Skua fields (Stricker et al., 2016b).

The occurrence of pressure dissolution at quartz grain contacts has previously been identified as an important control on reservoir quality and potential porosity preservation. Several studies have suggested that sheet silicates (e.g., mica) need to be present along grain contacts for preferential dissolution to occur (Bjørkum, 1996; Oelkers et al., 1996). Bjørkum et al. (1998) proposed the rate-limiting step in quartz cementation is the rate of nucleation and precipitation in the pore space, and quartz cementation is relatively insensitive to the effective stress on the grain framework. However, more recent experimental studies have provided strong support for the role of isotropic fabrics and effective stress in controlling chemical compaction in sandstones (Sheldon et al., 2003). It has been demonstrated that vertical effective stress and its rate of build-up during burial has played a critical role in inhibiting porosity loss in the Skagerrak Formation sandstones of the Central Graben.

The petrographically observed results of this study complement the empirical porosity and VES trends discussed by Grant et al. (2014). They looked at trends in total porosity within the Skagerrak Formation derived from petrophysical log analysis using Vshale and thickness filters to remove facies and bed-scale variability. These trends strongly suggested that compaction is the dominant factor controlling average reservoir porosity. The modelling done here, in conjunction with the petrographic observations, helps to substantiate this model and provide petrographic evidence for the processes involved. Even at the grain scale, the compaction state shows a correlation to the modelled estimated maximum VES during burial. Maximum VES typically occurred around 10 Ma, before late burial and fluid pressure inflation.

When looked at carefully, it is clear that other influences, beside VES, can play a key role in determining reservoir quality. Chlorite coatings and the presence of microquartz rims (e.g., Osborne and Swarbrick, 1999; Taylor et al., 2015; Stricker et al., 2016b) dictate the ability of authigenic quartz cements to form at detrital grain surfaces and potentially occlude porosity. Low VES due to overpressure development helps retard pressure dissolution and thus restricts the amount of locally sourced silica available to enter into solution. In the absence of significant cementation, compaction is left to play its over-arching role.

7.7 Conclusion

1. Excellent reservoir quality with anomalously high porosity is preserved in many HPHT reservoirs of the Skagerrak Formation in the Central Graben, North Sea. However, despite similar diagenetic histories, reservoir quality and preserved porosity can vary from excellent (>25% porosity) to poor quality (<10% porosity) in HPHT reservoirs of the Central Graben area.
2. Excellent reservoir quality with anomalously high porosities of up to 35% at burial depths >3500 m below seafloor is preserved in the UK sectors of the Central Graben. Shallow onset and continuous increase of overpressure has maintained low VES through time in the Heron, Jade, Judy and Skua fields and resulted in under-compaction of the fluvial channel reservoirs for their present-day depths of burial.
3. In the Norwegian Cod and Gaupe fields, by comparison with the UK fields, the reservoir quality is low, with porosities <10%, related to later and deeper onset of overpressure and consequently high VES.
4. This research has demonstrated the importance of identifying the timing of overpressure generation and its maintenance for arresting mechanical compaction during progressive burial. The results are consistent with a model where VES affects both the compaction state and subsequent cementation of the reservoir. It has clearly identified the importance of VES in reservoir quality studies especially for HPHT basins.

Chapter VIII

Synthesis of results, conclusion, and future work

8.1 Reservoir quality studies and overpressure

As progressively more petroleum exploration occurs in HPHT regimes of the world, understanding the reservoir quality under HPHT conditions is paramount for successful exploration of hydrocarbons. The effect of pore fluid pressure, low VES, and hence reduced mechanical compaction is well known, according to Terzaghi's concept of effective stress. Nevertheless, relatively few studies have tried to appraise the role of overpressure for reservoir quality (Ramm and Bjørlykke, 1994; Osborne and Swarbrick, 1999; Bloch et al., 2002; Taylor et al., 2010), while other studies have overlooked or underestimated the impact of low VES on reservoir quality within overpressured basins (e.g., Bjørlykke, 2014; Taylor et al., 2015).

Bloch et al. (2002) used simple numerical compaction and cementation models for lithic-rich and quartz-rich sands to analyse the impact of shallow overpressure and reduced VES on the reservoir quality of deeply buried sandstone reservoirs. However, the study by Bloch et al. (2002) was purely theoretical and lacked connections to sedimentary basins or reservoirs. Gluyas and Cade (1997), on the other hand, investigated the impact of overpressure on reservoir quality empirically by using present-day porosity and overpressures. They developed an empirical approach for porosity loss as a function of effective stress and proposed that 1 MPa overpressure offsets the increase in VES due to 80 m burial with hydrostatic pore pressures, so overpressure leads to less mechanical compaction. This equation can offer some useful guidance for the porosity prediction in compacted sands. However, the overpressure initiation depth and the VES evolution during progressive burial are both critical to predict and quantify the effect of pore fluid overpressure on reservoir quality.

Multidisciplinary studies, combining the modelling of overpressure and empirical or petrographic analysis, are rare. Therefore, a multidisciplinary approach comprising petrographic, SEM, fluid inclusion and burial history modelling studies has been adopted in the present study to understand the evolution of reservoir quality with the explicit focus on the impact of vertical effective stress.

8.2 Reservoir quality of the Skagerrak Formation

The HPHT reservoir sandstones of the Skagerrak Formation in the Central Graben, Central North Sea, exhibit exceptionally high reservoir quality and anomalously high porosities of up to 35% for their depth of burial. However, reservoir quality can vary strongly from excellent (>30% porosity) to poor (<10% porosity) within the Skagerrak Formation.

8.2.1 Early onset of pore fluid overpressure and low VES arrests mechanical compaction and porosity loss.

The shallow development or early onset of pore fluid overpressure has been recognised as a key mechanism for porosity preservation within the Skagerrak Formation. Low VES and reduced mechanical compaction have been identified as critical for the present-day reservoir quality (e.g., Swarbrick et al., 2000; Nguyen et al., 2013; Grant et al., 2014). Nguyen et al. (2013) and Grant et al. (2014) proposed a geological scenario where shallow overpressure onset, creation of low VES and reduced compaction preserve reservoir quality within the Skagerrak Formation of the J-Ridge area (UK Quadrant 30). Taylor et al. (2015), in contradiction, questioned the contribution made by overpressure and low VES for porosity preservation within the ETAP area (UK Quadrant 22).

This research has identified the shallow onset of overpressure as a key parameter for the preservation of reservoir quality and high porosities. Porosity decreases generally under hydrostatic conditions, leading to strong porosity reductions from ~45% (Beard and Weyl, 1973) to ~25% porosity (or IGV) at 2-3 km burial depth (Paxton et al., 2002). Shallow onset of pore fluid overpressure limits the increase in VES during burial where high primary porosities are present. The overpressure onset depth is a crucial factor for enhanced porosity preservation; it defines the maximum of the preservable primary porosity. Therefore, the shallower the overpressure onset depth, the higher is the preservation potential for primary porosity. This has been highlighted by the comparison of the UK and Norwegian Skagerrak Formation reservoir sandstones (Figure 8.1, Figure 8.2 & Figure 8.3), where poorer reservoir quality and lower porosities (~10%) resulted from deeper overpressure onset within Norwegian reservoir sandstones (Figure 8.3).

In summary, shallow overpressure onset and reduction of VES preserved primary porosity from an early stage onwards.

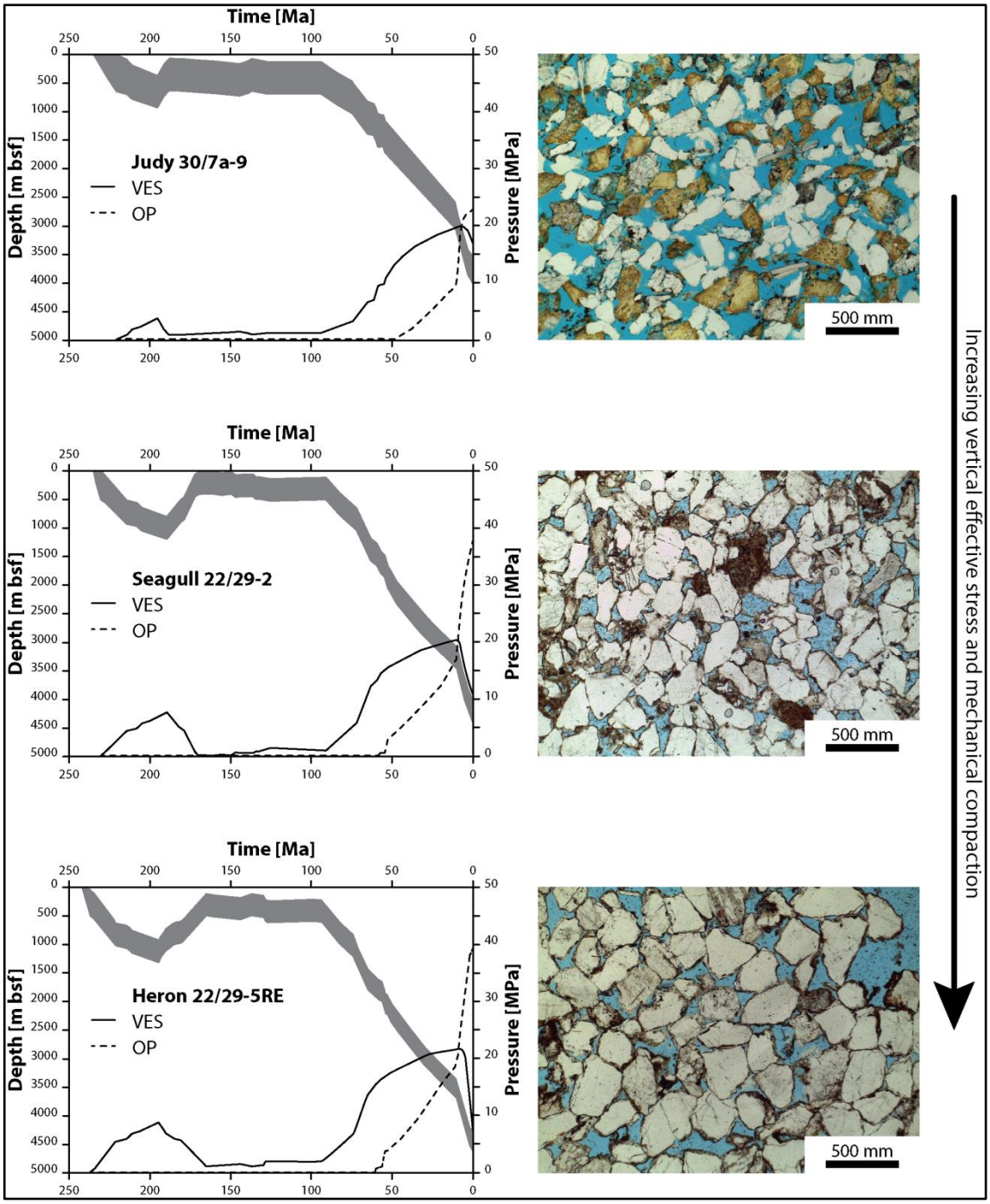

Figure 8.1 Burial depth (grey), pore fluid overpressure (OP) and vertical effective stress (VES) evolution with micrographs, showing the porosity distribution and mechanical compaction state of the Judy field (30/7a-9; 12077.00), Seagull field (22/29-2; 13584'10'') and Heron field (22/29-5RE; 15715'10'').

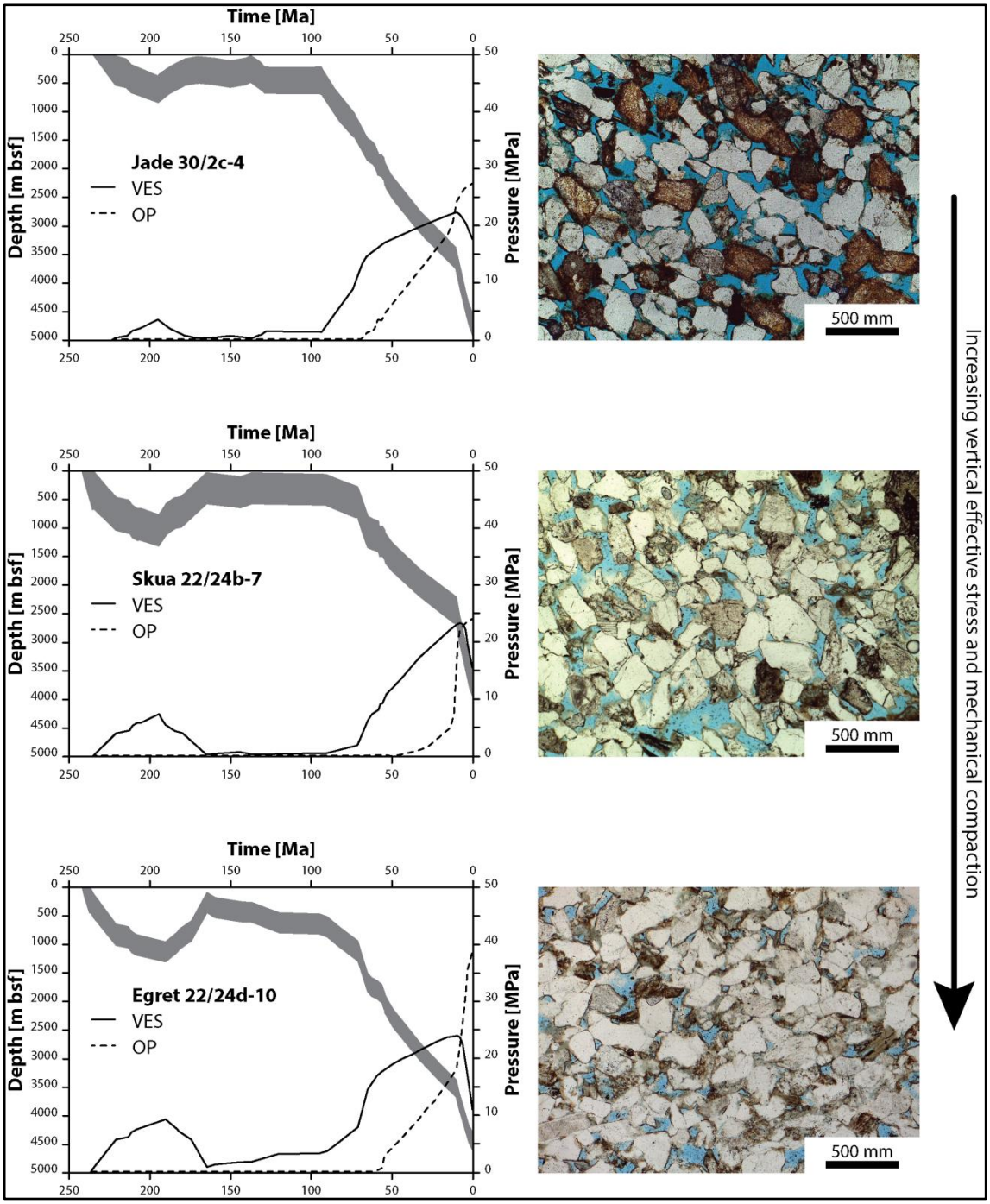

Figure 8.2 Burial depth (grey), pore fluid overpressure (OP) and vertical effective stress (VES) evolution with micrographs, showing the porosity distribution and mechanical compaction state of the Jade field (30/2c-4; 15748.00), Skua field (22/24b-7; 11882'2'') and Heron field (22/24d-10; 14593'11'').

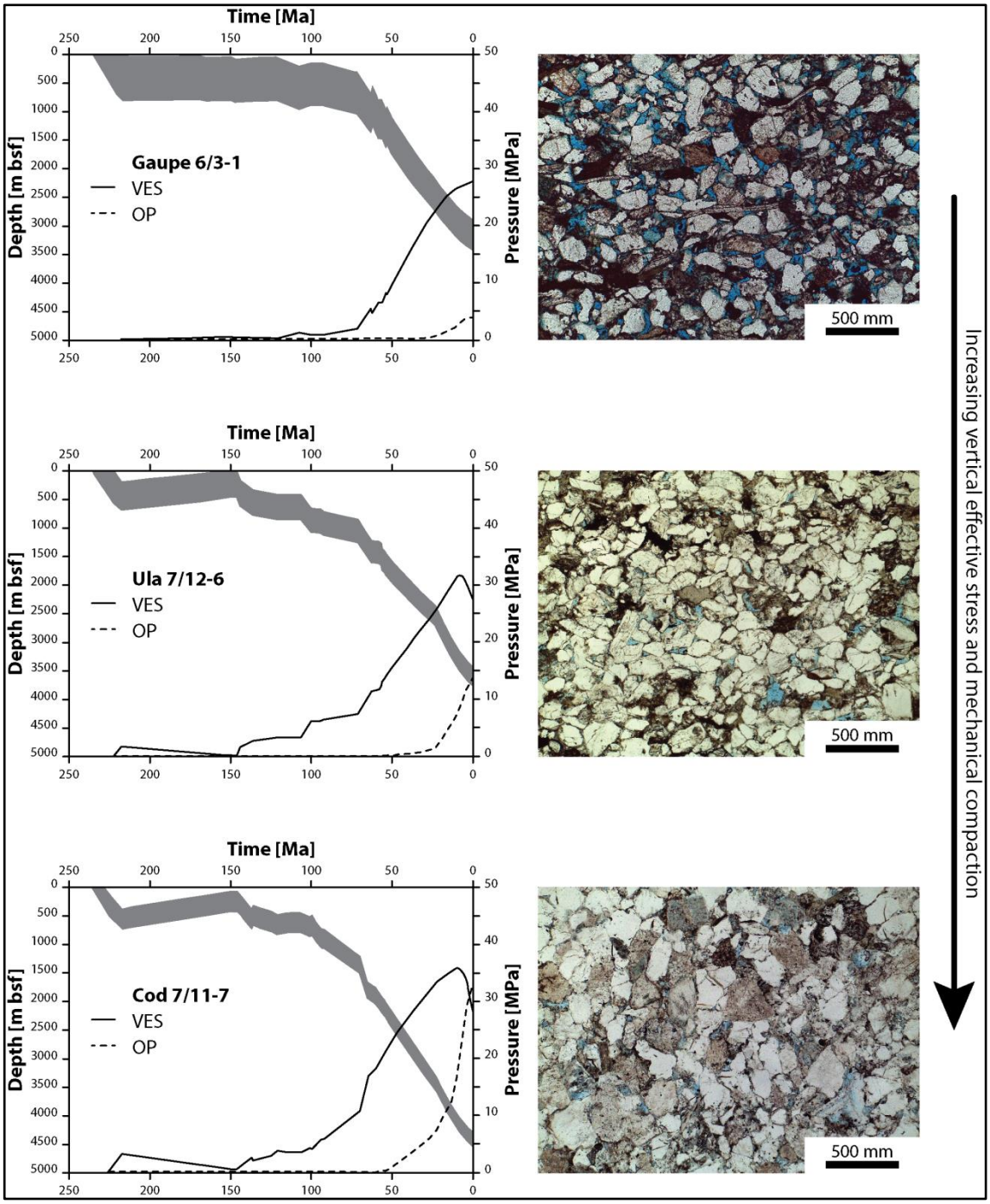

Figure 8.3 Burial depth (grey), pore fluid overpressure (OP) and vertical effective stress (VES) evolution with micrographs, showing the porosity distribution and mechanical compaction state of the Gaupe field (6/3-1; 3072.00), Ula field (7/12-6; 3530.42) and Cod field (7/11-7; 4608.44).

8.2.2 Overpressure development and the rate of overpressure increase (accrual rate) are important for the preservation of reservoir quality.

Porosity preservation by pore fluid overpressure has been the subject of several studies (e.g., Jeans, 1994; Ramm and Bjørlykke, 1994; Gluyas and Cade, 1997). However, the development of the overpressure (i.e., timing, increase rate and maintenance) and the evolution of the vertical effective stress throughout the burial history have not been considered (e.g., Gluyas and Cade, 1997). The interaction of pore fluid overpressure and VES must be considered throughout the burial history to predict porosity preservation by limited mechanical compaction. Late development of overpressure at greater depth by fluid transfer or hydrocarbon charge cannot be associated with a reduced compaction state (Swarbrick and Osborne, 1998).

Overpressure and VES evolution have been investigated for various Skagerrak Formation reservoir sandstones in the Central North Sea (Figure 3.1B). The VES evolution has been identified as crucial for reservoir quality and porosity preservation. The reservoir quality of the Skagerrak Formation sandstones can vary from excellent to poor, and commonly reflects the maximum VES experienced throughout the burial history (Figure 8.4). The maintenance and continuous increase of overpressure with subsequent burial has been identified as one of the key factors, beside the overpressure onsets, to preserve excellent reservoir quality (e.g., the Judy field). VES is sensitive to overpressure changes and increases immediately to hydrostatically pressured VES values if the overpressure is lost (Grant et al., 2014).

In summary, shallow overpressure onset and continuous overpressure increase created low VES throughout the burial history and preserved primary porosity from an early stage to depth.

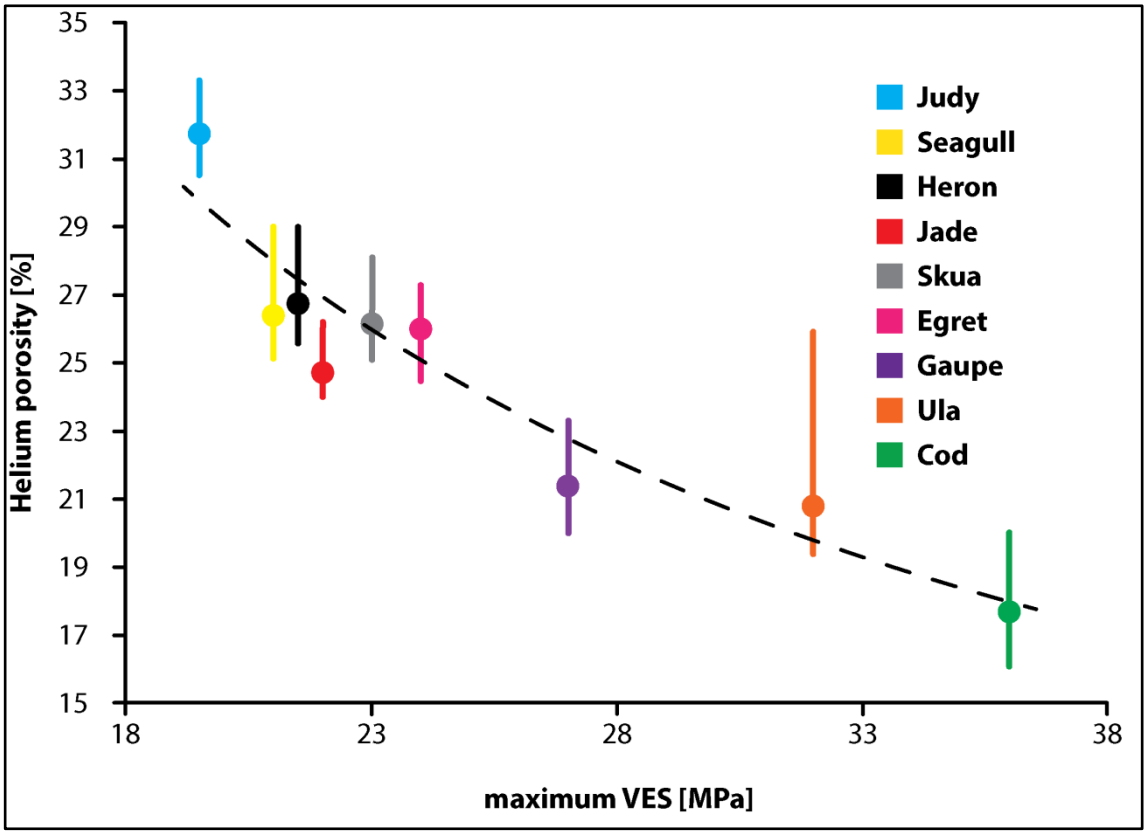

Figure 8.4 Maximum helium porosities (20 highest values) of Judy (30/7a-9), Seagull (22/29-2), Heron (22/29-5RE), Jade (30/2c-4), Skua (22/24b-7), Egret (22/24d-10), Gaupe (6/3-1), Ula (7/12-6) and Cod (7/11-7) core plug samples plotted against maximum vertical effective stress (VES) with a best-fit trend line for average values (points).

8.2.3 Low VES inhibits extensive quartz cementation within the Skagerrak Formation sandstones.

The pore fluid overpressure and the VES evolution have been proven to play a crucial role for the mechanical compaction state of the Skagerrak Formation sandstones and their resulting reservoir quality. Pore fluid overpressure has been shown to induce low VES and to retard mechanical compaction throughout the burial process (e.g., Lander and Walderhaug, 1999; Paxton et al., 2002). However, this study has also identified the importance of pore fluid overpressure for the retardation of quartz cement. Low VES reduces the effect of pressure dissolution at quartz grain contacts and thus restricts the amount of locally sourced silica available to enter into solution. Similar observations

have been made by Osborne and Swarbrick (1999), who recognised the importance of overpressure in arresting (inhibiting) quartz cementation and preserving porosity in the Jurassic Fulmar Formation of the Central Graben, North Sea. The restricted availability of silica in solution is highlighted by the high homogenization temperatures for aqueous quartz overgrowth fluid inclusions in Skagerrak Formation sandstone samples (Table 5.4 & Table 6.2). The reduced availability of silica restricted quartz precipitation at elevated temperatures (70-80˚C; McBride, 1989; Walderhaug, 1994a; Worden and Morad, 2000) and delayed silica dissolution and quartz cementation to higher temperatures (Walderhaug, 1996; Worden and Morad, 2000; Sheldon et al., 2003; Ajdukiewicz and Larese, 2012).

In summary, shallow development and constant maintenance of overpressure reduced the VES during progressive burial and preserved primary porosity by a retarding mechanical compaction and arresting quartz precipitation by restricting the internal supply of dissolved silica within the Skagerrak Formation.

8.2.4 Occurrence of clay mineral coatings and porosity maintenance

Authigenic clay mineral coatings are often closely linked with high porosities and the absence of quartz cement in deeply buried sandstones (e.g., Pittman et al., 1992; Ehrenberg, 1993; Berger et al., 2009; Ajdukiewicz and Larese, 2012). The retardation of quartz cement by authigenic clay mineral coatings, especially chlorite coatings, plays an important role in porosity maintenance within the Skagerrak Formation sandstones (e.g., Hillier, 1994; McKie and Audretsch, 2005; Nguyen et al., 2013; Taylor et al., 2015). The authigenic clay mineral coatings are generally well developed and widely distributed, but may vary locally in their appearance (Nguyen et al., 2013; Stricker and Jones, 2016). The chlorite coatings of the ETAP area (UK Quadrant 22) show the thickest development and highest coverage rates. Taylor et al. (2015) presented a strong

inverse correlation for grain coatings and quartz cement, which proves the quartz retardation potential of the chlorite coating within the ETAP sandstone reservoirs.

Ajdukiewicz and Larese (2012) described the inhibition of quartz nucleation by chlorite coatings for temperatures of up to 115˚C. But they observed nucleation microquartz at temperatures above 115˚C below chlorite coatings within the Norphlet Formation, Gulf of Mexico. Ajdukiewicz and Larese (2012) speculated that chlorite coatings effectiveness as a nucleation barrier may decrease with increasing temperatures as the diffusivity rates and/or kinetic energy of silica molecules in pore fluids increase, allowing more silica to diffuse through the coating to open grain surfaces between chlorite particles and nucleate there. Similar observations for macroquartz and microquartz have been made for the Skagerrak Formation. Macroquartz cementation is sparse, only present at coating breaks or gaps, and shows high homogenization temperatures for aqueous fluid inclusions (Table 5.4 & Table 6.2). Microquartz below the authigenic clay mineral coatings is more common within the Skagerrak Formation sandstone samples (Figure 5.6C & D, Figure 5.9A & C & Figure 6.9D). The Skagerrak Formation samples provide prove of the quartz cement inhabitation potential of well-developed and complete clay mineral coatings to high temperatures of up to 170˚C.

In summary, the combination of shallow development and maintenance of overpressure reduced the VES during progressive burial, stalled the internal silica supply and, in combination with well-developed authigenic clay mineral coatings, preserved high primary porosities within the Skagerrak Formation.

8.2.5 The reservoir sandstones of the Skagerrak Formation show regional reservoir quality variations in the wider Central Graben area.

Reservoir quality of the Skagerrak Formation sandstones can vary regionally from excellent (>30% porosity) to poor (<10% porosity) within the Central Graben area. Regional variations within the Central North Sea are induced by the compartmentalisation of the Skagerrak Formation in the isolated mini-basins. The compartmentalisation of the Skagerrak Formation allowed different burial histories with different rates of burial for the isolation of the mini-basins. Burial history variations between the mini-basins led to local variations of erosional events, horizon thickness, overpressure onset, overpressure development, and the VES evolution (Figure 8.1, Figure 8.2 & Figure 8.3)

In summary, regional reservoir quality variations between the UK quadrants and the Norwegian quadrant are driven by mechanical and chemical compaction and reflect regional variation of overpressure onset and VES evolution (Figure 8.4).

8.2.6 Intra-basin reservoir quality variations within the Skagerrak Formation.

Strong intra-basinal reservoir quality variations have been encountered in the Judy Sandstone Member of the Seagull field (Figure 6.3). Reservoir quality varies significantly between the centre (22/29-2) and the mini-basin margin (22/29-3), despite similar burial histories with similar temperature and VES histories (Figure 6.4). Intra-basinal reservoir quality variations are commonly linked to facies variations due to coeval halokinesis and depositional variations, especially in fluvial settings where the coeval halokinesis dictates the distribution of fluvial channels and accommodation space. Banham and Mountney (2013a, 2013b) have shown that depositional variations induced by contemporaneous salt movement create variable reservoir potentials

between central and marginal mini-basin areas, with more stacked channel sandstones in the mini-basin centre. However, a facies-dependent comparison of channel sandstones from the Seagull field revealed also a strong diagenetic influence on the spatial distribution of reservoir quality, with an inverse relationship between porosity and pore-filling authigenic clay minerals (Figure 6.8). The intra-basinal variations of the clay mineral content correlate with the occurrence of fractures and disaggregation bands. Fractures and disaggregation bands represent pathways for meteoric and/or saline fluid influx and for enhanced infiltration of allogenic clay minerals. This highlights the impact of contemporaneous salt movement and salt-related tectonics on the reservoir potential and the spatial variations of the reservoir quality within a mini-basin.

In summary, the central areas of the salt-walled mini-basins are likely to have higher reservoir potential and to exhibit better reservoir quality than marginal mini-basin areas due to higher ratios of stacked channel sandstones, less infiltration of allogenic clay minerals, and less diagenetic alterations.

8.3 Summary & implications

1. Existing potential for good to excellent reservoir quality with anomalously high porosities in deeply buried (>4000 m) complex fluvial HPHT sandstones.
2. Early/shallow onset of pore fluid overpressure and low vertical effective stress arrests mechanical compaction and maintains primary porosity to depth (up to 35% at burial depths >3500 m).
3. The rate of pore fluid overpressure increase (accrual rate) with ongoing burial plays a crucial role for reservoir quality preservation by pore fluid overpressure.
4. The occurrence of authigenic clay mineral coatings, in particular chlorite coatings, has been crucial for the porosity maintenance within the Skagerrak Formation, in particular at elevated temperatures of up to 180°C.
5. The continuous reduction of vertical effective stress, due to shallow overpressure onset, reduced the amount of quartz cementation within the Skagerrak Formation sandstones by reducing pressure dissolution at detrital quartz grain contacts.
6. The reservoir sandstones of the Skagerrak Formation show strong regional reservoir quality variations, due to different rates of pore fluid overpressure build-up and varying vertical effective stress evolutions.
7. Intra-basin reservoir quality of the Skagerrak Formation sandstones demonstrate spatial variations, due to depositional and diagenetic variations caused by contemporaneous salt movement and local pore-fluid chemistry variations associated with clay infiltration and disaggregation bands.

8.4 Suggestions for future work

Results from this research have shown the obvious importance of high pore pressure in preserving sandstone porosity in the mechanical compaction regime. Many – but by no means all – believe that the rate of quartz cementation is controlled primarily by precipitation kinetics, which are in turn a function of temperature. For a given time-temperature history, the amount of quartz cement is then predictable, with porosity a dual function of (a) cement volume and (b) porosity at the start of cementation; that pre-cement porosity is controlled by the effective stress at the threshold temperature of cementation. In this context alone, pore pressure history is central to reservoir quality prediction.

There are several further developments that could be undertaken to expand this research, including the following:

1. *Evolution and prediction of reservoir quality in thrust tectonic/compressional regimes.*

   Whilst the idea of high pore pressure preserving sandstone porosity in the mechanical compaction regime is now mature, it has been derived from basins where the maximum stress is vertical and the ratio of vertical to horizontal stress is relatively constant (North Sea, in particular the Skagerrak and overlying Fulmar Formations, CNS). Few studies have tested the models in tectonically stressed settings, where horizontal stresses need to be considered, despite their obvious importance for petroleum production (e.g., New Zealand, Borneo, Colombia, Trinidad, and Venezuela). Because sediment compaction is based on effective stress, not burial, it is essential to track pore pressure and effective stress in the basin through time to predict porosity and better evaluate reservoir quality. In addition, if effective stress influences the rate of quartz pressure dissolution and thus the rate of

cementation, we should observe differences in stylolitisation style, quartz cement patterns and the volume of quartz cement precipitated in tectonically stressed sandstones.

2. *Quantitative petrography in horizontal stress regimes*

   Quantitative petrographical descriptions, combined with fluid inclusion data and stable oxygen isotope data from high resolution, in situ secondary ion mass spectrometry (SIMS) to determine quartz cementation histories from tectonically stressed regimes. These can be compared with histories predicted from standard quartz cementation models, using time-temperature histories generated from 1D and 2D basin models (e.g., Touchstone).

3. *Hydrothermal reactor experiments*

   Our lack of understanding of the changes that occur to bulk compositions of sandstones and the precipitation of quartz cements and clay mineral coatings under increasing temperature and especially pressure needs to be better addressed. Experimental modelling and laboratory experiments using hydrothermal reactors to model effects of high pressure (>40 MPa) and high temperature (>200°C) on chemical diagenesis of sandstones undergoing deep burial would mark a significant step forward in our knowledge of burial diagenesis processes in HPHT reservoirs. Results would test the principles underlying reservoir quality simulation software, such as Touchstone or PetroMod. It would allow a better understanding of what may be happening to sandstones in ultra-HPHT basinal settings such as the Malay Basin.

Appendix I

Petrographic data

UK sector 22

Skua (well 22/24b-7)

Sample	Depth	TVDSS	FCG	GS	Porosity	IGV	COPL	CEPL	Q	F	L	SEM	CL
	[m]	[m]	[%]	[mm]	[%]	[%]	[%]	[%]	[%]	[%]	[%]	[-]	
11877'1"	3620.14	3598.80	91.0	0.170	18.7	34.3	16.2	12.0	64.7	32.6	2.7	RP	
11878'2"	3620.47	3599.13	74.7	0.164	12.8	25.0	26.7	8.1	69.0	25.4	5.6		
11880'8"	3621.23	3599.89	91.7	0.179	32.2				67.7	27.5	4.8		
11882'2"	3621.68	3600.35	78.3	0.208	11.4	21.6	29.8	6.6	70.9	24.7	4.4	RP	
11887'	3623.34	3602.00		0.170	4.2								CL
11892'	3624.68	3603.35	99.3	0.192	10.0								
11895'1"	3625.62	3604.29	73.3	0.219	4.2								
11895'7"	3625.77	3604.44	40.7	0.202	17.2				76.8	21.0	2.2		CL
11900'	3627.12	3605.78		0.127	3.1	19.0	32.1	10.4					
11903'2"	3628.09	3606.75	77.0	0.143	6.1	22.7	28.9	10.9					
11906'	3628.95	3607.61	31.7	0.172	4.4								
11908'3"	3629.63	3608.30	4.0	0.222	6.0								
11909'4"	3629.96	3608.63	16.3	0.203	18.6	24.3	27.3	4.1	78.6	14.6	6.8		
11912'	3630.78	3609.44	41.3	0.232	14.2	19.6	31.5	4.6	66.1	20.1	13.8		
11915'5"	3631.82	3610.48			0.5								
11919'	3632.91	3611.58			2.7								
11929'6"	3636.11	3614.78			0.7								
11932'	3636.87	3615.54	19.7	0.193	11.0	26.0	25.6	11.4	58.9	31.5	9.6		
11937'5"	3638.52	3617.19	52.0	0.136	6.0	21.9	29.6	9.6					
11939'3"	3639.08	3617.75	89.0	0.146	24.3	21.0	30.4	10.7	70.8	24.0	5.2	TS	
11939'6"	3639.16	3617.82	92.0	0.189	6.2								
11943'10"	3640.48	3619.14	80.7	0.124	48.9	21.6	29.8	7.7	64.7	28.6	6.7		
11945'	3640.84	3619.50	88.0	0.150	6.4								
11952'4"	3643.07	3621.74	88.7	0.137	12.9	28.6	22.9	6.2	58.4	37.2	4.4	RP	
11960'4"	3645.51	3624.17	83.7	0.157	5.3								
11966'7"	3647.41	3626.08		0.162	3.8								
11971'1"	3648.79	3627.45	91.3	0.168	11.6	27.6	23.9	6.6	72.5	25.1	2.4	RP	CL
11971'2"	3648.81	3627.48	90.3	0.097	6.5								
11972'10"	3649.32	3627.98			3.8								
11973'	3649.37	3628.03	92.7	0.168	13.3	27.0	24.7	8.3	70.7	27.0	2.3		
12086'3"	3683.89	3662.55	73.7	0.194	12.1	33.6	17.1	15.8	64.8	34.2	1.0		
12087'3"	3684.19	3662.86	91.7	0.114	14.4	25.0	26.7	13.6	77.8	15.1	7.1		

Table I.1 Petrographic data for the Skua samples, with driller's depth (Depth), true vertical depth below mean sea level (TVDSS), fraction of coated grains (FCG), average grain size (GS), optical porosity (porosity), intergranular volume (IGV), compactional porosity loss (COPL), cementational porosity loss (CEPL), Fraction of quartz grains (Q), fraction of feldspar grains (F), fraction of lithic grains (L), and indication of being used as a sample for scanning electron microscopy (SEM) or cathodoluminescence (CL).

Egret (well 22/24d-10)

Sample	Depth	TVDSS	FCG	GS	Porosity	IGV	COPL	CEPL	Q	F	L	SEM	CL
	[m]	[m]	[%]	[mm]	[%]	[%]	[%]	[%]	[%]	[%]	[%]	[-]	[-]
14379'4"	4382.82	4355.69		0.126	2.0	33.0	17.9	27.1					
14380'8"	4383.23	4356.1	99.0	0.128	7.8								
14382'10"	4383.89	4356.76	70.7	0.140	8.2								
14385'10"	4384.8	4357.67	83.0	0.152	13.1	33.6	17.1	8.6	56.5	32.6	10.9		
14387'	4385.16	4358.03		0.085	2.9								
14391'11"	4386.66	4359.53		0.099	3.7								
14393'11"	4387.27	4360.14	92.7	0.123	7.1	27.0	24.7	12.1					
14396'2"	4387.95	4360.82	93.3	0.143	8.8								
14400'2"	4389.17	4362.04	84.0	0.112	4.8								
14402'8"	4389.93	4362.81	22.3	0.091	6.5								
14405'10"	4390.9	4363.77		0.120	2.7								
14409'8"	4392.07	4364.94		0.155	0.9								
14411'3"	4392.55	4365.42		0.142	4.0								
14415'4"	4393.79	4366.67	96.0	0.145	6.2								
14416'5"	4394.12	4367	93.7	0.151	6.0								
14418'11"	4394.89	4367.76	92.3	0.179	10.1	16.3	34.3	5.3	54.3	37.2	8.4	RP	
14419'7"	4395.09	4367.96	93.0	0.169	6.8								
14421'10"	4395.77	4368.65		0.170	4.3								
14423'	4396.13	4369		0.176	0.8								
14424'9"	4396.66	4369.54		0.087	2.2								
14425'6"	4396.89	4369.77	89.0	0.084	5.2								
14427'8"	4397.55	4370.43		0.064	5.8								
14432'5"	4399	4371.87		0.092	2.4								
14434'4"	4399.58	4372.46		0.112	2.4								
14439'	4401.01	4373.88		0.027	1.7								
14442'8"	4402.12	4375	85.3	0.108	6.1								
14444'7'	4402.71	4375.58	94.0	0.131	7.1								
14445'10"	4403.09	4375.96		0.155	3.5								
14447'7"	4403.62	4376.5	95.7	0.117	13.2	23.3	28.3	8.4	63.8	33.8	2.4		CL
14449'5"	4404.18	4377.06	98.0	0.122	5.2								
14451'5"	4404.79	4377.66	95.7	0.102	6.5								
14454'9"	4405.81	4378.68	95.0	0.098	7.4								
14455'10"	4406.14	4379.01		0.123	6.6	26.7	25.0	16.5					
14457'5"	4406.62	4379.49	82.0	0.115	10.4								
14461'6"	4407.87	4380.74	95.0	0.109	6.5								
14463'4"	4408.42	4381.3	94.0	0.101	8.3								
14465'5"	4409.06	4381.93	91.7	0.122	4.2	26.0	25.7	16.6					
14469'3"	4410.23	4383.1		0.167	0.7								
14475'8"	4412.18	4385.06	93.0	0.142	5.4								
14478'7"	4413.07	4385.95	94.3	0.137	6.9								
14482'1"	4414.14	4387.01	91.0	0.169	9.5								
14483'8"	4414.62	4387.49		0.179	1.2								
14484'11"	4415	4387.88	92.7	0.154	6.8								
14488'6"	4416.09	4388.97		0.103	3.3								
14490'9"	4416.78	4389.65	94.3	0.168	7.3								
14494'7"	4417.95	4390.82	96.7	0.126	5.1	26.0	25.7	13.9					
14495'7"	4418.25	4391.13	97.0	0.127	5.3	21.0	30.4	11.4					
14497'10"	4418.94	4391.81		0.126	1.7	12.7	37.0	7.8					
14500'	4419.6	4392.47	95.0	0.141	8.3							TS	
14502'11"	4420.49	4393.36		0.099	2.0								
14505'4"	4421.23	4394.1	93.0	0.130	4.7								
14508'10"	4422.29	4395.17		0.170	2.2								
14511'11"	4423.23	4396.11	71.7	0.205	7.2								
14517'9"	4425.01	4397.88	80.0	0.220	6.6								
14522'10"	4426.56	4399.43		0.154	0.8								
14524'5"	4427.04	4399.92	64.0	0.160	3.4								
14526'9"	4427.75	4400.63	83.3	0.168	3.4								
14528'11"	4428.41	4401.29	67.3	0.114	5.7								
14530'3"	4428.82	4401.69	97.3	0.164	8.9				70.8	19.4	9.9	TS	
14537'11"	4431.16	4404.03	75.3	0.168	5.0								
14539'5"	4431.61	4404.49	53.3	0.100	0.8								
14541'11"	4432.38	4405.25	92.7	0.146	5.5								
14543'8"	4432.91	4405.78	93.3	0.239	7.7								

Sample	Depth	TVDSS	FCG	GS	Porosity	IGV	COPL	CEPL	Q	F	L	SEM	CL
	[m]	[m]	[%]	[mm]	[%]	[%]	[%]	[%]	[%]	[%]	[%]	[-]	[-]
14545'8"	4433.52	4406.39	95.7	0.139	4.4								
14552'7"	4435.63	4408.5	96.3	0.164	5.0								
14555'7"	4436.54	4409.41	89.3	0.178	6.4								
14557'7"	4437.15	4410.02	91.0	0.163	6.0								
14560'5"	4438.02	4410.89	96.3	0.172	6.4								
14565'11"	4439.69	4412.56	92.3	0.132	6.9								
14573'2"	4441.9	4414.77	96.3	0.125	5.8	20.3	31.0	12.0					
14576'6"	4442.92	4415.79	98.0	0.131	4.3								
14581'7"	4444.47	4417.34	98.3	0.254	8.2								
14583'6"	4445.05	4417.92	96.7	0.200	12.4	22.6	28.9	5.5	55.9	32.7	11.4		
14586'4"	4445.91	4418.79	94.7	0.227	14.1	21.0	30.4	4.4	66.4	26.0	7.6		CL
14589'1"	4446.75	4419.63	97.0	0.219	7.7								
14591'10"	4447.59	4420.46		0.052	3.8								
14593'11"	4448.23	4421.1	76.3	0.135	7.4								
14598'4"	4449.57	4422.44		0.069	3.8								
14602'5"	4450.82	4423.69	85.7	0.098	10.2	24.3	27.3	8.7	63.3	29.5	7.2		
14606'	4451.91	4424.78	91.7	0.157	8.4								
14987'3"	4568.11	4540.99	88.7	0.138	8.5								
14990'1"	4568.98	4541.85		0.070	7.0								
14993'4"	4569.97	4542.84	14.3	0.179	5.9								
14997'2"	4571.14	4544.01	86.3	0.114	10.7	16.0	34.5	3.7	53.1	42.0	4.9	RP	
14999'11"	4571.97	4544.85	45.3	0.161	3.5								
15003'11"	4573.19	4546.07	83.0	0.089	9.9								
15005'11"	4573.8	4546.68	83.7	0.100	10.5	19.6	31.5	4.1	62.1	35.6	2.3		
15006'11"	4574.11	4546.98	89.7	0.104	8.6								
15009'7"	4574.92	4547.79	94.7	0.133	2.1								
15014'4"	4576.37	4549.24		0.133	0.3								
15018'10"	4577.74	4550.61	90.0	0.135	11.0	23.6	27.9	7.2	56.3	40.5	3.2		
15020'11"	4578.38	4551.25	90.0	0.132	13.6	19.6	31.5	3.2	57.7	36.5	5.8	RP	
15020'7"	4578.27	4551.15	93.0	0.151	11.3	25.0	26.6	10.8	61.8	35.4	2.8		
15027'11"	4580.51	4553.38	100.0	0.103	11.7	10.6	38.4	1.6	60.6	38.2	1.2	RP	
15032'3"	4581.83	4554.7	92.0	0.090	7.1								
15035'6"	4582.82	4555.69	95.0	0.135	10.1	20.6	30.7	6.2	53.0	39.6	7.4		
15041'9"	4584.73	4557.6		0.112	1.2								
15042'10"	4585.06	4557.93	97.0	0.154	10.3	11.3	38.0	1.2	55.0	40.0	5.0	RP	
15046'6"	4586.17	4559.05	94.3	0.148	13.1	19.6	31.5	3.9	62.3	32.5	5.2		
15048'10"	4586.88	4559.76		0.168	2.7								
15056'6"	4589.22	4562.09	80.3	0.128	13.8	13.0	36.8	1.1	58.4	39.1	2.5		
15061'10"	4590.85	4563.72	93.0	0.142	7.1								
15065'8"	4592.02	4564.89	67.7	0.123	10.9	23.0	28.6	5.2	63.5	35.5	1.0		
15068'11"	4593.01	4565.88	2.0	0.199	11.1	17.3	33.5	4.7	61.0	363.3	5.7		CL
15070'8"	4593.54	4566.41		0.101	1.5								
15075'10"	4595.11	4567.99		0.124	5.7	36.0	14.1	28.1					

Table I.2 Petrographic data for the Skua samples, with driller's depth (Depth), true vertical depth below mean sea level (TVDSS), fraction of coated grains (FCG), average grain size (GS), optical porosity (porosity), intergranular volume (IGV), compactional porosity loss (COPL), cementational porosity loss (CEPL), Fraction of quartz grains (Q), fraction of feldspar grains (F), fraction of lithic grains (L), and indication of being used as a sample for scanning electron microscopy (SEM) or cathodoluminescence (CL).

Seagull (well 22/29-2)

Sample	Depth	TVDSS	FCG	GS	Porosity	IGV	COPL	CEPL	Q	F	L	SEM	CL
	[m]	[m]	[%]	[mm]	[%]	[%]	[%]	[%]	[%]	[%]	[%]	[-]	[-]
13504'10"	4116.27	4089.15	86.7	0.148	5.8								
13511'8"	4118.36	4091.23	75.7	0.210	17.4	35.0	15.4	16.1	77.8	16.4	5.8		
13514'4"	4119.17	4092.04	85.3	0.299	10.1	29.3	22.2	12.2	81.7	14.9	3.4		
13521'0"	4121.20	4094.07	84.3	0.272	10.5	32.3	18.7	16.5	77.7	19.3	3.0		
13532'1"	4124.58	4097.45	72.7	0.192	5.2								
13538'4"	4126.48	4099.36	94.3	0.162	12.2	36.0	14.1	20.9	69.7	28.2	2.1	RP	
13547'3"	4129.20	4102.07	89.3	0.125	6.0								
13556'0"	4131.87	4104.74	79.3	0.166	5.7								
13567'2"	4135.27	4108.15	67.7	0.183	7.0								
13572'4"	4136.85	4109.72	85.0	0.165	7.3								
13576'9"	4138.19	4111.07	74.0	0.158	8.2	34.3	16.2	19.0	69.7	20.2	10.1		
13584'10"	4140.66	4113.53	83.3	0.194	10.6	27.7	24.0	11.2	68.5	25.9	5.6		
13590'5"	4142.36	4115.23	88.0	0.114	7.0	38.3	10.8	27.1	64.1	32.3	3.6		
13597'3"	4144.44	4117.31	91.7	0.104	7.3	34.0	16.7	20.0	77.5	16.0	6.4		
13608'0"	4147.72	4120.59	78.7	0.179	9.8	23.7	27.9	6.7	72.1	22.6	5.3		
13618'3"	4150.84	4123.72	66.3	0.188	9.2	20.0	31.3	7.8	68.9	21.9	9.2		CL
13627'11"	4153.79	4126.66	98.3	0.190	6.4							RP	
13645'10"	4159.25	4132.12	87.0	0.121	5.5								
13649'6"	4160.37	4133.24	63.0	0.271	4.6								
13662'2"	4164.23	4137.10	62.7	0.166	10.3	29.0	22.5	11.6	66.3	30.7	2.9		
13666'1"	4165.42	4138.30	96.0	0.240	2.1								
13674'7"	4168.01	4140.89	98.7	0.129	3.5								
13676'7"	4168.62	4141.50	27.3	0.198	6.4								
13688'4"	4172.20	4145.08											
13692'6"	4173.47	4146.35	58.7	0.168	13.7	29.7	21.8	10.9	68.9	24.4	6.7		
13695'0"	4174.24	4147.11	43.7	0.154	9.8	28.0	23.6	12.5	66.4	26.6	7.0		
13703'9"	4176.90	4149.78	22.3	0.124	6.1								
13709'4"	4178.60	4151.48	50.0	0.189	3.6								
13719'11"	4181.83	4154.70	98.0	0.216	12.3	36.0	14.1	14.3	72.8	21.5	5.8		
13730'0"	4184.90	4157.78		0.141	3.3								
13741'10"	4188.51	4161.38	96.7	0.169	4.9							TS	
13761'4"	4194.45	4167.33	65.3	0.096	5.8								
13786'0"	4201.97	4174.85	7.7	0.231	5.1	40.0	8.3	31.5	67.2	21.1	11.7		CL
13807'2"	4208.42	4181.30	73.7	0.181	6.3							RP	
13813'9"	4210.43	4183.30											
13819'8"	4212.23	4185.11	41.3	0.195	7.2								
13858'4"	4224.02	4196.89	43.7	0.100	3.6								
13880'3"	4230.70	4203.57	88.3	0.160	3.8							RP	

Table I.3 Petrographic data for the Skua samples, with driller's depth (Depth), true vertical depth below mean sea level (TVDSS), fraction of coated grains (FCG), average grain size (GS), optical porosity (porosity), intergranular volume (IGV), compactional porosity loss (COPL), cementational porosity loss (CEPL), Fraction of quartz grains (Q), fraction of feldspar grains (F), fraction of lithic grains (L), and indication of being used as a sample for scanning electron microscopy (SEM) or cathodoluminescence (CL).

Seagull (well 22/29-3)

Sample	Depth	TVDSS	FCG	GS	Porosity	IGV	COPL	CEPL	Q	F	L	SEM	CL
	[m]	[m]	[%]	[mm]	[%]	[%]	[%]	[%]	[%]	[%]	[%]	[-]	[-]
13775'0"	4198.62	4172.71	72.0	0.154	3.7							RP	
13776'3"	4199.00	4173.09	76.0	0.124	2.3								
13778'6"	4199.69	4173.78	78.3	0.134	4.3								
13781'4"	4200.55	4174.64	39.3	0.121	3.5								
13787'3"	4202.35	4176.45	61.7	0.141	2.6								
13790'10"	4203.45	4177.54	40.7	0.143	3.0								CL
13799'6"	4206.09	4180.18	58.3	0.146	2.4							RP	
13805'4"	4207.87	4181.96		0.127	3.4								
13815'6"	4210.96	4185.06	35.7	0.189	2.5								
13822'1"	4212.97	4187.06	54.0	0.163	3.5								
13828'1"	4214.80	4188.89		0.097	5.7	42.3	4.6	34.3	66.2	33.1	0.7		
13834'1"	4216.63	4190.72	44.3	0.210	5.2	27.7	24.0	15.2	71.3	21.1	7.7	RP	
13840'4"	4218.53	4192.63	56.0	0.096	6.7								
13845'0"	4219.96	4194.05		0.120	2.8								
13849'6"	4221.33	4195.42		0.142	5.8	23.7	27.9	15.6	62.4	32.3	5.3		
13854'0"	4222.70	4196.79		0.167	3.0								
13860'4"	4224.63	4198.72											
13869'7"	4227.45	4201.54		0.108	4.6								
13875'4"	4229.20	4203.29		0.127	4.3								
13882'0"	4231.23	4205.33		0.163	2.5								
13887'2"	4232.81	4206.90		0.183	4.8								
13895'2"	4235.25	4209.34	86.0	0.153	3.3								CL
13899'3"	4236.49	4210.58	98.3	0.146	6.8	32.0	19.1	22.6	66.0	25.3	8.8	RP	
13910'0"	4239.77	4213.86	96.0	0.159	3.9	33.7	17.1	22.4	64.6	27.2	8.2	TS	
13950'5"	4252.09	4226.18		0.114	5.4	28.3	23.3	18.9	61.5	32.7	5.9		
13966'9"	4257.07	4231.16		0.109	6.5								
13971'0"	4258.36	4232.45		0.118	5.4	24.6	27.1	12.9	58.0	38.7	3.3		
13976'5"	4260.01	4234.10	99.0	0.123	6.1	28.3	23.3	16.4	53.9	39.8	6.3		
13981'5"	4261.54	4235.63		0.166	3.4								
13988'5"	4263.67	4237.76		0.115	2.2								

Table I.4 Petrographic data for the Skua samples, with driller's depth (Depth), true vertical depth below mean sea level (TVDSS), fraction of coated grains (FCG), average grain size (GS), optical porosity (porosity), intergranular volume (IGV), compactional porosity loss (COPL), cementational porosity loss (CEPL), Fraction of quartz grains (Q), fraction of feldspar grains (F), fraction of lithic grains (L), and indication of being used as a sample for scanning electron microscopy (SEM) or cathodoluminescence (CL).

Heron (well 22/29-5RE)

Sample	Depth	TVDSS	FCG	GS	Porosity	IGV	COPL	CEPL	Q	F	L	SEM	CL
	[m]	[m]	[%]	[mm]	[%]	[%]	[%]	[%]	[%]	[%]	[%]	[-]	[-]
15237'7"	4644.42	4316.23		0.083	1.7								
15243'4"	4646.17	4317.45		0.061	2.6								
15246'7"	4647.16	4318.14		0.083	2.3								
15248'7"	4647.77	4318.56		0.068	1.5								
15250'9"	4648.43	4319.02		0.055	0.5								
15279'1"	4657.06	4325.03			1.0								
15287'10"	4659.73	4326.88			0.2								
15293'3"	4661.38	4328.03		0.054	1.2								
15455'8"	4710.89	4362.47	98.3	0.083	2.4								
15463'5"	4713.25	4364.11	97.3	0.094	3.5								
15465'7"	4713.91	4364.57	92.0	0.084	1.9								
15467'4"	4714.44	4364.94	89.7	0.087	3.6								
15469'8"	4715.15	4365.44	88.7	0.095	4.0								
15471'8"	4715.76	4365.86	86.0	0.099	2.9								
15473'2"	4716.22	4366.18	83.7	0.166	3.0								
15475'7"	4716.96	4366.69	75.7	0.168	9.9								
15479'3"	4718.08	4367.47	93.7	0.122	4.2	23.0	28.6	12.1					
15483'10"	4719.47	4368.44	84.7	0.108	4.1								
15487'11"	4720.72	4369.31											
15488'9"	4720.97	4369.48		0.153	7.4								
15490'4"	4721.45	4369.82	79.3	0.120	3.1								
15492'7"	4722.14	4370.30	94.7	0.123	1.9	13.0	36.8	7.0					
15503'7"	4725.49	4372.63		0.171	2.1								
15509'6"	4727.30	4373.88	57.7	0.170	10.7	26.3	25.3	3.9	63.7	29.3	7.0		
15519'11"	4730.47	4376.09	84.7	0.151	8.2								
15524'9"	4731.94	4377.12	61.3	0.180	7.6								
15526'7"	4732.50	4377.50	84.7	0.110	5.2								
15529'9"	4733.47	4378.18		0.099	2.8								
15537'7"	4735.86	4379.84	78.0	0.114	5.3								
15542'8"	4737.40	4380.91	92.7	0.139	4.8								
15547'8"	4738.93	4381.97	91.7	0.098	2.9								
15551'7"	4740.12	4382.80	76.3	0.102	4.6								
15552'9"	4740.48	4383.05	40.7	0.167	3.4								
15566'10"	4744.77	4386.04			0.7								
15569'9"	4745.66	4386.66	61.0	0.129	6.7	22.7	28.9	10.7					
15571'6"	4746.19	4387.03	47.0	0.118	1.7								
15582'7"	4749.57	4389.38	30.7	0.189	6.7								
15588'9"	4751.45	4390.68		0.177	1.1								
15589'7"	4751.71	4390.86		0.154	2.9								
15591'10"	4752.39	4391.34	85.3	0.131	4.3								
15599'10"	4754.83	4393.03	99.0	0.160	10.3	23.3	28.2	8.1	65.3	31.0	3.7	RP	
15603'1"	4755.82	4393.72		0.049	3.9								
15607'8"	4757.22	4394.70		0.080	2.4								
15614'9"	4759.38	4396.20	89.7	0.165	16.8	31.0	20.3	6.9	57.1	40.0	2.9	RP/TS	
15623'8"	4762.09	4398.09	86.3	0.202	5.8								
15624'5"	4762.32	4398.25	60.0	0.327	5.5								
15627'10"	4763.36	4398.97		0.194	4.8								
15638'10"	4766.72	4401.30		0.072	1.4								
15642'10"	4767.94	4402.15	92.3	0.120	5.4								
15643'6"	4768.14	4402.29	94.3	0.125	5.7	22.0	29.5	8.2					
15645'8"	4768.80	4402.75	82.0	0.123	3.9	23.7	27.9	13.0					
15647'3"	4769.28	4403.09		0.136	1.4								
15648'8"	4769.71	4403.39		0.074	1.1								
15651'8"	4770.63	4404.02	80.0	0.107	4.0								
15657'7"	4772.43	4405.28	97.7	0.106	2.6								
15660'11"	4773.45	4405.99	97.3	0.140	2.5								
15662'11"	4774.06	4406.41	89.3	0.141	4.3								
15665'8"	4774.90	4406.99	94.7	0.148	4.5								
15669'9"	4776.14	4407.86	80.0	0.184	6.1								
15675'10"	4777.99	4409.15	76.0	0.183	10.2	20.6	30.6	3.0	63.5	30.0	6.5		
15678'8"	4778.86	4409.75	27.0	0.227	6.8								
15679'8"	4779.16	4409.96	45.3	0.164	5.3								
15681'6"	4779.72	4410.35											

Sample	Depth	TVDSS	FCG	GS	Porosity	IGV	COPL	CEPL	Q	F	L	SEM	CL
	[m]	[m]	[%]	[mm]	[%]	[%]	[%]	[%]	[%]	[%]	[%]	[-]	[-]
15684'5"	4780.61	4410.97	79.0	0.166	8.8								
15689'	4782.01	4411.94	61.0	0.188	9.0								
15689'8"	4782.21	4412.08	38.0	0.209	9.1								
15691'6"	4782.77	4412.47	22.0	0.219	11.7	24.6	26.9	5.6	71.6	22.3	6.1		CL
15692'4"	4783.02	4412.65	14.3	0.186	12.9	28.6	22.9	10.3	59.0	26.7	14.3		CL
15695'4"	4783.94	4413.28			0.7								
15697'11"	4784.73	4413.83	82.0	0.151	3.5								
15699'8"	4785.26	4414.20		0.065	2.1								
15702'11"	4786.25	4414.89	92.7	0.093	3.6								
15703'11"	4786.55	4415.10	97.3	0.086	2.5								
15706'3"	4787.27	4415.60	94.3	0.117	8.4								
15709'5"	4788.23	4416.27	99.7	0.084	4.5								
15711'7"	4788.89	4416.73	93.0	0.178	24.5	35.3	14.9	6.2	66.3	23.7	10.0		
15712'10"	4789.27	4416.99	93.0	0.090	6.4								
15714'7"	4789.81	4417.36	93.3	0.267	30.9	42.3	4.7	2.7	70.0	23.5	6.5	TS	
15715'10"	4790.19	4417.63	85.3	0.268	26.0	29.3	22.2	4.2	67.5	27.8	4.7	RP	
15716'9"	4790.47	4417.82	84.0	0.225	7.7								
15718'10"	4791.10	4418.27	91.3	0.249	18.4	22.6	28.9	4.3	65.8	26.3	7.9	RP	
15722'2"	4792.12	4418.97	89.7	0.140	5.1								
15724'11"	4792.95	4419.55	53.7	0.206	11.1	21.6	29.8	5.6	71.0	24.1	4.9		
15725'9"	4793.21	4419.73			0.5								
15728'10"	4794.15	4420.39		0.092	1.3								
15733'8"	4795.62	4421.41		0.163	1.6								
15736'10"	4796.59	4422.08	79.7	0.154	7.9								
15738'10"	4797.20	4422.51	82.7	0.202	12.2	20.0	31.3	4.4	63.7	30.7	5.6		
15741'10"	4798.11	4423.14	86.3	0.157	6.5								
15743'8"	4798.67	4423.53	92.7	0.155	12.8	26.6	29.8	5.6	69.5	27.2	3.3	RP	
15745'10"	4799.33	4423.99	76.7	0.189	22.8	34.6	15.8	10.6	67.6	23.8	8.6		
15747'10"	4799.94	4424.41	86.0	0.173	8.9								
15749'1"	4800.32	4424.68	64.0	0.197	18.6	28.3	23.3	6.1	61.5	29.7	8.8		
15752'2"	4801.26	4425.33	96.3	0.140	7.7								
15754'7"	4802.00	4425.84	85.7	0.115	6.7								
15757'11"	4803.01	4426.55	39.3	0.206	13.8	50.7	-11.5	47.6	70.4	23.4	6.2		
15760'11"	4803.93	4427.19	53.0	0.140	15.8	20.7	30.6	2.1	63.4	32.8	3.8		
15762'7"	4804.44	4427.54	59.3	0.124	12.9	20.0	31.3	5.7					
15763'9"	4804.79	4427.79	93.0	0.095	5.4								
15766'11"	4805.76	4428.46	89.3	0.083	3.6								
15768'7"	4806.26	4428.81	92.7	0.128	4.6	24.3	27.3	10.4					
15770'2"	4806.75	4429.15	79.0	0.151	9.4								
15772'5"	4807.43	4429.63	93.0	0.187	13.4				80.9	18.4	0.7		CL
15774'10"	4808.17	4430.14	64.7	0.272	9.7								
16218'3"	4943.32	4524.15	91.3	0.096	1.1								
16219'9"	4943.78	4524.47		0.155	2.3								
16228'5"	4946.42	4526.31	69.7	0.129	1.0	22.3	29.2	14.9					
16230'11"	4947.18	4526.84			0.2								
16232'11"	4947.79	4527.26	89.7	0.150	4.9								
16234'2"	4948.17	4527.53	94.3	0.135	4.6								
16235'5"	4948.56	4527.79	54.3	0.154	4.5								
16238'9"	4949.57	4528.50		0.056	1.0								
16242'2"	4950.61	4529.22											
16242'11"	4950.84	4529.38		0.077	1.3								
16243'8"	4951.07	4529.54		0.119	2.7								
16245'10"	4951.73	4530.00	84.7	0.135	3.5								
16248'2"	4952.44	4530.49	99.7	0.131	2.7								
16251'5"	4953.43	4531.18	77.3	0.111	1.2								
16252'9"	4953.84	4531.47	100.0	0.115	3.0								
16254'10"	4954.47	4531.91	89.7	0.130	5.1	22.7	28.9	14.0					
16256'	4954.83	4532.15	84.7	0.121	1.1	30.0	21.4	22.5					
16257'4"	4955.24	4532.44			0.7								
16260'9"	4956.28	4533.16	87.3	0.154	6.2								
16262'8"	4956.86	4533.57		0.125	1.7	44.3	1.2	36.6					
16263'5"	4957.09	4533.73		0.071	1.1								
16267'6"	4958.33	4534.59		0.079	1.8								
16271'8"	4959.60	4535.48		0.121	1.2	28.7	22.9	22.1					
16274'	4960.32	4535.97		0.114	2.9								

Sample	Depth	TVDSS	FCG	GS	Porosity	IGV	COPL	CEPL	Q	F	L	SEM	CL
	[m]	[m]	[%]	[mm]	[%]	[%]	[%]	[%]	[%]	[%]	[%]	[-]	[-]
16279'6"	4961.99	4537.14		0.088	1.5								
16283'2"	4963.11	4537.91		0.064	1.7								
16284'7"	4963.54	4538.21	72.7	0.085	3.7								
16285'9"	4963.90	4538.46		0.095	3.2								
16289'2"	4964.94	4539.19	85.3	0.131	2.1								
16291'6"	4965.65	4539.68		0.094	2.3								
16293'9"	4966.34	4540.16	71.7	0.179	6.9								
16296'10"	4967.27	4540.81		0.205	5.6								
16297'2"	4967.38	4540.88	70.0	0.092	1.7								
16298'8"	4967.83	4541.20											
16301'5"	4968.67	4541.78	95.0	0.096	2.8								
16304'10	4969.71	4542.51	91.0	0.090	2.4								
16306'10"	4970.32	4542.93											

Table I.5 Petrographic data for the Skua samples, with driller's depth (Depth), true vertical depth below mean sea level (TVDSS), fraction of coated grains (FCG), average grain size (GS), optical porosity (porosity), intergranular volume (IGV), compactional porosity loss (COPL), cementational porosity loss (CEPL), Fraction of quartz grains (Q), fraction of feldspar grains (F), fraction of lithic grains (L), and indication of being used as a sample for scanning electron microscopy (SEM) or cathodoluminescence (CL).

UK sector 30

Jade (well 30/2c-4)

Sample	Depth	TVDSS	FCG	GS	Porosity	IGV	COPL	CEPL	Q	F	L	SEM	CL
	[m]	[m]	[%]	[mm]	[%]	[%]	[%]	[%]	[%]	[%]	[%]	[-]	[-]
15057.15	4589.42	4474.62	94.0	0.106	2.9	13.7	36.3	3.6					
15591.44	4752.27	4637.47	97.0	0.113	0.0	14.3	35.8	7.7					
15593.00	4752.75	4637.95		0.067	0.1								
15615.94	4759.74	4644.94	57.0	0.212	11.7	28.0	23.6	1.3	44.9	53.2	1.9		
15618.50	4760.52	4645.72	18.3	0.285	16.8	23.0	28.6	2.1	48.9	40.5	10.6		
15645.00	4768.60	4653.80	38.7	0.176	14.3	21.7	29.8	0.9	42.3	52.4	5.3		
15660.00	4773.17	4658.37	10.7	0.189	16.4	24.0	27.6	4.3	51.4	42.3	6.3		
15660.33	4773.27	4658.47	56.3	0.169	17.5	30.0	21.4	1.0	54.5	40.6	5.0		
15678.00	4778.65	4663.85	71.7	0.205	15.6	25.3	26.3	4.4	57.5	38.8	3.7		
15690.88	4782.58	4667.78	97.3	0.128	2.7	15.7	34.8	3.5					
15693.00	4783.23	4668.43	97.0	0.131	5.1	15.0	35.3	4.3					
15700.69	4785.57	4670.77		0.076	0.4								
15712.00	4789.02	4674.22	76.3	0.121	12.3	21.3	30.1	4.4	44.5	50.7	4.8		
15742.16	4798.21	4683.41	73.0	0.107	1.9	13.3	36.5	4.2					
15748.00	4799.99	4685.19	19.3	0.218	15.1	18.3	32.7	1.3	47.1	45.8	7.1		
15754.13	4801.86	4687.06		0.092	0.1								
15761.00	4803.95	4689.15		0.073	0.0								
15792.16	4813.45	4698.65		0.169	0.7								

Table I.6 Petrographic data for the Skua samples, with driller's depth (Depth), true vertical depth below mean sea level (TVDSS), fraction of coated grains (FCG), average grain size (GS), optical porosity (porosity), intergranular volume (IGV), compactional porosity loss (COPL), cementational porosity loss (CEPL), Fraction of quartz grains (Q), fraction of feldspar grains (F), fraction of lithic grains (L), and indication of being used as a sample for scanning electron microscopy (SEM) or cathodoluminescence (CL).

Judy (well 30/7a-7)

Sample	Depth	TVDSS	FCG	GS	Porosity	IGV	COPL	CEPL	Q	F	L	SEM	CL
	[m]	[m]	[%]	[mm]	[%]	[%]	[%]	[%]	[%]	[%]	[%]	[-]	[-]
11291.00	3441.50	3416.20			1.0								
11291.54	3441.66	3416.36	46.0	0.089	5.1							TS	
11294.85	3442.67	3417.37	28.3	0.080	2.1							TS	
11309.70	3447.20	3421.90	35.3	0.093	8.6								
11317.59	3449.60	3424.30			0.7							TS	
11325.13	3451.90	3426.60	41.7	0.087	8.0							TS	
11333.00	3454.30	3429.00			1.6								
11344.00	3457.65	3432.35	38.3	0.084	11.9	30.7	20.7	4.2	47.0	51.4	1.6		
11351.38	3459.90	3434.60			1.6							TS	
11366.80	3464.60	3439.30										RP	
11442.68	3487.73	3462.43	39.7	0.101	4.8	23.0	28.6	7.9				TS	
11446.00	3488.74	3463.44	36.0	0.085	9.2								
11465.35	3494.64	3469.34			1.3							TS	
11496.00	3503.98	3478.68	16.0	0.128	19.0	23.3	28.3	1.9	56.7	40.6	2.8	TS	
11503.31	3506.21	3480.91	33.0	0.149	5.4	31.7	19.5	16.4				TS	
11506.33	3507.13	3481.83			0.1							TS	
11512.00	3508.86	3483.56			1.2								
11519.19	3511.05	3485.75	52.3	0.106	6.0	42.0	5.2	33.8				TS	
11521.00	3511.60	3486.30	14.7	0.096	14.9	32.3	18.7	3.5	54.1	44.3	1.6		
11537.11	3516.51	3491.21	35.0	0.072	4.7							TS	

Table I.7 Petrographic data for the Skua samples, with driller's depth (Depth), true vertical depth below mean sea level (TVDSS), fraction of coated grains (FCG), average grain size (GS), optical porosity (porosity), intergranular volume (IGV), compactional porosity loss (COPL), cementational porosity loss (CEPL), Fraction of quartz grains (Q), fraction of feldspar grains (F), fraction of lithic grains (L), and indication of being used as a sample for scanning electron microscopy (SEM) or cathodoluminescence (CL).

Judy (well 30/7a-8)

Sample	Depth	TVDSS	FCG	GS	Porosity	IGV	COPL	CEPL	Q	F	L	SEM	CL
	[m]	[m]	[%]	[mm]	[%]	[%]	[%]	[%]	[%]	[%]	[%]	[-]	[-]
11428.00	3483.25	3456.43											
11432.25	3484.55	3457.73											
11631.00	3545.13	3518.31	19.0	0.239	6.4								
11656.90	3553.02	3526.20	39.7	0.146	12.4	28.3	23.3	7.4	58.6	38.9	2.5		
11660.00	3553.97	3527.15	51.3	0.118	18.3	31.3	19.9	5.3	47.7	51.8	0.5		
11683.04	3560.99	3534.17	42.7	0.158	13.0	19.3	31.8	3.0	65.1	29.3	5.7	TS	
11688.00	3562.50	3535.68	40.3	0.189	13.2	23.3	28.3	6.0	60.6	39.4	0.0		
11692.16	3563.77	3536.95	42.7	0.216	12.5	25.7	26.0	5.4	60.5	34.4	5.1	TS	
11708.56	3568.77	3541.95	18.3	0.249	19.9	26.7	25.0	2.5	55.5	36.2	8.3		
11730.00	3575.30	3548.48	22.0	0.210	6.8								
11731.00	3575.61	3548.79	14.3	0.209	23.9	25.0	26.7	2.9	52.4	47.6	0.0		
11748.00	3580.79	3553.97	0.0		0.1								
11763.00	3585.36	3558.54	9.7	0.170	26.1	25.3	26.3	2.5	62.1	37.9	0.0		
11789.00	3593.29	3566.46	0.0										
11798.00	3596.03	3569.21	16.7	0.209	25.7	28.0	23.6	1.3	50.9	47.2	1.9		
11820.00	3602.74	3575.91	27.7	0.220	28.1	23.0	28.6	0.7	62.2	36.4	1.3		
11864.83	3616.40	3589.58											
11875.00	3619.50	3592.68											
11886.58	3623.03	3596.21										TS	
11911.00	3630.47	3603.65											
11928.00	3635.65	3608.83											
11935.70	3638.00	3611.18											

Table I.8 Petrographic data for the Skua samples, with driller's depth (Depth), true vertical depth below mean sea level (TVDSS), fraction of coated grains (FCG), average grain size (GS), optical porosity (porosity), intergranular volume (IGV), compactional porosity loss (COPL), cementational porosity loss (CEPL), Fraction of quartz grains (Q), fraction of feldspar grains (F), fraction of lithic grains (L), and indication of being used as a sample for scanning electron microscopy (SEM) or cathodoluminescence (CL).

Judy (well 30/7a-9)

Sample	Depth	TVDSS	FCG	GS	Porosity	IGV	COPL	CEPL	Q	FR	L	SEM	CL
	[m]	[m]	[%]	[mm]	[%]	[%]	[%]	[%]	[%]	[%]	[%]	[-]	[-]
12024.00	3664.92	3621.02	11.7	0.124	5.3	23.3	28.3	9.3					
12029.10	3666.47	3622.58		0.052	2.0								
12034.50	3668.12	3624.22		0.046	0.4								
12056.00	3674.67	3630.78	62.0	0.072	0.0								
12077.00	3681.07	3637.18	21.0	0.160	27.3	23.7	27.9	0.7	38.9	58.4	2.7		
12079.00	3681.68	3637.79	62.7	0.066	2.0								
12105.00	3689.60	3645.71	80.0	0.105	0.2	25.0	26.7	5.4					
12110.30	3691.22	3647.33	14.3	0.139	20.3	35.0	15.4	7.1	40.7	58.8	0.5		
12135.60	3698.93	3655.04		0.054	0.3								
12167.00	3708.50	3664.61	25.7	0.239	24.1	26.3	25.3	3.0	45.9	50.5	3.6		
12186.00	3714.29	3670.40		0.151	0.3								

Table I.9 Petrographic data for the Skua samples, with driller's depth (Depth), true vertical depth below mean sea level (TVDSS), fraction of coated grains (FCG), average grain size (GS), optical porosity (porosity), intergranular volume (IGV), compactional porosity loss (COPL), cementational porosity loss (CEPL), Fraction of quartz grains (Q), fraction of feldspar grains (F), fraction of lithic grains (L), and indication of being used as a sample for scanning electron microscopy (SEM) or cathodoluminescence (CL).

Judy (well 30/7a-11Z)

Sample	Depth	TVDSS	FCG	GS	Porosity	IGV	COPL	CEPL	Q	F	L	SEM	CL
	[m]	[m]	[%]	[mm]	[%]	[%]	[%]	[%]	[%]	[%]	[%]	[-]	[-]
11424.00	3482.04	3456.74	51.7	0.221	3.9								
11438.98	3486.60	3461.30	57.3	0.177	18.9	37.0	12.7	3.5	67.0	26.4	6.6	RP	
11446.00	3488.74	3463.44	77.0	0.095	0.6								
11482.02	3499.72	3474.42	78.3	0.093	3.7							RP	
11502.69	3506.02	3480.72	63.0	0.114	6.4	35.3	14.9	17.0					
11510.00	3508.25	3482.95	59.3	0.163	12.4	30.7	20.7	10.6	83.9	32.7	5.4		
11583.07	3530.52	3505.22	62.3	0.102	14.2	34.0	16.7	5.6	57.5	38.1	3.9	RP	
11626.00	3543.60	3518.31	60.7	0.178	9.5								
11647.00	3550.01	3524.71	73.0	0.108	0.6	21.7	29.8	11.0					
11660.53	3554.13	3528.83	62.0	0.143	21.1	36.0	14.1	1.1	51.0	38.3	2.4	RP	
11682.00	3560.67	3535.38	61.0	0.134	12.7	36.3	13.6	3.7	66.3	29.9	3.8		
11683.43	3561.11	3535.81	41.7	0.153	18.6	36.3	13.6	4.3	54.7	42.5	2.8		

Table I.10 Petrographic data for the Skua samples, with driller's depth (Depth), true vertical depth below mean sea level (TVDSS), fraction of coated grains (FCG), average grain size (GS), optical porosity (porosity), intergranular volume (IGV), compactional porosity loss (COPL), cementational porosity loss (CEPL), Fraction of quartz grains (Q), fraction of feldspar grains (F), fraction of lithic grains (L), and indication of being used as a sample for scanning electron microscopy (SEM) or cathodoluminescence (CL).

Judy (well 30/7a-P3)

Sample	Depth	TVDSS	FCG	GS	Porosity	IGV	COPL	CEPL	Q	F	L	SEM	CL
	[m]	[m]	[%]	[mm]	[%]	[%]	[%]	[%]	[%]	[%]	[%]	[-]	[-]
12954.36	3948.49	3356.90	21.7	0.317	25.7	33.3	17.5	1.7	57.8	35.7	6.5		
13033.14	3972.50	3377.60	59.3	0.131	16.1	31.7	19.5	3.8	62.3	37.7	0.0		
13046.85	3976.68	3381.21	38.3	0.189	18.5	28.3	23.3	1.5	67.5	28.7	3.8		
13057.22	3979.84	3383.93	43.0	0.152	13.8	26.7	25.0	4.0	55.8	35.4	8.7		
13072.51	3984.50	3387.95	44.3	0.121	12.5	29.7	21.8	1.8	60.6	36.9	2.5		
13085.20	3988.37	3391.29	67.7	0.099	2.7								
13145.44	4006.73	3407.11	32.3	0.167	19.6	26.0	25.7	2.2	60.9	36.7	2.3		

Table I.11 Petrographic data for the Skua samples, with driller's depth (Depth), true vertical depth below mean sea level (TVDSS), fraction of coated grains (FCG), average grain size (GS), optical porosity (porosity), intergranular volume (IGV), compactional porosity loss (COPL), cementational porosity loss (CEPL), Fraction of quartz grains (Q), fraction of feldspar grains (F), fraction of lithic grains (L), and indication of being used as a sample for scanning electron microscopy (SEM) or cathodoluminescence (CL).

Judy (well 30/13-5)

Sample	Depth	TVDSS	FCG	GS	Porosity	IGV	COPL	CEPL	Q	F	L	SEM	CL
	[m]	[m]	[%]	[mm]	[%]	[%]	[%]	[%]	[%]	[%]	[%]	[-]	[-]
12939.24	3943.88	3897.25			0.5								
12957.87	3949.56	3902.93										TS	
12978.81	3955.94	3909.31			0.4								
12988.32	3958.84	3912.21	28.7	0.191	18.4	25.0	26.7	5.6	62.8	30.3	6.9		
12990.78	3959.59	3912.96	46.0	0.168	25.4	30.0	21.4	2.6	57.8	40.3	1.9		
12996.06	3961.20	3914.57	47.0	0.136	18.0	22.3	29.2	2.1	58.6	36.9	4.5		
12997.34	3961.59	3914.96	37.0	0.159	26.0	25.0	26.7	1.0	56.6	40.6	2.7		
12997.38	3961.60	3914.97	38.3	0.180	21.0	27.3	24.3	2.5	62.3	32.1	5.7		
12999.64	3962.29	3915.66	41.7	0.220	18.6	29.7	21.8	5.0	63.5	32.0	4.5	TS	
13007.48	3964.68	3918.05	45.7	0.159	23.8	34.7	15.8	7.3	56.5	36.6	6.8	TS	
13008.69	3965.05	3918.42	38.7	0.200	13.6	25.7	26.0	3.2	67.9	28.0	4.1		
13020.87	3968.76	3922.13	48.7	0.166	13.0	31.3	19.9	2.1	59.5	35.5	5.0		
13040.32	3974.69	3928.06	37.0	0.157	6.7							TS	
13089.53	3989.69	3943.06		0.177	8.4								
13111.65	3996.43	3949.80		0.139	3.3	25.3	26.3	10.3					

Table I.12 Petrographic data for the Skua samples, with driller's depth (Depth), true vertical depth below mean sea level (TVDSS), fraction of coated grains (FCG), average grain size (GS), optical porosity (porosity), intergranular volume (IGV), compactional porosity loss (COPL), cementational porosity loss (CEPL), Fraction of quartz grains (Q), fraction of feldspar grains (F), fraction of lithic grains (L), and indication of being used as a sample for scanning electron microscopy (SEM) or cathodoluminescence (CL).

Norwegian sector 2

Well 2/5-10

Sample	Depth	TVDSS	FCG	GS	Porosity	IGV	COPL	CEPL	Q	F	L	SEM	CL
	[m]	[m]	[%]	[mm]	[%]	[%]	[%]	[%]	[%]	[%]	[%]	[-]	[-]
15026.98	4580.00		26.0	0.388	0.8							RP	
15033.54	4582.00		16.0	0.229	0.2								
15041.74	4584.50		17.7	0.474	1.6								
15049.95	4587.00		26.7	0.201	0.1								
15056.51	4589.00		20.3	0.189	0.5								

Table I.13 Petrographic data for the Skua samples, with driller's depth (Depth), true vertical depth below mean sea level (TVDSS), fraction of coated grains (FCG), average grain size (GS), optical porosity (porosity), intergranular volume (IGV), compactional porosity loss (COPL), cementational porosity loss (CEPL), Fraction of quartz grains (Q), fraction of feldspar grains (F), fraction of lithic grains (L), and indication of being used as a sample for scanning electron microscopy (SEM) or cathodoluminescence (CL).

Well 2/8-12S

Sample	Depth	TVDSS	FCG	GS	Porosity	IGV	COPL	CEPL	Q	F	L	SEM	CL
	[m]	[m]	[%]	[mm]	[%]	[%]	[%]	[%]	[%]	[%]	[%]	[-]	[-]
17148.15	5226.50		38.3	0.140	9.2								
17151.10	5227.40		17.0	0.199	0.1								
17158.65	5229.70		6.0	0.222	7.0							RP	
17176.69	5235.20			0.028	0.4								
17179.32	5236.00			0.168	2.7								
17202.45	5243.05		16.7	0.254	0.3								
17482.48	5328.40		18.7	0.200	0.4								

Table I.14 Petrographic data for the Skua samples, with driller's depth (Depth), true vertical depth below mean sea level (TVDSS), fraction of coated grains (FCG), average grain size (GS), optical porosity (porosity), intergranular volume (IGV), compactional porosity loss (COPL), cementational porosity loss (CEPL), Fraction of quartz grains (Q), fraction of feldspar grains (F), fraction of lithic grains (L), and indication of being used as a sample for scanning electron microscopy (SEM) or cathodoluminescence (CL).

Norwegian sector 6

Gaupe (well 6/3-1)

Sample	Depth	TVDSS	FCG	GS	Porosity	IGV	COPL	CEPL	Q	F	L	SEM	CL
	[m]	[m]	[%]	[mm]	[%]	[%]	[%]	[%]	[%]	[%]	[%]	[-]	[-]
3025.72	3025.72	2902.72		0.228	5.0	23.3	28.3	15.3	52.5	40.2	7.3		
3025.72	3025.72	2902.72	5.0	0.226	0.3	9.3	39.3	1.8	59.8	38.3	1.9		
3027.40	3027.40	2904.40	94.7	0.297	7.3								
3027.40	3027.4	2904.40	53.3	0.269	1.3								
3028.65	3028.65	2905.65			2.1								
3030.45	3030.45	2907.45	46.7	0.346	12.6								
3030.45	3030.45	2907.45	11.7	0.347	1.6								
3033.70	3033.70	2910.70	71.3	0.384	5.6								
3035.05	3035.05	2912.05		0.603	2.6								
3036.70	3036.70	2913.70	31.7	0.324	15.3								
3036.70	3036.7	2913.70	4.7	0.411	6.6							RP	
3037.40	3037.4	2914.40	10.7	0.590	11.1								
3038.40	3038.4	2915.40	8.7	0.493	9.9								
3039.45	3039.45	2916.45		0.270	4.2								
3040.65	3040.65	2917.65			2.6								
3041.50	3041.5	2918.50			0.2								
3042.45	3042.45	2919.45	100.0	0.171	3.0	34.3	16.2	28.8	69.8	28.0	2.1		
3043.00	3043	2920.00			0.6								
3044.65	3044.65	2921.65		0.121	6.1								
3045.65	3045.65	2922.65		0.148	2.3	22.7	28.9	16.1	72.2	26.9	0.9		
3046.00	3046	2923.00	100.0	0.161	6.4	27.3	24.3	13.9	63.5	33.1	3.3		
3047.45	3047.45	2924.45	37.7	0.256	9.1								
3048.50	3048.5	2925.50	29.7	0.551	13.7								
3049.35	3049.35	2926.35	34.3	0.401	21.4	28.0	23.6	7.9	77.9	15.0	7.0		
3050.60	3050.6	2927.60	21.7	0.435	15.4								
3051.00	3051	2928.00	23.3	0.415	14.6								
3052.65	3052.65	2929.65	100.0	0.195	3.2	34.7	15.8	25.8	51.1	43.5	5.4		
3053.35	3053.35	2930.35	100.0	0.193	3.7	30.7	20.7	22.5	60.1	34.4	464.0		
3055.65	3055.65	2932.65	100.0	0.305	5.9								
3056.35	3056.35	2933.35		0.290	7.0								
3057.10	3057.1	2934.10	87.3	0.299	6.2	23.7	27.9	11.3	80.2	12.8	7.0		
3058.35	3058.35	2935.35	13.3	0.219	0.5	20.7	30.7	7.9	55.6	41.8	2.7		
3059.65	3059.65	2936.65			3.8								
3060.65	3060.65	2937.65	100.0	0.220	3.4	23.3	28.3	15.8	52.7	45.9	1.4		
3061.10	3061.1	2938.10	75.0	0.193	8.1	23.3	28.3	14.8	59.2	31.9	8.9		
3061.95	3061.95	2938.95			1.2								
3063.00	3063	2940.00	100.0	0.171	7.2	29.3	22.2	22.3	55.2	40.4	4.4		
3064.05	3064.05	2941.05	28.3	0.335	19.7	26.7	25.0	5.5	70.0	17.5	12.4		
3064.05	3064.05	2941.05	48.3	0.329	6.2								
3065.05	3065.05	2942.05	64.3	0.326	7.5								
3066.30	3066.3	2943.30	60.7	0.306	8.5								
3067.00	3067	2944.00	100.0	0.290	8.3								
3068.00	3068	2945.00	97.3	0.429	16.1								
3069.40	3069.4	2946.40	1.3	0.652	16.9								
3069.40	3069.4	2946.40	3.0	0.719	7.4								
3070.95	3070.95	2947.95	100.0	0.177	5.2	31.3	19.9	21.6	77.6	17.3	5.1		
3071.60	3071.60	2948.60	28.0	0.326	13.0								
3072.00	3072.00	2949.00	31.7	0.278	16.5	24.3	27.3	12.1	57.2	34.1	8.7		
3072.00	3072	2949.00	14.0	0.241	2.6								
3073.35	3073.35	2950.35	100.0	0.289	4.8								
3074.00	3074	2951.00	14.3	0.290	24.9	21.7	29.8	0.9	63.6	29.8	6.6		
3074.00	3074	2951.00	17.3	0.311	5.3								
3075.10	3075.1	2952.10		0.183	4.8	40.0	8.3	36.7	69.5	27.3	3.1	TS	
3075.60	3075.6	2952.60	69.7	0.331	5.4								
3077.00	3077	2954.00	5.0	0.533	14.3								
3077.95	3077.95	2954.95	11.3	0.424	11.7								
3079.00	3079	2956.00	9.7	0.541	0.6								
3079.25	3079.25	2956.25			18.6								
3082.35	3082.35	2959.35		0.200	4.0	30.0	21.4	22.5	63.4	33.7	2.9		
3083.35	3083.35	2960.35	10.0	0.355	21.4								
3083.35	3083.35	2960.35	11.0	0.329	4.8								

Sample	Depth	TVDSS	FCG	GS	Porosity	IGV	COPL	CEPL	Q	F	L	SEM	CL
	[m]	[m]	[%]	[mm]	[%]	[%]	[%]	[%]	[%]	[%]	[%]	[-]	[-]
3084.10	3084.10	2961.10	5.0	0.517	9.2								
3084.65	3084.65	2961.65	10.3	0.467	10.1								
3085.65	3085.65	2962.65		0.118	5.2								
3085.65	3085.65	2962.65	29.7	0.136	0.2								
3086.00	3086	2963.00	4.3	0.502	15.2								
3087.00	3087	2964.00	100.0	0.187	3.4				74.5	24.8	0.7		
3088.30	3088.3	2965.30	22.7	0.461	13.1								
3088.65	3088.65	2965.65		0.586	20.4								
3089.35	3089.35	2966.35		0.367	6.9								
3090.80	3090.8	2967.80	29.0	0.333	12.9								
3090.80	3090.8	2967.80	10.3	0.329	2.9								
3091.05	3091.05	2968.05		0.312	4.9								
3092.07	3092.07	2969.07			19.4								
3093.07	3093.07	2970.07	100.0	0.184	5.6								
3094.35	3094.35	2971.35	80.3	0.201	5.4	18.7	32.3	9.2	63.7	33.3	3.0		
3095.00	3095.00	2972.00	40.0	0.219	17.9	17.7	33.2	4.2	73.4	23.7	2.9		
3095.00	3095	2972.00	16.3	0.206	1.5	18.0	32.9	6.0	67.2	31.5	1.2		
3096.35	3096.35	2973.35	100.0	0.120	4.9								
3100.35	3100.35	2977.35	100.0	0.143	7.3	25.3	26.3	15.0	55.8	43.3	0.9		
3101.65	3101.65	2978.65	100.0	0.136	3.2	18.0	32.9	8.7	63.8	35.8	0.4		
3102.03	3102.03	2979.03	72.0	0.234	13.3	16.7	34.0	4.2	62.0	31.0	6.9		
3103.65	3103.65	2980.65	23.3	0.457	7.7								
3105.65	3105.65	2982.65	43.7	0.442	25.1								
3106.10	3106.10	2983.10	56.0	0.377	16.1							RP	
3107.77	3107.77	2984.77	93.3	0.223	8.1	20.0	31.3	8.7	61.2	37.1	1.8		
3108.75	3108.75	2985.75	85.3	0.208	6.1	27.0	24.7	19.1	66.8	24.2	9.0		
3109.65	3109.65	2986.65		0.248	3.6	25.0	26.7	17.4	70.1	19.6	10.3		
3110.00	3110	2987.00	40.3	0.285	15.3								
3110.00	3110	2987.00	20.3	0.298	1.5								
3111.45	3111.45	2988.45	64.3	0.379	11.6								
3112.05	3112.05	2989.05	15.0	0.358	18.9								
3113.52	3113.52	2990.52		0.114	5.6								
3114.18	3114.18	2991.18	14.0	0.446	6.5	30.7	20.7	22.2	68.1	20.1	11.8	TS	
3115.65	3115.65	2992.65	94.3	0.261	8.0								
3116.17	3116.17	2993.17	0.2	0.160	3.3	27.3	24.3	20.4	70.5	27.0	2.5		

Table I.15 Petrographic data for the Skua samples, with driller's depth (Depth), true vertical depth below mean sea level (TVDSS), fraction of coated grains (FCG), average grain size (GS), optical porosity (porosity), intergranular volume (IGV), compactional porosity loss (COPL), cementational porosity loss (CEPL), Fraction of quartz grains (Q), fraction of feldspar grains (F), fraction of lithic grains (L), and indication of being used as a sample for scanning electron microscopy (SEM) or cathodoluminescence (CL).

Norwegian sector 7

Brynhild (well 7/7-2)

Sample	Depth	TVDSS	FCG	GS	Porosity	IGV	COPL	CEPL	Q	F	L	SEM	CL
	[m]	[m]	[%]	[mm]	[%]	[%]	[%]	[%]	[%]	[%]	[%]	[-]	[-]
10978.55	3346.10		45.0	0.248	5.6								
10996.27	3351.50			0.254	6.2								
10997.91	3352.00		20.0	0.240	2.6								
11011.04	3356.00		21.3	0.247	9.6								
11017.60	3358.00		42.7	0.238	2.6								
11020.88	3359.00		87.0	0.338	6.6								
11024.16	3360.00		88.0	0.310	5.4								
11027.44	3361.00		25.3	0.197	1.3								
11030.72	3362.00			0.278	2.5								

Table I.16 Petrographic data for the Skua samples, with driller's depth (Depth), true vertical depth below mean sea level (TVDSS), fraction of coated grains (FCG), average grain size (GS), optical porosity (porosity), intergranular volume (IGV), compactional porosity loss (COPL), cementational porosity loss (CEPL), Fraction of quartz grains (Q), fraction of feldspar grains (F), fraction of lithic grains (L), and indication of being used as a sample for scanning electron microscopy (SEM) or cathodoluminescence (CL).

Krabbe (well 7/8-3)

Sample	Depth	TVDSS	FCG	GS	Porosity	IGV	COPL	CEPL	Q	F	L	SEM	CL
	[m]	[m]	[%]	[mm]	[%]	[%]	[%]	[%]	[%]	[%]	[%]	[-]	[-]
12351.00	3764.40		36.0	0.117	0.8								
12355.26	3765.70		23.3	0.132	0.0								
12359.86	3767.10		23.3	0.155	0.1								
12361.17	3767.50		25.0	0.171	3.0								

Table I.17 Petrographic data for the Skua samples, with driller's depth (Depth), true vertical depth below mean sea level (TVDSS), fraction of coated grains (FCG), average grain size (GS), optical porosity (porosity), intergranular volume (IGV), compactional porosity loss (COPL), cementational porosity loss (CEPL), Fraction of quartz grains (Q), fraction of feldspar grains (F), fraction of lithic grains (L), and indication of being used as a sample for scanning electron microscopy (SEM) or cathodoluminescence (CL).

Cod (well 7/11-7R)

Sample	Depth	TVDSS	FCG	GS	Porosity	IGV	COPL	CEPL	Q	F	L	SEM	CL
	[m]	[m]	[%]	[mm]	[%]	[%]	[%]	[%]	[%]	[%]	[%]	[-]	[-]
4561.64	4561.64	4307.69	35.0	0.409	4.4	18.0	32.9	9.8	72.4	19.1	8.5		
4565.29	4565.29	4311.23			1.8								
4566.82	4566.82	4312.71		0.126	2.9	21.0	30.4	14.6	59.1	32.5	8.4		
4568.95	4568.95	4314.78		0.120	3.2								
4569.87	4569.87	4315.66	63.3	0.333	2.6	19.7	31.5	12.6	50.4	36.2	13.4		
4575.96	4575.96	4321.57		0.175	2.1	21.3	30.1	14.9	63.2	31.6	5.3		
4577.06	4577.06	4322.63		0.152	3.7	34.3	16.2	28.8	80.1	14.3	5.6		
4578.40	4578.40	4323.93		0.367	6.5								
4582.06	4582.06	4327.47	36.7	0.443	5.7	29.9	21.6	19.6	66.7	26.4	6.9		
4583.89	4583.89	4329.24		0.098	1.8								
4585.72	4585.72	4331.02	72.0	0.245	2.1	17.3	33.5	11.3	60.3	31.8	7.9		
4586.63	4586.63	4331.90		0.182	2.3	19.0	32.1	12.4	47.2	46.0	6.8		
4587.24	4587.24	4332.49		0.107	5.9								
4588.76	4588.76	4333.97		0.209	6.1	18.7	32.4	12.6	61.7	32.8	5.5		
4589.68	4589.68	4334.85		0.187	7.2	20.0	31.3	13.1	57.9	33.6	8.5		
4590.29	4590.29	4335.44		0.144	10.3	23.7	27.9	12.5	58.0	38.5	3.4		
4592.12	4592.12	4337.22		0.116	2.9								
4593.34	4593.34	4338.40	69.3	0.208	1.7	20.3	31.0	13.3	61.1	32.9	6.0		
4594.86	4594.86	4339.87	31.3	0.210	3.9	15.7	34.8	8.9	63.7	33.9	2.4		
4595.77	4595.77	4340.76		0.075	2.3								
4596.57	4596.57	4341.53		0.097	5.2								
4597.48	4597.48	4342.41		0.058	0.6								
4598.82	4598.82	4343.71		0.067	0.6								
4599.43	4599.43	4344.30		0.150	3.7	15.0	35.3	9.3	54.1	40.9	5.0		
4600.35	4600.35	4345.19											
4601.26	4601.26	4346.07	72.0	0.169	5.9	22.3	29.2	15.6	59.1	37.8	3.1		
4602.17	4602.17	4346.95	5.7	0.368	6.1	16.0	34.5	1.3	55.1	40.8	4.1		
4606.00	4606.00	4350.66	3.0	0.445	0.1								
4606.40	4606.40	4351.05	6.0	0.317	0.9								
4608.44	4608.44	4351.09	33.7	0.178	5.6	22.3	29.2	13.0	53.1	46.5	0.4		

Sample	Depth	TVDSS	FCG	GS	Porosity	IGV	COPL	CEPL	Q	F	L	SEM	CL
	[m]	[m]	[%]	[mm]	[%]	[%]	[%]	[%]	[%]	[%]	[%]	[-]	[-]
4609.19	4609.19	4353.75	28.3	0.308	5.5	18.0	32.9	5.4	51.0	42.3	6.6		
4610.10	4610.10	4354.64			3.3								
4610.40	4610.40	4354.93		0.132	0.0								
4610.40	4610.40	4354.93											
4612.23	4612.23	4356.70		0.088	3.4								
4614.06	4614.06	4358.47	27.0	0.137	3.0	17.0	33.7	9.1	63.3	24.2	12.5		
4616.20	4616.20	4360.54	38.3	0.335	3.7								
4617.42	4617.42	4361.72	76.3	0.207	5.9	28.3	23.3	16.9	62.0	37.6	0.5		
4673.43	4673.43	4415.98	0.2										

Table I.17 Petrographic data for the Skua samples, with driller's depth (Depth), true vertical depth below mean sea level (TVDSS), fraction of coated grains (FCG), average grain size (GS), optical porosity (porosity), intergranular volume (IGV), compactional porosity loss (COPL), cementational porosity loss (CEPL), Fraction of quartz grains (Q), fraction of feldspar grains (F), fraction of lithic grains (L), and indication of being used as a sample for scanning electron microscopy (SEM) or cathodoluminescence (CL).

Mime (well 7/11-10S)

Sample	Depth	TVDSS	FCG	GS	Porosity	IGV	COPL	CEPL	Q	F	L	SEM	CL
	[m]	[m]	[%]	[mm]	[%]	[%]	[%]	[%]	[%]	[%]	[%]	[-]	[-]
14427.87	4397.40		40.3	0.241	0.0								
14432.13	4398.70		56.0	0.196	3.5								
14435.51	4399.73		51.3	0.384	3.2								
14438.37	4400.60		14.3	0.602	4.4								
14442.31	4401.80			0.091	2.6								
14444.60	4402.50			0.096	0.6								

Table I.19 Petrographic data for the Skua samples, with driller's depth (Depth), true vertical depth below mean sea level (TVDSS), fraction of coated grains (FCG), average grain size (GS), optical porosity (porosity), intergranular volume (IGV), compactional porosity loss (COPL), cementational porosity loss (CEPL), Fraction of quartz grains (Q), fraction of feldspar grains (F), fraction of lithic grains (L), and indication of being used as a sample for scanning electron microscopy (SEM) or cathodoluminescence (CL).

Ula (well 7/12-6)

Sample	Depth	TVDSS	FCG	GS	Porosity	IGV	COPL	CEPL	Q	F	L	SEM	CL
	[m]	[m]	[%]	[mm]	[%]	[%]	[%]	[%]	[%]	[%]	[%]	[-]	[-]
11551.15	3520.62	3494.88	16.0	0.252	4.9								
11560.87	3523.58	3497.84	46.7	0.343	9.8	34.7	15.8	19.4	68.9	23.3	7.8		
11562.47	3524.07	3498.33											
11583.31	3530.42	3504.68	60.3	0.607	5.4								
11596.69	3534.50	3508.76		0.166	3.1	43.3	2.9	39.7	85.7	11.8	2.5		
11607.03	3537.65	3511.91		0.120	6.4								
11617.69	3540.90	3515.16	75.0	0.140	2.4	34.7	15.8	28.9	80.0	19.4	0.6	RP	
11642.63	3548.50	3522.77		0.131	1.8	30.0	21.4	23.3	81.6	17.8	0.6		
11665.60	3555.50	3529.77	10.3	0.296	6.8								
11679.21	3559.65	3533.92		0.139	2.9								
11690.53	3563.10	3537.37	38.0	0.282	6.4								
11698.41	3565.50	3539.77	87.7	0.172	3.6	34.7	15.8	27.8	63.9	35.6	0.5		
11708.25	3568.50	3542.77	36.0	0.185	6.5	38.7	10.3	26.6	59.3	33.3	7.3		
11737.45	3577.40	3551.67	95.0	0.177	2.1	35.7	14.5	30.2	61.4	34.4	4.2		
11749.26	3581.00	3555.27	90.0	0.174	14.2	40.3	7.8	21.2	72.0	28.0	0.0		
11760.02	3584.28	3558.55	79.0	0.267	16.6	34.7	15.8	16.6	67.7	21.5	10.8	TS	
11765.34	3585.90	3560.17	16.3	0.399	9.0							RP	
11765.67	3586.00	3560.27	84.3	0.383	16.1	43.3	2.9	26.9	69.5	22.6	7.9		
11766.98	3586.40	3560.67	73.0	0.407	17.9	37.0	12.7	14.6	66.5	23.8	9.7		
11768.23	3586.78	3561.05	70.7	0.303	24.4	42.0	5.2	14.2	68.7	26.4	4.9		
11778.43	3589.89	3564.16	93.3	0.275	4.8								
11799.92	3596.44	3570.71	80.0	0.251	9.2								
11808.15	3598.95	3573.22	72.0	0.349	18.6	37.7	11.8	19.4	71.8	26.0	2.2	TS	
11811.60	3600.00	3574.27	11.7	0.220	5.7	31.0	20.3	14.3	62.7	34.2	3.1		
11822.99	3603.47	3577.74	92.7	0.169	3.6	42.7	4.1	39.0	64.4	32.5	3.1		
11838.41	3608.17	3582.44	62.3	0.371	18.8	33.3	17.5	10.5	70.8	29.2	0.0	TS	
11847.10	3610.82	3585.09	78.0	0.153	9.6	43.7	2.4	42.6	73.4	24.7	1.9		
11861.90	3615.33	3589.60	24.3	0.297	6.4								
11880.24	3620.92	3595.19	91.7	0.183	3.9	25.5	26.2	18.6	71.2	22.0	6.8		
11889.69	3623.80	3598.07	88.0	0.161	4.1	26.0	25.7	16.6	65.0	32.5	2.5		
11892.80	3624.75	3599.02		0.107	0.3								
11908.09	3629.41	3603.68	62.0	0.238	7.9	22.0	29.5	12.0	53.2	40.8	6.0		
11922.66	3633.85	3608.12		0.099	0.0								

Sample	Depth	TVDSS	FCG	GS	Porosity	IGV	COPL	CEPL	Q	F	L	SEM	CL
	[m]	[m]	[%]	[mm]	[%]	[%]	[%]	[%]	[%]	[%]	[%]	[-]	[-]
11931.52	3636.55	3610.82	50.3	0.220	8.7								
11962.49	3645.99	3620.26	49.0	0.312	5.9								

Table I.20 Petrographic data for the Skua samples, with driller's depth (Depth), true vertical depth below mean sea level (TVDSS), fraction of coated grains (FCG), average grain size (GS), optical porosity (porosity), intergranular volume (IGV), compactional porosity loss (COPL), cementational porosity loss (CEPL), Fraction of quartz grains (Q), fraction of feldspar grains (F), fraction of lithic grains (L), and indication of being used as a sample for scanning electron microscopy (SEM) or cathodoluminescence (CL).

Well 7/11-6

Sample	Depth	TVDSS	FCG	GS	Porosity	IGV	COPL	CEPL	Q	F	L	SEM	CL
	[m]	[m]	[%]	[mm]	[%]	[%]	[%]	[%]	[%]	[%]	[%]	[-]	[-]
13598.10	4144.50		9.7	0.289	0.3								
13599.55	4144.94			0.110	4.5								
13600.73	4145.30		43.7	0.485	11.0								
13605.32	4146.70		28.7	0.408	11.0								
13608.28	4147.60		24.3	0.387	16.4							RP	
13612.05	4148.75		38.3	0.303	0.5								
13616.15	4150.00			0.112	2.4								
13619.92	4151.15		8.7	0.421	5.2								
13621.60	4151.66		17.0	0.439	6.5								
13625.53	4152.86			0.085	2.0								
13628.29	4153.70		11.7	0.413	8.8								
13633.87	4155.40		31.7	0.245	0.3								
13638.46	4156.80			0.207	2.8								
13639.05	4156.98				0.6								
13640.69	4157.48			0.123	3.5								

Table I.21 Petrographic data for the Skua samples, with driller's depth (Depth), true vertical depth below mean sea level (TVDSS), fraction of coated grains (FCG), average grain size (GS), optical porosity (porosity), intergranular volume (IGV), compactional porosity loss (COPL), cementational porosity loss (CEPL), Fraction of quartz grains (Q), fraction of feldspar grains (F), fraction of lithic grains (L), and indication of being used as a sample for scanning electron microscopy (SEM) or cathodoluminescence (CL).

Well 7/11-8

Sample	Depth	TVDSS	FCG	GS	Porosity	IGV	COPL	CEPL	Q	F	L	SEM	CL
	[m]	[m]	[%]	[mm]	[%]	[%]	[%]	[%]	[%]	[%]	[%]	[-]	[-]
12222.05	3725.10		50.0	0.246	6.3								
12228.94	3727.20		50.0	0.381	7.6								
12231.01	3727.83		91.3	0.274	7.1								
12235.73	3729.27		84.3		10.7								
12237.15	3729.70		47.7	0.183	4.7								
12243.74	3731.71		54.7	0.329	9.3								
12246.33	3732.50		50.3	0.258	8.6								
12249.94	3733.60		48.0	0.172	1.8								
12251.12	3733.96		65.0	0.354	2.2								
12256.11	3735.48		41.0	0.158	7.7								
12258.14	3736.10		5.7	0.332	5.2								
12261.10	3737.00		44.3	0.360	6.8								
12263.85	3737.84			0.351	1.1								
12266.90	3738.77			0.072	0.3								
12269.92	3739.69			0.115	3.0								
12275.53	3741.40		35.0	0.158	1.7								
12277.83	3742.10		83.7	0.153	5.3								
12281.11	3743.10		79.3	0.215	4.7								

Table I.22 Petrographic data for the Skua samples, with driller's depth (Depth), true vertical depth below mean sea level (TVDSS), fraction of coated grains (FCG), average grain size (GS), optical porosity (porosity), intergranular volume (IGV), compactional porosity loss (COPL), cementational porosity loss (CEPL), Fraction of quartz grains (Q), fraction of feldspar grains (F), fraction of lithic grains (L), and indication of being used as a sample for scanning electron microscopy (SEM) or cathodoluminescence (CL).

Appendix II

SEM images & SEM-EDS data

SEM images UK sector 22

Skua (well 22/24b-7)

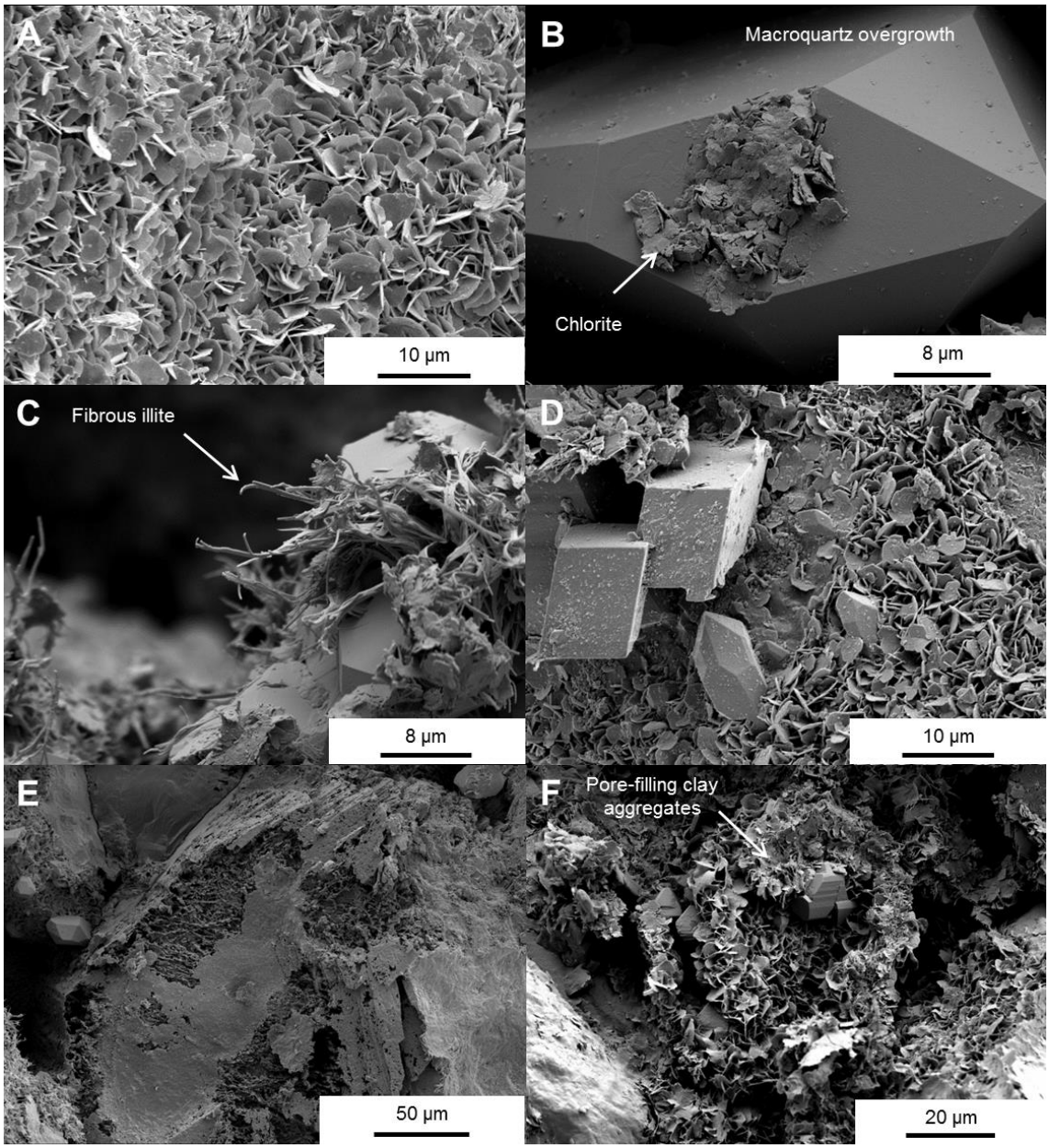

Figure II.1 SEM images of A) chlorite grain coating (22/24b-7; 11877'1''); B) macroquartz overgrowth inter-growing with chlorite platelets (22/24b-7; 11971'1''); C) authigenic illite fibres inter-growing with quartz overgrowth (22/24b-7; 11971'1''); D) pore-filling dolomite crystals and grain coating chlorite (22/24b-7; 11882'2''); E) partly dissolved feldspar (22/24b-7; 11971'1''); F) pore-filling clay chlorite aggregates (22/24b-7; 11952'4'').

Egret (well 22/24d-10)

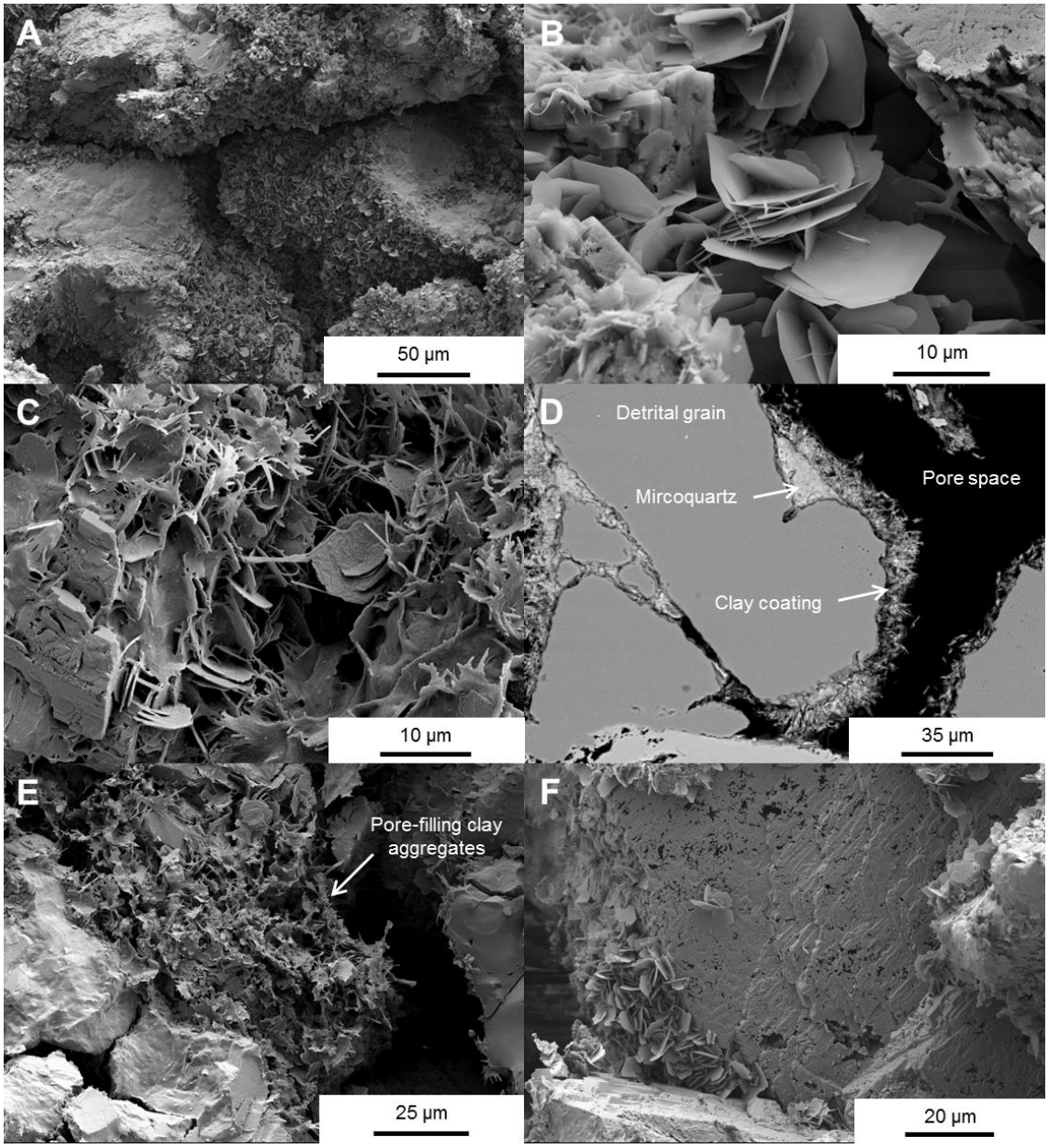

Figure II.2 SEM images of A) well-developed chlorite grain coatings (22/24d-10; 14997'2''); B) well-developed chlorite platelets (22/24d-10; 15042'10''); C) mixed clay mineral coating of authigenic chlorite and authigenic illite (22/24d-10; 14418'11''); D) cross-section of thickly developed clay mineral coatings, with microquartz overgrowth between the detrital quartz grain and the clay mineral coating (22/24d-10; 114500'0''); E) pore-filling clay mineral aggregates, consisting of authigenic chlorite and authigenic illite (22/24d-10; 14418'11''); F) partly dissolved K-feldspar with partial chlorite coating (22/24d-10; 14997'2'').

Seagull (well 22/29-2)

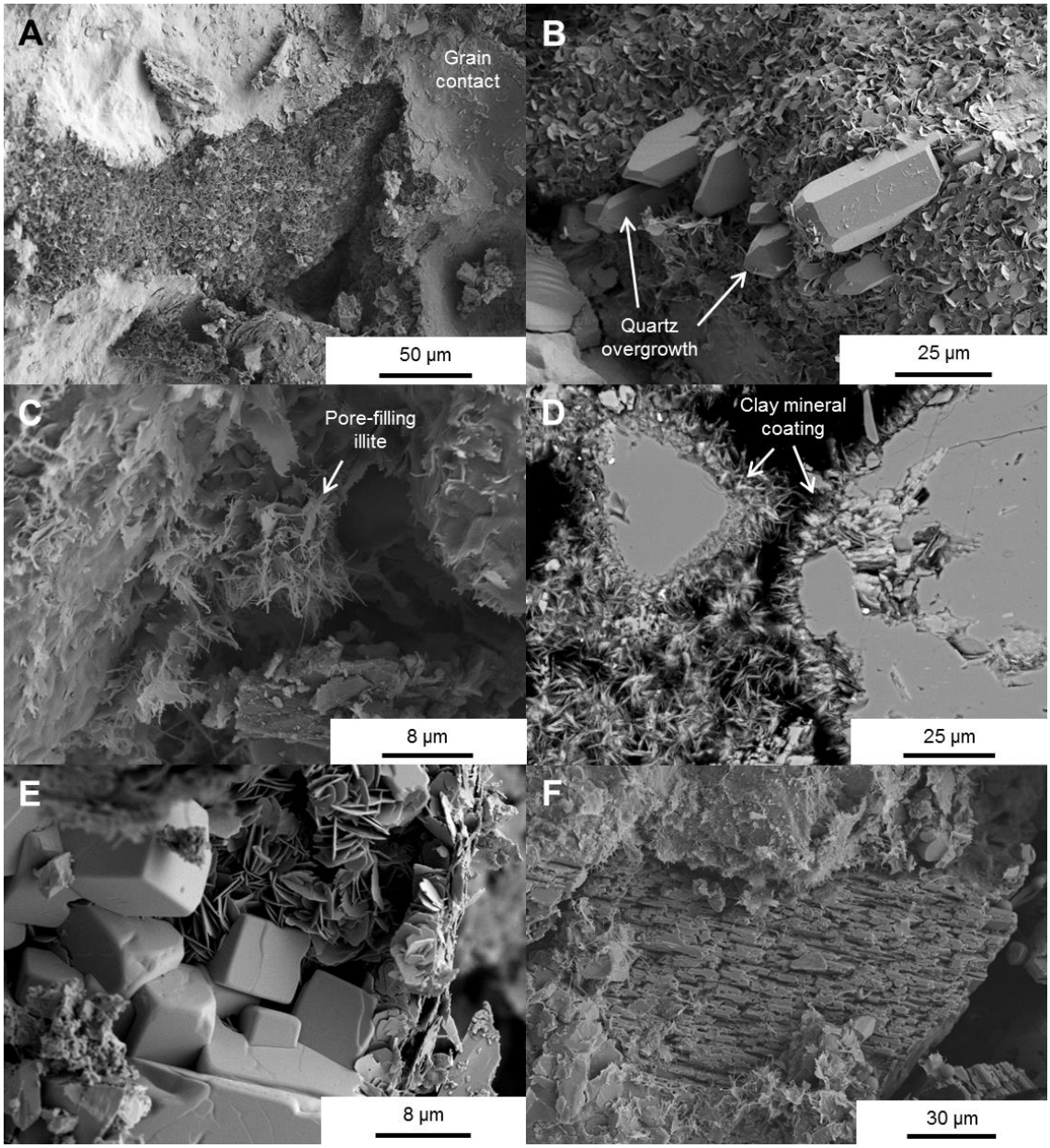

Figure II.3 SEM images of A) well-developed chlorite grain coatings with a visible root zone at the former grain contact (22/29-2; 13627'11''); B) well-developed chlorite coating with single quartz overgrowth crystals (22/29-2; 13538'4''); C) authigenic illite grain coating with pore-filling fibres (22/29-2; 13730'0''); D) cross-section of thickly developed clay mineral coatings and pore-filling clay mineral aggregates (22/29-2; 13741'10''); E) pore-filling salt crystals (22/29-2; 13627'11''); F) partly dissolved K-feldspar (22/29-2; 13730'0'').

Seagull (well 22/29-3)

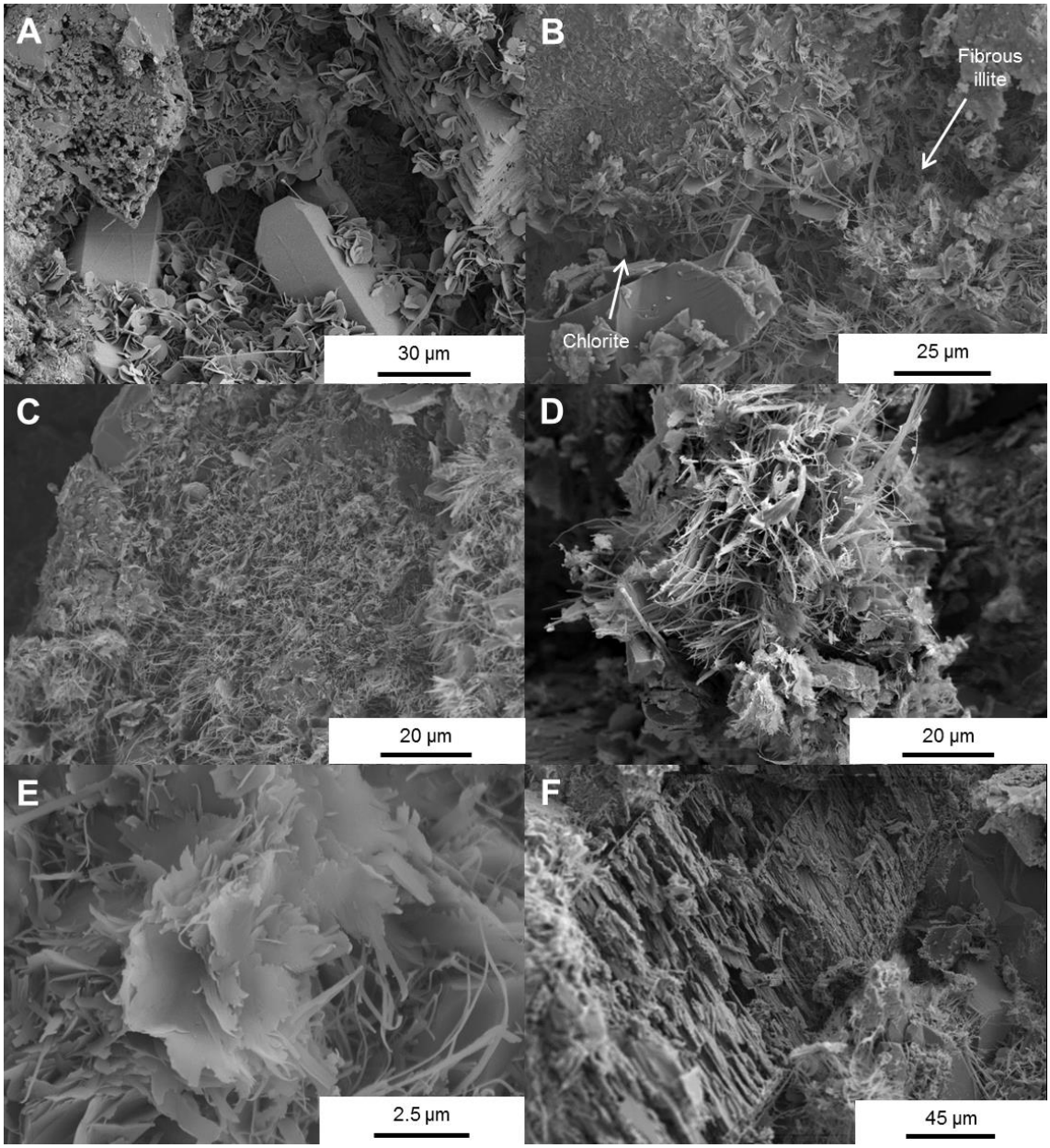

Figure II.4 SEM images of A) well-developed grain-coating chlorite platelets with quartz overgrowths and a partly dissolved K-feldspar (22/29-3; 13899'3''); B) mixed clay mineral coating with authigenic fibrous illite and authigenic chlorite (22/29-3; 13790'10''); C) well-developed authigenic illite grain coating (22/29-3; 13790'10''); D) pore-filling illite aggregate (22/29-3; 13799'6''); E) flaky illite in a flower-like or rosette-like structure (22/29-3; 13799'6''); F) partly dissolved K-feldspar (22/29-3; 13790'10'').

Heron (well 22/29-5RE)

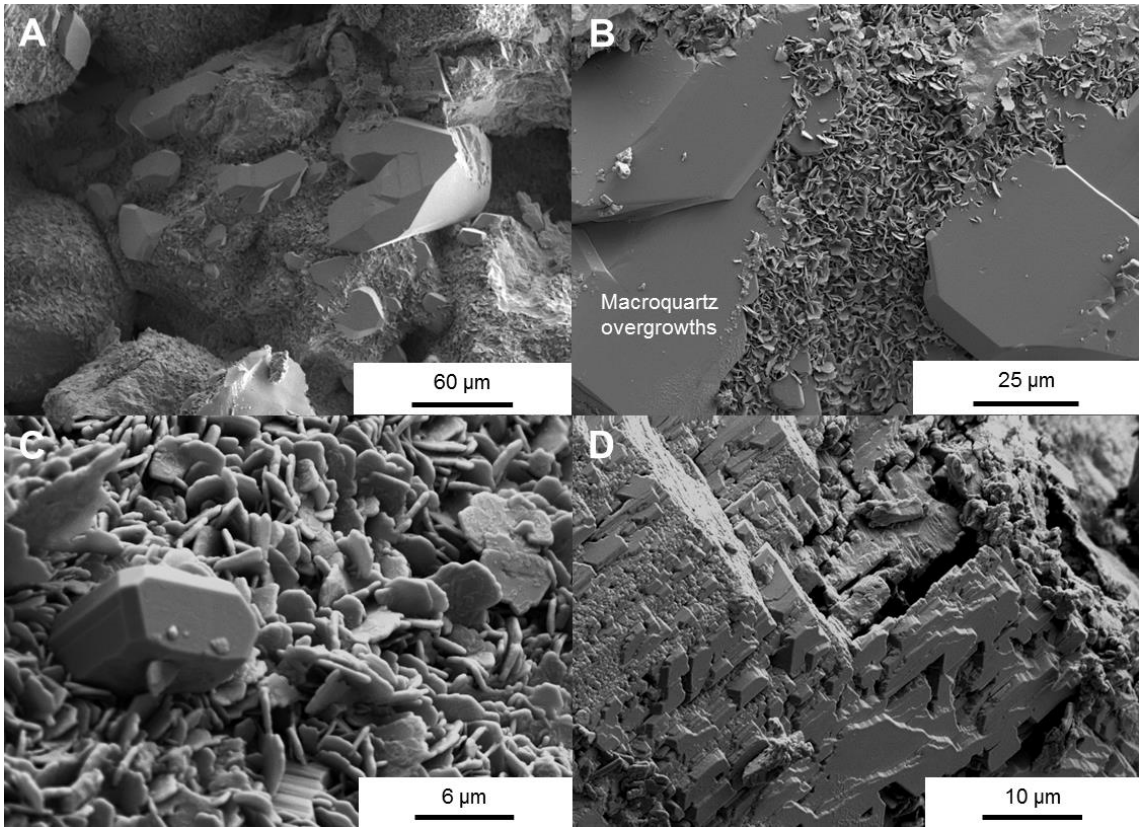

Figure II.5 SEM images of A) chlorite coated grains and partly coated grains with macroquartz overgrowths (22/29-5RE; 15599'10''); B) Macroquartz overgrowths interacting with grain-coating chlorite (22/29-5RE; 15718'10''); C) well-developed grain-coating chlorite platelets with an inter-growing microquartz (22/29-5RE; 15718'10''); D) partly dissolved K-feldspar (22/29-5RE; 15614'9'').

SEM images UK sector 30

Judy (well 30/7a-7)

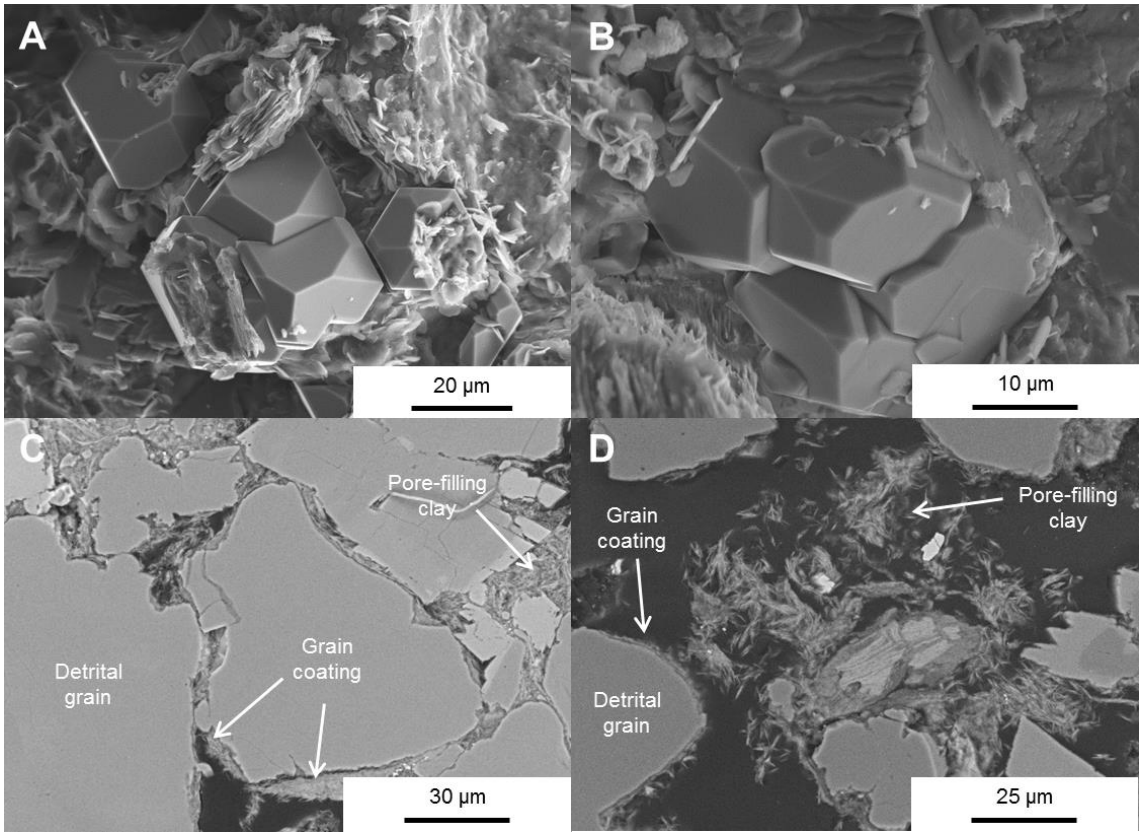

Figure II.6 SEM images of A) grain-coating chlorite and macroquartz overgrowth (30/7a-7; 3464.60); B) macroquartz overgrowth (30/7a-7; 3464.60); C) cross-section of the grain arrangement and clay mineral coatings (30/7a-7; 3442.67); D) pore-filling clay minerals (30/7a-7; 3441.6).

Judy (well 30/13-5)

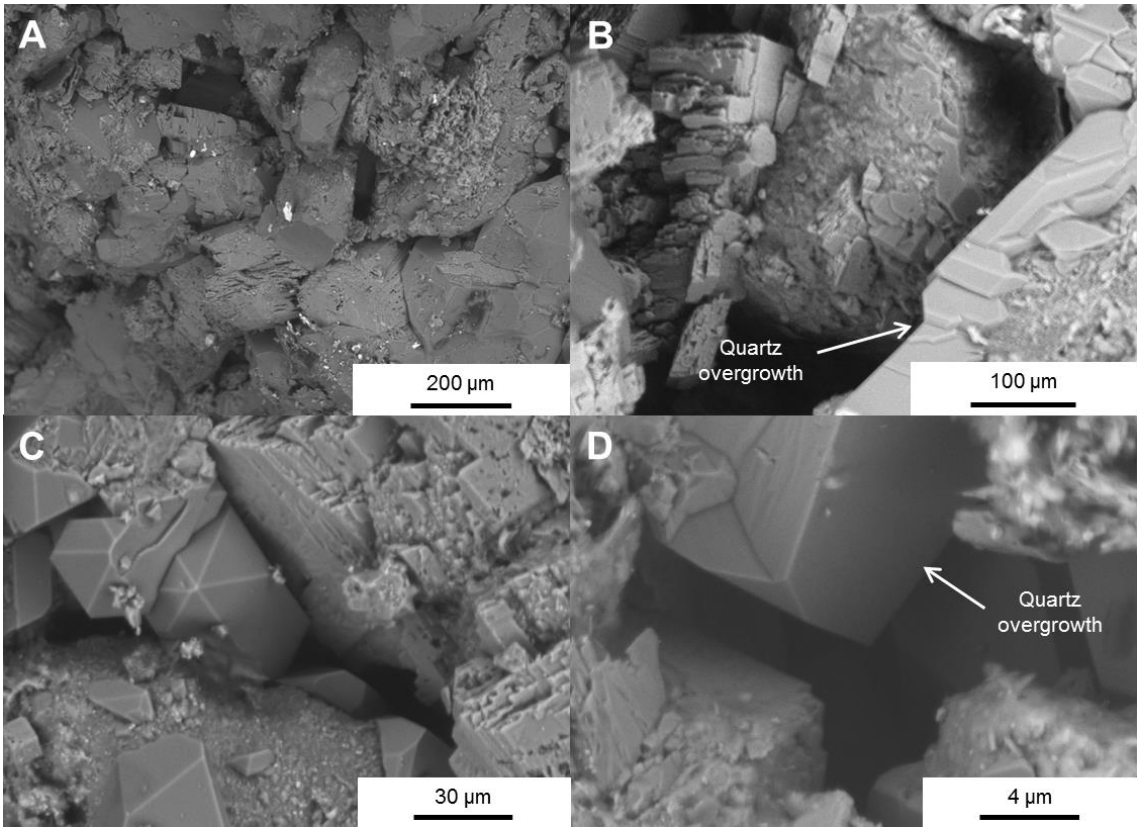

Figure II.7 SEM images of A) grain and pore space arrangement (30/13-5; 3949.56); B) macroquartz overgrowth (30/13-5; 3949.56); C) partly dissolved feldspar and macroquartz overgrowth on clay-coated grain(30/13-5; 3964.68); D) pore-filling macroquartz overgrowth (30/13-5; 3974.69).

SEM images Norwegian sector 2

Well 2/5-10

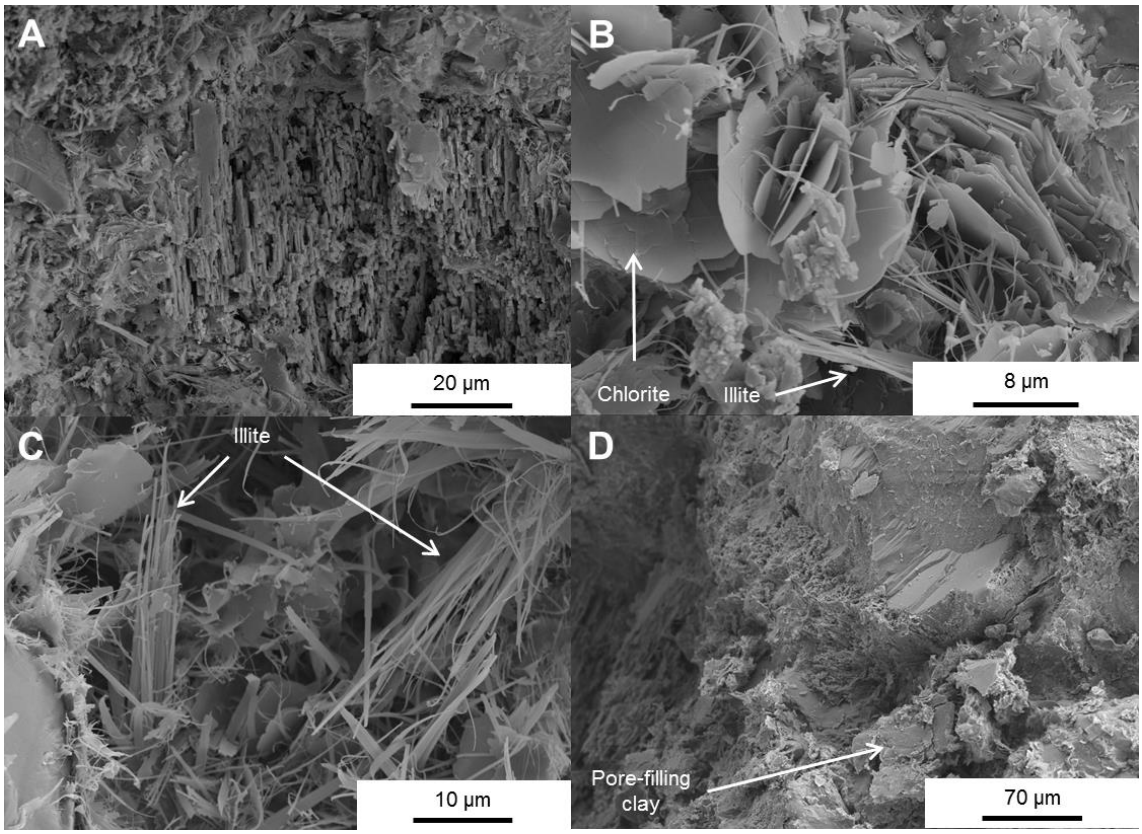

Figure II.8 SEM images of A) dissolved K-feldspar (2/5-10; 4580); B) authigenic chlorite platelets with authigenic illite fibres (2/5-10; 4580); C) authigenic pore-filling illite fibres (2/5-10; 4580); D) pore-filling clay within the dense grain arrangement (2/5-10; 4580).

Well 2/8-12S

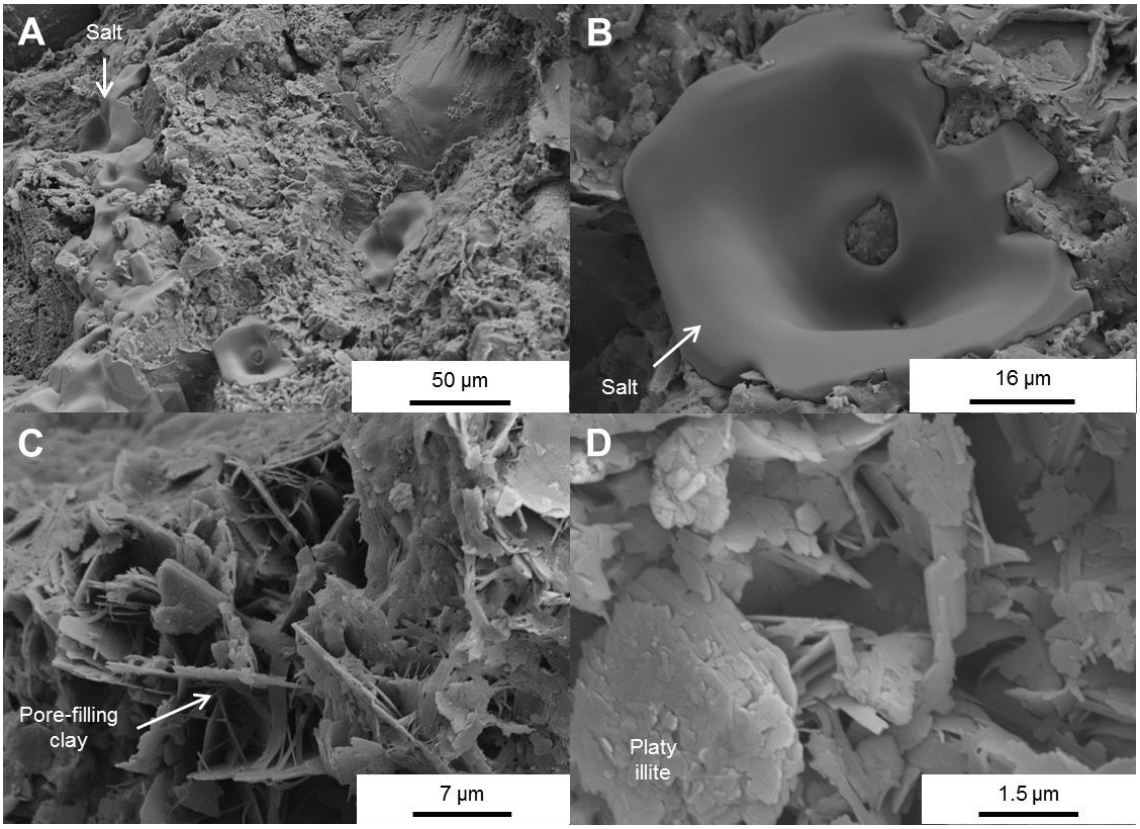

Figure II.9 SEM images of A) pore-filling salt (2/8-12S; 5229.7); B) pore-filling salt on clay mineral coating (2/8-12S; 5229.7); C) authigenic pore-filling clay (2/8-12S; 5229.7); D) platy illite crystals (2/8-12S; 5229.7).

SEM images Norwegian sector 6

Gaupe (well 6/3-1)

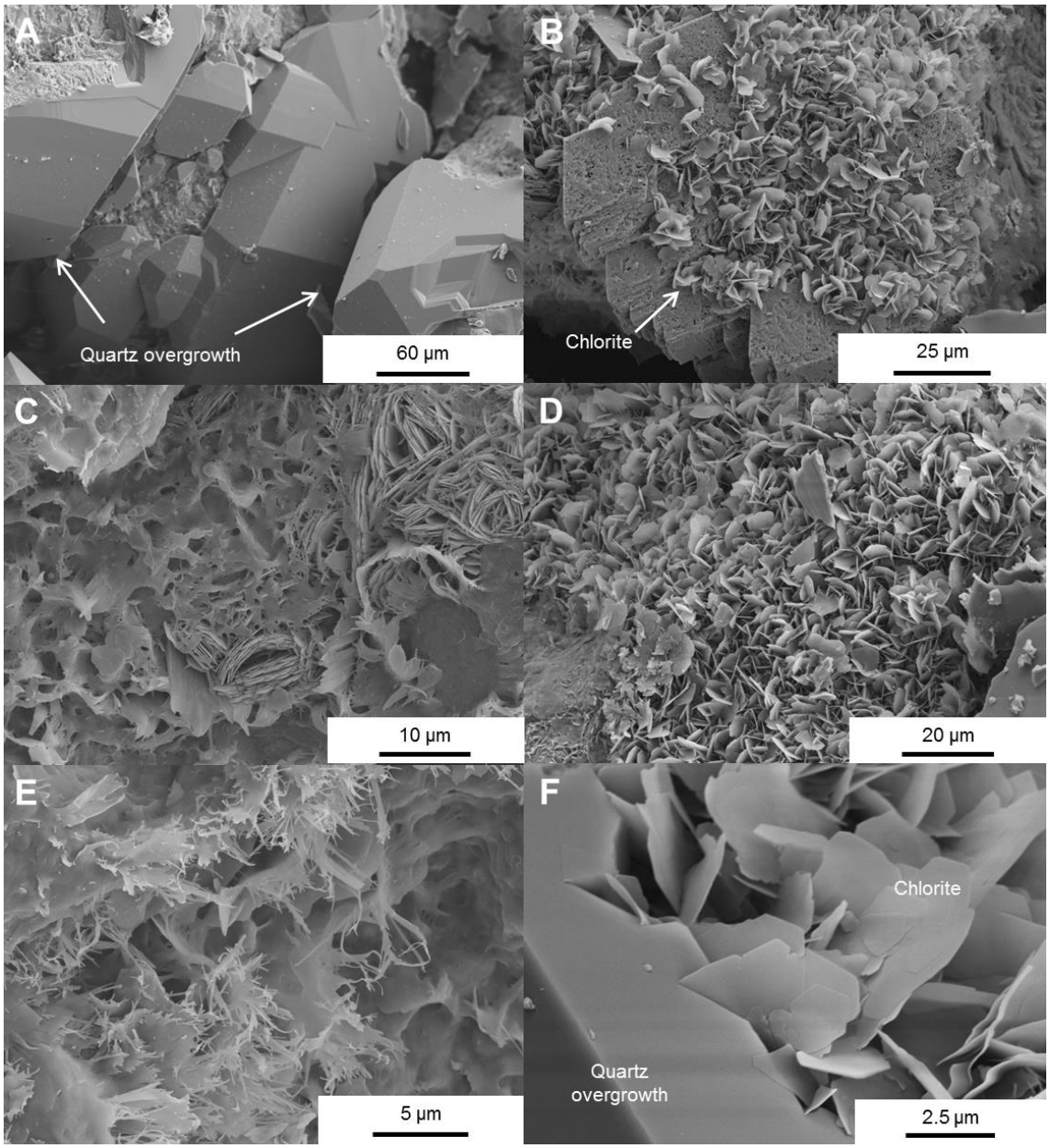

Figure II.10 SEM images of A) quartz overgrowths on detrital quartz grains (6/3-1; 3036.7); B) chlorite platelets on feldspar with partial dissolution (6/3-1; 3106.10); C) authigenic clay mineral coating, mixture of chlorite and illite (6/3-1; 3036.7); D) authigenic grain-coating chlorite (6/3-1; 3106.10); E) authigenic fibrous illite (6/3-1; 3036.7); F) intergrowth of authigenic chlorite crystals and quartz overgrowth (6/3-1; 3106.10).

SEM images Norwegian sector 7

Ula (well 7/12-6)

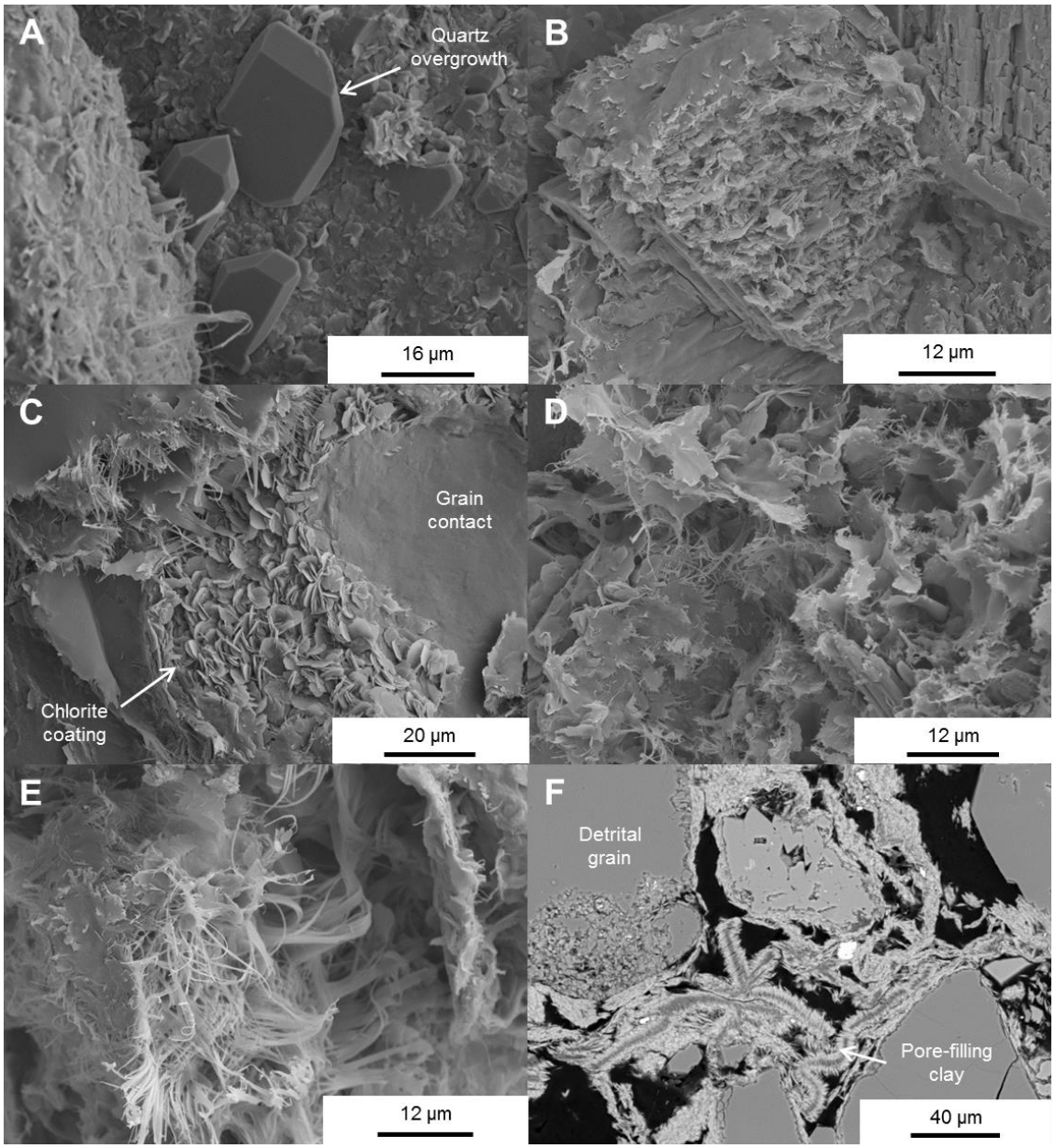

Figure II.11 SEM images of A) Quartz overgrowths on clay mineral-coated grain (7/12-6; 3585.90); B) authigenic clay minerals on partially dissolved feldspar grain (7/12-6; 3540.90); C) authigenic chlorite grain coating (7/12-6; 3585.90); D) authigenic flaky illite (7/12-6; 3540.90); E) authigenic fibrous illite (7/12-6; 3540.90); F) cross-section of elongated pore-filling clay aggregates (7/12-6; 3584.28).

Well 7/11-6

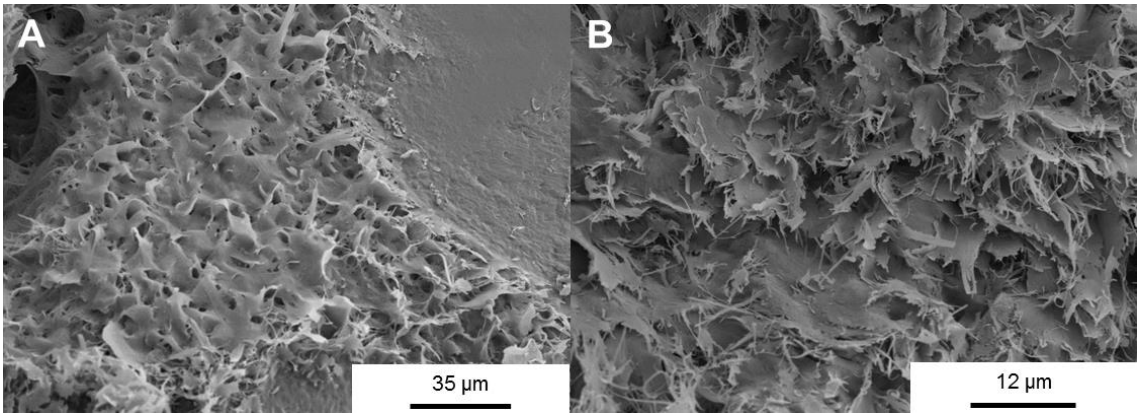

Figure II.12 SEM images of A) authigenic grain-coating illite (7/11-6; 4147.60); B) authigenic fibrous illite (7/11-6; 4147.60).

SEM-EDS data UK sector 22

Skua (well 22/24b-7)

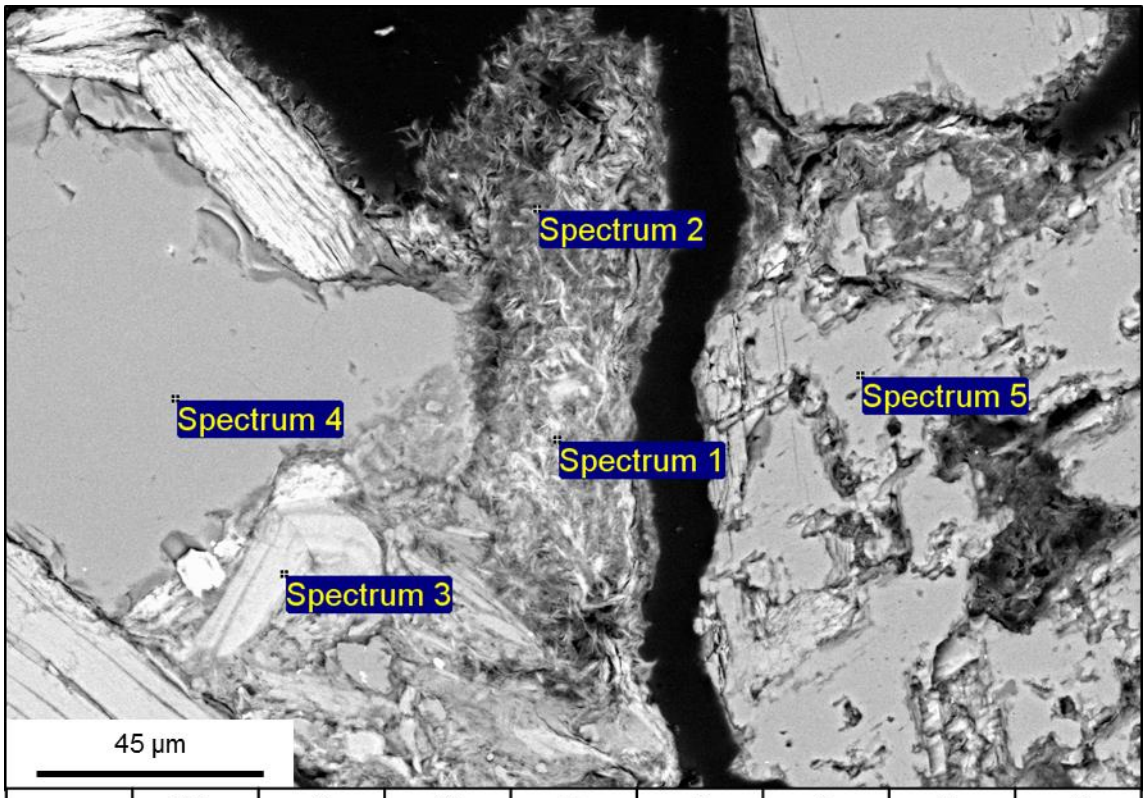

Spectrum	Mg	Al	Si	P	K	Ca	Fe	O
	[%]	[%]	[%]	[%]	[%]	[%]	[%]	[%]
1	7.83	13.44	16.56		0.42	1.31	18.54	41.90
2	8.36	14.01	19.01		0.81	0.93	12.99	43.88
3	14.15	13.12	15.35				14.71	42.68
4			46.74					53.26
5	8.53	9.85	32.67					48.95

Figure II.5 SEM-EDS analysis of a clay mineral coating and grains in the sample 11939'3'' (well 22/24b-7), analysis in atomic % normalised to oxygen by stoichiometry.

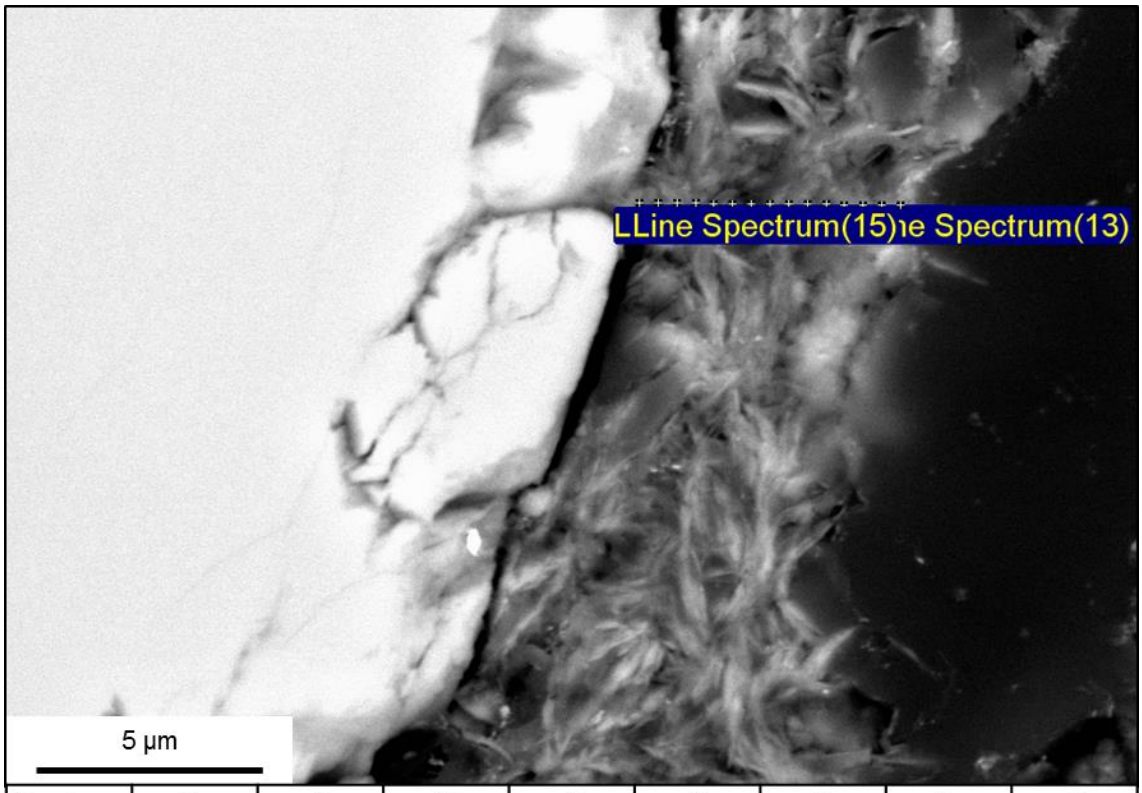

Spectrum	Mg	Al	Si	P	K	Ca	Fe	O
	[%]	[%]	[%]	[%]	[%]	[%]	[%]	[%]
1	4.34	10.95	22.41		7.91	0.46	10.90	43.04
2	4.71	11.78	22.62		6.77		10.39	43.72
3	6.66	12.71	22.24		4.14		9.62	44.63
4	7.35	13.81	21.90	0.76	2.82		7.57	45.79
5	7.45	13.79	22.14		2.14		9.04	45.43
6	7.79	15.06	20.32		1.30		10.57	44.96
7	8.27	14.73	20.58				11.22	45.20
8	8.71	14.41	19.60		0.53		12.26	44.50
9	9.07	14.68	18.23		0.84		12.72	43.85
10	8.51	13.83	17.44		0.83	0.54	16.09	42.76
11	8.14	13.70	16.54		0.45	0.55	18.60	42.02
12	8.84	13.82	16.72				18.23	42.39
13	8.86	13.38	17.06			0.48	17.77	42.45
14	8.93	13.76	16.47		0.50		18.17	42.18
15	8.54	13.39	16.34				19.88	41.84

Figure II.14 SEM-EDS analysis of a clay mineral coating in the sample 11939’3’’ (well 22/24b-7), analysis in atomic % normalised to oxygen by stoichiometry.

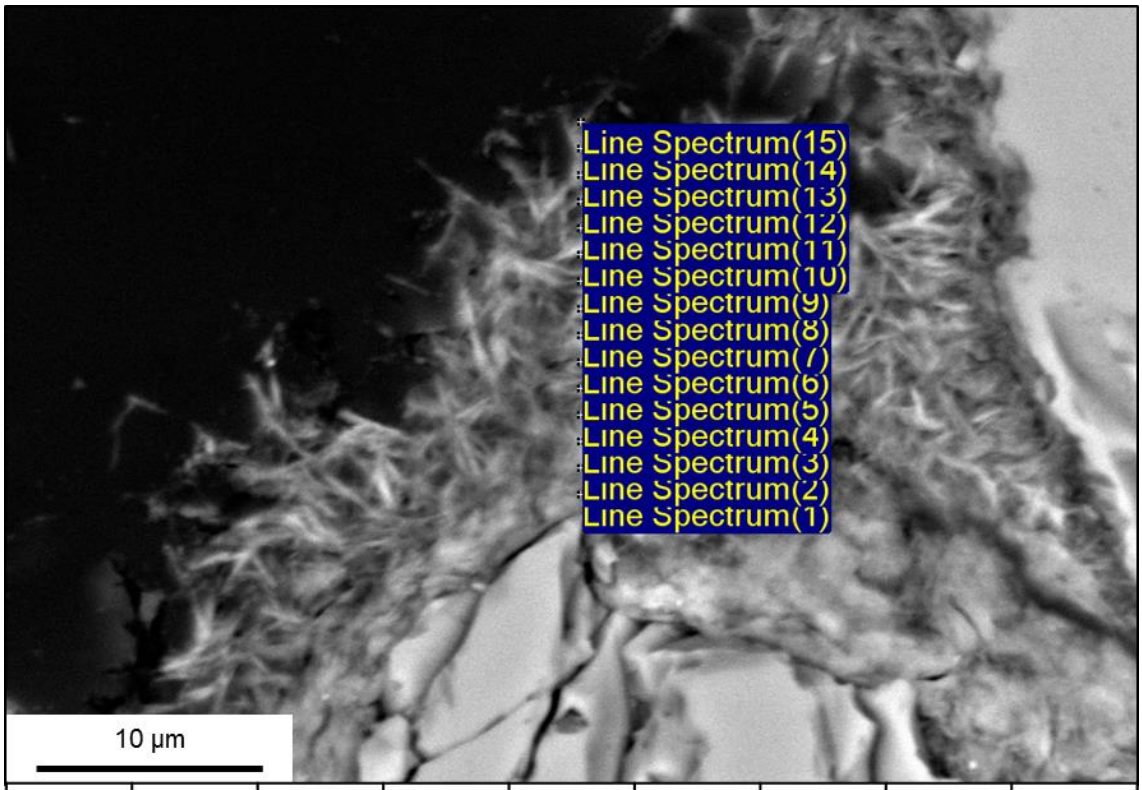

Spectrum	Mg	Al	Si	P	K	Ca	Fe	O
	[%]	[%]	[%]	[%]	[%]	[%]	[%]	[%]
1	3.50	12.31	26.34		4.58		7.06	46.22
2	6.13	13.16	21.68		2.81	0.53	11.25	44.44
3	8.48	14.02	18.92		0.68	0.41	13.67	43.82
4	7.49	13.82	18.28		0.78		16.64	42.98
5	8.10	13.96	18.15		0.59	0.83	15.15	43.22
6	7.68	13.70	16.81		0.71	0.63	18.40	42.06
7	8.22	13.15	16.85			0.62	19.13	42.03
8	8.15	13.86	17.33		0.72		17.37	42.56
9	7.82	13.79	17.11				18.94	42.33
10	8.33	13.24	17.14			0.44	18.57	42.28
11	8.06	13.05	16.95			0.89	19.03	42.02
12	8.10	13.03	16.47				20.77	41.63
13	9.14	13.11	15.89			0.63	19.58	41.64
14	8.64	12.60	16.12			0.72	20.49	41.42
15	9.28	12.74	15.57			0.97	20.12	41.33

Figure II.15 SEM-EDS analysis of a clay mineral coating in the sample 11939'3'' (well 22/24b-7), analysis in atomic % normalised to oxygen by stoichiometry.

Egret (well 22/24d-10)

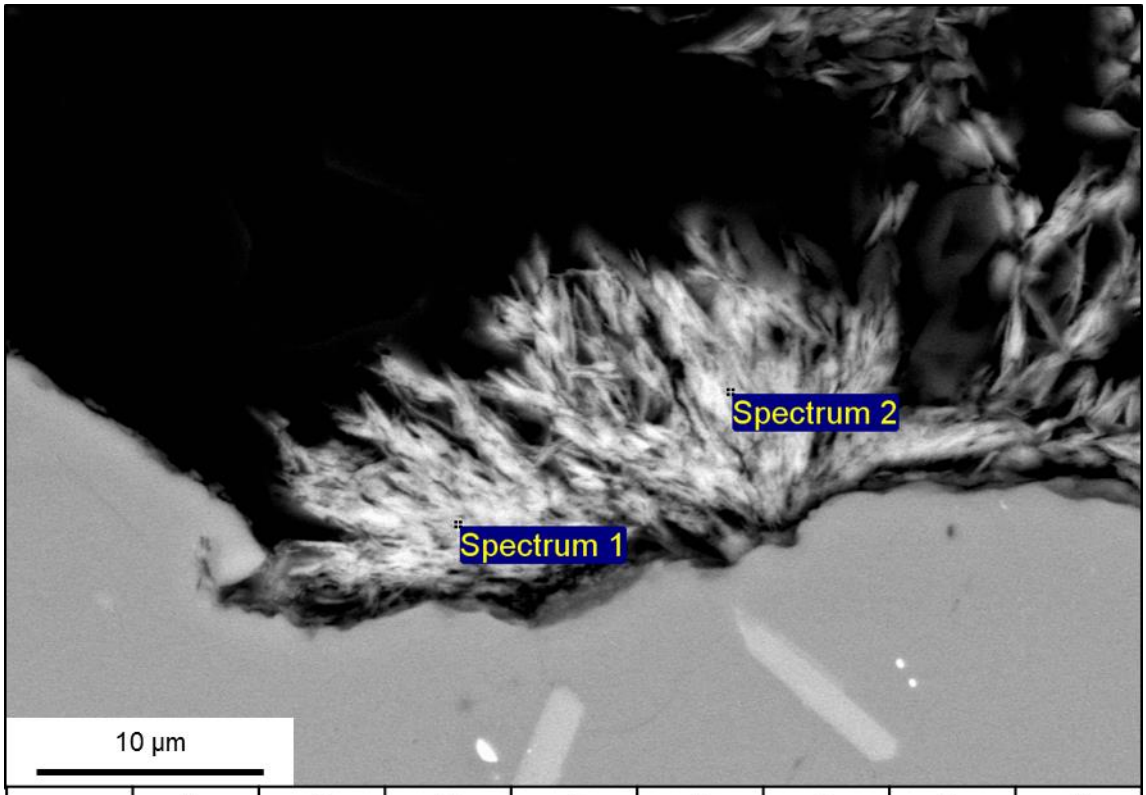

Spectrum	Mg	Al	Si	P	K	Ca	Fe	O
	[%]	[%]	[%]	[%]	[%]	[%]	[%]	[%]
1	7.89	10.18	13.34	0.81	0.19	0.20	7.61	59.78
2	8.47	10.03	12.51	0.98		0.30	8.21	59.50

Figure II.16 SEM-EDS analysis of a clay mineral coating in the sample 14500’0’’ (well 22/24d-10), analysis in atomic % normalised to oxygen by stoichiometry.

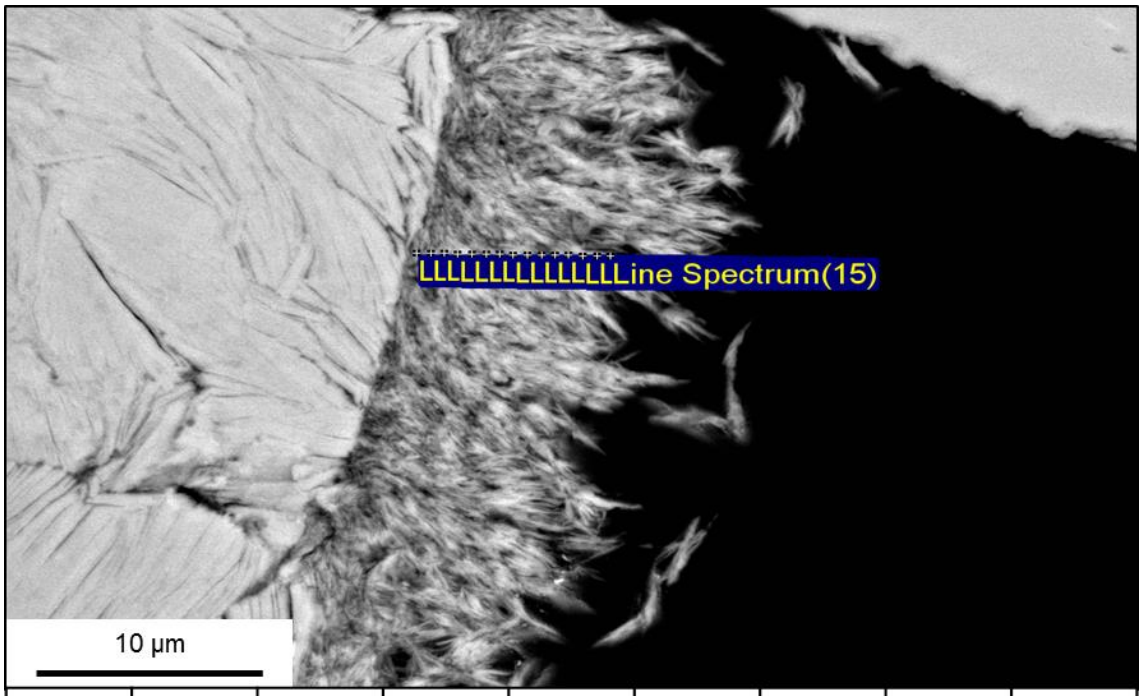

Spectrum	Mg	Al	Si	P	K	Ca	Fe	O
	[%]	[%]	[%]	[%]	[%]	[%]	[%]	[%]
1	8.64	10.03	14.00				7.83	59.51
2	8.81	10.32	13.29	0.47			7.53	59.58
3	8.46	10.47	12.96	0.69			7.80	59.62
4	8.52	10.69	13.16	0.32			7.82	59.49
5	9.20	10.24	12.92	0.40		0.23	7.68	59.32
6	9.04	10.12	13.91				7.43	59.49
7	8.84	10.57	13.27				8.03	59.28
8	8.45	10.91	12.93			0.23	8.30	59.19
9	8.72	10.42	12.97	0.33			8.22	59.34
10	8.31	11.05	13.46				7.69	59.49
11	8.94	10.49	13.04	0.46			7.60	59.48
12	8.58	10.59	12.71	0.73		0.2	7.62	59.55
13	8.72	10.39	12.18	1.19		0.24	7.71	59.58
14	9.05	10.60	12.65	0.54			7.78	59.38
15	8.85	11.08	13.18				7.52	59.36

Figure II.17 SEM-EDS analysis of a clay mineral coating in the sample 14500'0'' (well 22/24d-10), analysis in atomic % normalised to oxygen by stoichiometry.

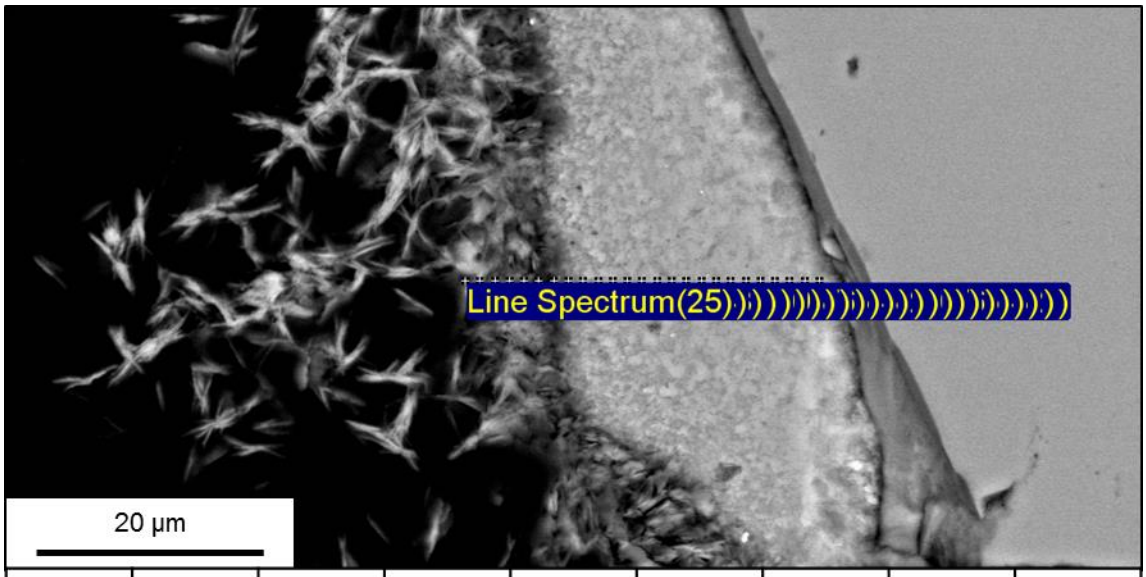

Spectrum	Mg	Al	Si	P	K	Ca	Fe	O
	[%]	[%]	[%]	[%]	[%]	[%]	[%]	[%]
1			33.33					66.67
2			33.33					66.67
3			33.02	0.27				66.71
4			33.26			0.11		66.63
5			33.23			0.15		66.62
6			33.09					66.70
7			33.33					66.67
8			33.03	0.20		0.11		66.66
9			33.33					66.67
10			33.33					66.67
11			33.03	0.26				66.71
12			33.33					66.67
13			32.88	0.39				66.73
14			32.47	0.59			0.25	66.68
15			33.04	0.258				66.71
16			33.33					66.67
17			33.33					66.67
18	0.27	0.16	32.60	0.18	0.19		0.19	66.42
19	1.92	2.06	28.74	0.37			1.75	65.16
20	1.67	2.03	29.45		0.24		1.43	65.17
21	6.14	7.55	19.13		0.24	0.20	5.36	61.39
22	8.17	10.12	14.79	0.39			6.31	60.22
23	8.45	10.21	14.31				7.32	59.71
24	8.40	9.78	14.47	0.59			6.63	60.13
25	9.08	11.04	13.76				6.48	59.64

Figure II.18 SEM-EDS analysis of a clay mineral coating and microquartz in the sample 14500'0'' (well 22/24d-10), analysis in atomic % normalised to oxygen by stoichiometry.

Seagull (well 22/29-2)

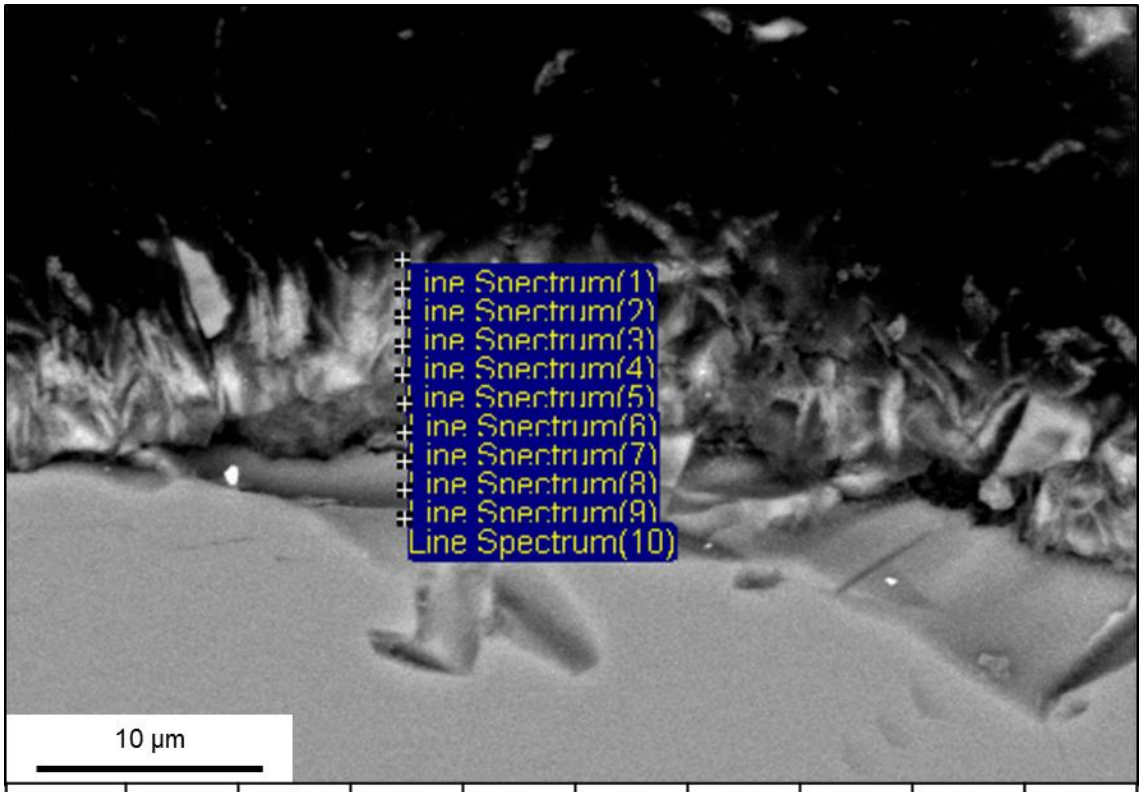

Spectrum	Mg	Al	Si	S	Cl	K	Ti	Fe	O
	[%]	[%]	[%]	[%]	[%]	[%]	[%]	[%]	[%]
1	8.27	10.91	12.41	0.56	0.50			8.11	59.24
2	9.41	10.58	12.88					8.05	59.08
3	9.81	10.55	12.98		0.34			7.36	58.95
4	9.12	10.19	13.32	0.37				7.41	59.58
5	7.33	9.74	16.07					6.39	60.47
6	4.08	7.66	19.55					7.02	61.69
7	2.57	4.97	19.77					11.55	61.13
8	0.41	0.89	31.43					1.32	65.94
9			33.21					0.19	66.60
10		0.35	32.90					0.20	66.54

Figure II.19 SEM-EDS analysis of a clay mineral coating in the sample 13741'10'' (well 22/29-2), analysis in atomic % normalised to oxygen by stoichiometry.

Seagull (well 22/29-3)

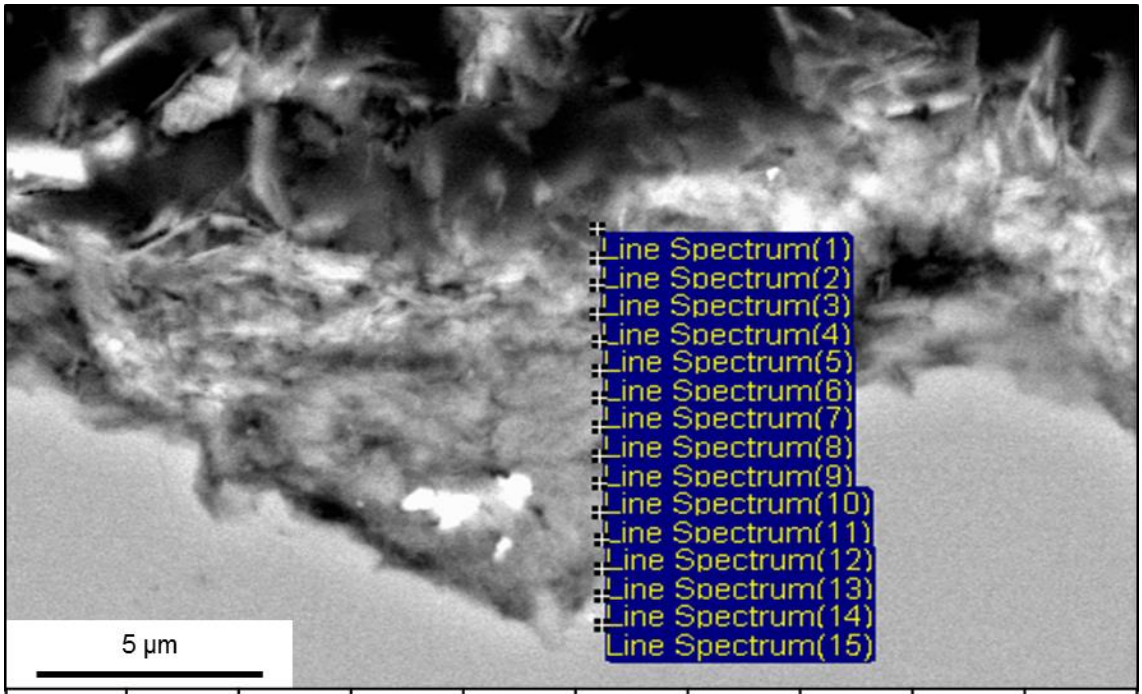

Spectrum	Mg	Al	Si	P	Cl	K	Ti	Fe	O
	[%]	[%]	[%]	[%]	[%]	[%]	[%]	[%]	[%]
1	6.87	10.97	14.16		0.47	0.53		7.54	59.45
2	5.67	12.55	14.03		0.36	0.75		6.85	59.78
3	6.11	10.86	14.71			0.73		7.71	59.89
4	5.24	10.86	16.26			1.36		5.78	60.51
5	4.06	10.83	17.81			2.28		3.99	61.04
6	2.64	10.15	20.57			3.32		1.32	61.99
7	2.02	10.38	20.91			3.61		0.93	62.15
8	1.93	10.60	20.74			3.65		0.96	62.11
9	1.80	10.44	20.82			3.95		0.95	62.03
10	1.78	9.98	21.30			3.68		1.03	62.23
11	1.82	9.84	20.92	0.46		3.45		1.10	62.40
12	1.70	8.69	22.39	0.38		3.04		0.89	62.90
13	1.41	6.74	24.61			2.53	0.28	0.93	63.50
14	0.84	4.16	28.06			1.62		0.65	64.66
15	0.43	2.15	30.41			0.83	0.24	0.29	65.65

Figure II.20 SEM-EDS analysis of a clay mineral coating in the sample 13910’0’’ (well 22/29-3), analysis in atomic % normalised to oxygen by stoichiometry.

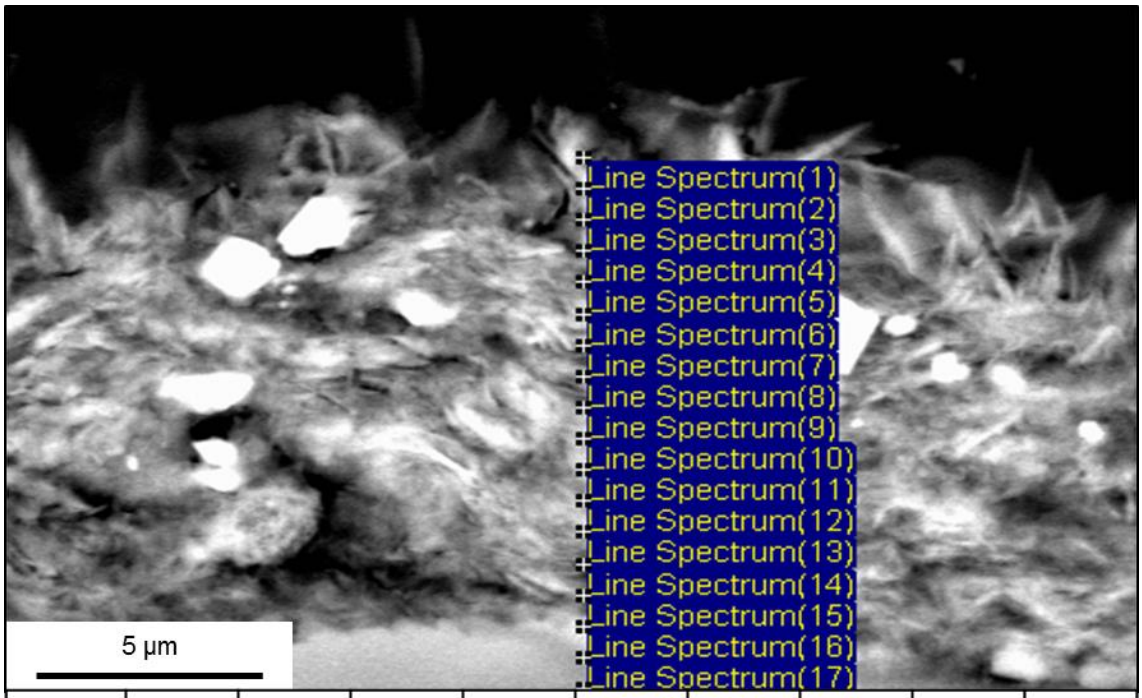

Spectrum	Mg	Al	Si	P	Cl	K	Ti	Fe	O
	[%]	[%]	[%]	[%]	[%]	[%]	[%]	[%]	[%]
1	7.88	11.92	13.21					7.40	59.59
2	6.44	9.57	11.02				4.41	8.45	60.11
3	6.56	10.34	12.60				2.22	8.29	60.00
4	6.80	10.72	13.37				1.38	7.67	60.06
5	6.65	11.17	13.72			0.40	0.85	7.23	59.98
6	6.45	11.01	13.06			0.33	1.94	7.04	60.17
7	6.51	9.77	11.55			0.41	5.04	6.07	60.64
8	4.95	9.13	11.21	0.47		0.79	6.61	5.48	61.35
9	6.24	10.56	13.94			0.96	1.14	7.21	59.94
10	6.97	11.05	14.00			0.49		7.84	59.64
11	6.83	11.21	13.76			0.47		8.17	59.57
12	6.52	10.72	14.49			0.76		7.78	59.74
13	6.50	11.16	14.38			0.91		7.30	59.75
14	5.96	10.50	15.86			0.84		6.50	60.34
15	5.26	8.83	17.85			0.97		6.20	60.89
16	3.37	5.70	23.29			0.78		3.99	62.87
17	0.61	1.77	30.91			0.36		0.54	65.81

Figure II.21 SEM-EDS analysis of a clay mineral coating in the sample 13910’0’’ (well 22/29-3), analysis in atomic % normalised to oxygen by stoichiometry.

Heron (well 22/29-5RE)

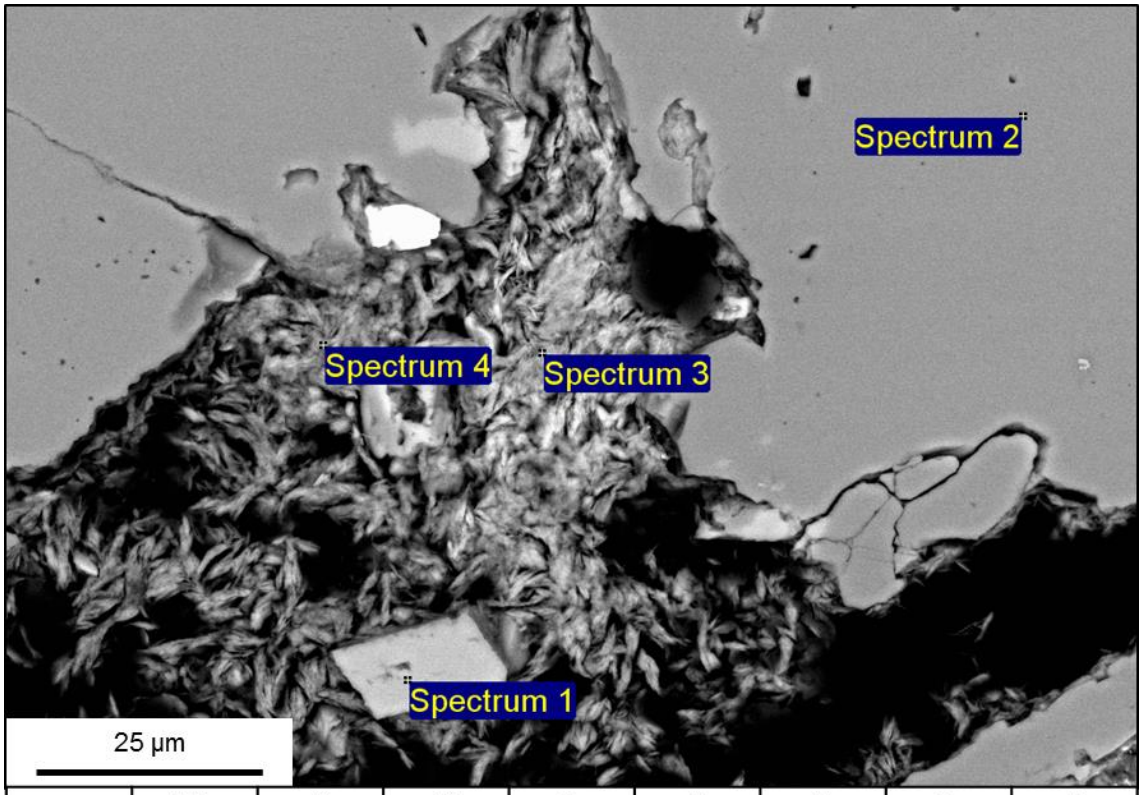

Spectrum	Mg	Al	Si	P	K	Ca	Fe	O
	[%]	[%]	[%]	[%]	[%]	[%]	[%]	[%]
1		9.26	31.36		12.80			46.58
2			46.74					53.26
3	7.56	13.19	18.64		1.02		16.66	42.93
4	7.21	11.64	15.91		0.64		24.28	40.31

Figure II.22 SEM-EDS analysis of a clay mineral coating and grains in the sample 15714’7’’ (well 22/29-5RE), analysis in atomic % normalised to oxygen by stoichiometry.

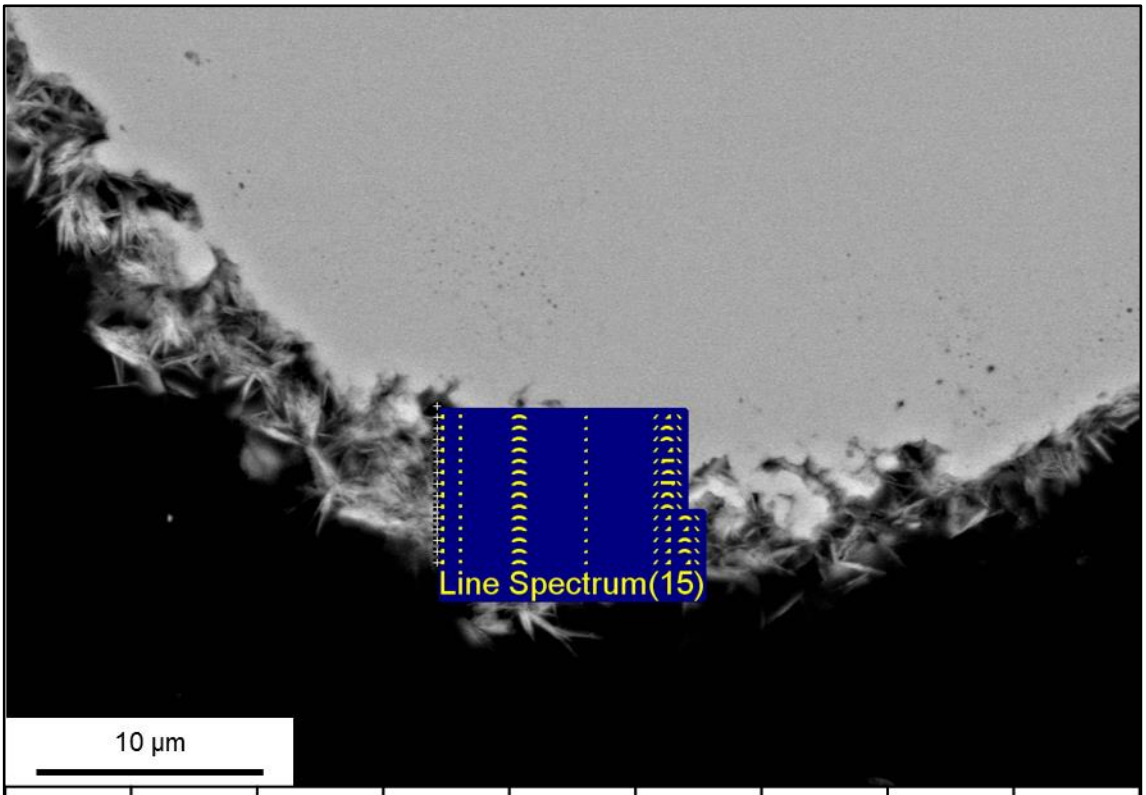

Spectrum	Mg	Al	Si	P	K	Ca	Fe	O
	[%]	[%]	[%]	[%]	[%]	[%]	[%]	[%]
1	0.27	0.23	32.96					66.54
2	2.11	2.46	28.24				2.45	64.74
3	1.80	1.98	29.22				1.89	65.11
4	4.02	4.62	24.18				3.93	63.25
5	3.19	3.54	25.97				3.42	63.87
6	3.42	3.82	25.40				3.70	63.66
7	4.79	6.37	21.57				4.90	62.37
8	6.28	8.01	18.34				6.20	61.17
9	6.73	8.98	16.89		0.23		6.55	60.63
10	7.17	9.99	15.43		0.54		6.78	60.08
11	7.92	10.70	14.24		0.28		7.13	59.73
12	8.02	10.37	13.88		0.21		8.04	59.48
13	7.99	10.67	13.67				8.16	59.50
14	7.44	10.33	14.02				8.62	59.59
15	7.59	10.42	13.13				9.69	59.17

Figure II.23 SEM-EDS analysis of a clay mineral coating in the sample 15714’7’’ (well 22/29-5RE), analysis in atomic % normalised to oxygen by stoichiometry.

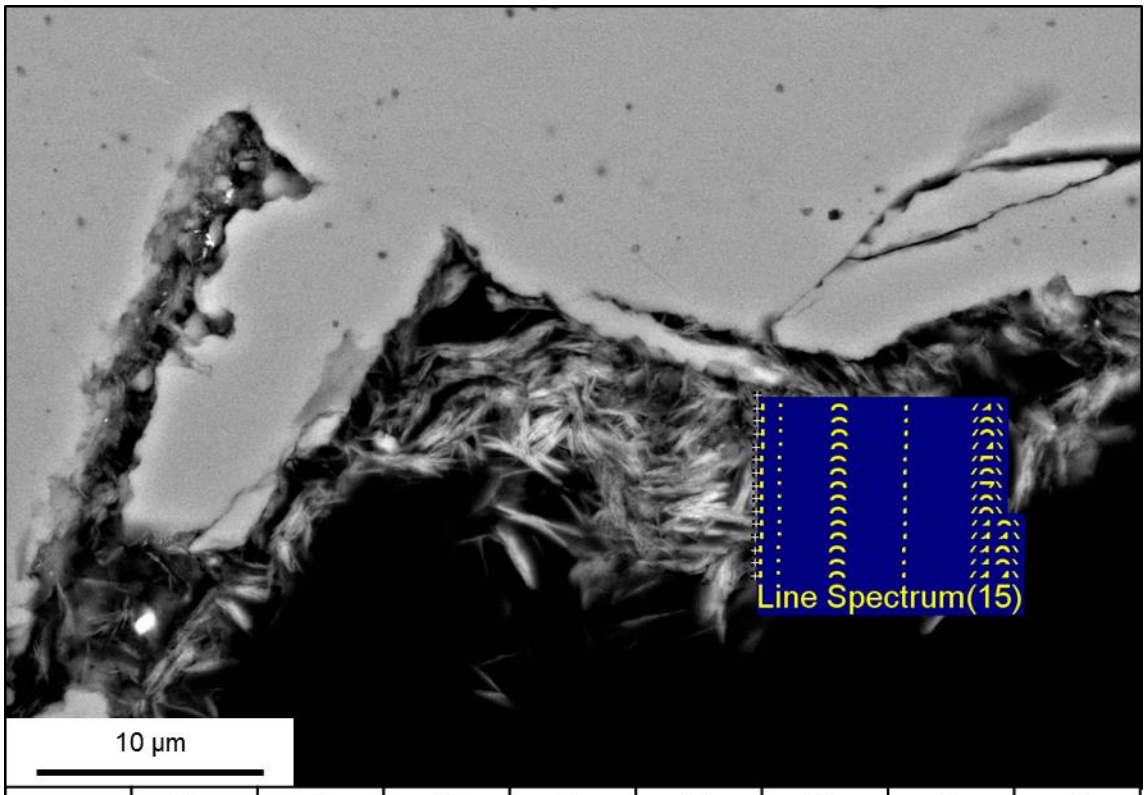

Spectrum	Mg	Al	Si	P	K	Ca	Fe	O
	[%]	[%]	[%]	[%]	[%]	[%]	[%]	[%]
1	4.65	7.05	19.40				7.44	61.46
2	6.19	8.96	15.98				8.65	60.23
3	6.44	9.23	14.74				9.91	59.68
4	7.93	9.89	14.16				8.46	59.55
5	7.86	11.15	13.70				7.65	59.64
6	8.43	10.88	13.89				7.14	59.66
7	8.72	11.12	13.44		0.30	0.25	6.74	59.43
8	8.05	10.86	13.72	0.35			7.18	59.84
9	8.25	11.22	13.51				7.46	59.56
10	8.09	10.83	13.60				7.97	59.51
11	8.13	11.36	12.88		0.23		8.18	59.22
12	7.73	10.61	13.85				8.24	59.58
13	7.49	10.38	13.08		0.26	0.36	9.36	59.07
14	8.15	11.19	13.16				8.12	59.38
15	8.50	11.42	13.15				7.50	59.43

Figure II.24 SEM-EDS analysis of a clay mineral coating in the sample 15714’7’’ (well 22/29-5RE), analysis in atomic % normalised to oxygen by stoichiometry.

Appendix III

Fluid inclusion data

UK sector 22

Skua (well 22/24b-7; sample 11909’4’’)

Sample: 22/24b-7; 11909'4''								
Host	Type	Th	±	Axes		Tm	Salinity	Note
				Long	Short			
		[°C]	[°C]	[µm]	[µm]	[°C]	[wt% NaCl eq.]	
Quartz Overgrowth Aqueous	P(L+V>L)	139.9	0.5	5	5	-14.5	18.3	
Quartz Overgrowth Aqueous	P(L+V>L)	144.2	0.4	16	5	-12.7	16.7	
Quartz Overgrowth Aqueous	P(L+V>L)	143.0	0.4	5	3	-12.4	16.4	
Quartz Overgrowth Aqueous	P(L+V>L)	142.3	0.4	3	4	-15.0	18.7	
Quartz Overgrowth Aqueous	P(L+V>L)	141.5	0.4	4	4	-15.9	19.4	
Quartz Overgrowth Aqueous	P(L+V>L)	154.5	0.7	4	3	-5.4	8.4	
Quartz Overgrowth Aqueous	P(L+V>L)	140.8	0.5	5	4	-15.7	19.3	
Quartz Overgrowth Aqueous	P(L+V>L)	137.3	0.6	4	4	-20.7	23.0	
Quartz Overgrowth Aqueous	P(L+V>L)	144.0	0.4	4	4	-15.0	18.7	
Quartz Overgrowth Aqueous	P(L+V>L)	156.2	0.8	3	3	-5.4	8.4	
Quartz Overgrowth Aqueous	P(L+V>L)	133.4	0.6	7	3	-16.5	19.9	
Quartz Overgrowth Aqueous	P(L+V>L)	137.1	0.6	7	3	-14.7	18.4	
Quartz Overgrowth Aqueous	P(L+V>L)	140.8	0.5	6	3	-12.9	16.8	
Quartz Overgrowth Aqueous	P(L+V>L)	140.4	0.5	7	5	-21.4	23.6	
Quartz Overgrowth Aqueous	P(L+V>L)	135.8	0.6	4	4	-15.6	19.2	
Quartz Overgrowth Aqueous	P(L+V>L)	135.9	0.6	14	12	-16.2	19.7	
Quartz Overgrowth Aqueous	P(L+V>L)	137.3	0.6	8	4	-14.3	18.1	
Quartz Overgrowth Aqueous	P(L+V>L)	145.7	0.3	11	5	-15.9	19.4	
Quartz Overgrowth Aqueous	P(L+V>L)	146.8	0.3	7	6	-14.1	17.9	
Quartz Overgrowth Aqueous	P(L+V>L)	144.6	0.4	7	4	-12.4	16.4	
Quartz Overgrowth Aqueous	P(L+V>L)	139.3	0.5	5	4	-13.9	17.7	
Quartz Grain Oil	S(L+V>L)	87.9	0.3	7	1	oil	oil	
Quartz Grain Oil	S(L+V>L)	91.7	0.4	6	1	oil	oil	
Quartz Grain Oil	S(L+V>L)	85.7	0.3	6	1	oil	oil	
Quartz Grain Oil	S(L+V>L)	88.9	0.4	7	5	oil	oil	
Quartz Grain Oil	S(L+V>L)	88.7	0.4	8	4	oil	oil	
Quartz Grain Oil	S(L+V>L)	118.2	0.9	15	4	oil	oil	
Quartz Grain Oil	S(L+V>L)	100.5	0.6	9	5	oil	oil	
Quartz Grain Oil	S(L+V>L)	85.6	0.3	17	6	oil	oil	
Quartz Grain Oil	S(L+V>L)	88.6	0.4	7	3	oil	oil	
Quartz Grain Oil	S(L+V>L)	81.6	0.3	8	6	oil	oil	
Quartz Grain Oil	S(L+V>L)	91.0	0.4	7	4	oil	oil	
Quartz Grain Oil	S(L+V>L)	100.1	0.6	8	4	oil	oil	
Feldspar Oil	F(L+V>L)	87.9	0.3	7	1	oil	oil	
Feldspar Oil	F(L+V>L)	91.7	0.4	6	1	oil	oil	
Feldspar Oil	F(L+V>L)	85.7	0.3	6	1	oil	oil	
Feldspar Oil	F(L+V>L)	88.9	0.4	7	5	oil	oil	
Feldspar Oil	F(L+V>L)	88.7	0.4	8	4	oil	oil	
Feldspar Oil	F(L+V>L)	118.2	0.9	15	4	oil	oil	
Feldspar Oil	F(L+V>L)	100.5	0.6	9	5	oil	oil	
Feldspar Oil	F(L+V>L)	85.6	0.3	17	6	oil	oil	
Feldspar Oil	F(L+V>L)	88.6	0.4	7	3	oil	oil	
Feldspar Oil	F(L+V>L)	81.6	0.3	8	6	oil	oil	
Feldspar Oil	F(L+V>L)	91.0	0.4	7	4	oil	oil	
Feldspar Oil	F(L+V>L)	100.1	0.6	8	4	oil	oil	

Table III.1 Aqueous and Non-aqueous fluid inclusion data table, including the inclusion host mineral and inclusion type, homogenization temperature (Th) with error (±), fluid inclusion dimensions with long and short axes, final melt temperature (Tm) and salinity, with uft: unable to freeze; M: metastable.

Skua (well 22/24b-7; sample 11931’0’’)

Sample: 22/24b-7; 11931'0''								
Host	**Type**	**Th**	**±**	**Axes**		**Tm**	**Salinity**	**Note**
				Long	**Short**			
		[°C]	**[°C]**	**[µm]**	**[µm]**	**[°C]**	**[wt% NaCl eq.]**	
Quartz Overgrowth Aqueous	P(L+V>L)	136.1	0.6	7	6	-14.9	18.6	
Quartz Overgrowth Aqueous	P(L+V>L)	132.6	0.6	8	5	-15.4	19.0	
Quartz Overgrowth Aqueous	P(L+V>L)	133.1	0.6	5	3	-16.9	20.2	
Quartz Overgrowth Aqueous	P(L+V>L)	139.9	0.5	11	2	-13.9	17.7	
Quartz Overgrowth Aqueous	P(L+V>L)	133.3	0.6	5	4	-17.1	20.4	
Quartz Overgrowth Aqueous	P(L+V>L)	138.6	0.5	4	4	-13.2	17.1	
Quartz Overgrowth Aqueous	P(L+V>L)	137.3	0.6	5	3	-13.6	17.5	
Quartz Overgrowth Aqueous	P(L+V>L)	133.5	0.6	5	4	-13.6	17.5	
Quartz Overgrowth Oil	P(L+V>L	83.3	0.3	6	2	oil	oil	
Feldspar Oil	F(L+V>L)	88.1	0.4	9	4	oil	oil	
Feldspar Oil	F(L+V>L)	83.6	0.3	7	7	oil	oil	
Carbonate Cement Aqueous	F(L+V>L)	141.8	0.4	15	14	-25.9	26.5	
Carbonate Cement Aqueous	F(L+V>L)	138.5	0.5	9	3	-25.4	26.2	
Carbonate Cement Aqueous	F(L+V>L)	140.0	0.5	12	6	-30.6	28.0	
Carbonate Cement Aqueous	F(L+V>L)	142.4	0.4	5	5	-27.6	27.3	
Carbonate Cement Aqueous	F(L+V>L)	143.4	0.4	7	6	-30.5	28.0	
Carbonate Cement Aqueous	F(L+V>L)	142.1	0.4	5	3	-30.5	28.0	
Carbonate Cement Aqueous	F(L+V>L)	142.3	0.4	4	2	-27.7	27.4	
Carbonate Cement Aqueous	F(L+V>L)	141.5	0.4	8	5	-31.4	28.3	
Carbonate Cement Aqueous	P(L+V>L)	140.4	0.5	6	5	-32.1	28.6	
Carbonate Cement Aqueous	P(L+V>L)	142.7	0.4	11	4	-28.5	27.6	
Carbonate Cement Aqueous	P(L+V>L)	144.5	0.4	6	6	-29.5	27.7	
Carbonate Cement Oil	P(L+V>L)	111.6	0.8	28	8	oil	oil	
Carbonate Cement Oil	P(L+V>L)	87.4	0.3	4	4	oil	oil	
Carbonate Cement Oil	P(L+V>L)	107.3	0.7	4	4	oil	oil	
Carbonate Cement Oil	P(L+V>L)	79.4	0.3	10	6	oil	oil	
Carbonate Cement Oil	P(L+V>L)	87.2	0.3	11	8	oil	oil	
Carbonate Cement Oil	P(L+V>L)	84.0	0.3	5	4	oil	oil	
Carbonate Cement Oil	P(L+V>L)	88.0	0.3	5	3	oil	oil	
Carbonate Cement Oil	P(L+V>L)	80.4	0.3	4	4	oil	oil	

Table III.2 Aqueous and Non-aqueous fluid inclusion data table, including the inclusion host mineral and inclusion type, homogenization temperature (Th) with error (±), fluid inclusion dimensions with long and short axes, final melt temperature (Tm) and salinity, with uft: unable to freeze; M: metastable.

Egret (well 22/24d-10; sample 15068’11’’)

Sample: 22/24d-10; 15068'11''								
Host	Type	Th	±	Axes		Tm	Salinity	Note
				Long	Short			
		[°C]	[°C]	[µm]	[µm]	[°C]	[wt% NaCl eq.]	
Quartz Overgrowth Aqueous	P(L+V>L)	160.1	1.1	12	10	-9.2	13.2	
Quartz Overgrowth Aqueous	P(L+V>L)	153.4	0.6	17	8	-9.2	13.2	
Quartz Overgrowth Aqueous	P(L+V>L)	155.8	0.8	3	2	-9.0	12.9	
Quartz Overgrowth Aqueous	P(L+V>L)	147.9	0.3	5	2	-9.6	13.6	
Quartz Overgrowth Aqueous	P(L+V>L)	146.0	0.3	7	5	-9.6	13.6	
Quartz Overgrowth Aqueous	P(L+V>L)	150.2	0.4	8	4	-10.1	14.1	
Quartz Overgrowth Aqueous	P(L+V>L)	149.4	0.4	5	4	-10.2	14.2	
Quartz Overgrowth Aqueous	P(L+V>L)	155.0	0.7	4	4	-9.1	13.0	
Quartz Overgrowth Aqueous	P(L+V>L)	150.7	0.4	4	4	-9.2	13.2	
Quartz Overgrowth Aqueous	P(L+V>L)	166.6	1.1	6	3	-8.8	12.7	
Quartz Overgrowth Aqueous	P(L+V>L)	152.3	0.5	7	6	-9.5	13.5	
Quartz Overgrowth Aqueous	P(L+V>L)	150.2	0.4	8	4	-9.5	13.5	
Quartz Overgrowth Aqueous	P(L+V>L)	151.6	0.5	5	2	-9.9	13.9	
Quartz Overgrowth Aqueous	P(L+V>L)	154.4	0.7	8	4	-10.1	14.1	
Quartz Overgrowth Aqueous	P(L+V>L)	171.0	1.0	7	4	-5.1	8.0	
Quartz Overgrowth Aqueous	P(L+V>L)	166.5	1.1	4	3	-8.8	12.7	
Quartz Overgrowth Aqueous	P(L+V>L)	152.2	0.5	5	3	-10.4	14.4	
Quartz Overgrowth Aqueous	P(L+V>L)	149.0	0.3	5	3	-10.8	14.8	
Quartz Overgrowth Aqueous	P(L+V>L)	145.4	0.3	4	3	-10.2	14.2	
Feldspar Aqueous	P(L+V>L)	148.2	0.3	15	12	-27.4	27.2	
Feldspar Aqueous	P(L+V>L)	145.7	0.3	11	4	-27.4	27.2	
Feldspar Aqueous	P(L+V>L)	147.0	0.3	8	8	-27.4	27.2	

Table III.3 Aqueous and Non-aqueous fluid inclusion data table, including the inclusion host mineral and inclusion type, homogenization temperature (Th) with error (±), fluid inclusion dimensions with long and short axes, final melt temperature (Tm) and salinity, with uft: unable to freeze; M: metastable.

Seagull (well 22/29-2; sample 13786’0’’)

Sample: 22/29-2; 13786'0''								
Host	Type	Th	±	Axes		Tm	Salinity	Note
				Long	Short			
		[°C]	[°C]	[µm]	[µm]	[°C]	[wt% NaCl eq.]	
Quartz Overgrowth Aqueous	P(L+V>L)	137.9	0.6	11	5	-19.7	22.3	
Quartz Overgrowth Aqueous	P(L+V>L)	143.4	0.4	5	3	-22.5	24.3	
Quartz Overgrowth Aqueous	P(L+V>L)	136.2	0.6	6	6	-20.3	22.7	
Quartz Grain Oil	S(L+V>L)	75.0	0.3	7	2	oil	oil	
Quartz Grain Oil	S(L+V>L)	72.3	0.3	3	2	oil	oil	
Quartz Grain Oil	S(L+V>L)	82.1	0.3	6	4	oil	oil	
Quartz Grain Oil	S(L+V>L)	108.6	0.7	5	4	oil	oil	
Quartz Grain Oil	S(L+V>L)	72.7	0.3	3	3	oil	oil	
Quartz Grain Oil	S(L+V>L)	72.9	0.3	3	2	oil	oil	
Intergranular Dolomite Aqueous	P(L+V>L)	135.8	0.6	14	5	-13.8	17.7	
Intergranular Dolomite Aqueous	P(L+V>L)	134.5	0.6	3	3	-15.3	18.9	
Intergranular Dolomite Aqueous	P(L+V>L)	84.8	0.3	10	5	-20.5	22.9	
Intergranular Dolomite Aqueous	P(L+V>L)	125.0	0.3	6	4	-16.6	20.0	
Intergranular Dolomite Aqueous	P(L+V>L)	116.7	0.9	14	5	-19.0	21.8	
Intergranular Dolomite Aqueous	P(L+V>L)	85.9	0.3	8	8	-20.5	22.9	

Table III.4 Aqueous and Non-aqueous fluid inclusion data table, including the inclusion host mineral and inclusion type, homogenization temperature (Th) with error (±), fluid inclusion dimensions with long and short axes, final melt temperature (Tm) and salinity, with uft: unable to freeze; M: metastable.

Seagull (well 22/29-2; sample 13875’4’’)

Sample: 22/29-3; 13875'4''								
Host	Type	Th	±	Axes		Tm	Salinity	Note
				Long	Short			
		[°C]	[°C]	[µm]	[µm]	[°C]	[wt% NaCl eq.]	
Quartz Overgrowth Aqueous	P(L+V>L)	134.7	0.7	4	4	-17.4	20.6	
Quartz Overgrowth Aqueous	P(L+V>L)	142.3	0.4	3	3	-16.2	19.7	
Quartz Overgrowth Aqueous	P(L+V>L)	144.0	0.4	5	5	-16.5	19.9	
Quartz Overgrowth Aqueous	P(L+V>L)	136.1	0.6	3	3	-17.5	20.7	
Quartz Overgrowth Aqueous	P(L+V>L)	130.9	0.5	6	3	-17.8	20.9	
Quartz Overgrowth Aqueous	P(L+V>L)	143.4	0.4	6	1	-17.5	20.7	
Quartz Overgrowth Aqueous	P(L+V>L)	139.3	0.5	6	2	-15.8	19.4	
Quartz Overgrowth Aqueous	P(L+V>L)	129.5	0.5	3	2	-21.7	23.8	
Quartz Overgrowth Aqueous	P(L+V>L)	134.1	0.6	3	2	4.7	-4.7	
Feldspar Aqueous	F(L+V>L)	135.9	0.6	12	7	-22.2	24.1	
Feldspar Aqueous	F(L+V>L)	136.1	0.6	5	5	-22.3	24.1	
Feldspar Aqueous	F(L+V>L)	137.0	0.6	4	3	-22.2	24.1	
Feldspar Aqueous	F(L+V>L)	133.7	0.6	3	3	-22.2	24.1	
Feldspar Aqueous	F(L+V>L)	132.5	0.6	12	4	-22.3	24.1	
Feldspar Oil	F(L+V>L)	79.3	0.3	7	4	oil	oil	
Feldspar Oil	F(L+V>L)	76.4	0.3	14	8	oil	oil	
Feldspar Oil	F(L+V>L)	68.4	0.3	10	6	oil	oil	
Feldspar Oil	F(L+V>L)	76.4	0.3	14	4	oil	oil	
Feldspar Oil	F(L+V>L)	115.7	0.9	18	2	oil	oil	
Feldspar Oil	F(L+V>L)	81.9	0.3	11	1	oil	oil	
Feldspar Oil	F(L+V>U)			23	9	oil	oil	
Feldspar Oil	F(L+V>L)	74.4	0.3	6	1	oil	oil	
Feldspar Oil	F(L+V>L)	79.8	0.3	7	2	oil	oil	
Feldspar Oil	F(L+V>L)	84.9	0.3	4	1	oil	oil	
Feldspar Oil	F(L+V>L)	97.9	0.5	6	5	oil	oil	
Feldspar Oil	F(L+V>L)	138.5	0.5	4	2	oil	oil	
Feldspar Oil	F(L+V>L)	80.0	0.3	5	1	oil	oil	
Feldspar Oil	F(L+V>L)	78.6	0.3	5	1	oil	oil	
Feldspar Oil	F(L+V>L)	75.6	0.3	4	1	oil	oil	
Feldspar Oil	F(L+V>L)	74.3	0.3	4	1	oil	oil	

Table III.5 Aqueous and Non-aqueous fluid inclusion data table, including the inclusion host mineral and inclusion type, homogenization temperature (Th) with error (±), fluid inclusion dimensions with long and short axes, final melt temperature (Tm) and salinity, with uft: unable to freeze; M: metastable.

Seagull (well 22/29-3; sample 13834’1’)

Sample: 22/29-3; 13834'1''								
Host	Type	Th	±	Axes		Tm	Salinity	Note
				Long	Short			
		[°C]	[°C]	[µm]	[µm]	[°C]	[wt% NaCl eq.]	
Quartz Overgrowth Aqueous	P(L+V>L)	132.9	0.6	4	4	-13.5	17.4	
Quartz Overgrowth Aqueous	P(L+V>L)	138.1	0.6	8	4	-13.7	17.6	
Quartz Overgrowth Aqueous	P(L+V>L)	141.1	0.5	6	6	-15.1	18.8	
Quartz Overgrowth Aqueous	P(L+V>L)	135.7	0.6	6	6	-15.1	18.8	
Quartz Overgrowth Aqueous	P(L+V>L)	139.0	0.5	10	7	-18.8	21.7	
Quartz Overgrowth Aqueous	P(L+V>L)	145.4	0.3	6	2	-13.3	17.2	
Quartz Overgrowth Aqueous	P(L+V>L)	141.3	0.5	7	4	-13.6	17.5	
Quartz Grain Oil	P(L+V>L)	65.0	0.3	7	5	oil	oil	

Table III.6 Aqueous and Non-aqueous fluid inclusion data table, including the inclusion host mineral and inclusion type, homogenization temperature (Th) with error (±), fluid inclusion dimensions with long and short axes, final melt temperature (Tm) and salinity, with uft: unable to freeze; M: metastable.

Seagull (well 22/29-3; sample 13875’4’’)

Sample: 22/29-3; 13875'4''								
Host	**Type**	**Th**	**±**	**Axes**		**Tm**	**Salinity**	**Note**
				Long	**Short**			
		[°C]	**[°C]**	**[µm]**	**[µm]**	**[°C]**	**[wt% NaCl eq.]**	
Quartz Overgrowth Aqueous	P(L+V>L)	132.0	0.6	5	2	-17.4	20.6	
Quartz Overgrowth Aqueous	P(L+V>L)	128.5	0.4	8	2	-16.2	19.7	
Quartz Grain Aqueous	S(L+V>L)	134.3	0.6	5	1	-10.7	14.7	
Quartz Grain Aqueous	S(L+V>L)	136.6	0.6	3	3	-11.0	15.0	
Quartz Grain Aqueous	S(L+V>L)	131.3	0.5	4	2	-11.0	15.0	
Quartz Grain Aqueous	S(L+V>L)	144.0	0.4	4	2	-6.0	9.2	
Quartz Grain Aqueous	S(L+V>L)	142.6	0.4	3	2	-6.0	9.2	
Feldspar Oil	F(L+V>L)	67.0	0.3	11	5	oil	oil	
Feldspar Oil	F(L+V>L)	69.4	0.3	9	3	oil	oil	
Feldspar Oil	F(L+V>L)	68.4	0.3	6	1	oil	oil	
Feldspar Oil	F(L+V>L)	67.1	0.3	3	2	oil	oil	
Feldspar Oil	F(L+V>L)	67.1	0.3	3	2	oil	oil	

Table III.7 Aqueous and Non-aqueous fluid inclusion data table, including the inclusion host mineral and inclusion type, homogenization temperature (Th) with error (±), fluid inclusion dimensions with long and short axes, final melt temperature (Tm) and salinity, with uft: unable to freeze; M: metastable.

Heron (well 22/29-5RE; sample 15691’6’’)

Sample: 22/29-5RE; 15691'6''								
Host	**Type**	**Th**	**±**	**Axes**		**Tm**	**Salinity**	**Note**
				Long	**Short**			
		[°C]	**[°C]**	**[µm]**	**[µm]**	**[°C]**	**[wt% NaCl eq.]**	
Quartz Overgrowth Aqueous	P(L+V>L)	104.0	0.6	10	9	-13.6	17.5	
Quartz Overgrowth Aqueous	P(L+V>L)	116.0	0.9	8	4	-16.3	19.8	
Quartz Overgrowth Aqueous	P(L+V>L)	111.0	0.8	7	3	-16.5	19.9	
Quartz Overgrowth Aqueous	P(L+V>L)	106.0	0.7	3	3	-20.6	22.9	
Quartz Overgrowth Oil	P(L+V>L)	69.8	0.3	7	3	oil	oil	
Quartz Overgrowth Oil	P(L+V>L)	75.3	0.3	10	4	oil	oil	
Quartz Overgrowth Oil	P(L+V>L)	76.3	0.3	22	14	oil	oil	
Quartz Overgrowth Oil	P(L+V>L)	76.1	0.3	8	4	oil	oil	
Quartz Overgrowth Oil	P(L+V>L)	72.1	0.3	4	3	oil	oil	
Quartz Grain Aqueous (Oil assoc.)	s(L+V>L)	137.4	0.6	7	5	-10.7	14.7	
Quartz Grain Aqueous (Oil assoc.)	S(L+V>L)	138.8	0.5	16	8	-10.1	14.1	
Quartz Grain Aqueous (Oil assoc.)	S(L+V>L)	131.1	0.5	16	7	-14.7	18.4	
Quartz Grain Aqueous (Oil assoc.)	S(L+V>L)	135.8	0.6	7	4	-10.1	14.1	
Quartz Grain Aqueous (Oil assoc.)	S(L+V>L)	138.9	0.5	6	3	-12.6	16.6	
Quartz Grain Aqueous (Oil assoc.)	S(L+V>L)	139.1	0.5	7	5	-12.5	16.5	
Quartz Grain Aqueous (Oil assoc.)	S(L+V>L)	135.1	0.7	6	4	0.7	-0.7	M
Quartz Grain Aqueous (Oil assoc.)	S(L+V>L)	138.3	0.6	5	3	2.0	-2.0	M
Quartz Grain Oil	S(L+V>L)	72.8	0.3	15	4	oil	oil	
Quartz Grain Oil	S(L+V>L)	76.0	0.3	5	4	oil	oil	
Quartz Grain Oil	S(L+V>L)	74.9	0.3	12	10	oil	oil	
Quartz Grain Oil	S(L+V>L)	73.8	0.3	3	2	oil	oil	
Quartz Grain Oil	S(L+V>L)	76.4	0.3	7	4	oil	oil	
Quartz Grain Oil	S(L+V>L)	76.7	0.3	5	3	oil	oil	
Quartz Grain Oil	S(L+V>L)	76.6	0.3	4	3	oil	oil	
Feldspar Oil	F(L+V>L)	77.8	0.3	17	9	oil	oil	
Feldspar Oil	F(L+V>L)	75.4	0.3	15	8	oil	oil	
Feldspar Oil	F(L+V>L)	87.9	0.3	16	8	oil	oil	
Feldspar Oil	F(L+V>L)	78.9	0.3	8	7	oil	oil	
Feldspar Oil	F(L+V>L)	75.5	0.3	25	14	oil	oil	
Feldspar Oil	F(L+V>L)	77.3	0.3	9	1	oil	oil	
Feldspar Oil	F(L+V>L)	77.0	0.3	6	3	oil	oil	
Feldspar Oil	F(L+V>L)	61.9	0.3	8	6	oil	oil	
Feldspar Oil	F(L+V>L)	61.4	0.3	6	3	oil	oil	
Feldspar Oil	F(L+V>L)	60.0	0.3	5	2	oil	oil	
Feldspar Oil	F(L+V>L)	62.3	0.3	5	5	oil	oil	

Table III.8 Aqueous and Non-aqueous fluid inclusion data table, including the inclusion host mineral and inclusion type, homogenization temperature (Th) with error (±), fluid inclusion dimensions with long and short axes, final melt temperature (Tm) and salinity, with uft: unable to freeze; M: metastable.

Heron (well 22/29-5RE; sample 15721’11’’)

Sample: 22/29-5RE; 15721'11''								
Host	Type	Th	±	Axes		Tm	Salinity	Note
				Long	Short			
		[°C]	[°C]	[µm]	[µm]	[°C]	[wt% NaCl eq.]	
Quartz Overgrowth Aqueous	P(L+V>L)	143.6	0.4	6	4	-13.6	17.5	
Quartz Overgrowth Aqueous	P(L+V>L)	145.4	0.3	15	4	-13.6	17.5	
Quartz Overgrowth Aqueous	P(L+V>L)	144.4	0.4	5	4	-14.5	18.3	
Quartz Overgrowth Aqueous	P(L+V>L)	143.1	0.4	6	5	-13.9	17.7	
Quartz Overgrowth Aqueous	P(L+V>L)	141.5	0.4	11	9	-13.8	17.7	
Quartz Overgrowth Aqueous	P(L+V>L)	133.7	0.6	3	3	-15.1	18.8	
Quartz Overgrowth Aqueous	P(L+V>L)	162.2	1.1	7	5	-21.7	23.8	
Quartz Overgrowth Aqueous	P(L+V>L)	163.3	1.1	4	4	-20.7	23.0	
Quartz Overgrowth Aqueous	P(L+V>L)	75.0	0.3	7	6	oil	oil	
Feldspar Oil	F(L+V>L)	74.4	0.3	4	4	oil	oil	
Feldspar Oil	F(L+V>L)	76.4	0.3	6	5	oil	oil	
Feldspar Oil	F(L+V>L)	75.5	0.3	4	4	oil	oil	
Feldspar Oil	F(L+V>L)	44.8	0.3	5	5	oil	oil	
Feldspar Oil	F(L+V>L)	81.4	0.3	4	4	oil	oil	
Feldspar Oil	F(L+V>L)	77.1	0.3	10	6	oil	oil	
Feldspar Oil	F(L+V>L)	75.3	0.3	8	4	oil	oil	
Feldspar Oil	F(L+V>L)	75.6	0.3	10	6	oil	oil	
Feldspar Oil	F(L+V>L)	76.2	0.3	5	5	oil	oil	
Feldspar Oil	F(L+V>L)	74.3	0.3	6	6	oil	oil	
Feldspar Oil	F(L+V>L)	79.9	0.3	8	5	oil	oil	
Feldspar Oil	F(L+V>L)	75.5	0.3	8	4	oil	oil	
Feldspar Oil	F(L+V>L)	73.9	0.3	17	5	oil	oil	
Feldspar Oil	F(L+V>L)	70.7	0.3	9	8	oil	oil	
Feldspar Oil	F(L+V>L)	95.4	0.5	7	6	oil	oil	
Feldspar Oil	F(L+V>L)	71.2	0.3	6	3	oil	oil	
Feldspar Oil	F(L+V>L)	70.8	0.3	5	3	oil	oil	
Feldspar Oil	F(L+V>L)	72.9	0.3	6	5	oil	oil	
Feldspar Oil	F(L+V>L)	77.0	0.3	8	7	oil	oil	
Feldspar Oil	F(L+V>L)	75.9	0.3	7	2	oil	oil	
Feldspar Oil	F(L+V>L)	75.9	0.3	5	4	oil	oil	
Feldspar Oil	F(L+V>L)	74.9	0.3	3	3	oil	oil	
Feldspar Oil	F(L+V>L)	72.9	0.3	5	1	oil	oil	
Feldspar Oil	F(L+V>L)	66.7	0.3	4	4	oil	oil	
Feldspar Oil	F(L+V>L)	74.7	0.3	5	5	oil	oil	
Feldspar Oil	F(L+V>L)	76.4	0.3	5	5	oil	oil	
Feldspar Oil	F(L+V>L)	67.0	0.3	6	5	oil	oil	
Feldspar Oil	F(L+V>L)	73.7	0.3	8	7	oil	oil	

Table III.9 Aqueous and Non-aqueous fluid inclusion data table, including the inclusion host mineral and inclusion type, homogenization temperature (Th) with error (±), fluid inclusion dimensions with long and short axes, final melt temperature (Tm) and salinity, with uft: unable to freeze; M: metastable.

Norwegian sector 7

Cod (well 7/11-7; sample 14966’0’’)

Sample: 7/11-7; 14966'0''								
Host	Type	Th	±	Axes		Tm	Salinity	Note
				Long	Short			
		[°C]	[°C]	[µm]	[µm]	[°C]	[wt% NaCl eq.]	
Quartz Overgrowth Aqueous	P(L+V>L)	144.2	0.4	8	5	-9.8	13.8	
Quartz Overgrowth Aqueous	P(L+V>L)	142.7	0.4	5	4	-15.0	18.7	
Quartz Overgrowth Aqueous	P(L+V>L)	139.5	0.5	3	3	-12.7	16.7	
Carbonate Aqueous	P(L+V>L)	134.2	0.6	6	4	-21.4	23.5	
Carbonate Aqueous	P(L+V>L)	133.5	0.6	7	5	-23.2	24.8	
Carbonate Oil	P(L+V>L)	98.5	0.5	3	3	oil	oil	
Carbonate Oil	P(L+V>L)	93.3	0.4	5	4	oil	oil	
Carbonate Oil	P(L+V>L)	106.2	0.7	7	2	oil	oil	
Carbonate Oil	P(L+V>L)	84.3	0.3	6	2	oil	oil	
Carbonate Oil	P(L+V>L)	98.8	0.5	9	5	oil	oil	
Carbonate Oil	P(L+V>L)	91.7	0.4	5	4	oil	oil	
Carbonate Oil	P(L+V>L)	97.0	0.5	3	2	oil	oil	
Carbonate Oil	P(L+V>L)	97.0	0.5	2	2	oil	oil	
Carbonate Oil	P(L+V>L)	83.5	0.3	7	5	oil	oil	
Carbonate Oil	P(L+V>L)	87.1	0.3	6	5	oil	oil	
Carbonate Oil	P(L+V>L)	94.8	0.5	4	4	oil	oil	
Carbonate Oil	P(L+V>L)	87.9	0.3	5	4	oil	oil	
Carbonate Oil	P(L+V>L)	92.5	0.4	8	4	oil	oil	
Carbonate Oil	P(L+V>L)	94.7	0.5	3	3	oil	oil	
Carbonate Oil	P(L+V>L)	95.2	0.5	5	3	oil	oil	
Carbonate Oil	P(L+V>L)	93.5	0.4	7	3	oil	oil	
Carbonate Oil	P(L+V>L)	95.5	0.5	7	6	oil	oil	
Carbonate Oil	P(L+V>L)	89.9	0.4	3	3	oil	oil	
Carbonate Oil	P(L+V>L)	91.5	0.4	5	5	oil	oil	
Carbonate Oil	P(L+V>L)	88.6	0.4	11	10	oil	oil	
Carbonate Oil	P(L+V>L)	90.0	0.4	8	5	oil	oil	
Carbonate Oil	P(L+V>L)	95.2	0.5	10	3	oil	oil	
Carbonate Oil	P(L+V>L)	90.0	0.4	4	3	oil	oil	
Carbonate Oil	P(L+V>L)	94.9	0.5	6	5	oil	oil	
Carbonate Oil	P(L+V>L)	89.0	0.4	4	2	oil	oil	
Carbonate Oil	P(L+V>L)	87.6	0.3	4	2	oil	oil	
Carbonate Oil	P(L+V>L)	93.4	0.4	3	3	oil	oil	
Carbonate Oil	P(L+V>L)	89.5	0.4	4	3	oil	oil	
Carbonate Oil	P(L+V>L)	96.2	0.5	7	3	oil	oil	
Carbonate Oil	P(L+V>L)	85.7	0.3	5	4	oil	oil	
Carbonate Oil	P(L+V>L)	94.1	0.4	7	3	oil	oil	
Carbonate Oil	P(L+V>L)	92.0	0.4	4	3	oil	oil	
Carbonate Oil	P(L+V>L)	88.0	0.3	4	3	oil	oil	
Carbonate Oil	P(L+V>L)	83.5	0.3	7	5	oil	oil	
Carbonate Oil	P(L+V>L)	86.7	0.3	11	4	oil	oil	
Carbonate Oil	P(L+V>L)	93.5	0.4	4	3	oil	oil	
Carbonate Oil	P(L+V>L)	89.1	0.4	3	3	oil	oil	
Carbonate Oil	P(L+V>L)	82.9	0.3	5	3	oil	oil	
Carbonate Oil	P(L+V>L)	95.4	0.5	8	6	oil	oil	
Carbonate Oil	P(L+V>L)	92.9	0.4	5	5	oil	oil	
Carbonate Oil	P(L+V>L)	93.4	0.4	4	4	oil	oil	
Carbonate Oil	P(L+V>L)	84.0	0.3	5	4	oil	oil	
Carbonate Oil	P(L+V>L)	90.4	0.4	6	3	oil	oil	
Carbonate Oil	P(L+V>L)	88.4	0.4	3	3	oil	oil	
Carbonate Oil	P(L+V>L)	113.2	0.8	3	3	oil	oil	

Table III.10 Aqueous and Non-aqueous fluid inclusion data table, including the inclusion host mineral and inclusion type, homogenization temperature (Th) with error (±), fluid inclusion dimensions with long and short axes, final melt temperature (Tm) and salinity, with uft: unable to freeze; M: metastable.

Ula (well 7/12-6; sample 3530.42)

Sample: 7/12-6; 3530.42								
Host	Type	Th	±	Axes		Tm	Salinity	Note
				Long	Short			
		[°C]	[°C]	[µm]	[µm]	[°C]	[wt% NaCl eq.]	
Detrital Quartz Grain Oil	S(L+V>L)	94.3	0.4	5	2	oil	oil	
Detrital Quartz Grain Oil	S(L+V>L)	94.4	0.4	5	2	oil	oil	
Detrital Quartz Grain Oil	S(L+V>L)	124.0	0.3	7	2	oil	oil	
Detrital Quartz Grain Oil	S(L+V>L)	94.7	0.5	11	3	oil	oil	
Detrital Quartz Grain Oil	S(L+V>L)	95.8	0.5	4	3	oil	oil	
Detrital Quartz Grain Oil	S(L+V>L)	99.6	0.5	3	3	oil	oil	

Table III.11 Aqueous and Non-aqueous fluid inclusion data table, including the inclusion host mineral and inclusion type, homogenization temperature (Th) with error (±), fluid inclusion dimensions with long and short axes, final melt temperature (Tm) and salinity, with uft: unable to freeze; M: metastable.

Ula (well 7/12-6; sample 3636.55)

Sample: 7/12-6; 3636.55								
Host	Type	Th	±	Axes		Tm	Salinity	Note
				Long	Short			
		[°C]	[°C]	[µm]	[µm]	[°C]	[wt% NaCl eq.]	
Carbonate Aqueous	P(L+V>L)	87.5	0.3	5	3	-25.7	26.4	
Carbonate Aqueous	P(L+V>L)	103.5	0.6	17	6	0.7	-0.7	
Carbonate Aqueous	P(L+V>L)	79.3	0.3	7	3	-26.1	26.6	
Carbonate Aqueous	P(L+V>L)	83.8	0.3	4	3	utf	utf	
Carbonate Aqueous	P(L+V>L)	85.4	0.3	5	5	utf	utf	
Carbonate Aqueous	P(L+V>L)	84.0	0.3	5	4	-25.3	26.2	
Carbonate Aqueous	P(L+V>L)	108.3	0.7	6	5	-21.3	23.4	
Carbonate Aqueous	P(L+V>L)	108.1	0.7	6	5	-20.9	23.2	
Carbonate Aqueous	P(L+V>L)	138.7	0.5	14	6	utf	utf	
Carbonate Aqueous	P(L+V>L)	135.9	0.6	5	2	-9.6	13.6	
Carbonate Aqueous	P(L+V>L)	136.7	0.6	6	4	-23.2	24.8	
Carbonate Aqueous	P(L+V>L)	78.7	0.3	11	7	-23.4	24.9	
Carbonate Aqueous	P(L+V>L)	134.3	0.6	15	9	-13.5	17.4	
Carbonate Aqueous	P(L+V>L)	129.5	0.5	5	3	-13.5	17.4	
Carbonate Aqueous	P(L+V>L)	111.8	0.8	7	3	-11.1	15.1	
Carbonate Aqueous	P(L+V>L)	121.8	0.5	14	3	utf	utf	
Carbonate Aqueous	P(L+V>L)	117.9	0.9	5	6	utf	utf	
Carbonate Aqueous	P(L+V>L)	108.8	0.7	10	10	-21.6	23.7	
Carbonate Aqueous	P(L+V>L)	122.5	0.3	4	4	utf	utf	
Carbonate Aqueous	P(L+V>L)	112.7	0.8	3	3	-10.1	14.1	
Carbonate Aqueous	P(L+V>L)	108.3	0.7	10	7	-11.0	15.0	
Carbonate Aqueous	P(L+V>L)	77.6	0.3	8	3	-24.5	25.7	
Carbonate Aqueous	P(L+V>L)	104.2	0.6	8	5	-11.3	12.4	
Carbonate Aqueous	P(L+V>L)	135.9	0.6	3	3	-8.1	11.9	
Carbonate Aqueous	P(L+V>L)	137.0	0.6	7	5	-9.0	12.9	
Carbonate Aqueous	P(L+V>L)	83.1	0.3	6	3	-25.9	26.5	
Carbonate Aqueous	P(L+V>L)	105.0	0.6	3	3	-12.8	16.8	
Carbonate Aqueous	P(L+V>L)	111.8	0.8	3	3	-12.6	16.6	
Carbonate Aqueous	P(L+V>L)	132.6	0.6	11	3	-10.5	14.5	

Table III.12 Aqueous and Non-aqueous fluid inclusion data table, including the inclusion host mineral and inclusion type, homogenization temperature (Th) with error (±), fluid inclusion dimensions with long and short axes, final melt temperature (Tm) and salinity, with uft: unable to freeze; M: metastable.

Appendix IV

XRD data

Bulk rock XRD data Seagull (well 22/29-2)

Sample	Depth	Illite/ Smectite	Illite & Mica	Kaolinite	Chlorite	Quartz	K-Feldspar	Plagioclase	Calcite	Dolomite	Siderite	Barite	Pyrite	Total
	[ft]	[%]	[%]	[%]	[%]	[%]	[%]	[%]	[%]	[%]	[%]	[%]	[%]	[%]
A	13692.50	0.0	3.1	0.0	1.8	81.7	7.9	3.5	0.0	0.0	0.0	2.1	0.0	100
B	13695.00	TR	9.4	0.0	2.0	71.5	9.6	5.1	0.0	0.0	0.0	2.3	0.0	100
C	13703.75	0.0	17.4	0.0	7.6	58.2	9.5	6.8	0.0	0.0	0.0	0.6	0.0	100
D	13709.33	0.0	8.8	0.0	3.8	73.8	7.8	4.9	0.0	0.0	0.0	0.9	0.0	100
E	13719.92	0.0	8.0	0.0	6.0	74.4	7.1	4.0	0.0	0.0	0.0	0.5	0.0	100
F	13730.00	0.0	12.6	0.0	3.0	68.5	9.5	6.2	0.0	0.0	TR	0.0	TR	100

Table IV.1 Bulk rock XRD results for the Seagull samples A-F from the well 22/29-2, with the weight percentage of the clay fraction relative to the bulk sample.

Clay fraction XRD data Seagull (well 22/29-2)

Sample	Depth	Wt. % <2µm	Illite/smectite				Illite			Kaolinite			Chlorite			Quartz		Barite	
			A	B	Order	Illite	A	B	Crys	A	B	Crys	A	B	Crys	A	B	A	B
	[ft]		[%]	[%]		[%]	[%]	[%]		[%]	[%]		[%]	[%]		[%]	[%]	[%]	[%]
A	13692.50	4.7	0.0	0.0			51.0	2.4	P	0.0	0.0		37.7	1.8	M	3.8	0.2	7.6	0.4
B	13695.00	4.1	TR	TR	O	70-80	47.6	2.0	P	0.0	0.0		42.4	1.7	M	3.9	0.2	6.1	0.2
C	13703.75	4.6	0.0	0.0			42.7	2.0	M	0.0	0.0		48.5	2.2	M	6.3	0.3	2.5	0.1
D	13709.33	2.8	0.0	0.0			33.5	0.9	P	0.0	0.0		59.6	1.7	M	3.5	0.1	3.5	0.1
E	13719.92	3.0	0.0	0.0			15.5	0.5	P	0.0	0.0		77.9	2.3	M	3.9	0.1	2.7	0.1
F	13730.00	2.4	0.0	0.0			55.5	1.4	P	0.0	0.0		36.4	0.9	M	8.1	0.2	0.0	0.0

Table IV.2 Clay fraction XRD results for the Seagull samples A-F from the well 22/29-2, with the weight percentage of the clay fraction (Wt.% <2µm), the weight percentage of the clay minerals relative to the size fraction (A), the weight percentage of the clay fraction relative to the bulk sample (B), the mixed-layer ordering of illite/smectite (Order; RI: Random Interstratified (R0); O: Ordered Interstratification (R1); LR: Long-range Ordering (R3)) and the crystallinity of the clay minerals (Crys; VW: Very Well Crystallised; W: Well Crystallised; M: Moderately Crystallised; P: Poorly Crystallised)

Bulk rock XRD data Seagull (well 22/29-3)

Sample	Depth	Illite/ Smectite	Illite & Mica	Kaolinite	Chlorite	Quartz	K-Feldspar	Plagioclase	Calcite	Dolomite	Siderite	Barite	Pyrite	Total
	[ft]	[%]	[%]	[%]	[%]	[%]	[%]	[%]	[%]	[%]	[%]	[%]	[%]	[%]
G	13781.33	TR	9.3	0.0	3.3	76.3	8.2	2.8	0.0	0.0	0.0	0.0	0.0	100
H	13787.25	TR	8.2	0.0	3.4	79.6	6.6	2.2	0.0	0.0	0.0	0.0	0.0	100
I	13790.83	TR	10.8	0.0	2.8	78.9	6.2	1.2	0.0	0.0	0.0	0.0	0.0	100
J	13799.50	0.0	15.1	0.0	2.2	73.6	8.5	0.6	0.0	0.0	0.0	0.0	0.0	100
K	13805.33	TR	15.3	0.0	2.3	74.6	7.8	0.0	0.0	0.0	0.0	0.0	0.0	100
L	13815.50	0.0	6.2	0.0	1.5	86.7	5.2	0.4	0.0	0.0	0.0	0.0	0.0	100

Table IV.3 Bulk rock XRD results for the Seagull samples G-L from the well 22/29-3, with the weight percentage of the clay fraction relative to the bulk sample.

Clay fraction XRD data Seagull (well 22/29-3)

Sample	Depth	Wt. % <2µm	Illite/smectite				Illite			Kaolinite			Chlorite			Quartz		Barite	
			A	B	Order	Illite	A	B	Crys	A	B	Crys	A	B	Crys	A	B	A	B
	[ft]		[%]	[%]		[%]	[%]	[%]		[%]	[%]		[%]	[%]		[%]	[%]	[%]	[%]
G	13781.33	3.8	TR	TR	O	70-80	40.1	1.5	M	0.0	0.0		54.8	2.1	M	5.1	0.2	0.0	0.0
H	13787.25	4.8	TR	TR	O	70-80	33.2	1.6	M	0.0	0.0		62.9	3.0	M	3.9	0.2	0.0	0.0
I	13790.83	3.0	TR	TR	O	70-80	32.4	1.0	M	0.0	0.0		63.4	1.9	M	4.2	0.1	0.0	0.0
J	13799.50	3.4	0.0	0.0			57.3	1.9	M	0.0	0.0		38.3	1.3	M	4.4	0.1	0.0	0.0
K	13805.33	3.7	TR	TR	O	70-80	52.0	1.9	M	0.0	0.0		43.9	1.6	M	4.1	0.1	0.0	0.0
L	13815.50	3.2	0.0	0.0			51.6	1.7	M	0.0	0.0		41.0	1.3	M	7.5	0.2	0.0	0.0

Table IV.4 Clay fraction XRD results for the Seagull samples G-L from the well 22/29-3, with the weight percentage of the clay fraction (Wt.% <2µm), the weight percentage of the clay minerals relative to the size fraction (A), the weight percentage of the clay fraction relative to the bulk sample (B), the mixed-layer ordering of illite/smectite (Order; RI: Random Interstratified (R0); O: Ordered Interstratification (R1); LR: Long-range Ordering (R3)) and the crystallinity of the clay minerals (Crys; VW: Very Well Crystallised; W: Well Crystallised; M: Moderately Crystallised; P: Poorly Crystallised

Bibliography

Aagaard, P., J. S. Jahren, A. O. Harstad, O. Nilsen, and M. Ramm, 2000, Formation of grain-coating chlorite in sandstones. Laboratory synthesized vs. natural occurrences: Clay Minerals, v. 35, no. 1, p. 261–261, doi:10.1180/000985500546639.

Aase, N. E., P. A. Bjørkum, and P. H. Nadeau, 1996, The Effect of Grain-Coating Microquartz on Preservation of Reservoir Porosity: AAPG Bulletin, v. 80, no. 10, p. 1654–1673, doi:10.1306/64EDA0F0-1724-11D7-8645000102C1865D.

Aase, N. E., and O. Walderhaug, 2005, The effect of hydrocarbons on quartz cementation: diagenesis in the Upper Jurassic sandstones of the Miller Field, North Sea, revisited: Petroleum Geoscience, v. 11, no. 3, p. 215–223, doi:10.1144/1354-079304-648.

Abercrombie, H. J., I. E. Hutcheon, J. D. Bloch, and P. de Caritat, 1994, Silica activity and the smectite-illite reaction: Geology, v. 22, no. 6, p. 539–542, doi:10.1130/0091-7613(1994)022<0539:SAATSI>2.3.CO.

Ahn, J. H., D. R. Peacor, and D. S. Coombs, 1988, Formation mechanisms of illite, chlorite and mixed-layer illite-chlorite in Triassic volcanogenic sediments from the Southland Syncline, New Zealand: Contributions to Mineralogy and Petrology, v. 99, no. 1, p. 82–89, doi:10.1007/BF00399368.

Ajdukiewicz, J. M., and R. H. Lander, 2010, Sandstone reservoir quality prediction: The state of the art: AAPG Bulletin, v. 94, no. 8, p. 1083–1091, doi:10.1306/intro060110.

Ajdukiewicz, J. M., and R. E. Larese, 2012, How clay grain coats inhibit quartz cement and preserve porosity in deeply buried sandstones: Observations and experiments: AAPG Bulletin, v. 96, no. 11, p. 2091–2119, doi:10.1306/02211211075.

Ajdukiewicz, J. M., P. H. Nicholson, and W. L. Esch, 2010, Prediction of deep reservoir quality using early diagenetic process models in the Jurassic Norphlet Formation, Gulf of Mexico: AAPG Bulletin, v. 94, no. 8, p. 1189–1227, doi:10.1306/04211009152.

Allen, P. A., and J. R. Allen, 2005, Basin Analysis: Principls and Applications: Oxford, Wiley-Blackwell, 560 p.

Altaner, S. P., and R. F. Ylagan, 1997, Comparison of structural models of mixed-layer illite/smectite and reaction mechanisms of smectite illitization: Clays and Clay Minerals, v. 45, no. 4, p. 517–533, doi:10.1346/CCMN.1997.0450404.

Andrews-Speed, C. P., E. R. Oxburgh, and B. A. Cooper, 1984, Temperature and depth-dependent heat flow in western North Sea: AAPG Bulletin, v. 68, no. 11, p. 1764–1781.

Anjos, S. M. C., L. F. De Ros, and C. M. A. Silva, 2003, Chlorite authigenesis and porosity preservation in the Upper Cretaceous marine sandstones of the Santos Basin, offshore eastern Brazil: International Association of Sedimentology Special Publication, v. 34, p. 291–316.

Antonellini, M. A., A. Aydin, and D. D. Pollard, 1994, Microstructure of deformation bands in porous sandstones at Arches National Park, Utah: Journal of Structural Geology, v. 16, no. 7, p. 941–959, doi:10.1016/0191-8141(94)90077-9.

Aplin, A. C., S. R. Larter, M. A. Bigge, G. Macleod, R. E. Swarbrick, and D. Grunberger, 2000, PVTX history of the North Sea's Judy oilfield: Journal of Geochemical Exploration, v. 69-70, p. 641–644, doi:10.1016/S0375-6742(00)00066-2.

Archer, S. G., G. I. Alsop, a. J. Hartley, N. T. Grant, and R. Hodgkinson, 2012, Salt tectonics, sediments and prospectivity: an introduction: Geological Society, London, Special Publications, v. 363, no. 1, p. 1–6, doi:10.1144/SP363.1.

Archer, S., S. Ward, S. Menad, I. Shahim, N. T. Grant, H. Sloan, and A. Cole, 2010, The Jasmine discovery, Central North Sea, UKCS, *in* Petroleum Geology: From Mature Basins to New Frontiers—Proceedings of the 7th Petroleum Geology Conference: Geological Society of London, p. 225–243, doi:10.1144/0070225.

Audet, D. M., 1996, Compaction and overpressuring in Pleistocene sediments on the Louisana Shelf, Gulf of Mexico: Marine and Petroleum Geology, v. 13, no. 5, p. 467–474.

Audet, D. M., and J. D. C. McConnell, 1992, Forward modelling of porosity and pore pressure evolution in sedimentary basins: Basin Research, v. 4, no. 2, p. 147–162.

Bahlis, A. B., and L. F. De Ros, 2013, Origin and impact of authigenic chlorite in the Upper Cretaceous sandstone reservoirs of the Santos Basin, eastern Brazil: Petroleum Geoscience, v. 19, no. 2, p. 185–199, doi:10.1144/petgeo2011-007.

Banham, S. G., and N. P. Mountney, 2013a, Controls on fluvial sedimentary architecture and sediment-fill state in salt-walled mini-basins: Triassic Moenkopi Formation, Salt Anticline Region, SE Utah, USA: Basin Research, v. 25, no. 6, p. 709–737, doi:10.1111/bre.12022.

Banham, S. G., and N. P. Mountney, 2013b, Evolution of fluvial systems in salt-walled mini-basins: A review and new insights: Sedimentary Geology, v. 296, p. 142–166, doi:10.1016/j.sedgeo.2013.08.010.

Barclay, S. A., and R. H. Worden, 2000, Effects of Reservoir Wettability on Quartz Cementation in Oil Fields, *in* R. H. Worden, and S. Morad, eds., Quartz Cementation in Sandstones: Oxford, UK, Blackwell Publishing Ltd., p. 103–117, doi:10.1002/9781444304237.ch8.

Barclay, S. A., R. H. Worden, J. Parnell, D. L. Hall, and S. M. Sterner, 2000, Assessment of Fluid Contacts and Compartmentalization in Sandstone Reservoirs Using Fluid Inclusions: An Example from the Magnus Oil Field, North Sea: AAPG Bulletin, v. 84, no. 4, p. 489–504, doi:10.1306/C9EBCE2D-1735-11D7-8645000102C1865D.

Barde, J.-P., P. Chamberlain, M. Galavazi, P. Gralla, J. Harwijanto, J. Marsky, and F. van den Belt, 2002, Sedimentation during halokinesis: Permo-Triassic reservoirs of the Saigak Field, Precaspian Basin, Kazakhstan: Petroleum Geoscience, v. 8, no. 2, p. 177–187, doi:10.1144/petgeo.8.2.177.

Bayliss, P., 1975, Nomenclature of the Trioctahedral Chlorites: Canadian Mineralogist, v. 13, p. 178–180.

Beard, D. C., and P. K. Weyl, 1973, Influence of texture on porosity of unconsolidated sands: AAPG Bulletin, v. 57, no. 2, p. 349–369, doi:10.1306/819A4272-16C5-11D7-8645000102C1865D.

Becker, S. P., P. Eichhubl, S. E. Laubach, R. M. Reed, R. H. Lander, and R. J. Bodnar, 2010, A 48 m.y. history of fracture opening, temperature, and uid pressure: Cretaceous Travis Peak Formation, East Texas basin: Bulletin of the Geological Society of America, v. 122, no. 7-8, p. 1081–1093, doi:10.1130/B30067.1.

Berger, A., S. Gier, and P. Krois, 2009, Porosity-preserving chlorite cements in shallow-marine volcaniclastic sandstones: Evidence from cretaceous sandstones of the Sawan gas field, Pakistan: AAPG Bulletin, v. 93, no. 5, p. 595–615, doi:10.1306/01300908096.

Du Bernard, X., P. Eichhubl, and A. Aydin, 2002, Dilation bands: A new form of localized failure in granular media: Geophysical Research Letters, v. 29, no. 24, p. 21–29, doi:10.1029/2002GL015966.

Billault, V., D. Beaufort, A. Baronnet, and J. C. Lacharpagne, 2003, A nanopetrographic and textural study of grain-coating chlorites in sandstone reservoirs: Clay Minerals, v. 38, no. 3, p. 315–328, doi:10.1180/0009855033830098.

Bishop, D. J., 1996, Regional distribution and geometry of salt diapirs and supra-Zechstein Group faults in the western and central North Sea: Marine and Petroleum Geology, v. 13, no. 4, p. 355–364, doi:10.1016/0264-8172(95)00081-X.

Bjørkum, P. A., 1996, How Important is Pressure in Causing Dissolution of Quartz in Sandstones? p. 147–154, doi:10.1306/D42682DE-2B26-11D7-8648000102C1865D.

Bjørkum, P. A., E. H. Oelkers, P. H. Nadeau, O. Walderhaug, and W. M. Murphy, 1998, Porosity Prediction in Quartzose Sandstones as a Function of Time, Temperature, Depth, Stylolite Frequency, and Hydrocarbon Saturation: AAPG Bulletin, v. 82 (1998), no. 4, p. 637–647, doi:10.1306/1D9BC5CF-172D-11D7-8645000102C1865D.

Bjørkum, P. A., O. Walderhaug, and N. E. Aase, 1993, A model for the effect of illitization on porosity and quartz cementation of sandstones: Journal of Sedimentary Research, v. 63, no. 6, p. 1089–1091.

Bjørlykke, K., 1999, An Overview of Factors Controlling Rates of Compaction, Fluid Generation and Flow in Sedimentary Basins, *in* B. Jamtveit, and P. Meakin, eds., Growth, Dissolution and Pattern Formation in Geosystems: Dordrecht, Springer, p. 381–404, doi:10.1007/978-94-015-9179-9_18.

Bjørlykke, K., 2014, Relationships between depositional environments, burial history and rock properties. Some principal aspects of diagenetic process in sedimentary basins: Sedimentary Geology, v. 301, p. 1–14, doi:10.1016/j.sedgeo.2013.12.002.

Bloch, S., R. H. Lander, and L. M. Bonnell, 2002, Anomalously high porosity and permeability in deeply buried sandstone reservoirs: Origin and predictability: AAPG Bulletin, v. 86, no. 2, p. 301–328, doi:10.1306/61EEDABC-173E-11D7-8645000102C1865D.

Bredehoeft, J. D., R. D. Djevanshir, and K. R. Belitz, 1988, Lateral fluid flow in a compacting sand-shale sequence: South Caspian basin.: American Association of Petroleum Geologists Bulletin, v. 72, no. 4, p. 416–424, doi:10.1306/703C9A1E-1707-11D7-8645000102C1865D.

Burrus, J., 1998, Overpressure models for clastic rocks, their relation to hydrocarbon expulsion: a critical re-evaluation: AAPG Memoir, v. 70, p. 35–63.

Carr, A. D., 2003, Thermal history model for the South Central Graben, North Sea, derived using both tectonics and maturation: International Journal of Coal Geology, v. 54, no. 1-2, p. 3–19, doi:10.1016/S0166-5162(03)00017-X.

Charpentier, D., R. H. Worden, C. G. Dillon, and A. C. Aplin, 2003, Fabric development and the smectite to illite transition in Gulf of Mexico mudstones: An image analysis approach: Journal of Geochemical Exploration, v. 78-79, no. 03, p. 459–463, doi:10.1016/S0375-6742(03)00073-6.

Chen, G., G. Du, G. Zhang, Q. Wang, C. Lv, and J. Chen, 2011, Chlorite cement and its effect on the reservoir quality of sandstones from the Panyu low-uplift, Pearl River Mouth Basin: Petroleum Science, v. 8, no. 2, p. 143–150, doi:10.1007/s12182-011-0127-z.

Chuhan, F. A., A. Kjeldstad, K. Bjørlykke, and K. Høeg, 2002, Porosity loss in sand by grain crushing - Experimental evidence and relevance to reservoir quality: Marine and Petroleum Geology, v. 19, no. 1, p. 39–53, doi:10.1016/S0264-8172(01)00049-6.

Clark, J. A., J. A. Cartwright, and S. A. Stewart, 1999, Mesozoic dissolution tectonics on the West Central shelf, UK Central North Sea: Marine and Petroleum Geology, v. 16, no. 3, p. 283–300, doi:10.1016/S0264-8172(98)00040-3.

Crocker, M. E., and L. M. Marchin, 1988, Wettability and Adsorption Characteristics of Crude-Oil Asphaltene and Polar Fractions: Journal of Petroleum Technology, v. 40, no. 04, p. 470–474, doi:10.2118/14885-PA.

Deer, W. A., R. A. Howie, and J. Zussman, 1992, An Introduction to the rock-forming minerals: Harlow, Pearson Eduction Limited, 510 p.

Dewers, T., and P. Ortoleva, 1991, Influences of clay minerals on sandstone cementation and pressure solution: Geology, v. 19, no. 10, p. 1045–1048, doi:10.1130/0091-7613(1991)019<1045:IOCMOS>2.3.CO;2.

Dixon, S. A., D. M. Summers, and R. C. Surdam, 1989, Diagenesis and preservation of porosity in Norphlet Formation (Upper Jurassic), southern Alabama: AAPG Bulletin, v. 73, no. 6, p. 707–728.

Dowey, P. J., D. M. Hodgson, and R. H. Worden, 2012, Pre-requisites, processes, and prediction of chlorite grain coatings in petroleum reservoirs: A review of subsurface examples: Marine and Petroleum Geology, v. 32, no. 1, p. 63–75, doi:10.1016/j.marpetgeo.2011.11.007.

Drummond, C., and J. Israelachvili, 2002, Surface forces and wettability: Journal of Petroleum Science and Engineering, v. 33, no. 1-3, p. 123–133, doi:10.1016/S0920-4105(01)00180-2.

Dugan, B., and P. B. Flemings, 2000, Overpressure and Fluid Flow in the New Jersey Continental Slope: Implications for Slope Failure and Cold Seeps: Science, v. 289, no. 5477, p. 288–291, doi:10.1126/science.289.5477.288.

Ehrenberg, S. N., 1995, Measuring sandstone compaction from modal analyses of thin sections; how to do it and what the results mean: Journal of Sedimentary Research, v. 65, no. 2a, p. 369–379, doi:10.1306/D42680C7-2B26-11D7-8648000102C1865D.

Ehrenberg, S. N., 1993, Preservation of Anomalously High Porosity in Deeply Buried Sandstones by Grain-Coating Chlorite: Examples from the Norwegian Continenatl Shelf: AAPG Bulletin, v. 77, no. 7, p. 1260–1286.

Ehrenberg, S. N., 1990, Relationship between diagenesis and reservoir quality in sandstones of the Garn Formation, Haltenbanken, mid-Norwegian Continental Shelf: p. 1538–1558.

Ehrenberg, S. N., P. H. Nadeau, and Ø. Steen, 2008, A megascale view of reservoir quality in

producing sandstones from the offshore Gulf of Mexico: AAPG Bulletin, v. 92, no. 2, p. 145–164, doi:10.1306/09280707062.

Ehrenberg, S. N., P. H. Nadeau, and Ø. Steen, 2009, Petroleum reservoir porosity versus depth: Influence of geological age: AAPG Bulletin, v. 93, no. 10, p. 1281–1296, doi:10.1306/06120908163.

Emery, D., P. C. Smalley, N. H. Oxtoby, K. V. Ragnarsdottir, P. Aagaard, A. Halliday, M. L. Coleman, and R. Petrovich, 2016, Synchronous oil migration and Cementation in Sandstone Reservoirs Demonstrated by Quantitative Description of Diagenesis: Philosophical Transactions: Physical Sciences and Engineering, v. 344, no. 1670, p. 115–125.

Erratt, D., G. M. Thomas, and G. R. T. Wall, 1999, The evolution of the Central North Sea Rift: Petroleum Geology of Northwest Europe: Proceedings of the 5th Conference on the Petroleum Geology of Northwest Europe, v. 1, p. 63–82, doi:10.1144/0050063.

Evans, D., C. Graham, A. Armour, and P. Bathurst, 2003, The Millennium Atlas: petroleum geology of the central and northern North Sea: London, UK, Geological Society, 390 p.

Fossen, H., and A. Bale, 2007, Deformation bands and their influence on fluid flow: AAPG Bulletin, v. 91, no. 12, p. 1685–1700, doi:10.1306/07300706146.

Fossen, H., R. A. Schultz, Z. K. Shipton, and K. Mair, 2007, Deformation bands in sandstone: a review: Journal of the Geological Society, v. 164, no. 4, p. 755–769, doi:10.1144/0016-76492006-036.

Fox, J. F., 1998, Salt / sediment interaction: The Leading Edge, no. 1992, p. 1033–1041.

French, M. W., and R. H. Worden, 2013, Orientation of microcrystalline quartz in the Fontainebleau Formation, Paris Basin and why it preserves porosity: Sedimentary Geology, v. 284-285, p. 149–158, doi:10.1016/j.sedgeo.2012.12.004.

French, M. W., R. H. Worden, E. Mariani, R. E. Larese, R. R. Mueller, and C. E. Kliewer, 2012, Microcrystalline Quartz Generation and the Preservation of Porosity In Sandstones: Evidence from the Upper Cretaceous of the Subhercynian Basin, Germany: Journal of Sedimentary Research, v. 82, no. 6, p. 422–434, doi:10.2110/jsr.2012.39.

Friis, H., N. Molenaar, and T. Varming, 2014, Chlorite meniscus cement - implications for diagenetic mineral growth after oil emplacement: Terra Nova, v. 26, no. 1, p. 14–21, doi:10.1111/ter.12061.

Gaarenstroom, L., R. A. J. Tromp, M. C. de Jong, and A. M. Brandenburg, 1993, Overpressures in the Central North Sea: implications for trap integrity and drilling safety: Petroleum Geology of Northwest Europe: Proceedings of the 4th Conference on Petroleum Geology of NW. Europe, at the Barbican Centre, London, v. 2, no. 1990, p. 1305–1313, doi:10.1144/0041305.

Gaupp, R., A. Matter, J. Platt, K. Ramseyer, and J. Walzebuck, 1993, Diagenesis and fluid evolution of deeply buried Permian (Rotliegende) gas reservoirs, northwest Germany: AAPG Bulletin, v. 77, no. 7, p. 1111–1128, doi:10.1306/BDFF8E0C-1718-11D7-8645000102C1865D.

Gibbs, A. D., 1984, Structural evolution of extensional basin margins: Journal of the Geological Society, v. 141, no. 4, p. 609–620, doi:10.1144/gsjgs.141.4.0609.

Gibling, M. R., 2006, Width and Thickness of Fluvial Channel Bodies and Valley Fills in the Geological Record: A Literature Compilation and Classification: Journal of Sedimentary Research, v. 76, no. 5, p. 731–770, doi:10.2110/jsr.2006.060.

Giles, M. R., 1997, Diagenesis: A quantitative perspective: Implications for basin modelling and rock property prediction: Dordrecht, Kluver Academic Publishers, 526 p.

Glennie, K. W., 1998, Petroleum Geology of the North Sea: Oxford, UK, Blackwell Science Ltd, 656 p., doi:10.1002/9781444313413.

Glennie, K. W., J. Higham, and I. Stemmerik, 2003, Permian, *in* D. Evans, C. Graham, A. Armour, and P. Bathurst, eds., The Millennium Atlas: Petroleum Geology of the Central and Northern North Sea: London, UK, Geological Society of London, p. 91–103.

Gluyas, J. G., 1997, Poroperm Prediction for Reserves Growth Exploration: Ula Trend, Norwegian North Sea: Reservoir quality prediction in sandstones and carbonates: AAPG Memoir 69, p. 201–210.

Gluyas, J. G., and C. A. Cade, 1997, Prediction of Porosity in Compacted Sands: AAPG Memoir, v. 69, p. 19–27.

Gluyas, J. G., A. G. Robinson, D. Emery, S. M. Grant, and N. H. Oxtoby, 1993, The link between petroleum emplacement and sandstone cementation: Petroleum Geology of Northwest Europe: Proceedings of the 4th Conference on Petroleum Geology of NW. Europe, at the Barbican Centre, London, v. 2, p. 1395–1404, doi:10.1144/0041395.

Goldsmith, P. J., G. Hudson, and P. van Veen, 2003, Triassic, *in* D. Evans, C. Graham, A. Armour, and P. Bathurst, eds., The Millennium Atlas: Petroleum Geology of the Central and Northern North Sea: London, UK, Geological Society of London, p. 105–127.

Goldsmith, P. J., B. Rich, and J. Standring, 1995, Triassic correlation and stratigraphy in the South Central Graben, UK North Sea: Geological Society, London, Special Publications, v. 91, no. 1, p. 123–143, doi:10.1144/GSL.SP.1995.091.01.07.

Goldstein, R. H., and T. J. Reynolds, 1994, Systematics of fluid inclusions in diagenetic minerals: Tulsa, Society for Sedimentary Geology, 199 p., doi:10.2110/scn.94.31.

Goldstein, R. H., and C. Rossi, 2002, Recrystallization in quartz overgrowths: Journal of Sedimentary Research, v. 72, no. 3, p. 432–440, doi:10.1306/110201720432.

Gowers, M. B., and A. Saeboe, 1985, On the structural evolution of the Central Trough in the Norwegian and Danish sectors of the North Sea: Marine and Petroleum Geology, v. 2, no. 4, p. 298–318, doi:10.1016/0264-8172(85)90026-1.

Grant, N. T., A. J. Middleton, and S. Archer, 2014, Porosity trends in the Skagerrak Formation, Central Graben, United Kingdom Continental Shelf: The role of compaction and pore pressure history: AAPG Bulletin, v. 98, no. 6, p. 1111–1143, doi:10.1306/10211313002.

Grigsby, J. D., 2001, Origin and growth of authigenic chlorite in sandstones of the Lower Viksburg Formation, South Texas: Journal of Sedimentary Research, v. 71, no. 1, p. 27–36.

Grove, C., and D. A. Jerram, 2011, JPOR: An ImageJ macro to quantify total optical porosity from blue-stained thin sections: Computers and Geosciences, v. 37, no. 11, p. 1850–1859, doi:10.1016/j.cageo.2011.03.002.

Guven, N., W. F. Hower, and D. K. Davies, 1980, Nature of Authigenic Illites in Sandstone Reservoirs: Journal of Sedimentary Research, v. 50, no. 3, p. 761–766, doi:10.1306/212F7ADB-2B24-11D7-8648000102C1865D.

Haddad, S. C., R. H. Worden, D. Prior, and P. C. Smalley, 2006, Quartz Cement in the Fontainebleau Sandstone, Paris Basin, France: Crystallography and Implications for Mechanisms of Cement Growth: Journal of Sedimentary Research, v. 76, no. 2, p. 244–256, doi:10.2110/jsr.2006.024.

Haile, B. G., H. Hellevang, P. Aagaard, and J. S. Jahren, 2015, Experimental nucleation and growth of smectite and chlorite coatings on clean feldspar and quartz grain surfaces: Marine and Petroleum Geology, v. 68, p. 664–674, doi:10.1016/j.marpetgeo.2015.02.006.

Haimson, B., and H. Lee, 2004, Borehole breakouts and compaction bands in two high-porosity sandstones: International Journal of Rock Mechanics and Mining Sciences, v. 41, no. 2, p. 287–301, doi:10.1016/j.ijrmms.2003.09.001.

Harrison, W. J., and L. L. Summa, 1991, Paleohydrology of the Gulf of Mexico basin: American Journal of Science, v. 291, no. 2, p. 109–176, doi:10.2475/ajs.291.2.109.

Hart, B. S., P. B. Flemings, and A. Deshpande, 1995, Porosity and pressure. Role of compaction disequilibrium in the development of geopressures in a Gulf Coast Pleistocene basin: Geology, v. 23, no. 1, p. 45–48, doi:10.1130/0091-7613(1995)023<0045.

Haszeldine, R. S., M. Wilkinson, D. Darby, C. I. Macaulay, G. D. Couples, A. E. Fallick, C. G. Fleming, R. N. T. Stewart, and G. McAulay, 1999, Diagenetic porosity creation in an overpressured graben, *in* Petroleum Geology of Northwest Europe: Proceedings of the 5th Conference on the Petroleum Geology of Northwest Europe: p. 1339–1350, doi:10.1144/0051339.

Heald, M. T., and R. E. Larese, 1974, Influence of coatings on quarzt cementation: Journal of Sedimentary Petrology, v. 44, no. 4, p. 1269–1274.

Helgeson, D. E., 1999, Structural development and trap formation in the Central North Sea HP/HY play: Petroleum Geology of Northwest Europe: Proceedings of the 5th Conference

on the Petroleum Geology of Northwest Europe, v. 2, p. 1029–1036, doi:10.1144/0051029.
Hendry, J. P., and N. P. Trewin, 1995, Authigenic quartz microfabrics in Cretaceous turbidites: evidence for silica transformation preocesses in sandstones: p. 380–392.
Hillier, S., 1994, Pore-Lining Chlorites in Siliciclastic Reservoir Sandstones: Electron Microprobe, SEM and XRD Data, and Implications for Their Origin: Clay Minerals, v. 29, p. 665–679, doi:10.1180/claymin.1994.029.4.20.
Hillier, S., and B. Velde, 1992, Chlorite Interstratified With a 7 A Mineral: an Example From Offshore Norway and Possible Implications for the interpretation of the composition of diagenetic chlorites: Clay Minerals, v. 27, p. 475–486.
Hirst, J. P. P., 1992, Variations in Alluvial Architecture Across the Oligo-Miocene Huesca Fluvial System, Ebro Basin, Spain: The Three-Dimensional Facies Architecture of Terrigenous Clastic Sediments and Its Implications for Hydrocarbon Discovery and Recovery, v. 3, p. 111–121, doi:10.2110/csp.91.03.0103.
Hodgson, N. A., J. Farnsworth, and A. J. Fraser, 1992, Salt-related tectonics, sedimentation and hydrocarbon plays in the Central Graben, North Sea, UKCS: Geological Society, London, Special Publications, v. 67, no. 1, p. 31–63, doi:10.1144/GSL.SP.1992.067.01.03.
Houseknecht, D. W., 1987, Assessing the Relative Importance of Compaction Processes and Cementation to Reduction of Porosity in Sandstones: AAPG Bulletin, v. 71, no. 6, p. 633–642.
Houseknecht, D. W., 1988, Intergranular pressure solution in four quartzose sandstones: Journal of Sedimentary Research, v. 58, no. 2, p. 228–246, doi:10.1306/212f8d64-2b24-11d7-8648000102c1865d.
Hudec, M. R., and M. P. A. Jackson, 2007, Terra infirma: Understanding salt tectonics: Earth-Science Reviews, v. 82, no. 1-2, p. 1–28, doi:10.1016/j.earscirev.2007.01.001.
Hudec, M. R., M. P. A. Jackson, and D. D. Schultz-Ela, 2009, The paradox of minibasin subsidence into salt: Clues to the evolution of crustal basins: Bulletin of the Geological Society of America, v. 121, no. 1-2, p. 201–221, doi:10.1130/B26275.1.
Hudec, M. R., I. O. Norton, M. P. A. Jackson, and F. J. Peel, 2013, Jurassic evolution of the Gulf of Mexico salt basin: AAPG Bulletin, v. 97, no. 10, p. 1683–1710, doi:10.1306/04011312073.
Humphreys, B., S. J. Kemp, G. K. Lott, Bermanto, D. A. Dharmayanti, and I. Samsori, 1994, Origin of grain-coating chlorite by smectite transformation; an example from Miocene sandstones, North Sumatra back-arc basin, Indonesia: Clay Minerals, v. 29, no. 4, p. 681–692, doi:10.1180/claymin.1994.029.4.21.
Humphreys, B., S. A. Smith, and G. E. Strong, 1989, Authigenic chlorite in late Triassic Sandstones from the Central Graben, North Sea: Clay Minerals, v. 24, p. 427–444.
Isaksen, G. H., 2004, Central North Sea hydrocarbon systems: Generation, migration, entrapment, and thermal degradation of oil and gas: AAPG Bulletin, v. 88, no. 11, p. 1545–1572, doi:10.1306/06300403048.
Jahren, J. S., and M. Ramm, 2000, The Porosity-Preserving Effects of Microcrystalline Quartz Coatings in Arenitic Sandstones: Examples from the Norwegian Continental Shelf, *in* R. H. Worden, and S. Morad, eds., Quartz Cementation in Sandstones: Blackwell Science Ltd, p. 271–280, doi:10.1002/9781444304237.ch18.
Jeans, C. V., 1994, Clay diagenesis, overpressure and reservoir quality; an introduction: Clay Minerals, v. 29, no. 4, p. 415–424, doi:10.1180/claymin.1994.029.4.02.
de Jong, M. C., D. Smith, D. S. Nio, and N. Hardy, 2006, Subsurface correlation of the Triassic of the UK southern Central Graben: New Look at an Old Problem: First Break, v. 24, no. 2, p. 536–539, doi:10.2353/ajpath.2010.090880.
Kantorowicz, J. D., 1990, The influence of variations in illite morphology on the permeability of Middle Jurassic Brent Group sandstones, Cormorant Field, UK North Sea: Marine and Petroleum Geology, v. 7, no. 1, p. 66–74, doi:10.1016/0264-8172(90)90057-N.
Kape, S., O. Diaz de Souza, I. Bushnaq, M. Hayes, and I. Turner, 2010, Predicting production behaviour from deep HPHT Triassic reservoirs and the impact of sedimentary architecture on recovery, *in* Petroleum Geology: From Mature Basins to New Frontiers—Proceedings

of the 7th Petroleum Geology Conference: p. 405–417, doi:10.1144/0070405.
Knox, R. W. O., and W. G. Cordey, 1992, Lithostratigraphic nomenclature of the UK North Sea: Nottingham, British Geological Survey.
Kvenvolden, K. A., and E. Roedder, 1971, Fluid inclusions in quartz crystals from South-West Africa: Geochimica et Cosmochimica Acta, v. 35, no. 12, p. 1209–1229, doi:10.1016/0016-7037(71)90112-8.
Lander, R. H., R. E. Larese, and L. M. Bonnell, 2008, Toward more accurate quartz cement models: The importance of euhedral versus noneuhedral growth rates: AAPG Bulletin, v. 92, no. 11, p. 1537–1563, doi:10.1306/07160808037.
Lander, R. H., and O. Walderhaug, 1999, Predicting porosity through simulating sandstone compaction and quartz cementation: AAPG Bulletin, v. 83, no. 2-3, p. 433–449, doi:10.1306/00AA9BC4-1730-11D7-8645000102C1865D.
Lanson, B., D. Beaufort, G. Berger, J. Baradat, and J.-C. Lacharpagne, 1996, Illitization of diagenetic kaolinite-to-dickite conversion series: Late-stage diagenesis of the Lower Permian Rotliegend sandstone reservoir, offshore of the Netherlands: Journal of Sedimentary Research, v. 66, no. 3, p. 501–518, doi:10.1306/D4268392-2B26-11D7-8648000102C1865D.
Lanson, B., D. Beaufort, G. Berger, A. Bauer, A. Cassagnnère, and A. Meunier, 2002, Authigenic kaolin and illitic minerals during burial diagenesis of sandstones: a review: Clay Minerals, v. 37, no. 1, p. 1–22, doi:10.1180/0009855023710014.
Larter, S. R., and A. C. Aplin, 1995, Reservoir geochemistry: methods, applications and opportunities: Geological Society, London, Special Publications, v. 86, no. 1, p. 5–32, doi:10.1144/GSL.SP.1995.086.01.02.
Lervik, K.-S., 2006, Triassic lithostratigraphy of the Northern North Sea Basin: Norwegian Journal of Geology, v. 86, no. 1989, p. 93–117.
Lima, R. D., and L. F. De Ros, 2002, The role of depositional setting and diagenesis on the reservoir quality of Devonian sandstones from the Solimoes Basin, Brazilian Amazonia: Marine and Petroleum Geology, v. 19, no. 9, p. 1047–1071, doi:10.1016/S0264-8172(03)00002-3.
Lines, M. D., and H. A. Auld, 2004, A petroleum charge model for the Judy and Joanne Fields, Central North Sea: application to exploration and field development: Geological Society, London, Special Publications, v. 237, no. 1, p. 175–206, doi:10.1144/gsl.sp.2004.237.01.11.
Lundegard, P. D., 1992, Sandstone porosity loss; a ‘big picture’ view of the importance of compaction: Journal of Sedimentary Research, v. 62, no. 2, p. 250–260, doi:10.1306/D42678D4-2B26-11D7-8648000102C1865D.
Mallon, A. J., and R. E. Swarbrick, 2002, A compaction trend for non-reservoir North Sea Chalk: Marine and Petroleum Geology, v. 19, no. 5, p. 527–539, doi:10.1016/S0264-8172(02)00027-2.
Mallon, A. J., and R. E. Swarbrick, 2008, Diagenetic characteristics of low permeability, non-reservoir chalks from the Central North Sea: Marine and Petroleum Geology, v. 25, no. 10, p. 1097–1108, doi:10.1016/j.marpetgeo.2007.12.001.
Mallon, A. J., R. E. Swarbrick, and T. J. Katsube, 2005, Permeability of fine-grained rocks: New evidence from chalks: Geology, v. 33, no. 1, p. 21–24, doi:10.1130/G20951.1.
Mandl, G., L. N. J. DeJong, and A. Maltha, 1977, Shear zones in granular material: Rock Mechanics, v. 9, no. 2-3, p. 95–144, doi:10.1007/BF01237876.
Mann, D. M., and A. S. Mackenzie, 1990, Prediction of pore fluid pressures in sedimentary basins: Marine and Petroleum Geology, v. 7, no. 1, p. 55–65, doi:10.1016/0264-8172(90)90056-M.
Marchand, A. M. E., P. C. Smalley, R. S. Haszeldine, and A. E. Fallick, 2002, Note on the importance of hydrocarbon fill for reservoir quality prediction in sandstones: AAPG Bulletin, v. 86, no. 9, p. 1561–1571, doi:10.1306/61EEDD00-173E-11D7-8645000102C1865D.
Matlack, K. S., D. W. Houseknecht, and K. R. Applin, 1989, Emplacement of clay into sand by infiltration: Journal of Sedimentary Petrology, v. 59, no. 1, p. 77–87,

doi:10.1306/212F8F21-2B24-11D7-8648000102C1865D.
Matthews, W. J., G. J. Hampson, B. D. Trudgill, and J. R. Underhill, 2007, Controls on fluviolacustrine reservoir distribution and architecture in passive salt-diapir provinces: Insights from outcrop analogs: AAPG Bulletin, v. 91, no. 10, p. 1367–1403, doi:10.1306/05310706123.
McBride, E. F., 1989, Quartz cement in sandstones: a review: Earth-Science Reviews, v. 26, no. C, p. 69–112, doi:10.1016/0012-8252(89)90019-6.
McKie, T., 2011, Architecture and behaviour of dryland fluvial reservoirs, Triassic Skagerak Formation, Central North Sea: SEPM Special Publication, v. 97, p. 189–214.
McKie, T., 2014, Climatic and tectonic controls on Triassic dryland terminal fluvial system architecture, central North Sea, *in* From Depositional Systems to Sedimentary Successions on the Norwegian Continental Margin: Chichester, UK, John Wiley & Sons, Ltd, p. 19–57, doi:10.1002/9781118920435.ch2.
McKie, T., and P. Audretsch, 2005, Depositional and structural controls on Triassic reservoir performance in the Heron Cluster, ETAP, Central North Sea: Petroleum Geology: North-West Europe and Global Perspectives - Proceedings of the 6th Petroleum Geology Conference, v. 6, p. 285–297, doi:10.1144/0060285.
McKie, T., S. J. Jolley, and M. B. Kristensen, 2010, Stratigraphic and structural compartmentalization of dryland fluvial reservoirs: Triassic Heron Cluster, Central North Sea: Geological Society, London, Special Publications, v. 347, no. 1, p. 165–198, doi:10.1144/SP347.11.
McKie, T., and P. M. Shannon, 2011, Comment on 'The Permian-Triassic transition and the onset of Mesozoic sedimentation at the northwestern peri Tethyan domain scale: Palaeogeographic maps and geodynamic implications' by S. Bourquin, A. Bercovici, J. Lopez-Gomez, J. B. Diez, J. Broutin, A.: Palaeogeography, Palaeoclimatology, Palaeoecology, v. 311, no. 1-2, p. 136–143, doi:10.1016/j.palaeo.2011.07.016.
McKie, T., and B. Williams, 2009, Triassic palaeogeography and fluvial dispersal across the northwest European Basins: Geological Journal, v. 44, no. 6, p. 711–741, doi:10.1002/gj.1201.
McKinley, J. M., R. H. Worden, and A. H. Ruffell, 2003, Smectite in sandstones: A review of the controls on occurrence and behaviour during diagenesis: International Association of Sedimentologists Special Publications, v. 34, p. 109–128.
Meissner, F. F., 1978, Petroleum Geology of the Bakken Formation Williston Basin, North Dakota and Montana, *in* D. Estelle, and R. Miller, eds., The Economic Geology of the Williston Basin, 1978 Williston Basin Symposium: Montana Geological Society, p. 207–230.
Molenaar, N., J. Cyziene, S. Sliaupa, and J. Craven, 2008, Lack of inhibiting effect of oil emplacement on quartz cementation: Evidence from Cambrian reservoir sandstones, Paleozoic Baltic Basin: Bulletin of the Geological Society of America, v. 120, no. 9-10, p. 1280–1295, doi:10.1130/B25979.1.
Morad, S., K. Al-Ramadan, J. M. Ketzer, and L. F. De Ros, 2010, The impact of diagenesis on the heterogeneity of sandstone reservoirs: A review of the role of depositional fades and sequence stratigraphy: AAPG Bulletin, v. 94, no. 8, p. 1267–1309, doi:10.1306/04211009178.
Morad, S., B. H. N. Ismail, L. F. De Ros, I. S. Al-Aasm, and N.-E. Serrhini, 1994, Diagenesis and formation water chemistry of Triassic reservoir sandstones from southern Tunisia: Sedimentology, v. 41, no. 6, p. 1253–1272, doi:10.1111/j.1365-3091.1994.tb01452.x.
Moraes, M. a. S., and L. F. de Ros, 1990, Infiltrated Clays in Fluvial Jurassic Sandstones of Reconcavo Basin, Northeastern Brazil: Journal of Sedimentary Research, v. Vol. 60, no. 6, p. 809–819, doi:10.1306/212F928C-2B24-11D7-8648000102C1865D.
Munz, I. A., 2001, Petroleum inclusions in sedimentary basins: Systematics, analytical methods and applications: Lithos, v. 55, no. 1-4, p. 195–212, doi:10.1016/S0024-4937(00)00045-1.
Munz, I. A., H. Johansen, and I. Johansen, 1999, Characterisation of Composition and PVT Properties of Petroleum Inclusions: Implications of Reservoir Filling and Compartmentalisation, *in* SPE Annual Technical Conference and Exhibition: Society of

Petroleum Engineers, p. 7, doi:10.2118/56519-MS.
Murphy, W. M., E. H. Oelkers, and P. C. Lichtner, 1989, Surface reaction versus diffusion control of mineral dissolution and growth rates in geochemical processes: Chemical Geology, v. 78, no. 3-4, p. 357–380, doi:10.1016/0009-2541(89)90069-7.
Nedkvitne, T., D. A. Karlsen, K. Bjørlykke, and S. R. Larter, 1993, Relationship between reservoir diagenetic evolution and petroleum emplacement in the Ula Field, North Sea: Marine and Petroleum Geology, v. 10, no. 3, p. 255–270, doi:10.1016/0264-8172(93)90108-5.
Neumann, V., 2006, Numerical modeling and phase prediction in deep overpressured basinal settings of the Central Graben, North Sea: 192 p.
Nguyen, B. T. T., S. J. Jones, N. R. Goulty, A. J. Middleton, N. T. Grant, A. Ferguson, and L. Bowen, 2013, The role of fluid pressure and diagenetic cements for porosity preservation in Triassic fluvial reservoirs of the Central Graben, North Sea: AAPG Bulletin, v. 97, no. 8, p. 1273–1302, doi:10.130e/01151311163.
Oakes, C. S., R. J. Bodnar, and J. M. Simonson, 1990, The system NaCl-CaCl2-H2O: I. The ice liquidus at 1 atm total pressure: Geochimica et Cosmochimica Acta, v. 54, no. 3, p. 603–610, doi:10.1016/0016-7037(90)90356-P.
Oelkers, E. H., P. A. Bjørkum, and W. M. Murphy, 1996, A petrographic and computational investigation of quartz cementation and porosity reduction in North Sea sandstones: American Journal of Science, v. 296, no. 4, p. 420–452, doi:10.2475/ajs.296.4.420.
Osborne, M. J., and R. E. Swarbrick, 1999, Diagenesis in North Sea HPHT clastic reservoirs-consequences for porosity and overpressure prediction: Marine and Petroleum Geology, v. 16, no. 4, p. 337–353, doi:10.1016/S0264-8172(98)00043-9.
Osborne, M. J., and R. E. Swarbrick, 1997, Mechanisms for Generating Overpressure in Sedimentary Basins: A Reevaluation: AAPG Bulletin, v. 81, no. 6, p. 1023–1041, doi:10.1306/E4FD2D89-1732-11D7-8645000102C1865D.
Ostermeier, R. M., 1995, Deepwater Gulf of Mexico Turbidites - Compaction Effects on Porosity and Permeability: SPE Formation Evaluation, v. 10, no. 02, p. 79–85, doi:10.2118/26468-PA.
Oxtoby, N. H., A. W. Mitchell, and J. G. Gluyas, 1995, The filling and emptying of the Ula Oilfield: fluid inclusion constraints: Geological Society, London, Special Publications, v. 86, no. 1, p. 141–157, doi:10.1144/GSL.SP.1995.086.01.11.
Parsons, I., P. Thompson, M. R. Lee, and N. Cayzer, 2005, Alkali feldspar microtextures as provenance indicators in siliciclastic rocks and their role in feldspar dissolution during transport and diagenesis: Journal of Sedimentary Research, v. 75, p. 921–942, doi:10.2110/jsr.2005.071.
Paxton, S. T., J. O. Szabo, and J. M. Ajdukiewicz, 2002, Construction of an intergranular volume compaction curve for evaluating and predicting compaction and porosity loss in rigid-grain sandstone reservoirs: AAPG Bulletin, v. 86, no. 12, p. 2047–2067.
Peng, J., J. Liu, Y. Wang, and J. Liu, 2009, Origin and controlling factors of chlorite coatings-an example from the reservoir of T3x Group of the Baojie area, Sichuan Basin, China: Petroleum Science, v. 6, no. 4, p. 376–382, doi:10.1007/s12182-009-0057-1.
Péron, S., S. Bourquin, F. Fluteau, and F. Guillocheau, 2005, Paleoenvironment reconstructions and climate simulations of the Early Triassic: Impact of the water and sediment supply on the preservation of fluvial systems: Geodinamica Acta, v. 18, no. 6, p. 431–446, doi:10.3166/ga.18.431-446.
Pittman, E. D., R. E. Larese, and M. T. Heald, 1992, Clay coats: Occurence and relevance to preservation of porosity in sandstones, *in* Origin, diagenesis and petrophysics of clay minerals in sandstones: SEPM Special Publication 47: p. 241–255, doi:10.2110/pec.92.47.0241.
Pittman, E. D., and D. N. Lumsden, 1968, Relationship Between Chlorite Coatings on Quartz Grains and Porosity, Spiro Sand, Oklahoma: Journal of Sedimentary Research, v. 38, no. 2, p. 668–670.
Pooler, J., and M. Amory, 1999, A subsurface perspective on ETAP - an integrated development of seven Central North Sea fields: Petroleum Geology Conference

Proceedings, v. 5, no. 0, p. 993–1006, doi:10.1144/0050993.
Preto, N., E. Kustatscher, and P. B. Wignall, 2010, Triassic climates - State of the art and perspectives: Palaeogeography, Palaeoclimatology, Palaeoecology, v. 290, no. 1-4, p. 1–10, doi:10.1016/j.palaeo.2010.03.015.
di Primio, R., and V. Neumann, 2008, HPHT reservoir evolution: A case study from Jade and Judy fields, Central Graben, UK North Sea: International Journal of Earth Sciences, v. 97, no. 5, p. 1101–1114, doi:10.1007/s00531-007-0206-y.
Ramm, M., and K. Bjørlykke, 1994, Porosity/depth trends in reservoir sandstones: assessing the quantitative effects of varying pore-pressure, temperature and mineralogy: Norwegian shelf data: Clay Minerals, v. 24, p. 475–490, doi:10.1180/claymin.1994.029.4.07.
Ramm, M., A. W. Forsberg, and J. S. Jahren, 1997, Porosity-depth trends in deeply buried Upper Jurassic reservoirs in the Norwegian Central Graben; an example of porosity preservation beneath the normal economic basement by grain-coating microquartz: Reservoir quality prediction in sandstones and carbonates., v. 69, p. 177–199.
Roberts, A. M., J. D. Price, and T. S. Olsen, 1990, Late Jurassic half-graben control on the siting and structure of hydrocarbon accumulations: UK/Norwegian Central Graben: Geological Society, London, Special Publications, v. 55, no. 1, p. 229–257, doi:10.1144/GSL.SP.1990.055.01.11.
Rowan, M. G., M. P. A. Jackson, and B. D. Trudgill, 1999, Salt-related fault families and fault welds in the northern Gulf of Mexico: AAPG Bulletin, v. 83, no. 9, p. 1454–1484, doi:10.1306/E4FD41E3-1732-11D7-8645000102C1865D.
Saigal, G. C., K. Bjørlykke, and S. R. Larter, 1992, The effects of oil emplacement on diagenetic processes - examples from the Fulmar Reservoir sandstones, central North Sea: p. 1024–1033, doi:IDS Number: JA235.
Sathar, S., and S. Jones, 2016, Fluid overpressure as a control on sandstone reservoir quality in a mechanical compaction dominated setting: Magnolia Field, Gulf of Mexico: Terra Nova, v. 28, no. 3, p. 155–162, doi:10.1111/ter.12203.
Sathar, S., R. H. Worden, D. R. Faulkner, and P. C. Smalley, 2012, The Effect of Oil Saturation On the Mechanism of Compaction In Granular Materials: Higher Oil Saturations Lead To More Grain Fracturing and Less Pressure Solution: Journal of Sedimentary Research, v. 82, no. 8, p. 571–584, doi:10.2110/jsr.2012.44.
Schneider, F., and S. Hay, 2001, Compaction model for quartzose sandstones application to the Garn Formation, Haltenbanken, Mid-Norwegian Continental Shelf: Marine and Petroleum Geology, v. 18, no. 7, p. 833–848, doi:10.1016/S0264-8172(01)00032-0.
Schneider, F., and S. Wolf, 2000, Quantative HC potential evaluation using 3D basin modelling: application to Franklin structure, Central Graben, North Sea, UK.: Marine and Petroleum Geology, v. 17, p. 841–856.
Sclater, J. G., and P. A. F. Christie, 1980, Continental stretching: An explanation of the post-mid-Cretaceous subsidence of the Central North Sea basin: Journal of Geophysical Research, v. 85, no. 7, p. 3711–3739.
Shadravan, A., and M. Amani, 2012, HPHT 101: What Every Engineer or Geoscientist Should Know about High Pressure HighTemperature Wells, *in* SPE Kuwait International Petroleum Conference and Exhibition: Society of Petroleum Engineers, doi:10.2118/163376-MS.
Sheldon, H. A., J. Wheeler, R. H. Worden, and M. J. Cheadle, 2003, An Analysis of the Roles of Stress, Temperature, and pH in Chemical Compaction of Sandstones: Journal of Sedimentary Research (SEPM), v. 73, no. 1, p. 64–71.
Smith, R. I., N. Hodgson, and M. Fulton, 1993, Salt control on Triassic reservoir distribution , UKCS Central North Sea: Petroleum Geology of Northwest Europe: Proceedings of the 4th Conference on Petroleum Geology of NW. Europe, at the Barbican Centre, London, p. 547–557, doi:10.1144/0040547.
Środoń, J., 1999, Nature of Mixed-Layer Clays and Mechanisms of their Formation and Alteration: Annual Review of Earth and Planetary Sciences, v. 27, no. 1, p. 19, doi:10.1146/annurev.earth.27.1.19.
Storvoll, V., K. Bjørlykke, D. A. Karlsen, and G. C. Saigal, 2002, Porosity preservation in

reservoir sandstones due to grain-coating illite: A study of the Jurassic Garn Formation from the Kristin and Lavrans fields, offshore Mid-Norway: Marine and Petroleum Geology, v. 19, no. 6, p. 767–781, doi:10.1016/S0264-8172(02)00035-1.

Stricker, S., and S. J. Jones, 2016, Enhanced porosity preservation by pore fluid overpressure and chlorite grain coatings in the Triassic Skagerrak, Central Graben, North Sea, UK: Geological Society, London, Special Publications, v. 435, doi:10.1144/SP435.4.

Stricker, S., S. J. Jones, and N. T. Grant, 2016a, Importance of vertical effective stress for reservoir quality in the Skagerrak Formation, Central Graben, North Sea: Marine and Petroleum Geology, doi:10.1016/j.marpetgeo.2016.03.001.

Stricker, S., S. J. Jones, S. Sathar, L. Bowen, and N. Oxtoby, 2016b, Exceptional reservoir quality in HPHT reservoir settings: Examples from the Skagerrak Formation of the Heron Cluster, North Sea, UK: Marine and Petroleum Geology, v. 77, p. 198–215, doi:10.1016/j.marpetgeo.2016.02.003.

Sun, Z. X., Z. L. Sun, J. Yao, M. L. Wu, J. R. Liu, Z. Dou, and C. R. Pei, 2014, Porosity preservation due to authigenic chlorite coatings in deeply buried upper Triassic Xujiahe Formation sandstones, Sichuan Basin, Western China: Journal of Petroleum Geology, v. 37, no. 3, p. 251–267, doi:10.1111/jpg.12582.

Swarbrick, R. E., 2012, Review of pore-pressure prediction challenges in high-temperature areas: The Leading Edge, v. 31, no. 11, p. 1288–1294, doi:10.1190/tle31111288.1.

Swarbrick, R. E., R. W. Lahann, S. A. O'Connor, and A. J. Mallon, 2010, Role of the Chalk in development of deep overpressure in the Central North Sea: Petroleum Geology: From Mature Basins to New Frontiers—Proceedings of the 7th Petroleum Geology Conference, v. 7, p. 493–507, doi:10.1144/0070493.

Swarbrick, R. E., and M. J. Osborne, 1998, Mechanisms that generate abnormal pressures: an overview: AAPG Memoir, v. 70, p. 13–34.

Swarbrick, R. E., M. J. Osborne, D. Grunberger, G. S. Yardley, G. Macleod, A. C. Aplin, S. R. Larter, I. Knight, and H. A. Auld, 2000, Integrated study of the Judy Field (Block 30/7a) - an overpressured Central North Sea oil/gas field: Marine and Petroleum Geology, v. 17, no. 9, p. 993–1010, doi:10.1016/S0264-8172(00)00050-7.

Swarbrick, R. E., M. J. Osborne, and G. S. Yardley, 2002, Comparison of Overpressure Magnitude Resulting from the Main Generating Mechanisms: AAPG Memoir, v. 76, p. 1–12.

Taylor, T. R., M. R. Giles, L. A. Hathon, T. N. Diggs, N. R. Braunsdorf, G. V. Birbiglia, M. G. Kittridge, C. I. MacAulay, and I. S. Espejo, 2010, Sandstone diagenesis and reservoir quality prediction: Models, myths, and reality: AAPG Bulletin, v. 94, no. 8, p. 1093–1132, doi:10.1306/04211009123.

Taylor, T. R., M. G. Kittridge, P. Winefield, L. T. Bryndzia, and L. M. Bonnell, 2015, Reservoir quality and rock properties modeling - Triassic and Jurassic sandstones, greater Shearwater area, UK Central North Sea: Marine and Petroleum Geology, v. 65, p. 1–21, doi:10.1016/j.marpetgeo.2015.03.020.

Taylor, T. R., R. Stancliffe, C. I. Macaulay, and L. Hathon, 2004, High temperature quartz cementation and the timing of hydrocarbon accumulation in the Jurassic Norphlet sandstone, offshore Gulf of Mexico, USA: Geological Society, London, Special Publications, v. 237, no. 1, p. 257–278, doi:10.1144/gsl.sp.2004.237.01.15.

Thomson, A., 1979, Preservation of porosity in the deep Woodbine/Tuscaloosa trend, Louisuana: Journal of Petroleum Technology, v. 34, no. 5, p. 396–403.

Ungerer, P., E. Behar, and D. Discamps, 1981, Tentative calculation of the overall volume expansion of organic matter during hydrocarbon genesis from geochemistry data. Implications for primary, *in* M. Bjorøy, P. Albrecht, C. Cornfeld, K. de Groot, G. Eglinton, E. Galimov, D. Leythaeuser, R. Pelet, J. Rullkoetter, and G. Speers, eds., Advances in organic geochemistry: John Wiley & Sons, p. 129–135.

Vagle, G. B., A. Hurst, and H. Dypvik, 1994, Origin of quartz cements in some sandstones from the Jurassic of the inner Moray Firth (UK): Sedimentology, v. 41, no. 2, p. 363–377, doi:10.1111/j.1365-3091.1995.tb02107.x.

Vollset, J., and A. G. Dore, 1984, A revised Triassic and Jurassic lithostratigraphic

nomenclature for the Norwegian North Sea: p. 53.
Walderhaug, O., 1990, A Fluid Inclusion Study of Quartz-Cemented Sandstones from Offshore Mid-Norway--Possible Evidence for Continued Quartz Cementation During Oil Emplacement: Journal of Sedimentary Research (SEPM), v. 60, no. 2, p. 203–210.
Walderhaug, O., 1996, Kinetic modeling of quartz cementation and porosity loss in deeply buried sandstone reservoirs: AAPG Bulletin, v. 80, no. 5, p. 731–745, doi:10.1306/64ED88A4-1724-11D7-8645000102C1865D.
Walderhaug, O., 1994a, Precipitation rates for quartz cement in sandstones determind by fluid-incsuion microthermometry and temperature-history modeling: Journal of Sedimentary Research, v. 64, no. 2, p. 324–333, doi:10.2110/jsr.64.324.
Walderhaug, O., 1994b, Temperatures of Quartz Cementation in Jurassic Sandstones from the Norwegian Continental Shelf--Evidence from Fluid Inclusions: SEPM Journal of Sedimentary Research, v. Vol. 64A, no. 2, p. 311–323, doi:10.1306/D4267D89-2B26-11D7-8648000102C1865D.
Warren, E. A., and A. J. Pulham, 2001, Anomalous Porosity and Permeability Preservation in Deeply Buried Tertiary and Mesozoic Sandstones in the Cusiana Field, Llanos Foothills, Colombia: Journal of Sedimentary Research, v. 71, no. 1, p. 2–14, doi:10.1306/081799710002.
Weibel, R., 1998, Diagenesis in oxidising and locally reducing conditions - an example from the Triassic Skagerrak Formation, Denmark: Sedimentary Geology, v. 121, no. 3-4, p. 259–276, doi:10.1016/S0037-0738(98)00085-2.
Weibel, R., 1999, Effects of Burial on the Clay Assemblages in the Triassic Skagerrak Formation, Denmark: Clay Minerals, v. 34, no. 4, p. 619–635, doi:10.1180/claymin.1999.034.4.08.
Weibel, R., H. Friis, A. M. Kazerouni, J. B. Svendsen, J. Stokkendal, and M. L. K. Poulsen, 2010, Development of early diagenetic silica and quartz morphologies - Examples from the Siri Canyon, Danish North Sea: Sedimentary Geology, v. 228, no. 3-4, p. 151–170, doi:10.1016/j.sedgeo.2010.04.008.
Wilkinson, M., D. Darby, R. S. Haszeldine, and G. D. Couples, 1997, Secondary porosity generation during deep burial associated with overpressure leak-off: Fulmar formation, United Kingdom Central Graben: AAPG Bulletin, v. 81, no. 5, p. 803–813, doi:10.1306/522B484D-1727-11D7-8645000102C1865D.
Wilkinson, M., and R. S. Haszeldine, 2011, Oil charge preserves exceptional porosity in deeply buried, overpressured, sandstones: Central North Sea, UK: Journal of the Geological Society, v. 168, no. 6, p. 1285–1295, doi:10.1144/0016-76492011-007.
William J. Plumley, 1980, Abnormally High Fluid Pressure: Survey of Some Basic Principles: AAPG Bulletin, v. 64, no. 3, p. 414–422, doi:10.1306/2F919409-16CE-11D7-8645000102C1865D.
Wilson, M. D., and E. D. Pittman, 1977, Authigenic Clays in Sandstones: Recognition and Influence on Reservoir Properties and Paleoenvironmental Analysis: SEPM Journal of Sedimentary Research, v. 47, no. 1, p. 3–31, doi:10.1306/212F70E5-2B24-11D7-8648000102C1865D.
Wilson, M. J., L. Wilson, and I. Patey, 2014, The influence of individual clay minerals on formation damage of reservoir sandstones: a critical review with some new insights: Clay Minerals, v. 49, no. 2, p. 147–164, doi:10.1180/claymin.2014.049.2.02.
Winefield, P., R. Gilham, and R. Elsinger, 2005, Plumbing the depths of the Central Graben: towasrds an integrated pressure, fluid and charge model for the Central North Sea HPHT play: Petroleum Geology Conference Series, v. 6, p. 1301–1315, doi:10.1144/0060389.
Worden, R. H., M. W. French, and E. Mariani, 2012, Amorphous silica nanofilms result in growth of misoriented microcrystalline quartz cement maintaining porosity in deeply buried sandstones: Geology, v. 40, no. 2, p. 179–182, doi:10.1130/G32661.1.
Worden, R. H., and S. Morad, 2003, Clay Minerals in Sandstones: Controls on Formation, Distribution and Evolution, *in* Special Publications of the international Association of Sedimentologists: Oxford, UK, Blackwell Publishing Ltd., p. 1–41, doi:10.1002/9781444304336.ch1.

Worden, R. H., and S. Morad, 2000, Quartz Cementation in Oil Field Sandstones: A Review of the Key Controversies: Special Publications of the international Association of Sedimentologists, v. 29, p. 1–20, doi:10.1002/9781444304237.ch1.

Worden, R. H., N. H. Oxtoby, and P. C. Smalley, 1998, Can oil emplacement prevent quartz cementation in sandstones? Petroleum Geoscience, v. 4, no. 2, p. 129–137, doi:10.1144/petgeo.4.2.129.

Yardley, G. S., and R. E. Swarbrick, 2000, Lateral transfer: A source of additional overpressure? Marine and Petroleum Geology, v. 17, no. 4, p. 523–537, doi:10.1016/S0264-8172(00)00007-6.